



LCLS-II Conceptual Design Report

LCLSII-1.1-DR-0001-R0



This material is based upon work supported by the U.S. Department of Energy,
Office of Science, under Contract No. DE-AC02-76SF00515.

***LCLS-II* CONCEPTUAL DESIGN REPORT**

Table of Contents

Nov. 26, 2013

1. Executive Summary

- 1.1. Background
- 1.2. BESAC Subpanel Recommendations
- 1.3. Capability Gap
- 1.4. Mission Need
- 1.5. Key Features of LCLS-II
 - 1.5.1. Soft X-ray Source
 - 1.5.2. Soft X-ray Optics and Instruments
 - 1.5.3. Hard X-ray Source
 - 1.5.4. Hard X-ray Optics and Instruments
- 1.6. Cost Range
- 1.7. Schedule
- 1.8. Alternates Analysis
 - 1.8.1. Status Quo
 - 1.8.2. Proposed LCLS-II Configuration
 - 1.8.3. LCLS-II in a "Green Field"
- 1.9. Acquisition Strategy
- 1.10. References

2. Scientific Objectives

- 2.1. Science from LCLS-I to LCLS-II
- 2.2. Transformative Capabilities of LCLS-II
 - 2.2.1. Advanced Methods and Techniques
- 2.3. Scientific Questions and Methods Addressed with LCLS-II
 - 2.3.1. Chemistry
 - 2.3.2. Materials
 - 2.3.3. Biology
- 2.4. LCLS-II Short and Long Term Plans
 - 2.4.1. Longest Term Horizon
 - 2.4.2. Long Term: Five Years After LCLS-II First Light (before 2025)
- 2.5. Short Term: Toward LCLS-II Commissioning (LCLS-II Project Period)
- 2.6. References

3. Machine Performance and Parameters

- 3.1. Description of Parameter Choices
 - 3.1.1. Beam Parameters
 - 3.1.2. Linac

- 3.1.3. Undulators
- 3.1.4. Sensitivities
- 3.1.5. Alternative Configuration and Parameter Impact
- 3.2. Performance Parameters
- 3.3. Beam Operating Modes
 - 3.3.1. "One-Shot Mode"
 - 3.3.2. "Single-Bunch, 1-Hz Mode"
 - 3.3.3. "Single-Bunch, 60-Hz Mode"
 - 3.3.4. "100-Bunch Mode"
 - 3.3.5. "1000-Bunch Mode"
- 3.4. References

4. Project Overview

- 4.1. Overview
- 4.2. Injector
- 4.3. SCRF Linac
- 4.4. Bunch Compression and Beam Transport
- 4.5. X-ray Production and Delivery
- 4.6. Experimental Systems
- 4.7. Infrastructure and Facilities
- 4.8. Coordinate System and Alignment
- 4.9. Beam Commissioning
 - 4.9.1. Pre-Beam Commissioning
 - 4.9.2. Beam and System Commissioning
 - 4.9.3. Beam and System Characterization
- 4.10. Management
- 4.11. Cost and Schedules
- 4.12. References

5. Electron Injector

- 5.1. Introduction and Overview
- 5.2. Drive Laser Systems
 - 5.2.1. Photocathode Drive Laser Requirements
 - 5.2.2. Laser Heater Requirements
- 5.3. Photo-Cathode
- 5.4. Electron Gun and Buncher
 - 5.4.1. The VHF Electron Gun
 - 5.4.2. Buncher and Solenoids
- 5.5. Injector Accelerator
- 5.6. Injector Beam Dynamics

- 5.7. Injector Alignment
- 5.8. References

6. Superconducting Linac Technologies

- 6.1. Introduction and Overview
- 6.2. Choice of RF Technology
- 6.3. Operating Gradient
- 6.4. Radio Frequency Parameters
 - 6.4.1. Q_0 Baseline
 - 6.4.2. Cavity Tuner Requirements
 - 6.4.3. HOM Damping
 - 6.4.4. Amplitude and Phase Stability
 - 6.4.5. Cavity Alignment
 - 6.4.6. Maximal Cavity Detuning
 - 6.4.7. Loaded Q and RF Power Requirements
 - 6.4.8. Cryo-module Dynamic Load
- 6.5. RF Cavities
 - 6.5.1. The TESLA Cavity Design
 - 6.5.2. Cavity Material, Processing and Cryogenic RF Testing
 - 6.5.3. Alternative Materials and Cavity Design
 - 6.5.4. Input Coupler
 - 6.5.5. HOM Couplers
 - 6.5.6. Cavity Tuners
- 6.6. Cryomodules and Components
 - 6.6.1. Top-Level Parameters for Cryomodules
 - 6.6.2. 1.3 GHz Cryomodule Baseline Concept
 - 6.6.3. Elements of a Functional Specification
 - 6.6.4. Pre-production Cryomodule Concept and Goals
 - 6.6.5. Injection Cryomodule
 - 6.6.6. Cryomodule Risks and Risk Mitigation Concepts
 - 6.6.7. Engineering and Design Process
 - 6.6.8. Conclusion
- 6.7. Cryogenics
 - 6.7.1. Functional Requirements
 - 6.7.2. Helium Refrigerator Description and Choice
 - 6.7.3. Operating Modes
 - 6.7.4. Warm Helium Compressors
 - 6.7.5. Gas Management and Storage System
 - 6.7.6. LN₂ Precooling System
 - 6.7.7. Vacuum System

- 6.7.8. Cryogenic Distribution System
- 6.7.9. Utilities
- 6.7.10. Component Location and Area Requirements
- 6.7.11. Large Equipment Installation
- 6.7.12. Control System
- 6.7.13. Applicable Safety Standards
- 6.8. Superconducting Magnets, BPMs and Warm Sections
 - 6.8.1. Superconducting Magnets
 - 6.8.2. Beam Position Monitors
 - 6.8.3. Diagnostics and Warm Sections
- 6.9. RF Controls, LLRF, and Feedback
 - 6.9.1. RF Control Stations
 - 6.9.2. 3.9 GHz LLRF Systems
 - 6.9.3. Resonance Control
 - 6.9.4. Cryomodule Interlocks
- 6.10. RF Power Systems
 - 6.10.1. 1.3 GHz System Requirements
 - 6.10.2. Technology Options
 - 6.10.3. Source Selection
 - 6.10.4. 3.9-GHz RF Sources for the Harmonic Linearizer
 - 6.10.5. Other RF Sources
 - 6.10.6. Vendor Qualification and Pre-production Plan
- 6.11. RF Harmonic Linearizer
 - 6.11.1. Introduction/Overview
 - 6.11.2. The FLASH ACC39 RF Harmonic Linearizer
 - 6.11.3. Modifications for CW Operation
 - 6.11.4. Alternate Compression Schemes
- 6.12. Linac Beam Dynamics and Tolerances
 - 6.12.1. Single Bunch Emittance Dilutions
 - 6.12.2. Multi-Bunch Emittance Effects
 - 6.12.3. HOM Heating Effects
- 6.13. RF Commissioning
- 6.14. References

7. Electron Compression and Transport

- 7.1. Introduction and Overview
- 7.2. Linac Lattice
- 7.3. Alignment
- 7.4. Laser Heater System
- 7.5. Bunch Compression

- 7.5.1. Parameters
- 7.5.2. Longitudinal Tracking
- 7.5.3. Microbunching Instability and Laser Heater Optimization
- 7.6. Electron Diagnostic Sections
 - 7.6.1. Injector Diagnostic Section
 - 7.6.2. Post-BC1 Diagnostic Section
 - 7.6.3. Post-BC2 Diagnostic Section
 - 7.6.4. Pre-Undulator Diagnostic Sections
 - 7.6.5. Dumplines Diagnostic Sections
- 7.7. Beam Transport and Switching
 - 7.7.1. The Linac Extension
 - 7.7.2. Bypass Line
 - 7.7.3. Transport from Bypass Line to Undulators
 - 7.7.4. Beam Spreader System
- 7.8. Collimation and Beam Halo Management
 - 7.8.1. Collimation Requirements
 - 7.8.2. Beam Halo
 - 7.8.3. Collimation Scheme
- 7.9. Main Electron Dump Transport
- 7.10. Kickers, Septa, and Specialized Components
 - 7.10.1. Diagnostic Kickers
 - 7.10.2. Septum Magnets
 - 7.10.3. RF Spreader Cavity
- 7.11. References

8. FEL Systems

- 8.1. Introduction and Overview
- 8.2. FEL Requirements and Electron Beam Parameters
- 8.3. Layout and Operating Range of the Soft and Hard X-Ray FELs
 - 8.3.1. Layout
 - 8.3.2. Nominal X-Ray Parameters and Operating Ranges
 - 8.3.3. Electron Beam Arrival Time
 - 8.3.4. Pulse Duration
 - 8.3.5. Photon Energy
 - 8.3.6. Bandwidth
 - 8.3.7. Pulse Energy
 - 8.3.8. Coherence
- 8.4. Undulator Beamline Components
 - 8.4.1. Segments
 - 8.4.2. Quadrupole & Trajectory Correctors

- 8.4.3. Collimator
- 8.4.4. RF-BPM
- 8.4.5. Phase Shifter
- 8.4.6. Ambient Field Correctors
- 8.4.7. Beam Loss Monitors
- 8.5. FODO Lattice Optimization
- 8.6. Undulator Magnetic Measurements and Tuning
 - 8.6.1. Undulator Tuning
 - 8.6.2. Magnetic Measurement Systems
 - 8.6.3. Magnetic Measurement Facility
 - 8.6.4. Earth's Magnetic Field
 - 8.6.5. Fiducializing Large Undulators
 - 8.6.6. Throughput
- 8.7. Undulator Magnet Design
 - 8.7.1. Choice of Magnetic Material
 - 8.7.2. Magnetic Design
 - 8.7.3. Magnetic Tuning Strategies
 - 8.7.4. Mechanical Design
- 8.8. Undulator Alignment
 - 8.8.1. Alignment Strategy
 - 8.8.2. Conventional Alignment
 - 8.8.3. Beam-Based Alignment
- 8.9. Radiation Damage Issues
 - 8.9.1. Introduction
 - 8.9.2. Damage Mechanisms
 - 8.9.3. Radiation Protection
- 8.10. Temperature and Position Stability
 - 8.10.1. Temperature Monitoring
 - 8.10.2. Gap Monitoring
 - 8.10.3. Wire Position Monitors
 - 8.10.4. Undulator Hall Floor Stability
- 8.11. Undulator Vacuum Chamber
- 8.12. Self-Seeding
 - 8.12.1. Self-Seeding for the Soft X-ray Undulator
 - 8.12.2. Self-Seeding for the Hard X-ray Undulator
- 8.13. References

9. Electron Beam Diagnostics

- 9.1. Diagnostics Requirements
- 9.2. Beam Position Monitors

- 9.2.1. Cold Cavity BPM
- 9.2.2. Warm Cavity BPM
- 9.2.3. BPM electronics
- 9.3. Transverse Profile Monitors
 - 9.3.1. Wire Scanners
 - 9.3.2. Screens
 - 9.3.3. Other Transverse Profile Monitors
- 9.4. Halo Monitors
- 9.5. Bunch Length Monitors
 - 9.5.1. Relative BLM CW Heat Loading
 - 9.5.2. Advanced BLM Options
- 9.6. Transverse RF Deflectors
- 9.7. Toroids, Beam Current, and Loss Monitors
 - 9.7.1. Timescales
 - 9.7.2. Devices
- 9.8. Arrival Time Monitors
- 9.9. Beam-Based Feedback
- 9.10. References

10. Start-to-End Tracking Simulations

- 10.1. Introduction and Overview
- 10.2. Injector Simulations
- 10.3. Linac Simulations
- 10.4. FEL Simulations
 - 10.4.1. SXR SASE Simulations
 - 10.4.2. SXR Self-Seeded Simulations
 - 10.4.3. HXR SASE Simulations
 - 10.4.4. HXR Self-Seeded Simulations
- 10.5. Single Bunch Sensitivities and Tolerances
- 10.6. Multi-Bunch Sensitivities and Tolerances
- 10.7. Beam-Based Corrections and Tuning Strategies
 - 10.7.1. Electron Trajectory Correction
 - 10.7.2. Electron Beam Matching
 - 10.7.3. Electron Dispersion Correction
 - 10.7.4. Emittance Measurements and Minimization
 - 10.7.5. RF Phasing
- 10.8. References

11. Photon Transport and Diagnostics

- 11.1. Introduction and Overview

- 11.2. High Average Power Photon Beamline Requirements
 - 11.2.1. Undulator Performance
 - 11.2.2. Photon Delivery Requirements
 - 11.2.3. Photon Power and Power Density
- 11.3. X-ray Damage Considerations
 - 11.3.1. Normal Incidence
 - 11.3.2. Optical Surfaces
- 11.4. X-ray Mirror Acceptance and Reflectivity Considerations
 - 11.4.1. Flux and Image Preservation
 - 11.4.2. Harmonic Attenuation
- 11.5. Wavefront Preservation in X-ray Transport Systems
 - 11.5.1. Brightness Preservation
 - 11.5.2. Variable Image Size
 - 11.5.3. Thermal and Mechanical Deformation
- 11.6. Monochromators and Pulse Length Considerations in X-ray Transport Systems
 - 11.6.1. Monochromators
 - 11.6.2. Pulse Length Considerations
- 11.7. X-ray Diagnostics
 - 11.7.1. Diagnostics for X-ray Tuning
 - 11.7.2. X-ray Diagnostics Chamber
 - 11.7.3. Intensity Monitors
 - 11.7.4. Wave Front Sensors
 - 11.7.5. In-line Spectrometer
 - 11.7.6. Arrival Time Monitors
- 11.8. Photon Beamline Layouts
 - 11.8.1. SXR Beamline Configuration
 - 11.8.2. HXR Beamline Configuration
 - 11.8.3. Transport Line/Experimental Area Alignment
- 11.9. References

12. Experimental Instruments

- 12.1. Introduction and Overview
- 12.2. Soft X-ray Beamline and End Station
- 12.3. Hard X-Ray Beamline Upgrades
- 12.4. Detector Systems
- 12.5. Controls, Data Acquisition, and Computing
- 12.6. Laser Systems
- 12.7. Timing Systems
- 12.8. Scientific Support Infrastructure

12.9. References

13. Timing and Synchronization

13.1. Master Clock, Frequency Selection, and Conversion

13.2. Triggering System

13.3. Timing Distribution to Experiments

13.3.1. Undulator Beam Arrival Time Monitor

13.3.2. RF Laser Locking

13.3.3. Laser Femtosecond Timing

13.3.4. X-ray / Optical Cross Correlator

13.4. References

14. Controls and Safety Systems

14.1. Control System Overview

14.1.1. Controls Requirements

14.1.2. Operations Requirements

14.1.3. Reliability

14.2. Global Systems

14.2.1. Control System Architecture

14.2.2. Controls Hardware Architecture

14.2.3. Timing and Event System

14.2.4. Beam-based Feedback System

14.3. Beam Diagnostic Systems

14.3.1. Sampling ADC based diagnostics

14.3.2. Image Acquisition

14.4. Power Supplies and Power Conversion

14.4.1. Scope

14.4.2. Power Supply Designs

14.4.3. Power Supply Controls

14.5. Low Level RF Controls

14.6. Undulator Controls

14.6.1. Undulator Motion Control

14.6.2. Undulator Temperature Monitoring

14.7. Beamline Instrumentation and Controls

14.7.1. Vacuum Controls System

14.7.2. Controls System Interface to Conventional Facilities

14.7.3. Basic Motion Controls

14.7.4. Temperature Monitoring

14.8. Controls Software

14.8.1. Operations Software

- 14.8.2. Central Database
- 14.8.3. High Level Applications
- 14.9. Safety Systems
 - 14.9.1. Personnel Protection System
 - 14.9.2. Beam Containment System
 - 14.9.3. Machine Protection System
- 14.10. X-Ray Transport and Experiment Systems Controls
 - 14.10.1. Front End Enclosure
 - 14.10.2. Data Acquisition
 - 14.10.3. Relocation of AMO and SXR Instruments
- 14.11. References

15. Infrastructure and Facilities

- 15.1. Introduction and Overview
- 15.2. Infrastructure Requirements
 - 15.2.1. Injector
 - 15.2.2. Cryogenic Plant Infrastructure
 - 15.2.3. Linac Facility Sectors 0 Through Sector 10
 - 15.2.4. Beam Switchyard
 - 15.2.5. Beam Transport Hall
 - 15.2.6. Undulator Hall
 - 15.2.7. Electron Beam Dump
 - 15.2.8. Front End Enclosure
 - 15.2.9. Near Experimental Hall
- 15.3. Site Civil Utilities Design
 - 15.3.1. Architectural Standards
 - 15.3.2. Structural Standards
 - 15.3.3. Mechanical Systems Standards
 - 15.3.4. Electrical Systems Standards
 - 15.3.5. Site Utilities Standards
 - 15.3.6. Environmental Standards
- 15.4. Sustainability Standards
- 15.5. References

16. Environment, Safety, Health, and Quality

- 16.1. Introduction and Overview
- 16.2. Preliminary Hazards Analysis (PHA)
- 16.3. Construction Hazards (LCLS-II PHA-1)
- 16.4. Natural Phenomena Hazards (LCLS-II PHA-2)
- 16.5. Environmental Hazards (LCLS-II PHA-3)

- 16.6. Waste Hazards (LCLS-II PHA-4)
- 16.7. Fire Hazards (LCLS-II PHA-5)
- 16.8. Electrical Hazards (LCLS-II PHA-6)
- 16.9. Noise and Vibration Hazards (LCLS-II PHA-7)
- 16.10. Cryogenic Hazards (LCLS-II PHA-8)
- 16.11. Confined-Space Hazards (LCLS-II PHA-9)
- 16.12. Ozone Hazards (LCLS-II PHA-10)
- 16.13. Chemical and Hazardous Materials (LCLS-II PHA-11)
- 16.14. Accelerator/Beamline Hazards (LCLS-II PHA-12)
- 16.15. Ionizing Radiation Hazards (LCLS-II PHA-13)
- 16.16. Non-Ionizing Radiation (LCLS-II PHA-14)
- 16.17. Material Handling (LCLS-II PHA-15)
- 16.18. Experimental Operations (LCLS-II PHA-16)
- 16.19. NEPA and NHPA
- 16.20. Quality Assurance
- 16.21. References

17. Radiological Considerations

- 17.1. Overview and Design Requirements
- 17.2. Criteria for Shielding and Radiation Safety Systems
- 17.3. LCLS-I and LCLS-II Beam Distribution System
 - 17.3.1. Dump Performance Parameters
 - 17.3.2. Upgrade Scenarios
- 17.4. Preliminary Shielding Design
 - 17.4.1. LCLS-II Injector, LINAC and Beam Switch Yard
 - 17.4.2. Shielding of LINAC penetrations
 - 17.4.3. Shielding of TDKIKB
 - 17.4.4. Head House, BTH, Undulator and Roof Buildings
 - 17.4.5. Tune-up Dump Shielding
 - 17.4.6. Shielding of Main Dumps DUMP/DUMPB
 - 17.4.7. Shielding and Beam Collimations for NEH Access
 - 17.4.8. Experimental Systems and Hutches
- 17.5. PPS, BCS Requirements
 - 17.5.1. PPS Design Requirements for LCLS-II
 - 17.5.2. BCS Design Requirements for LCLS-II
- 17.6. Radiological Environmental Issues
 - 17.6.1. Skyshine Dose at Site Boundary and Monitoring Systems
 - 17.6.2. Radioactive Air Effluent and Monitoring Systems
 - 17.6.3. Groundwater Protection and Soil Activation and Monitoring Systems
 - 17.6.4. LCW Systems, Wastewater Management and Stormwater Protection
- 17.7. Operational Radiation Protection Issues
 - 17.7.1. Radiation Damage Fields to Beam-Line Components

- 17.7.2. Repair and Maintenance Considerations
- 17.7.3. LCW System Design and Activation of Water in Dumps
- 17.8. References

18. Future Upgrade Options

- 18.1. Introduction and Overview
- 18.2. Electron Energy Upgrade
 - 18.2.1. Higher Gradients in Pulsed Mode
 - 18.2.2. Additional Installed Cryomodules
- 18.3. Future FEL Lines
 - 18.3.1. New Beam Transport, Undulator Hall, and Experiment Hall to the South
 - 18.3.2. Repurposing End Stations A and B
- 18.4. Self-Seeding and Other Techniques for Improving Coherence
 - 18.4.1. Self-Seeding
 - 18.4.2. External Seeding
 - 18.4.3. Two-Stage HGHG
 - 18.4.4. HHG Modification
 - 18.4.5. EHG Modification
 - 18.4.6. Two-Bunch Seeding Option
 - 18.4.7. Improvement of Temporal Coherence by *iSASE*
 - 18.4.8. Improvement of Temporal Coherence by *pSASE*
- 18.5. Upgrade to Self-Seeding Schemes
 - 18.5.1. Self-Seeding for the Soft X-ray Undulator
 - 18.5.2. Self-Seeding for the Hard X-ray Undulator
- 18.6. Polarization Control for the SXR FEL
- 18.7. Beyond 1 MHz
- 18.8. References

1

Introduction and Executive Summary

TECHNICAL SYNOPSIS

The revised scope of the LCLS-II Project has been aligned with the findings and recommendations of the Basic Energy Sciences Subcommittee report of 25 July 2013, which identified the importance of a high repetition rate X-ray free-electron laser source. The project will construct a 4 GeV continuous-wave (CW) superconducting linear accelerator in the first kilometer of the SLAC linear accelerator tunnel. The linac will provide pulses of electrons at rates of up to 1 MHz to two new undulators in the existing LCLS Undulator Hall. The two undulators will cover the spectral ranges 0.2-1.2 keV and 1-5 keV, respectively, when receiving electrons from the new linac. The existing LCLS linac will continue to operate, providing hard X-rays up to 25 keV. Existing X-ray instruments will be repurposed to exploit these new capabilities.

1.1 Background

Planning for the LCLS-II Project (LCLS-II) began in 2009, shortly after the LCLS Project demonstrated lasing at 8 keV. Critical Decision 0 (CD-0) for LCLS-II was approved by the Office of Science in May 2010. The project received CD-1 approval in October 2011 and completed all requirements for approval of CD-2 in August 2012. In March 2013 a “continuing resolution” Federal budget appropriation bill was enacted; consequently the LCLS-II Project did not receive line-item approval to start construction. The resultant delay has allowed the project to revise its conceptual design in response to most recent recommendations given to the Department of Energy Basic Energy Sciences (BES) Program by the BESAC Subcommittee on Future X-Ray Light Sources [1,2 and see chapter 1.2]. SLAC proposes to meet the scientific needs described in the BESAC Subcommittee report with a new design that is now responsive to the revised Mission Need Statement, approved in September 2013. The reconfigured LCLS-II Project is described in this Conceptual Design Report (CDR).

1.2 BESAC Subpanel Recommendations

The following quotes from the BESAC Subcommittee report [2] summarize the key capabilities that motivate the new LCLS-II design concept:

- “It is considered essential that the new light source have the pulse characteristics and **high repetition rate** necessary to carry out a broad range of coherent “pump probe” experiments, in addition to a sufficiently broad photon energy range (**at least ~0.2 keV to ~5.0 keV**).”
- “It appears that such a new light source that would meet the challenges of the future by *delivering a capability that is beyond that of any existing or planned facility worldwide is now within reach. However, no proposal presented to the BESAC light source subcommittee meets these criteria.*”
- “The panel recommends that a decision to proceed toward a new light source with revolutionary capabilities be accompanied by a robust R&D effort in accelerator and detector technology that will maximize the cost-efficiency of the facility and fully utilize its unprecedented source characteristics.”
- “...the best approach for a light source with the characteristics just enumerated would be a linac-based, seeded, free electron laser (FEL). To meet anticipated high demand for this linear device, the linac should feed multiple independently tunable undulators, each of which could service multiple end-stations. It is considered essential that the new light source have the pulse characteristics and high repetition rate necessary to carry out a broad range of coherent ‘pump-probe’ experiments, in addition to a sufficiently broad photon energy range (at least ~0.2 keV to ~5.0 keV) and pulse energy necessary to carry out novel ‘diffract before destroy’ structural determination experiments important to a myriad of molecular systems.”

The LCLS facility [3] already produces extremely intense pulses of X-rays spanning 280-10,000 eV. It also produces spatially coherent, short-duration temporally coherent pulses, near the Fourier transform limit in the range of 5-9 keV [4]. LCLS will soon produce similarly short and temporally coherent pulses in the range of 500-1,000 eV [5]. The facility produces sufficiently high energy per pulse for a wide variety of “diffract before destroy” experiments. However, neither LCLS nor the original LCLS-II concept could provide a sufficiently high repetition rate for the scientific objectives targeted by the BESAC Subcommittee.

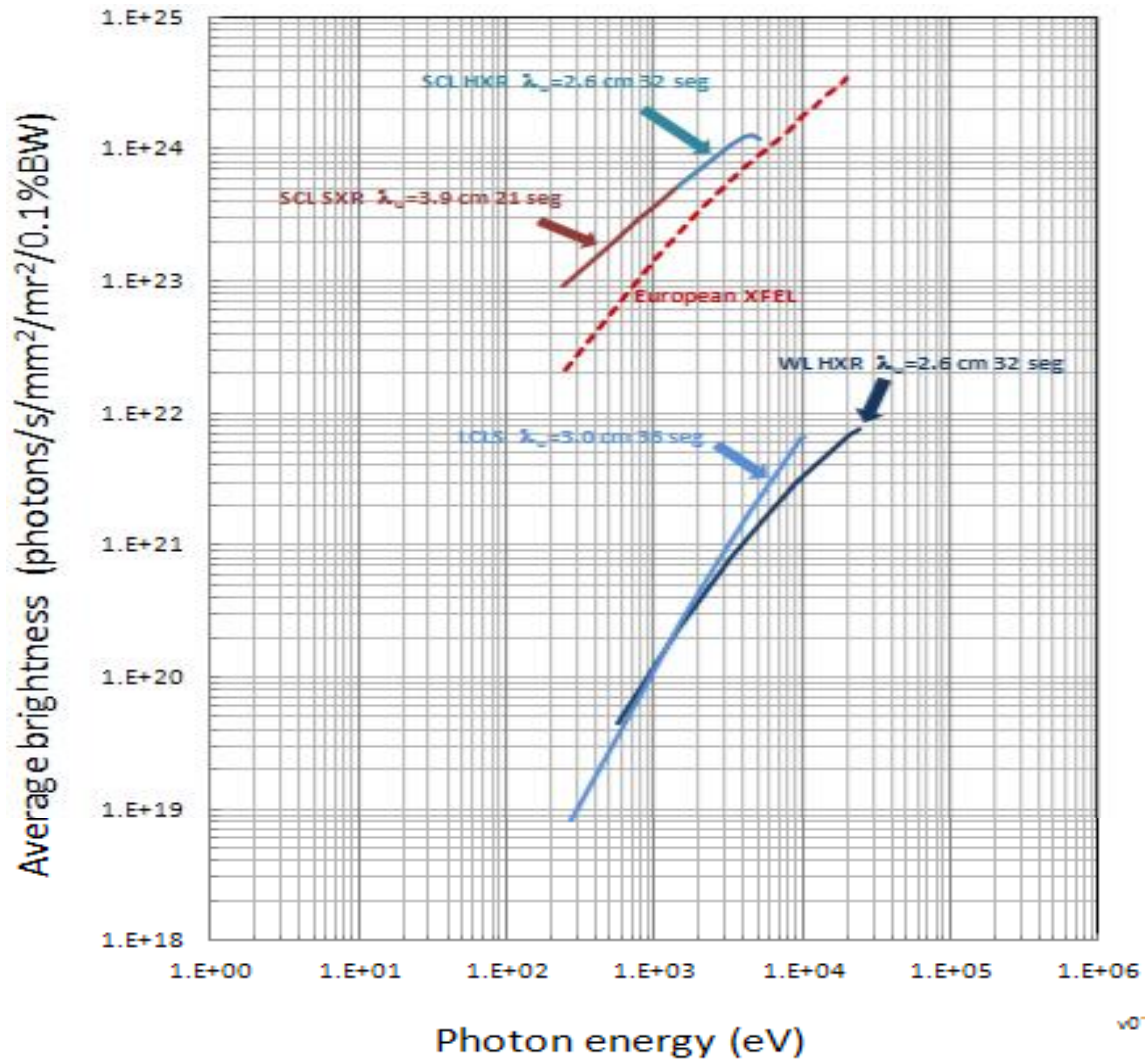


Figure 1: Nominal average brightness ranges for the two LCLS-II undulators at saturation. The dashed line indicates expected performance of the European XFEL Facility. The two-color (red + blue) solid line shows the average brightness of the two new LCLS-II undulators when they are operated with the new superconducting linac. The dark blue line shows the average brightness of the new hard x-ray (“HXR”) undulator source operating with the existing copper LCLS linac. The light blue line shows the performance of existing LCLS undulator and linac.

Since the former LCLS-II design had been predicated on use of Sectors 10-20 of the existing SLAC linac to provide electrons to the new X-ray sources, SLAC invested significant effort in exploring the repetition rate limits of “normal conducting” linacs. A repetition rate of 360 Hz would be relatively easy to achieve, since the SLAC linac was designed to run at this rate. A repetition rate of 1 kHz might be achieved by an extensive modification of all the SLAC linac modulators and klystrons. Repetition rates above 1 kHz require that LCLS-II build a new high repetition rate linac. For this reason LCLS-II will employ a superconducting linac that will, as shown in Figure 1, provide up to a thousandfold increase in average brightness compared to LCLS today.

1.3 Capability Gap

The revised Mission Need Statement (MNS) acknowledges the “capability gap” between LCLS performance and the abovementioned capabilities, which the BESAC Subcommittee identified as essential to realize the research potential of future X-ray free-electron lasers.

SLAC has responded to this need in the new configuration of LCLS-II by proposing the addition of a superconducting linac and two variable gap undulators. This combination will greatly expand both the capabilities and capacity of the LCLS complex.

1.4 Mission Need

The revised MNS lists “mission-level assumptions,” which anticipate the “key performance parameters” (KPPs) of the project, to be finalized in the approved Critical Decision 2 document, expected in 2015. These mission-level assumptions are:

- A new superconducting linear accelerator
- Expanded spectral reach, from 200 to 20,000 eV
- High repetition rate operations from 200 to 5,000 eV
- Capability to provide “pump” pulses over an extended range of photon energies to a sample, synchronized to LCLS-II X-ray probe pulses with controllable time delay
- Increase of user access through parallel rather than serial beam use

The revised MNS states that, if these assumptions are met,

“LCLS-II will expand the existing U.S. capacity and capability in X-FEL science and leverage the LCLS investment in a cost effective way. It assures international competitiveness of the U.S. x-ray program for decades to come.”

1.5 Key Features of LCLS-II

The LCLS-II concept responds fully to all mission-level assumptions of the revised Mission Need Statement. The concept includes:

- Replacement of the existing linac and associated RF systems in Sectors 0-10 by a CW 4 GeV superconducting linac and electron source, with a nominal bunch output frequency of 1 MHz.
- Installation of a helium liquefaction plant, needed for operation of the linac, in the vicinity of Sector 4
- Use of existing transport lines to bypass the middle portion of the SLAC linac as well as the LCLS linac in Sectors 11-30
- Replacement of the existing LCLS undulator with a variable gap system capable of receiving electrons from either the normal-conducting LCLS linac or the new 4 GeV superconducting (SC) linac
- Installation of a soft X-ray undulator source with self-seeding capability on the north side of the LCLS undulator hall
- Modification of the existing beam dumps, X-ray optics and soft X-ray instruments to exploit the new linac and X-ray sources
- Installation of new x-ray transport, optics and diagnostics for the new soft x-ray source to support two soft x-ray experiment stations

- Modification of the existing hard x-ray transport and optics to enable use of the new high repetition rate x-ray source by existing hard x-ray experiment stations

The layout of the SLAC linac tunnel is shown in Figure 2.

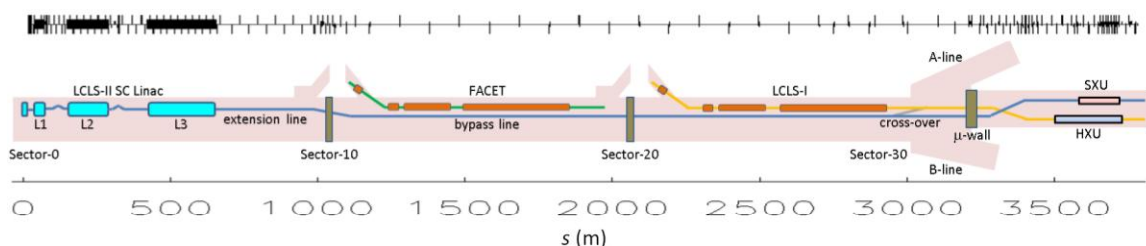


Figure 2. Layout of the SLAC linac tunnel with LCLS-II located in first 650 m of the tunnel, followed by the extension line to Sector-10, the bypass line to sector-30, and the beam transport to the SXU and HXU undulators.

1.5.1 Soft X-ray Source

The new soft X-ray (SXR) undulator source is intended to cover a spectral range of 200-1,200 eV. In particular, the SXR source will cover 250-1,200 eV with 4 GeV electrons from the new SC linac, as shown in Figure 1. This source will provide either SASE radiation or narrow-bandwidth radiation (via self-seeding) over its operating range. This source will be installed on the north side of the access aisle in the LCLS Undulator Hall.

1.5.2 Hard X-ray Source

The hard X-ray (HXR) undulator source will be installed on the south side of the aisle in the LCLS Undulator Hall, in place of the existing LCLS undulator. This undulator will receive electrons from either the new superconducting linac or the existing LCLS linac. When fed by the SC linac, it will operate over the spectral range of 1-5 keV at selectable high (approximately 100 kHz) pulse frequencies. When fed by the LCLS “copper” (Cu) linac, the HXR undulator will span 0.28-25 keV, by means of varying both the linac energy and the gap of the undulator. The two light-blue solid line segments in Figure 1 show the average brightness of the new HXR undulator over its full range of operation, utilizing both the new superconducting linac and the existing LCLS linac.

1.5.3 X-ray Transport and End Stations (XTES)

The project will provide two x-ray beam paths, one for each undulator. These beam paths, shown schematically in Figure 3, include the components necessary to filter, attenuate and collimate the x-ray beam.

LCLS-II XTES

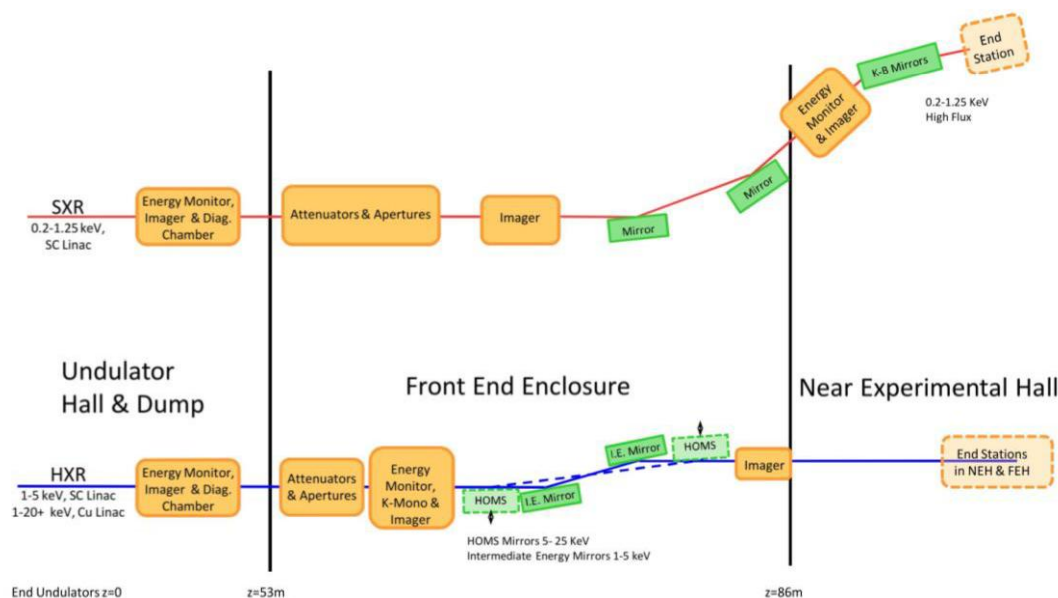


Figure 3: Schematic layout of LCLS-II x-ray transport and end stations. See Chapter 11 for a complete description.

The “south side” beam path must transport 1-5 keV photons produced by the new linac in addition to photons up to 24 keV produced by the existing (“copper”) LCLS linac. The x-ray beam is deflected horizontally by a pair of mirrors to ensure that gamma rays and very hard spontaneous radiation cannot exit the front end enclosure. Two pairs of mirrors will be provided; one pair will be used to transport 1-5 keV photons and the other pair will be used for harder x-rays. The south x-ray beam path will also provide gas and solid attenuators, non-invasive intensity monitors, imagers and a “K monochromator” that will be used to set the gaps of the new undulators. The south side beam path will incorporate collimators, shutters, diagnostics for imaging, wavefront monitoring and non-invasive pulse energy measurement.

The “north side” x-ray beam path will be dedicated to the new soft x-ray undulator, which will receive electrons from the new north-side undulator and the superconducting linac. This beam path will include attenuators, imagers, non-invasive intensity monitors, and a Kirkpatrick-Baez focusing system. The north-side x-ray beam path is designed to permit later addition of additional deflecting mirrors which will be used to direct x-rays to multiple instruments.

1.5.3.1 Soft x-ray Instruments

Existing LCLS soft x-ray instruments will be “re-purposed” (disassembled and reconfigured reusing original components to the extent possible) for use with the new soft x-ray source provided by LCLS-II. The capabilities of the: Atomic/Molecular/Optical Physics “HFP” end station, the coherent scattering “LAMP” end station and the resonant soft x-ray scattering

“REDSOX” end station will be available at the LCLS-II soft x-ray instrument by installing the end station required by each experiment’s needs. A concept for a resonant inelastic x-ray scattering (RIXS) instrument has been under development by LCLS scientists for some time, and the layout of the new beam path and end station will permit later implementation of this instrument.

As the soft x-ray research program matures, it is expected that the LCLS Near Experiment Hall will someday be dedicated to soft x-ray research as additional beam paths and end stations are set up. It is expected that, when this scenario is realized, the capabilities of the x-ray pump/probe (XPP) instrument will be re-created in the Far Experiment Hall, most likely in the X-ray Correlation Spectrometry (XCS) enclosure.

1.5.3.2 Hard X-ray Transport, Optics and Diagnostics

X-rays from the HXR source will be delivered to the existing four hard X-ray instruments (XPP, CXI, XCS, MEC). The high repetition rate of the SC linac is expected to be especially important to the XPP and XCS programs. Two sets of mirrors (one pair for x-rays up to 5 keV and another pair for harder x-rays) are required to cover the full spectrum of the HXR source; the project will provide a pair of mirrors designed for 1-5 keV x-rays.

1.5.3.3 Hard X-ray Instruments

The existing LCLS hard x-ray instruments in Hutches 4-6 will be adapted for use with either the high repetition rate x-ray source or the existing LCLS beam. The Matter in Extreme Conditions (MEC) instrument will most likely operate with harder x-rays from the copper linac.

1.5.4 High Repetition Rate Capability

The new superconducting linac will be capable of producing and accelerating electron bunches at up to 1 MHz and delivering over 1 MW of electron beam power. It is important to recognize that an important figure of merit for x-ray experimenters is the x-ray power delivered to the experiment. Due to considerations such as sample heating and x-ray optics stability, it is anticipated that the maximum practical x-ray power in high repetition rate operation will be approximately 20 watts, regardless of repetition rate. LCLS-II can exceed this x-ray power by a considerable factor, while using less than 120 kW of electron beam power. For this reason the new LCLS-II electron beam dumps will be designed to handle 120 kW.

Other considerations may lead to a limit on linac repetition rate. For example, pump/probe experiments will be limited by the pump laser repetition rate; imaging experiments may be limited by the state-of-the-art in readout of 2-D detectors and data archiving rates. One-dimensional detectors, integrating detectors and electron spectrometers can operate at MHz repetition rates.

LCLS-II will provide a DAQ for basic high-repetition rate detectors (such as a one-dimensional array that can operate at 1 MHz and an integrating 2-D detector). The LCLS-II Project will not undertake the development of fast (1-10 kHz) 2-D detectors. SLAC and other labs

working at extending the state-of-the-art in fast readout, and LCLS-II will provide faster detectors to fully exploit LCLS-II capabilities.

1.6 Cost Range

The cost range will be subject to an independent cost review as part of the CD-1 approval process. The total project cost (TPC) has been estimated to be \$895M. Table 1 shows the funding profile assumed in developing the project schedule. The 2014 Omnibus Appropriation is not reflected in this table; it is now known that LCLS-II will receive \$10M OPC and \$75M TEC in FY2014. It is expected that FY2015 funding for TEC+OPC will be reduced to \$115M. Funding in FY2016 and beyond will be reduced to maintain the TPC at \$895M.

Table 1. Assumed funding profile from 2010 through 2019 for LCLS-II in units of M\$.

Fiscal Year	FY 10	FY 11	FY 12	FY 13	FY 14	FY 15	FY 16	FY 17	FY 18	FY 19	Total
OPC and Pre-Ops	1.2	9.4	8.0		0.7	9.3	5.0		8.0	7.0	48.6
TEC-LLP			40.0		0	50.0	20.0				110.0
TEC-PED			2.0	5.0	4.0	21.0	15.0				47.0
TEC-Construction			2.5	17.5	39.7	67.7	169.0	185.1	168.0	39.9	689.4
Total Project Cost	1.2	9.4	52.5	22.5	44.4	148.0	209.0	185.1	176.0	46.9	895.0

1.7 Schedule

The proposed funding profile and schedule for the LCLS-II Project supports the achievement of “first light” from the new undulator sources during FY2019(early finish date). The project can be completed on this schedule if it is executed by a coordinated multi-institutional collaboration as described in the acquisition strategy. Achievement of this schedule is contingent on the following:

- Sufficient funding to support the work plan
- Superconducting RF accelerating modules acquired from two suppliers working in parallel
- Certain key long-lead procurements that can be awarded early in FY2015, after approval of CD-3A
- Reduction of LCLS operation for scientific users by a total of seven months compared to the routine operating schedule (which includes a total of three months of shutdown per year) in order to install all the necessary equipment in the existing LCLS Undulator Hall.

The overview LCLS-II construction schedule is shown in Figure 3. Level 1 milestones for Critical Decision approvals are listed in Table 2.

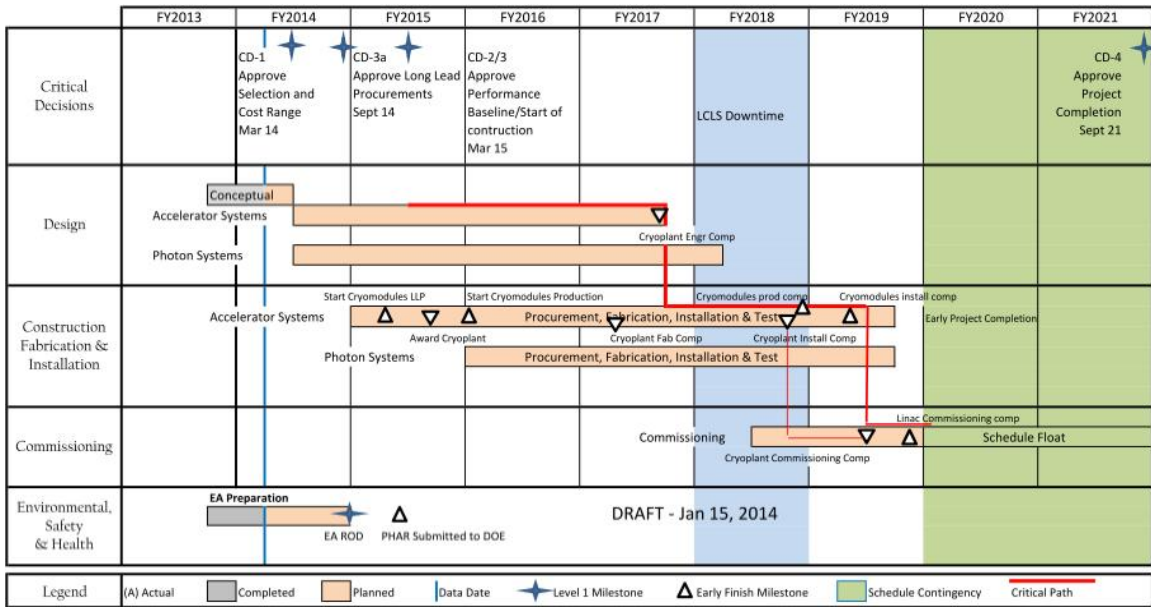


Figure 3. Preliminary schedule for construction of LCLS-II.

Table 2. Proposed Level 0 Milestones for the LCLS-II Project.

Level 1 Milestones	Date
CD-0, approve mission need	4/22/10 (actual)
Revise Mission Need Statement	09/27/2013 (actual)
CD-1, approve alternative selection and cost range	March 2014
CD-3A, approve long lead procurements	September 2014
CD-2, approve performance baseline	March 2015
CD-3, approve start of construction	March 2015
CD-4, approve project completion	September 2021

1.8 Alternatives Analysis

The Department of Energy has considered three alternatives for fulfilling the revised Mission Need Statement considered in creating the acquisition strategy:

- Maintain the status quo: build no new facility and use existing facilities at SLAC or elsewhere in the world.
- Build LCLS-II at SLAC.
- Build a comparable facility in a “green field.”

1.8.1 Status Quo

As observed in the BESAC report [2] and quoted in section 1.3 of this report, the United States lacks key research capabilities that are essential to the mission of the BES program and the

Office of Science. Therefore the status quo does not properly support the BES mission. Since no existing or planned FEL facility anywhere in the world can provide high-brightness X-ray pulses at about 100 kHz, as proposed in this conceptual design, the Mission Need cannot be fulfilled by use of any other facility in the world. Construction of a new facility or enhancement of an existing facility is thus required.

1.8.2 Proposed LCLS-II Configuration

The LCLS-II proposal meets the requirements in the BES Subcommittee report. Construction of LCLS-II at SLAC permits: reuse of approximately \$400M in existing facilities and infrastructure at SLAC; the \$500M invested in the LCLS facility to date; and the experience and expertise of the SLAC/LCLS staff. Since obtaining “first light” at LCLS in April 2009, SLAC and the LCLS staff have shown unprecedented productivity in the form of high-impact groundbreaking scientific output at LCLS. SLAC has, in the four years since LCLS operations began, exceeded every performance goal of the LCLS Project in terms of peak power, femtosecond-scale pump/probe timing capability and peak brightness. SLAC personnel are well-prepared to fully exploit the new capabilities provided by LCLS-II upon its completion. Furthermore, LCLS-II will support a wide range of enhancements to the LCLS facility, as described in Chapter 18 of this report. These enhancements make maximal use of existing SLAC infrastructure, ensuring LCLS can maintain its position at the forefront of x-ray research in the most cost-effective way possible for decades to come.

1.8.3 LCLS-II in a “Green Field”

This option would fulfill the Mission Need. However this option is far more expensive than construction of the proposed LCLS-II configuration. As described in the LCLS-II Acquisition Strategy, construction of a facility equivalent to LCLS-II in a green field would incur approximately \$3.5 billion in additional life cycle cost, compared to constructing LCLS-II as described in this report. The additional cost would result from duplicating SLAC facilities, operating them and decommissioning/demolishing them at a future date. It is therefore far more cost-effective to construct the LCLS-II facilities at SLAC.

1.9 Acquisition Strategy

The Acquisition Strategy selects Stanford University, DOE’s Managing & Operating contractor for SLAC, to directly manage the LCLS-II acquisition. The acquisition of large research facilities is within the scope of the DOE contract for the management and operations of SLAC and consistent with the general expectation of the responsibilities of DOE M&O contractors.

SLAC will assign responsibility for the design and fabrication of major LCLS-II subsystems to other DOE Laboratories or eventually an NSF Laboratory that possess the expertise and infrastructure to best accomplish these tasks. In particular, Lawrence Berkeley National Laboratory (LBNL) will continue to design and production-engineer the undulators for LCLS-II,

and will provide the electron source around which LCLS-II will be designed. Fermi National Accelerator Laboratory (Fermilab) and Thomas Jefferson National Accelerator Facility possess the expertise to design and fabricate cryogenic acceleration modules (“cryomodules”). Argonne National Laboratory will provide undulator vacuum chambers and will develop an alternative undulator design. Argonne will also support FNAL with chemical processing facilities for niobium accelerating structures. In addition, Cornell University will provide development support for improving cryomodule performance. NSF-funded research at Cornell may yield an alternative choice for the LCLS-II electron gun.

Most of the assembly, installation, testing, and commissioning of the LCLS-II Project will be performed by the SLAC LCLS-II scientific and technical staff. Much of the subcontracted work to be performed for LCLS-II consists of hardware fabrication. Since a significant fraction of this work requires shutdown of SLAC accelerator facilities, every effort will be made to minimize interruptions to LCLS operation.

1.10 References

- [1] Charge to Professor John C. Hemminger, chair of the Basic Energy Sciences Advisory Committee, from William F. Brinkman, January 2013; stored at the BESAC website <http://science.energy.gov/~media/bes/besac/pdf/2013-brinkman-to-hemminger.pdf>.
- [2] “Report of the BESAC Subcommittee on Future X-ray Light Sources,” stored at the BESAC website http://science.energy.gov/~media/bes/besac/pdf/Reports/Future_Light_Sources_report_BESAC_approved_72513.pdf.
- [3] C. Bostedt, et al., “Ultra-fast and ultra-intense x-ray sciences: first results from the Linac Coherent Light Source free-electron laser,” *J. Phys. B: At. Mol. Opt. Phys.* **46** [164003](#).
- [4] J. Amann, et al., “Demonstration of self-seeding in a hard x-ray free-electron laser,” *Nature Photonics* **6**, pp. 693-698 (2012); ISSN: 1749-4885.
- [5] Y. Feng, et al., “System Design for Self-Seeding the LCLS at Soft X-ray Energies”, Proceedings of the 2012 Free Electron Laser Conference, Nara, Japan, [TUOBI01](#), pp. 205-212, ISBN 978-3-95450-123-6.

2

SCIENTIFIC OBJECTIVES

TECHNICAL SYNOPSIS

LCLS-II is a next-generation time-resolved microscope that can view structure and function in the material and chemical world down to the fundamental length- and time-scales of individual molecules and atoms. It combines the most advanced features of X-ray science and laser science, including high power, high time resolution, and high coherence, in an X-ray source with exquisite control over its spatial and temporal characteristics.

This chapter describes the scientific objectives of LCLS-II by building upon the results from LCLS-I, as well as the proposals for LCLS-II [1] and the Next Generation Light Source Facility [2]. The scientific objectives have driven the specifications for scope and design of the LCLS-II facility described in this report. This overall approach meets the recommendations of the BESAC lightsource subcommittee issued on July 24, 2013 [3] and endorsed by the full BESAC committee.

LCLS-II will enable groundbreaking science addressing a broad range of scientific challenges, including some of the “Grand Challenges” identified by BESAC [4]. Understanding the fundamental mechanisms of chemical reactivity, tailoring materials to transport and store energy efficiently, and solving the nanoscale functionality of biological systems will all benefit from the transformative capabilities provided by LCLS-II.

The key new capabilities of LCLS-II are:

- 1. High pulse repetition rate over a broad energy range from ~0.2 to 5 keV*
- 2. Control over the pulse bandwidth (including transform-limited pulses) and polarization*
- 3. Increased photon energy range compared to LCLS-I (in particular, exceeding 10 keV)*
- 4. Ability to produce multiple pulses with arbitrary delays and full control of pulse energy, duration, and bandwidth.*

These capabilities will drive discovery across scientific disciplines and enhance the understanding and ability to control nature’s fundamental systems. They will enable X-ray laser science with much greater flexibility for coherently manipulating and probing matter – control that has been obtainable in the past only with optical lasers -- but with near-atomic resolution that optical techniques generally lack. The high repetition rate and control over pulse properties will open up laser spectroscopies that exploit the element-specific resonances below 5keV. The high scattering cross section in this energy range will enable high-efficiency imaging of biological structures with nanometer resolution. In addition to the revolutionary new capability that LCLS-II will provide, the project will double the number of independent FEL sources at the LCLS facility. The independent sources will provide more than a simple increase in capacity,

since they have complementary scientific capabilities. This synergy creates new opportunities that will be welcomed by the growing LCLS user community.

LCLS-II is a big step forward in the overall plan to maintain the LCLS as the world's premier X-ray laser facility. The investment in a continuous-wave superconducting accelerator forms a backbone for future expansion. It will allow for the later addition of more undulator sources with special characteristics, which will further augment capability and capacity.

This chapter explains how LCLS-II will provide a path to understanding -- how control over the X-ray bandwidth will provide knowledge to control chemical transformation on the molecular level, how the high repetition rate will enable the study of the dynamics of electrons at the quantum level with unprecedented resolution, and how the extended photon energy range will yield new molecular structures of complex biological systems and bioinspired materials.

2.1 Science from LCLS-I to LCLS-II

The path to scientific discovery at LCLS-II builds upon an experimental foundation developed during the first four years of operation of LCLS-I, where the unprecedented properties of an X-ray free-electron laser have sparked the development of new methodologies. LCLS has enabled the first steps toward comprehensive investigation of the fundamental behavior of matter at the atomic length-scale and femtosecond time-scale. We describe below a few important examples of LCLS research presenting clear avenues for new discoveries at LCLS-II and beyond.

LCLS-I Highlights

Single-shot nanoscale imaging has been demonstrated for a variety of nanostructures including a single mimivirus [5], ferromagnetic order in a nanostructure [6] and aerosol particles [7]. Experiments at LCLS have confirmed that iterative techniques for recovering real images from diffraction patterns of illuminated objects are effective for Ångstrom-wavelength FEL radiation and nanoscale samples. Enough information is contained in a single-shot diffraction pattern for good image reconstruction.

Diffract-before-destroy experiments have demonstrated that Serial Femtosecond X-ray Crystallography of proteins [8] is a viable method for determining the structures of hard-to-crystallize proteins at high resolution [9]. *De novo* phasing has been shown to be possible using the LCLS source [10] and novel structures previously inaccessible at synchrotrons have been solved [11]. The technique has been used for studies on Photosystem II as well as on the extremely important G Protein-Coupled Receptor (GPCR) family of membrane proteins. These results have demonstrated the ability to extract useful information from very weakly scattering samples, if a large enough number of measurements is performed [12].

LCLS has been used to explore several fundamental **nonlinear optical processes that govern the response of matter to high intensity X-ray radiation in atomic, molecular and bulk materials**. An understanding of how **small quantum systems like atoms, molecules and clusters behave under the high electric fields** from intense FEL radiation is critical for

understanding materials in extreme environments and interpreting the most demanding experiments. The first LCLS experiments observed the full ionization of neon due to sequentially absorbed photons [13]. Studies of nonlinear ionization dynamics and ionization dynamics for larger, nanoscale clusters of atoms followed [14,15,16], providing data which is critical for testing models of more complex X-ray/matter interactions.

Researchers have also demonstrated population inversion and stimulated X-ray emission of inner shell processes leading to a narrow bandwidth atomic X-ray laser [17] that could eventually be used for high resolution spectroscopic studies. In bulk materials the mixing of X-ray and optical fields [18] promises a new method for atomic-scale imaging of valence electron density as well as the local polarizability. Such nonlinear and stimulated optical processes offer important insight toward understanding electron correlations and energy and coherence transfer, and could form the basis of multi-dimensional X-ray spectroscopies of chemical and materials dynamics.

The femtosecond X-ray pulses of LCLS have already revolutionized our ability to follow atomic-scale electronic and nuclear dynamics using stroboscopic optical pump, X-ray probe time-resolved spectroscopy. Such ultrafast pump-probe measurements have been applied to a wide range of scientific questions. The dynamics of photoinduced bond breaking has been observed: (1) in the ring molecule cyclohexadiene-hexatriene [19], which is a model system in photochemistry; and (2) as carbon monoxide molecules are desorbed from a ruthenium substrate [20], which is a key step for an important class of catalytic reactions. Pump-probe methods have also been used to align molecular gases in the laboratory to enable X-ray studies in the molecular frame [21,22]. The photo-induced evolution of the charge and spin ordering for electrons associated with specific atomic sites has been studied (1) on the nanoscale in ferromagnetic GdFeCo [23], (2) in the stripe order of LaSrNiO₄ [24], and (3) to study the insulator-metal transition in Fe₃O₄ [25]. Ultrafast three-dimensional images of lattice dynamics in gold nanocrystals have been measured [26]. Time-domain phonon dispersion measurements were recently demonstrated [27], reaching exquisite energy and momentum resolution using broadband pulses without monochromators or analyzers.

Methods for characterizing X-ray pulses were critical to the development of many of the aforementioned experiments. Measuring the arrival time of X-ray pulses with respect to optical pulses down to a few femtoseconds has been demonstrated [22, 28]. Single pulse wavefront measurements of hard X-rays have been collected [29].

These experiments show that many of the underlying techniques needed to achieve the scientific objectives outlined below in Section 2.3 are viable. The pioneering experiments at LCLS-I point toward a new class of experiments that require the much brighter, more stable, advanced laser X-ray source that will be provided by LCLS-II.

Moving beyond one-photon-at-a-time experiments

A common theme of among many of these LCLS-I experiments is the use of resonant processes near K, L or M X-ray absorption edges. Resonant excitation of core electrons to unoccupied valence states provides elemental and chemical specificity, and through polarization-

dependent effects enables the separation of charge- and spin-based phenomena. The choice of the spectral range is based on the energy of atom-specific absorption features of some of the most important elements in the periodic table – the K-edges of the second and third row elements (C, N, O, Al, Si, P, S) which provide information of the p bonding orbitals, the L-edges of the fourth row elements (Ca – Zn) which reveal the valence properties of the d-orbitals, and the important f valence states of the rare earths which are probed through M-edge excitation. An example of the prominence of such element-specific bonding resonances is given in Figure 1.

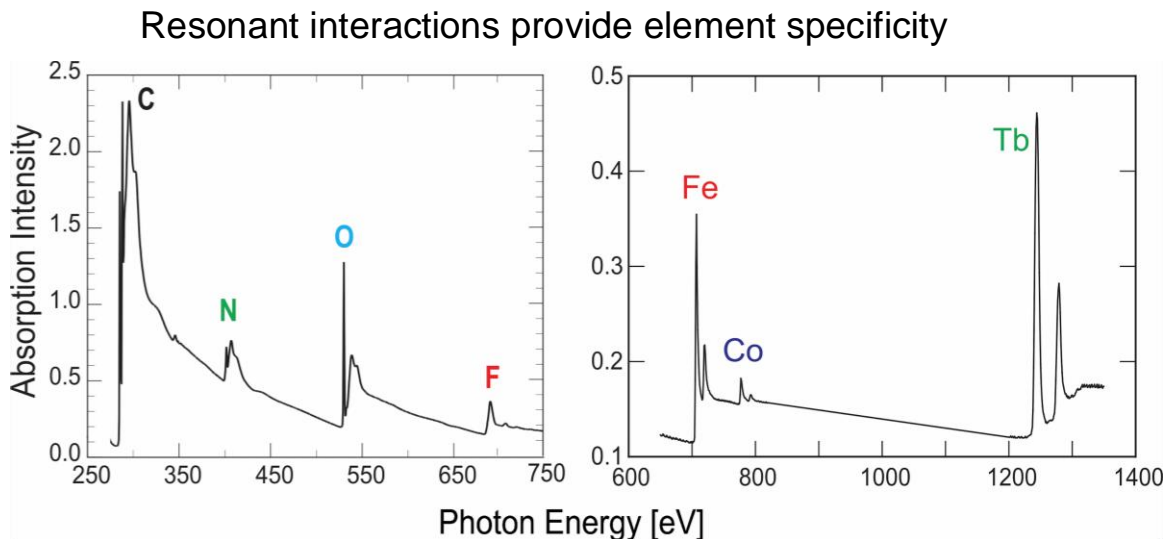


Figure 1. Example of the dominance of resonant over non resonant interactions in the soft X-ray region. Utilization of the large cross section associated with such resonances forms the basis of soft X-ray investigations of matter through techniques like X-ray absorption, diffractive coherent imaging, X-ray microscopy, and resonant elastic and inelastic X-ray scattering. The large cross section of resonant processes also allow extension of coherent control through nonlinear coupling of X-ray laser pulses with matter, extending the power of NMR and optical multi-dimensional spectroscopy techniques into the X-ray region.

These prominent element-specific resonances in conjunction with the spatial coherence provided by X-ray free electron lasers enables a revolutionary scientific development. It is based on the control of resonant electronic processes by multi-photon, multi-dimensional spectroscopy which can now be extended into the soft X-ray region as illustrated in Figure 2. This concept follows the enabling development of powerful sources of electromagnetic waves such as radar microwave sources in the 1940s that fueled the development of nuclear magnetic resonance (NMR) techniques, and the invention of the laser in 1960 which led to unprecedented control of light-matter interactions.

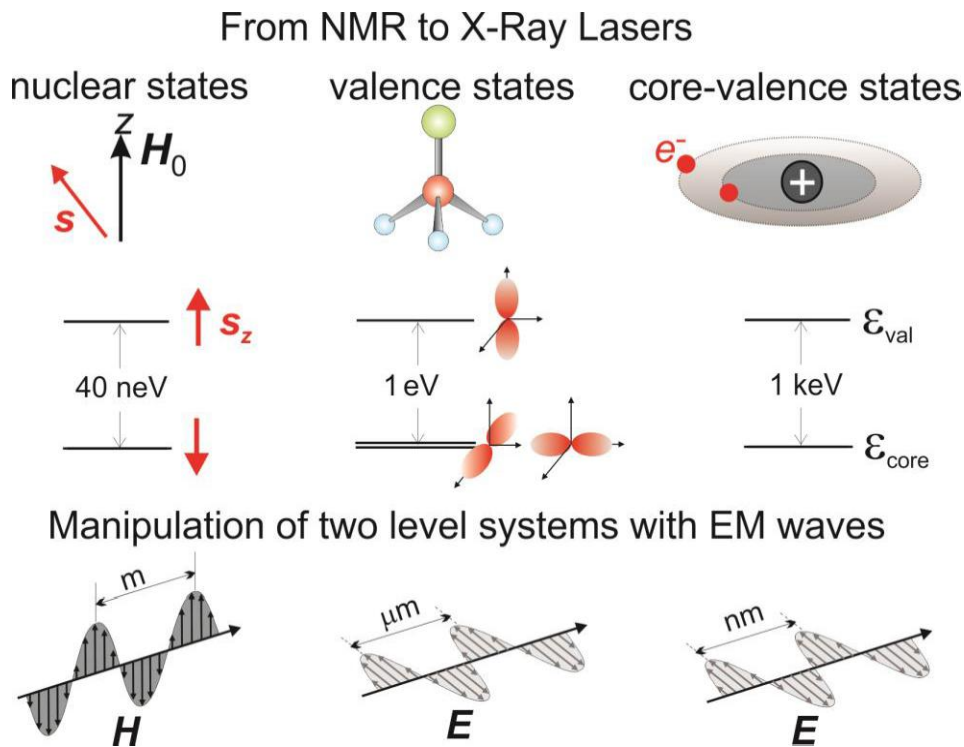


Figure 2: The evolution of multidimensional spectroscopy from NMR in the 1940s to optical lasers in the 1960s to X-rays with the advent of X-ray lasers around 2010.

Imaging with Nanometer Resolution

Another common theme of many high-impact experiments at LCLS over the past four years has been the use of coherent scattering as a nanoscale imaging method. LCLS-I and its instrumentation are optimized to provide imaging capabilities in the range of photon energies below 2 keV or above 5 keV. A higher energy range is desired because it can support higher spatial resolution; however, X-ray imaging involves a number of additional factors that complicate this simple drive to shorter wavelength FELs.

- For non-crystalline imaging of single molecules, the sample heterogeneity may ultimately limit the resolution to about 4 Å, even for hard X-rays.
- Because the scattering signal increases as λ^2 and the number of photons per laser pulse also scales with λ , assuming a fixed detector efficiency, measurements should be made at the longest possible wavelength that supports the desired (or achievable) resolution.
- The fact that the sample is completely destroyed by a single shot, forces the need to collect the maximum amount of information in that one shot, so optimization of the photon energy for the given sample is crucial.

In certain situations, the currently inaccessible range between 2 and 5 keV would be ideally suited for structural biology studies. The increased repetition rate at LCLS-II, could markedly

increase data collection speed leading to revolutionary results, provided data from each pulse is individually read out from the detectors and the pulse intensity is sufficient to produce signal above noise at the desired resolution on every pulse. Results achieved at LCLS-I with sub-micron crystals using soft X-rays support the feasibility of transformative science by imaging single objects at nanometer resolution with improved focusing and an optimized photon energy range.

2.2 Transformative Capabilities of LCLS-II

To enter the “Control Age” where we design and tailor materials and systems at a fundamental level in order to solve problems related to energy, information science, and medicine requires a deep understanding of the mechanisms governing nature. Arriving at a deep level of understanding demands answers to scientific questions in chemistry, materials physics and biology across a wide range of parameters such as: time—to explore the dynamical nature of processes; energy—to understand how electrons influence order giving materials new emergent properties; and space—to discover how the structure of complex molecules describe their function in living systems. The unique capabilities of LCLS-II will be essential for pursuing the scientific objectives outlined in this chapter.

Key New Capabilities Driven by the Scientific Objectives of LCLS-II

1. High pulse repetition rate over a broad energy range from ~0.2 to 5 keV

High X-ray pulse repetition rate is a key element of accelerating experimental discovery. Even with the intense pulses produced by a free-electron laser, many experiments are starved for signal (because very weak effects are being studied, or because the FEL beam must be filtered into a very small portion of phase space). Other experiments benefit from the high coherence of the FEL beam but involve samples which must not be modified by intense pulses, requiring the FEL pulse intensity to be reduced. All of these experiments will benefit from a pulse repetition rate much higher than the 120 Hz offered by LCLS-I. LCLS-II, with a CW superconducting accelerator, will offer pulse repetition rates of 100 kHz or more.

2. Control over the pulse bandwidth (including transform limited pulses) and polarization

The ability for X-rays to “see” specific elements arises from resonant spectroscopic contrast. Control over the photon energy and stability is important for efficient spectroscopic studies. Narrower energy bandwidth can provide further access to isolate chemical environments. This control will be provided by a combination of self-seeding and monochromatization at LCLS-II.

3. Increased photon energy range compared to LCLS-I (in particular, exceeding 10keV)

Understanding systems in their “natural state” often requires an ability to probe their full three-dimensional extent. The symmetries of liquids, the nature of

interfaces and the flow of energy through materials can be explored with coherent high-energy X-rays from LCLS-II. Photon energies greater than 10 keV allow these photons to penetrate deep into samples. The short wavelengths of high-energy X-rays compress the distribution of scattered photons, allowing a greater fraction of the total diffraction pattern to be collected by a detector of modest size. An extended energy range will afford LCLS-II the capability to probe a greater fraction of reciprocal space, while studying dynamics in crystals and in non-periodic systems like liquids and glasses. In addition, the extended energy range will permit the use of standard MAD phasing techniques for protein crystallography.

4. *Ability to produce multiple pulses with arbitrary delays and full control of pulse energy, duration, and bandwidth*

Understanding the dynamics of electronic structure and the mechanisms of energy flow will require advanced time-resolved coherent spectroscopy methods. These methods will develop over time at LCLS-II as capabilities including two-color operation and polarization control are realized. These developments will provide LCLS-II with capability for nonlinear and stimulated spectroscopic methods.

2.2.1 Advanced Methods and Techniques

Because the LCLS-II source characteristics draw closer to those of an ideal laser source, spectroscopic methods can be considered which have not previously been possible using X-rays.

2.2.2 Time-Domain Spectroscopies

The short pulses from LCLS-II imply broad bandwidth that is not well-matched to standard synchrotron spectroscopy methods that employ low throughput monochromators and spectrometers. Fortunately, the high coherence properties, high repetition rate, and high stability of LCLS-II means that superior spectral resolution could be obtained by time-domain methods analogous to those used in the optical laser spectroscopy community, such as frequency combs and Fourier transform spectroscopy as well as pump-probe and multi-dimensional spectroscopies. Because these methods work in the time-domain, they are appropriate not only for equilibrium properties but also nonequilibrium dynamics and rare-events far from equilibrium that cannot be captured by other means. The time-domain is also natural for studying the coupling between modes during the return to equilibrium. The challenge with these techniques is that they require high levels of coherence either in the source, the excited state of the sample, or in some cases both the source and the sample.

A recent example of X-ray time-domain spectroscopy is the measurement of phonon-dispersion with sub meV resolution using broad-band (>50eV) X-ray pulses. [30] In these experiments an external laser pulse initiates temporal coherence in the sample, in the form of squeezed correlate pairs of phonons of equal and opposite momentum. A time-delayed hard X-

ray pulse scatters from the squeezed vibrations of the crystal in stroboscopic fashion. The scattered X-rays have imprinted on them, as a function of time, correlations corresponding to phonon modes spanning the entire Brillouin zone. By detecting the scattering signal with an area detector, massively parallel detection across a broad momentum distribution can be obtained at once. The phonon frequencies and lifetimes are obtained from a simple temporal Fourier transform of the time- and momentum-resolved data. This method can also be used to track the evolution of nonthermal populations during hot electron relaxation, relevant for high speed electronic and optoelectronic devices, as well as for energy conversion in photovoltaic and thermoelectric devices.

The challenges of these experiments are in the signal-to-noise obtained at 120 Hz operation, as well in generating time-synchronous large-amplitude coherence. Multiple-pulse X-ray experiments, with and without external excitation, would allow for direct measurement of excitations spanning from microelectron-Volts to electron-Volts with the same X-ray pulse. Research and development are needed in advanced X-ray optics that allow full coherent manipulation of these pulse pairs with attosecond control over many picoseconds or even nanoseconds of separation. Such a capability would be transformative for answering frontier questions in chemical reactivity and materials dynamics.

2.2.3 Multi-Dimensional Spectroscopies

Multidimensional spectroscopy is a powerful example of coherent time-domain methods. The power of X-ray multidimensional spectroscopy lies in the capability to follow the coherent flow of charge and spin excitations and the associated flow and dissipation of energy between selected atoms or functional groups. In contrast to multidimensional NMR spectroscopy which monitors low energy *nuclear spin* processes through sequences of radio-frequency pulses and multidimensional infrared and optical spectroscopy which probe *vibrational* degrees of freedom, X-ray laser pulses provide direct access to the full range of electronic states (unrestricted by dipole selection rules) and their evolution on the fundamental (attosecond to femtosecond) time scales of their couplings, with the ability to obtain an atom-projected view of the processes, owing to core-to-valence transitions. X-rays can therefore provide critical new insight to correlated electronic and spin interactions in materials and molecular complexes.

Multi-dimensional X-ray spectroscopy and nonlinear X-ray science will be hallmarks of LCLS-II as they require capabilities that are not currently available. The three key ingredients for multi-dimensional X-ray spectroscopy are:

- Utilization of soft X-ray resonances which provide nonlinear cross sections that are comparable to non-resonant optical cross sections.
- Exploitation of high temporal coherence, which can be expressed as a large photon degeneracy, for X-ray laser pulses of 1-100 fs duration. These experiments will require high repetition rate pulses with full polarization control and improved longitudinal coherence control, and the availability of multi-color pulses. Pulse-to-pulse intensity fluctuations must be minimized for improved sensitivity.

- Development of an X-ray optics toolbox that allows the splitting and relative time delay of pulses, with the requirement of adjustable pulse directions through the sample for wave-vector control.

2.3 Scientific Questions and Methods Addressed with LCLS-II

The scientific objectives for LCLS-II are divided here by discipline: chemistry and molecular physics; materials physics; and biology and biochemistry. Each section provides scientific motivation followed by relevant questions to form the scientific objective. Experiments that will provide insight are described in terms of the methods and techniques enabled or improved at LCLS-II. This is not intended to be an exhaustive scientific case.

2.3.1 Chemistry and Molecular Physics

Chemical and molecular science investigates the arrangement of electrons and nuclei on the Ångstrom to nanometer length-scale as a means of controlling the function of molecular materials. Coherent, ultrashort duration X-ray pulses present many unique opportunities to characterize the structure and dynamics of electrons and nuclei in all molecular media. The ability of LCLS-II to address critical questions in energy conversion and chemical catalysis merit focus, but should not be viewed as the only research opportunities in the molecular and chemical sciences enabled by LCLS-II.

The world faces many challenges concerning the production and storage of energy and the reduction of the environmental impact of energy production and usage. Nearly all chemical processes involved in energy conversion utilize catalytic chemical transformations at interfaces between solids and liquids or gases. Enhancing our understanding of chemical catalysis on the molecular level presents a critical opportunity to improve the efficiency and cleanliness of energy production and usage.

Understanding and controlling chemical transformations on the molecular level represents one of the grand scientific challenges, and is central to generating cost-effective and environmentally benign energy sources. Such processes often occur at local catalytic reaction centers and their tracking is aided by the atomic and chemical specificity of X-rays. Manipulation of electronic and nuclear structure and dynamics on the Ångstrom length-scale resides at the heart of chemical transformations. Control of chemical reactivity will lead to the synthesis of many new useful products, efficient and compact energy storage and release by chemical bond manipulation, and the ability to influence key biological reactions and functions. The ultrafast X-ray pulses from LCLS-II present an excellent opportunity to track these dynamics with the temporal and spatial resolution required to push towards a comprehensive and predictive understanding of chemical reactivity.

2.3.1.1 Characterization and Control of Molecular Energy Conversion

Reactions triggered by optical photons from the sun power nearly all biological functions, either directly or indirectly. Light-driven processes also present a risk to life; for example, the

absorption of UV light by DNA can lead to mutation and cancer. In all of these cases, light absorption disturbs the valence electrons, which bind nuclei together and thus stabilize the molecule in a particular geometry. In the ground state, all forces among nuclei and electrons are balanced. If a photon is absorbed, the electrons reorganize, and the equilibrium is disturbed. What follows is a highly intertwined motion of nuclei and electrons. To perform a certain function, the motion of the molecule has to be directed into a particular channel. For example, a bond may need to be altered, as in the photochemical bond rotation that occurs in vision.

Despite extensive investigation, we still lack a quantitative understanding of photochemical reactivity, much less a predictive understanding. The powerful tools we use to understand chemical reactivity in the electronic ground state of molecules, such as transition state theory and density functional theory, cannot be simply extended to photochemical reactions where non-equilibrium trajectories determine the rate and reaction pathway. Controlling artificial photosynthetic and photovoltaic processes requires understanding the coupled quantum evolution of the electronics and nuclei in highly non-equilibrium configurations that evolve on the femtosecond to many picosecond time-scale.

Experimental characterization of these optically induced trajectories will benefit greatly from tools able to resolve structure, both electronic and nuclear, with a sub-Ångstrom spatial resolution and sub-picosecond time resolution. The spatial resolution of soft X-ray spectroscopy relies not on the wavelength of the X-rays, which is typically much larger than the molecule, but rather on the sub-Ångstrom spatial extent of the core electronic states of oxygen, nitrogen, sulfur, or other atoms that can be targets for excitation within the molecule. Thus this research area will benefit significantly from the expansion of the photon energy range at LCLS-II, which will enlarge the number of accessible atomic edges.

The characterization and control of complex chemical phenomena requires a multifaceted approach involving a diverse range of molecular systems, chemical environments, and experimental techniques. Both the intra-molecular structure of reactive molecules and the environment surrounding the molecules critically influence the outcome of photochemical processes. Understanding and controlling the coupled quantum evolution of the electrons and nuclei in highly non-equilibrium configurations consequently requires studying chemical systems in an array of chemical environments. The novel technical capabilities of LCLS-II will enable critical chemical reactions to be investigated in a wide array of environments from the gas phase, to solution, including heterogeneous environments such as catalytic surfaces and interfaces. The opportunities are too great to be covered fully in this document, but we will highlight a few characteristic areas where LCLS-II will provide transformative experimental opportunities.

2.3.1.2 Molecular Energy Conversion in Isolated Quantum Systems

The approach to understanding the photochemistry of isolated molecules is based on a very close interplay between experiment and theory. At the current state of the art, it is impossible to predict any but the most trivial molecular behavior during chemical transformations without serious approximations. The most widely employed approximations are the Born-Oppenheimer

approximation (BOA), which decouples nuclear and electronic degrees of freedom; and various mean field descriptions of electron-electron interactions, such as the Hartree-Fock approximation. While these approximations often prove valid for the description of chemical reactions in the electronic ground state, they have dubious applicability for most electronic excited state phenomena, where electron correlation and non-Born-Oppenheimer dynamics play a crucial role and still render calculations extremely challenging [31,32].

To illustrate the challenges, we plot part of an electronically excited potential energy surface for the special case of the nucleobase uracil in Figure 3. The light absorption launches a molecular vibrational wave-packet in the Franck-Condon point from where it relaxes to lower points 2 and 3 on the 2d potential energy surface. The exact shape of the potential is highly controversial leading to conflicting simulations statements about the nuclear relaxation on the PES as well as the non-BOA transitions to other electronic states (see Ref. [33] and references therein).

Understanding the photochemistry of DNA

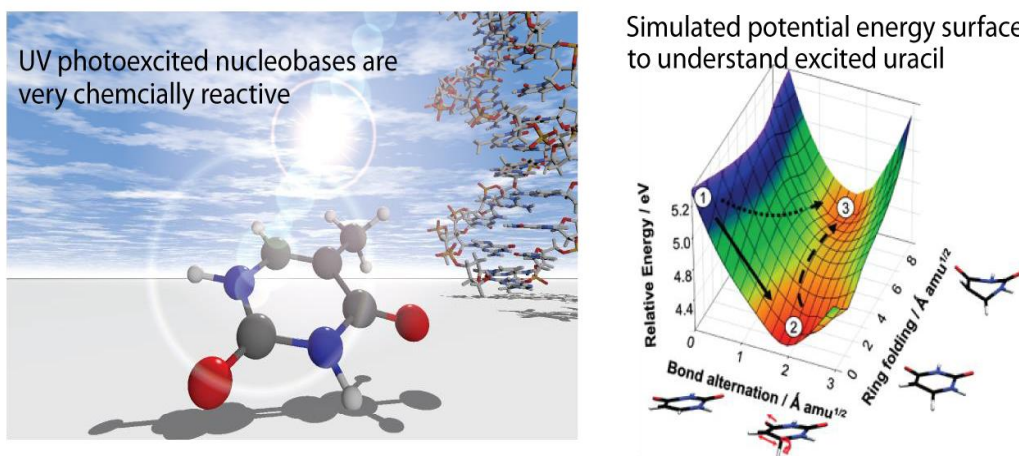


Figure 3. Simulated excited state potential energy surface (PES) of the nucleobase uracil plotted as a function of two effective nuclear coordinates. Light absorption promotes the molecule on point 1. The gradient at 1 directs the wavepacket towards point 2 where it is trapped by a reaction barrier towards point 3, where a non-BOA coupling elements funnel population into a different electronic state. The gradient as well as the barrier depend sensitively on the *ab initio* approach chosen [From Hudock, H. R. *et al. J. Phys. Chem. A* 111, 8500 (2007)].

Three overarching questions regarding the chemical reactivity of electronic excited states must be addressed before the chemical sciences will be able to rationally design molecular systems for solar energy conversion. (1) How does the redistribution of electrons induced by photo-excitation dictate excited state nuclear dynamics? This involves accurate experimental characterization of photo-excited PES gradients which will provide important input for benchmarking *ab initio* methods. (2) How do the valence electrons respond to photo-excitation and the nuclear dynamics on the photo-excited PES? This question addresses transient changes in

electronic structure induced by non-BOA coupling. Tracking the time and spatial evolution of the valence electrons will provide critical information for characterizing theoretical methods for describing the non-BOA dynamics that occur in reactive electronic excited states [32,34]. (3) What is the spatial extent of the excited electron wavefunction and how does electron correlation influence the time dependent electronic wavefunction? This question is directly related to electron correlation [35] and can help designing more sophisticated quantum chemistry methods.

Experimental studies of valence excited state dynamics generally utilize optical pulses to initiate the dynamics, though we will discuss X-ray Raman excitation of valence electrons below. Ultrafast X-rays allow excited molecular dynamics to be followed with atomic spatial resolution and atomic and site selectivity. While a diverse range of methods can be used to detect the X-ray molecule interaction, the high repetition rate and peak flux of LCLS-II will enable completely new methods for dilute gas phase targets such as resonant inelastic scattering, photoelectron spectroscopy, and multi-particle correlation spectroscopy. This expansion in X-ray methods not only increases the information content of the experiment, but also allows measurements with a stronger connection to molecular theory to be achieved.

These highlighted ultrafast X-ray methods enabled by LCLS-II require single X-ray photon interactions with individual molecules, and thus the single pulse intensity has an upper bound. Once such a boundary has been reached, improvement in signal quality can only be achieved by increasing the repetition rate of the source. Resonant soft X-ray cross-sections and space charge broadening in photoelectron spectroscopy set this cross-section sufficiently low that most measurements relying on single photon absorption events per pulse per molecule cannot utilize the full flux achievable at a low repetition rate X-ray FEL. A higher repetition rate will therefore lead to optimal use of photons as compared to lower repetition rate sources with similar integrated flux. All methods mentioned above will therefore benefit from the machine parameters. Lower-repetition-rate FEL sources like LCLS-I make photoelectron spectroscopy and X-ray fluorescence spectroscopy difficult at best, and generally ineffective. Consequently, LCLS-I experiments have emphasized Auger electron and photo-ion detection, but these methods do not lend themselves to unambiguous interpretation. Compared to Auger spectroscopy, photoelectron and X-ray fluorescence spectra can be simulated with higher reliability; the final states of photoemission are cationic in contrast to the more complex dicationic states after Auger decay. Multi-particle coincidence (MPC) techniques are based on the simultaneous detection of multiple photo-ions, electrons, or both emerging from a *single* molecule due to the absorption of a *single* X-ray photon. This tight constraint absolutely requires a high repetition rate source and up until now these measurements were most successfully performed on ground-state systems at synchrotrons. Implementation of MPC techniques as a probe of optically generated valence excited state dynamics represents an exciting and novel opportunity for studying chemical dynamics in isolated molecular systems that requires the capabilities of a source like LCLS-II.

Nonlinear, time resolved X-ray methods have been proposed in recent theoretical studies [36]. Robust implementation of these methods requires high repetition rates and high peak flux. The simplest in the developed experimental protocols is an X-ray pump-probe experiment, in

which a first pulse resonantly excites a highly localized coherent superposition of valence electronic states that propagates through the molecule. This wave-packet is probed at another location by a time delayed X-ray pulse (of similar or different energy than the first pulse). The experiment probes the spatial extent of electronic wave-functions through the molecule, for instance by transient shifts in core photoelectron lines. The spatial shape of wave-functions is a sensitive probe for electron interactions as comparative approaches between mean field and highly correlated methods show (see [35] and references therein). Experimental schemes that aim at a better determination of electron correlation in optically excited states employ pulse pair Raman excitation leaving the molecule in a valence excitation without creating a core hole. These schemes are more advanced and the full experiment requires at least three coherent time- and space-separated X-ray pulses.

2.3.1.3 Molecular Energy Conversion in Complex Chemical Environments

Proteins provide compelling examples of the diversity of chemical phenomena that can be controlled with atomically engineered reaction environments. Proteins control photo-induced charge transfer in photosynthesis and photo-induced isomerization in bacteriorhodopsin to fuel life. Proteins also use photo-induced charge transfer and photoisomerization to control circadian rhythms, to see, to repair DNA, and to trigger motion [37, 38, 39, 40, 41, 42]. Such systems provide clear demonstrations of effective light conversion for a wide range of biological processes. By understanding, mimicking, and manipulating these ultrafast processes, we have the opportunity to identify both molecular and supramolecular design rules for constructing artificial light-conversion materials and devices.

Photo-isomerization reactions in bacteriorhodopsin highlight the current limits of our present understanding of how a protein environment controls chemical reactivity. Ultrafast spectroscopy measurements have demonstrated that photo-isomerization of the retinal chromophore differs significantly from photo-isomerization in solution [43,44]. Ultrafast spectroscopy studies on bacteriorhodopsin mutants also demonstrate that modification of the protein environment significantly influences the photo-isomerization dynamics and reaction pathway. While biochemical synthesis and ultrafast optical measurements have a demonstrated ability to influence and observe the outcome of photon-driven chemistry, these studies have not been able to explain these observations or identify the physical and chemical properties of the protein environment that dictate the outcome of photochemical reactions. Understanding how proteins control chemical reactivity requires time-resolved studies of the structure of both the isomerizing chromophore and the protein environment.

The ability of ultrafast X-ray spectroscopic tools to allow excited molecular dynamics to be followed with atomic spatial resolution and atomic and site selectivity presents a unique opportunity to characterize chemical dynamics with a level of detail presently unachievable. Nobel Laureate Arieh Warshel has proposed that proteins control chemical reactivity by sculpting an electrostatic environment that stabilizes the transition state structure, but this critical hypothesis has been controversial and remains largely untested. Characterizing how the local reaction environment, be it a protein, solvent, or catalytic interface, influences the dynamic

evolution of the excited state electron density is essential for understanding chemical catalysis. These measurements, coupled to ultrafast structure determination at LCLS-I and advanced molecular theory and simulation, will enable chemical dynamics to be characterized with unprecedented detail. Such characterization will be the first step towards the control of photo-driven phenomena in artificial molecular systems on a level analogous to biological systems.

Inorganic complexes catalyze a wide array of chemical reactions and strongly absorb visible radiation, which makes them targets for the development of artificial photosynthetic catalysts. Research in artificial photosynthesis uses natural photosynthesis as a template for designing materials and devices to efficiently and cost-effectively convert photons into fuel. Following light absorption, the first step in natural photosynthesis is the fast and efficient splitting of light-driven electronic excited states into charge-separated electrons and holes [45]. The effective design of an artificial photosynthetic reaction center must incorporate ultrafast charge separation and minimize the perturbation to the nuclear structure induced by the light-driven electronic excited state to inhibit undesirable photochemical and photophysical relaxation channels. Consequently, the ability to understand and eventually design molecular systems for solar applications requires a detailed understanding of electronic excited-state chemical dynamics and the molecular properties that govern them.

Scientists have designed and synthesized a wide variety of inorganic complexes that can generate charge-separated excited states, but ultrafast relaxation of the charge-separated state greatly inhibits performance in many of these systems because a photocatalyst must reside in the excited state to drive a chemical conversion [46, 47,48]. Controlling the excited-state dynamics of inorganic artificial photosynthetic systems first requires the characterization of the time-dependent charge distribution of the electron and hole and how this charge distribution influences the rate of electron excited-state relaxation.

Understanding and eventually controlling molecular conversion of light to electricity and fuel in inorganic chemistry requires understanding the non-adiabatic and correlated dynamics of electronic excited states, which in turn requires understanding the coupled motion of electrons and nuclei. This proves more challenging in inorganic chemistry than in organic chemistry because of the myriad energetically accessible electronic spin states and stronger spin-orbit coupling in these systems. X-ray spectroscopic methods provide an excellent set of tools for studying these aspects of electronic structure and dynamics. As highlighted above, soft X-ray spectroscopy, including X-ray absorption, fluorescence and inelastic X-ray scattering, provides a unique set of tools for tracking time-dependent changes in charge distribution of atomic specificity and Ångstrom resolution.

2.3.1.4 Mechanistic Studies of Catalyzed Reactions at Interfaces

Understanding the fundamental dynamics of catalysis

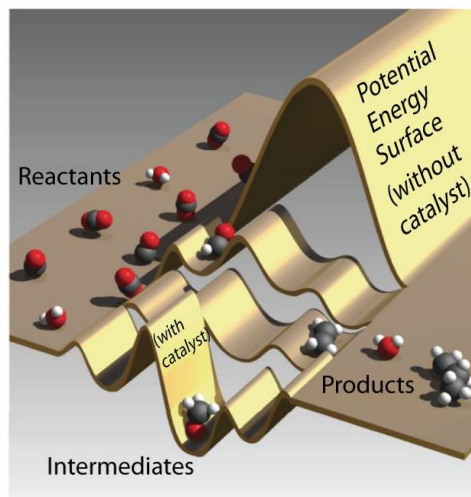


Figure 4. Schematic picture of the potential energy surface of a surface chemical reaction from reactants to products via 3 different intermediates.

The reaction mechanism of many surface chemical reactions contains several elementary dynamical steps proceeding on different time scales. Figure 4 shows a schematic reaction energy diagram going from reactants to products via different intermediates. The number of molecules that react at a specific time during a catalytic reaction is usually very low (typical turnover frequencies of a good catalyst is one per surface atom per second). If we monitor the various species on the surface using *in situ* techniques under steady-state reaction conditions we might observe the adsorbed reactants and products as well as intermediates as shown in the figure. The intermediate (with catalyst) in the deep energy well will have a long residence time. However, the other two intermediates will only be populated during short time-scales and the overall concentration at steady state conditions will be very low. In order to understand the reaction mechanism it is essential that the transient short-lived intermediates can be detected and characterized under ultrafast time scales.

To achieve a predictive understanding of surface chemical reactions, we need to determine the molecular forces, and the motions that these forces induce during chemical change, that lead to bond making and breaking at surfaces with atomic specificity. Furthermore, there are experimental indications from gas-surface dynamics studies that important energy dissipation channels exist that result in strong non-adiabatic coupling in adsorption and dissociation processes [49]. It has been suggested that the non-adiabatic damping of vibrational motion close to the activation barrier for the dissociation process is due to creation of electron-hole pairs in the substrate. It is therefore important to probe not only the transient species but also how charge and energy flow in the surface region during each individual elementary reaction step.

An ultrafast laser pulse can induce a rapid rise in the electron and phonon temperatures, leading to an increase in the population of reactive species [49, 50, 51, 52, 53, 54]. An

investigation of the dynamics of CO desorption from a Ru surface has been performed at the LCLS. This study identified a transient precursor state weakly interacting with the surface and clearly points the way towards a new era of surface dynamics [20].

The X-rays from LCLS II would allow probing the surface with X-ray emission spectroscopy (XES), X-ray absorption spectroscopy (XAS) and X-ray photoelectron spectroscopy (XPS). All these techniques have the unique ability to provide an atom-specific probe of the electronic structure and application of these techniques to ultra-fast spectroscopy have opened entirely new windows into the realm of atomic motion and electronic structure rearrangements, and thereby chemical dynamics. In particular, using selective excitation in the resonant inelastic X-ray scattering aspect of XES at different incident energies corresponding to specific XAS resonances, we can selectively detect unique subensembles of molecules on the surface that may exist only transiently [55]. By rapidly refreshing the reaction surface between each pulse, the high repetition rate at LCLS-II would allow for extremely rapid measurements of data, doing in minutes what currently at LCLS takes one week. This would open up for systematic investigations with various temperatures, pressures, laser power, surface compositions and structures that currently are not possible. Furthermore, nonlinear spectroscopy such as stimulated emission could allow for much higher fluorescence yield and in a pump-probe scheme would allow to follow electron transfer on 1 fs time-scales during reactions. The high repetition rate would also open for XPS that today is not realistically possible due to severe space charge limitations at low repetition rate machine such as LCLS. Chemical shift measurements will give a high chemical specificity for both molecules on the surface and the substrate.

Since XES and XAS are photon-in and photon-out spectroscopies and the laser excitation energies are typically below any molecular electronic transition in the gas phase, these experiments can also be carried out at high pressures. In the case of XPS, differential pumping will allow for pressures in the few torr range which can be extended to even higher pressures using photon energies in the few keV range giving rise to high kinetic photoelectrons with a substantially longer mean free path. Sample environments can be developed to create unique environments in terms of both single crystal substrates and supported nanoparticles in contact with either gases or liquids allowing for both thermal and photo- and electro- induced chemistry.

2.3.2 Materials

The sustainability of modern society depends on our ability to convert and use energy efficiently with minimal environmental impact. Solutions to our energy problems require our ability to understand, design and control the physical processes of materials behind energy conversion, dissipation, storage and transport. Novel, coherent X-ray sources that can access the ultrafast time-scales of these processes with atomic-scale resolution and element specificity will transform our potential for new materials solutions. LCLS-II will provide revolutionary opportunities for addressing these frontier questions from the level of electrons and atoms and the long-range, mesoscopic to macroscopic properties that emerge. These opportunities arise from the unprecedented combination of high-repetition rate, polarization control, short pulse duration

and high coherence of LCLS-II. Examples of problems where the LCLS-II will have a transformative impact are: (i) the mechanisms for emergent behavior in correlated materials, (ii) understanding the dynamics of energy dissipation in nanoscale materials for novel electronics and optoelectronics (graphene, etc), (iii) the crossover between the ballistic and diffusive regime of heat and charge transport in nanoscale materials, (iv) energy transport in photovoltaic and thermoelectric materials, (v) spintronics and information storage, (vi) ultrafast probes of non-trivial atomic correlations in non-periodic systems such as glasses and soft matter, and the role that inhomogeneity plays in determining the tunable properties of advanced materials.

It is natural to look towards ultrafast methods for both initiating and measuring dynamics associated with the above problems. For example, LCLS-II will allow momentum-resolved spectroscopic measurements of the evolution of spin, charge and nuclear structure in both equilibrium and far-from equilibrium conditions. Combinations of time and frequency domain-methods are required to access this information. For near equilibrium studies the combination of high-repetition rate and short pulses are key to achieving high temporal resolution without the measurement dramatically altering the system under study. For far-from-equilibrium studies, especially in extreme environments, the high peak power of the FEL allows one to concentrate the photons during the brief instants in which the system can be held at such conditions. In both cases the coherence properties of the pulse allows for unprecedented imaging of spatial and temporal inhomogeneity. Below we expand upon a few examples of where the LCLS-II will enable scientists to answer frontier problems in materials science.

2.3.2.1 What are the Mechanisms of Emergent Phenomena Exhibited in Quantum Materials?

Grand challenges of correlated materials remain at the forefront of modern condensed matter physics. LCLS-II will enable exquisite new spectroscopic tools for investigating the complex interplay of the intertwined orders in quantum materials on the fundamental time- and length-scales, aimed at uncovering the mechanisms of emergent phenomena.

Many phenomena exhibited by correlated materials are known as “emergent”, in which electrons form a variety of exotic quantum phases bearing little resemblance to the expectations derived from the constituents of the materials alone. Because many of the emergent quantum phases exhibit extreme properties, such as high-temperature superconductivity and colossal magnetoresistance, correlated electron materials may satisfy our need for future smaller, faster, and lower-power electronics. Tailoring these materials for applications requires an understanding of the interplay between electron correlation (including their, charge, orbital and spin degrees of freedom) and nanoscale heterogeneity.

To understand such complex interplay requires a paradigm shift from the conventional solid state theories. The phase diagrams of such materials are astonishingly rich, with multiple phases occurring on comparable energy scales at high temperatures [56]. Moreover, local forms of “fluctuating order” extend well outside the corresponding phase boundaries [57]. It is increasingly clear that these orders cannot be thought of as isolated phenomena, or even strictly as

“competing orders”, but that rather they are “intertwined” in a complex manner, all reflecting different aspects of the underlying quantum physics of the strongly correlated electron fluid. Even precisely identifying the nature of the broken symmetry states that occur in these materials has proven to be a remarkably difficult undertaking, and disentangling the nature of the mesoscale order that arises at intermediate time and length scales is a still more daunting task.

The control of emergent properties in quantum materials is a further grand challenge of materials science. It is now possible to use ultrafast excitations to alter the strongly intertwined spin, charge and lattice degrees of freedom, leading to new transient states that are inaccessible in thermal equilibrium [58,59,60,61]. For example, photo-induced metal-insulator transitions [60] and even superconductivity [61] have recently been reported in transition metal oxides. These transient non-equilibrium phenomena, and their relation to equilibrium properties are still poorly understood. These are remarkable examples of non-thermal phenomena. Much effort is underway to identify and speed up the limiting time-scale of material switches, which has obvious applications for advanced technology including in memory and storage applications.

Angle-resolved photoemission spectroscopy (ARPES) [62] and inelastic and resonant inelastic X-ray scattering (IXS [e.g. Sette] RIXS [63]) are directly sensitive to the single-particle spectral function and collective excitations of materials respectively. The high-repetition-rate femtosecond pulses from LCLS-II will allow these methods to be extended to the time-domain with exquisite sensitivity and resolution that is not possible with existing sources. All time-domain methods including Fourier transform [27] and multidimensional coherent spectroscopy allow for the combination of the best spectral resolution and phase-sensitive detection but are limited by the jitter and/or interferometric stability when pushing to high energy. Optimal time-resolved or frequency-domain techniques require an appropriate balance between spectral and time resolution. For example, the high repetition rate and tunable control over pulses will enable new high-resolution methods based on multiple-pulse ARPES or IXS, with unprecedented spectral resolution limited by the inverse of the pulse pair time delay. When combined with all time-resolved frequency domain spectroscopies this can provide unique opportunities to uncover the dynamic mechanisms responsible for emergence in both equilibrium and photo-induced non-equilibrium conditions.

Tracking the evolution of collective excitations via RIXS

Rapid development of RIXS in the soft X-ray regime has allowed the investigation of low-energy excitations at an energy range of 100 meV that bear the hallmark of the symmetry-broken states. With this resolution, a number of the collective excitations, such as magnon [64], paramagnon [65], triplon [66], two-spinon [67], phonons [68], and orbiton [67], have been resolved in the energy-momentum space. The need for higher energy resolution cannot be overstated. The new LCLS-II instrumentation would make possible an ultrahigh-energy-resolution RIXS instrument with complete polarization analysis of the scattering photons that can resolve collective charge and magnetic excitations with energies comparable with the characteristic energy scales near the Fermi level (< 30 meV) (for example, the superconducting gap and pseudogap in high- T_c superconductors [62]), with the temporal resolution (>70 fs) required for

studying the dynamics of these excitations. Measuring low-energy excitations while the sample is absorbing watts of energy from the X-ray beam requires careful thermal management. This can be achieved with the development of rapid sample translation systems and high capacity cryostats. These equilibrium state experiments are not only important for a fundamental understanding of the novel state, but also provide complementary information for the future time domain experiments.

Furthermore, the proximity of various phases in the phase diagrams, especially near a quantum critical point, can partition the material into electronically distinct domains that experience temporal and spatial fluctuations over many time- and length-scales. Quasistatic and dynamic inhomogeneities are ubiquitous in correlated systems. Momentum-resolved RIXS experiments, which can measure these responses, would reveal how, for example, the spatial fluctuations of the gap in a high- T_c superconductor are connected to the collective dynamics, or how the lattice relaxes locally in response to charge transfer that underlies Jahn-Teller phenomena in manganites and multiferroics. This would yield tremendous insights that would be felt across many areas of fundamental materials physics.

Time Resolved RIXS: Tracking Bosonic Excitations

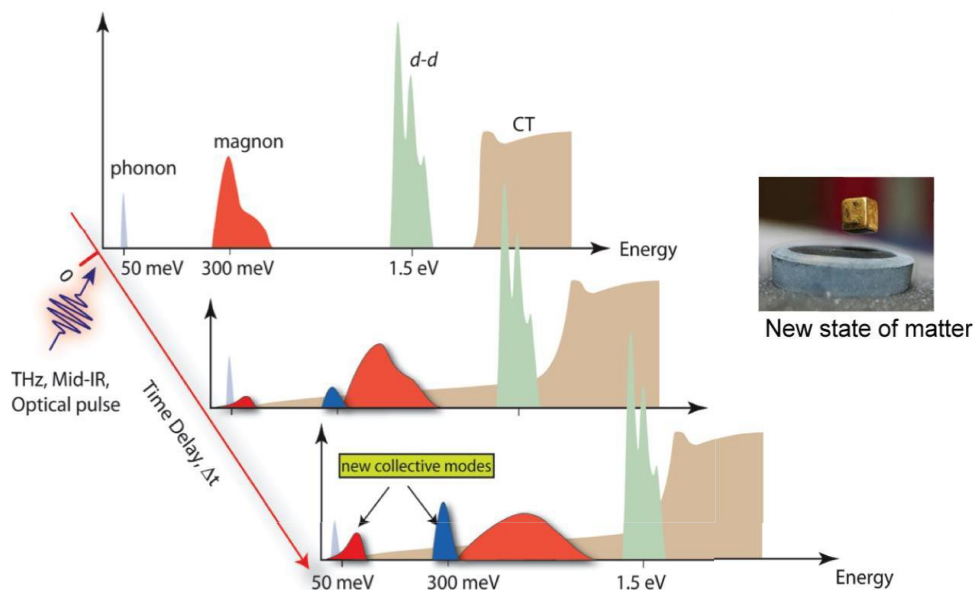


Figure 5. RIXS instrument at the LCLS-II with uncertainty-principle-limited energy and temporal resolution can track the evolution of the elementary excitations in the photo-induced transient states. If a new symmetry-broken state is induced, new collective modes associated with this new state could also be detected. “d-d” and “CT” stand for the excitations with d-orbital manifold and charge transfer excitations, respectively.

Time-resolved RIXS at enabled by the high-repetition-rate ultrafast pulses from LCLS-II will be a unique probe of collective excitations of photo-excited transient states. As schematically shown in **Figure 5**, one can readily probe the temporal evolution of elementary excitations, such as magnon and phonons during a photo-induced transient state. Momentum-dependent

information about these elementary excitations is inaccessible using table-top time-resolved spectroscopy, and is essential to identify the dominant interactions relevant to the underlying electronic states. Furthermore, with sufficient energy resolution enabled by the high brightness LCLS-II beam, one could also detect collective modes arising from the symmetry-broken state induced by an ultrafast photon pump pulse. The energy-momentum dispersion and the time scales of the collective modes bear the hallmarks of the photo-induced new phase.

2.3.2.2 Analysis of Elementary Scattering Processes at the Fermi Surface via ARPES

ARPES is a powerful tool for analyzing electronic structures with high energy and momentum resolution and has played a crucial role in the study of correlated materials, particularly the high- T_c superconductors [62]. The high-repetition-rate ultrafast X-ray pulses from LCLS-II will augment the capabilities of ARPES. These femtosecond X-ray pulses that will extend ARPES into the time-domain (Tr-ARPES) can access the dynamics and collective excitations of band structures and order parameters of broken symmetry ground states [69]. Spin resolved ARPES (S-ARPES) requires a high repetition rate source and will provide new insights into the electronic states of spin-textured materials [70]. LCLS-II will also allow for high energy, keV measurements (H-ARPES), which provide sensitivity to bulk electronic structures and buried interfaces [71,72].

Currently Tr-ARPES and high efficiency S-ARPES experiments are primarily performed using table-top laser systems at low photon energy (< 10 eV), which only have finite momentum access, insufficient to cover the full Brillouin zone. High harmonic generation laser systems permit Tr-ARPES measurements over much of the Brillouin zone in most cases, but are limited to low pulse energy and sub-keV photon energies. LCLS-II enables a new era of Tr-ARPES and S-ARPES, where the high repetition rate mitigates space charging and increases the dynamic range. Furthermore, the X-ray FEL pulse with tunable time-energy bandwidth within the uncertainty principle allows Tr-ARPES and S-ARPES to be performed at optimal resolution; something that is difficult for HHG-based Tr-ARPES. In addition, the high photon flux due to the high repetition rate could enable S-ARPES and Tr-ARPES in a single combined measurement. Such an instrument will allow us to probe the full single-particle dynamics near the Fermi surface in energy, time, momentum, and spin domains.

Finally, LCLS-II also enables bulk sensitive H-ARPES using multi-keV photons, which is currently limited by low cross-sections. LCLS-II's multi-keV capability at high repetition rate mitigates this drawback of H-ARPES. The prospects for femtosecond time-resolved H-ARPES are exciting. Fundamental new insights about the interfacial dynamics of heterostructures in correlated materials may be obtained.

2.3.2.3 Dynamics of Energy Relaxation Processes in Modern Materials and Nanostructures for Energy Conversion

Heat transport at the nanoscale

The problem of heat conduction at nanoscale dimensions [73] is of fundamental interest and sets stringent physical limits to the current trend of shrinking micro-electronic devices. At

nanometer length-scales comparable with the phonon mean free path, conventional heat diffusion based on Fourier law does not hold and can even exhibit the opposite ballistic conduction behavior [74]. At the same time, modern materials processing enables the fabrication of nanoscale structures that can be designed to obtain some control of phonon properties for thermoelectric applications [75, 76] as well as for “phonon engineering” analogous to photonics in optics[77]. However, progress is limited by the lack of probes of the transport dynamics across all phonon wavelengths with subpicosecond resolution.

There are clear opportunities for a transformative impact by LCLS-II. Although there are extensive optical and time-resolved X-ray diffraction reports on the dynamics of phonon propagation we still lack detailed, momentum-dependent information on, for example, the mean free path of short-wavelength phonons which are the main carriers of heat [73]. Neutron scattering measurements of phonon branches provide momentum resolution [78] but cannot access the intrinsic dynamics of the fundamental phonon propagation and scattering processes. A recent LCLS experiment on bulk GaAs [79] showed that a highly-nonequilibrium distribution of high-wavevector phonons is observed at ~ 5 ps after laser photoexcitation. This behavior was observed in other semiconductors and hints at being a somewhat general behavior. This experiment demonstrates the feasibility of such measurements and paves the way for a new momentum- and time-resolved technique for measuring, microscopically, the phonon contributions to the thermal conductivity and their anharmonicity at the nanoscale. The future capabilities of LCLS-II will be transformative: (1) high repetition rate will provide exquisite signal to noise, (2) wavelength stability promises a tremendous increase in the amount of useful data in experiments such as [79] with the ability to probe with high momentum resolution throughout the Brillouin zone, (3) the ability to reach higher photon energies opens the possibilities of measuring higher momentum transfer or higher Brillouin zones.

Relaxation of charge carriers by phonon emission in materials for energy conversion

The relaxation of energetic charge carriers by phonon emission is an important energy challenge in modern functional materials. The performance of photovoltaic conversion and optoelectronic materials is typically limited by the effect of electron-phonon scattering in carrier mobility. In thermoelectrics the figure of merit has remained low because of challenges in designing materials with low thermal conductivity that can also transport charge efficiently. Many of these challenges could be addressed by a top-down control of phonon propagation and decay channels. For example in thermoelectrics the thermal conductivity could be reduced with a clever design of nanostructures to scatter the main carriers of heat, thus increasing the figure of merit [75, 76].

LCLS-II provides new opportunities to understand the fundamental processes of energy dissipation with the ability to probe, with large signal-to-noise, the dynamics of the lattice as carriers relax back to equilibrium. As mentioned above, results from LCLS-I show that the emission of zone boundary phonons in bulk GaAs occur on the ~ 5 picosecond time scale [79]. The high repetition rate of the new machine will push these measurements to new level enabling sensitivity to small changes in the weak X-ray diffuse scattering, for example due to the emission

of non-equilibrium phonon populations by hot carriers in nanoscale films and two-dimensional materials.

2.3.2.4 How Does Ultrafast Magnetization Depend on the Nanoscale Dynamics?

The recent observation of all-optical magnetic switching provides a radically new approach to reversing the magnetization of a sample using ultrafast and non-thermal effects of circularly polarized femtosecond laser pulses as the external stimulus [80]. Such an all-optical switching scheme can also be used to write nanoscale, topologically-protected magnetic structures [81] that can be viewed as magnetic bits in future data storage devices. This raises two questions for fundamental science whose answers will have a significant impact on technology.

First, what is the origin and proper theoretical description of the strongly non-equilibrium state following optical excitation? This state is commonly described by phenomenological assigning an electron temperature out-of-equilibrium with the lattice. It is, however, currently debated to what degree spin angular momentum is transferred to the lattice. This non-equilibrium state is also the cause of so-called superdiffusive spin currents that can transport spin angular momentum across nanometer distances [82].

Second, what are the channels for ultrafast angular momentum transfer between magnetic sub-lattices? Currently, all-optical switching requires the use of transition metal rare earth alloys with antiferromagnetic alignment of the elemental magnetic constituents. Understanding the ultrafast spin transfer processes and possible changes in the magnetic exchange coupling with the sample far from equilibrium will enable us to predict the use of more commonly accessible magnetic materials for future applications.

LCLS-II provides a path toward techniques to address these fundamental mysteries of nanoscale magnetism. Seeded, polarized, femtosecond soft X-ray pulses from LCLS II will be instrumental in providing these answers either via resonant scattering [23] from repetitive processes or via single-shot holography of non-periodic processes [6]. Current nanoscale magnetic images at LCLS reveal a modest 50-100 nm spatial resolution. High-flux circularly polarized X-rays at LCLS-II could allow single-shot snapshots of magnetic domain formation on a ~10 nm length scale.

2.3.2.5 Electron Dynamics Following THz Excitations of Solids

One of the great drivers for understanding the spectacular, yet complex properties of quantum materials is the desire to ultimately transcend the use of semiconductor electronics [83]. Clearly, probing materials properties in the time domain is of technological interest, e.g. in establishing the speed limits for electronic switching [25]. However, it has also served basic science, allowing us to disentangle competing interactions in complex materials in the time domain. Exploring the materials' response, such as insulator-metal transitions, to external electro-magnetic stimuli will be instrumental for developing future oxide electronics applications [84]. The extended THz spectral region is of special importance: intense single cycle THz pulses mimic the ultimate electrical switch in devices while narrow-band multi-cycle stimuli launch lattice dynamics that may ultimately allow us to induce novel forms of superconductivity [61].

Disentangling the complex interactions between electronic, spin, and lattice degrees of freedom of quantum materials in the time domain is usually done using multi-cycle electromagnetic excitation. In this way energy can be directly pumped into quasiparticle excitations such as phonons that may trigger an electronic response for instance leading to insulator-metal transitions [85]. A very different approach has recently been demonstrated at LCLS [86]. It is based on pumping momentum into the electronic system via the use of single cycle THz pulses [87]. In a Mott insulator this was shown to lead to an increase of the electronic hopping kinetic energy, causing the system to become metallic for THz electric field strengths above 0.1 GV/m. This opens the door for novel ways to manipulate electronic correlations in quantum materials.

The 100 kHz operation of LCLS-II represents nothing less than a game changer. Intense single-cycle THz pulses (0.1-1 ps duration, giving 1 GV/m electric field strength) can be ideally generated using electron bunches accelerated via superconducting accelerator technology. Seeded soft X-rays are ideally suited to study the interplay between electrons and spins on the nanometer length and on the femtosecond time-scales. Resonant inelastic X-ray scattering will be able to probe spin and electronic excitations in time-energy space close to the Heisenberg limit. Finally the high repetition rates at LCLS-II will enable soft X-ray time-resolved photoemission studies with bulk sensitivity.

2.3.3 Biology

The understanding of life and the biochemical processes that sustain it has obvious importance to society at large. It is primarily through structural knowledge, which may be used to deduce function of the proteins, complexes and control pathways involved in disease, that one begins to devise a cure or treatment. In the search for discoveries that directly impact society, there can be no better example than the determination of the structure and function of biomolecules and processes involved in a human disease and the use of this information to design new drugs to control or cure the disease. Prominent examples where structures played a key role in drug development include HIV protease, reverse transcriptase, and fusion inhibitors that made HIV a largely manageable disease; the kinase inhibitor Gleevec that is remarkably effective in treating certain types of leukemia; and the recent BRAF kinase inhibitor Zelboraf that is used to treat metastatic melanoma in patients with a certain mutation (about 50% of the patients have this mutation).

As illustrated in Figure 6, X-ray macromolecular crystallography is today the primary technique used to solve the structure of life's machinery on the molecular and atomic levels and it is expected to continue to be as important in the future.

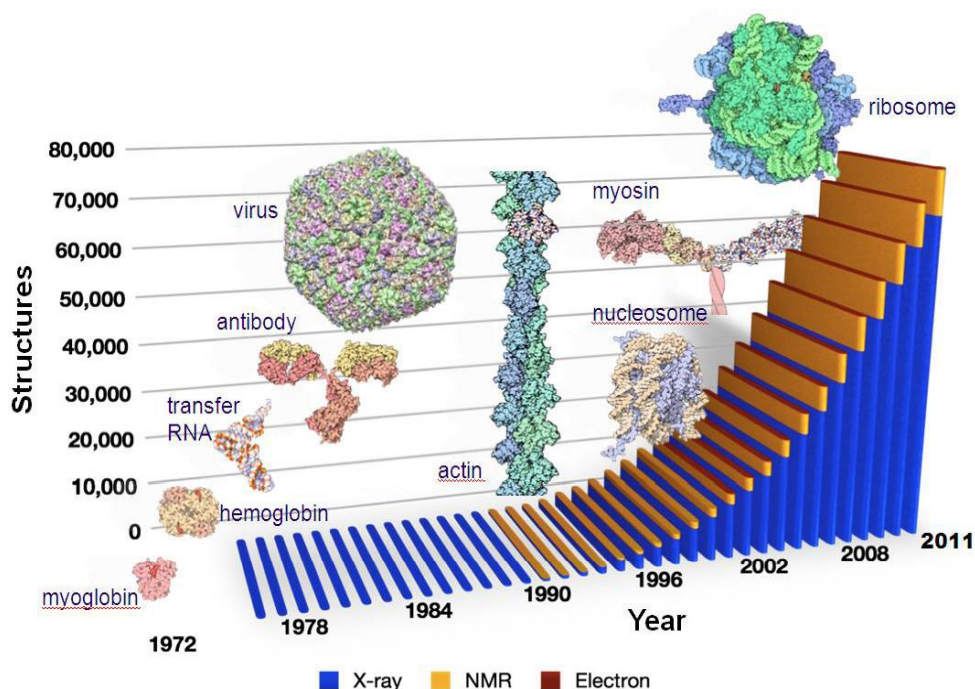


Figure 6: Cumulative number of structures in the Protein Data Bank and breakdown of structures solved by different techniques. (C. Abad-Zapatero, *Acta Cryst. D68* (2012)).

The technique of macromolecular X-ray crystallography has progressed from studying individual proteins and enzymes in a reductionist approach to biology to providing a system-level view of large protein assemblies, in many cases interacting with DNA, RNA, lipids and carbohydrates that carry out many of the key biological functions. As the macromolecular assemblies being investigated increase in size and complexity, the essential requirement of growing macroscopic diffraction-quality crystals becomes more and more challenging. Despite more than half a century of intense efforts, determining crystallization conditions for biological macromolecules remains unpredictable and requires exhaustive experimentation. The inability to obtain large-enough high-quality, well-diffracting crystals for conventional synchrotron-based studies is a significant limitation to macromolecular crystallography and structure determination of large complexes and of some other classes of proteins. The problem is exacerbated in cases of integral membrane proteins, which are very often more difficult to crystallize than soluble proteins. This represents a very important challenge in biology because many of the important processes of life occur at the boundary between the cell interior and the outside, *i.e.* at the membrane lipid bilayers, and many of these processes are today very poorly understood due to the lack of structural information. As of mid-2012, out of more than 82,500 structures deposited in the Protein Data Bank, fewer than 350 represent membrane proteins. Any tool that can be developed to facilitate the structural determination of membrane proteins would be immense value. Likewise, the number of macromolecular complexes determined is still dwarfed by the number of known individual structures.

In addition to the challenges of crystallization, the problem of X-ray-induced radiation damage has hindered progress in structure determination, in particular at high resolution. Nearly all crystals used in synchrotron experiments must be cryogenically cooled to minimize such damage. Cryo-cooling precludes the study of conformational changes that are often present at room temperature. There are also active metal centers in some very radiation sensitive proteins, such as photosystem II, that are rapidly photo-damaged by the synchrotron beam before an intact structure can be determined.

LCLS-I has provided a path to discovery for many more difficult-to-crystallize or easily-damaged proteins by allowing much smaller crystals to be used successfully when compared to what is possible at conventional synchrotron X-ray sources. The revolutionary ultra-bright and ultra-short X-ray pulses from LCLS-I have removed the link between crystal size and radiation damage. The extremely high peak-power of the pulses permits measurable and interpretable high-resolution diffraction from crystals that are typically of a micron size. The femtosecond duration of the LCLS pulse lets diffraction outrun radiation damage, leading to a “diffract-before-destroy” approach that allows X-ray doses far above the conventional damage threshold. By exposing many individual crystals to the beam one-by-one, fully hydrated and at room temperature, a complete undamaged diffraction data set can be determined at high resolution, despite the fact that the crystals are destroyed by the beam. In this way, LCLS-I pulses can be used to achieve higher resolution for crystals that are sensitive to radiation damage, avoiding the loss of resolution caused by even a single exposure at synchrotron sources.

LCLS-II will provide new capabilities to study biological samples using the so-far-inaccessible photon energy ranges between 2 and 5 keV and above 11 keV. In general, higher energy is desirable for data collection to higher resolution and using heavy atoms with high-energy absorption edges for *de novo* phasing. However, in certain situations, the currently inaccessible range between 2 and 5 keV can be ideally suited for XFEL crystallography experiments, using absorption edges in this energy range or using single particle structure determination. LCLS-II will provide new opportunities by extending photon energy ranges with higher repetition rate and/or higher power per pulse by extending the fundamental energy into a range where previously only weaker higher harmonics were available at LCLS-I.

2.3.3.1 Nanocrystallography on Ever Smaller Crystals

Published results from LCLS-I have demonstrated interpretable diffraction from crystals as small as 6x6x6 unit cells (less than 300 unit cells total). However, these results were obtained using soft X-rays below 2 keV, where the resolution was limited. Studies of crystals of similar sizes using hard X-rays between 6 and 10 keV have not surprisingly yielded much weaker signals due to the reduced scattering cross-section at higher energies. Published results from LCLS-I typically utilize much larger crystals for high resolution structures using hard X-rays, with crystals of 5 microns or more being relatively common [88, 89]. Only for well-known proteins with high quality small unit cell crystals such as lysozyme could crystals size around or below 1 micron be used for structural studies [9]. For larger unit cell samples such as Photosystem II [89], much larger crystals were used, typically along with lower photon energies, in an attempt to

maximize the signal by utilizing the longest wavelength that can support the desired or achievable resolution. LCLS-II can have a large impact on difficult-to-crystallize samples, where many small crystals are obtained but no high quality large ones. It is reasonable to expect that many of these small crystals will have limited quality. It is likely that the presence of defects is one of the factors limiting in the growth of crystals. Therefore, with crystals of limited diffraction quality, optimizing the photon energy will be critical to maximize the information content from every shot. Photon energies between 2 and 5 keV can support resolution down to 4-2 Å with detectors arranged to collect diffracted light in all forward directions ($2\theta \leq 90^\circ$). Even with a planar detector with 2k x 2k pixels covering a smaller solid angle, resolutions down to 3.5 Å should be possible at 5 keV. Any structural information of extremely large protein complex with unknown structures can be more than sufficient to produce new key scientific knowledge. LCLS-II, with its ability to produce high-peak-power pulses in the 2-5 keV range, will enable the study of smaller and smaller crystals while not sacrificing too much on the resolution.

2.3.3.2 *De Novo* Structure Determination Utilizing the Extended Photon Energy Range of LCLS-II

In order to have a true impact on structural biology XFELs need to enable structural determination of molecules that are entirely unknown *a priori*. This requires the ability to solve structure *de novo* using independent phasing techniques. Recently, this was demonstrated to be feasible at LCLS using Single-wavelength Anomalous Dispersion (SAD) phasing with gadolinium bound to lysozyme providing the anomalous signal above the 7.24 keV Gd L_{III}-edge [90]. Unfortunately, not every protein can bind heavy atoms suitable for such SAD experiments, but over 70% of all proteins contain one or both of the sulfur-bearing amino acids cysteine or methionine. Sulfur can be substituted by Se in these amino acids to take advantage of another widely used phasing method known as Multiple-wavelength Anomalous Dispersion (MAD). The MAD method is largely based on the anomalous signal from the K-edge of Selenium at 12.7 keV, and the LCLS-II project will widen the energy range to reach photon energies above 12.7 keV. This will open the door for phasing of a much broader range of protein crystals. LCLS-II will also allow phasing of entirely native sulfur-containing samples with access to photon energies close to the sulfur edge, allowing the anomalous signal to be maximized by taking advantage of the high repetition rate for in-vacuum serial femtosecond crystallography. The range 2-5 keV will also provide access to other potentially interesting absorption edges such as the L-edge of iodine, M-edges of actinides, and the K-edges of phosphorous and calcium, to name just a few. The SAD and MAD techniques, as well as other phasing techniques based on anomalous scattering, will benefit directly from the extended energy range of LCLS-II from below 5 keV and above the current high energy cutoff of ~11 keV.

Radiation-Damage-Free Structures at Room Temperature

Even in some macromolecules that can produce large crystals, synchrotron sources can cause radiation damage at the active site, so that the structure of metal centers in the molecules can only be determined in a radiation-damaged state. This can be a problem even at cryogenic temperatures, but is a particular issue for studies at room temperature. This can often be the case

for metallo-proteins, where X-ray absorption in the protein and buffer leads to multiple, very rapid radiation damage events, including photo-reduction of the metal centers, even under cryogenic conditions. The manganese cluster in photosystem II is an example, where it is not possible to determine the structure at high resolution in the most important states during the water splitting cycle. LCLS-I and LCLS-II can help obtain damage-free structures in chemically important states, and the increased energy range of LCLS-II will provide more flexibility to tune the photon energy to maximize the signal and the achievable resolution.

Increased Resolution Provided by Harder X-rays

The increased photon energy range of LCLS-II, up to 16 keV and above, will provide the opportunity to obtain higher resolution using strongly diffracting crystals in a damage-free way, improving on the current limitations of LCLS-I. Such higher photon energy will also benefit cases where only small crystals are available by allowing improved resolution for strongly scattering crystals. Increasing the resolution measurable implies a need for larger dynamic range detectors. Also, higher photon energies may lead to reduced quantum efficiency in current LCLS-I detectors. For structural biology, the need to measure every pulse separately will ultimately also lead to a need for new detector development to better utilize the LCLS-II capabilities.

2.3.3.3 Single Molecule Imaging

With pulse energy comparable to the current LCLS-I, smaller spot size optimized for given samples, and more efficient optics, it should be possible to obtain close to a factor of 1000 increase in effective pulse intensity compared to previous LCLS protein nanocrystallography experiments at 2 keV. In those experiments diffraction was observed from crystals only 6 unit cells across, i.e., less than 300 total unit cells. The integrated Bragg signal scales linearly with total unit cells, giving confidence that measurements from single objects with this achievable factor of 1000 can be obtained. While some loss of signal will come from using photon energies larger than 2 keV, it can be advantageous to do so from geometrical perspectives. The photon energy range between 2 and 5 keV has been identified as the optimal range for biological imaging of non-periodic single particles. This range provides a good compromise between scattering signal and resolution. Also, the reduced absorption compared to softer X-rays limits the damage during the pulse and improves the ability for the X-rays to penetrate a thick sample. The tender X-ray range (2-5 keV) provided by LCLS-II is expected to provide the capabilities to pursue non-periodic imaging at resolution approaching 1 nm. As for the case of crystallography, imaging techniques require every pulse to be detected separately and thus imaging is not expected to make use of the ultimate repetition rate of LCLS-II. However, with new detector development, it should be possible to increase the usable repetition rate by a factor of 100 compared to current LCLS-I capabilities. While the ultimate success of single molecule imaging remains speculative as of today, the availability of the 2-5 keV range at LCLS-II at these higher repetition rates would represent a key enabling step towards more involved studies aimed at pushing the limits of the technique.

2.3.3.4 Spectroscopy, Small and Wide Angle X-ray Scattering

As previously mentioned, the techniques of crystallography and imaging require large area detectors capable of reading out every pulse individually, and it is not expected that such detectors will operate at 100 kHz. However, other techniques relevant to structural biology do not require individual pulses to be read out, and allow integrating measurements over multiple pulses. Such techniques could still benefit from the damage-free capabilities of the short pulses of LCLS-II, provided the sample is replaced between every shot. With the use of liquid jets or other fast-flowing sample delivery systems, it will be possible to rapidly obtain X-ray spectra from samples like PSII [89]. The same would be true of small or wide angle scattering (SAXS/WAXS) patterns. Coupled with optical pumps, it will be possible to rapidly map electronic structure changes in photosensitive samples or obtain medium-resolution information on structural changes. Such techniques can directly benefit from the full increase in repetition provided by LCLS-II, in particular when using transition-metal L-edge spectroscopies.

2.4 LCLS-II Short and Long Term Plans

The LCLS facility will continue to evolve beyond LCLS-II, driven by the requirements of its developing science mission. Care is being taken in planning LCLS-II to assure that reasonable upgrade paths exist and that no likely path will be compromised by the LCLS-II design. This section gives an overview of the current thinking about how science at LCLS will make use of LCLS-II and how it could develop in the longer term. More detail is given in Chapter 18.

2.4.1 Short Term: Toward LCLS-II Commissioning (LCLS-II Project Period)

X-ray instrumentation for exploiting the capabilities of LCLS-II will come on line in a phased approach, much of it funded independently of the LCLS-II project. Existing instrumentation for low-repetition-rate hard X-ray experiments will require minimal adjustment to take advantage of some of the new features of LCLS-II, notably the extended photon energy range. The current scientific program will continue to advance. New hard X-ray mirror, beam diagnostic and detector upgrades already in progress at LCLS will provide compatibility with the LCLS-II high-repetition-rate hard X-ray and tender X-ray operation—though performance at very high rates may be limited by thermal issues for some of the optics. Exploratory studies, at low rate, are planned in order to develop diagnostics and detectors in the 2-5 keV energy range. These studies are a natural part of LCLS research on biological imaging with tender X-rays. New soft X-ray spectrometers already under development will advance X-ray emission and resonant inelastic X-ray scattering methods toward nonlinear and multi-dimensional spectroscopic studies. Soft X-ray end stations under development will be available for use at the LCLS-II soft X-ray beamline when it turns on.

2.4.2 Long Term: Five Years after LCLS-II First Light (Before 2025)

During the first five years of LCLS-II operation, development efforts will concentrate on optimizing the source capability and X-ray instrumentation to enable initial experiments

exploring the science thrust areas described above. Just as the first five years of LCLS operation have seen continuous development of FEL source capability, X-ray optics and diagnostics, experimental stations, detectors, and data management systems, the first five years of LCLS-II operation are expected to be a very rich period for development of new experimental capability and new techniques. Since a key feature of the LCLS-II source is its high pulse repetition rate, many new developments will be aimed at taking best advantage of this feature. Source development will provide better control of pulse parameters such as bandwidth and polarization, and develop the ability to precisely control multiple pulses. X-ray systems will be developed for managing the high average power levels of a high-rate FEL, and manipulating the carefully-crafted pulses without distortion. High-rate detectors and data systems will turn the torrent of experimental data into useable form efficiently. In addition, specialized experimental stations will be developed for carrying out complex experiments.

2.4.3 Longest Term Horizon (Beyond 2025)

In the long term, the LCLS facility at SLAC will be able to continue to grow. Space exists within the SLAC accelerator complex for additional superconducting accelerator sections, which could boost the energy range of high-repetition-rate FEL pulses into the hard X-ray region. Space is also available for additional undulator halls and experiment halls, all fed from the same accelerator complex. As the science impact of FEL sources becomes more widely felt, and as additional X-ray FEL sources come on line around the world, LCLS intends to continue to maintain its position as the leader in terms of science capability, serving a sizeable and growing user community.

2.5 References

- 1 LCLS-II Proposal, SLAC-I-060-001-000-00 (May 13, 2010).
- 2 Next Generation Light Source Facility, Proposal for CD-0 (December, 2010).
- 3 Report of the BESAC Subcommittee on Future X-ray Light Sources
http://science.energy.gov/~media/bes/besac/pdf/Reports/Future_Light_Sources_report_BESAC_approved_72513.pdf
- 4 Directing Matter and Energy: Five Challenges for Science and the Imagination (2007)
http://science.energy.gov/~media/bes/pdf/reports/files/gc_rpt.pdf
- 5 M.M. Seibert, *et al.*, *Nature* **470**, 78–81 (2011).
- 6 T. Wang, *et al.*, *Phys. Rev. Lett.* **108** 267403 (2012).
- 7 N. D. Loh, *et al.*, *Nature* **486**, 513–517 (2012).
- 8 H.N. Chapman, *et al.*, *Nature* **470**, 73–77 (2011).
- 9 S. Boutet, *et al.*, *Science* **337** (6092) 362 (2012).
- 10 R. M. Barends, *et al.*, *Nature* (accepted).
- 11 L. Redecke, *et al.*, *Science* **339**, 6116 (2012).
- 12 D. Starodub, *et al.*, *Nature Communications* **3**, 1276 (2012).
- 13 L. Young, *et al.*, *Nature* **466**, 56 (2010).

- 14 L. Fang, *et al.*, *Phys. Rev. Lett.*, **105** (2010).
- 15 S. Schorb, *et al.*, *Phys. Rev. Lett.* **108**, 233401 (2012).
- 16 T. Gorkhover, *et al.*, *Phys. Rev. Lett.* **108** 245005 (2012).
- 17 N. Rohringer, *et al.*, *Nature* **481**, 488–491 (2012).
- 18 T. E. Glover, *et al.*, *Nature* **488**, 603–608 (2012).
- 19 V. S. Petrovic, *et al.*, *Phys. Rev. Lett.* **108** 253006 (2012).
- 20 M. Dell'Angela, *et al.*, *Science* **339** 6125 (2013).
- 21 J. P. Cryan, *et al.*, *Phys. Rev. Lett.* **105**, 083004 (2010).
- 22 J. M. Glowina, *et al.*, *Opt. Express*, **18**, 17620 (2010).
- 23 C. E. Graves, *et al.*, *Nature Materials* **12**, 293–298 (2013).
- 24 W.S. Lee, *et al.*, *Nature Communications* **3**, 838 (2012).
- 25 S. de Jong, *et al.*, *Nature Materials* --- (2013).
- 26 J. N. Clark, *et al.*, *Science* **341**, 6141 (2013).
- 27 M. Trigo, *et al.*, *Nature Physics* (2013).
- 28 M. Harmand, *et al.*, *Nature Photonics* (2013).
- 29 S. Rutishauser *et al.*, *Nature Communications* **3**, 947 (2012)
- 30 M. Trigo, *et al.*, *Nature Physics* (2013) doi:10.1038/nphys2788
- 31 F. Plasser, F., *et al.*, *Theor. Chem. Acc.* **131**, 1073 (2012).
- 32 J. Tully, *et al.*, *J. Chem. Phys.* **137**, 22A301 (2012).
- 33 J. Gonzalez-Vasquez, *et al.*, *Phys. Chem. Chem. Phys.* **11**, 3927 (2009).
- 34 M. Ben-Nun, *et al.*, *J. Phys. Chem. A* **104**, 5161 (2000).
- 35 A. Kuleff, *et al.*, *Chem. Phys* **399**, 245 (2012).
- 36 S. Mukamel S. *et al.*, *Acc. Chem. Res.* **42**, 553(2009).
- 37 A. R. Cashmore, *et al.*, *Science*, **284** (5415):760– 765 (1999).
- 38 N.C. Rockwell, *et al.*, *Chem. Phys. Chem.*, **11**(6):1172–1180 (2010).
- 39 A. Sancar *et al.*, *Chemical Reviews-Columbus* **103**(6):2203–2238 (2003).
- 40 L. Song, *et al.*, *Science*, **261**(5123):891 (1993).
- 41 M. A van der Horst, *et al.*, *Accounts of chemical research*, **37**(1):13–20, 2004.
- 42 A.B. Wohri, *et al.*, *Science*, **328**, 5978 630 (2010).
- 43 L. Song, *et al.*, *Science*, **261**(5123):891 (1993).
- 44 P. Hamm, *et al.*, *Chemical Physics Letters*, 263(5):613–621 (1996).
- 45 G.R. Fleming, *et al.*, *Nature*, 333:190–192, (1988).
- 46 L. Duan, *et al.*, *Nature Chemistry*, **4**(5):418–423 (2012).
- 47 J.J. Concepcion, *et al.*, *Accounts of chemical research*, **42**(12):1954–1965 (2009).
- 48 M.R. Wasielewski, *et al.*, *Journal of organic chemistry*, **71**(14):5051–5066 (2006).
- 49 A.C. Luntz, A. Nilsson, L.G.M. Pettersson, J.K. Norskov (Eds.), *Chemical Bonding at Surfaces and Interfaces*. Elsevier, (2008).

-
- 50 E.H.G. Backus, *et al.*, *Science*, **310**, 1790 (2005).
- 51 L. Bartels, *et al.*, *Science* **305**, 648 (2004).
- 52 M. Bauer, *et al.*, *Phys. Rev. Lett.* **87**, 025501 (2001).
- 53 I.M. Fane, *et al.*, *Phys. Rev. Lett.* **97**, 186105 (2006).
- 54 C. Frischkorn, *et al.*, *Chem. Rev.* **106**, 4207 (2006).
- 55 M. Beye, *et al.*, *Phys. Rev. Lett.* **110**, 186101 (2013).
- 56 E. Dagotto, *Science* **309**, 257–262 (2005).
- 57 S. A. Kivelson, *et al.*, *Reviews of Modern Physics* **75**, 1201 (2003).
- 58 Tokura, *et al.*, *J. Phys. Soc. Jpn.* **75**, 011001 (2006).
- 59 H. Ichikawa *et al.*, *Nature Materials* **10**, 101-105 (2011).
- 60 R. Matteo, *et al.*, *Nature* **449**, 72-72 (2007).
- 61 D. Fausti, *et al.*, *Science* **331** 189-191 (2011).
- 62 A. Damasceli, *et al.*, *Rev. Mod. Phys.* **75**, 473 (2003).
- 63 L. J. P. Ament, *et al.*, *Rev. Mod. Phys.* **83**, 705 (2011).
- 64 M. Guarise *et al.*, *Phys. Rev. Lett.* **105**, 157006 (2010).
- 65 M. Le Tacon *et al.*, *Nature Phys.* **7**, 725-730 (2011).
- 66 J. Schlappa *et al.*, *Phys. Rev. Lett.* **103**, 047401 (2009).
- 67 J. Schlappa *et al.*, *Nature* **485**, 82 (2012).
- 68 W. S. Lee, *et al.* *Phys. Rev. Lett.* **110**, 265502 (2013).
- 69 F. Schmitt, *et al.*, *Science* **321**, 1649 (2008).
- 70 C. Jozwiak, *et al.*, *Nature Physics* **9**, 293 (2013).
- 71 T. Claesson, *et al.*, *Phys. Rev. Lett.*, **93** 136402 (2004).
- 72 A. X. Gray, *et al.*, *Nature Materials*, **10** 759-764 (2011).
- 73 D. G. Cahill *et al.*, *J. Appl. Phys.* **93**, 793 (2003).
- 74 M. N. Luckyanova, *et al.*, *Science* **338**, 936 (2012).
- 75 Y. Lan, *et al.*, *Advanced Functional Materials*, **20**, 357 (2009).
- 76 G. Pernot, *et al.*, *Nature Materials* **9**, 491 (2010).
- 77 R. P. Beardsley, *et al.*, *Phys. Rev. Lett.* **104**, 085501 (2010).
- 78 J. Ma, *et al.*, *Nature Nanotechnology* **8**, 445 (2013).
- 79 M. Trigo, *et al.*, LCLS L362 experiment, *in preparation*.
- 80 C. D. Stanciu, *Phys. Rev. Lett.*, **99**:047601 (2007).
- 81 M. Finazzi, *et al.*, *Phys. Rev. Lett.*, **110**, 177205, (2013).
- 82 Dennis Rudolf, *et al.*, *Nature Communications*, **3**:1037 (2012).
- 83 B. Keimer, *et al.*, *Nature Materials* **11**, 751–752 (2012).
- 84 Z. Yang, *et al.*, *Annu. Rev. Mater. Res.* **41**, 337 (2011).
- 85 M. Rini, *et al.*, *Nature*, **449**, 72-74 (2007).
- 86 A.X. Gray, *et al.* (unpublished).

- 87 Z.-G. Zhu, *et al.*, *Phys. Rev. B*, **82**, 235304 (2010).
- 88 L. Redecke, *et al.*, *Science*, **338** (2012).
- 89 J. Kern, *et al.*, *Science* (2013).
- 90 T.R.M. Barends, *et al.*, *Nature* (2013) accepted.

3

MACHINE PERFORMANCE AND PARAMETERS

TECHNICAL SYNOPSIS

The LCLS-II is a high-repetition-rate, high-average-brightness FEL facility based on the very successful LCLS-I, but now driven by a superconducting continuous wave (CW) 4-GeV linac, which supplies two separate free-electron lasers located in the existing LCLS undulator hall at SLAC. The SXR FEL is based on a 0.2 - 1.3 keV photon tuning range with self-seeding using the 4 GeV CW linac. The HXR FEL is a replacement of the existing LCLS-I undulator, with an adjustable gap device that can support either a 1-5 keV tuning range, when driven by the 4-GeV CW linac, or a 1-25 keV tuning range when driven by the existing 3-15-GeV copper linac at 120 Hz.

This chapter lists the high-level parameters for the accelerator facility. The LCLS-II parameter choices are described first, followed by the performance parameters for the various FEL configurations, which are presented in eight parameter tables. Finally, the chapter includes a brief description of possible low-power commissioning and startup modes.

3.1 Description of Parameter Choices

The LCLS-II design is based heavily on work performed for the New Light Source (NLS) in the UK [1], the Next Generation Light Source (NGLS) at the Lawrence Berkeley National Laboratory (LBNL) [2], the European X-Ray FEL Project (XFEL) [3], the Jefferson LAB (JLAB) 12-GeV Upgrade [4], the Cornell University Energy Recovery Linac [5], and the International Linear Collider designs [6]. Although the performance requirements are different, the LCLS-II parameter choices rely heavily on these preceding studies and projects.

The LCLS-II has been designed to deliver photons between 200 eV and 5 keV at repetition rates as high as 1 MHz using a superconducting RF linac (SCRF) while still providing pulses at short wavelengths and high-pulse energy using the existing 120 Hz Cu LCLS linac. The design was optimized to be responsive to the recommendations of the July 25, 2013 *Report of the BESAC Subcommittee on Future X-ray Light Sources* [7], as listed in Table 1. To cover the full photon energy range, the facility will include two variable-strength undulators, which will allow the possibility of generating transform-limited pulses by using self-seeding as well as downstream monochromators. A schematic of the accelerator facility is shown in Figure 1.

Table 1. BESAC Subcommittee recommendations and LCLS implementation.

Recommendation		Implementation
High repetition rate	✓	CW Linac with MHz capability
Broad energy range	✓	SC and Cu Linacs with variable gap undulators
Transform limited	✓	Self seeding narrows bandwidth with Monochomator used to control bandpass
Ultra-bright	✓	14GeV linac & high K undulator
Multiple undulator sources	✓	Two undulators

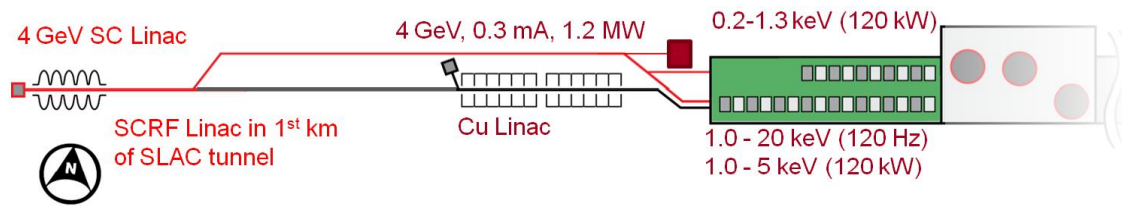


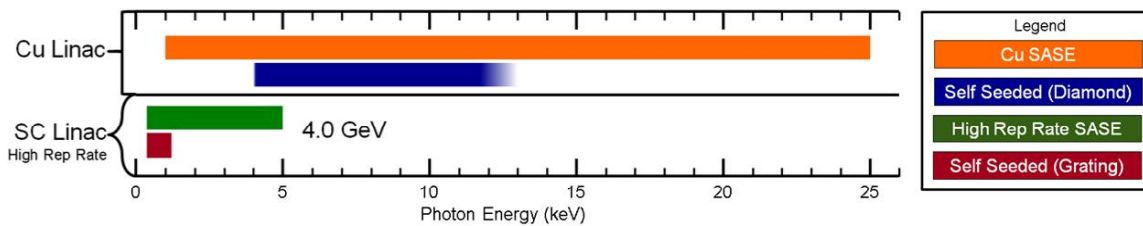
Figure 1. Schematic of the LCLS-II facility with the new SCRF linac and two new undulators, along with the existing copper (Cu) linac, undulator and experimental halls. The “Cu Linac” is in the 3rd km of the SLAC tunnel.

The two LCLS-II undulators, referred to as the Soft X-ray Undulator (SXR) and the Hard X-ray Undulator (HXR), will be installed in the existing LCLS Undulator Hall to minimize civil construction and project cost. This limits the maximum undulator length to roughly 150 meters.

The beam, undulator, and downstream optics parameters are then chosen to achieve the performance goals described below and illustrated schematically in Figure 2.

1. Soft X-ray photons from SASE and self-seeding between 0.2 and 1.3 keV at MHz rates, with an average X-ray power of less than 20 Watts (see Chapter 11);
2. Hard X-ray photons from SASE between 1.0 and 5.0 keV at MHz rates, with the possibility of an upgrade to self-seeding operation at energies between 1 and 4 keV with an average X-ray power of less than 20 Watts;
3. Hard X-ray photons with SASE above 20 keV and self-seeding between 4 keV and 13 keV, with performance comparable to or exceeding that of existing LCLS.

Figure 2. Photon energies from the SCRF and Cu linacs for both SASE and self-seeded



operation assuming 4.0 GeV SCRF electrons and 3-to-15 GeV Cu-Linac electron beams. Self-seeding for photon energies between 1.3 and 4 keV is possible with an upgrade, as described in Chapter. 18.

The beam, linac, and undulator parameter choices are described in the following sub-sections. These are then followed, in Section 3.1.4, by a description of the sensitivities about the present operating point and then, in Section 3.1.5, by a discussion of alternate technologies and the impact on the LCLS-II parameters.

3.1.1 Beam Parameters

The performance of the X-ray FEL depends sensitively on the achievable electron beam parameters. As noted, the LCLS-II design builds on previous studies for CW X-ray light sources, and Table 2 lists the beam parameters in the NLS and the NGLS design, along with those of the LCLS-II design. As discussed below, the bunch charge is determined by the desired amount of X-ray power, the electron average power limit, and the operating mode, while the beam emittance is determined by the injector technology and the bunch charge.

Table 2. Electron beam parameters of recent designs for CW X-ray FELs.

Parameter	NLS	NGLS	LCLS-II
Energy [GeV]	2.25	2.40	4.00
Bunch charge [pC]	200	300	100
Slice emittance [mm-mrad]	0.3	0.6	0.4
Slice energy spread [keV]	150	150	500
Peak current [kA]	0.97	0.5	1

The bunch charge and beam emittance are critical parameters. The nominal bunch charge in the LCLS-II is assumed to be 100 pC. The lower bunch charge allows the injector to be optimized for smaller beam emittances while still providing much more average X-ray power than the downstream optics can absorb. The bunch charge can be increased or decreased, along with a corresponding change in the beam emittance and bunch length, preserving the peak current, for special operating configurations. A maximum value of 500 pC is used to specify the injector laser requirements, and a low charge of 10 pC is used to specify diagnostic resolution requirements.

The LCLS-II design assumes an injector based on a low frequency, normal-conducting RF gun. This injector was developed extensively for the NGLS design, and an R&D project is underway at LBNL to demonstrate the proposed technology. The normalized emittance from the injector is simulated to be smaller than 0.6 mm-mrad at 300 pC and 0.3 mm-mrad at 100 pC. Similar parameters have been demonstrated at Cornell University with a DC gun and buncher, providing confidence that such emittance values will be attainable. A slice emittance of 0.43 mm-mrad at 100 pC is assumed for the baseline parameters.

The peak current that is achievable in the LCLS-II will depend on the beam energy and the compression ratio. The existing LCLS-I achieves a compression factor of roughly 100, taking a 45 Amp beam from the injector to 4 kA at the 5-GeV point in the linac. The injector assumed for the LCLS-II — either a low frequency RF gun or DC gun — generates a relatively low current beam. A compression factor of 100 would yield a peak current of 1 to 2 kA, with a peak current of 1 kA assumed as the baseline value.

Finally, the beam energy is determined by the shortest X-ray wavelength desired and by the undulator period. In the LCLS-II, the requirement that the HXR provide comparable performance to the existing LCLS-I, with beam from the existing *Cu* linac dictates that the period remain close to that of the existing LCLS-I, which is 30 mm. To reach FEL saturation at 5 keV, in a 150-m long, 30-mm period undulator would require an electron energy of at least 4.5 GeV.

However, the highest energy photons that the 30-mm period undulator could deliver using the existing *Cu* linac would be slightly less than the goal of 25 keV. Since the cost of the LCLS-II is a strong function of the linac energy, an electron energy of 4.0 GeV and an HXR undulator period of 26 mm has been chosen for the CDR. As will be shown in Section 3.1.3, a 150-m long undulator with a 26-mm period will deliver performance close to that of the LCLS-I over much of the common operating range. It will saturate at more than 25 keV with a 14-GeV incoming beam, and at 5 keV with a 4-GeV incoming beam.

As will be discussed in Section 3.1.3, this choice of parameters has little overhead at short wavelengths (5 keV); should the performance of the different systems fail to meet the specifications, the FEL may not saturate at 5 keV. In the future, the parameters, technology choices, and costs may be reexamined to establish a more robust working point.

3.1.2 Linac

To provide the high repetition rate beam, the new linac must be SCRF. Extensive technology development of SCRF has occurred over the last two decades, offering many technological options. As discussed in Chapter 6, the base technology will be the 1.3 GHz TESLA nine-cell cavity, the same as that of the European XFEL. The average gradient of the linac is chosen to be 16 MV/m, which is well within the capability of existing technology while minimizing the cost of the facility.

The LCLS-II is being designed to accommodate future upgrades, to be discussed in Chapter 18. The maximum electron beam power from the linac is chosen to be 1.2 MW, a sufficient electron beam power to generate more than 100 Watts of X-rays in up to 10 undulators in the long term. The initial maximum bunch repetition rate of the linac will be 0.93 MHz (the injector RF frequency: $1300/7 \text{ MHz} \approx 185.7 \text{ MHz}$, divided down to the drive laser oscillator frequency: $185.7/5 \text{ MHz} \approx 37.14 \text{ MHz}$, and reduced again to: $37.14/40 \text{ MHz} \approx 0.9286 \text{ MHz}$ to fill every 40th oscillator cycle). This is consistent with the 1.3-GHz linac, the low frequency RF injector, and the existing constraints of the SLAC timing system.

3.1.3 Undulators

In general, the photon energy range can be achieved by varying the undulator strength and/or the beam energy. Because it is straightforward to vary the beam energy of the normal conducting LCLS linac, this procedure is used to tune the photon energy in the current facility. Changing the beam energy in the LCLS-II SCRF linac may be more challenging for two reasons: first, when supplying beam to both HXR and SXR undulators, changing the beam energy impacts both undulators and may complicate scheduling of the experiments; second, the SCRF linac will operate with much higher beam power and, although CW operation should prove more stable than the existing LCLS operation, changing beam parameters may prove more challenging because of the high consequences of beam loss.

For these reasons, this project plans to primarily control the photon energy with the undulator strength. Two primary technologies were considered for the variable strength undulators: superconducting undulators (SCU) and variable-gap hybrid permanent magnet (VGPM) undulators. The potential of the SCUs is significant and would have important performance benefits which are discussed in Section 3.1.5.4. At the present time, however, the technology is still at an early stage of development; therefore the LCLS-II is based on VGPM undulators.

As noted, the maximum length of the existing LCLS Undulator Hall is roughly 150 meters. This will allow for the installation of 34 segments of the HXR, with each segment 3.4 meters in length and an interspace of 1.15 meters for a quadrupole, phase shifter, RF BPM, x and y steering coils, and a fixed-aperture protection collimator. To support self-seeding, two of these undulator slots will be reserved for self-seeding monochromators. The baseline will thus include 32 HXR segments plus slots, one of which containing the self-seeding monochromator and the other reserved for future upgrade. As illustrated in Figure 3, the HXR with a 26 mm period is able to just saturate at 5 keV in SASE mode when driven by the 4-GeV SCRF linac, and should be able

support self-seeded operation up to 4 keV. Self-seeding driven by the SCRF linac in the HXR between 1 and 4 keV would be supported as an upgrade and is described in Chapter 18.

In the HXR, a majority of the high-repetition rate experiments are expected to want photon energies between 1.5 and 5 keV. To operate at 1.5 keV with a 4-GeV beam in the 26-mm period undulator, a K of 2.4 is required. These conditions can be achieved in a VGPM with a magnetic gap of 7.2 mm, which is comparable to the LCLS-I undulator gap. Studies are underway to ensure that ensuing stay-clear is acceptable for the high power electron beams. To generate longer wavelength photons down to 1 keV, the SCRF linac energy will be reduced to ~3 GeV.

Similarly, the SXR is specified to support self-seeding over the range of 0.2 to 1.3 keV, with the majority of the experiments between 0.25 and 1.25 keV. To cover this range, the SXR will have a 39-mm period. It is expected that twelve 3.4-meter-long undulator segments would be sufficient to operate over the desired photon range in SASE-mode, and 19 undulator segments would be sufficient for self-seeding. To provide 20% margin in parameters, the baseline specifies 21 SXR 3.4-meter undulator magnet segments, separated by 1.15-m interspaces, just as with HXR. One empty slot in the SXR system is provided for the self-seeding monochromator insertion. As illustrated in Figure 3, in order to generate longer wavelength photons as low as 200 eV, the SCRF linac beam energy would be reduced to approximately 3 GeV.

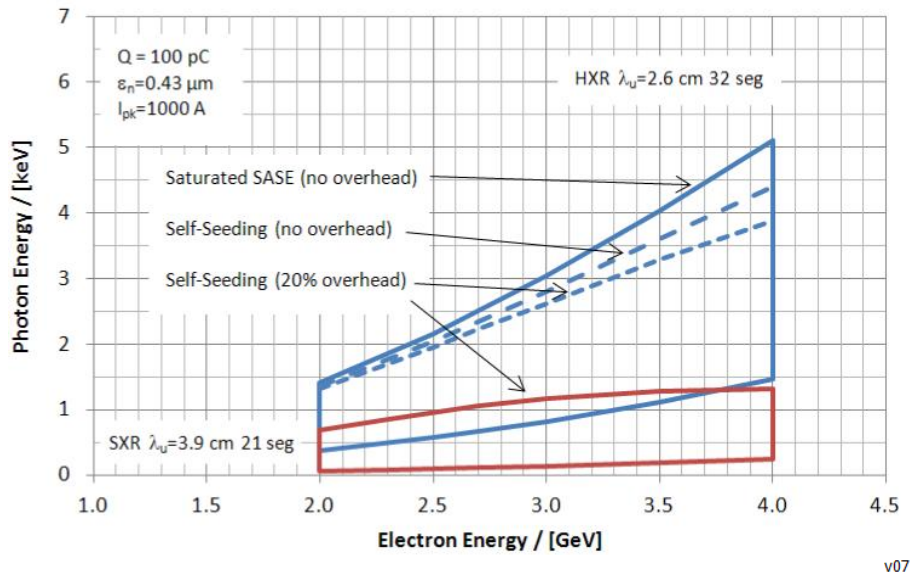


Figure 3. Illustration of the photon energy range for the HXR (blue) and the SXR (red) over the SCRF electron beam energy range: 2.0 to 4.0 GeV. Nominal operation is 4.0 GeV.

When driven by the high rate SCRF linac with the nominal 100-pC electron bunch, the SXR and HXR are expected to generate X-ray pulse energies between 100 μJ and a few mJ, as illustrated in Figure 4. The photon beam line optics are being designed for a maximum X-ray power of 20 Watts and thus, when operating at very high repetition rates, the FELs will need to be carefully tuned to prevent optics damage. This process will be accomplished by adjusting the bunch charge, energy chirp, transverse emittance, and beam rate.

Finally, the performance and tuning range of the HXR FEL, when driven by the existing *Cu* linac, is illustrated in Figure 5, along with the performance of the existing LCLS undulator. Because of the shorter undulator period, the X-ray pulse energy is slightly lower than that of the LCLS at photon energies of a few keV, but the LCLS-II HXR will be able to generate X-rays over a much wider range of wavelengths than the existing LCLS.

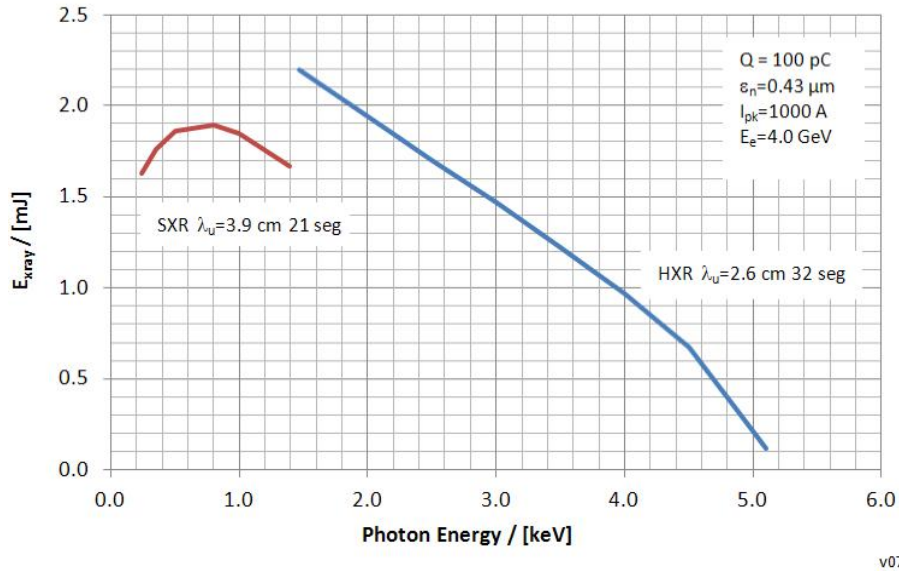


Figure 4. Expected X-ray pulse energy for the SXR (red) and HXR (blue) when driven by the SCRF linac. Much of the high repetition rate operation would require low bunch charge. For example, 1 mJ at 1 MHz would correspond to 1 kW of X-ray power.

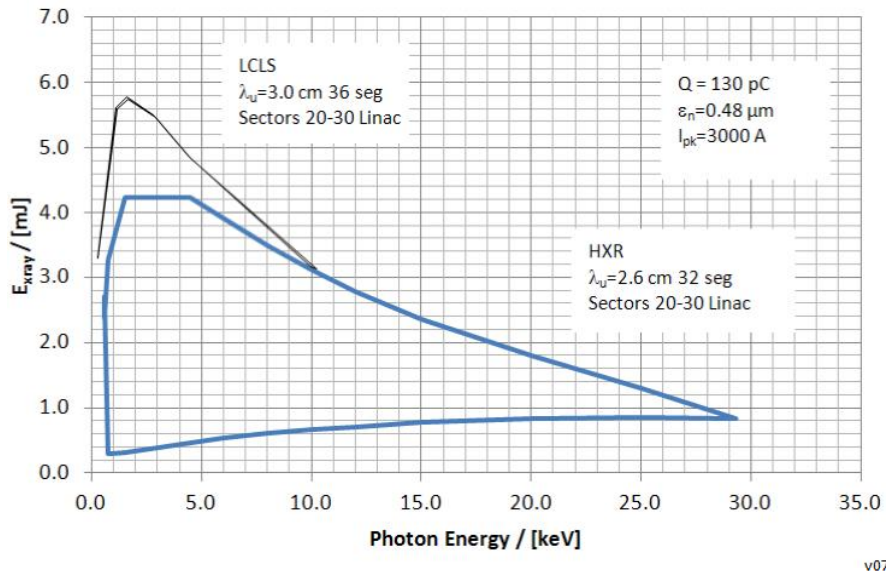


Figure 5. Expected performance — X-ray pulse energy versus photon energy (wavelength) — for HXR (blue) as driven by the existing *Cu* linac ("Sectors 20-30") at 120 Hz. The performance of the existing LCLS 30-mm-period undulator is also noted (black). The new HXR undulator would deliver comparable performance over the 1-to-10 keV photon energy range and would also be able to provide X-rays as high as 25 keV.

3.1.4 Sensitivities

The LCLS-II parameters have been chosen to meet the requirements described in Section 3.1.1. As noted, the parameters for the HXR FEL do not have much margin of error and may warrant re-optimization once cost and performance details are better understood. The sensitivity of the saturation length for SASE is shown in Figure 6, Figure 7, and Figure 8 for both the HXR and SXR FELs. As can be seen, the SXR performance is relatively insensitive to variations in parameters, although the same is not true for the HXR performance. While representing an operational risk for the present design, this sensitivity also points to minor design changes needed to make the design more robust. For example, a 5% increase in the electron beam energy would reduce the HXR saturation length by more than 20 percent. Similarly, increasing the peak current from 1.0 kA to 1.5 kA (still well below the LCLS parameters) would decrease the saturation length by about 15%. Finally, a decrease in the HXR undulator period from 26 mm to 24 mm would decrease the saturation length by more than 20%, although there would be a corresponding decrease in the high pulse energy performance when driven with the *Cu* linac.

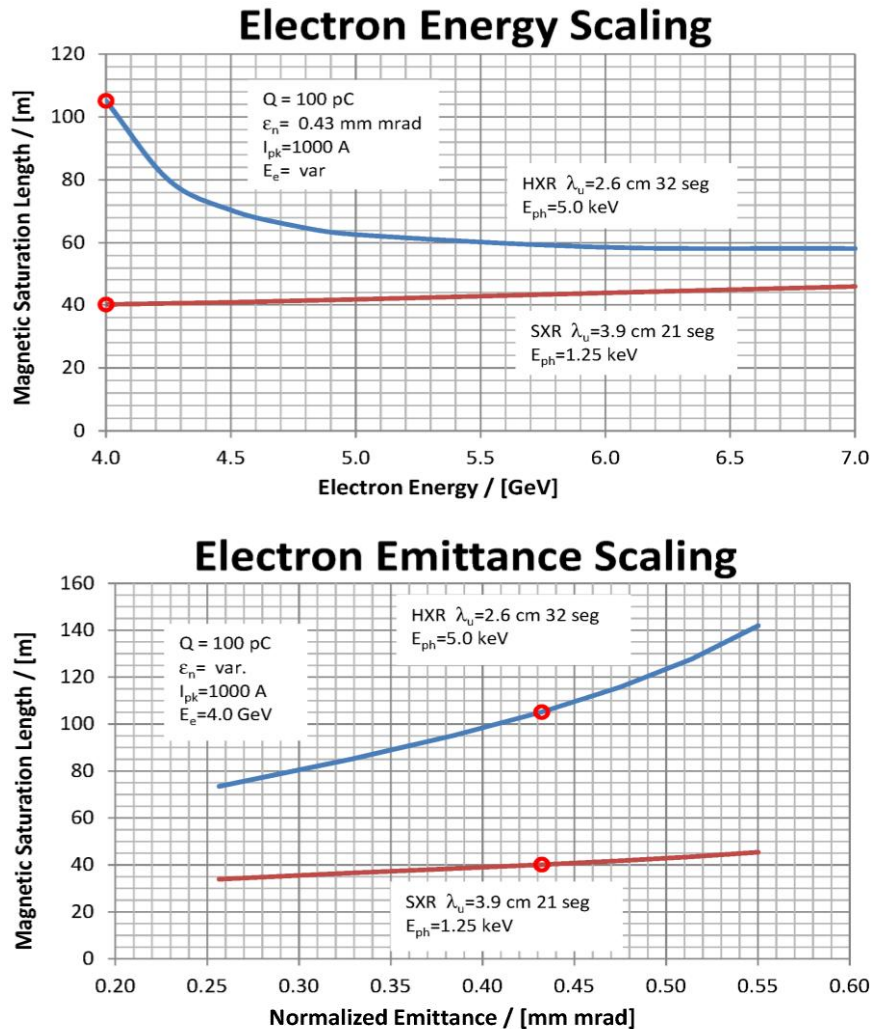


Figure 6. Dependence of the saturation length of the HXR (blue) and SXR (red) FELs to the SCRF electron beam energy (top) and the electron beam emittance (bottom).

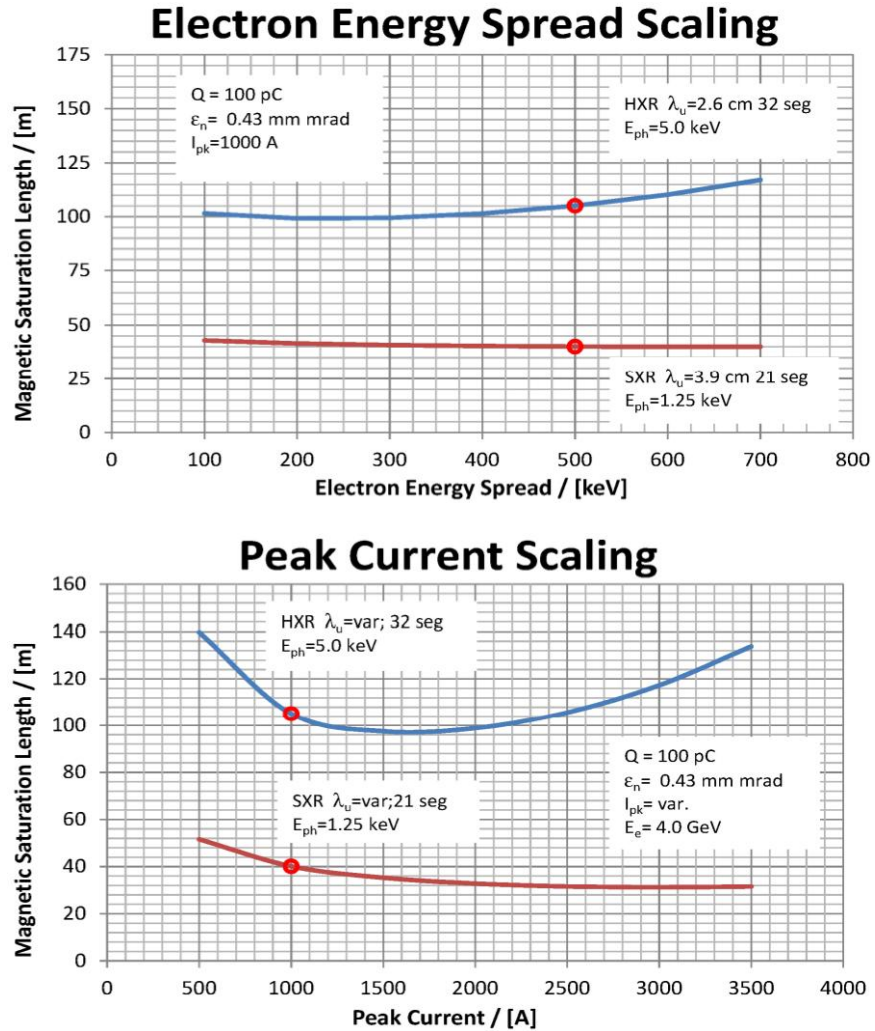


Figure 7. Dependence of the saturation length of the HXR (blue) and SXR (red) FELs to the rms electron beam energy spread (top) and the electron beam peak current (bottom).

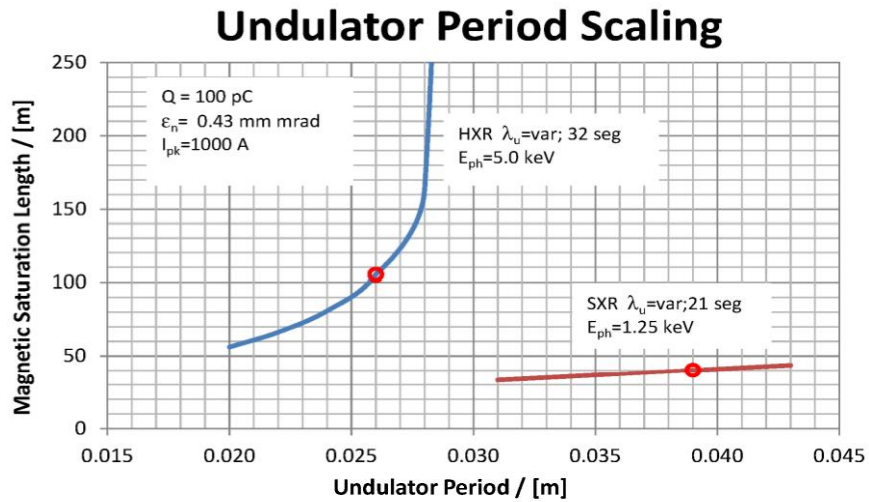


Figure 8. Dependence of the saturation length of the HXR (blue) and SXR (red) FEL's to the undulator period. The sensitivity to period reflects the low 4-GeV energy choice.

3.1.5 Alternative Configuration and Parameter Impact

The determination of the beam parameters for an FEL that can generate the desired photon requirements is described above. The most straight-forward implementation of an accelerator that can produce such high-repetition rate beams is the single-pass superconducting linac that is the basis of this CDR. This section will outline a few alternate configurations for the accelerator that have been considered and their impact on parameters. In addition to the topics described here, there are many details of the baseline SCRF technology that are being optimized and different options are being explored; these options are described in Chapter 6.

3.1.5.1 Normal-Conducting Linacs

The first alternatives that have been considered are variations on the normal-conducting RF linac technology that was used for the initial construction of the SLAC linac in the 1960's. It is relatively straight-forward to upgrade the existing SLAC linac to generate rf pulses at 360 Hz. Each RF pulse would be ~300 ns in duration and could accelerate a short train of bunches (~10) providing an effective repetition rate of >3kHz (10 x 360 Hz). Some initial testing has been performed on the existing hardware to demonstrate this option. In this option, the accelerating gradient is decreased by roughly a factor of two and to achieve the same beam energy as in the LCLS, one would need to utilize 2 km of the existing 3-km SLAC linac in order to accelerate to 15 GeV. Additions of new normal-conducting RF sources and/or acceleration structures could further increase the RF pulse repetition rate to a few kHz which would provide a beam repetition rate of a few 10's of kHz but at a very uneven rate with a burst of bunches at 10's of MHz followed by millisecond-scale delays.

3.1.5.2 Recirculating Superconducting Linacs

The next alternative is based on a recirculating superconducting linac which is similar in concept to the CEBAF facility at the Thomas Jefferson National Accelerator Facility. The advantage of such an approach is that the linac could be much lower energy since it is reused multiple times and therefore might be significantly less expensive. For example, assuming three times recirculation would reduce the minimum linac energy from the 4.0 GeV in the LCLS-II design to ~1.40 GeV (slightly more than 1/3 the final energy due to energy loss mechanisms in the recirculation). The challenge of such an approach is maintaining the beam quality and the flexibility to deliver the desired beams. In the LCLS-II design, the bunch is compressed by a factor of 100 using different RF phases in different portions of the linac. It would likely be difficult to implement such a scheme with such a large compression factor in a recirculating linac while preserving beam quality.

The recirculation concept was studied extensively for the New Light Source design in the UK and a chapter of the NLS CDR [1] was devoted to such a design. The conclusions that are described are similar to the ones mentioned here. Quoting from the summary of Chapter 14 in the NLS CDR: *“An alternative recirculating linac design has been studied in detail for the NLS, motivated mainly by the potential cost savings on both construction and operation. The proposal developed here needed many novel design concepts as well as optimization procedures to be*

developed in order to tackle the additional features in comparison to the single pass design, and to achieve the challenging bunch parameters for seeded FELs. The design optimization is complex due to limitations arising from incoherent and coherent synchrotron radiation as well as the interplay of higher order chromatics with the energy chirp needed for bunch compression.”

In conclusion, recirculation may offer some cost savings but these will likely come at a significant increase in risk and likely a reduction of the FEL performance. Future studies will attempt to understand the risk and performance issues further.

3.1.5.3 Energy Recovery Linacs

Another approach is to develop an Energy Recovery Linac (ERL) which might allow much higher beam power through the undulators. ERL designs and test facilities are being developed at KEK in Japan, Cornell in the US, and Germany and the concept has been demonstrated at the Jefferson Laboratory FEL program with >100 MeV beams and at lower energies at many facilities around the world. Typically, the ERL concept has been focused on the generation of diffraction-limited synchrotron radiation but the technology could be used to drive an X-ray oscillator FEL or a SASE-based X-ray FEL. One advantage is that the accelerator could provide much higher electron beam power to the undulators which would then generate much higher X-ray powers. Another advantage is that, in an FEL, 99% of the electron beam power does not go into X-rays and, rather than deposit the power into a complex high-power dump that generates extensive radiation, this excess power is recovered in order to reduce the RF power needs of the accelerator.

While attractive, this technology is relatively complex due to the need to handle multiple beams with differing energies and more complex timing constraints. The LCLS-II undulators already have the capability of generating far more X-ray power than the 20 Watts the downstream optics will be able to handle and thus there is little benefit in increasing the electron beam power. Thus, the relative benefit compared to the increased complexity of the ERL concept does not seem warranted. This capability may be desired for a future upgrade.

3.1.5.4 Superconducting Undulators

As described above, the use of the variable strength undulators allows tuning of the photon energy while operating at the maximum beam energy. Furthermore, the highest power X-rays are generated with the highest undulator fields. The baseline technology chosen for the LCLS-II is the variable-gap permanent magnet (VGPM) undulators as described in Section 3.1.2. At the undulator period of interest, superconducting undulators (SCU) can achieve much higher fields than permanent magnet technology. For example, with a 26 mm period, it is expected that a *NbTi* SCU could operate with fields twice as large as the VGPM technology. The SCU would allow for a very different optimization of the undulators for both the SXR and the HXR where the undulator period would be decreased while the maximum field is increase. Examples are shown in Table 3 and Table 4 for *NbTi* SCU technology where the required undulator length is significantly reduced while the peak photon power is increased; *Nb₃Sn* superconductor provides even higher fields. The increased performance could be translated into decreased undulator

length as illustrated in Table 3 and Table 4, reduced electron beam energy, or higher X-ray pulse energies.

Table 3. Comparison of SCU (*NbTi*) and VGPM undulators for HXR with 4.0 GeV electron beam.

	Period	Undulator Length	Kmax	Sat. Length @ 1.5 keV	Sat. Energy @ 1.5 keV	Sat. Length @ 5.0 keV	Sat. Energy @ 5.0 keV
HXR VGPM	26 mm	144.5	2.4	42.2	2.28 mJ	147.9	0.07 mJ
HXR SCU	21 mm	94.4	3.1	35.1	2.15 mJ	78.6	0.55 mJ

Table 4. Comparison of SCU (*NbTi*) and VGPM undulators for SXR with 4.0 GeV electron beam.

	Period	Undulator Length	Kmax	Sat. Length @ 0.25 keV	Sat. Energy @ 0.25 keV	Sat. Length @ 1.3 keV	Sat. Energy @ 1.3 keV
SXR VGPM	39 mm	94.4	5.5	35.1	1.73 mJ	54.1	1.71 mJ
SXR SCU	29 mm	76.2	6.4	27.3	1.85 mJ	42.2	1.78 mJ

In addition, SCU's are believed to be much less sensitive to the damaging effects of an accumulated radiation dose, an issue that will require great care with collimation and masking in a permanent magnet approach, especially at the very high repetition rate of the LCLS-II.

Although the SCU undulators have great potential, the technology is not yet ready to be adopted by the project. R&D efforts are progressing at a number of laboratories around the world. The LCLS-II project is working with SCU R&D groups at ANL and LBNL to help focus those programs on the critical issues that are relevant for the LCLS-II. If significant advances are achieved in the next two years, it may be possible for the project to adopt the technology.

3.2 Performance Parameters

For convenient reference, the high-level performance parameters for the electrons, accelerator, undulators, and FELs in their various configurations are listed below, with electron parameters listed in

Table 5; the accelerator, lattice and compression parameters in

Table 6; RF and cryogenic parameters in Table 7; SXR undulator parameters in Table 8; HXR undulator parameters Table 9; SXR FEL and X-ray parameters (as driven by the CW linac) in Table 10; HXR FEL and X-ray parameters, as driven by the CW linac, in Table 11, and the HXR FEL and X-ray parameters, as driven by the copper linac, in Table 12.

Table 5. Electron beam operational parameters at the SRF linac end, including rms stability goals.

Electron Beam Parameters	symbol	nominal	range	units
Final electron energy (operational)	E_f	4.0	2.0-4.0	GeV
Maximum upgrade energy (or reduced duty factor)	E_{max}	10	-	GeV
Electron bunch charge (limited by beam power)	Q_b	0.10	0.01-0.5	nC
Maximum bunch repetition rate in linac (CW)	f_b	0.2	0-1 (10)	MHz
Average electron current in linac	I_{av}	0.02	0.001-0.3	mA
Average electron beam power at linac end (limit)	P_{av}	0.08	0-1.2	MW
Normal rms transverse slice emittance (nom. charge)	$\gamma\epsilon_{1-s}$	0.45	0.2-0.7	μm
Final peak current	I_{pk}	1000	500-1500	A
Final rms bunch length	σ_{zf}	8.3	0.6-52	μm
Final useable bunch duration fraction (FWHM)	$\Delta\tau_f/\tau_f$	50	-	%
Total magnetic compression (cathode to undulators)	C_T	85	25-150	-
Final slice energy spread (rms)	σ_{Es}	500	125-1500	keV
<i>Estimated RMS Stability Goals:</i>				
Relative rms electron energy stability at 4 GeV	$(\Delta E/E_f)_{rms}$	< 0.01	-	%
Relative rms peak current stability at 1 kA	$(\Delta I/I_{pk})_{rms}$	< 5	-	%
Bunch arrival time stability (rms)	$(\Delta t_b)_{rms}$	< 20	-	fs
Transverse position stability (rms)	$\Delta x_{rms}/\sigma_x$	< 10	-	%

Table 6. Accelerator, lattice and compression parameters at nominal bunch charge.

Accelerator Parameters	symbol	nominal	range	units
Injector cathode	-	CsTe	-	-
Drive-laser pulse length (FWHM)	τ_{DL}	33	20-70	ps
Maximum bunch repetition rate in the linac	f_{rep}	0.929	-	MHz
Laser heater-induced energy spread (rms)	σ_E	6	0-20	keV
RF phase of L1 linac	φ_1	-21.0	-30-0	deg
RF phase of L2 linac	φ_2	-21.0	-30-0	deg
RF phase of L3 linac	φ_3	0.0	-10-10	deg
BC1 R_{56}	$ R_{56-1} $	55	20-75	mm
BC2 R_{56}	$ R_{56-2} $	60	0-75	mm
Electron energy at laser heater	E_{LH}	98	90-120	MeV
Electron energy at BC1	E_{BC1}	250	200-300	MeV
Electron energy at BC2	E_{BC2}	1600	1400-1800	MeV
Length of full cryomodule with 8 cavities	L_{CM}	11.99	-	m
Active length of L0 linac (all cavities)	L_{L0}	8.30	-	m
Active length of L1 linac (all 1.3-GHz cavities)	L_{L1}	16.6	-	m
Active length of HL linac (all 3.9-GHz cavities)	L_{HL}	4.15	-	m
Active length of L2 linac (all cavities)	L_{L2}	99.6	-	m
Active length of L3 linac (all cavities)	L_{L3}	166	-	m
Bypass line length (RW-wake removes chirp)	L_{byp}	2200	-	m
Bypass line bore radius (stainless steel)	r_{byp}	24.5	-	mm

Table 7. Radio frequency (RF) operational parameters, including rms stability goals.

RF Parameters (CW SRF Linac)	symbol	nominal	units
RF frequency (main linac)	f_{RF}	1.3	GHz
Average RF gradient (powered cavities only)	E_{acc}	16	MV/m
Active length of 9-cell 1.3-GHz cavity	L_{cav}	1.038	m
Installed 1.3-GHz voltage (all cavities)	V_{13}	4.6	GV
Fraction of unpowered cavities (installed spares)	V_{off}	6%	-
Mean cavity quality factor (unloaded)	Q_0	> 2.7	10^{10}
Mean cavity quality factor (loaded)	Q_L	< 4	10^7
Cavity operating temperature	T_{cryo}	2.0	K
No. of 9-cell cavities per cryomodule (1.3 GHz)	N_{cav}	8	-
Active length of one 9-cell 3.9-GHz cavity	L_{cav39}	0.346	m
Cavities per power amplifier in L0, HL, and L1	-	1	-
Cavities per power amplifier in L2 & L3	-	48	-
Total installed cryomodules (1.3 GHz)	N_{CM}	35	-
RF power per cavity (average)	P_{cav}	6.3	kW
Total number of 3.9-GHz cavities	-	12	-
Max. 3.9-GHz crest voltage	V_{39}	60	MV
No. installed 8-cavity CMs in L0	N_{CM0}	1	-
No. installed 8-cavity CMs in L1	N_{CM1}	2	-
No. installed 3.9-GHz CMs as linearizer	N_{CMLH}	3	-
No. installed 8-cavity CMs in L2	N_{CM2}	12	-
No. installed 8-cavity CMs in L3	N_{CM3}	20	-
SC Cryogenic AC Power	P_{Cryo_AC}	5.4	MW
RF AC Power	P_{RF_AC}	3.5	MW
Estimated RMS Stability Goals:			
RF phase stability (rms, pulse-to-pulse)	$(\Delta\phi_{RF})_{rms}$	0.01	deg
RF amplitude stability (rms, pulse-to-pulse)	$(\Delta V/V_{RF})_{rms}$	0.01	%

Table 8. SXR Undulator operational parameters.

SXR Undulator Parameters (SASE/SS)	symbol	nominal	units
Undulator type	-	Hybrid PM	-
Gap type	-	variable	-
Wiggle plane	-	horizontal	-
Full-height of magnetic gap (min)	g_m	7.2	mm
Undulator period	λ_u	39	mm
Undulator parameter (peak, max)	K	5.5	-
Magnetic field (peak, max)	$ B_y $	1.5	T
Magnetic length of each undulator segment	L_{seg}	3.40	m
Length of each break section	L_{brk}	1.15	m
Total number of segments	N_{seg}	21	-
Total magnetic undulator length	$N_{seg}L_{seg}$	71.2	m
Total undulator beamline length (incl. chicane)	$L_{u,bl}$	98.9	m
Average beta function in undulator	$\langle\beta_{x,y}\rangle$	12	m
Monochromator location (after N_1 segments)	N_1	8	-
Monochromator length (e^- chicane)	L_{mono}	< 4	m
Monochromator resolving power (FWHM)	R_{res}	10,000	-
Monochromator efficiency (not incl. BW)	M_{eff}	2	%
RMS Undulator Tolerances:			
Undulator parameter tolerances	$(\Delta K/K)_{rms}$	~ 0.04	%
First field integral per segment	$ \int B_y ds $	< 40	μTm
Second field integral per segment	$ \int\int B_y ds $	< 50	μTm^2
Radiation phase error per segment	$\Delta\phi_{rms}$	< 5	deg

Table 9. HXR Undulator operational parameters.

HXR-Undulator Parameters (SASE/SS)	symbol	nominal	units
Undulator type	-	Hybrid PM	-
Gap type	-	variable	-
Wiggle plane	-	horizontal	-
Full-height of magnetic gap (min)	g_m	7.2	mm
Undulator period	λ_u	26	mm
Undulator parameter (peak, max)	K	2.4	-
Magnetic field (peak, max)	$ B_y $	1.0	T
Magnetic length of each undulator segment	L_{seg}	3.40	m
Length of each break section	L_{brk}	1.15	m
Total number of segments	N_{seg}	32	-
Total magnetic undulator length	$N_{seg}L_{seg}$	108	m
Total undulator beamline length (incl. chicane)	$L_{u,bl}$	149	m
Average beta function in undulator	$\langle \beta_{x,y} \rangle$	13	m
Monochromator location (after N_1 segments)	N_1	15	-
Monochromator length (e^- chicane)	L_{mono}	< 4	m
Monochromator resolving power (FWHM)	R_{res}	15,000	-
Monochromator efficiency (not incl. BW)	M_{eff}	2	%
RMS Undulator Tolerances:			
Undulator parameter tolerances	$(\Delta K/K)_{rms}$	~ 0.02	%
First field integral per segment	$ \int B_y ds $	< 40	μTm
Second field integral per segment	$ \int \int B_y ds $	< 50	μTm^2
Radiation phase error per segment	$\Delta \varphi_{rms}$	< 5	Deg

Table 10. Baseline SXR FEL (SASE/SS[§]) SC linac operational parameters, including rms stability goals. The values are for 4 GeV electron energy and 100 pC bunch charge and include post-saturation tapering, where applicable.

SXR FEL Parameters (SASE/SS [§])	symbol	$E_{r,min}$	$E_{r,max}$	units
Photon energy (tuning range, fundamental)	E_r	0.25	1.3	keV
Photons per pulse (fundamental)	N_{ph}	46	7.8	10^{12}
X-ray pulse length (FWHM)	$\Delta\tau$	60	60	fs
FEL pulse energy (fundamental, SASE)	$E_r N_{ph}$	1,800	1,600	μJ
FEL peak power (fundamental, SASE)	P_{FEL}	18	16	GW
Peak brightness (SASE)	$B_{pk,SASE}$	9.3	45	$\times 10^{30}$ *
Peak brightness (SS [§])	$B_{pk,SS}$	140	670	$\times 10^{30}$ *
Average ⁺ brightness (max delivered, SS [§])	$B_{av,SASE}$	930	4,500	$\times 10^{20}$ *
Power gain length (3D, magnetic)	L_G	1.4	2.4	m
FEL parameter (SASE, 3D)	ρ_{3D}	1.3	0.75	10^{-3}
Bandwidth (FWHM, SASE)	BW_{SASE}	0.77	3.5	eV
Bandwidth (FWHM, SS [§])	BW_{SS}	0.03	0.06	eV
Photon source size (rms)	σ_s	23	18	μm
Photon far-field divergence (FWHM)	ϑ_s	38	8.8	μrad
Beam rate in this FEL	f_{FEL}	ss [†] -100**	ss [†] -100**	kHz
Average electron beam power in this FEL (max.)	P_e	120	120	kW
Average X-ray beam power delivered in this FEL	P_{xray}	< 20	< 20	W
Polarization purity (linear horizontal)	$\langle P \rangle$	100	100	%

* photons per second, per mm^2 , per mrad^2 , per 0.1% bandwidth

† single shot

§ self-seeded

+ @ 100 kHz rep rate

** 1 MHz is possible, but at a much lower bunch charge to limit the average power

Table 11. Baseline HXR FEL (SASE/SS[§]) SC Linac operational parameters, including rms stability goals; the values are for 4 GeV electron energy and 100 pC bunch charge and include post-saturation tapering, where applicable.

HXR FEL (SC-Linac) Parameters (SASE/SS [§])	symbol	$E_{r,min}$	$E_{r,max}$	units
Photon energy (tuning range, fundamental)	E_r	1.5	5.0	keV
Photons per pulse (fundamental)	N_{ph}	9.1	0.25	10^{12}
X-ray pulse length (FWHM)	$\Delta\tau$	60	60	fs
FEL pulse energy (fundamental, SASE)	$E_r N_{ph}$	2,200	200	μJ
FEL peak power (fundamental, SASE)	P_{FEL}	22	2.0	GW
Peak brightness (SASE)	$B_{pk,SASE}$	53	121	$\times 10^{30}$ *
Peak brightness (SS [§])	$B_{pk,SS}$	790	1,800	$\times 10^{30}$ *
Average ⁺ brightness (max delivered, SS [§])	$B_{av,SASE}$	5,300	12,000	$\times 10^{20}$ *
Power gain length (3D, magnetic)	L_G	1.9	5.6	m
FEL parameter (SASE, 3D)	ρ_{3D}	0.66	0.21	10^{-3}
Bandwidth (FWHM, SASE)	BW_{SASE}	1.1	1.7	eV
Bandwidth (FWHM, SS [§])	BW_{SS}	0.075	0.25	eV
Photon source size (rms)	σ_s	18	17	μm
Photon far-field divergence (FWHM)	Θ	8.5	2.7	μrad
Beam rate in this FEL	f_{FEL}	ss [†] -100**	ss [†] -100**	kHz
Average electron beam power in this FEL (max.)	P_e	120	120	kW
Average X-ray beam power delivered in this FEL	P_{xray}	< 20	< 20	W
Polarization purity (linear horizontal)	$\langle P \rangle$	100	100	%

* photons per second, per mm², per mrad², per 0.1% bandwidth

† single shot

§ self-seeded

+ @ 100 kHz rep rate

** 1 MHz is possible, but at a much lower bunch charge to limit the average power

Table 12. Baseline HXR FEL (SASE/SS[§]) Cu Linac operational parameters, including rms stability goals. The values are for 2.5 to 15 GeV electron energy and 130 pC bunch charge and include post-saturation tapering, where applicable.

HXR FEL (Cu-Linac) Parameters (SASE/SS [§])	symbol	$E_{r,min}$	$E_{r,max}$	units
Photon energy (tuning range, fundamental)	E_r	1.0	25	keV
Photons per pulse (fundamental)	N_{ph}	3.4-18	0.020	10^{12}
X-ray pulse length (FWHM)	$\Delta\tau$	43	43	fs
Electron beam energy	E_e	2.5-15	15	GeV
FEL pulse energy (fundamental, SASE)	$E_r N_{ph}$	550-2,900	1,500	μJ
FEL peak power (fundamental, SASE)	P_{FEL}	13-67	35	GW
Peak brightness (SASE)	$B_{pk,SASE}$	42-89	840	$\times 10^{30}$ *
Peak brightness (SS [§])	$B_{pk,SS}$	66-2,200	13,000	$\times 10^{30}$ *
Average ⁺ brightness (max delivered, SS [§])	$B_{av,SASE}$	2.3-4.6	240	$\times 10^{20}$ *
Power gain length (3D, magnetic)	L_G	1.7-4.3	4.7	m
FEL parameter (SASE, 3D)	ρ_{3D}	0.50-0.79	0.27	10^{-3}
Bandwidth (FWHM, SASE)	BW_{SASE}	1.1-4.3	18	eV
Bandwidth (FWHM, SS [§])	BW_{SS}	0.05	1.2	eV
Photon source size (rms)	σ_s	26-19	8.9	μm
Photon far-field divergence (FWHM)	Θ	11-9.4	1.1	μrad
Beam rate in this FEL	f_{FEL}	ss [†] -0.120**	ss [†] -0.120**	kHz
Average electron beam power in this FEL (max.)	P_e	0.5	0.3	kW
Average X-ray beam power delivered in this FEL	P_{xray}	0.05-0.35	0.18	W
Polarization purity (linear horizontal)	$\langle P \rangle$	100	100	%

* photons per second, per mm^2 , per mrad^2 , per 0.1% bandwidth

† single shot

§ self-seeded

+ @ 120 Hz rep rate

** 360 Hz is possible in the future, but requires 2 km of linac to produce a 14 GeV bunch

3.3 Beam Operating Modes

The very high average power of the accelerated CW electron beam makes it undesirable to terminate the beam anywhere other than in specially-designed beam dumps. Materials struck by the full-power beam in a persistent manner for more than roughly 100 microseconds may be damaged, possibly leading to a breach of the vacuum chamber. For this reason, several accelerator operating modes are envisioned for initial low-power commissioning, recovery from RF trips, recovery from beam-loss trips, and startup from shut-down periods. These modes are configured to allow machine setup and diagnosis, but are defined at much lower average power levels in order to protect the beamline components during these less controlled, more transient startup periods. Beams sent to different destinations may operate in different modes at the same time. For example, it should be possible to tune up low power beams going to one undulator while simultaneously delivering full power beams to the other.

Reducing the average beam power can be done in a number of ways: (1) by reducing the charge per bunch; (2) by creating a bunch train with a reduced duty factor; or (3) by reducing the frequency of bunches, or a combination of these methods. (Note that the RF power in the cavities remains continuously energized for all of these settings.) Changing the bunch charge is the least desirable method here, as it can have a large effect on the single bunch energy, timing, compression, and trajectory. For this reason we choose to preserve the 1 μ s linac bunch spacing (or 10 μ s at 100 kHz) in all of the schemes below, with consecutive bunches (sometimes only one) forming a bunch train, with the train repeated at a low repetition rate. Table 13 defines six different operating modes with constant single-bunch charge, but most with much lower duty factor with respect to the CW (1.2 MW) beam. They are defined in more detail below.

Table 13. Accelerator operating modes for initial low-power commissioning, trip recovery, and startup from shut-down. The average power levels are shown assuming a 1 MHz CW nominal bunch rate (as an example) and a 300 pC bunch charge (worst case).

Operating Mode	Bunch Train Length (μ s)	Number of Bunches in Train	Train Repetition Rate (Hz)	Duty Cycle	Avg. Current (μ A)	Avg. Power at 4 GeV (W)
One-Shot (on demand)	(no train)	(no train)	-	-	~ 0	~ 0
Single-Bunch, 1-Hz	(no train)	1	1	10^{-6}	0.0003	1.2
Single-Bunch, 60-Hz	(no train)	1	60	6×10^{-5}	0.018	72
100-Bunch	100	100	60	0.006	1.8	7200
1000-Bunch	1000	1000	60	0.06	18	72000
CW	inf.	inf.	CW	1	300	1200000

3.3.1 “One-Shot Mode”

This is a single 100-pC bunch accelerated to 4 GeV and used during initial commissioning when the beam is first shot through sensitive beamlines, such as the undulators. A second bunch in this mode can be triggered at any time after this pulse, but no sooner than 1 second later. This

one-shot mode might also be requested by scientific users as well and can be delivered to either FEL, possibly on synchronous demand from a user-generated trigger.

3.3.2 “Single-Bunch, 1-Hz Mode”

The “Single-Bunch, 1-Hz” mode is basically a single-shot mode repeated at the maximum “one-shot” rate of 1 Hz. This mode might be used to recover from conditions of full beam loss before establishing higher beam power.

3.3.3 “Single-Bunch, 60-Hz Mode”

The “Single-Bunch, 60-Hz” mode serves as the next step-up in power and allows feedback loops to converge in a reasonable time frame. These are used for initial commissioning or startup periods after initial beam transport has been established and with little beam loss.

3.3.4 “100-Bunch Mode”

The “100-Bunch” mode is the next step-up in power and allows nearly steady-state loading conditions along the bunch train, enabling rough beam tune-up with low average power. This provides a 0.6 percent duty cycle and only 100 bunches per train at 60 Hz, still preserving the steady-state 1- μ s bunch spacing.

3.3.5 “1000-Bunch Mode”

Finally, the “1000-Bunch” mode may not be needed, but is the next step-up in power and clearly establishes steady-state loading conditions along the bunch train. This provides a 6 percent duty cycle and 1000 bunches per train at 60 Hz. Finally, the “CW” mode is used for nominal operation, although the 1 MHz rate may be rarely used with only two (initial) FELs installed.

3.4 References

1. <http://www.newlightsource.org/documents/NLS%20CDR%20Consolidated%20Final.pdf>
2. <http://www.lbl.gov/ngls/>
3. <http://www.xfel.eu/>
4. <http://www.jlab.org/12GeV/>
5. <http://erl.chess.cornell.edu/>
6. <http://www.linearcollider.org/>
7. “Report of the BESAC Subcommittee on Future X-ray Light Sources,” stored at the BESAC website, http://science.energy.gov/~media/bes/besac/pdf/Reports/Future_Light_Sources_report_BESAC_approved_72513.pdf

4

PROJECT OVERVIEW

TECHNICAL SYNOPSIS

The LCLS-II project is described briefly here in overview with separate sections on the injector, linac, X-ray production, experimental systems, infrastructure and facilities, beam commissioning, management, and a cost and schedule summary. The facility that is described is designed to achieve the high level parameters as described in Chapter 3.

4.1 Overview

As has been described in Chapters 1 and 3, the LCLS-II project consists of a new high repetition rate (MHz) injector, a CW superconducting RF (SCRF) linac that accelerates the beam to 4.0 GeV, the re-use of an existing 2.4 km long bypass line from the end of the SCRF linac to the Beam Switch Yard (BSY) after Sector 30 of the SLAC linac and then transport to the LCLS Undulator Hall where two new undulators, the SXR (soft X-ray) and the HXR (hard X-ray), will be installed. The transport from the BSY to the HXR undulator will use the existing LCLS Linac-To-Undulator (LTU) beamline while the transport from the BSY to the SXR will use a newly constructed LTU beamline.

As described, the facility is constructed to either deliver high rate beam from the SCRF linac to both the SXR and HXR undulators or to deliver the high rate beam to the SXR undulator and deliver beam from the existing LCLS linac at 120 Hz to the HXR undulator. The critical technologies in the LCLS-II design are the beam injector which determines the beam emittance for a given bunch charge, the SCRF linac which accelerates the high rate beam and the variable strength undulators which allow the large, independent photon tuning range for the SXR and HXR FEL's.

The LCLS-II facility will utilize the existing accelerator tunnels at SLAC. The injector and SCRF linac will be installed in the 1st km of the existing SLAC linac tunnel after the existing equipment (the SLAC S-band linac) is removed from this portion of the linac tunnel. The layout of the LCLS-II is shown in Figure 1, which is only approximately drawn to scale and with separate scales in the horizontal and vertical directions (the tunnel width in the main linac is just 11 feet wide). The beamline component symbols along the top of the plot are from the design optics file (*MAD* file) and the beam optics are plotted in Figure 2 from the exit of the injector cryomodule CM01 where the beam energy is ~ 100 MeV to the beam dump after the SXR undulator; the optics for the beamline to the HXR undulator are similar.

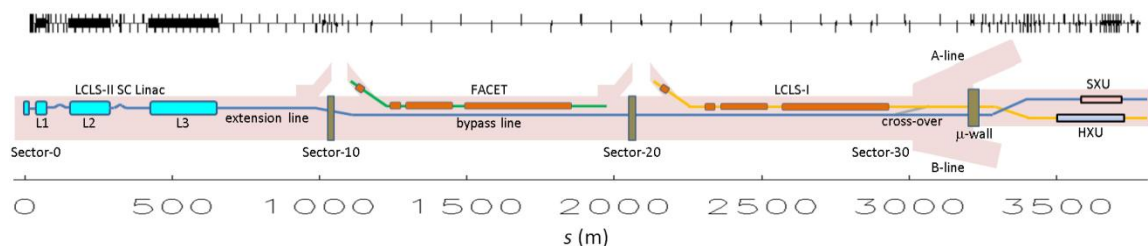


Figure 1. Layout of SLAC linac tunnel with LCLS-II located in first 650 m of tunnel followed by the extension line to sector-10, the bypass line to sector-30, and the beam transport to the SXR and HXR undulators.

The facility will be summarized in the following sections: the injector in Section 4.2; the linac and beam transport in Sections 4.3 and 4.4; the X-ray production and delivery in Section 4.5; the experimental systems in Section 4.6; the infrastructure and facilities in Section 4.7; the alignment systems in Section 4.8; beam commissioning in Section 4.9; and finally, management

and cost and schedule in Sections 4.10 and 4.11. The LCLS-II parameters are described in Chapter 3 and additional design details can be found in the dedicated chapters following this Project Overview chapter.

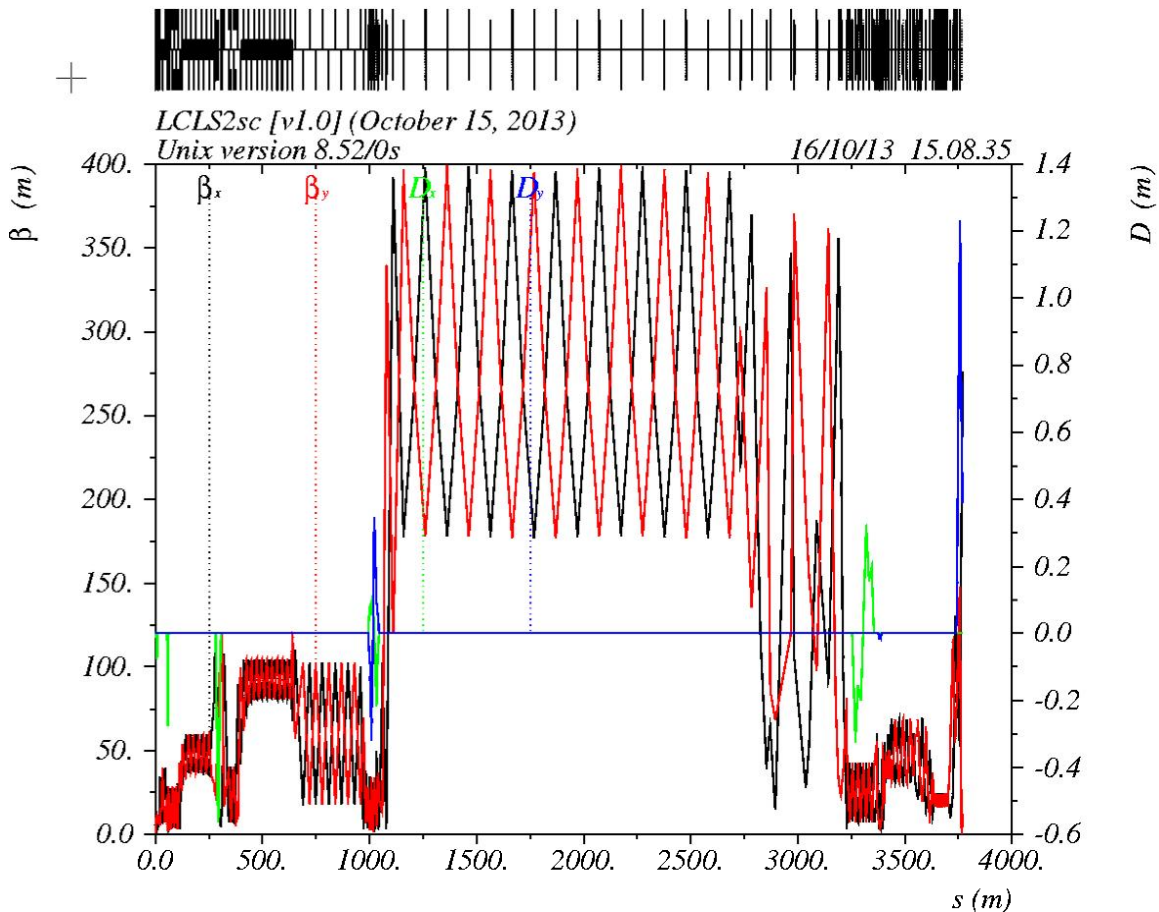


Figure 2. Beta and dispersion functions over the entire LCLS-II accelerator from the exit of the CM01 cryomodule to the electron dump after the SXR undulator.

4.2 Injector

An electron gun with the required LCLS-II brightness and high repetition rate has not yet been experimentally demonstrated. However, several technologies have simulated results that meet or exceed the performance requirements of LCLS-II. The relatively low repetition rate FEL guns, such as those developed at the LCLS at SLAC and PITZ in Berlin, cannot be directly scaled to higher repetition rates because the high frequency (>1 GHz) room-temperature RF technology cannot operate continuously at the MHz repetition rates required for LCLS-II. For the LCLS-II baseline, a CW normal conducting low frequency RF (VLF) gun has been chosen as the primary candidate for the electron source due to a combination of the simplicity of operation and the highest achieved gradient in a CW gun, potentially allowing for lower beam emittances. The high gradient is especially significant at high bunch charges where beam quality can suffer due to space charge.

We have chosen CsTe as the photo-cathode material due to its long history of use at FLASH and other facilities. We also take advantage of the availability of a proven cathode storage/transport system (“a vacuum suitcase”) and a load lock for transferring cathodes into and out of the gun. CsTe has demonstrated the few percent quantum efficiency (QE) with lifetimes in excess of one week as required for a user facility. An IR laser with ~ 30 W average power, frequency converted to the UV with ~ 1 W average power is necessary to produce up to 500 pC at 1 MHz from a CsTe cathode. Future cathode development is expected to result in higher QE and emission with visible light as opposed to UV light, thereby simplifying the laser systems and reducing their power requirements. The low frequency normal conducting gun can operate CW with low vacuum pressure. The power density from RF currents in the cavity is low enough to be cooled by conventional water channels when operating in CW mode with the high electric fields required by a high brightness photo-injector. Furthermore, the long RF wavelength allows for numerous high-conductance vacuum ports machined into the cavity necessary for achieving the UHV vacuum conditions required for CsTe and other semiconductor cathodes. Additionally, the use of a large number of non-evaporable getter vacuum pump (NEG) modules as the main pumping system allows efficient removal of those molecules (for example H₂O, O₂, CO, CO₂, ...) that are particularly deleterious for semiconductor cathodes. A cross section of the normal conducting CW gun is shown in Figure 3.

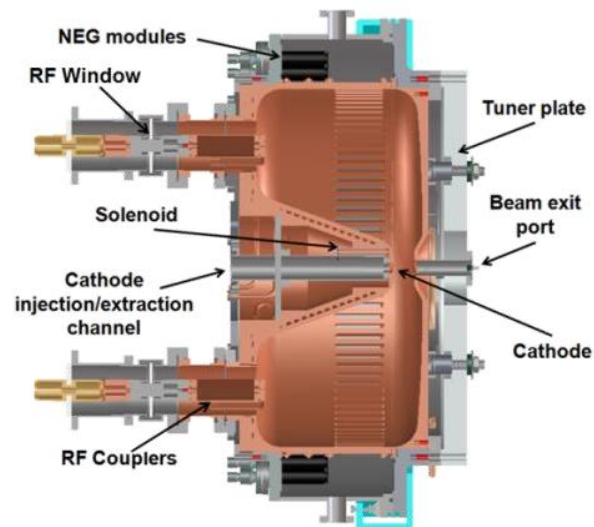


Figure 3. Normal conducting CW RF gun cross-section, showing the cavity main components.

The energy of beam exiting the low frequency normal conducting gun is only 750 keV with bunch lengths up to 40 ps FWHM to reduce space charge forces. Following the gun is a normal conducting CW 1.3 GHz buncher cavity and two emittance compensating solenoids to control the longitudinal and transverse phase space respectively. Further acceleration up to ~ 100 MeV is achieved with an LCLS-II linac cryomodule consisting of eight, TESLA-like 9-cell cavities. Each cavity is powered by a separate RF power source to provide individual amplitude and phase control. Additional beam diagnostics for characterizing the longitudinal and transverse phase space are located downstream of the accelerator section. Beam tuning will occur in two modes.

Initial setup will be conducted using a low rate of < 100 Hz and beam charges of ~ 100 pC. Final beam tuning occurs at full rate. High repetition rate non-intercepting diagnostics include BPMs in all sections as well as dedicated offset diagnostic lines into which bunches are deflected at a low rate < 120 Hz. A laser heater to control the energy spread and suppress micro-bunching instabilities downstream is also included after the injector accelerator.

Simulations run at LBNL and SLAC using ASTRA predict a 100% projected normalized emittance of 0.35 mm-mrad with 100 pC per bunch, 33 ps long flat-top laser with 2 ps rise and fall times, and 0.77 mm diameter flat-top transverse profile. The beam emittance is predicted to scale roughly with the square-root of the bunch charge and emittances of less than 1 mm-mrad are simulated to be possible at charges as high as 500 pC. Additional simulations and study are needed to understand the effects of the RF power coupler asymmetries and if additional phase and amplitude controls on the cells at the lowest energies are required.

The APEX experiment at LBNL will demonstrate the VLRF gun performance at 30 MeV over the parameter range of interest in late FY15. The primary concern of the VLRF gun technology is the relatively high dark current which has been measured at ~ 10 μ Amps; much of this dark current is accelerated and becomes a source of radiation. Another concern is the relatively large minimum bunch spacing of 5.4 ns which likely precludes the option of two-bunch self-seeding. Alternate technologies such as a DC gun, which has demonstrated parameters very close to the nominal beam parameters, will also be explored. More detail on the injector design can be found in Chapter 5.

4.3 SCRF Linac

A CW SCRF linac will accelerate the electron beam from the electron gun to a final energy of 4.0 GeV. It will be based on existing SRF technology to the greatest extent possible and to take advantage of the developments in TESLA/ILC/XFEL designs that have been made worldwide; CW SCRF technology developments at TJNAF and at Cornell University will also be utilized. The linac is based on the 1.3 GHz TESLA 9-cell superconducting cavities which are roughly 1-meter in length. The linac consists of thirty-five 1.3 GHz cryomodules, each containing 8 cavities. Additionally, twelve 3.9 GHz cavities installed in three cryomodules are used to linearize the longitudinal phase space. The linac operates at an average gradient of 16 MV/m and can generate a 1.2 MW electron beam.

As illustrated in Figure 1 of Section 4.1, the linac is divided into four different sections:

1. L0: one cryomodule in the injector follows the electron gun and accelerates the beam from 0.75 MeV to ~ 100 MeV at which point there is a laser heater, collimation, and diagnostics
2. L1: two 1.3 GHz cryomodules which accelerate the beam from 100 MeV to 250 MeV and three 3.9 GHz linearizer cryomodules lead to BC1, the first bunch compressor

3. L2: twelve 1.3 GHz cryomodules which accelerate the beam from 250 MeV at BC1 to BC2, the second bunch compressor, at ~ 1.5 GeV
4. L3: twenty: 1.3 GHz cryomodules which accelerate the beam from 1.5 GeV at BC2 to the final energy of 4.0 GeV

The linac will be installed on the north side of the existing SLAC linac tunnel. The linac tunnel is only 11 feet wide and thus the cryomodules will be a tight fit. Figure 4 shows a schematic of two 1.3 GHz cryomodules in the SLAC tunnel, one installed on the left and one being transported on the right.

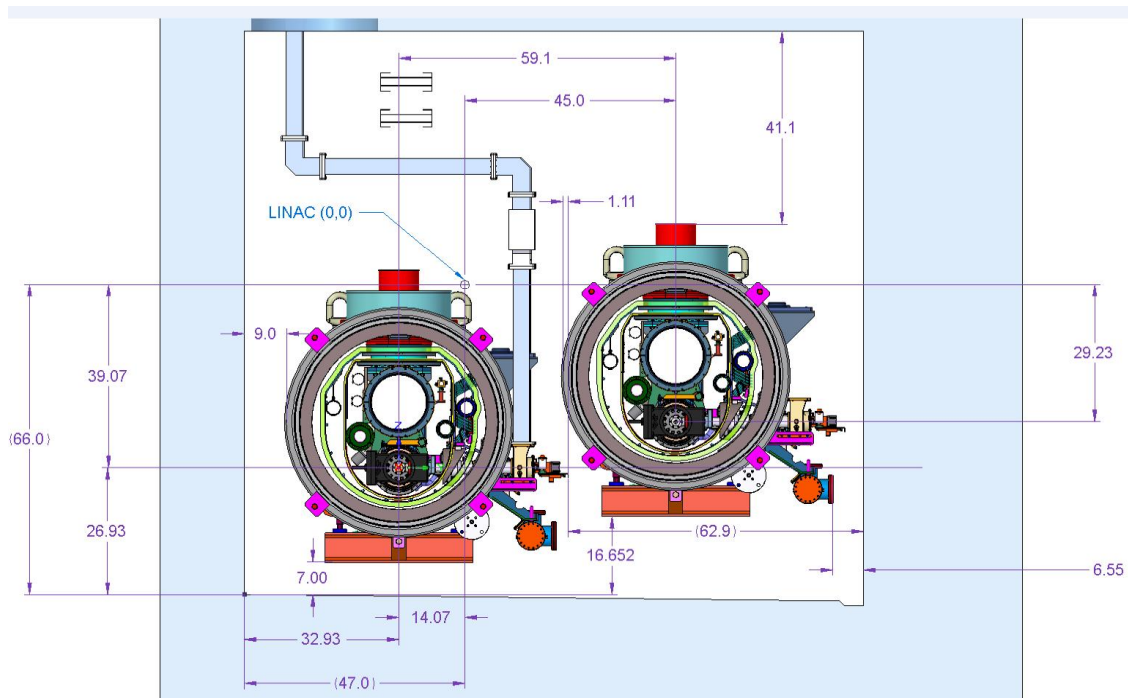


Figure 4. Schematic of LCLS-II cryomodules in the SLAC linac tunnel; the module on the left is in the installed position while the module on the right is being transported; all dimensions are in inches.

The linac cavity and cryomodule design is based on that developed for TESLA [1], the European XFEL [2] and the International Linear Collider [3]. This technology is mature, well understood, and thoroughly industrialized [4]. By the date foreseen for LCLS-II project construction more than 1000 nine-cell 1300 MHz SRF cavity resonators of this identical design will have been fabricated by industry and tested in institutions involved in the above three project efforts. More than 110 cryomodules of this design will also have been built and tested.

A key element in this design is the roughly 13 m long cryomodule that supports the operation of eight cavities, a superconducting focusing and correction magnet package, and a beam position monitor (BPM). The cryomodules themselves can be built and tested at partner labs including, Fermilab and Thomas Jefferson Lab, and then transported to SLAC for installation in the LCLS-II accelerator enclosure. Once in the enclosure, the cryomodules are directly connected end-to-

end to form a single cryostat vacuum-insulation volume. The main advantage of this is cost and space saving as there is no need for a secondary cryogenic distribution system – the cryomodules themselves contain a set of three helium gas circuits. An additional advantage is that the cavities are better isolated from ambient (warm) temperature vacuum systems and are therefore less susceptible to incidental contamination. The main disadvantage of this scheme is that removal of a failed cryomodule requires the warming-up of a large fraction (typically $\frac{1}{2}$) of the linac and the storage of the helium coolant in large external tanks. We will follow the path set forth by the European XFEL and expect to be guided by their experience – both during the construction and operational phases of the project.

The primary differences to be realized for LCLS-II are the adaptation of the cryomodule to support CW operation at 16 MV/m at 2 degrees K temperature, and development of high- Q_0 cavity production. The high- Q_0 allows the full LCLS-II linac system to be realized with only one cryoplant and results in considerable cost-saving. The cryomodule heat load will be dominated by the dynamic (RF-dependent) heat load by a 4:1 margin over the static (thermal isolation) heat leakage. Internal cryomodule cryogen handling and cavity cooling have to be somewhat modified from the European XFEL and ILC design and improved cavity cryogenic load-reducing surface treatment processes must be adopted to achieve the required Q_0 . There are several promising developments, especially at lower temperature (1.8 K) that may provide further performance improvements.

The power losses absorbed by the 2 K cryogenics systems are predicted to be about 90 W per cryomodule. The cryogenic systems will distribute 2.3 K liquid, cooled to 2 K by expansion at each cryomodule. Installed cryoplant capacity is about 4 kW at 2 K, taking into account uncertainty and overcapacity factors. Examples of large-scale cryo-systems of similar size to those needed for LCLS-II exist at JLab and at CERN; similar relevant experience also exist for high power pulsed systems (SNS) and smaller scale tests at Cornell, HZB in Berlin, and DESY in Hamburg.

High power RF for the cryomodules will be provided by a combination of single-cavity solid-state amplifiers (SSA) (first three and last two cryomodules) and five 300 kW klystron sources feeding 48-cavities (for all other 1.3 GHz cryomodules). It is expected that existing low-level-RF technology will be suitable to control cavity accelerating voltage for the SSA-fed cavities but that tests are needed to show that fast electro-mechanical (piezo-electric pusher) actuators work well enough for the LLRF control in the multi-cavity rf sources case. Key issues are control of Lorentz-force detuning and coupled-cavity disturbances. These will be tested in cryomodule tests and in existing dual-cavity horizontal test systems.

More detail on the SCRF linac design can be found in Chapter 6.

4.4 Bunch Compression and Beam Transport

The bunch compression and beam transport includes a laser heater chicane (LH) at a beam energy of roughly 100 MeV, the first bunch compressor chicane (BC1) at 250 MeV, a second

bunch compressor chicane (BC2) at 1.5 GeV, beam focusing and steering within the linac cryomodules, and the transport from the end of the linac to the SXR and HXR undulators as illustrated in Figure 1 in Section 4.1.

The bunch length from the RF gun is roughly 40 ps. This is ballistic and velocity bunched to about 2 ps rms before the laser heater. The laser heater system is designed to increase the bunch uncorrelated energy spread to roughly 5 keV to suppress the micro-bunching instability. The warm section housing the laser heater also includes collimation of the beam energy spread and the transverse phase space to limit beam losses in the downstream cryomodules. In addition, there is an offset diagnostic line into which bunches are continuously deflected at a low rate (~100 Hz). This line includes a short S-band transverse deflecting cavity and it will provide a continuous analysis of the beam phase space including the slice emittance and longitudinal phase space.

The bunch length is then compressed in two bunch compressors by roughly a factor of 100 to a peak current between 500 and 1,500 Amps. Each bunch compressor will consist of a four bending-magnet chicane followed by a collimation and matching region before the next SCRF linac section. There will be an additional offset diagnostic line after BC1 into which beam is continuously deflected at a low rate (~100 Hz). This line includes a short S-band transverse deflecting cavity and it will provide an ongoing analysis of the beam phase space including the slice emittance and longitudinal phase space.

At the end of the SCRF linac, an extension line transports the beam for roughly 300 meters to Sector 10 in the SLAC linac at which point the beam is deflected up to an existing bypass line that will transport the beam for roughly 2 km past the existing S-band linac that is used for the LCLS as well as a possible future project that would be located in the middle third of the SLAC linac. The bypass line will contain additional energy and transverse collimation to remove all tails before the beam is sent into the undulators. At the end of the bypass line, the beam enters a spreader that will be able to send bunches in an arbitrary pre-determined pattern to either or both of the HXR or SXR undulators or a high power dump that will be located in the BSY.

One of the beamlines from the spreader will connect to the existing LCLS Linac-to-Undulator (LTU) beamline that will go to the new HXR undulator. A new LTU beamline will be constructed that leads to the SXR undulator from the beam spreader in the BSY. This line will start at the beam spreader to the south and above the existing LCLS LTU and will cross over and descend until it is at the same elevation as illustrated in Figure 1.

Start-to-End simulations have verified the fundamental performance of the design including the injector (Chapter 5), the acceleration (Chapter 6), bunch compression and beam transport (Chapter 7), and the FEL process in the undulators (Chapter 8). The Start-to-End simulations are described in Chapter 10. Finally, studies of beam loss and the collimation requirements have been made and are described in Chapter 7 while the radiological concerns related to handling this high-power beam are described in Chapter 17.

4.5 X-Ray Production and Delivery

There will be two new variable gap permanent-magnet hybrid undulator systems installed in the existing LCLS undulator hall. The HXR undulator will be installed on the south side of the hall, replacing the existing LCLS undulator. The SXR undulator will be installed parallel to the HXR undulator but 2.5 meters to the north as illustrated in Figure 5.

The electron beam from the SC linac will be directed to either the HXR or SXR undulator line on a pulse-by-pulse basis. The SXR system will operate with beam from the SCRF linac over the energy range from 0.2 to 1.3 keV. The HXR undulator system, which will replace the existing undulator on the south side of the tunnel, will cover the energy range from 1 to 5 keV at high rep-rate driven by beam from the SCRF linac. Alternately, the HXR undulator can receive beam from the existing warm LCLS linac at lower rate to operate with higher X-ray pulse energy at photon energies up to 25 keV. The LCLS-II undulator lines will initially operate in the Self-Amplified Spontaneous Emission (SASE) regime with self-seeding capability. There will be a grating based self-seeding on the SXR line. The existing diamond monochromator self-seeding capabilities will be maintained on the HXR. A concept for self-seeding in the intermediate energies between 1-4 keV is discussed in chapter 8.

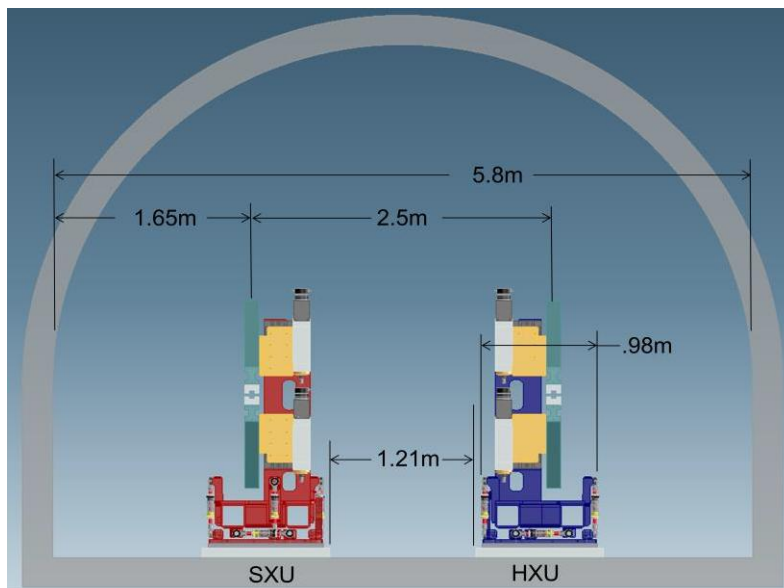


Figure 5. Schematic of the SXR and HXR undulators in the LCLS undulator hall looking down-beam; the undulators are described in greater detail in Chapter 8.

The X-ray transport and experimental systems (XTES) are laid out to deliver the two FEL beams to experimental stations in existing LCS facilities as illustrated in Figure 6. The beam from the SXR undulator system will be delivered to two reconfigured SXR experimental stations in the Near Experimental Hall (NEH). The beam from the HXR system will be delivered to the four existing HXR stations, one in the NEH and the three in Far Experimental Hall (FEH). The X-ray transport system is required to deliver the FEL beams to experimental stations with a minimal loss in flux and wavefront distortion. To accomplish this, the number of mirrors is kept to a

minimum. The delivered flux is dependent on the grazing angle of the optics, the optical coating, number of optics and the acceptance of the mirrors. The wave front distortion is principally dependent on the figure error of the optics and diffraction from mirror and other apertures in the beam path. The requirement for both the HXR and SXR optical systems is to deliver the beam well focused at the sample. Both the SXR and HXR beamline systems will provide diagnostics to both characterize the beams for FEL tuning and to support the experimental programs at high rep-rates. The undulator systems and X-ray optics transport are being designed for initial operations at ≤ 1 MHz, with the potential for future upgrades to higher rates.

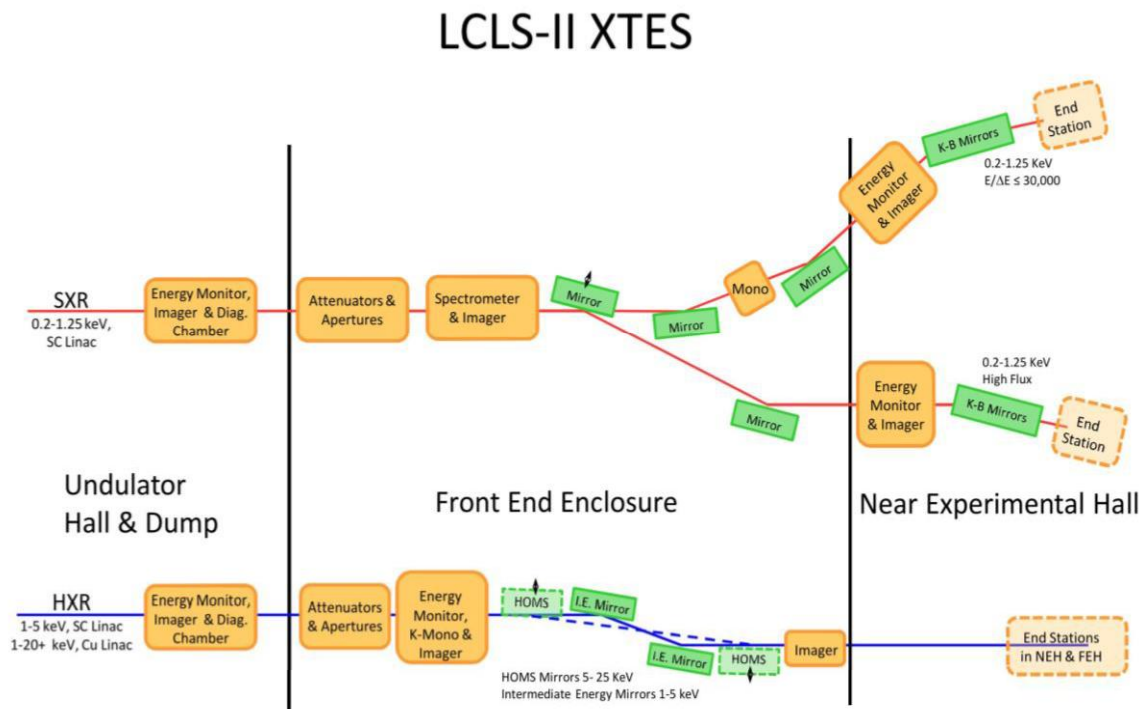


Figure 6. Schematic layout of the X-ray transport. The SXR line is on the north side of the LCLS Undulator Hall and the HXR line on the south. The two lines start just downstream of the bend magnets to the dumps, continue through the Front End Enclosure and deliver beam to the existing LCLS experimental instruments.

Finally, the LCLS-II X-ray transport is a flexible system with significant potential for future expansion and upgrade. A number of possible upgrades for the X-ray Production and Experimental Systems are described in chapters 12 and 18.

4.6 Experimental Systems

The experimental systems for LCLS-II include both upgrades to existing instruments as well as new systems within the project scope. There is one soft X-ray beamline that will transport the beam from the soft X-ray undulator to an experimental end station area located in the Near Experimental Hall. Experimental end stations currently in use or in development at LCLS will be used on this beamline. These end stations are specialized for: coherent scattering, atomic,

molecular and optical physics as well as resonant diffraction. To accommodate the higher repetition rate beam from the LCLS-II SCRF linac, laser, detector and data acquisition developments are needed. The control system will be upgraded and relocated and the data acquisition system will require additional space in close proximity to the soft X-ray experimental areas.

The X-ray transport and delivery system to the four hard X-ray instruments will need new, larger aperture mirrors that are water cooled to accommodate the lower photon energy and high average power from the LCLS-II FEL's. These upgrades will enable X-ray beam delivery to the hard X-ray instruments.

Overall, the current LCLS experimental infrastructure combined with the experimental systems in the LCLS-II project scope provide a foundation for developing state-of-the-art experimental capabilities to exploit the unique properties of the LCLS-II X-ray beam. To fully leverage these instruments, investment beyond the project scope in sample delivery, excitation laser, area detection and data acquisition systems will be required. The Experimental Systems are described in greater detail in Chapter 12.

4.7 Infrastructure and Facilities

The infrastructure systems to be provided include electrical and mechanical systems support for the new injector, the superconducting linac, and a facility for the cryoplat that will be installed mid-way along the new SCRF linac. Additional support will be provided for mechanical wet and dry side utilities, electrical power, and compressed air in the Beam Transport Hall, (BTH), the Undulator Hall, (UH), the Electron Beam Dump, (EBD), the Front End Enclosures, (FEE), and in the Near Experimental Hall, (NEH). The existing injector area will be reconfigured, and a new injector system installed for the superconducting RF cavities. As explained in Chapter 15, the linac tunnel between Sectors 0 through Sector 10 will require reconfiguration of existing utilities, as required, to support the new superconducting linac and to meet the current building codes and federal requirements. Existing infrastructure will be re-used, as possible, or replaced, as necessary, with code-compliant installations. The gallery structure, housing equipment above the linac tunnel, will undergo a similar reconfiguration to meet building codes and federal regulations. Most of the beam transport is in underground tunnels but, at the end of the Beam Switch Yard, the Beam Transfer Hall (BTH) crosses the SLAC Research Yard (RSY) above ground and connects to the Undulator Hall (UH) tunnel. The BTH will require additional radiation shielding and access restrictions due to increased beam power and radiation protection considerations. The new beam line requires additional power, cooling and reconfiguration of existing utilities in the BTH area. The Undulator Hall extends under the ridge between the Research Yard and the existing LCLS-I experimental and office facilities. The new undulator installations will require existing utility reconfigurations and additional support utilities. The new beam line, new electron beam dumps (EBD), and beam optics in the EBD and the X-ray optics in the Front End Enclosure (FEE) will require structural and utility reconfigurations. The Near Experimental Hall is where new experimental stations will be

installed. The new experiment configuration will require structural, architectural and utility reconfigurations. More detail on the infrastructure and facilities can be found in Chapter 15.

4.8 Coordinate System and Alignment

The SLAC linear accelerator (linac) coordinate system is used for the LCLS injector and accelerator structures and systems installed in the accelerator enclosure and will also be used for LCLS-II. The alignment coordinate system is a cartesian right-handed system with the y-axis opposite the direction of the gravity vector at the origin and the z-axis in the direction of the linac. The origin is at the beginning of the linac and the z-axis follows the (straight) beam line. There are 100 alignment stations along the linac and the station number datum are located on this z-axis. The beam axis of the linac is not level with respect to gravity and has approximately a 0.5% slope as explained below. The linac coordinate system will be used from the Injector through the linac and in the BSY.

The SLAC accelerator is designed with a downward slope heading eastward, with respect to the local gravity vector, of $\phi_{50} = 5.000000$ mrad at station-50 (in the middle of the linac). This downward slope, due to the Earth’s curvature, becomes $\phi_{100} = 4.760000$ mrad at station-100 at the end of the linac. The layout is depicted in **Figure 7**, where the (x, y, z) coordinates (in blue) are established along the existing linac axis (with $z = 3048$ m at station-100), while the (x', y', z') coordinates (in red) are vertically normal to the Earth’s surface under the LCLS-I undulator’s (rounded to the nearest meter) center. The undulator coordinate system as defined in **Figure 7** will be used for LCLS-II downstream of the BSY. Local coordinate systems for the convenience of the designers might be derived from the undulator system by adding offsets and by rotating the system around the y-axis.

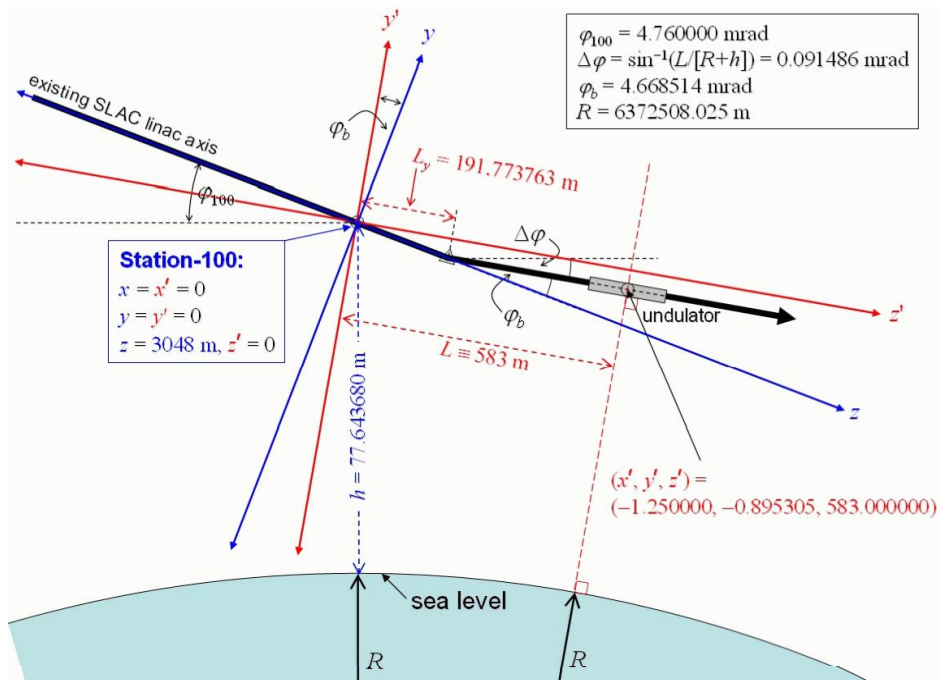


Figure 7. SLAC linac coordinate system (x, y, z) , and LCLS undulator system (x', y', z') .

An alignment monument network will be installed and mapped in all areas. All components will be aligned by referencing this alignment network. During installation, conventional alignment methods will be used to position components to their individual tolerances. Position adjustments will be applied mechanically. Where remote movers exist, corrections to the positions will be applied after post processing the alignment data. The initial alignment of X-ray components follows the same procedure as above, after which additional steps might have to be used depending on the component (*e.g.*, setting the roll of mirrors with auto-collimation techniques).

The different machine sections will have different functions and tolerances. In general the new alignment network will build up on existing network installations and component installations. For some areas, new tunnel networks need to be installed. The relatively weak links between machine sections make it necessary to support the tunnel networks with a surface network.

Common to all parts of the machine, free-stationed laser trackers, oriented to at least four neighboring points, are used for the absolute positioning measurements. The tracking capabilities of these instruments will significantly aid in facilitating the control of any alignment operation, *e.g.*, moving components into position. Once the above steps are completed, the components will be mapped as a quality control measure. If any positional residuals exceed the tolerance, a second iteration needs to be carried out. A quality control survey will always follow the completion of the alignment process.

4.9 Beam Commissioning

The LCLS-II electron beam commissioning will occur in several dedicated phases, based on the installation schedule (SCRF commissioning is described in Chapter 6). The main beam commissioning phases envisioned and their estimated durations are as follows, where each of two FELs are commissioned independently:

Table 1. LCLS-II beam commissioning phases for two FEL lines.

Commissioning phase	Systems to commission	Estimated duration
Injector	Drive laser, gun, injector linac, laser heater, 3.9-GHz RF system, BC1, diagnostics	3 months
Main Linac	LLRF systems, HLRF systems, cavities and cryomodules, BC2, diagnostics	5 months
Beam Transport	Matching sections, deflector switching, septa, diagnostics, MPS kickers	2 months
Undulator & Dump	Undulator segments, break sections, dump line, electron and photon diagnostics	3 months/FEL

Injector commissioning will likely be concurrent with downstream installation activities to isolate the injector beam commissioning from the FEL installation activities downstream of this point.

The bunch charge will be chosen as a compromise between high-charge impedance and stability issues, and low-charge diagnostics resolution limitations. A bunch charge of 50-100 pC will likely be used to commission the injector, linac, and FEL lines, with higher (300 pC) and lower (10-50 pC) charge levels tested as well.

Linac commissioning will be centered on RF processing, low-level RF commissioning, and bunch compression issues. The new SCRF systems will require special attention for longer time spans than the other commissioning periods, requiring at least 5 months of dedicated effort (see Chapter 6). During this period the electron beam will be dumped on the special diagnostic dump located in the undulator hall, or one of the undulators will be fully extracted (or the gap fully opened) and the beam taken to its main dump. Upon first beam transport through the linac, the RF phases will be unknown as well as the cold cavity BPM (mounted in the cryomodules) position readback signs, so a very low charge (10-20 pC) and low pulse rate (1-10 Hz) will be applied initially (see Chapter 3 on Operating Modes), until the RF phases can be more accurately set using cavity signals with RF off and BPM signals from the chicanes. The cold quadrupole magnets in the cryomodules will need to be initially scaled down in gradient with the RF switched off, but will be easily scaled back up to their nominal settings after RF power and phase settings have been established.

FEL commissioning will be focused initially on spontaneous radiation and trajectory correction using beam-based alignment, and then on the observation and optimization of FEL X-ray production, using the accelerator controls to improve and test the FEL performance. Low-power (low rate) operation will be used until the FEL and electron beam is well established.

Each machine commissioning phase is broken down into different commissioning levels as well, including pre-beam commissioning, beam and system commissioning, and beam and system characterization. It will be important to build up the commissioning procedure in a pyramid fashion, where the operation of each component is first well established using post-installation testing in the tunnel, followed by beam-based testing; the electron beam is established with minimal losses, reasonable trajectory, empirical matching, and operation of all personal protection, machine protection, and beam containment systems verified; and *only* then is beam characterization pursued (*e.g.*, emittance, energy spread, peak current, FEL gain, etc.). The definition and order of these levels is as follows:

4.9.1 Pre-beam Commissioning

The pre-beam commissioning is performed after component installation and is focused on local system and component testing performed in the tunnel or service buildings as necessary, and carried out by the physicist responsible for that area or system. This checkout is not meant to replace engineering tests performed earlier on the bench or in the tunnel. The goal is to verify full performance after installation with local observations (*e.g.*, measuring magnetic fields and

polarities of an installed quadrupole) using, as much as possible, the actual control system to set and adjust the device using both a local instrument (*e.g.*, Hall probe) and the main control system to verify its response and readback accuracy. Detailed pre-beam check lists will be prepared with all expected polarities, connections, and expected responses clearly listed so that detailed analysis or polarity interpretations do not have to be carried out in the tunnel. The lists will include many aspects per device (*e.g.*, polarity, field type, local label accuracy, proper installed location along beam line, connectivity to other components, cooling water flow, motor function, limit switch operation, etc) and check-boxes to mark with dates, physicist's initials, and notes, etc, in order to fully document every step in the pre-beam check list. When finished, each area will be ready for beam with high confidence of proper operation on every system and component.

4.9.2 Beam and System Commissioning

Basic beam commissioning is performed only after pre-beam commissioning is finished and is focused on demonstrating the basic beamline performance, such as transmission, linear beam optics, verifying beam-based readbacks (*e.g.*, BPMs), machine protection system operation, beam-based radiation surveys, accelerator controls, trajectory correction, beam matching software, high-level software applications, etc. Beam-based component verification will follow these pre-beam tests to verify components, using a lower-power beam, wherever possible (*e.g.*, steering correctors, BPMs, screens, wires, RF deflectors, etc.). This level of commissioning is executed in order to verify beamline operation, its controls, and its proper installation. It is *not* intended to do beam characterization or more complex physics analysis of beam quality. This level is reserved for the final level of commissioning.

4.9.3 Beam and System Characterization

Beam and system characterization is performed only after beam and system commissioning is finished and is focused on measuring, correcting, and demonstrating beam quality and detailed system performance. This is the stage at which (for example) emittance measurements are made and careful corrections are applied. Prior to this level any similar measurements are made only to check out software, diagnostics, or the beam analysis algorithm. Measurements and corrections to be made at this final level include emittance, bunch length, energy spread, sliced beam analysis, beam matching, trajectory optimization, FEL gain length, etc. The beam rate (power) will typically be kept low during these stages and ramped up to full power slowly only after full system verifications are completed.

4.10 Management

DOE has selected the SLAC National Accelerator Laboratory (SLAC) to manage and execute the LCLS-II acquisition. The acquisition of large research facilities is within the scope of the DOE contract for the management and operations of SLAC and consistent with the general expectation of the responsibilities of DOE M&O contractors.

SLAC does not currently possess all the necessary core competencies to design, procure and construct LCLS-II. To address this, SLAC envisions collaborating with other DOE national labs and Universities (Partners) to perform significant portions of the LCLS-II scope of work.

At the time of writing this document, the Partner institutions anticipated to support LCLS-II are the Thomas Jefferson National Accelerator Facility (TJNAF), Argonne National Laboratory (ANL), Fermi National Accelerator Laboratory (FNAL), Lawrence Berkeley National Laboratory (LBNL), and Cornell University. Memoranda of Understanding and Memorandum Purchase Orders have been awarded to participating labs to secure their help in preparing this Conceptual Design Report. Any work accomplished through Universities will be completed via standard DOE format University agreements. Procurements authorized by Partner institutions will be via approved DOE purchasing systems.

By approving “critical decisions”, the Department of Energy will authorize the Project to proceed in steps, from conceptual design (Critical Decision 1, or CD-1) to “baseline”, i.e. the Project technical deliverables, cost and schedule plan (CD-2) to start of construction (CD-3). At Project completion, DOE will verify that the Project has been constructed and is functioning in fulfillment of the baseline requirements defined at the time of CD-2. Satisfactory Project completion is marked with the approval of Critical Decision 4 by DOE.

DOE project management policies, procedures and requirements for approval of Critical Decisions are defined in a series of orders and guides such as [DOE O 413.3B](#) and related [directives](#) in the 413 series [5]. Project Critical Decision Authorities have been modified for Office of Science Projects, as described in a [letter](#) issued by William Brinkman in January 2011.

The Project organization will integrate Partner Laboratories into a single functional organization and chain of command that creates, adjusts and then works in accordance with the approved Project baseline cost and schedule to fulfill the Mission Need approved by DOE. Changes to the baseline cost, schedule and technical definitions of the Project can be made subject to approvals of Project management at SLAC and DOE in accordance with approval thresholds defined by the Project Execution Plan.

The basic ground rules of collaboration between SLAC and the Partners are documented in a Memorandum of Understanding signed by the Laboratory Directors or equivalent authorities of the Partners. In addition, SLAC and the Partners will enter into more specific memoranda of understanding (MoUs) defining plans for work and funding commitments for the coming 6-12 months. These MoUs will be updated as necessary to reflect the Project’s plan and funding commitments.

4.11 Costs and Schedules

The Project is managed to a resource loaded logically linked schedule which is maintained in Primavera P6. As host laboratory, SLAC maintains the definitive P6 file and all Project collaborators status and maintain that file per the host laboratory EVMS procedure ([SLAC-I-051-101-000-00-R007](#)). The cost and schedule estimates are done at the activity level by number of

hours and skill code and unburdened M&S dollars. Work scheduled at Project collaborator laboratories is estimated by that laboratory using their resource skill codes. The Project P6 file is processed through COBRA, applying skill code rates, labor and M&S burden, and escalation to the cost estimate, to calculate the total project cost.

The cost estimates include design maturity and judgment factors at the level of individual activities. These factors are used to estimate the scale of a possible cost overrun for each activity and hence the management reserve that should be held for each activity. In addition, a risk registry is maintained which lists significant Project risks, mitigations for those risks and their potential impact. The bottoms-up contingency estimate and the risk factors are combined statistically using Monte Carlo modeling techniques to assess the management reserve needed for the Project. Management reserve is held by the Project Office and applied when needed through the Project change control process.

The status of all activities that are or are scheduled to be currently underway is reported monthly by the Control Account Manager responsible for the activity. Major variances in the cost or schedule are analyzed and documented with a corrective action plan and future projection. The status of the Project schedule is reviewed monthly by Project management.

Changes to the Project baseline may be proposed by the Control Account Manager. Potential changes are vetted by technical reviews and by the Integration Management Team. A baseline change request (BCR) is brought to the Project Change Control Board (CCB) for evaluation by the System Manager.

4.12 References

1. http://tesla.desy.de/new_pages/TDR_CD/start.html.
2. <http://www.xfel.eu/>
3. <http://www.linearcollider.org/>
4. M. Ross, "Industrialization of the ILC Project," <http://accelconf.web.cern.ch/AccelConf/IPAC2013/papers/weib202.pdf>
5. See <https://www.directives.doe.gov/directives/current-directives/directives-current-400-series> for relevant DOE project management requirements and guides explaining methods of compliance with these requirements.

5

ELECTRON INJECTOR

TECHNICAL SYNOPSIS

The requirement for the LCLS-II of being a MHz-class repetition rate accelerator has fundamental implications for the electron gun. Indeed, an electron gun with the required brightness at such high repetition rate has not yet been demonstrated.

The results of the relatively low repetition rate FEL guns, as the ones of the LCLS at Stanford or PITZ in Berlin, cannot be directly scaled to higher repetition rates because the high frequency room-temperature RF technology they use cannot operate at MHz repetition rates. The available technologies for high-repetition-rate guns, and the need to keep dark current within acceptable values, push the accelerating gradient in the electron gun down to values significantly smaller than in the lower repetition rate case. Beam dynamics in this “low gradient” regime assumes quite different characteristics; although simulations indicate the capability of achieving the required results in this regime, an experimental demonstration has yet to be performed.

The large majority of high-brightness gun schemes use photocathode systems for the flexibility they offer in controlling the electron bunch distribution. The high repetition rate and the available laser technology require the use of high quantum efficiency (QE) photocathodes. The robust metal cathodes deployed in the low repetition rate injectors cannot be used due to low QE. The “delicate” semiconductor cathodes must be used to achieve the necessary QE, but they also require significantly lower vacuum pressures to obtain the desired lifetimes.

This chapter describes the issues mentioned above in more detail and presents our solutions for the LCLS-II injector.

5.1 Introduction and Overview

Table 1 summarizes the requirements for the injectors and electron gun that must be simultaneously satisfied to operate in LCLS-II. In the following part of this chapter, the table requirements will be analyzed and addressed in more detail.

Table 1. LCLS-II Injector and Gun Requirements.

Parameter	Symbol	Unit	Min. Value	Nom. Value	Max. Value
Bunch repetition rate at injector and linac	f_G	MHz	0	0.2	1
Charge per bunch	Q	pC	10	100	500*
Normalized transverse emittance (slice, rms)	$\epsilon_{nx,ny}$	μm	0.2	0.45	<1
Beam energy at the gun exit	E_G	MeV		0.75	
Beam energy at injector exit	E_I	MeV		98	
Electric field at the cathode during photoemission	E_C	MV/m		20	
Dark current	I_D	nA		see text	
Laser pulse length at the cathode (rms)	σ_t	ps	~5	~10	~20
Peak current at the injector exit	I_{pl}	A		12	50
Average current at the injector exit	I_{ave}	mA		0.02	0.3
Operational vacuum pressure	P_G	nTorr		~1	
Cathode quantum efficiency at 257.5 nm	QE	%	0.5	2	10
Laser energy at the cathode per pulse	E_{Laser}	μJ	0.001	0.1	0.5

* The average beam power stays constant as the bunch charge exceed 300 pC by using a lower bunch rate.

Figure 1 illustrates the layout of the LCLS-II injector, including the drive laser (UV), the RF photocathode gun (186 MHz), the 1.3 GHz buncher cavity, a dark-current sweeper (pulsed) magnet to reduce the accelerated dark current, a 12-meter-long cryomodule with eight 9-cell L-band cavities (each powered separately), a laser heater system to damp the micro-bunching instability (see Chapter 7), a pulse-stealing kicker magnet used to direct a low power beam (about 100 Hz) into a special off-axis beam diagnostic line, and a short beam collimation and matching section. The diagnostic line allows continual emittance and energy spread measurements at low average power and includes an RF deflecting cavity (S-band), so that these measurements can also be time resolved (*i.e.*, along the bunch length).

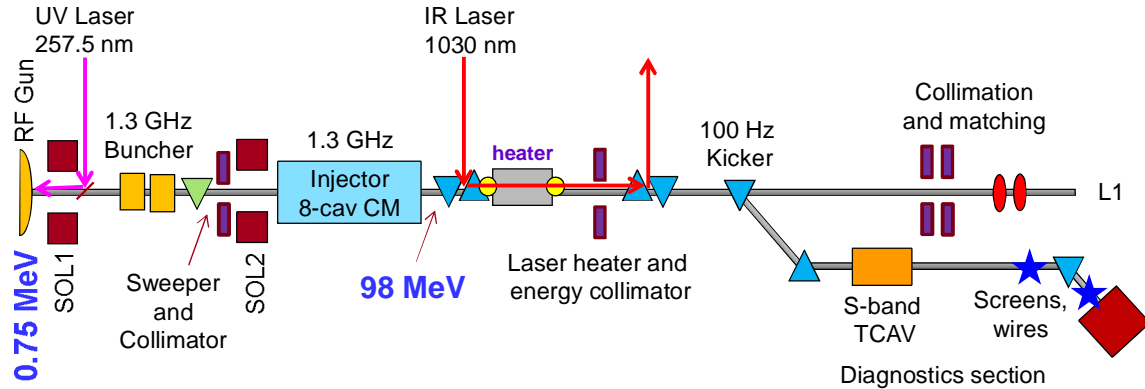


Figure 1. LCLS-II Injector layout.

A continuous wave (CW), normal conducting low-frequency RF gun was chosen for the electron source due to a combination of the simplicity of operation and the highest achieved gradient in a CW gun. The high gradient is especially significant at high bunch charges where beam quality can suffer due to space charge. The high gradient also generates significant field emission or dark current which must be mitigated. A DC gun was considered but operates at significantly lower gradient leading to larger beam sizes at high bunch charge and reduced beam quality. DC guns currently operate around 350 kV and have not yet demonstrated reliable operation at 500 kV. Superconducting RF guns have not reached the necessary maturity at this time to be considered a reliable option for a user facility.

5.2 Drive Laser System

The LCLS-II photoinjector drive lasers systems consist of (1) a photocathode drive laser system and (2) a laser-heater laser system. In combination with the photocathode and the injector RF cavity, the photocathode illumination laser defines spatial and temporal characteristics of the injector electron bunch. The laser heater generates an uncorrelated energy spread in the electron beam to suppress micro-bunching instabilities. The design of both laser systems is driven by the simultaneous requirements for high average power, transverse and longitudinal beam quality, stability, and high reliability.

5.2.1 Photocathode Drive Laser Requirements

Summary requirements of the photocathode drive laser are given in Table 2. The proposed photocathodes for the LCLS-II injector are made of a semiconductor compound such as cesium telluride (Cs_2Te) that has demonstrated QE of greater than 10 percent, but have work functions of more than 4 eV, requiring UV illumination. Taking 0.5 percent as a lower limit of QE before cathode replacement, and selecting a wavelength of about 257.5 nm, the maximum bunch charge of 500 pC requires 0.5 μJ of laser light on cathode per electron bunch, or 0.5 W average power at 1 MHz repetition rate. Losses from spatial and temporal beam conditioning, together with beam transport losses, are estimated to be of order 90 percent, requiring 5 W average power in the UV.

The UV light will be generated through harmonic generation of an IR laser with an expected efficiency of 10 percent, requiring an average power of 50 W in the IR.

No commercially available lasers exist that can meet all of the requirements of the LCLS-II photoinjector, but there are several technologies that can be extended and developed to meet these requirements. Candidate laser system technologies include Ti:sapphire oscillator/amplifier systems, SESAM mode-locked thin disk oscillators [1] and fiber oscillator/amplifier systems. Of these technologies, the fiber oscillator/amplifier systems currently have the best combination of average power scalability, beam quality, and power and timing stability. Fiber-based laser systems with 10 W output power, MHz repetition rate, and high transverse and longitudinal beam quality are commercially available [2] today. The drive laser system for the Advanced Photoinjector EXperiment (APEX) gun test facility at Lawrence Berkeley National Laboratory (LBNL) is very similar to the required laser system [3].

Table 2. Photocathode Laser Parameters.

Parameter	Unit	Value
IR wavelength	nm	1030
UV wavelength	nm	257.5
Maximum average IR power	W	45.9
Maximum average UV power from laser	W	4.6
Maximum average UV power at cathode	W	0.5
Minimum UV power stability (RMS)	%	1%
Minimum pointing stability (RMS)	μm	10
Beam size on cathode (RMS)	μm	50-500
Transverse beam shape on cathode		uniform
Pulse duration on cathode (flat-top)	ps	20-60
Maximum intensity variation on cathode during pulse	%	10
Maximum pulse rise/fall time on cathode	ps	2
Oscillator repetition rate	MHz	37.14
Oscillator period	ns	26.92
Maximum timing jitter relative to RF (RMS)	fs	100
Laser output repetition rate	MHz	0.93
Laser output period	μs	1.08
Output pulse timing variation for beam spreader (±)	ns	26.92

Infrared emission at 1030-1070 nm can be obtained from Ytterbium (Yb^{3+}) doped fibers. Direct pumping at 980 nm is possible, with small quantum defect. Ytterbium-doped fiber oscillators deliver very stable sub-ps pulses to the amplification stage. The oscillator frequency (37.14 MHz) is the 35th sub-harmonic of the accelerating RF frequency (1.3 GHz) and the 5th sub-harmonic of the electron gun (185.7 MHz) frequency. The synchronization between the accelerating cavity frequency and the laser will be assured by a feedback loop around the laser oscillator, controlling the cavity length via a fast piezo-actuator (multi-kHz bandwidth). Timing jitter detection and feedback electronics will be similar to the existing LCLS or APEX systems. These systems operate with timing jitter of less than 100 fs RMS, and significantly better performance is expected with a fiber oscillator due to the inherently low phase noise.

Ytterbium-doped silica fibers can be used as amplifying media in chirped pulse amplification (CPA) schemes, taking the average power up to tens of Watts. The gain bandwidth of such fibers supports sub-picosecond pulses, and the high saturation fluence allows the generation of high-energy pulses. The large bandwidth allows also for fast rise/fall time. The demand for very short rise/fall time comes from the need to control the beam halos, which is a major concern in high-repetition-rate machines, mainly for equipment protection.

Acousto-optic pulse pickers at the pre-amplification stage can be used to take the repetition rate down to the targeted ~ 1 MHz. Some flexibility in the precise timing of individual electron bunches is required for bunch selection with an RF deflecting cavity. The pulse pickers will enable gating oscillator pulses shifted in time by one period of the oscillator (e.g. ± 26.92 ns for a 37.14 MHz oscillator frequency). Changing the timing between amplified pulses by approximately 3 percent of the normal period may result in corresponding changes in the pulse energy of adjacent pulses. If the variation in pulse energy is unacceptably large, an energy correction scheme could be developed using electro-optic modulators in the pre-amp stage.

The LCLS-II specification calls for a uniform, hard-edged transverse laser profile which can be achieved by using an adjustable telescope, a hard aperture, and a relay-imaging system to project the beam profile at the aperture onto the cathode. The beam size on the aperture can be selected to determine the exact spatial distribution that is projected onto the cathode. For a highly uniform beam profile, more than 50 percent of the pulse energy is lost with this scheme. A three-lens telescope system in front the aperture can be designed to offer flexibility on the choice of beam size and fluence at the cathode.

The temporal structure requirements for the photoinjector is a “flat-top” pulse of 20-60 picoseconds, with rising and falling edges of less than 2 ps. The required temporal laser shaping can be achieved by pulse stacking schemes using birefringent crystals have been demonstrated to be both reliable and efficient. In such systems, a train of delayed replicas of the original input pulse, each with orthogonal polarization, is generated by means of a chain of birefringent crystals with different thicknesses [4]; these pulse replicas will partially overlap in time, forming a quasi-flat-top beam. The rise and fall time of the shaped pulse depends on the initial pulse length. The appealing characteristics of this scheme are simplicity and efficiency (around 90 percent when

using anti-reflection coated crystals). The drawback is the lack of flexibility in pulse time duration, which can only be changed from the nominal by factors of two. More flexibility can be gained at the detriment of simplicity and efficiency. As an example, grating-based “4f” shapers [5] allow continuous span of pulse length along extended ranges. Experience from the development of the LCLS laser system has shown that such direct temporal shaping schemes have significant complexity, poor reliability, and do not match the performance of pulse stacking methods.

The laser needs the capability to switch continuously from 1 MHz to 1 Hz in order to allow different machine operation modes, such as beam diagnostics or beam-based alignment. Electro-Optic Modulator (EOM) Pockels cells would be the first choice as pulse pickers because of their high-efficiency and high-damage threshold, however few EOM products for pulses at MHz rep-rate are currently commercial available due to the challenges of driving high voltage at high rep-rate and suppressing acoustic resonances in electro-optic crystals. An alternative is to use acousto-optic modulators (AOM) that can operate up to many MHz repetition rate. The diffracted beam coming out from the crystal has a different angle with respect to the zero order beam, and the efficiency can be as high a 75 percent. Depending on the laser pulse peak power, different materials can be chosen, but usually the ones with the highest damage thresholds are not the ones with the highest efficiency. Both EOM and AOM technologies will be evaluated for efficiency, contrast ratio, peak power handling, rep-rate flexibility, and commercial availability.

The beam transport from the laser room to the photoinjector cave will follow the model of LCLS, using relay imaging optics and transport through an evacuated beam pipe to minimize contamination of optics and the detrimental influence of air currents on the beam profile and beam-pointing stability. Near the gun imaging optics with the required magnification will image the aperture to the cathode plane.

Laser system diagnostics will include cameras to monitor the beam profile; calibrated photodiodes and power meters to monitor energy and power stability; IR and UV cross-correlation diagnostics to monitor pulse duration; and position sensitive detectors (cameras and/or quad photodiodes) to monitor and provide feedback to beam pointing stabilization systems. The gun area will have a virtual cathode diagnostic consisting of a camera that will be placed in an equivalent optical plane as the cathode to monitor the beam profile of a small fraction of the laser energy.

The MHz repetition rate of the laser will enable measurements of beam pointing and energy jitter with high enough bandwidth that effective feedback loops can be put in place to correct noise at many kHz bandwidth. For example, beam-pointing jitter from mechanical vibrations in the laser, beam transport, and photoinjector could be corrected by using feedback loops to drive mirrors with high-speed piezo-actuators.

5.2.2 Laser Heater Requirements

Summary requirements of the laser heater laser are given in **Table 3**. In most regards, the requirements are quite close to those of the photocathode drive laser, and it is beneficial to have the two lasers be as similar as possible for operational efficiency and redundancy. The minimum pulse energy required for maximum level of beam heating (20 keV RMS) is 7.5 μJ for 40 ps laser pulse duration and identical sizing of the laser beam and electron beam in the heater undulator. In order to relieve the drift and jitter effects from perfect alignment between beams, the laser beam size can be doubled, requiring twice the pulse energy, 15 μJ . Beam transport losses are estimated at 25 percent, requiring 20 μJ at the input to the beam transport. A pulse stacker will be used to produce a 40 ps flat-top. The stacking scheme produces two orthogonal polarizations, but only photons with polarization parallel to the undulator's wobble plane will interact with the electrons and heat the beam. Thus the stacker efficiency is estimated to be 40 percent and the required average IR power is 50 W.

Table 3. Heater Laser Parameters.

Parameter	Unit	Value
Heater wavelength	nm	1030
Electron bunch duration (rms)	ps	7
Heater pulse duration (FWHM)	ps	40
Peak power	MW	0.13
Minimum pulse energy for maximum heating	μJ	7.5
Spatial overlap of laser and e-beam	%	200%
Minimum laser energy for maximum heating and overlap	μJ	15
Beam transport transmission efficiency	%	75%
Minimum laser energy into beam transport	μJ	20
IR laser pulse stacker transmission efficiency	%	40%
Minimum IR laser energy into pulse stacker	μJ	50
Laser repetition rate	MHz	1
Minimum laser average power	W	50

The 50 W power levels are similar to the photocathode drive laser requirement, which is higher than current state-of-the-art commercial systems. The power requirement can be reduced by decreasing the duration of the pulse and/or by reducing the beam size in the undulator. If longer pulse duration and larger beam size are determined to be critical to performance, alternative laser technology may be suitable for the laser heater. For example, conventional

master oscillator power amplifier (non-CPA) laser systems directly producing tens of picosecond pulses and tens of W of average power are already commercially available [6] and this technology could be extended to meet the specific requirements of the heater.

As is the case for the existing LCLS, we could consider using the residual IR after harmonic generation from the photocathode drive laser as the laser heater beam. This would reduce the costs and has the advantage of perfect timing synchronization of the two beams. However, this is not an ideal solution in terms of power or spatial and temporal quality of the heater beam. The conversion efficiency from the IR to the second harmonic will be of order 40 percent, reducing the available IR to about 18 W. The harmonic conversion process is nonlinear with laser intensity, resulting in a distorted spatial and temporal profile of the residual IR, which will reduce the effectiveness of the laser heater.

Synchronization, pulse timing, beam transport, and diagnostics for the laser heater system will mirror those for the photocathode drive laser.

5.3 Photocathode

The photocathode for the LCLS-II requires high quantum efficiency, low intrinsic emittance, long operating lifetime and prompt response time. Significant progress has been made in the three years since the cathode options were described [7], including the validation of the three-step model for the intrinsic model of a semiconductor cathode by two independent groups [8-9]. This progress was made in addition to the tremendous advances in operating high QE cathodes in high average current guns. The DC gun results from Cornell University are especially exciting, showing a bi-alkali cathode producing 75 mA of beam without any lifetime limit [10]. More information about recent cathode development can be found at the Physics of Photocathodes for Photoinjectors (P3) Workshop website [11].

The LCLS-II cathode system will consist of a cathode fabrication chamber, a UHV “suitcase” for storing and transporting the cathodes, and a load lock for inserting and removing cathodes in both the fabrication chamber and the gun. The suitcase and load lock is based upon the INFN Milan LASA design developed for the European XFEL project. This system has supplied Cs₂Te cathodes for testing at the PITZ gun facility in Berlin and for operations at the FLASH FEL in Hamburg. This equipment allows cathodes fabricated in Milan, Italy, to be transported using the suitcase to the facilities in Germany. The suitcase is also used to transport spent cathodes back to Milan for post-mortem analysis. A similar approach will be used for LCLS-II. The fabrication will be done at a cathode lab at either LBNL or SLAC, and then the suitcase will be used to transport cathodes into the load lock for insertion into the LCLS-II gun.

The Cs₂Te cathode has been chosen as the baseline cathode for LCLS-II due to its long history of use at the FLASH facility, the availability of a proven cathode storage and transport system (suitcase), and a load lock for transferring cathodes into and out of the gun. An INFN Milan LASA cathode suitcase and load lock has been purchased by LBNL as part of the development work for the NGLS project. The LASA group also fabricated Cs₂Te cathodes, which

were shipped to LBNL in the suitcase. Figure 2 and Figure 3 show the equipment installed and in use at the APEX facility. The LASA Cs₂Te cathodes still had a QE greater than 10 percent after a year's storage in the suitcase, and are currently being used in the APEX beam studies.



Figure 2. Ultra-high vacuum suitcase used to transport and store cathodes.



Figure 3. Left: loadlock system CAD view. Right: Apex gun with cathode load lock and suitcase attached.

While Cs₂Te is the current baseline for the LCLS-II project, the cathode system has enough flexibility to produce and use other cathode types, which have lower intrinsic emittance or reduce the complexity and cost of the drive laser and optics. Other cathodes built on the same style plug can be installed in the suitcase and transferred to the gun. A possible cathode material is K₂CsSb, which emits electrons with visible light and has both high QE and relatively low intrinsic emittance. It also has the required operational robustness. This cathode's survivability has been demonstrated in work by Cornell University, where such a cathode produced several mA of average current in a HVDC gun for several hours with essentially no decrease in the QE [10]. In addition independent results from Cornell and LBNL show that K₂CsSb also has relatively low intrinsic emittance and high QE at approximately 500 nm wavelength [8, 9]. This longer wavelength potentially simplifies the drive laser by eliminating the need for a UV laser and optics. K₂CsSb cathodes are already being fabricated in the LBNL cathode lab (see Figure 4) for testing in the APEX gun. Another prospective cathode material is sodium potassium antimonide,

Na₂K₂Sb, which has also operated at high average current with high-QE and relatively low intrinsic emittance [12].

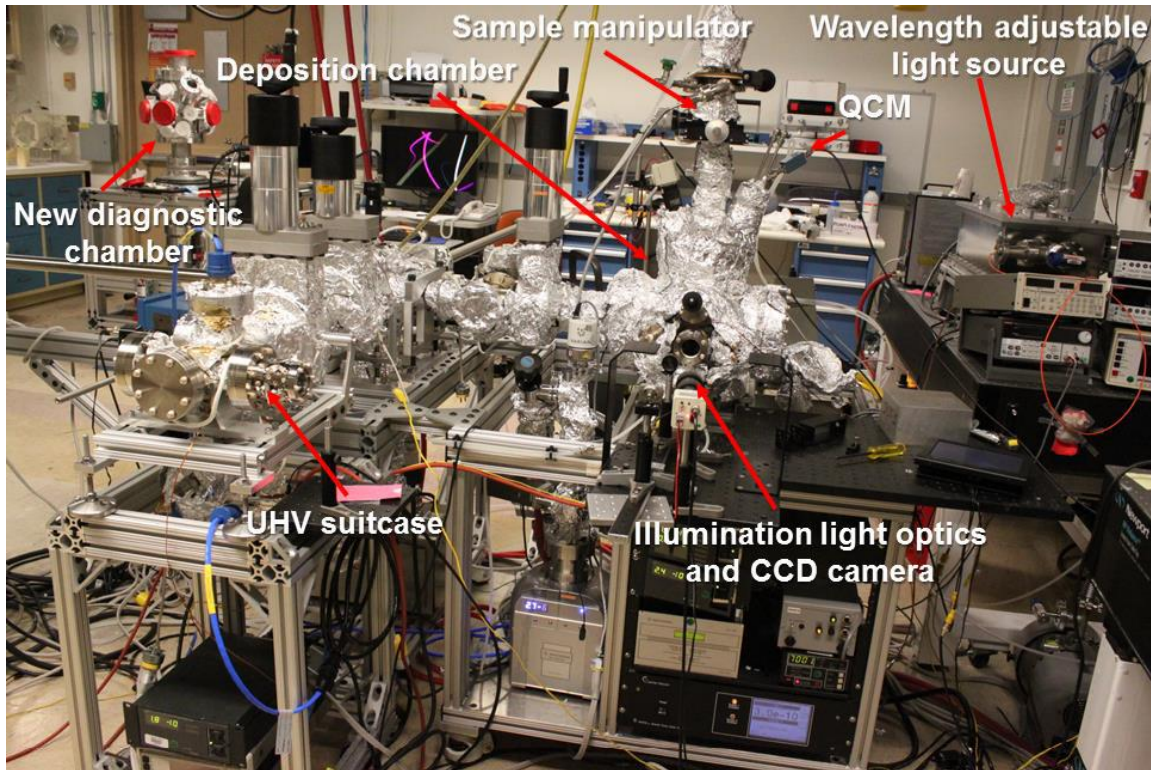


Figure 4. The cathode lab at LBNL used to produce K₂CsSb and other cathodes for APEX [Photo courtesy H. Padmore, LBNL].

5.4 Electron Gun and Buncher

Several different gun technologies with high repetition rate capability exist already or are under active development, but none has yet satisfied all the broad requirements of Table 1. Schemes include direct current (DC) guns, superconducting radio-frequency (SRF) guns, and low frequency normal-conducting radio-frequency (NCRF) guns, the choice we have adopted for the LCLS-II. The main characteristics of these technologies and the rationale behind our specific choice are described here. In DC gun schemes, a static voltage is applied between the cathode, where the electrons are generated and a hollow electrode at the beam exit (the anode) to create the static electric field that accelerates the electrons. Low energy (approximately 100 keV) DC guns with thermionic cathodes are the backbone of a very large number of injectors in applications where a relatively modest brightness is required. DC guns present a number of appealing characteristics. They can operate at very high repetition rates, limited only by the capability of the cathode system being used. They are also compatible with magnetic fields in the cathode/gun region. The low pressures required to operate delicate high QE photocathodes can be achieved despite the relatively large volume of DC gun vacuum chambers. This is made possible by the opening of large-vacuum-conductivity apertures and locating the pumping units inside the main

chamber. As notable examples, DC guns with GaAs:Cs and other semi-conductor photocathodes operating with beam energies up to about 350 kV have demonstrated reliable operation up to 77 pC per bunch, with relatively high-brightness and GHz-class repetition rates [13,14]. To achieve the higher brightness at the high charge per bunch required by X-ray FELs such as LCLS-II, the beam energy at the gun exit and the accelerating gradient at the cathode must be increased beyond the values presently achieved. Several groups are pursuing schemes designed to operate at 500 kV with cathode gradients approaching 10 MV/m. Major issues to be resolved include voltage breakdown and “punctuation,” a discharge caused by charge build-up through the large ceramic that insulates the cathode from the anode and which results in a hole through the insulator wall. Different solutions have been proposed and are being tested. Promising initial results have been obtained by segmenting the ceramic to reduce voltage across each ceramic element, and by separating such parts with metallic electrodes shaped to shield the ceramics from field-emitted electrons [15]. Similar solutions are under test at Cornell and JLAB. To prevent high voltage breakdowns in DC guns, the biased parts of the system are typically housed in an inert gas (e.g. SF₆) environment. This process requires that components of the gun must be placed in large inert gas tanks, thus increasing the overall size and complexity of the system.

SRF technology is a natural candidate for consideration in the development of high-repetition-rate electron guns. The accelerating field is generated in resonant structures, which can operate in CW mode and allow for repetition rates limited only by the frequency of the SRF structure and/or by the maximum power that can be fed through the RF couplers. Indeed, a number of groups worldwide are proposing and developing schemes based on such technology, using frequencies ranging from less than 100 MHz to more than 1 GHz. Gradients in SRF guns are typically higher than those in DC guns, and in some designs values in the ballpark of 40 MV m⁻¹ are being targeted [16]. While such large gradients can be advantageous for beam dynamics, they may also increase the amount of dark current as a result of field emission from the gun parts. This is an issue of particular importance in high-repetition-rate injectors, and requires careful evaluation. The effective cryopumping by the superconducting wall allows for the low pressures required by high QE photocathodes, although contamination and compatibility issues between cathode materials and the super-conducting structures need to be carefully evaluated and experimentally tested. On this issue, results at Rossendorf, Germany, with Cs₂Te photocathodes in a SRF gun have shown promising results [17]. Because of field exclusion by the superconducting walls (Meissner effect), and of the magnetic field quenching threshold, magnetic fields in the cathode region cannot be easily applied. Schemes under study include those where the required solenoidal magnetic field configuration is generated by exciting a particular high-order mode in one of the gun accelerating-cells, or where cryo-compatible solenoids are housed inside the cryostat. SRF technology requires cryostats and refrigeration systems, and therefore significant system complexity.

A significant number of normal-conducting radio frequency guns operating in L-band (about 1 to 2 GHz) and S-band (about 2 to 4 GHz) have been developed and successfully operated in photoinjector schemes. Remarkable examples are the FLASH L-band gun at DESY [18] and the

LCLS S-band gun at SLAC [19], both of which are reliably operating beams with the brightness required by their respective X-ray FELs. NCRF guns are a reliable and mature technology with several important features. They have successfully achieved gradients during photoemission at the cathode greater than 60 MV/m, which allow running high charge bunches with relatively short bunch lengths. The NCRF guns are also compatible with most cathode types and with the presence of magnetic fields in the cathode area. However, at these high frequencies, the size of the resonating structures is relatively small. Consequently, the power density on the cavity walls assumes significantly larger values when the cavities are operated at the required gradients. Removing heat from the structure becomes a challenge, and studies have shown that this issue can limit the maximum achievable repetition rate for these guns to about 10 kHz [20]. In addition, because of the small RF wavelength in such guns, field distortion and preservation of RF performance do not allow for large pumping apertures. This limits the overall vacuum performance and, potentially, the compatibility with the most “sensitive” cathodes.

In order to preserve the positive characteristics of high-frequency NCRF guns and to extend their capability to operate at higher repetition rates, several groups developed schemes using NCRF structures resonating at lower frequencies. At these lower frequencies, the resonant structures become larger and the power density on the walls decreases. Below a certain frequency, the cavities can start to run in CW mode. Indeed, a CW NCRF gun, resonating at 700 MHz and equipped with a state-of-the-art cooling system has been developed and successfully conditioned at full-power at Los Alamos National Laboratory [21]. If the RF gun frequency is pushed further down in the VHF band (30–300 MHz), the power density on the walls becomes sufficiently small to be handled by conventional water-cooling techniques. Such schemes are based on mature RF and mechanical technology. They offer remarkable simplicity, and their performance in terms of reliability is promising. Moreover, because of their long wavelength, significantly large apertures can be opened in the cavity walls with negligible field distortion. This allows for high-vacuum conductance when connected to vacuum pumps located outside of the cavity walls. This way, extensive pumping can be used to obtain the low pressure in the gun. As is true for their higher frequency counterparts, low frequency NCRF guns are also fully compatible with the presence of magnetic fields in the cathode region. However, lower frequencies also imply lower accelerating fields. The values for such a quantity are substantially higher than those for DC guns, but are significantly smaller than those of the high frequency NCRF case. The VHF NCRF we adopted for LCLS-II gun operates at 186 MHz with approximately 20 MV/m. More details on the gun are included in the next section.

5.4.1 The VHF Electron Gun

The VHF gun has been developed at LBNL [22-23] in the framework of the APEX project, and has been designed to satisfy the requirements of Table 4 using reliable and mature mechanical and RF technologies. The core of the gun is a normal-conducting copper RF cavity resonating at 186 MHz in the VHF band. Figure 5 shows a cross section of the VHF cavity with the main components, while Table 4 includes its main parameters.

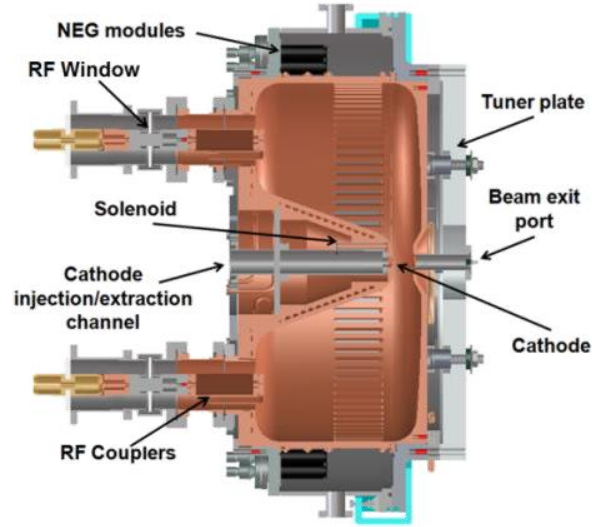


Figure 5. VHF cavity cross-section, showing the cavity's main components.

Table 4. LBNL VHF gun parameters list.

Parameter	Symbol	Unit	Min. Value	Nom. Value	Max. Value
Frequency	f_G	MHz	-	186	-
Operation mode				CW	
Beam energy at the gun exit	E_G	keV		750	-
Field at the cathode at photoemission	E_C	MV/m		19.5	
Quality factor (ideal conductor)	Q_0			30900	-
Shunt impedance	R	M Ω	-	6.5	-
Nominal RF power for Q_0	P_0	kW		88	
Stored energy	E_S	J	-	2.3	-
Peak surface field	E_P	MV/m	-	-	24.1
Peak wall power density	P_W	W/cm ²	-	-	25
Accelerating gap		cm		4	
Diameter/length		cm		69.4/35.0	
Design operating pressure		Torr		$\sim 10^{-10}$ - 10^{-9}	

Two major goals were targeted by this design: the CW operation capability and the low vacuum pressure performance. Indeed, because of the low frequency, the structure body is large enough to withstand the heat load present when operating in CW mode with the high electric fields required by a high brightness photoinjector. Furthermore, the long RF wavelength allows

for the large high-conductance vacuum ports (the numerous slots visible along the “equator” of the cavity in Figure 5), which are necessary for achieving the desired vacuum pressure. Additionally, the use of a large number of NEG modules as the main pumping system allows efficient removal of those molecules like H₂O, O₂, CO, CO₂, which are particularly detrimental semiconductor cathodes. A vacuum load lock system, based on the INFN design [24] in use at FLASH, will allow the quick replacement of photocathodes under vacuum.

The resonant copper structure is surrounded by a stainless steel shell (visible in Figure 5) which ensures the required mechanical rigidity and the proper vacuum sealing. No sliding tuner is present, and the required frequency tuning is achieved by a mechanical system that slightly pushes or pulls the cavity wall at the beam exit port side. The RF power is supplied through two magnetic loop couplers diametrically opposed on the cathode back wall of the cavity. The 186 MHz frequency choice is the seventh sub-harmonic of 1.3 GHz, the frequency of the SC linac technology selected for the LCLS-II linac.

The design includes an embedded solenoid in the cathode nose, the primary function of which is that of “bucking” coil to nullify the magnetic field on the cathode surface. The achievable field intensity is large enough to allow for generating the correlation in the beam transverse plane required by emittance exchange techniques.

The relatively moderate peak field value of about 24 MV/m (about 20 MV/m at the cathode) was selected as a tradeoff between beam dynamics requirements and the need to minimize dark current. Values of dark current in the few μ A range have been measured in the VHF gun operating in APEX at the nominal field of \sim 20 MV/m. Simulation studies using those values and a linac layout similar to the one of the LCLS-II, indicate that the dark current beam power is borderline acceptable. Techniques on how to reduce dark current (different cavity wall cleaning, or active removal) are being studied and will be tested at APEX (more details in Section 5.4.2). It should be also mentioned that if a further reduction of dark current is required, a moderate decrease of the accelerating field in the gun, would minimally affect the transverse brightness performance while significantly reducing the dark current emission due to the exponential dependence on applied field. For example, based on simulations and APEX measurements, a 20% field decrease (16 MV/m) in the gun would increase the transverse emittance by roughly 10% while reducing dark current by about a factor 5.

Extensive multipacting simulations with several different codes (already confirmed by experimental results) showed that a broad region around the operating voltage is free of multipacting resonances. These same validated codes will be used to eliminate any possible resonances inside the buncher cavity over the desired range of RF powers.

With the theoretical quality factor shown in Table 4, the cavity would require approximately 90 kW to generate the desired field intensity. The actual quality factor after fabrication is typically on the order of 10 percent lower, and for reliability reasons the power source should not operate at its maximum power. Accounting for these two factors, we specify the source for a maximum CW power value of 120kW. Different RF power technologies can be used for the

development of the 186 MHz, 120 kW CW RF source. Solid state amplifiers reached the required level of maturity to deliver the necessary reliability and probably represent the least expensive solution. Schemes based on tetrodes tubes have already demonstrated performance and reliability in this frequency range and represent a viable option.

An R&D program targeting the demonstration of the performance of an injector based on the VHF gun is underway at LBNL under the name of the Advanced Photoinjector Experiment (APEX). APEX has already demonstrated a number of fundamental milestones, including CW operation, design energy, and vacuum performance [25]. Additional tests demonstrate QE lifetimes compatible with user facility operation with Cs₂Te cathodes that generate several hundred pC bunches at MHz repetition rate [26]. Experiments to measure the emittance at 100-500 pC charges at 30 MeV beam energies are planned in FY2015.

5.4.2 Buncher and Solenoids

Aside from the gun, the injector includes several other subsystems to accelerate the beam to relativistic energies while preserving beam brightness and simultaneously compressing the bunch length to the level required by the downstream linac. A room temperature, 1.3 GHz CW RF buncher cavity is located between the VHF gun and the injector accelerator in order to initiate the bunch compression in the injector. The cavity, shown in Figure 6, is a scaled version of the 1.5 GHz third harmonic cavities developed for the Advanced Light Source at LBNL. Because of the relatively low energy of the electron beam at the buncher position, the required fields can be achieved in CW mode by the reliable and simple room temperature technology. The choice for buncher frequency to be the same as the main linac satisfies beam dynamics requirements while reducing the complexity of the RF power system. The RF power source for the buncher cavity must be capable to deliver about 20 KW of CW power. The buncher cavity design includes three dummy ports rotated every 90 degrees from the coupler port to eliminate dipole and quadrupole field components and work is in progress to reduce the required power and evaluate thermal effects due to the rf coupler. Due to the long bunches needed to minimize space charge at the highest bunch charges, we will explore the need to replace the 1.3 GHz buncher with a 650 MHz subharmonic buncher to better linearize the longitudinal phase space and increase the fraction of electrons that are able to contribute to the lasing process.

The two solenoids upstream and downstream of the buncher generate the magnetic fields required by the emittance compensation process. The relatively low energy of the beam allows for compact magnets with conventional water-cooling. The fields required for emittance compensation (and for solenoid scans during thermal emittance measurements) are obtained with a magnetic length of about 20 cm and magnetic fields of up to a few kG. The magnets are installed on remotely controlled actuators that allow for the complete online alignment of the magnets. Each magnet is also equipped with normal and skew quadrupole coils for the correction of undesired multipolar component of the magnetic field.

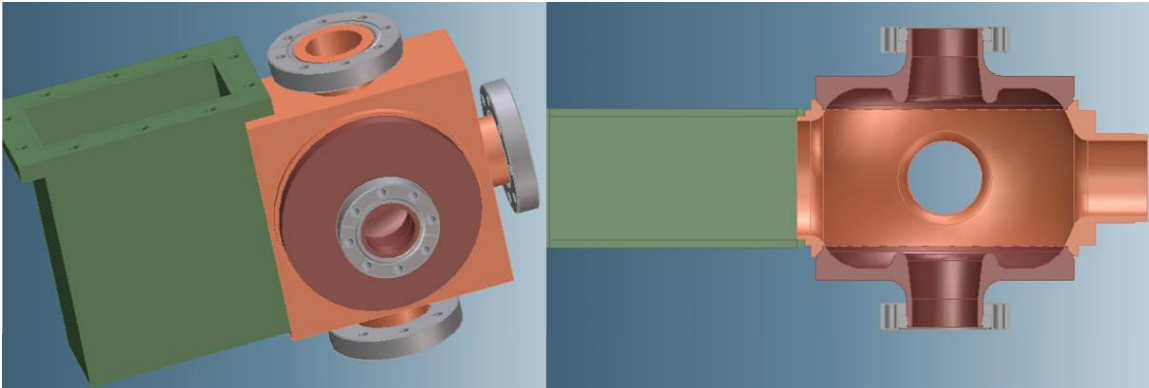


Figure 6. The LCLS-II injector buncher cavity and input coupler. Left: 3D CAD view. Right: cross section view.

In addition to the buncher and solenoids, a dark current mitigation technique is needed to reduce the dark current to acceptable levels. Due to the high gradient achievable in the RF gun, a significant amount of dark current can be emitted. R&D will be needed to minimize the dark current which, due to the high beam power ($1 \mu\text{A}$ at 4 GeV is 4 kW), can damage downstream components. A possible solution might be to add a temporally varying “sweeper” that allows the desired electron bunches through unchanged but imparts a transverse momentum to other undesirable bunches that are subsequently lost on a dump before the injector accelerator. Feasibility studies on such a device are underway at APEX and R&D is required for the LCLS-II gun. Moreover, there is evidence that if the gun surface is cleaned according to superconducting cavity or other promising recipes the dark current could be reduced to levels similar to those of superconducting cavities, making additional mitigations unnecessary [27-28]. Experiments to confirm this hypothesis are also necessary.

And finally a wakefield budget will be established for the low energy section of the injector between the gun and cryomodule and an analysis will determine the need for any wakefield mitigation. If necessary, the designs for bellows liners and plugs for view screen crosses which were used in LCLS-I can easily be adapted to the LCLS-II gun-to-linac beamline.

5.5 Injector Accelerator

In the LCLS-II injector, the 750 keV electron beam from the gun is accelerated to 98 MeV by eight, 9-cell 1.3 GHz SRF cavities of the Tesla type in a single 12 m long cryomodule. The cavities are of the same type as in the LCLS-II main linac but with individual control of RF phase and power for each cavity, in order to properly control the emittance compensation and the velocity bunching processes along the injector. Couplers should be located at the downstream end at the highest beam energy to minimize emittance growth. In addition, simulations indicate that the first few cavities will require symmetrized RF couplers and modified HOM absorbers in order to reduce dipole and quadrupole field components that introduce emittance growth at low energy. We will explore the benefits of adding additional symmetrized RF couplers for every n cells instead of the single coupler for all 9 cells in the first cavity. This will allow additional amplitude

and phase adjustments at low energy to further control emittance growth and velocity bunching instead of operating with fixed phase advance between cells.

In general, the LCLS-II injector linac will use standard diagnostics systems, which are described in Chapter 9 of this report and shown in Figure 1. Tune-up of the beam will be conducted using a lower repetition rate than nominal to avoid exceeding beam containment and machine protection system thresholds. Beam tuning will occur in two modes. Initial setup will be conducted using the off axis diagnostic line at a low rate of less than 100 Hz with beam charges of about 100 pC. Final beam tuning occurs at full rate with beam switched back to the main transport line. The lower initial repetition rate will allow diagnostic systems to operate in pulse-by-pulse mode.

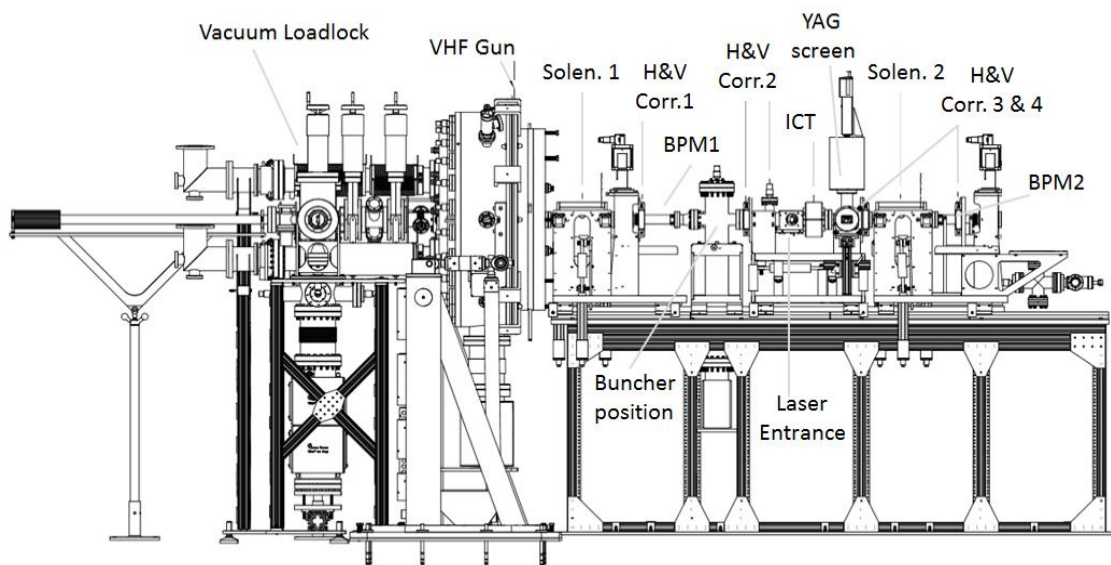


Figure 7. APEX low energy beamline with components and diagnostics. LCLS-II low energy injector beamline will clone the APEX layout.

In order to tune components in the low energy injector section (less than 750 keV) before the injector accelerator, it is essential to measure the beam orbit, current and profiles utilizing two sets of stripline BPMs, one ICT, one beam profile system (based on a YAG screen), and several horizontal and vertical steering magnets in order to allow for beam energy, thermal emittance, average current, and single bunch charge measurements. The YAG screen will be used for beam imaging and emittance measurements. It will also allow gun energy optimization and calibration. Using this screen, thermal emittance measurements at very low charge are possible by using the solenoid scan technique. The layout of the low energy diagnostics is shown in Figure 7.

The injector accelerator will contain the standard systems for RF amplitude and phase control. Each 9-cell cavity will be controlled independently, and is fed by an independent klystron; the last cavity is not powered, to be available as a spare. Independent amplitude and phase control are critical requirements to allow optimum control of the transverse and longitudinal phase space during acceleration of the low energy beam.

A laser heater (LH) is included to induce a controllable growth in the uncorrelated energy spread as a way to suppress the microbunching instability. A permanent magnet (PM) undulator positioned in the middle of a small magnetic chicane causes an interaction between the electron beam and a co-propagating conventional laser pulse that modulates the electron beam energy. This modulation then turns into the desired uncorrelated energy spread as the beam exits the chicane and the electrons slip longitudinally with respect to one another because of their finite transverse emittance. The total uncorrelated beam energy spread is the quadrature sum of the LH-induced contribution and the typically small natural energy spread at the injector exit (on the order of 1-2 keV rms). The laser wavelength is 1030 nm with 7.5 μ J/pulse energy to allow the LH laser to be nearly identical to the cathode drive laser; the corresponding undulator period based on the undulator resonance condition is 4.71 cm, with 10 periods corresponding to a few percent bandwidth. It is expected that 6 keV rms energy spread is sufficient to suppress the microbunching instability, although we set a 20 keV rms requirement for the maximum heating capacity. A more detailed description of the laser heater, including initial simulation results, is included in Chapter 7.

Downstream of the laser heater, the primary beamline contains the standard non-destructive BPM diagnostics and ICT, plus an emittance and beam matching section. A separate diagnostics section as shown in Figure 1 will include a deflecting cavity (TCAV) for longitudinal phase space measurements including bunch-length, energy spread, timing jitter as well as slice emittance measurements. YAG screens are included to measure beam profiles and allow fast routine emittance measurements at low duty cycle. In addition, a wire scanner system is included to eliminate the effect of coherent optical transition radiation on emittance measurements due to the laser heater chicane. The machine protection system will be specifically designed to prevent insertion of diagnostics devices at beam rates and/or charges that pose a risk of device damage.

5.6 Injector Beam Dynamics

The LCLS-II injector consists of a 186 MHz normal conducting RF gun and a single-cell 1300 MHz normal conducting buncher, two solenoids used for emittance compensation, and one cryomodule with eight 9-cell superconducting cavities. The 186 MHz RF gun accelerates the electron beam to 0.75 MeV. From a beam dynamics perspective, the 186 MHz RF gun is equivalent to a DC gun as the transit time across the 4 cm gun gap is only 0.2 ns, which is much smaller than the 5.38 ns period of the RF gun. The 1300 MHz buncher is used to compress the bunch length from 5-15 ps rms down to about 3 ps rms, with zero-crossing phase technique and the first two accelerating cavities can provide additional compression. The first seven accelerator cavities boost the electron beam energy to 98 MeV, while the eighth cavity is typically not powered but available as a spare.

As the relatively low energy of the beam at the gun exit, which leads to stronger space charge effects, relatively long laser pulses (30-60 ps flat-top and 2 ps rise/fall time) are needed to generate the electron beam and to reduce space charge effects. A conservative cathode intrinsic emittance

of 1 $\mu\text{m}/\text{mm}$ -rms is included for the beam dynamics simulation with the ASTRA code [29]. Multi-objective genetic algorithms are used to optimize a larger number of parameters for the injector performance [30]. Table 5 shows the example of the parameters range for optimizations.

Table 5. Injector Optimization Parameter List with Function and Range.

Parameter Name	Function	Range of Values
Electron gun phase (wrt crest)	Initial energy, gun transit time	(-15) – (15) deg
Solenoid 1, 2 strength	Emittance compensation, transverse beam size control	0.01 – 0.2 T
Buncher peak field and phase (wrt crest)	Longitudinal compression	0 – 4 MV/m, (-120) - (-50) deg.
1st and 2nd 1.3 GHz cavity peak field and phase (wrt crest)	Longitudinal compression emittance compensation	5 – 29.5 MV/m (-70) – (70) deg.
6th and 7th 1.3 GHz cavity phase (wrt crest)	Remove linear chirp	(-70) – (70) deg.
Beam diameter and bunch length at the cathode	Initial size, emittance and bunch length control	0.050 – 2 mm, 20 – 60 ps

The first objective of the optimization process is to minimize the transverse, normalized emittance, and the second objective is to achieve the desired bunch length or peak current at the injector exit for a given charge. Additional objectives are defined by the need to control longitudinal profile symmetry and reduce higher order correlations and tails in the longitudinal phase space. Figure 8 shows the example of the optimization process for a 100 pC bunch. In this case, only two objectives were considered (emittance and bunch length). The longitudinal phase space for a 100 pC solution is shown in Figure 9, along with the current profile and slice emittance of the beam. As seen in this figure, the peak current is about 12 A, while the slice emittance is less than 0.3 mm-mrad for 95 percent of particles. The evolution of the emittance and the longitudinal rms bunch length along the injector transport is shown in Figure 10. Table 6 summarizes the main beam quantities for 100 pC charge and Figure 11 shows an example of a 300 pC charge solution satisfying the requirements at the injector exit. Further optimizations for nominal 100 pC and higher charge (300-500 pC) are underway.

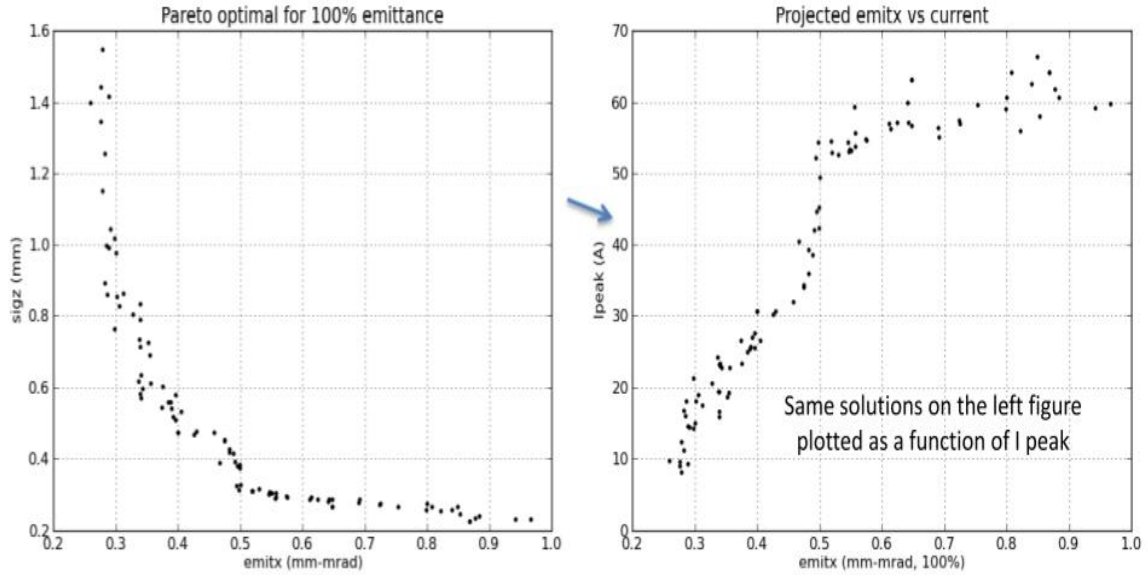


Figure 8. Optimized solutions for 100 pC. Left: rms bunch length vs 100% projected emittance. Right: peak current vs 100% projected emittance, each calculated at the injector exit.

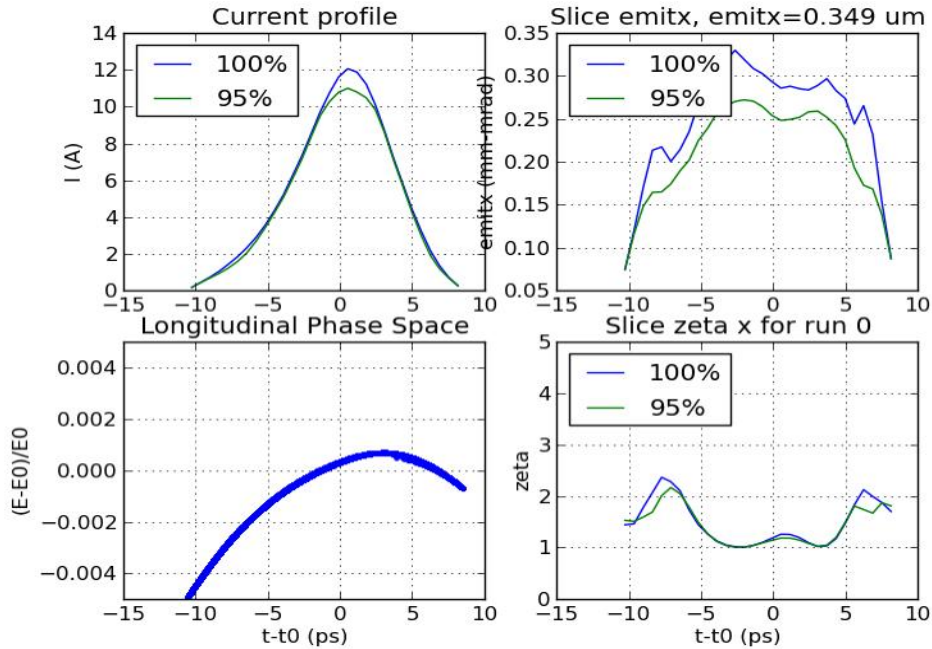


Figure 9. Properties of the optimized beam for 100 pC at the injector exit. Note zeta is the transverse mismatch parameter which indicates how well each slice is matched to the projected beam where a value of 1 indicates a perfect match.

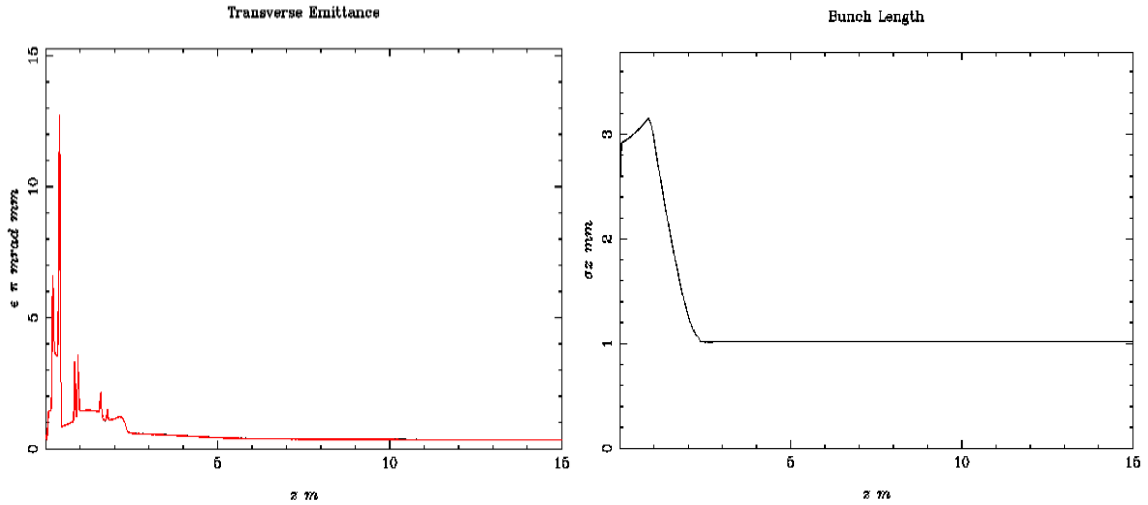


Figure 10. Evolution of transverse normalized rms emittance (left) and rms bunch length (right) along the injector transport for 100 pC.

Table 6. Optimized Values and Main Beam Parameters for 100 pC beam.

Property	Value	Units
Gun gradient	~20	MV/m
Gun phase (with zero defined as max. acceleration)	-8.4	Deg
Laser pulse length flattop/rise/fall	33/2/2	ps
Beam diameter at cathode (uniform distribution)	0.77	mm
Intrinsic emittance	1	$\mu\text{m}/\text{mm}\text{-rms}$
Charge	100	pC
Buncher gradient, phase (with zero defined as max. acceleration)	3.67, -84.5	MV/m, deg
Projected emittance 100%/95%	0.37/0.28	mm-mrad
Sliced emittance 100%/95%	0.35/0.26	mm-mrad
Bunch length at injector exit	~3	ps rms
Peak current	12	A
Beam energy	97.6	MeV

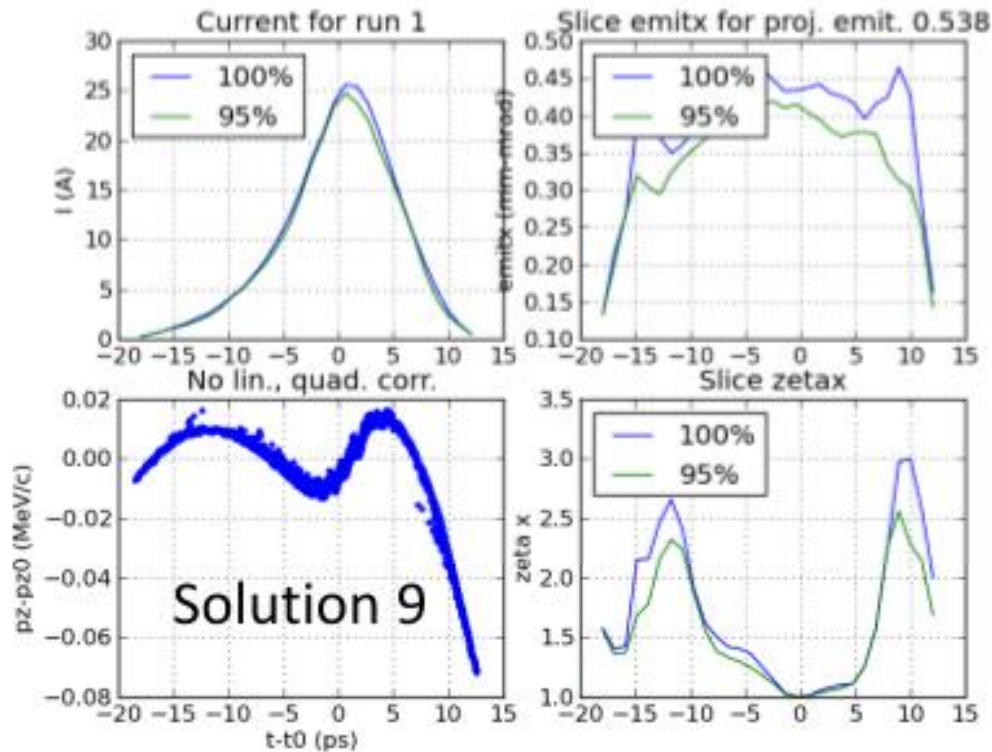


Figure 11. Example of properties of a 300 pC beam at the injector exit.

5.7 Injector Alignment

The injector network will support the survey and alignment of the injector components. Standard networking design and measurement techniques can be used since the injector components have fairly conventional positioning tolerance requirements. The network needs to be in place before any shielding wall is installed, which limits line of sight for highest network monument accuracy. A horizontal sight pipe through the shielding wall needs to be designed to allow a connection of the reference systems in the injector and Linac tunnels during operations. The alignment of injector components will be done using alignment fixtures (balls) attached to a viewable outside surface of the component which have been referenced to either functional internal surfaces or to a measured electrical or magnetic axis of that device. For example, the alignment fixtures on the solenoids should have a known position with respect to the magnetic axis as determined by magnetic measurements, and those on the gun should be referenced to the cathode and gun nosecone. These fixtures should be located on the device to be viewable within the alignment network.

5.8 References

1. Saraceno, C.J.; Schriber, C.; Emaury, F.; Heckl, O.H.; Baer, C.R.E.; Hoffmann, M.; Beil, K.; Kränkel, C.; Golling, M.; Südmeyer, T.; Keller, U. Cutting-Edge High-Power Ultrafast Thin Disk Oscillators. *Appl. Sci.* (2013) 3, 355.

2. See for example: <http://www.imra.com/products/product-lines/fcpa-microjewel/>
3. D. Filippetto et al., "The Photocathode Laser System for the APEX High Repetition Rate Photoinjector", Proceedings of 2013 FEL Conf., New York, NY USA (2013).
4. Shian Zhou, et al., Applied Optics, Vol. 46, Issue 35, pp. 8488-8492 (2007) 248.
5. See for example, Cialdi S., et al, Appl Opt, (2007) 46, 4959.
6. See for example: http://www.ipgphotonics.com/qswitch_ylps20.htm, or <http://www.trumpf-laser.com/en/products/solid-state-lasers/short-pulsed-lasers/trumicro-series-5000.html>
7. D.H. Dowell, et al., Nucl. Instrum. Methods Phys. Res. A 622 (2010) 685.
8. I. Bazarov et al., "Thermal emittance measurements of a cesium potassium antimonide photocathode," Appl. Phys. Lett. 98, 224101 (2011).
9. T. Vecchione et al., "A low emittance and high efficiency visible light photocathode for high brightness accelerator-based X-ray light sources," Appl. Phys. Lett. 99, 034103 (2011).
10. Bruce Dunham et al., "Record high-average current from a high-brightness photoinjector," Appl. Phys. Lett. 102, 034105 (2013).
11. See <http://www.ins.cornell.edu/Events/Photocathode2012/WebHome.html>.
12. L. Cultrera et al., "Growth and characterization of rugged sodium potassium antimonide photocathodes for high brilliance photoinjector," Appl. Phys. Lett. 103, 103504 (2013).
13. B. Dunham, et al., Proc. of 2012 Int. Part. Accel. Conf., New Orleans, LA, USA, 2012, 20-2.
14. T. Siggins, et al., Nucl. Instrum. Methods Phys. Res. A 475 (2001) 549.
15. N. Nishimori, et al., Appl. Phys. Lett. 102, (2013) 234103.
16. R. Legg, et al., Proc. of 2012 Int. Part. Accel. Conf., New Orleans, LA, USA, 2012, 661.
17. R. Xiang, et al., Proc. of 2012 Int. Part. Acc., New Orleans, LA, USA, 2012, 1524.
18. S. Rimjaem, et al., Proc. of 2009 FEL Conf., Liverpool, UK, 2009, 251.
19. C. Limborg, et al., LCLS TN-05-3, February 2005.
20. J. W. Staples, S. P. Virostek and S. M. Lidia, Proc. of 2004 European Part. Accel. Conf., Lucerne, Switzerland, 2004, 473.
21. D. C. Nguyen, et al., Nuclear Instr. Meth. A 528, (2004) 71.
22. J. Staples, F. Sannibale, and S. Virostek., VHF-band Photoinjector, CBP Tech Note 366. Berkeley, October 26, 2006.
23. K. Baptiste, et al., Nuclear Instr. Meth. Phys. Res. A 599 (2009) 9.
24. D. Sertore, et al., Nucl. Instr. and Meth. Phys. Res. A 445 (2000) 422.
25. F. Sannibale, et al., Phys. Rev. ST - Accel. and Beams 15 (2012) 103501.
26. F. Sannibale, et al., Recent Results from the APEX Project at LBNL, in Proceedings of the 2013 NAPAC2103, Pasadena, CA, August 2013.
27. F. Stephan et al., New Experimental Results from PITZ, in Proceedings of the LINAC2008, Victoria, Canada, Sept./Oct. (2008) 474.
28. A. Brinkmann, D. Reschke, J. Ziegler, Various Applications of Dry-Ice Cleaning in the Field of Accelerator Components at DESY, in Proceedings of the LINAC2008, Victoria, Canada, Sept./Oct. (2008)
29. K. Floettmann, Astra code, DESY, October 2011.

30. C. Papadopoulos et al., Injector optimization for a high-repetition rate X-ray FEL, FEL 2012.

6

SUPERCONDUCTING LINAC TECHNOLOGIES

TECHNICAL SYNOPSIS

Choices for beam energy and pulse repetition rates are motivated by the scientific need for X-ray laser pulses and FEL technology and necessitate the adoption of continuous wave (CW) superconducting RF (SRF) technology for the linac. Designed to accept up to 500 pC electron bunches, up to 1 MHz bunch rate, and approximately 100 MeV beam energy from the injector, the linac provides bunch compression and acceleration up to 4 GeV before directing the beam for distribution into the separate FEL undulator lines. The proposed linac layout, based on the choice of 1.3 GHz TESLA/ILC-like superconducting cavity technology, consists of seven main sections. The first section, the laser heater, connects the linac to the injector, and is intended to control the beam's uncorrelated energy spread and to stabilize the beam dynamics. The beam is then accelerated in Linac 1 (with approximately 200 MeV energy gain), conditioned by passage through a 3.9 GHz third-harmonic RF structure, compressed through a single-chicane bunch compressor at about 300 MeV energy, and then further accelerated to about 1500 MeV in Linac 2. A second bunch compressor allows for further manipulations of the longitudinal phase space, and the final energy of 4 GeV is achieved in Linac 3, with a peak current of approximately 1 kA and bunch length of approximately 100 fs. The linac maximum beam power is limited to 1.2 MW.

The LCLS-II linac conceptual design employs the XFEL cryomodule design, with minimal modifications to accommodate CW operation meeting LCLS-II requirements. Cryomodules containing the cavities and support systems, including cryogen distribution, will be in contiguous sections, with magnets and diagnostics in cold sections near the ends of the cryomodules. The cavity tuners and couplers are to be developed from existing designs. Our choice of an accelerating gradient of approximately 16 MV/m is conservative in terms of present-day cavity capabilities; however it is within a broad optimum of accelerating gradients when full construction and operating costs for CW operation are considered. The average unloaded Q is 2.7×10^{10} at an operating temperature of 2 K, utilizing the most recent advances in SRF technology, and existing cryoplant design. Harmonic cavities are used to linearize the correlated energy spread in the electron bunches, and are based on the 3.9 GHz design successfully implemented at FLASH. Main linac RF cavities are independently powered up to the first bunch compressor, following which single klystrons power multiple cavities in six cryomodule segments.

In addition to supporting the desired high-bunch repetition rates, CW operation of the SRF linac also allows for automated broadband feedback control to ensure stability and uniformity of the electron bunches, with jitter in X-ray pulse parameters perhaps 10 times smaller than that currently achieved with normal-conducting free electron lasers.

6.1 Introduction and Overview

Choices for beam energy and pulse repetition rates are dictated by the scientific needs for X-ray laser pulses and FEL technology, and necessitate the adoption of CW SRF technology for the linac. The major sections of the linac are shown in Figure 6.1.1. Most notable among the LCLS-II design features are a high-repetition-rate (MHz), high-brightness electron source, and a superconducting radio-frequency electron linac operating in CW mode, which will provide bunches at high rate, high average beam power, and with flexible bunch spacing. This chapter discusses the options for the superconducting linac design, and our choices to meet the needs for LCLS-II.

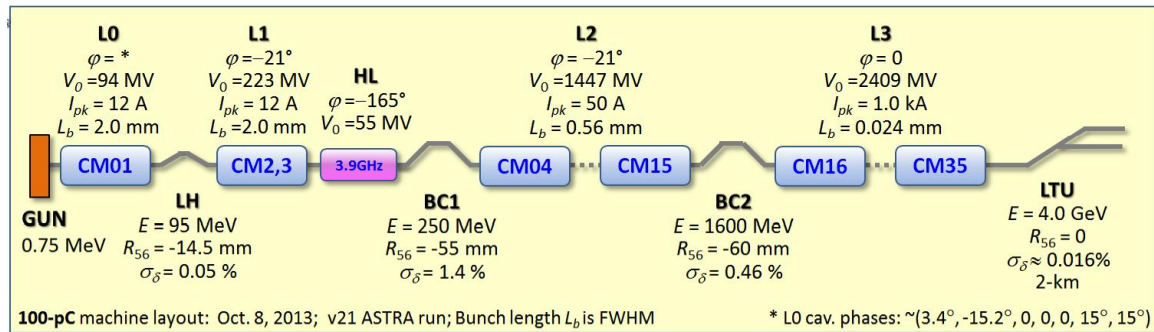


Figure 6.1.1. Schematic layout of LCLS-II injector, linac, bunch compressors, and beam transport with key parameters listed for CW operation with 100-pC per bunch. The eighth cavity in the injector cryomodule (L0) is not used.

The CW SRF linac will provide the backbone for delivery of electron beams initially to two FEL undulators, and with the potential for driving an array of several independent FEL undulators. The machine design concept is for a nominal 1 MHz repetition rate with an average current of 300 μ A, a maximum bunch charge of 500 pC, and upgrade paths consistent with a range of lower bunch charge at increased rate while maintaining average beam power up to 1.2 MW at the linac exit. A variety of bunch time structures may be accommodated by the injector and linac, and our conceptual design allows flexibility to support the desired scientific scope.

As shown in Figure 6.1.1, the injector delivers beam to Linac 0 (L0, with one cryomodule and approximately 100 MeV of energy gain), which is followed by a laser heater that increases the beam's uncorrelated energy spread to suppress the microbunching instability. The beam is then accelerated in Linac 1 (L1, with 2 cryomodules and approximately 200 MeV energy gain), passed through twelve "harmonic linearizer" cavities, compressed in a single-chicane bunch compressor at about a 250 MeV energy, and then further accelerated to approximately 1600 MeV in Linac 2 (L2, with 12 cryomodules). A second bunch compressor allows for further bunch compression, and the final energy of 4 GeV is achieved in Linac 3, the last linac section (L3, with 20 cryomodules). Given the 30-50 A range for the peak current out of the injector, a net bunch compression factor of about 20 to 30 is required. Bunch length varies from 7 ps in L0 to 80 fs (FWHM) in L3.

We propose to use existing SRF technology to the greatest extent possible and to take advantage of the developments in TESLA/ILC/XFEL designs that have been made worldwide.

These developments have resulted in extensive infrastructure for SRF components and systems based on the TESLA 1.3 GHz cavities, including a build-up of cavity and cryomodule assembly and testing capabilities at FNAL during the last decade. CW SRF technology developments at TJNAF (CEBAF, its 12 GeV upgrade, and the JLAB FEL), and at Cornell University (energy recovery linac and injector prototype) will also be utilized.

The LCLS-II accelerator will be based on the 1-meter-long TESLA 9-cell fine-grain niobium cavity, which is used successfully at the FLASH FEL facility at DESY in Hamburg. It will be used at the XFEL facility, now under construction, and is also planned for use in the International Linear Collider. To operate at the required gradient in CW mode, modifications to accommodate the increased heat flow within the cavity helium bath and its connection to the 2 K two-phase pipe are required. Also, the cooling of the cavity end-groups, in particular the HOM antennas, needs to be improved. The LCLS-II design uses an adjustable coaxial fundamental power coupler similar to that used at XFEL, and with enhanced cooling to accommodate incident average power per cavity up to about 10 kW. 3.9 GHz cavities, operating at the third harmonic of the accelerating cavity RF frequency, are needed to control the electron bunch energy distribution. Pulsed versions of 3.9 GHz harmonic linearizer cavities have been designed and built at FNAL and successfully demonstrated at FLASH, and will be adapted for CW operation at LCLS-II. Active control of the cavity resonant frequency is needed for LCLS-II, and an end-lever tuner is proposed for LCLS-II cavities. The tuner, controlled by the low-level RF (LLRF) system, will reduce phase and amplitude variations of RF fields caused by the mechanical vibration of the cavities and pressure fluctuations in the helium system.

The linac will contain 280 TESLA-like superconducting accelerating cavities operating at 1.3 GHz and 12 superconducting cavities operating at the harmonic frequency of 3.9 GHz. They are assembled in 38 cryomodules cooled by 2 K superfluid helium. The cryomodule concept is based on the XFEL design, with contiguous linac sections and transitions to warm sections at the electron gun, laser heater, bunch compressors, and at the exit of the linac. Cryogenics transport lines are built into the cryomodules, and bypasses are required only in the short warm sections, saving cost and space in the tunnel. The 1.3 GHz accelerating cryomodules will each contain 8 RF cavities, and the 3.9 GHz linearizer cryomodules will each contain 4 RF cavities. Magnets, diagnostics and HOM absorbers will be located in the cold sections at the end of each main linac cryomodule.

The design accelerating gradient of approximately 16 MV/m is well within current state of the art and minimizes combined construction and operating costs. The unloaded Q (Q_0) is an important parameter in specifying cryogenic systems and has a significant impact on cryogenic system capital costs and operational costs. The LCLS-II design is for Q_0 of 2.7×10^{10} , at an operating temperature of 2 K. A single cryoplant similar to that built for the 12 GeV upgrade project at TJNAF will provide cooling of the SRF components. R&D in cavity processing techniques to achieve the Q_0 required for LCLS-II in production cavities is under way.

Higher order modes (HOMs) in the cavities impact beam dynamics and are well characterized for the TESLA-type cavities. Simulations show that LCLS-II bunches excite a broad spectrum of

modes extending well into the THz range, and that HOM damping requirements are similar to those of XFEL. LCLS-II will use a HOM damping scheme similar to that planned for XFEL, with annular distributions of RF-power absorptive materials inserted in the sections between cryomodules.

The nominal RF power required is approximately 6 kW per cavity. Using a single power supply per cavity is particularly advantageous before BC1 in order to obtain optimal control of bunch compression; solid-state amplifiers are preferred for these cavities. After the first bunch compressor, a single klystron will deliver power to 48 cavities in 6 cryomodules, providing a cost-effective system for accelerating beam to final energy.

Heat transport of approximately 10 W per cavity, through 2 K liquid helium to the evaporative surface, places new requirements on pipe sizing to ensure cavity cooling. Attention must also be given to heat transport within the cavity helium tank, and at cavity end groups. Power losses absorbed by the 2 K cryogenics systems are predicted to be about 90 W per cryomodule. The cryogenic systems will distribute 2.3 K liquid, cooled to 2 K by expansion at each cryomodule. Installed cryoplant capacity is about 4 kW at 2 K, taking into account uncertainty and overcapacity factors. Examples of large-scale cryosystems of similar size to those needed for LCLS-II exist at JLab and at CERN; similar relevant experience also exist for high power pulsed systems (SNS) and smaller scale tests at Cornell, HZB in Berlin, and DESY in Hamburg.

Integrated LLRF and beam-based broadband feedback control of the CW SRF systems and the injector will ensure stability and uniformity of the electron bunches and of the delivery of reproducible X-ray pulses. The goals for RF amplitude and phase stability of 0.01% and 0.01° (rms, for vector-sum control of 48 cavities) respectively have been demonstrated in operating systems.

The linac will be installed in the existing SLAC linac tunnel, with high power RF amplifiers, power supplies, and low-level RF controls installed in the klystron gallery above the tunnel. Waveguide distribution systems will connect power amplifiers in the klystron gallery to cavities in the tunnel. The cryogenics systems will be located centrally along the LCLS-II linac.

6.2 Choice of SRF Technology

For applications such as LCLS-II, which require high accelerating gradients of approximately 10 MV/m or greater with high average beam power (~MW) and CW operation, SRF is the logical choice. Substantial capital and operational cost savings will be realized by using SRF cavities for beam acceleration, primarily because of the substantially lower power dissipation compared with normal-conducting accelerators. The cavity dissipated power is proportional to E_{acc}^2 / Q_0 , where E_{acc} is the accelerating gradient and Q_0 is the cavity unloaded quality factor. Typical niobium SRF cavities have quality factors five or more orders of magnitude higher than do normal conducting copper cavities, resulting in substantially lower cost for power amplifiers and operation, thus substantially outweighing the costs of operating the cryogenic system.

SRF acceleration for CW accelerators has the advantage that the beam pipe diameter may be made much larger than for a normal conducting cavity because the substantially higher Q_0 allows for relaxation of the shunt impedance requirement without much impact on the dissipated power. A larger beam pipe reduces trapped HOM impedances, leading to a reduction of transverse beam instability, beam emittance growth, and beam break-up risk. A disadvantage of the larger beampipe aperture is the reduction in short-range longitudinal wakefield, which is useful in correcting correlated energy spread following bunch compression.

The choice of SRF cavity frequency (f) is driven by several factors. Arguments for higher frequency include reduced cost of niobium for the smaller cavities, which in turn impact the size and cost of associated component and cryomodule. Arguments for lower frequency include reduced longitudinal and transverse geometric wakefields, which scale as f^2 and f^3 , respectively, and lower losses from the superconducting current as described in the Bardeen, Cooper, and Schrieffer (BCS) theory, which scale as f^2 [1]. SRF cavity surface resistance R_s consists of three components:

$$R_s = R_{mag} + R_{res} + R_{BCS}$$

where R_{mag} is the resistance caused by trapped magnetic field vortices and may be reduced by magnetic shielding; R_{res} is the remaining residual resistance, which may be minimized by appropriate surface processing; and R_{BCS} is the BCS resistance, where:

$$R_{BCS} = A \frac{f^2}{T} \exp\left(-\frac{\Delta(T)}{kT}\right)$$

and A and Δ depend on the (niobium) material parameters [1]. A reduction in the cavity surface resistance leads directly to improvement of the cavity quality factor and decreased heat load to the cryogenic system. The choice of RF frequency is also influenced by the surface resistance being dominated by the temperature-independent residual and magnetic losses ($R_0 = R_{mag} + R_{res}$) as the frequency is lowered. Also, field emission may increase with the size of the cavity, as large cavities are difficult to clean reliably [2]. L-band technology (approximately 1-2 GHz) neatly satisfies these considerations, and indeed both 1.3 GHz and 1.5 GHz have been used extensively for electron acceleration, particularly at DESY and JLab, respectively. State-of-the-art cavity preparation techniques result in residual resistance of a few n Ω for L-band cavities, and operation at or below 2 K is favored to minimize dynamic losses dominated by BCS resistance. The choice of the TESLA 9-cell 1.3 GHz cavities and XFEL cryomodules meets the LCLS-II requirements, and minimizes development cost by taking advantage of existing, proven, technology and infrastructure. Recent advances in high- Q_0 capability at an operating temperature of 2 K minimizes losses and lower the overall cost for the cryogenic system.

6.3 Operating Gradient

The choice of a design operating acceleration gradient (E_{acc}) depends upon a combination of factors and is one of the most important decisions in the design of most linacs. The LCLS-II linac is no exception. The ramifications of the decision for the operating gradient range from

construction and operating costs to system reliability. For CW SRF linacs, the principal factor in establishing the design operating gradient is cost optimization of the integrated accelerator complex, including cryogenic plant.

Higher gradients lead to a shorter accelerator, and therefore reduced part count, which in turn lower the integrated costs for all accelerator systems, including cryomodules. On the other hand, higher gradients also result in a higher cryogenic load, which leads to increased construction and operating costs. Higher gradients may lead to higher levels of dark current and resulting X-ray flux, which could be detrimental to electronics and other radiation-sensitive accelerator components in the tunnel. Producing cavities that operate at higher gradients may also be more expensive as quality control standards tighten and/or production yield begins to suffer.

While most of the emphasis of the development of TESLA-style 1.3 GHz 9-cell cavities has been focused on achieving the highest possible gradients in pulsed mode, the design has been studied and tested for CW operation as well [3–6]. The CEBAF 12 GeV upgrade project has established that even higher CW operating gradients than those envisioned for LCLS-II can be produced reliably in operational cryomodules [7–9]. The continued evolution of cavity processing techniques and development of infrastructure has made realization of useful accelerating gradients for LCLS-II to be low risk.

A critical element in establishing the operating gradient is identification of the unloaded quality factor (Q_0) for the accelerating cavities. Higher Q_0 , and thus lower losses to the superfluid helium, may be achieved at lower temperature. This has little impact on selection of the gradient, however, since the reduction in heatload is typically offset by an increase in cryoplant costs at lower temperature. The choice of operating gradient is thus not dependent on the cavity temperature, unless the heatload requires a transition in cryoplant construction modularity (i.e. an additional coldbox), in the operating gradient region considered. Analysis of cryoplant cost and delivery schedule for LCLS-II indicates that exploiting existing plant designs at 2 K has significant advantages.

In support of the analysis to optimize the operating gradient, we have prepared models to capture the main elements that impact construction and operating costs as a function of cavity gradient [10]. Using the baseline Q_0 vs. E_{acc} specification described in section 6.4.1 ($Q_0 = 2.7 \times 10^{10}$ at 16 MV/m), the total dynamic load variation with gradient is presented in Figure 6.3.1. Figure 6.3.2 shows, in arbitrary units, the total linac cost of both construction and 10 year operations as a function of operating gradient. The dashed green curve represents the cost of the cryogenic system; the blue curve is the sum of the cost of the SRF cryomodules, RF power, and controls, which decreases at higher gradients due to the need for fewer cavities; the orange dashed curve is the estimated cost of 10 year AC power for linac and cryogenic systems; and the solid red curve is the modeled total construction cost plus the 10 year operating cost for the linac. The LCLS-II linac analysis differs significantly from other applications because the existing SLAC tunnel is considered as cost-free. A step in cost is seen between 18 and 19 MV/m, where an additional coldbox is required.

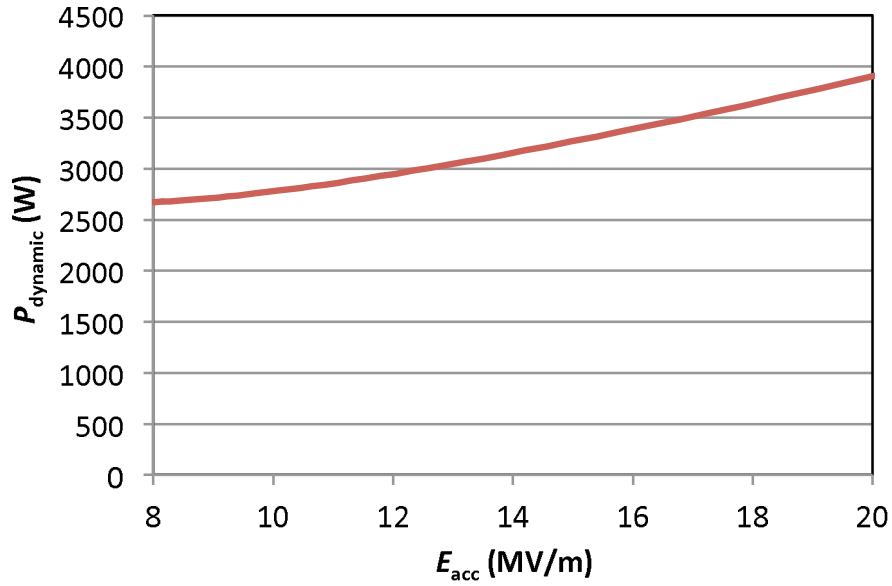


Figure 6.3.1: LCLS-II linac total 2 K dynamic heat load as a function of gradient.

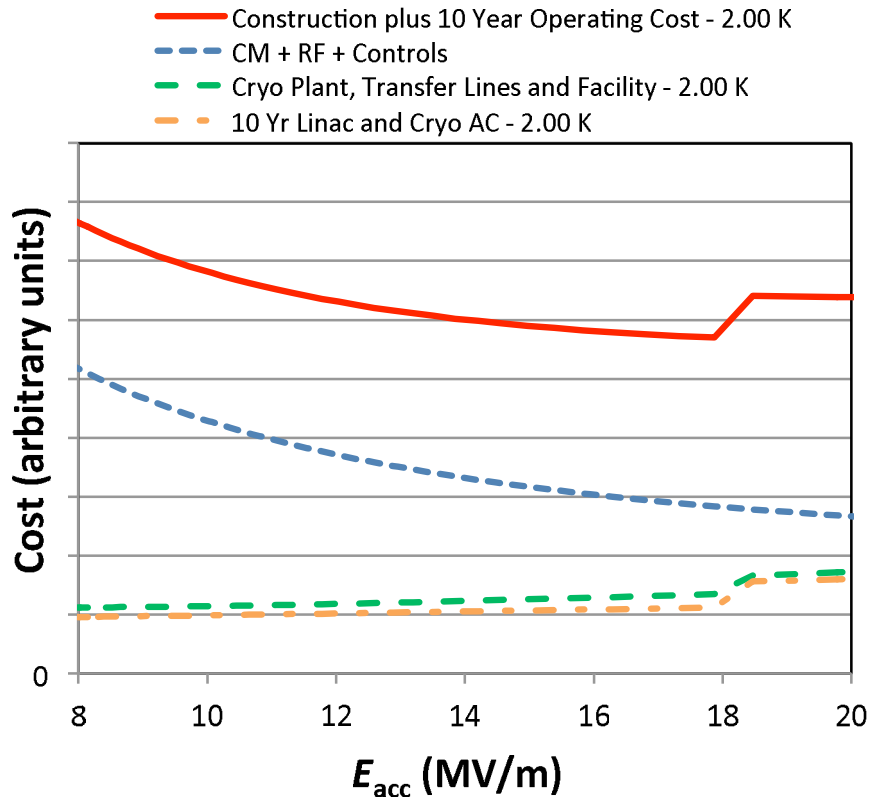


Figure 6.3.2: Model of relative LCLS-II linac cost as a function of operating gradient, at 2 K.

The choice of operating gradient of 16 MV/m for the LCLS-II cavities has been based upon both the anticipated total costs for the system (i.e., cryomodules, RF amplifiers, cryoplant, tunnel installation, and integrated system operational costs) and the best operational reliability. Amongst

the benefits of this choice of gradient are an improved cavity production yield that will result in lower cost, and field-emission-induced radiation is not anticipated to be a significant challenge in this operating gradient range. Consequently, we also expect to have somewhat increased reliability and availability compared to operation at higher gradients, as well as operational flexibility due to the redundancy provided by the cavities that should be operating below their performance limits.

6.4 Radio Frequency Parameters

The main RF parameters of LCLS-II linac are set by the choice of adopting the 1300 MHz TESLA cavity in this conceptual design (see Section 6.5). While a low-loss geometry might save ~15% on cryogenic losses compared to the TESLA cavity, the project schedule requires minimization of development work. Adoption of the TESLA cavity, together with development of high- Q_0 processing techniques (see Section 6.5.2) provides an effective route to reduced cryogenic losses, while retaining the benefits of existing TESLA cavity experience and infrastructure. Using the TESLA cavity parameters, the cavity operating gradient, and the beam characteristics previously discussed, it is possible to derive the operating conditions of the cavities and RF systems and calculate the expected operating point, including the projected load on the cryogenic system. Table 6.4.1 summarizes the major RF parameters for the LCLS-II main linac.

6.4.1 Q_0 Baseline

The cavity intrinsic quality factor Q_0 is related to the surface resistance via:

$$Q_0 = \frac{G}{R_s}$$

where G is a geometrical constant dependent on the cavity shape, and the RF surface resistance R_s is described in Section 6.2. The achievable Q_0 , as realized for fully dressed cavities installed in a cryomodule, is dependent on operating temperature, resonant structure geometry, niobium material processing history, magnetic field environment transitioning through T_c , and operating gradient.

Figure 6.4.1 shows Q_0 vs. E_{acc} and corresponding dynamic heatloads per cavity for three cases; 1) representative data measured at 2 K for a TESLA-style XFEL 9-cell cavity prepared by the present (ILC and XFEL) standard processing protocol, 2) recently published data from a new and improved processing protocol applied to single-cell TESLA-style cavities, and 3) the target performance for LCLS-II cavities. The latter is derived from Q_0 performance in the 14–20 MV/m accelerating gradient range extrapolated from recent theoretical and experimental work [11,12], and making allowance for in-cryomodule residual losses, which gives $Q_0 = 2.7 \times 10^{10}$ at 16 MV/m at 2 K, and thus 10 watts dynamic load from each cavity. This, together with renewed attention to minimizing in-cryomodule trapped flux, offers significantly higher Q_0 values than previously attainable with niobium [13–18].

Table 6.4.1 Main RF Parameters.

RF frequency	1300	MHz
Operating temperature	2	K
Average operating gradient	~16	MV/m
Average Q_0	2.7×10^{10}	-
Cavity length (L)	1.038	M
R/Q (r/Q)	1036 (998)	Ω (Ω/m)
Geometry constant (G)	270	Ω
Coarse (slow) tuner range	245	kHz
Fine (fast) tuner range	~1	kHz
HOM damped Q value (monopole and dipole)	$\leq 10^7$	-
Lorentz detuning	≤ 1.5	Hz/(MV/m) ²
Number of cryomodules	35	-
Number of cavities per CM	8	-
Cavity alignment requirements (RMS)	0.5	mm
Peak detune (with piezo tuner control)	10	Hz
Required cavity field amplitude stability [†]	0.01	% (rms)
Required cavity field phase stability [†]	0.01	deg (rms)
Q_{ext}	4×10^7	-
RF beam power per cavity (@300 μ A load)	5	kW
RF power needed per cavity	6.3	kW
Cavity dynamic load	10	W

[†]For the vector-sum configuration of 48 cavities driven by a single power supply. The stability requirement is relaxed to approximately 0.1% and 0.1° per cavity, for a single-source single-cavity configuration.

Pioneering work at FNAL has shown Q_0 higher than 3×10^{10} at 16 MV/m gradient in vertical test, following processing including a nitrogen-bake in many 1-cell cavities and a 9-cell cavity [14]. The nitrogen-doping process as currently implemented adds a small partial pressure ~mTorr of nitrogen to the furnace while still at 800°C, for few minutes at the end of the standard 800°C degassing cycle in UHV. Following the bake in a nitrogen atmosphere, a lighter than currently standard electropolish is applied and only a few microns of the cavity surface are removed. The optimum amount of material removal required following gas bake is found to depend on the gas exposure time and the temperature at which the gas injection occurs. Secondary ion mass spectrometry (SIMS) suggests that the final concentration of interstitial nitrogen leading to the best performance is ~100 ppm, about 10 times higher than achieved with the standard ILC/XFEL cavity processing. The beneficial effects of this interstitial nitrogen, which closely track the best theoretical performance of niobium [13] are presently understood as arising from a

combination of two factors: (1) shortening of the electron mean free path within the RF penetration depth, which decreases the BCS losses, and (2) preferentially occupying lattice defect sites which are empty at 800 C, but become readily occupied by H and O under atmospheric conditions at lower temperature, with the result of inhibiting the formation of chemical complexes associated with the parasitic losses associated with the so-called “mid-field Q slope.” Bake parameters can be optimized further to reduce cavity performance sensitivity to tolerances in material removal post gas bake. Section 6.5.2 further discusses cavity processing techniques.

Results of vertical test measurements of BCS and residual resistance at 1.3 GHz at 16 MV/m, for different surface processing techniques, are summarized in Table 6.4.2 [19]. Different types of surface processing affect R_{BCS} and R_{res} differently, and any optimization of operating temperature or gradient must take this into account [19]. As shown in the table, the recent breakthrough in cavity processing based on doping the surface with interstitials such as nitrogen or argon during bake sets a new BCS limit, and indicates that a target Q_0 of 2.7×10^{10} at 2 K can be considered feasible.

A high- Q_0 R&D program with participation from Cornell, FNAL and JLab has been formed, for the purpose of transitioning the established principle into a robust and reproducible surface processing recipe for 9-cell cavities suitable for LCLS-II cavity production.

Table 6.4.2. Measured values of R_{BCS} (at both 2 K and 1.8 K) and R_0 , for 1.3 GHz at 70 mT (16 MV/m). Surface treatment processes using electropolishing (EP), buffered chemical polishing (BCP), 120°C bake, and nitrogen bake are shown for comparison.

Surface treatment	$R_{BCS}(70 \text{ mT}, 2\text{K})$ [nΩ]	$R_{BCS}(70 \text{ mT}, 1.8\text{K})$ [nΩ]	$R_0(70 \text{ mT})$ [nΩ]
EP+120 C	10	5	~4-8
BCP+120 C	10	5	>8
Nitrogen bake +EP	4.5	1.5	1-3

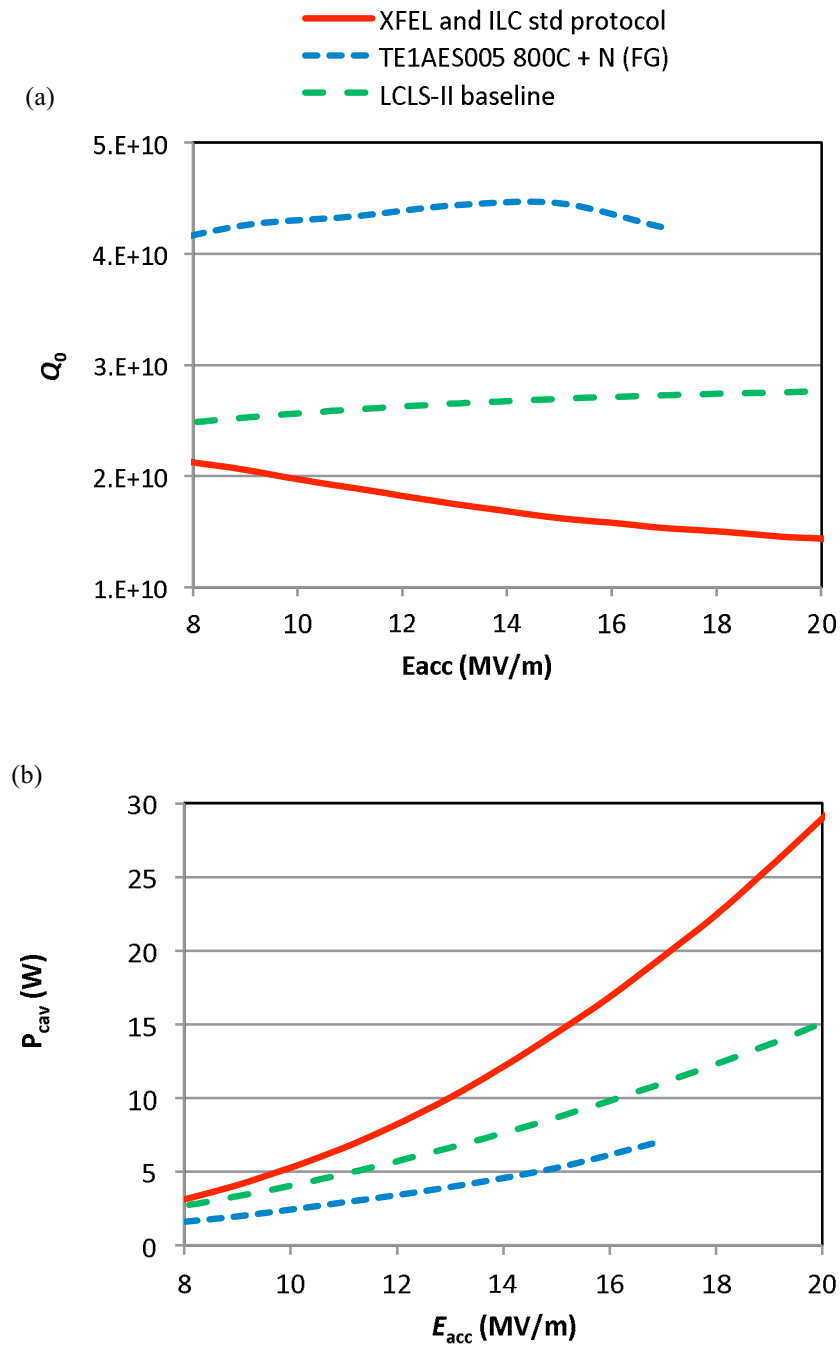


Figure 6.4.1. Cavity performance for XFEL and ILC cavities (solid red line), measured cavity performance with 800°C bake with nitrogen gas (dashed blue line), and LCLS-II design (dashed green line); (a), Q_0 vs. E_{acc} (b) corresponding heat load per cavity.

For high Q_0 operation, it is important to carefully control extrinsic factors in the cryomodule, which may contribute to surface resistance. Trapped magnetic flux, due to either unscreened remnant magnetic field or thermal currents during cooldown, is a well-understood factor leading

to the additional surface resistance R_{mag} . A good approximation to R_{mag} is given by the following expression [20]:

$$R_{mag} = (R_0 + R_1 B_{rf}) B_{ext}$$

where B_{ext} is the trapped magnetic field, B_{rf} is the magnitude of the RF field on the surface, $R_0 = 3.6 \text{ n}\Omega/\mu\text{T}$ [20], and $R_1 = 0.75 \times 10^{-2} \text{ n}\Omega/\mu\text{T/mT}$ [21].

For L-band SRF-based accelerators built to date, the test and operational specification has been for a magnetic field at the cavity of $< 1 \mu\text{T}$. Since for LCLS-II the cryogenic power dissipation has a large cost impact, the magnetic shielding specification will be designed to attenuate the ambient field at each cavity to reduce R_{mag} to $< 20\%$ of the total surface resistance. For $Q_0 = 2.7 \times 10^{10}$ at 16 MV/m (T=2K), $R_s = 10 \text{ n}\Omega$. Therefore, conservatively taking a 20% maximum contribution, $R_{res} < 2 \text{ n}\Omega$ at 16 MV/m ($B_{rf} = 70 \text{ mT}$). Using the equation for R_{mag} above leads to the requirement that for LCLS-II the remanent magnetic field must be attenuated to $< 0.5 \mu\text{T}$ at the cavity surface.

Different types of surface processing affect R_{res} differently, however, and the final design must take this into account using actual cavity parameters [19]. Magnetic shielding specification in the cryomodule must take into account the actual value of R_{res} for LCLS-II cavities as developed in the high- Q_0 R&D program. The magnetic shielding design will use verified permeability measurements and temperature dependence, and not rely on the manufacturer's data [22]. Assembly procedures must be specified to ensure the magnetic shielding material is not subject to mechanical impact. In addition, magnetic shielding design must account for the shielding holes which are necessary for helium vessel cryogenic piping, mechanical supports, etc. The shielding design for LCLS-II shall avoid holes close to the high surface magnetic field region of the cavity equators to the extent possible [23].

The lower Q_0 that has been observed when cavities are dressed and installed in cryomodules may also be attributed in part to additional flux trapping caused by thermocurrents generated by the bi-metal Nb-Ti vessel junctions, and higher residual ambient magnetic field at the cavity during cooldown. Tests at HZB [17], and Cornell University, have demonstrated that this problem can be circumvented by minimizing the thermal gradients in the cavity LHe bath during cooldown through the transition temperature. At Cornell, tests have successfully demonstrated that residual resistances of $1 \text{ n}\Omega$ in a 7-cell 1.3 GHz ERL cavity can be preserved in a cryomodule, via homogenous cooldown through T_c and thermal cycling to 10 to 15 K [24].

Should the specified Q_0 not be achieved with the nitrogen bake technique and with reasonable production costs, R&D in large grain material and low-loss cavity shapes may provide alternate routes to the required performance.

6.4.2 Cavity Tuner Requirements

Each cavity must be equipped with a tuner capable of performing the following functions:

1. Accommodating static effects by

- a. Tuning the cavity to the resonant frequency following cool-down.
 - b. Tuning the cavity far off resonance in the event of cavity failure.
2. Accommodating dynamic effects by
 - a. Compensating for changes to the cavity resonant frequency due to variations in helium bath pressure and mechanical vibrations (microphonics)
 - b. Compensating for changes in the cavity resonant frequency due to Lorentz-force detuning when the cavity field changes, especially during cavity field ramp-up.

These functions are commonly performed by a composite tuner consisting of an electro-mechanical static tuner in concert with a piezo-electric dynamic tuner. The static tuner is designed to tune the cavity over a wide frequency range, to accommodate the expected cavity-to-cavity variation in resonance frequency due to manufacturing tolerances, to adjust for the change in cavity resonant frequency following cool-down, and to tune the cavity off resonance in the event of failure. The piezo tuner provides the precision to finely adjust the cavity resonant frequency and the mechanical bandwidth to respond, within some design range, to dynamic excursions from the resonant frequency set point caused by pressure fluctuations, mechanical vibrations, and changes in Lorentz-force detuning. Cavity tuner designs are described in Section 6.5.6.

6.4.2.1 Static Tuner Requirements

The slow frequency tuner needs to be able to adjust the cavity resonant frequency to values close to the 1300 MHz operating point once the cavities are cold, and needs to compensate for possible slow drifts in resonant frequency, on the order of a few seconds. The required tuning range of the slow tuner (and thus the required maximum tuning force) is set by several components:

1. Accuracy of room temperature tuning, which is done before helium tank welding and final $\sim 10\ \mu\text{m}$ cavity material removal.
2. Variations in frequency spread during cavity cool down.
3. Providing preloading of the piezo actuators required for dynamic operation.
4. Providing sufficient tuning range to be able to tune a cavity far off resonance in the event of cavity failure.

These considerations lead to a required tuning range of $\sim 245\ \text{kHz}$ for the static LCLS-II tuner.

6.4.2.2 Dynamic Tuner Requirements

The expected peak microphonics level and the need to quickly compensate Lorentz-force detuning during cavity field ramp-up set the dynamic tuning range of the fast piezo-driven tuner. We estimate the Lorentz-force detuning constant of the cavity to be $1.5\ \text{Hz}/(\text{MV}/\text{m})^2$, and at 16

MV/m Lorentz-force detuning will require a fast tuning range of ~ 400 Hz. This requirement for dynamic tuning for LCLS-II can be satisfied by a DESY style dynamic tuner (see Section 6.5.6).

6.4.3 HOM Damping

For LCLS-II cavities the HOM damping is expected to be similar to that of the XFEL cavities. By using HOM dampers in the same configuration as XFEL, loaded Qs of approximately 10^5 are expected for high-impedance accelerating and deflecting HOMs. Beam dynamics and HOM heating calculations (see Section 6.12.2) show that this level of damping is far beyond that needed for LCLS-II, largely because beam current is much smaller for LCLS-II than for XFEL. Preliminary calculations indicate that HOM damping to produce loaded Q's in the 10^7 range should be adequate for LCLS-II baseline parameters (see Section 6.12.2), and the existing HOM damper design meets these requirements. There is a recognized need to ensure thermal stabilization of the HOM pickup probe. This will be addressed in a manner already demonstrated at JLab and/or in development at DESY and discussed in Section 6.5.5.

6.4.4 Amplitude and Phase Stability

The energy stability requirement for the full linac reflects on the single cavity and cryomodule RF stability, which will be accomplished by implementing a fully digital RF controller, described in Section 6.9. Including the off-crest phase in the low-energy parts of the linac and the energy spread generated by phase fluctuations there, we set the RMS amplitude and phase requirements to be 0.01% and 0.01 degrees respectively, to accommodate the $\leq 0.01\%$ energy jitter requirement on the beam for correlated fluctuations. These requirements are dominated by the vector-sum linac configuration, and are feasible. However, in the case of uncorrelated fluctuations – for example, when the cavities are fed by independent RF sources – the amplitude and phase stability requirements are reduced by a factor of ten.

6.4.5 Cavity Alignment

Cavity alignment requirements are determined by emittance dilution due to transverse wake fields excited by off-axis beam in the accelerating sections and by other sources (see Section 6.12). Table 6.12.1 shows the rms alignment tolerances for the main linac components, which are similar to the European XFEL design parameters.

6.4.6 Maximal Cavity Detuning

Mechanical vibrations of the cavity cause fluctuations in its resonant frequency, described by δf , the difference between the cavity resonant frequency and that of the RF source. LCLS-II cavities will operate with much narrower bandwidths (~ 30 Hz, determined by the cavity loaded quality factor Q_L , see Section 6.4.7) than the typical values used in pulsed linacs such as FLASH (approximately 200 Hz). The narrower bandwidths make the LCLS-II cavities more susceptible to detuning than their pulsed counterparts.

Microphonics levels measured at various machines are summarized in Table 6.4.3. As described in Reference [25], the peak cavity detuning is estimated at 6σ . It is important to note,

however, that even larger detuning has been observed occasionally. Detuning levels range between 0.6 Hz and 7 Hz RMS (4 to 40 Hz 6σ peak) and significant differences are commonly seen from cavity to cavity, even within the same cryomodule, although this phenomenon is not yet well understood. Typically, the dominant part of the microphonics spectrum occurs at vibration frequencies of several tens of Hz to a few hundred Hz (see Figure 6.4.2 and Table 6.4.3 for examples.)

Table 6.4.3. Measured Cavity Microphonic Frequency Deviations [2].

Machine	σ [Hz]	6σ [Hz]	Comments
CEBAF	2.5 (average)	15 (average)	Significant fluctuations between cavities
ELBE	1 (average)	6 (average)	
SNS	1 to 6	6 to 36	Significant fluctuations between cavities
TJNAF FEL	0.6 to 1.3	3.6 to 7.8	Center cavities more quiet
TTF	2 to 7	12 to 42	Pulsed. Significant fluctuations between cavities

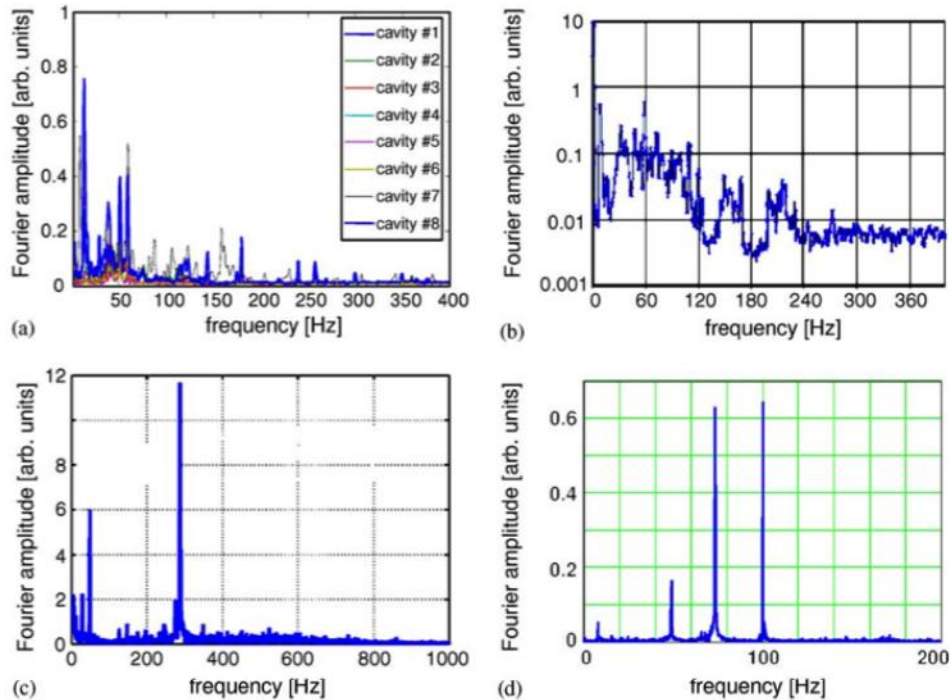


Figure 6.4.2. Examples of microphonics spectra. (a) TJNAF FEL (CEBAF upgrade module) [27]; (b) SNS module [28]; (c) TTF test cryostat (CHECHIA) [29]; (d) ELBE module [30].

For a fixed cavity bandwidth, the additional RF power required to maintain a stable cavity field increases with the square of the ratio of the peak detuning to the cavity half-bandwidth. To limit the capital and operating RF costs, peak detuning levels must be kept low (approximately

cavity half-bandwidth or less). The narrow bandwidths planned for the LCLS-II cavities make achieving low microphonics levels an important objective in the designs of the cavity, frequency tuner and cryomodule. Besides designing the cryomodule for minimal microphonics, a further reduction in microphonics amplitude can be achieved with active control schemes, making use of a fast frequency tuner. Active resonance stabilization is an area of active research in laboratories around the world, and initial studies have shown some promising results, as presented below. The success of such active, fast frequency control, however, strongly depends on the mechanical properties of the cavities and their environment, especially mechanical resonances and the local noise spectrum that may excite these. In general, feedback control bandwidths of a few Hz have been achieved; they are limited by mechanical resonances, allowing reliable compensation of slower frequency modulations and drifts. Adaptive feedforward can be used to compensate for individual, strong lines in the microphonics spectrum [26], unless several strong spectral lines are close to each other.

Extensive studies have been performed in the HoBiCaT test stand at HZB in Berlin using 9-cell 1.3 GHz TESLA style cavities operating at 2 K, with bandwidths between 20 and 40 Hz [26]. As shown in Figure 6.4.3, in the absence of active stabilization of the resonance frequency, variations of 12 Hz peak over periods as short as 10 seconds were measured [31]. With piezo feedback, the resonant frequency of the same cavity varied by less than 2 Hz peak over an equal measurement interval. During an extended test lasting 48 hours, the HoBiCaT piezo control system was able to stabilize the resonance frequency to better than 1 Hz RMS, but peak excursions of up to 15 Hz still were observed (see Figure 6.4.4) [26,32].

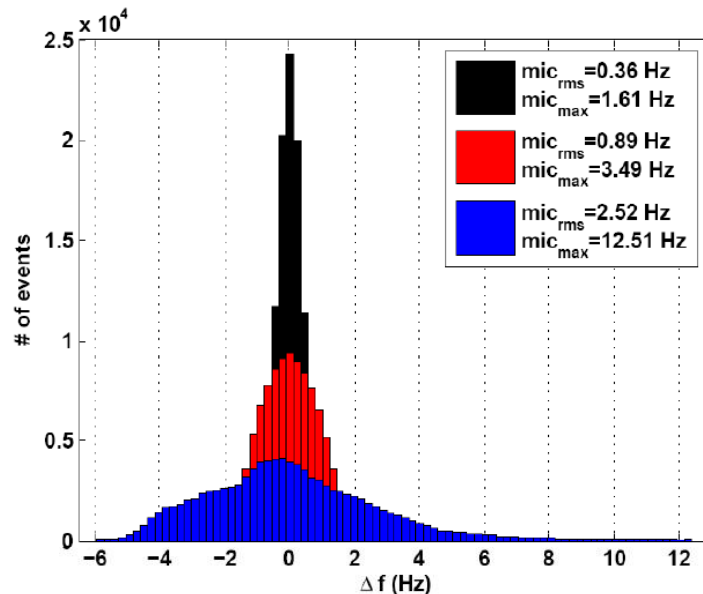


Figure 6.4.3. Microphonics distributions measured at HoBiCaT, using a combined detuning controller made up of a low-frequency proportional-integral feedback loop and an adaptive least-mean-square based FIR filter feedforward system. Detuning is measured over 100 s for open loop (blue), feedback control only (red) and the combined controller (black).

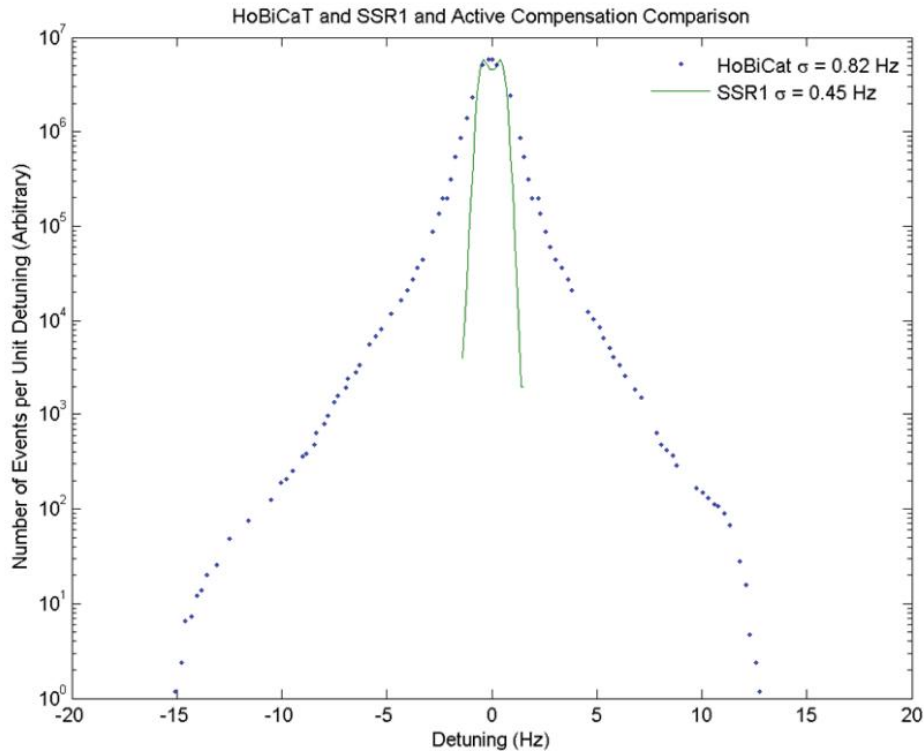


Figure 6.4.4. A comparison of the microphonics distributions measured at HoBiCaT and FNAL over a period of 48 hours. The variance of the HoBiCaT microphonics distribution was less than 1 Hz. During the same measurement interval, however, peak excursions larger than would be expected from a Gaussian distribution were observed.

While no active cavity tuning control systems currently operate in existing accelerators, the results from HZB and other laboratories suggest it is reasonable to expect that an active microphonics control system based on existing technology can be deployed to help stabilize the resonance frequency of each LCLS-II cavity. Compensating for slower frequency variations (modulation frequencies below a few Hz) and active compensation of Lorentz-force detuning has been demonstrated to work reliably at HZB, Cornell and elsewhere. Figure 6.4.5 shows an example of active Lorentz-force detuning compensation. Also notice that the peak microphonics detuning is kept below 20 Hz. Based on the information currently available on microphonics and its compensation, a peak detuning of less than or equal to 10 Hz appears to be a realistic target for LCLS-II. Measurements on LCLS-II prototype cryomodules and additional frequency control studies will confirm this value. As noted earlier, and detailed in Section 6.4.7, larger cavity detuning can be accommodated with additional RF power.

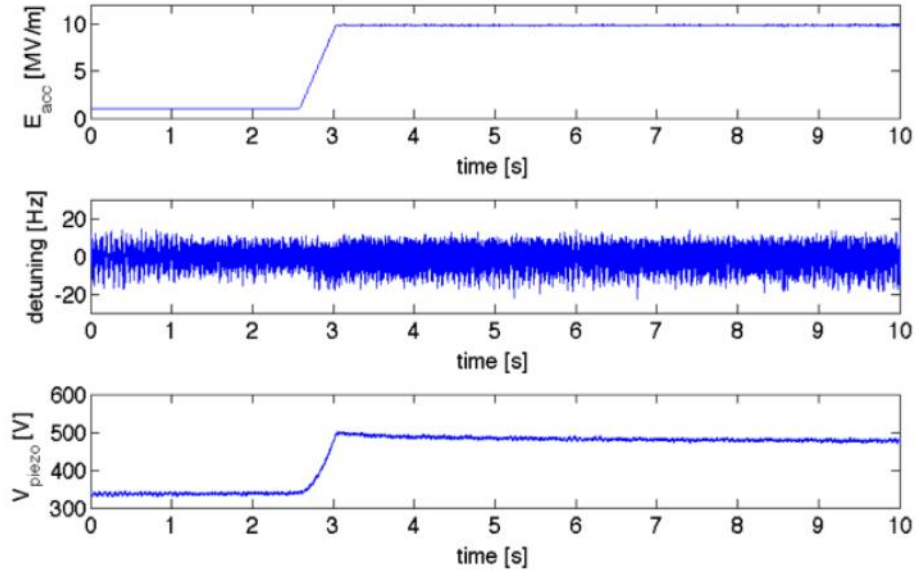


Figure 6.4.5. Example of active Lorentz-force detuning compensation by a piezo-tuner during field ramp-up of a 9-cell cavity with high loaded Q . Without compensation, the cavity would detune by more than 100 Hz (i.e., many bandwidths). The measurement was done at HoBiCaT with the Cornell LLRF control system [33,34].

6.4.7 Loaded Q and RF Power Requirements

The loaded quality factor of a cavity, Q_L , is defined in terms of the quality factors determined by losses in the cavity only (Q_0) and the losses external to the cavity (Q_{ext}):

$$\frac{1}{Q_L} = \frac{1}{Q_0} + \frac{1}{Q_{ext}}$$

Q_L determines the characteristic response time of the SRF systems to external stimulus ($\tau \sim Q_L/f$). In superconducting linacs, the coupling factor $\beta = Q_0/Q_{ext}$ is usually chosen to minimize the RF power needed to energize the cavities, including the beam load and the microphonics in the system. For on-crest operation, the optimal beta is

$$\beta_{opt} = \left[(1+b)^2 + (2Q_0 \delta f / f_0)^2 \right]^{1/2},$$

where the beam loading term $b = I_b(R/Q)Q_0/V$ and $\delta f/f_0$ is the relative microphonic frequency fluctuation. Assuming that the RF power is matched at the highest (worst case) operating current of 300 μA , and that the peak frequency fluctuation is 10 Hz, one obtains $\beta_{opt} = 485$, approximately equally split between the beam loading term and the micophonics term. This result leads to $Q_L = 4.1 \times 10^7$. Such a low Q_L will not match the beam load for average beam currents below the nominal 300 μA ; in this case, RF power will be absorbed in the RF system circulator loads.

The RF generator power per cavity (P_g) is calculated from:

$$P_g = \frac{(\beta+1)L}{4\beta Q_L(r/Q)} \left\{ (E_{acc} + I_b Q_L(r/Q) \cos \varphi_b)^2 + \left(2Q_L \frac{\delta f}{f_0} E_{acc} + I_b Q_L(r/Q) \sin \varphi_b \right)^2 \right\}$$

which in the case of $\beta \gg 1$ and $\varphi \sim 0$ is expressed as:

$$P_g = \frac{L}{4 Q_L(r/Q)} \left\{ (E_{acc} + I_b Q_L(r/Q))^2 + \left(2Q_L \frac{\delta f}{f_0} E_{acc} \right)^2 \right\}$$

where E_{acc} and I_b are the accelerating gradient and beam current in the cavity, respectively; r/Q is the geometric shunt impedance per unit length (Ω/m); φ_b is the phase of the beam relative to the field in the cavity E_{acc} ; δf is the difference between the cavity resonant frequency and that of the RF source, f_0 ; and L the cavity length (m).

As a result, we anticipate the generator will need to deliver an average of 5 kW per cavity at the entrance flange, or 40 kW per cryomodule, to support the required gradient with a beam current of 300 μA . We also need to provide sufficient power to correct for microphonics-induced frequency variations after piezo tuner correction. Consequently, the power installed will need to be a minimum of 6.3 kW per cavity or 50 kW per cryomodule taking into account RF power transmission losses of 6%, and overhead for control of 4%. The power RF and distribution systems are discussed in Section 6.10.

Should cavity frequency detuning exceed 10 Hz, more RF power may be required to maintain acceleration at required gradient of 16 MV/m. In Figure 6.4.6 the required RF power per cavity is shown as a function of the maximum cavity detune allowance for different cavity bandwidths (or equivalently for different Q_L) and for the nominal beam current of 300 μA . RF power transmission losses are 6%, and overhead for control is 4%. One can see that for a cavity detune of 20 Hz the required RF power per cavity is 8 kW, and for 30 Hz detune is 10 kW, respectively for the optimal coupling. However, the cavity Q_L is decreased in order to tolerate higher detune.

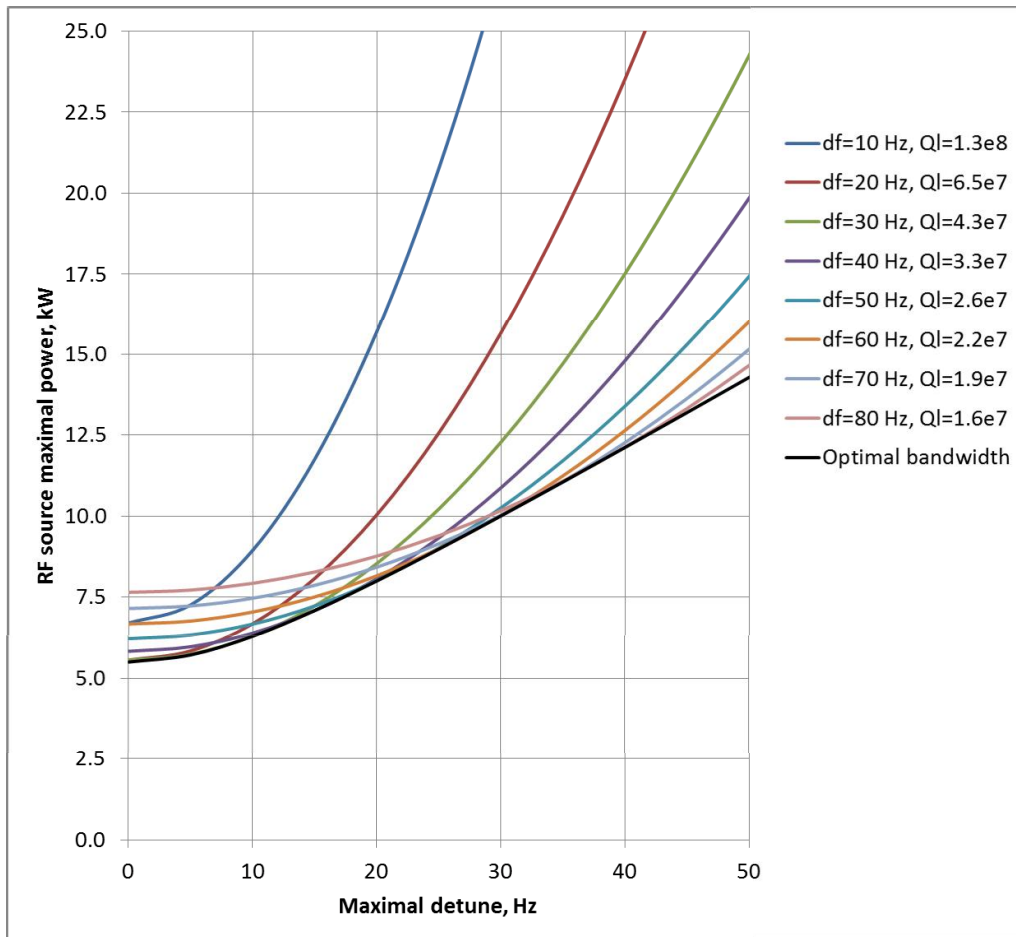
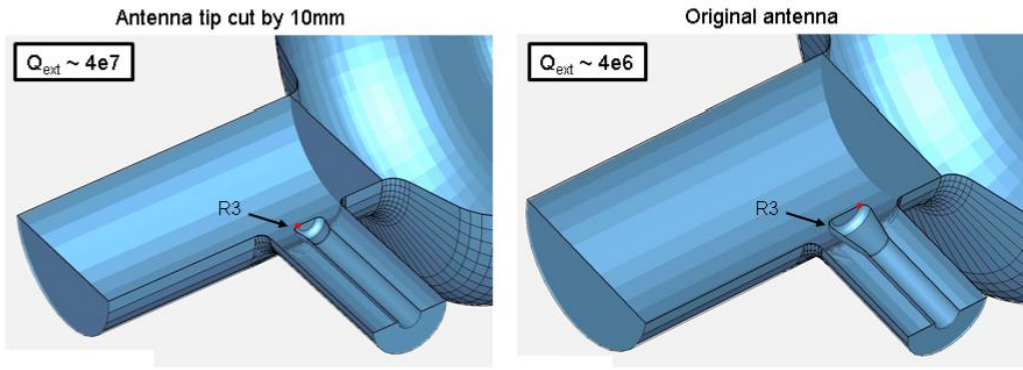


Figure 6.4.6. Maximum RF power per cavity versus the peak frequency fluctuation (cavity peak detuning) for different cavity bandwidth (or equivalently different Q_L), and nominal beam current of $300 \mu\text{A}$. The power versus the maximal detune for the optimal coupling for is shown in black (lower curve).

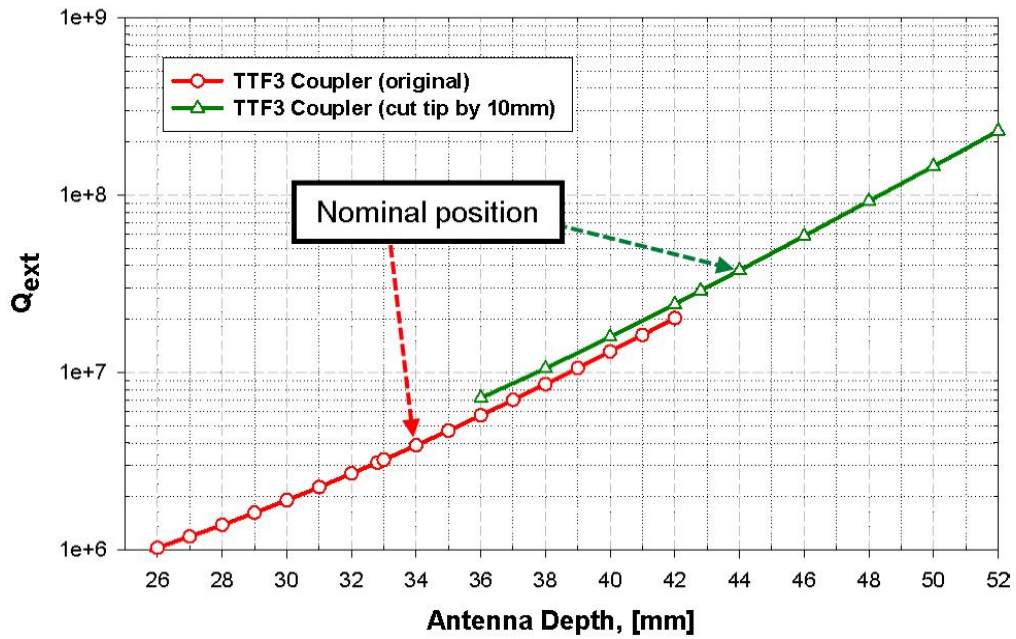
Note that TTF-III coupler provides Q_L in the range from 10^6 to 2×10^7 , and the nominal value is 4×10^6 . Q_L is adjusted by changing the coupler antenna length (see Figure 6.4.7.) providing flexibility. A maximum cavity detuning of 20 Hz would result in an optimal $Q_L = 2.6 \times 10^7$, requiring a small modification to the coupler antenna (see Figure 6.4.7), and an increase in RF power per cavity of $\sim 27\%$.

6.4.8 Cryomodule Dynamic Load

The RF operating conditions also allow us to calculate the dynamic load due to RF and beam-induced heating on the cryogenic system at 2 K. We estimate the total dynamic load at 2 K for a single cavity to be approximately 10 W and for the total cryomodule 91 W; Section 6.6 lists the cryogenic loads in more detail. Such high-heat loads require some modifications to the baseline XFEL-style cryomodule concept, described in Section 6.6. The cryogenic system is described in Section 6.7.



(a)



(b)

Figure 6.4.7. (a) Original configuration of the antenna tip of the TTF-III coupler (right) , and antenna tip length reduced by 10 mm (left); (b) Q_{ext} versus the distance of the antenna tip to the beamline axis for the two cases shown in (a).

6.5 RF Cavities

6.5.1 The TESLA Cavity Design

The TESLA 9-cell superconducting cavity is the baseline design for LCLS-II. The TESLA cavity design was introduced in the early 1990s [35] with the main goal of achieving a high gradient that would lower the cost of very long linacs operated in the TeV energy regime. The TESLA cavity was designed to achieve a lower-peak surface electric field in order to reduce field emission, a primary gradient-limiting mechanism devised two decades ago. Since then, significant progress has been made in overcoming the field emission limit as well as other limits, such as quench limit and high field Q-slope limit [36, 37]. Significant experience in TESLA

cavities has been accumulated at DESY, in the TESLA Test Facility (TTF) which later became FLASH. Currently, 800 9-cell TESLA cavities are being industrially produced for the European XFEL project. The TESLA cavity has also been adopted for the ILC, which has driven development of high gradient SRF cavities and other SRF components and systems and associated infrastructures. A major achievement in SRF cavity development is the realization of repeatable and reliable cavity processing procedures, leading to the demonstration of 90% production yield at an average gradient of 35 MV/m with $Q_0=8 \times 10^9$ for vertical qualification testing. By the time of publication of the ILC Technical Design Report (TDR) in June 2013 [38], a global SRF expertise and infrastructure was established. US industry, amongst others, is qualified to manufacture the 9-cell ILC cavities, and SRF facilities at JLab, FNAL/ANL are qualified to process and test full-scale 9-cell cavities with throughput considered to be appropriate for LCLS-II.

The TESLA/ILC cavity is shown in Fig.6.5.1. It operates in π mode at a resonant frequency of 1300 MHz, and consists of nine accelerating cells between two end group sections. One end group has a port for coupling RF power into the structure, and the other end has a port for a field sampling probe used to determine and control the accelerating field. Each end group also has a resonant higher order mode (HOM) coupler structure with a probe port and small electric field antenna for extracting HOM power and for diagnostics. The main parameters of a TESLA 9-cell cavity are given in Table 6.4.1; Table 6.5.1 shows additional detailed parameters for the cavities. The cavity effective length L is determined as $L=\lambda n/2$, where n is the number of cells and λ is the RF wavelength. For a TESLA-type cavity, L is 1.038 m. In this table, the shunt impedance R/Q relates the stored energy in the cavity to the accelerating voltage, according to $W = V^2 / (R/Q)\omega_0$, where $V = E_{acc} \cdot L$, E_{acc} is the operating gradient, and ω_0 is the reduced frequency. The basic useful relationship for this case is the power emitted from the fundamental power port with no beam loading:

$$P = V^2/Q(R/Q) = E_{acc}^2 L/Q(r/Q),$$

where $r/Q = (R/Q)/L$ is the shunt impedance per unit length in Ω/m . For a TESLA-type cavity $R/Q = 1036 \Omega$, and thus, $r/Q = 998 \Omega/m$.



Figure 6.5.1. LCLS-II baseline cavity: TESLA style 9-cell niobium cavity.

Table 6.5.1. TESLA Cavity Detailed Parameters.

Parameter	Value
Type of accelerating structure	Standing wave
Accelerating mode	TM010, π -mode
Type of cavity-cell shape	Tesla - type
Number of cells	9
Total length	1247 mm
Iris diameter	70 mm
Beam pipe diameter	78 mm
Cell to cell coupling	1.87%
Geometry constant	270 Ω
Lorentz detuning	$\leq 1.5 \text{ Hz}/(\text{MV}/\text{m})^2$
$B_{\text{peak}}/E_{\text{acc}}$	4.26 mT/(MV/m)
$\Delta f/\Delta L$	315 kHz/mm
Number of HOM couplers	2
Q_{ext} for high-impedance HOM	$< 10^5$

With the recent development of advanced surface processing and cleaning procedures, field emission in the gradient range of 15-20 MV/m is not expected to be a limitation.

Table 6.5-2. Typical Properties of High-Purity Niobium for Use in XFEL/ILC Cavities.

Element	Impurity content in ppm (wt)	Property	Value
Ta	≤ 500	RRR	≥ 300
W	≤ 70	Grain size	$\approx 50 \mu\text{m}$
Ti	≤ 50	Yield strength	$> 50 \text{ MPa}$
Fe	≤ 30	Tensile strength	100 MPa
Mo	≤ 50	Elongation at break	30%
Ni	≤ 30	Vickers hardness	
H	≤ 2	HV 10	≤ 50
N	≤ 10		
O	≤ 10		
C	≤ 10		

Considering that LCLS-II cavities are operated in CW mode, as opposed to the pulsed mode at XFEL or ILC, the heating at the end groups and HOM pickup probe are issues of concern, and

some adaptation may be needed, see Section 6.5.5. Experience in such adaptation has been accumulated in long-pulse and CW tests at DESY [39]; the CEBAF 12 GeV upgrade cavities which are operated in CW mode at 19.2 MV/m offers an existence proof of the technical capability needed for LCLS-II [40].

6.5.2 Cavity Material, Processing and Cryogenic RF Testing

The acceleration cells in a 9-cell TESLA cavity are fabricated by using high-purity sheet niobium with a typical RRR of 300 or greater. The raw materials are commercially produced and are available from vendors worldwide. Table 6.5.2 gives typical properties of high-purity niobium for use in XFEL/ILC cavities.

The technology for processing SRF cavity surfaces consists of a series of steps. This sequence, or “recipe,” was developed over the last 20 years by multiple SRF-focused institutions. The recipe, in its most basic form, requires removing the damaged layer from the RF surface by chemical etching or polishing; baking the cavity at high temperatures under vacuum to reduce the hydrogen dissolved in the niobium; and finishing with a final chemical etch or polish, followed by a high pressure water rinse in a cleanroom. The standard recipe developed for the ILC [38], listed in Table 6.5.3, has been implemented in large part by the Jefferson Lab C100 program and the European XFEL. For LCLS-II, a modified procedure that will include nitrogen surface diffusion (introduction of low pressure nitrogen at the end of the degas bake) and slow-cooldown steps is to be used. It may be further developed to possibly include the use of large-grain niobium or other means developed recently. An R&D program is underway to industrialize the process for high- Q_0 production at 2 K.

Following the completion of cavity processing, the cavity proceeds to qualification RF testing. In this test the cavity is mounted vertically in a cryogenic test stand and quality factor measured at 2 K, at gradients up to at least the required 16 MV/m, to validate adequate quality factor plus additional to-be-determined operational headroom. Characterization of any field emission using X-ray detection will occur simultaneously.

A helium tank is then welded to the qualified cavity and following an additional high-pressure rinsing cycle, auxiliary components (RF probe antenna, HOM antennas) are attached in a clean room to form a dressed cavity assembly. (Note: the XFEL procedure as outlined in the table may be followed.) Then eight cavities are assembled in a clean room into a string, which also includes the cold portion of the high power RF input coupler.

The modified cavity surface processing recipe offers the potential for significantly higher Q_0 in the gradient range of 15-20 MV/m over that used for XFEL / ILC (as described in section and 6.4.1) [41-44]. Data from more than 20 tests of nitrogen treated cavities shows significantly higher Q_0 than obtained with standard processing protocols (electropolish (EP), buffered chemical polish (BCP), 120°C bake), see Figure 6.5.2. The treatment consistently works in tests to date, and appears to be reliable. Additionally, a theoretical understanding of the physics responsible for the improvement is emerging. The nitrogen bake protocol produces a thick layer of nitrogen doped niobium (~10 microns), and surface removal of 3 to 7 microns has demonstrated consistent

high- Q_0 performance: this allows potential reprocessing (an additional few microns EP) of a dressed cavity, if needed, to overcome an independent contamination issue (field emission or quench). An advantage to these improved recipes is that they can be readily applied to the standard cavities using existing industrial expertise. High- Q_0 R&D for LCLS-II by a collaboration between Cornell University, FNAL and JLab includes efforts intended to optimize the procedure so that it may be applied by cavity companies during production.

Table 6.5.3. Cavity Processing and Preparation Recipe for ILC, XFEL, and JLab C100 projects.

Processing Step	Description
1 Bulk electropolishing or buffered chemical polishing	120-150 μm interior removal via electropolishing or buffered chemical polishing; 1 pass high-pressure rinse (HPR) and dry; industrial process.
2 Hydrogen degas bake	650-800°C vacuum bake; 2–10 hour hold; 1×10^{-5} mBar pressure.
4 RF tuning	Frequency, straightness, and field flatness adjustment to 95% or better.
5 Light electropolishing	20-30 μm interior removal at process temperature of $<25^\circ\text{C}$.
6 Low temperature bake	120°C bake, 48 hours, cavity under vacuum.
8 Vertical test preparation	High pressure deionized (DI) water rinse, assembly, and evacuation of cavity in class 10 cleanroom.
9 Vertical test	2.0 K RF performance measurement in vertical test cryostat; Q_0 vs. E_{acc} performance curves and field emission characterization.
10 Cavity dressing	Installation of helium vessel via TIG welding (note – for XFEL this step is done after step 8. LCLS-II may follow XFEL and adopt this preparation sequence).
11 Horizontal test or string assembly preparation	High pressure DI water rinse, assembly (including forward power coupler insertion), and evacuation of cavity in class 10 cleanroom. The same cleanroom sequence is followed to prepare the cavity either for horizontal test or string assembly
12 Horizontal test	2.0 K RF performance measurement in horizontal test cryostat; Q_0 vs. E_{acc} performance curves, field emission characterization, tuner and RF coupler performance. This step is considered a ‘spot-check’ and is not implemented for each production cavity.

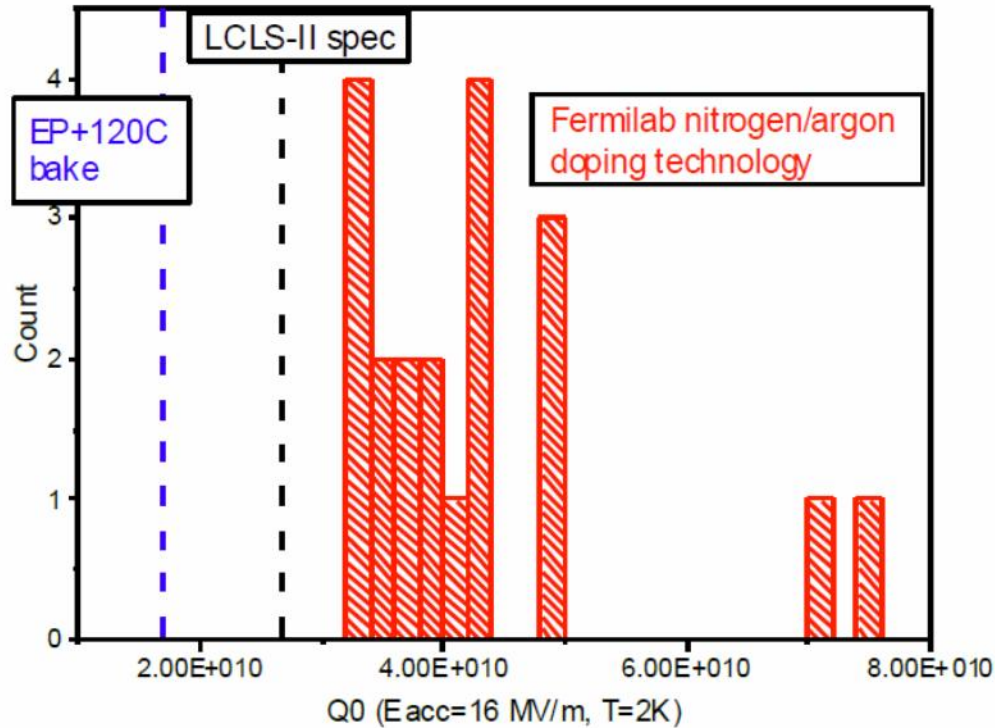


Figure 6.5.2. Results of 20 tests of cavities treated with a nitrogen bake protocol. The measured Q_0 is consistently improved over standard processing procedures, resulting in a mean Q_0 at 16 MV/m of 4.3×10^{10} and median of 4.0×10^{10} .

6.5.3 Alternative Materials and Cavity Design

Alternative cavity designs offer higher-shunt impedance and hence lower dynamic losses, achieved by using a different cell shape with a smaller aperture. The concept has been validated by the CEBAF upgrade low-loss shape cavities [45]. Other higher-efficiency cavity designs exist such as the low-surface-field (LSF) cavity [46], and the low-loss/ICHIRO cavity [47]. For the LCLS-II project, the availability of widespread existing TESLA-type cavity technology experience and production and development infrastructure, together with recent developments in high- Q_0 processing techniques, outweigh the advantages of these cavities.

Lower purity ingot niobium may offer lower residual surface resistance and reduced costs for cavities operated in the medium gradient range of 15-20 MV/m [48]. Residual resistance of ingot niobium cavities has shown an average value of 4 n Ω , as compared to an average 8 n Ω for standard fine-grain niobium cavities processed by using established procedures [49]. Eleven TESLA cavities built with ingot niobium have demonstrated an average Q_0 greater than 2×10^{10} at 2 K and greater than 3×10^{10} with E_{acc} of 14.7 MV/m at 1.8 K. Two such cavities have been tested with beam in FLASH. The third XFEL cryomodule “XM-3” contains seven ingot niobium cavities [50]. Although use of ingot niobium (of equivalent purity or of lower purity) is not fully deployed in industrial cavity production at the present time its possible development for LCLS-II cannot be excluded.

6.5.4 Input Coupler

Including a safety margin, the cavity fundamental input power coupler should be able to handle about 7 kW of average power. The TTF-III coupler [51] (Figure 6.5.3), with modifications, is proposed as the baseline design. The existing design cannot meet the average power requirements due to excessive heating on the warm side of the inner conductor. A possible simple solution is to increase the copper coating thickness of the warm inner conductor. RF-thermal effects of different copper coating thickness have been investigated using the software tool described in reference [52]. The modified couplers will be tested in CW regime at full power before mass production starts.

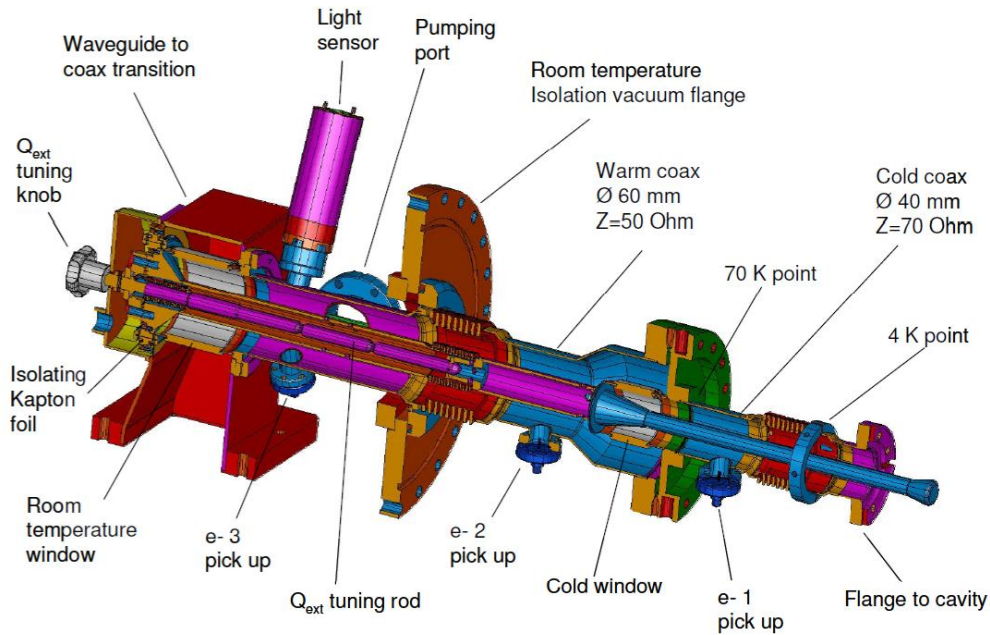


Figure 6.5.3. TTF-III Coaxial Power Coupler. The flange that connects the coupler to the cavity is at 2 degrees K.

Table 6.5.4 shows static and dynamic power losses at different temperature points (2 K, 4 K and 70 K) and maximum temperature T_{\max} of the bellows for different copper coating thickness. The average input RF power is 7 kW. P_{inner} are the losses in the inner conductor, P_{outer} are the losses in the outer conductor, P_{window} are the losses in the window, and P_{total} are total losses. Calculations were made for two values of the copper coating RRR: 10 and 100, respectively. For a tolerable temperature rise of under 400 K, copper thickness of 50 μm for RRR=10 would be sufficient assuming thermal intercept-straps as used for the XFEL cryomodule. Static and dynamic losses are highlighted for this case.

Table 6.5.4. Power losses in W for static (ST) and dynamic (DYN) load and the maximum temperature for copper coating with different thickness and RRR, with input power 7 kW. Suitable performance parameters are highlighted in bold underline. See text for explanation.

Coating thickness (μm)	RRR	Power 2K ST/DYN	Power 4K ST/DYN	$P_{\text{inner 70K}}$ ST/DYN	$P_{\text{outer 70K}}$ ST/DYN	$P_{\text{window 70K}}$ ST/DYN	P_{total} ST/DYN	T_{max} (K)
Inner/Outer								
30/10	10	0.02/0.09	0.2/0.52	0.85/6.8	1.06/2.8	0/1.35	2.13/11.6	420
<u>50/10</u>	<u>10</u>	<u>0.02/0.09</u>	<u>0.2/0.52</u>	<u>1.2/7.1</u>	<u>1.06/2.8</u>	<u>0/1.35</u>	<u>2.48/11.9</u>	<u>376</u>
100/10	10	0.02/0.09	0.2/0.52	1.95/7.8	1.06/2.8	0/1.35	3.23/12.6	327
30/10	100	0.095/0.12	0.5/0.66	0.88/6.81	0.73/2.36	0/1.35	3.06/11.2	396
50/10	100	0.095/0.12	0.5/0.66	1.24/7.26	0.73/2.36	0/1.35	3.42/11.65	364
100/10	100	0.095/0.12	0.5/0.66	2.05/8.2	0.73/2.36	0/1.35	4.23/12.6	322

6.5.5 HOM Couplers

Two HOM couplers are located in the beam pipe in the cavity end group assemblies, see Fig. 6.5.4. The design and angular position are defined by requirements for damping high order modes to the level of $Q_{\text{ext}} < 10^5$ necessary for the ILC, while minimizing coupling to the accelerating RF field, such that $Q_{\text{ext}} > 10^{11}$ at operating mode frequency. The current HOM coupler design allows CW operation for gradients ≤ 7 MV/m, limited by thermal quench of the HOM coupler antenna (or electrical pickup) due to high magnetic field near the antenna tip and poor cooling conditions [39]. One of the possibilities for reducing antenna heating is to modify the antenna tip, and preliminary simulation results show that trimming the antenna tip by ~ 5 mm reduces RF power losses by an order of magnitude, while reducing HOM damping by less than a factor of 10, an acceptable trade-off, taking into account that for LCLS II the maximum beam current is 0.3 mA compared to 9 mA in ILC, and HOMs should be damped to the level of $Q_{\text{ext}} < 10^7$. An additional improvement by increasing the diameter of the central conductor to improve heat transport of the HOM antenna, improving the thermal conductivity of the HOM antenna coaxial vacuum feed-through dielectric, and improving the thermal connection to the cylindrical body of the HOM coupler are also possible.

6.5.6 Cavity Tuners

Among the different tuner designs developed for and tested with pulsed 9-cell, 1.3 GHz cavities are the Saclay-I lever tuner (original Saclay type I tuner), the INFN blade tuner, and the KEK slide-jack tuner. Design parameters for each of these designs are compared in Table 6.5.5 [53].

Studies at Cornell and FNAL comparing the Saclay-I and blade tuner have concluded that the Saclay tuner is preferred for CW cavity operation [54-56]. The blade tuner has lower stiffness, and requires the LHe tank bellows to be located at a larger radius, which increases the sensitivity

of frequency variation due to LHe pressure changes. The blade tuner also has larger hysteresis and a much richer mechanical resonance spectrum, making active frequency control more challenging. The superior performance for CW operation and the proven track record of the Saclay-I tuner, with both pulsed and CW Tesla-style cavities, make Saclay-I a natural choice for the LCLS-II tuner.

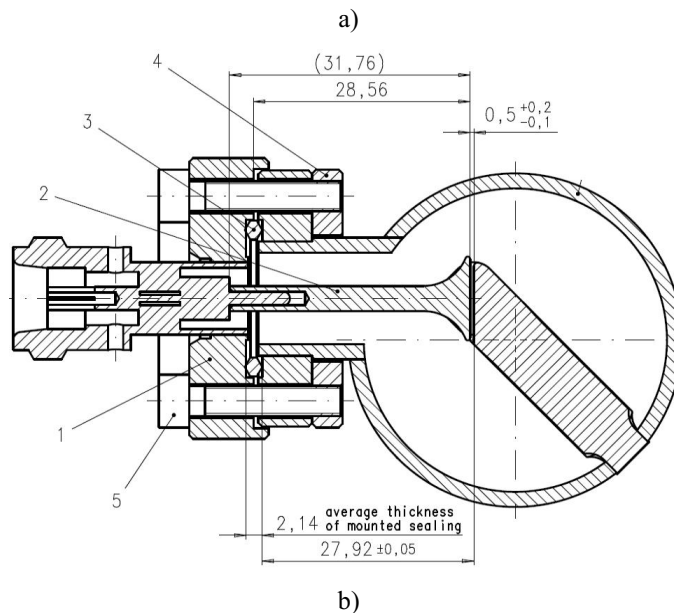


Figure 6.5.4. HOM couplers of the TESLA-like cavity: (a) photograph and (b) sketch: 1: HOM antenna flange; 2: HOM antenna Nb extension tip; 3: aluminum vacuum seal; 4: nut plate; 5: screw.

We propose to use a Saclay/DESY-type lever tuner (see Figures 6.5.5 and 6.5.6) which provides the required slow-tuning range of 245 kHz and the 1 kHz fast-tuning range. The tuning range can be increased to above 1 kHz by selecting appropriate piezo actuators, as was demonstrated at HZB and Cornell. Fast frequency control will require good linearity, resolution and small hysteresis, as has been demonstrated for the Saclay/DESY fast tuner (see the measurement shown in Figure 6.5.7 as an example).

Table 6.5.5. Design Parameters for Tuners Developed for 9-cell 1.3 GHz Elliptical Cavities [53].

	Saclay/DESY	KEK Slide-Jack	INFN Blade
CAVITY			
Cavity spring constant	3N/μm		3N/μm
Cavity sensitivity	300 Hz/μm	300 Hz/μm	300 Hz/μm
Dominant mechanical resonance	~200 Hz	~200 Hz	~300 Hz
TUNER			
Tuner mechanism	Lever	Ramp	Flexure
Tuner location	End	End or Central	Central
Tuner stiffness	40 N/μm	290 N/μm	30 N/μm
Slow Actuator			
Type	Stepping motor	Stepping motor	Stepping motor
Location	Cold	Warm	Cold
Steps per rotation	400		400
Gearbox			
Type	Harmonic drive	Bevel	Harmonic drive
Location	Cold	Cold	Cold
Reduction ratio			17600:1
Fast Actuator			
Type	Piezo Stack	Piezo Stack	Piezo Stack
Max Voltage (Warm)	200V	1000V	200V
Dimensions	10x10x35mm	35x50mm	10x10x40mm
Encapsulation	C-Clamp	Stainless tube	Stainless tube
Stroke (warm)	55 μF	40 μF	55 μF
Capacitance (cold)	2 μF	0.2 μF	4 μF
Blocking force	3 kN		4 kN
Static Performance			
Static tuning range	350 Hz	800 Hz	400 Hz
Static tuning sensitivity	1.1 Hz/Step	3 Hz/Step	1.4 Hz/Step
Dynamic Performance			
Dynamic tuning range	600 Hz	300 Hz	1000 Hz
Dynamic tuning sensitivity	<1 Hz/V	<1 Hz/V	<1 Hz/V

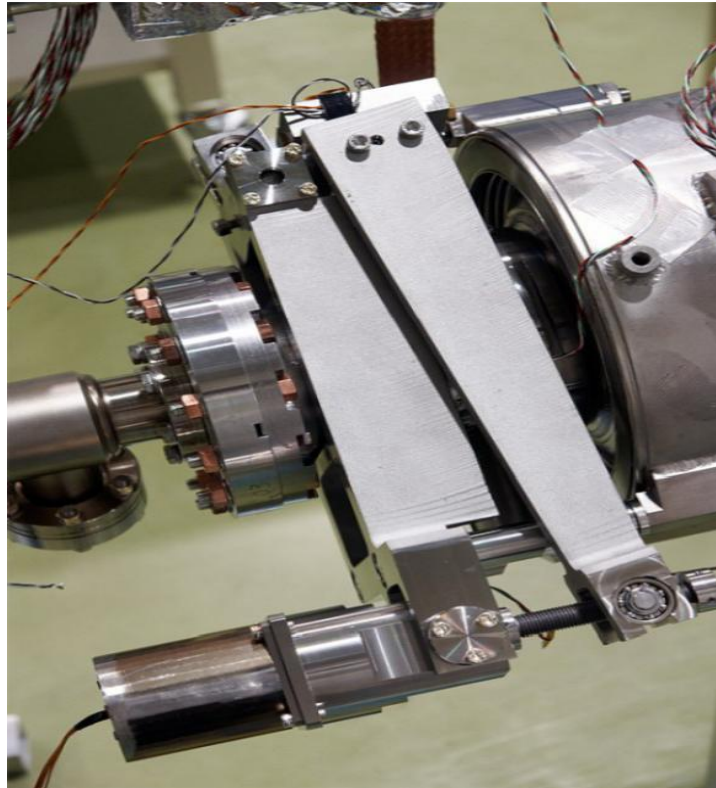


Figure 6.5.5. Saclay/DESY Lever Tuner. A stepper motor drives a compound lever system mounted on the end of the cavity to mechanically tune the resonance frequency.

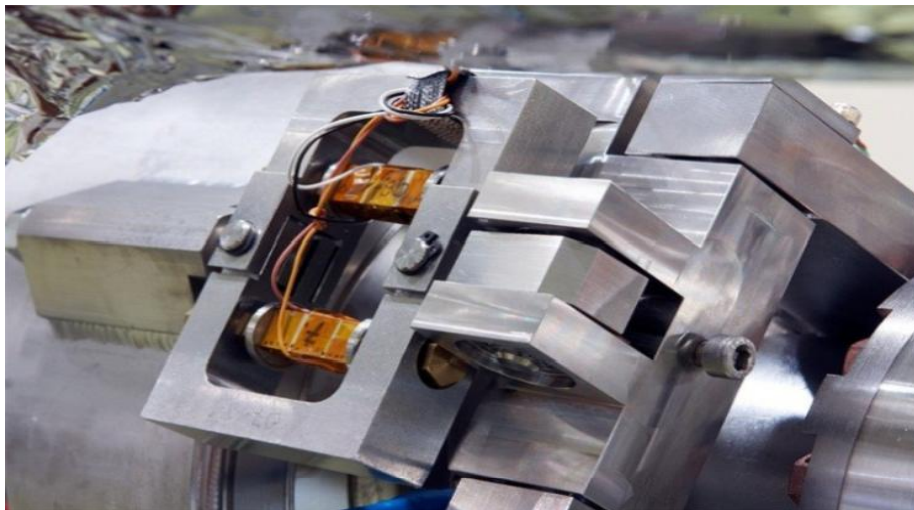


Figure 6.5.6. Saclay/DESY Fast Tuner. The fast tuner incorporates two piezo stack actuators for redundancy.

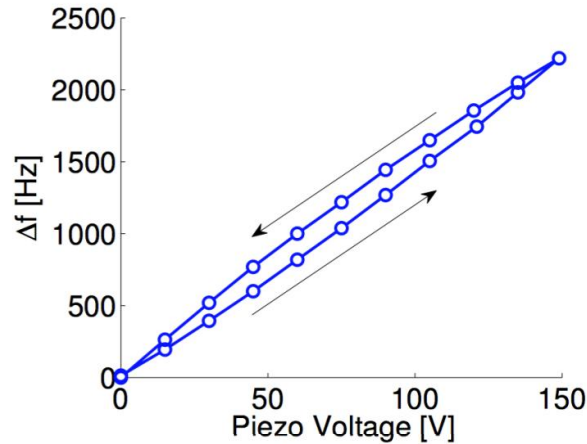


Figure 6.5.7: Frequency shift vs. piezo voltage measured with a modified Saclay-I tuner at Cornell. The measurements show excellent linearity and small hysteresis [53].

6.6 Cryomodules and Components

The function of the cryomodule is to support the dressed RF cavities, efficiently maintain them at the operating temperature of about 2 K, shield them from magnetic fields in excess of $0.5 \mu\text{T}$, ensure proper alignment, and accommodate associated hardware such as RF input couplers, HOM absorbers and instrumentation. A guiding concept for the LCLS-II superconducting linac is to utilize minimally modified XFEL cryomodules. This implies:

- An un-segmented “monolithic” cryogenic linac with insulating vacuum and piping connected from one cryomodule to the next
- Superferric (cold) conduction-cooled quadrupole/corrector package at the end of each cryomodule
- Cold beam position monitor (BPM)
- Cold electro-mechanical cavity tuner (an end-lever tuner)
- Adjustable coaxial coupler (modified TTF input coupler)

Some differences from the TESLA/ILC/XFEL model are necessary, however, to support CW operation in LCLS-II. The cryomodules will each add about 90 Watts of heat to the 2 K superfluid helium, mostly coming from RF cavity dynamic heating. This heat load and the 0.5% tunnel slope necessitate some modifications of the piping and liquid helium control scheme relative to the XFEL cryomodule. CW operation at a gradient of 16 MV/m also imposes some changes in the RF power input coupler and HOM couplers, as discussed in Section 6.5. Finally, close attention to system mechanical stiffness and avoiding flow-induced vibrations or other sources of microphonics will be required in order to minimize RF power requirements

6.6.1 Top-level Parameters for Cryomodules

Cavity parameters are listed in Section 6.4, while Table 6.6.1 lists key parameters for the cryomodules. Cryomodule requirements, heat loads, and cryogenic power estimates are derived from these parameters.

Table 6.6.1. Some Key Cavity and Cryomodule Parameters for the LCLS-II Linac.

Cryomodule (CM) Parameters	Symbol	nom. value	Units
Cavity operating temperature	T_{cryo}	2	K
No. of 9-cell cavities per cryomodule (1.3 GHz)	N_{cav}	8	-
Total installed cryomodules (1.3 GHz)	N_{CM}	35	-
Number of 3.9-GHz cavities per 3.9 GHz CM	-	4	-
Total installed 3.9 GHz cryomodules	-	3	-
No. installed 1.3 GHz cryomodules in L0	N_{CM0}	1	-
No. installed 1.3 GHz cryomodules in L1	N_{CM1}	2	-
No. installed 3.9-GHz cryomodules as linearizer	N_{CMLH}	3	-
No. installed cryomodules in L2	N_{CM2}	12	-
No. installed cryomodules in L3	N_{CM3}	20	-

Figure 6.6.1 illustrates the cryogenic flow schematic for a string of 1.3 GHz cryomodules. Helium flow circuits include a 2.3 K supply, which after conversion to 2 K at each cryomodule is returned as 2 K saturated vapor via the large 300 mm return pipe. Also included are a warm-up/cool-down line, a nominally 4.6 K thermal intercept circuit, and one nominally 40 K thermal radiation shield and thermal intercept circuit. Figure 6.6.1 also illustrates the plan to isolate 2 K liquid baths for each cryomodule while returning 2 K vapor in the large 300 mm pipe through the string of cryomodules in series, which we discuss further in Section 6.6.2. The schematic for 3.9 GHz cryomodules would be similar.

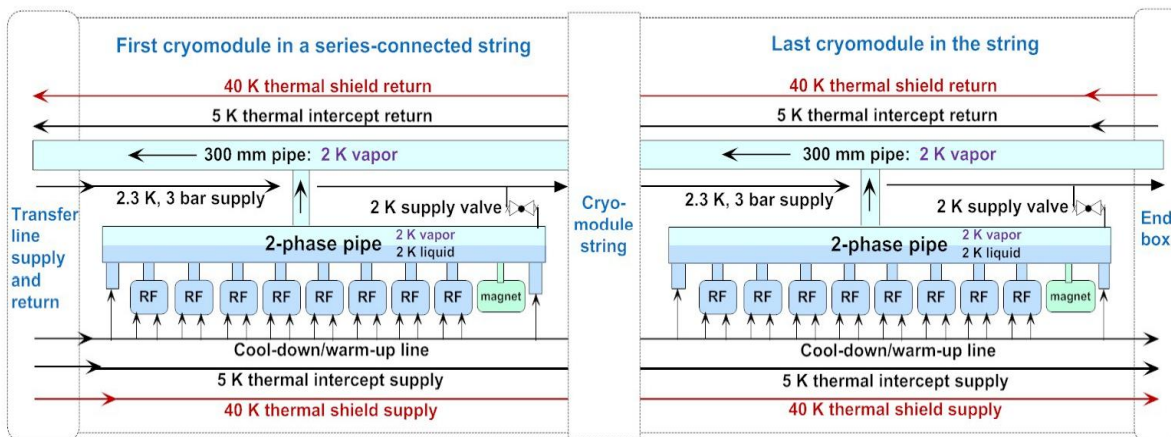


Figure 6.6.1. Cryomodule cooling flow schematic.

Cryomodule heat loads are among the key cryomodule parameters because they largely determine the size and operating cost of the cryogenic system. Table 6.6.2 shows estimates for the main linac heat loads, static and dynamic, on the 2 K, 5(4.6) K and 40 K circuits.

Table 6.6.2. Static and dynamic heat loads and linac total heat for 1.3 GHz LCLS-II cryomodules comprised of 8 cavities operating at an accelerating gradient of 16 MV/m, $Q_0 = 2.7 \times 10^{10}$, 2 K.

Cryomodule Heat Loads and Cryogenic Cooling Power	40 K	5 K	2 K
Predicted static heat per cryomodule (W)	100	12	6
Predicted dynamic heat per powered CM (W)	88	10	85
Total full power heat per cryomodule (W)	188	22	91
Total linac cryomodule heat (kW)	6.6	0.8	2.9
Total non-cryomodule heat (kW)	2.8	0.1	0.2
Predicted total linac heat (kW)	9.4	0.9	3.1

As shown in Table 6.6.2 and illustrated in Figure 6.6.2, dynamic heat loads at 2 K dominate the LCLS-II 1.3 GHz cryomodule requirements due to the CW operating conditions. Heat loads were estimated from a combination of known cavity parameters, extrapolations from the ILC reference design report (RDR) values, and measurements made on ILC type cavities, cryomodules and RF power couplers [53].

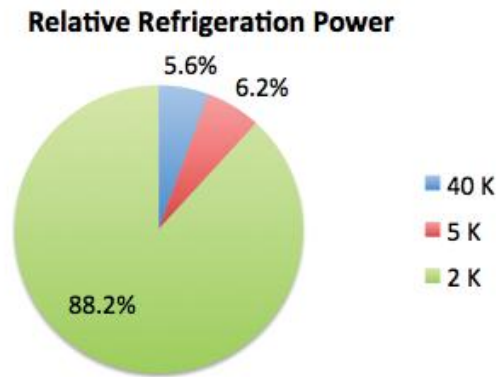


Figure 6.6.2. LCLS-II total heat loads converted to approximate percentage refrigeration power.

6.6.2 1.3 GHz Cryomodule Baseline Concept

An XFEL-style cryomodule (very similar to a TESLA/ILC style 3+) with minimal changes for CW operation has been selected as a baseline concept in order to provide as efficient and quick a start as possible toward cryomodule design and production. These would provide an unsegmented, “monolithic” cryogenic linac with insulating vacuum and piping connected from one cryomodule to the next.

RF cavities will be welded into titanium helium vessels, which contain the 2 K saturated liquid helium surrounding the RF cavities. Each cryomodule will include eight RF cavities, one superferric (cold) combined quadrupole, a corrector magnet package, and a cold beam position monitor. The length of an LCLS-II cryomodule is approximately 13 m. Each dressed cavity will incorporate a cold electro-mechanical, end-lever tuner, similar to that in XFEL, and an adjustable coaxial coupler. A “Type 3+” TESLA cryomodule, similar to those in XFEL but incorporating blade tuners and a few additional minor changes, is shown in Figure 6.6.3. Similarly to the TESLA/ILC dressed cavities, the maximum allowable working pressures will be 2 bar warm, 4 bar cold for the helium vessels and associated piping, and 20 bar for other piping.

Some differences from the XFEL (or Type 3+) design are necessary. Heat loads greater than 10 W per cavity at 2 K, with eight cavities per cryomodule, as opposed to 1-2 W per cavity for XFEL, result in some thermal and helium flow considerations which force changes from the XFEL design. Changes include some increased pipe sizes, to allow conduction of the heat from the cavities through the superfluid helium; limitation of the length of the 2 K 2-phase bath; omitting the 5 K radiation shield; and using modified input and HOM couplers and coupler cooling. A typical cross-section of such a modified cryomodule is shown in Figure 6.6.4. CW operation imposes tight constraints on cavity frequency in order to minimize RF power source requirements. Thus microphonics and cavity frequency variation with pressure need to be minimized, as will the magnetic shielding configuration to enable high Q_0 performance of the cavities according to the requirements given in Section 6.4.1.

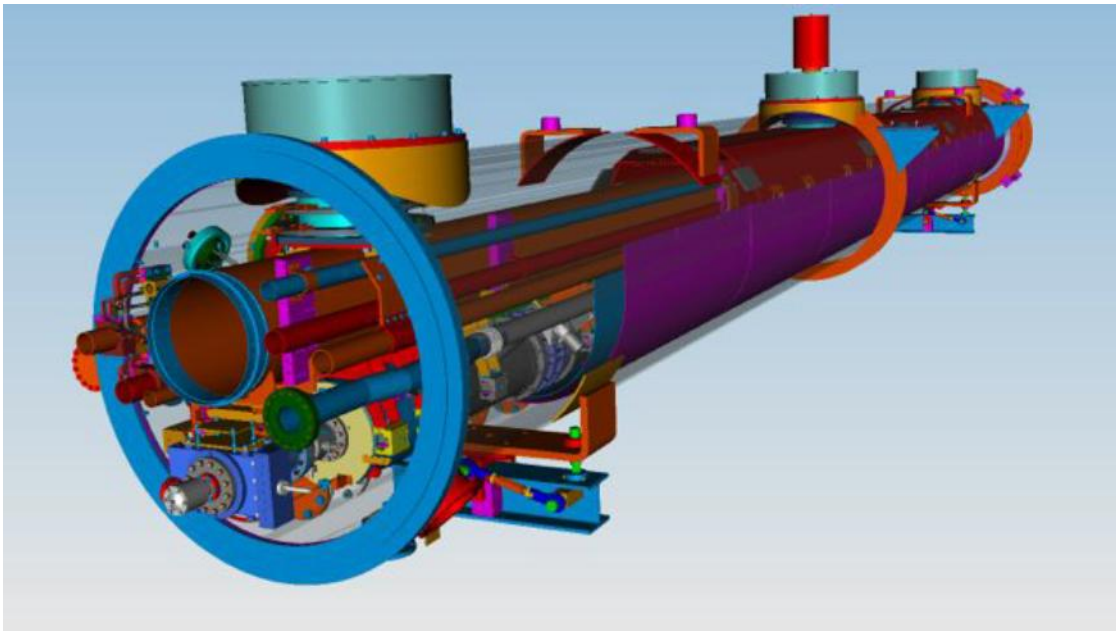


Figure 6.6.3. Type 3+ TESLA cryomodule; a slightly modified version is envisioned for LCLS-II.

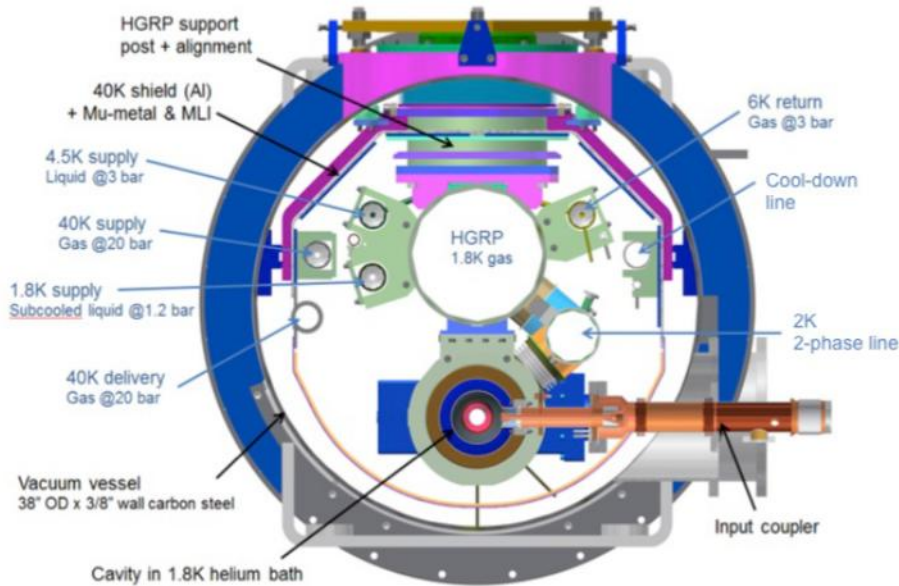


Figure 6.6.4: Cross-section of the Cornell-type CW cryomodule originally based on the ILC design with increased piping sizes.

Emergency venting may also drive certain line sizes and cryomodule features. Large flow rates may be generated by loss of insulating or beam vacuum, and the RF cavities will only be rated for a 4 bar maximum differential pressure. Accommodating these large flow rates, both for steady-state flow and venting flow, affects pipe sizing in the cryomodule. LCLS-II will require two-phase pipe size changes to accommodate the large vapor flow rate. Both the relatively large heat load of over 90 W at 2 K and the 0.5% tunnel slope make the division of 2 K liquid units desirable at the one-per-cryomodule level in order to adequately control helium mass flow rate and helium inventory in each cryomodule.

6.6.3 Elements of a Functional Specification

The following list of cryomodule requirements for LCLS-II provides highlights of the elements of a functional specification.

- Total voltage per cryomodule of 114 MV, ensemble average
- Cavity tuning resolution of less than 2 Hz
- Provide the required beam focusing (peak integrated gradient 2 T/m).
- Monitor beam position
- Provide the required insulating and beam vacuum reliably.
- Minimize cavity vibration and coupling of external sources to cavities.
- Provide good cavity alignment (tolerances shown in Section 6.4 and discussed in Section 6.12).

- Allow removal of up to 135 W at 2 K per cryomodule (including uncertainty in heat load).
- Protect the helium and vacuum spaces, including the RF cavity from exceeding allowable pressures.
- Provide high reliability in all aspects of the cryomodule (vacuum, alignment stability, mechanics, instrumentation), including after thermal cycles.
- Provide excellent magnetic shielding for high Q_0 by reducing residual magnetic field to below 0.5 μ T.
- Allow both slow and fast cool-down through the niobium critical temperature.

6.6.4 Pre-production Cryomodule concept and Goals

Utilizing existing ILC cavity and cryomodule hardware with some small modifications, two pre-production cryomodules will be assembled for the testing of LCLS-II requirements — one at Fermilab and one at JLab. Their construction will provide design and assembly experience for modified helium vessels for CW 1.3 GHz cavities. Key cryomodule objectives are:

- To demonstrate cavity performance in a cryomodule at 16 MV/m, CW operation, 2 K, baseline $Q_0 = 2.7 \times 10^{10}$.
- To test cavity-field control algorithms including, especially, multi-cavity single-RF-source schemes.
- To develop documentation and procedures. For example, establish of a cavity database, draft assembly and quality assurance travelers, and pressure safety and other safety documentation.
- To establish and exercise the close collaboration needed between Fermilab and JLab in building the same cryomodule design. For example, assess infrastructure and trained manpower needs for production modules

6.6.5 Injection Cryomodule

Cornell's low emittance studies have shown an advantage of having short cavities, with individual control of cavity RF field phase and amplitude at the low energy part of the accelerator, minimizing RF slippage. In addition, the transverse kicks to the low energy beam caused by the fundamental power input and HOM couplers should be kept at a minimum. Based on beam dynamics studies, the injector cryomodule might therefore be slightly different compared to the main linac modules:

- Shorter cavities (2-5 cells)
- Different power coupler with low transverse kick
- No HOM antennas, as they produce transverse field

- HOM beam line absorbers or waveguide absorbers in place of HOM antennas

6.6.6 Cryomodule Risks and Risk Mitigation Concepts

Experience with existing SRF cryomodules points to certain risks for which mitigation options will be considered: excessive cavity microphonics, problems with cavity tuner mechanical failure and input coupler thermal or cleanliness, overheating of HOM coupler, and cavity performance degradation in the cryomodule relative to initial vertical test results.

Mitigation measures under consideration include some level of segmentation of cryomodules into groups that can be warmed independently; access ports for tuners; and dual warm-up/cool-down supply ports for more uniform cool-down of the intermetallic joints on the RF cavity (mitigates residual trapped field strength).

6.6.7 Engineering and Design Process

All designs will be built to applicable SLAC engineering and safety standards. Fermilab and JLab's engineering and design work will also follow their respective laboratories' standards. Documentation will follow requirements of participating labs. Some joint decisions may be needed. (For example, pressure vessel and piping certifications must be agreed upon and followed.)

As part of the quality assurance process, a complete cryomodule traveler is to be developed, documenting all stages of materials inspection, cryomodule component fabrication, piping and weld inspection, cryomodule assembly, leak checking, and testing. All the designs will undergo reviews at the appropriate stages of design (such as conceptual, engineering and procurement readiness reviews).

6.7 Cryogenics

The linac cryogenic system consists of three major subsystems: the cryogenic plant, the cryogenic distribution system, and the associated auxiliary systems. The system is expected to operate for 20 years, with an estimated continuous operation of two to five years without a scheduled shutdown. The expected availability of the cryogenic system is 99%.

The cryogenic plant consists of warm recirculation compressors with associated cooling, oil-removal systems and dryers and cold boxes with ancillary support equipment. The system converts compressed, ambient-temperature helium into superfluid. The current refrigeration capacity of the cryogenic plant is estimated to be approximately 18 kW at 4.5 K equivalent. The capacity estimate is based on the assumed average cavity quality factor of $Q_0 2.7 \times 10^{10}$. It also includes 30% and 10% uncertainty factors associated with static and dynamic heat load estimates, and an additional 15% factor associated with cryogenic system overcapacity. Details of the LCLS-II cryogenic power requirements can be found in Table 6.7.1. Under these assumptions, the plant capacity is within the current existing designs for a single cold box. As a result, the baseline estimate assumes a CEBAF design CHL-II 4.5 K and 2 K cold box.

The cryogenic distribution system consists of the equipment needed to feed and return the cryogenics via vacuum insulated pipelines to the linac components needing these services throughout the entire linac. This equipment includes distribution boxes, cryogenic transfer lines, feed and end caps, and cryogenic bypasses to facilitate warm linac beamline elements.

Table 6.7.1. LCLS-II Cryogenic Systems Power Loads.

Item	Temperature Level		
	40 to 80 K	5 to 8 K	2 K
Predicted static heat load [kW]	6.44	0.54	0.38
Predicted dynamic heat load [kW]	2.95	0.33	2.74
Total predicted heat load [kW]	9.38	0.88	3.12
Static heat load uncertainty factor		1.3	
Dynamic heat load uncertainty factor		1.1	
Overcapacity factor for cryoplant		1.15	
Overall capacity multiplier	1.42	1.41	1.29
4.5 K equivalent capacity [kW @4.5 K]	1.0	1.1	15.8
Total 4.5 K equivalent capacity [kW @4.5 K]		17.94	

The auxiliary system consists of warm helium gas-storage tanks, interconnecting piping between the various systems and components, a liquid-nitrogen (LN₂) storage-dewar system, liquid-helium (LHe) storage dewar, a purifier system, an instrument air system, cold box chilled water system, and associated cryogenic safety systems.

6.7.1 Functional Requirements

The cryogenic system as a whole is required to perform the following functions:

- Provide sufficient cooling at appropriate temperature levels to enable operation of the SRF cavities and other cryogenic components within their respective operational conditions.
- Ensure that the system shall support controlled cool-down of cryomodules. The design of the SRF cryomodule limits the rate at which these components can be cooled down from room temperature to approximately 150 K.
- Ensure that the system and its components comply with the SLAC ES&H manual.
- Provide for proper protection of process fluids from contamination.

6.7.2 Helium Refrigerator Description and Choice

The linac refrigeration system consists of two integrated sections: a 4.5 K cold box and a 2 K sub-atmospheric cold box. A reduction in helium vapor pressure necessary to reach superfluid temperatures can be achieved either by including only cold compression or by using a combination of warm and cold compression, as shown Figure 6.7.1. The hybrid warm and cold compression cycle, as seen in Figure 6.7.1(a), has been used in at LHC and is being implemented for XFEL and Spallation Source. The full cold compressor cycle, illustrated in Figure 6.7.1 (b), has been implemented at CEBAF, SNS, and is planned for FRIB.

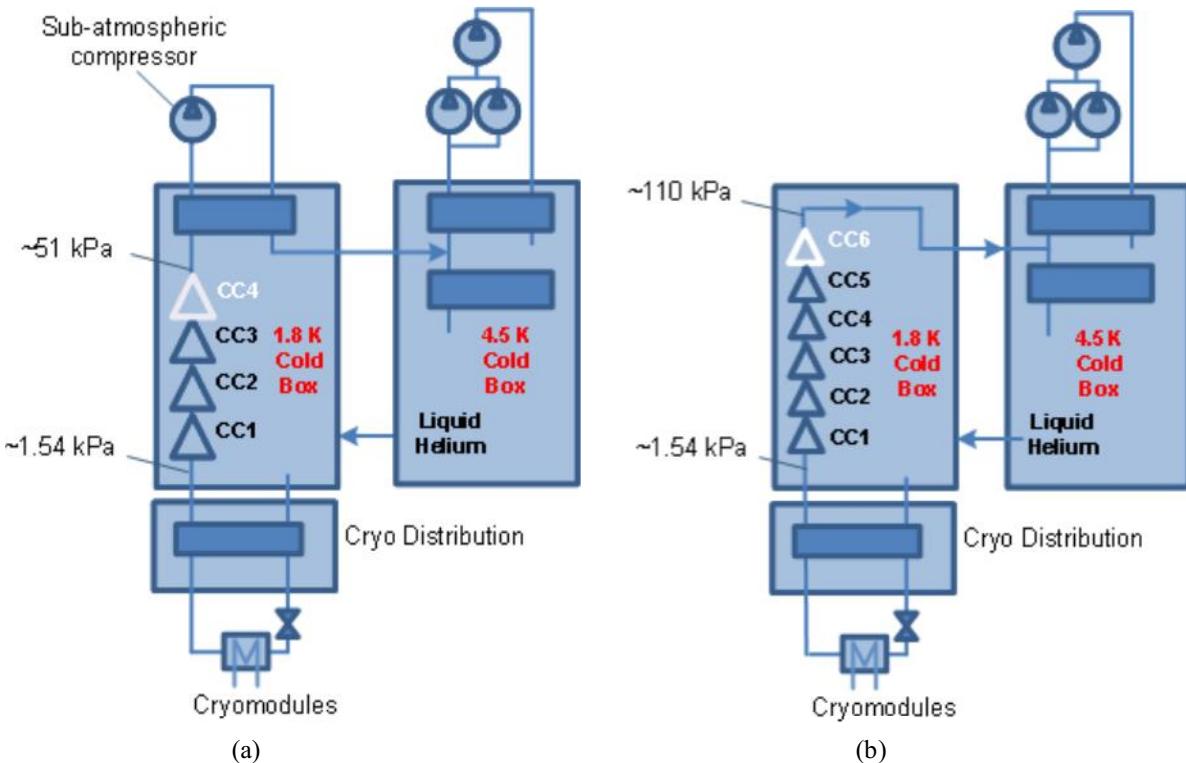


Figure 6.7.1 Superfluid helium refrigeration systems (1.8 K shown only as an example): (a) hybrid cycle; (b) full cold compressor cycle.

For the 4.5 K cold boxes, the plan is to reuse existing cold box designs with minimal modifications. The two options considered are the LHC 4.5 K refrigerator, and the CEBAF CHL-II. Both refrigerators have 18 kW at 4.5 K capacity. Reuse of either the LHC or CEBAF design would reduce the detailed engineering design phase, the critical path of the cryoplant procurement cycle, by five to nine months, as estimated by vendors. This reduces the technical risk of engineering a new plant and having learned from any shortcomings of the existing design, improvements can be incorporated. In addition, experience from commissioning and operation from these existing designs can be leverage to shorten the commissioning time for LCLS-II.

The designed cryogenic plant capacity is given in Table 6.7.2. The design capacity and temperature levels are consistent with the existing cryogenic plant design used by the JLab 12

GeV upgrade project. Since cryogenic plants of this type are custom designed, the use of an existing design offers a cost and schedule reduction by elimination of the vendor engineering and design phase. As a result, the baseline configuration for the LCLS-II cryogenic plant consists of the combined JLab 4.5 K and 2 K cold boxes, shown in Figure 6.7.2.

The cryogenic system is planned to be located in the center of the linac to balance the load, as shown in Figure 6.7.3. This allows the plant to cool the upstream cryomodule string independent of the downstream string.

Table 6.7.2. Design cryogenic capacity.

Temperature	Capacity
2 K	4.0 kW
5K to 8K	1.2 kW
40K to 80K	13.4 kW

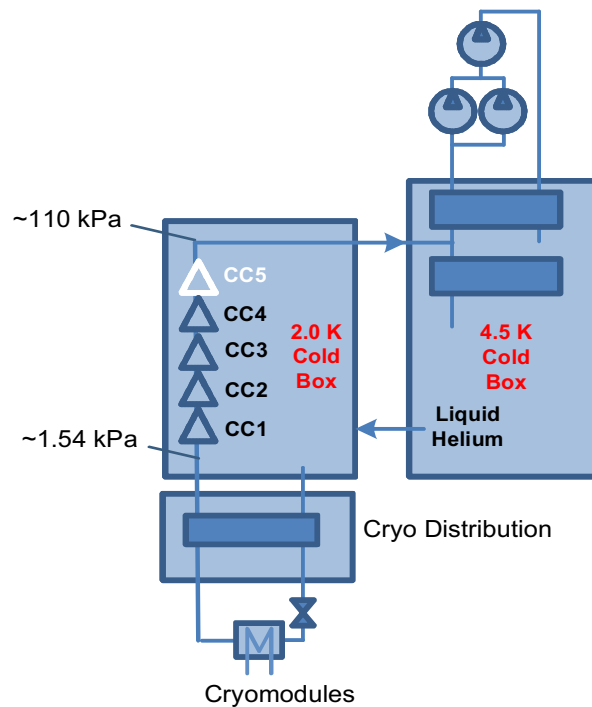


Figure 6.7.2. Full cold compressor 2K cycle adopted by LCLS-II.

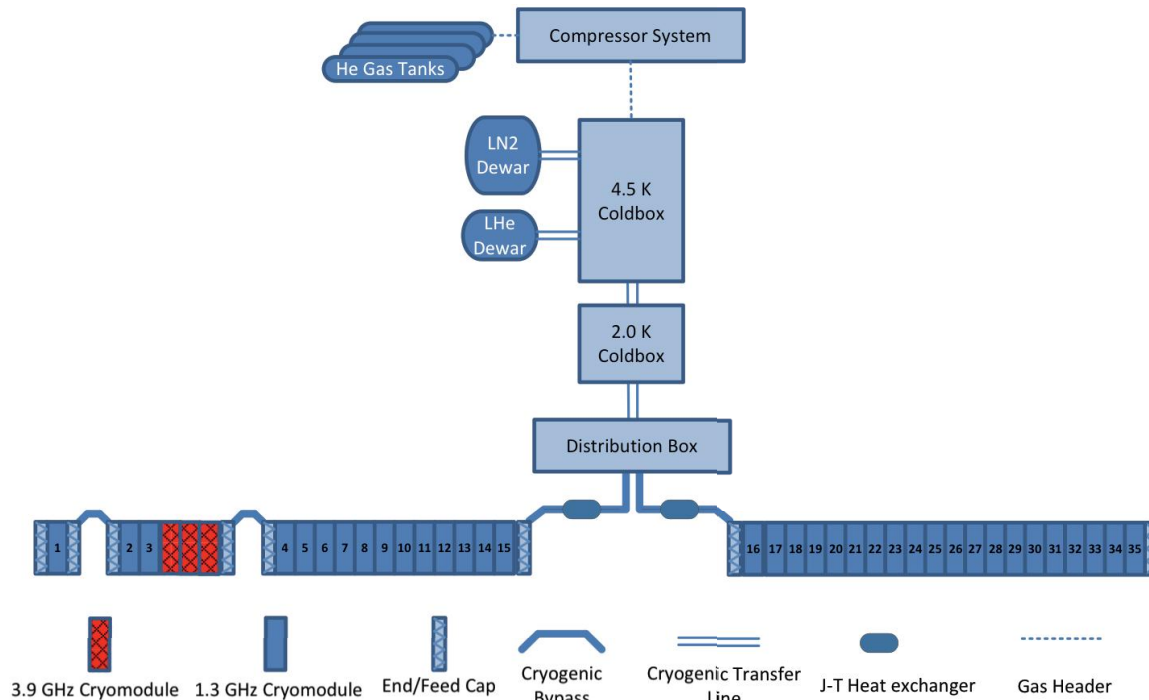


Figure 6.7.3. LCLS-II cryogenics systems layout. The refrigeration system is located centrally along the linac, and distributes cryogenic gas and liquid upstream and downstream.

6.7.3 Operating Modes

The cryogenic system is designed to operate as efficiently as is practical over a wide range of operating requirements. Efficiency is important for the operating modes that are expected to last for extended periods of time, such as normal linac operation at 2 K, 2 K standby (RF off) and 4.5 K standby. Operating modes for the cryogenic system include:

1. Controlled linac cool down and warm up.

The cryogenic system must be able to reliably cool down and warm up the cryomodule string within the cool down rate and temperature difference constraints imposed by the cryomodule design.

2. Linac liquid helium fill

This represents the 4.5K liquefaction capacity of the cryogenic system and determines the time required to fill the cryomodule string with 4.5K liquid helium.

3. 4.5 K standby

During extended shutdown periods, it is desirable to keep the cryomodule string cold while minimizing the operating cost as well as the risks by operating all circuits at positive pressure.

4. 2 K standby

During shorter shutdown periods, it is desirable to keep the cryomodule string at 2K. With the RF off, the heat load to the cryogenic system at 2K is about 12% of the nominal load.

5. 2 K nominal continuous wave operation

This represents the normal continuous wave operation of the linac at the estimated heat loads.

6. 2 K design operation

This represents the operation of the cryogenic system at its full design capacity.

7. 2 K pulsed mode operation

This represents a pulsed mode operation of the linac. Dynamic heat load is considerably reduced in this mode. It is desirable to be able to efficiently turn down the capacity of the cryogenic system to accommodate pulsed operation with an appropriately reduced operating cost.

6.7.4 Warm Helium Compressors

The 4.5 K helium refrigerator plant's compressors consist of multi-stage, oil-flooded screw compressors skid assemblies to compress ambient temperature helium gas from 1 atmosphere to the inlet service pressure required for the 4.5 K refrigerator operation. The estimated power use is 3.6 MW for the steady state plant operation. The compressor skids are grouped into low, medium and high pressure piping manifolds. Trace oil contained within the helium gas is removed from the supply process flow into the 4.5 K cold box to less than 1 ppb.

6.7.5 Gas Management and Storage Systems

The supply and return gas piping manifolds from the compressor system to the refrigerator is controlled by a gas management system – a series of valves which supply helium gas into and out of the cryogenic system from gas storage tanks and compressor bypass valves, which control pressures within the coldbox and the LHe stored in the linac cryomodels.. It is desirable to recovery the liquid as gas storage or, during a plant warm, up to ambient temperature. To accomplish this, four 4,000 scf gaseous helium storage tanks and one 10,000 liquid liter helium dewar are provided. One LHe dewar provides a refrigeration capacity buffer to stabilize the refrigeration supply between the refrigerator and the linac, and also enables performance testing of the refrigeration system prior to connection to the linac.

6.7.6 LN₂ Precooling System

Liquid nitrogen is supplied by one double-walled, vacuum-insulated 20,000 gallon horizontal dewar with a maximum allowable working pressure of 250 psi. External to the dewar, an ambient air vaporizer is used to provide pressurized nitrogen gas supply to the facility. The dewar and vaporizer will be located outdoors. Liquid nitrogen is fed to the facility by a single circuit, vacuum insulated transfer line. The transfer line is insulated with multilayer super insulation to minimize heat flux.

6.7.7 Vacuum Systems

Insulating vacuum: utility and guard vacuum systems are provided to support the operation of the refrigerators. The insulating vacuum systems are comprised of diffusion / mechanical vacuum

pump systems for the 4.5 K and 2 K cold boxes. Each is equipped with local controls for the pumps and their associated isolation valves and instrumentation to maintain the cold box insulating vacuum to 10^{-6} torr. In the event of a power failure, the system will automatically shut down and isolate the system from the cold box to maintain the insulating vacuum. Local and remote monitoring instrumentation is provided for determining the system performance and status.

A guard vacuum system is provided to guard relief devices and other boundaries that are part of the subatmospheric system, to minimize air contamination into the 2K systems during normal operation. The guard vacuum header therefore function as a relief discharge header. A vacuum system has been chosen over a helium guard system since a possible warm helium gas leak into the subatmospheric cryogenic process would develop a substantial process heat load and thermodynamic upset which can be difficult to locate the source.

Portable and fixed utility vacuum pumps, along with LN2 cooled traps, are used to decontaminate piping which have been opened to air during maintenance or repair. Typical use of the utility pumps include three evacuations of the process volumes with back fills of pure helium gas. LN2 cooled traps provide visual indication of the effectiveness of the moisture contamination removal and protection of the utility pump oil from degradation.

6.7.8 Cryogenic Distribution System

The cryogenic plants are connected to the cryomodule strings through a distribution system consisting of:

1. Distribution box

This device has one transfer line inlet from the plant and two transfer line outlets, one to each cryomodule string. Under normal operation, the plant cools both cryomodule strings. Valves within the box allow the strings to be isolated for independent warm-up.

2. Transfer lines

Large cryogenic transfer lines connect the plants to the distribution box and the distribution box to the two cryomodule strings. The cryomodule string transfer lines contain J-T heat exchangers for each cryomodule string. They are installed parallel the beamline between adjacent string feed caps in the tunnel.

3. Feed caps

Transfer lines from the distribution box connect to the cryomodule strings through transition feed caps. The feed cap connects to a cryomodule through a slightly modified cryomodule-cryomodule style interconnect. The vertical supply transfer line welds into the side of the feed cap. Since the feed cap represents the beginning of the cryomodule string, the forces of the maximum pressure of the internal circuits as well as the outer cryostat vacuum load must be transferred to the tunnel floor. This is accomplished through a weldment that also serves as a feed cap and cryomodule support.

4. End caps

The end caps represent the cryogenic ends of the two cryomodule strings. They are similar in function and design to the feed cap, except they do not have the side transfer line. An example of an end cap and support structure is shown in Figure 6.7.4.



Figure 6.7.4. Example of an end cap installed on cryomodule at the Fermilab New Muon Lab (NML).

5. Cryogenic bypasses

Cryogenic bypasses allow warm beamline space to exist within the cryomodule string by bypassing the cryogenic circuit. A bypass consists of two mirror image feed caps and an interconnecting transfer line. Three bypasses are planned in the upstream cryomodule string: one for a laser heater and two for bunch compressors.

6.7.9 Utilities

The cryogenic plant warm helium compressors represent a high inductive electrical load due to the motor drive of the compressors. The electric substation which provides power to the cryogenic plants must be sized to provide the magnetization start current of the largest compressor motor during the time when all other motors are running and when the starting applied voltage at the motor does not drop to less than 80% of nominal voltage rating. A complete redundant spare compressor skid is not included in the work scope. Although the cryogenic plant is only expected to use 3.6 MW of electric power during nominal operation, the substations are substantially larger due to the high percentage of inductive load and voltage drop during starting. The demonstrated successful and recommended substation for the cryogenic plant is 10 MVA. Information on compressor system motors for the refrigerator is listed in Table 6.7.3.

In addition to the electric load, the process compression heat generated by the compressors, turbines and vacuum pumps must be cooled by tower cooling water. The cryogenic plant requires a total of approximately 3,000 gallons per minute with a delta temperature difference of 14 degrees F at the equipment to remove 6 MW of total plant heat load.

Table 6.7.3. Compressor motors information.

QTY	HP	RPM	PHASE	VOLT
4	800	3600	3	4000
1	2500	3600	3	4000
1	120	3600	3	460

The cryogenic plants will require liquid nitrogen as a utility for precooling of the compressed helium gas within the 4.5 K cold box. LN₂ is delivered by trailer and stored in a single 20,000 gallon dewar.

A separate cooling loop to remove the heat extracted by the cryogenic expander brake loop is included in the planned work scope.

6.7.10 Component Location and Area Requirements

The total required cryogenic plant footprint requirement is estimated to be 150'x200'. Further work on specific component locations will be required during the project engineering phase to define the final locations and orientation of the equipment. Each subsystem location determination is planned with the goal of minimizing installation construction cost while providing ease of access required during the plant operation and maintenance.

Gas storage vessels are located next to the warm helium compressor facility. Four 4,000 scf gaseous helium storage vessels are located out of doors and occupy a total area of approximately 54'x85'. Each vessel is installed on low concrete support piers and adjacent to a helium gas/liquid off truck delivery loading station. The delivery station has two-trailer tractor-trailer delivery parking locations in which liquid or gas are exchanged for plant usage.

The cryogenic refrigerator plant requires an indoor warm helium compressor facility, comprised of six compressors skids. Each compressor facility area will be 75'x75' with provisions for 5 ton overhead crane service (21 foot hook height). The crane lift capacity is sufficient to replace the largest components of the compressor skid, i.e. the compressor body or drive motor. The compressor skids have an approximate dimension of 11'W x 26'L x 11'H, separated by 4.5 feet walkways. A common 32"W x 228"L x 84"H medium voltage motor control center for the compressor drive motors is also located within the facility. Compressor cooling water and helium gas piping are to be located below the floor, within piping trenches. Medium voltage and 480 V power conduits are to be located in the slab of the facility to minimize overhead piping congestion and to improve safety during large material handling. Civil interface boundaries for both the cooling water and motor control center are a common piping flange at the wall boundary of the facility for cooling water and the primary power cable connections to the motor control center. Civil interface boundaries of 480 V and 120/208 V are defined at the civil provided power distribution panels. All compressor interconnecting piping and electrical subfeeders from the motor control center to the compressor are provided in the installation budget of the refrigerator system.

The compressor facility does not require environmental controls other than four 20,000 scf/min rooftop ventilation fans and minimum building freeze protection. Due to the operation of the compressors, the compressor indoor facility is classified as a high-noise area, with levels as high as 104 dBA in the walkways between the compressor skids. Air ventilation intake louver sound baffling will be required to reduce external sound to acceptable levels. ODH sensors will be located on the ceiling with both visual/audio indoor and outdoor annunciation.

In addition to the main warm helium compressors, a 8kW emergency power generator for controls, a helium gas purifier, two redundant instrument air compressors, and one 18 g/s helium gas recovery compressor are installed within the compressor facility.

6.7.11 Large equipment installation

The helium refrigeration system is comprised of large industrial equipment which requires careful shipping coordination, material handling, and safety planning. The largest of these are the two cold box vessels, which comprise the 4.5 K refrigerator. Each 4.5 K cold box section weighs approximately 55 tons, with lengths up to 35 feet and shipping diameters of 12 feet. Delivery is on 48 wheeled tractor trailers.

The 2 K cold box, weighing an estimated 20 tons, will be shipped on a separate “low boy” standard open trailer. The cold box will be off-loaded horizontally at the refrigerator building roll-up door and rigged into the building using creepers.

6.7.12 Control System

The cryogenic plant and distribution controls is based on an industrial PLC system. The PLC is divided into four major groups: warm helium compressors, 4.5 K and 2 K refrigerators, auxiliary subsystems, and distribution system control. Each group communicates to a master control room via Ethernet connection to an IOC. In the event of an IOC or Ethernet failure, a local touch panel is supplied to access control loop parameters and plant functional control. All signal conversion and control loop conversion are done within the PLC. The PLC system performs all local equipment safety interlock functions of the cryogenic plant. All signals, control loop functions, alarms, and control parameters are transmitted from the PLC system to the main control room. Redundant PLC 24V power supplies are backed by emergency power.

6.7.13 Applicable Safety Standards

Cryogenic hazards due to the LCLS-II cryogenic plant include the potential for oxygen deficient atmospheres due to catastrophic failure of the cryogenic systems, thermal (cold burn) hazards from cryogenic components, pressure hazards, and electrical hazards. Initiators could include the failure/rupture of cryogenic systems from overpressure, failure of insulating vacuum jackets, mechanical damage/failure, deficient maintenance, or improper procedures.

ODH analysis will be conducted in areas at risk for releasing significant amounts of inert gases. Engineered and administrative controls will be implemented to mitigate the oxygen deficiency hazard. ODH mitigation will include employing oxygen deficiency sensors that alarm

locally and remotely when oxygen levels fall below preset levels. Emergency response procedures will be developed for responding to these alarm systems.

Engineered and administrative controls will be used to mitigate the thermal hazard.

All pressure vessels, piping systems and storage systems will be designed and installed to comply with applicable ASME and ANSI standards. The following list of codes in their latest edition shall be applied to the engineering, design, fabrication, assembly and tests of the cryogenic plant and its components:

- ASME B31.3 Process Piping
- ASME Boiler and Pressure Vessel (BPV) Code
- CGA Pressure Relief PLANT Standards
- EJMA standards
- NFPA 70, National Electric Code (NEC)
- NFPA 70E, Standard for Electrical Safety in the Workplace
- NFPA 79, Electrical Standard for Industrial Machinery
- OSHA Regulations (Standards - 29 CFR)

6.8 Superconducting Magnets, BPMs and Warm Sections

6.8.1 Superconducting Magnets

The magnet package generates a quadrupole field for beam focusing and dipole fields to correct the beam orbit in the vertical and horizontal planes. The main magnet specifications are shown in Table 6.8.1.

Most superconducting magnets designed and built for linear accelerators have been bath cooled [38, 57-63] and must be installed under clean room conditions during the SRF cavity string assembly. The conceptual design of the superconducting magnet package for LCLS-II is based on the latest experience and results obtained from the magnet design, fabrication, and tests for ILC, ASTA, Project-X, and the KEK SRF Cryomodule Test Facility [63-69]. For easy access and installation, the magnet package will be mounted at the end of a cryomodule (see Figure 6.8.1). The magnet is splittable in the vertical plane to facilitate magnet mounting around the beam pipe [67], is conduction-cooled, and does not have a helium vessel. This configuration allows more accurate magnet cold-mass positioning inside the cryomodule by eliminating the uncertainty in relative cold mass — liquid helium vessel position after cooling down. Magnet and current leads cooling is provided by pure aluminum thermal sinks.

The concept of a conduction-cooled splittable magnet has been proven by a number of tests of ILC magnet prototypes, which have a very tight specification related to the magnetic center stability [38]. A magnet with specifications similar to those for LCLS-II (see Table 6.8.1) has been built for ASTA [64] as a doublet quadrupole with dipole correctors. A single magnet of the

same design has also been built by a FNAL-KEK collaboration, and will be installed and tested in a cryomodule at KEK in early 2014. Even these magnets, with an integrated gradient of 36 T [67], have more than enough strength for LCLS-II needs (3 T at 50 A current). These magnets could be used as is, without any modifications at reduced current of 10 A in the quadrupole coils, or slightly modified by reducing the number of coil turns. Table 6.8.2 presents the magnet package parameters based on the proportional current reduction of a built quadrupole, and the parameters specified in Table 6.8.1.

Table 6.8.1 Linac quadrupole specifications.

Parameter	Unit	Value
Integrated peak gradient	T	0.6
Aperture	mm	78
Magnet effective length	mm	300
Peak gradient	T/m	2.0
Field non-linearity at 5 mm radius	%	0.05
Dipole trim coils integrated strength	T-m	0.01
Magnetic center offset in cryomodule	mm	0.3
Quadrupole azimuthal offset in cryomodule	mrاد	0.3
Liquid helium temperature	K	2.2

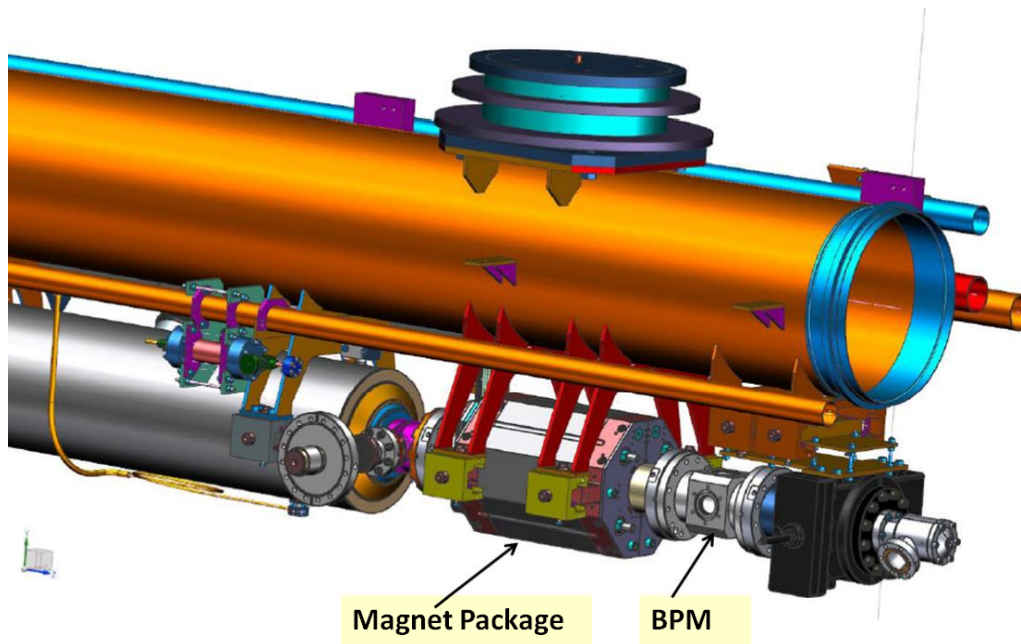


Fig. 6.8.1. 3D model of the magnet package and BPM inside the cryomodule.

Table 6.8.2. Magnet packaging parameters.

Parameter	Unit	Value
Magnet physical length	mm	315
Magnet width/height	mm	220
Pole tip distance	mm	90
Peak operating current	A	25
Number of quadrupole coils		4
Number of dipole coils		8
Type of superconducting coils		Racetracks
NbTi superconductor diameter	mm	0.5
Quadrupole inductance	mH	30
Liquid helium temperature	K	2.2
Quantity required		35

The magnet iron yoke and the superconducting coil geometry are shown in Fig. 6.8.2. The magnetic field analysis showed that the magnet yoke is not saturated (less than 1.5 T) and that a linear dependence exists between the operating current and the integrated gradient.

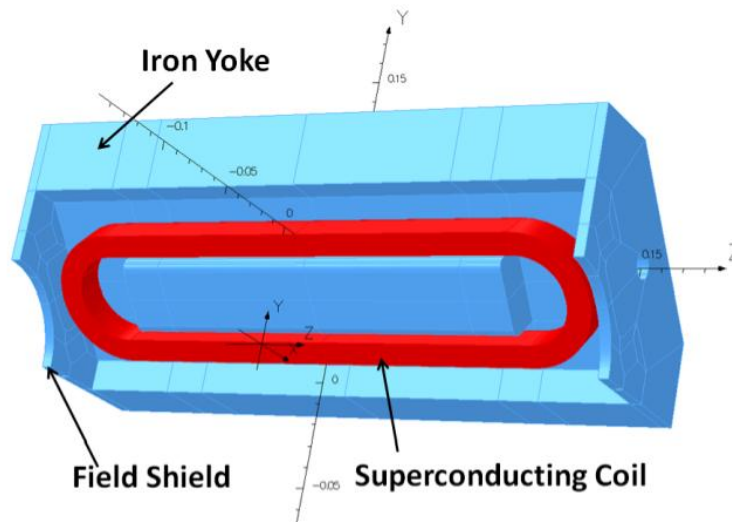


Figure 6.8.2. One quarter quadrupole view.

The quadrupole has a vertical split plane and is assembled from two half cores (see Figure 6.8.3) and has racetrack superconducting coils on the magnet poles.

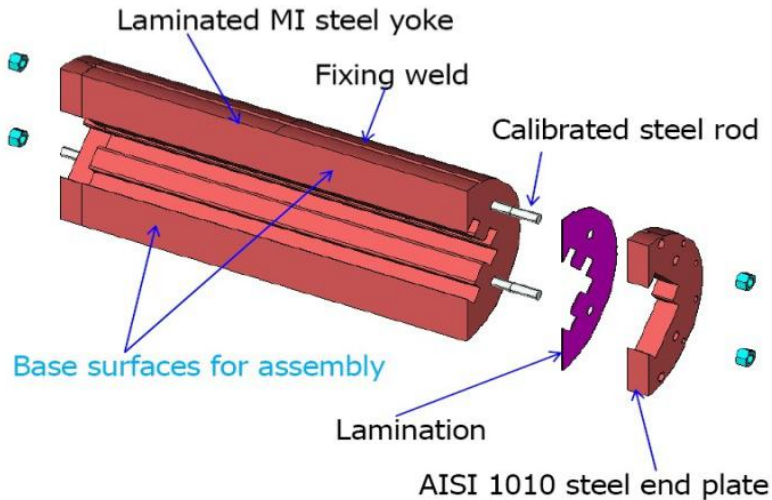


Figure 6.8.3. The FNAL-KEK magnet half core assembly.

The magnet halves are tightened to each other by end plate bolts. The magnet core is assembled from 1.5-mm-thick laser-cut laminations, fabricated from low carbon steel. The half core is pressed in a horizontal press and welded to sidebars and end plates forming a rigid mechanical structure. The magnet package has four racetrack type coils (see Figure 6.8.4), each wound into an aluminum channel. This channel is used for the coil epoxy vacuum impregnation forming a closed mold. Each coil has quadrupole, vertical dipole, and horizontal dipole sections spliced at the magnet forming the quadrupole and dipole windings.



Figure 6.8.4. Four racetrack coils before installation in the KEK cryomodule magnet yoke.

The magnet yoke assemblies are shown in Figure 6.8.5. After half core welding the split plane is carefully machined to provide the needed surface flatness to avoid any core and magnetic center motion due to magnetic forces during magnet operation.

The final assembly of the FNAL-KEK collaboration magnet is shown in Figure 6.8.6. All coils are cooled by pure Al thermal sinks, thermally connected to the Al coil body and a LHe supply pipe. The 2 K LHe line provides the conduction-cooling of this cryogen free magnet.



Figure 6.8.5. The magnet half yoke assemblies for the KEK cryomodule.

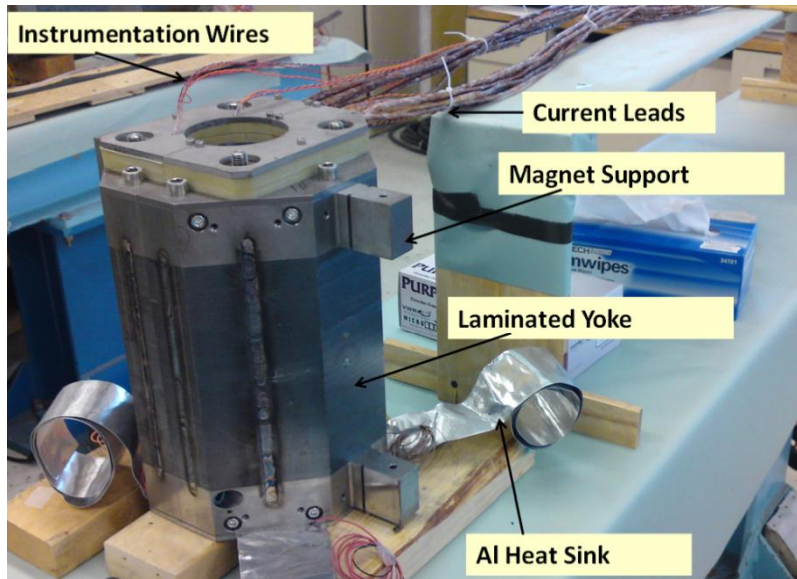


Figure 6.8.6. The KEK cryomodule magnet package final assembly.

The proposed magnet concept and performance have been demonstrated by tests for ILC magnets [59, 67–69] which have more stringent parameters, including 60 times higher integrated gradient, four times higher operating current, and two times longer length. The magnetic field quality is not an issue for these large aperture and small beam size magnets. The field quality is better than two units (2×10^{-4}) for a 10 mm diameter good field area. The magnetic center stability for the first splittable quadrupole was at the level of 6 μm , better than required for LCLS-II. The first ILC prototype magnets had active quench detection and protection systems. Recent tests at

KEK and FNAL with passive protection systems eliminated the active protection system. The magnet is self-protected by induced eddy currents in the coil aluminum case, and an external dump resistor is permanently connected to the magnet current leads. This substantially reduces the magnet system cost and increases the system reliability. The magnet will be installed in the cryomodule using standard SRF cavity supports, which provide magnet positioning with specified tolerances.

All magnets for LCLS-II will be subject to cold tests including magnetic measurements. FNAL has two test stands suitable for testing small superconducting magnets. Stand 3 is for magnet tests in a bath cooling mode. Stand 7, commissioned in 2013 and built in collaboration with KEK (see Figure 6.8.7), has a cryostat cooled by a single 1.5 W capacity cryocooler. It features a vertical room temperature tube in the center for high precision magnetic measurements and has five HTS current leads. The magnet under test is conductively cooled by thermal sinks connected to the cryocooler cold head.

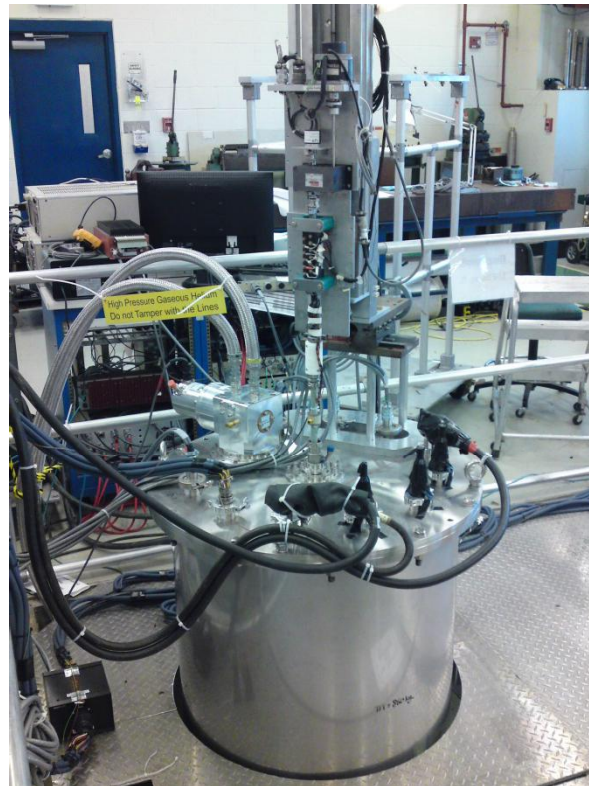


Figure 6.8.7. FNAL Stand 7 for conduction cooled magnet tests.

6.8.2 Beam Position Monitors

Low emittance beams must be transported without emittance dilution for reliable operation of the LCLS-II project. In order to keep a low beam emittance through the superconducting linac, Beam Position Monitors (BPMs) will be installed in every cryomodule with a quadrupole. These BPMs will be used to monitor the beam orbit and provide transverse beam position data for

beam steering. As cold BPMs are located inside the cryomodule, the reliability of the BPM must be very high. In order to provide 10 μm beam position resolution, a low single-bunch charge of 10 pC, these BPMs will be resonant cavities. We expect to use an L-band cavity BPM much like one intended for the ILC cryomodule, featuring common-mode-free couplers, a phase reference cavity per BPM, and Q around 1000 to take advantage of the microsecond between bunches (see Section 9.2). The “re-entrant cavity” BPM from the European XFEL is an existence proof of a design that has been successfully integrated into a cryomodule [70,71], including meeting requirements for UHV cleanliness in an SRF environment. This BPM should be able to meet the resolution requirements listed here, but this has not been demonstrated at the low-bunch charge expected, and puts much more strenuous requirements on electronics dynamic range and linearity.

6.8.3 Diagnostics and Warm Sections

The breaks between the cryomodules and the warm sections of the linac will require diagnostics which are described in Section 9. In addition beam correctors and quadrupole magnets are required. As described in Section 9.9, some of the correctors will need to be high bandwidth for fast beam feedback.

As the beam can generate substantial quantities (W to possibly a kW) of IR and visible coherent radiation from coherent synchrotron radiation (CSR) or coherent diffraction radiation (CODR), the break sections will need light shields to prevent this radiation from reaching the cryogenic components. The design of these shields needs to ensure that the shields themselves do not create CODR that can hit the cryogenic components.

6.9 RF Controls, LLRF, and Feedback

The low level RF (LLRF) system works to regulate the superconducting cavity frequencies, power couplings and RF field levels (amplitude and phase). The systems interface with the global phase/timing distribution system and the machine protection system, and include interlocks to protect the cavities. The linac will consist of four accelerating sections: L0, L1, L2 and L3. In sections L0, L1 and the end of L3, each cavity is powered by an individual power amplifier and the LLRF will consist of one controller per cavity (40 cavities total). In sections L2 and L3, 48 cavities will be powered by one high power amplifier and the LLRF controls cavity fields using a vector sum (240 cavities total). In addition, 12 linearizer superconducting cavities operating at 3.9 GHz will be controlled like those in L0 and L1. Figure 6.9.1 shows a block diagram of the installed LLRF systems. Reference and timing signal distribution is discussed in Chapter 13.

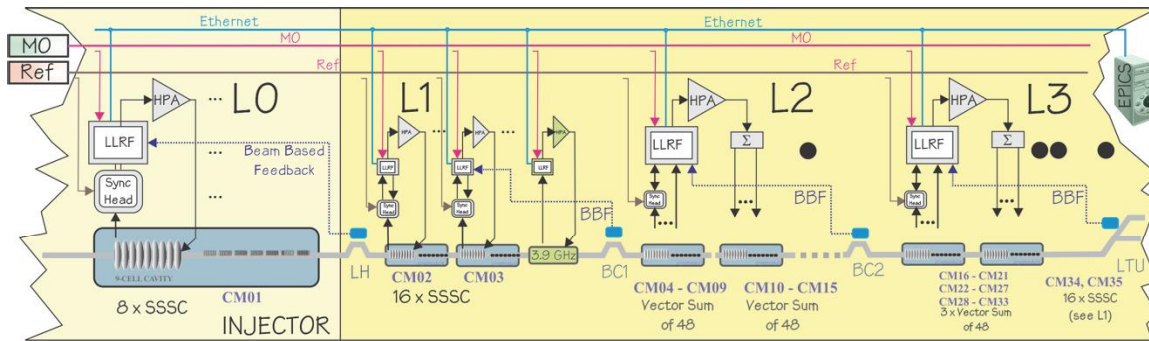


Figure 6.9.1. Schematic of the LCLS-II LLRF systems.

The cavity field control specifications are determined by the beam qualities needed for the FEL, and the cavities must meet the field control specifications and parameters listed in Table 6.9.1. The phase and amplitude stability requirements for L0, L1 and the 3.9 GHz cryomodules, are for each cavity. In the case of the vector sum systems (L2 and L3), the stability is for the vector sum of many cavities. In addition, the LLRF system must support the precise timing/jitter requirements for the electron beam, and the system will be closely coupled with the timing and synchronization system. The field stability requirements of 0.01 degree and 0.01% amplitude (over 1 second) for the vector-sum control is close to the state of the art, however it has been demonstrated at other laboratories, and allows for precise control of beam timing in addition to beam energy. Adopting a single-source single-cavity configuration would significantly relax the field stability requirements, as most driving terms are expected to be uncorrelated. Long term drifts and slow field control errors will be adjusted by beam based feedback.

Table 6.9.1. LLRF Field Control Parameters.

RF phase stability (rms, for vector sum)	$(\Delta\varphi_{RF})_{rms}$	0.01	deg	within 1 second
RF amplitude stability (rms, for vector sum)	$(\Delta V/V_{RF})_{rms}$	0.01	%	within 1 second
RF frequency	f_{RF}	1.3	GHz	
Average RF gradient (powered cavities only)	E_{acc}	16	MV/m	
Average electron current in linac	I_{av}	0.01–0.3	mA	
Mean cavity quality factor (loaded)	Q_L	4×10^7		
RF power per cavity (average)	P_{cav}	6.3	kW	
RF phase of L1 linac	φ_1	-22.0	deg	
RF phase of L2 linac	φ_2	-28.0	deg	
RF phase of L3 linac	φ_3	0.0	deg	

Because of the relatively high Q_L for matched cavities in LCLS-II (see Section 6.4.7), the cavity bandwidth approaches the microphonic detuning bandwidth of about 1.5 Hz rms and 10 Hz peak. The resulting large phase and amplitude variation of the cavity RF fields require active

feedback to maintain required stability. In the case of single-source, single-cavity control, the effects of microphonics on field stability can be damped using RF electronic feedback, as demonstrated at CEBAF, Cornell and HZB. In a vector sum controller with multiple cavities it is not possible to control the individual cavity microphonics using RF power. Therefore, we propose to use a fast piezo tuner (PZT) on each cavity to control slow drifts and partially compensate the microphonic detuning. Tests at FNAL and HZB on long pulse and CW operation have demonstrated that cavity fields can be controlled close to the LCLS-II specification, albeit with different cavity and cryomodule configurations [72,73].

An additional challenge to cavity control is detuning due to the RF field generated Lorentz force. The cavity resonant frequency detunes by many cavity bandwidths as the electromagnetic force of the RF fields distort the cavity during the initial turn on and when the RF power is fluctuating. In the single-source/single-cavity systems, a self-excited loop algorithm, in which the RF drive frequency is controlled to match the cavity resonant frequency, may be used to maintain control of the cavity fields in these circumstances. In the vector sum systems, the PZT will need to be employed to assist in the cavity resonant frequency control. An R&D project has been developed to verify that this is not an issue for the required gradient and Q_L in the vector sum configuration. An alternate is to eliminate the vector sum RF system and adopt single-source single-cavity systems.

The LLRF system will be adaptable, easy to program, have the ability to provide information and data quickly, a seamless interface with the EPICS global control system, and will be able to download digital firmware through the network. It will support beam-based feedback, and operate with pulsed RF. Calibration coefficients will be maintained both within the RF station and on the network. LLRF systems and cryomodule commissioning will be an integrated activity; each LLRF station will be programmed to support Q_L and Q_o measurements, including calorimetry, and will provide local analog outputs for diagnostics and trouble shooting.

The RF system proposed for linac sections L2 and L3 has not yet been operated in CW mode. In the pulsed mode, where it has been successful, the cavities typically have loaded Q_s an order of magnitude smaller than those for LCLS-II, making them less susceptible to microphonic vibrations. To determine systems performance and specifications, an accurate simulation of the CW vector sum system will be made, in addition to real-time tests performed at CW SRF facilities, such as at JLAB, and Cornell to demonstrate PZT control of cavities.

6.9.1 RF Control Stations

The LLRF system contains a number of subsystems, including cavity field control, resonance control (stepper tuner and PZT), and cavity/cryomodule interlocks. Peripheral subsystems such as cryomodule heaters and vacuum system may also be included.

6.9.1.1 Single Source Single Cavity Control (SSSC)

The technology for single source systems has been demonstrated at CW SC linacs, most notably CEBAF [74]. The field control system maintains the cavity field through electronic

feedback, typically a proportional-integral-derivative (PID) control algorithm. Figure 6.9.2 shows a block diagram of the L0 and L1 RF controls, which feature a single source single cavity configuration. The cavity field signal is converted down from 1.3 GHz to an intermediate frequency (IF), typically between 20 and 80 MHz. The IF is digitized using a technique known as “near” IQ sampling. This technique has the benefits of removing ADC non-linearities and simplifying the reference system by using the local oscillator as the clock reference [75]. Similarly, the reflected and forward-power signals and calibration-tone reference signals are digitized. Field programmable gate arrays (FPGAs) will perform the signal processing and control algorithms. The power amplifier drive signal will be converted to the IF frequency using a single DAC, and then the IF is converted back to 1.3 GHz using a mixer. In addition, the RF system will be able to generate a reference tone for self-calibration. The cavity’s resonance control algorithm (stepper motor and PZT) is also embedded in the LLRF FPGA.

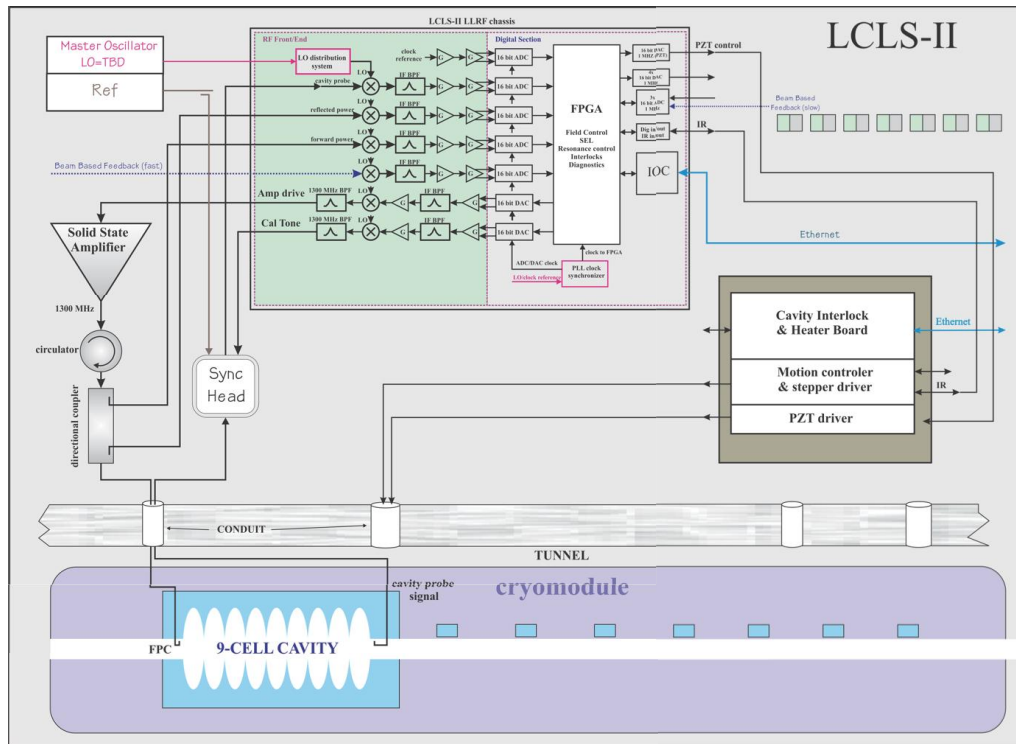


Figure 6.9.2. Block diagram of single source single cavity LLRF.

6.9.1.2 Single Source Multiple Cavity Control (Vector Sum)

Vector sum control of multiple cavities driven by a single source, as is used in pulsed SRF linacs such as XFEL [76], is proposed for L2 and L3 in LCLS-II. Figure 6.9.3 shows a block diagram of the vector sum system. The feedback algorithm and processing is similar to the single source single cavity case; however, the error signal is the sum of those of all 48 cavities. To make this feasible in CW operation, each cavity needs a broadband PZT (~400 Hz, see Section 6.4.2.2), providing active microphonic control.

For each klystron there will be three LLRF stations, with a master and two slaves. Each station will be able to receive and process 16 cavity signals, including field, forward, and reflected power. In effect, there will be one station for two cryomodules. A high-speed fiber link will transport the field vector sum information from the slave LLRF stations to the master station for final processing, and application to the klystron drive. Each RF station will provide resonant frequency control for the 16 cavities in its domain.

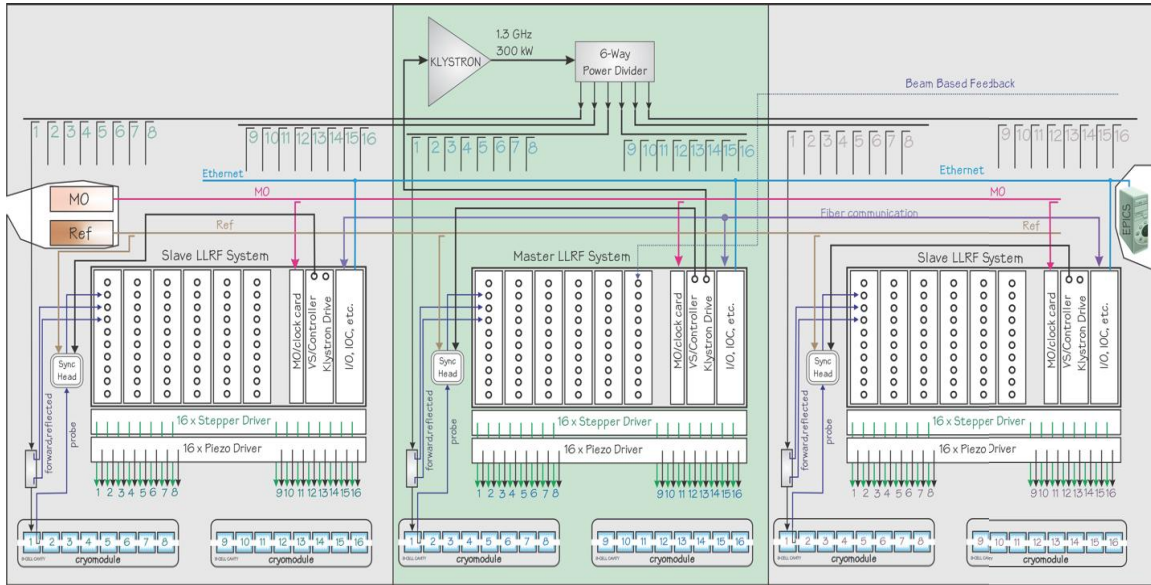


Figure 6.9.3. Block diagram of vector sum LLRF.

6.9.2 3.9 GHz LLRF Systems

The LCLS-II linac will include three cryomodules of four 3.9 GHz cavities each. The cavities will be operated under single-source, single-cavity control. Similar systems have been successfully operated in pulsed mode at FLASH, and will be operated in CW at LCLS-II. Field phase and amplitude stability requirements, and LLRF systems will be similar to those of the 1.3 GHz cavities.

6.9.3 Resonance Control

Cavity resonant frequency control is provided by a slow/coarse stepper motor and fast/fine piezo tuner (PZT). The stepper controller will consist of a chassis with eight stepper drivers. Communication with the cavity field control will be through a dedicated fiber link. As has been noted, the fast mechanical control of cavity resonant frequency is most needed in the vector sum systems. Each LLRF station must process the individual cavity field and forward power signals to determine its detuning angle. An algorithm then determines a control signal to apply to the PZT to keep the cavity close to the reference frequency. The controller and amplifier bandwidth needed for resonance control needs to be ~400 Hz. Section 6.10.1 discusses tuning techniques for different cavity and amplifier configurations.

6.9.4 Cryomodule Interlocks

Table 6.9.2 shows typical RF interlocks for a superconducting cryomodule and the speed with which the RF must turn off to protect the machine. In L2 and L3, an RF trip will take down all of the RF station's 48 cavities.

Table 6.9.2. Cryomodule Interlocks.

Interlock	RF Turn Off	Comment
Coupler arc	< 100 μ s	Typically PMT
Infrared	< 100 ms	Thermopile
Coupler e- pickup	< 100 μ s	
Coupler vacuum	< 1 ms	Ion pump
Beamline vacuum	< 1 ms	Ion pump
Quench	< 100 μ s	Internal to LLRF
He level	< 1 s	
He pressure	< 1 s	

6.10 RF Power Systems

6.10.1 1.3 GHz System Requirements

The basic RF power requirements are derived from physics requirements described in Chapter 7, and resulting operating parameters are listed in Chapter 3. The main requirements from an RF power perspective are the maximum gradient, which is about 16 MV/m, and the maximum beam current, which is 0.3 mA. Table 6.10.1 lists RF source power required per cavity given these values, including overheads such as the need to maintain gradient over a range of cavity frequency excursions due to microphonic mechanical vibrations. The number of cavities fed by each source is also a factor discussed below, as are transmission losses in the waveguide system and overhead to avoid operating at saturation. The cavity coupling (Q_{ext}) is chosen to minimize the power needed per cavity with a 10 Hz frequency excursion from microphonics. We believe peak excursions of 10 Hz are achievable but may require active suppression with piezo actuators.

There are a number of RF sources that can deliver more power than required per cavity in LCLS-II, and having a few higher power sources is generally cheaper than having many lower power ones. The cost benefit of powering multiple cavities per source must be balanced against bunch stability requirements; are the resulting energy variations within a string of cavities powered by one source and regulated as a group with “vector sum” control described in Section 6.9 (as is done at XFEL), tolerable? In the downstream portion of the linac, where the tolerances on local energy variation are less stringent, such a scheme is expected to work if the cavity energy gain excursions are less than $\sim 1\%$. As a practical choice, given the available sources to be discussed below, a ~ 300 kW klystron driving six cryomodules (48 cavities) is a reasonable upper

Table 6.10.1. Maximum RF Power Requirements per Cavity, Including Microphonic Effects.

Parameter	Value	Comment
Gradient	16 MV/m	On crest
Beam current	0.3 mA	
Cavity Q_{ext}	4.1×10^7	Minimizes power for 10 Hz microphonics offset
Maximum power per cavity (with microphonics, without overhead)	5.7 kW	Power with 10 Hz microphonics offset – no overhead
Maximum power per cavity (with microphonics, with overhead)	6.3 kW	Power with 10 Hz microphonics offset, 94% transmission efficiency and 4% overhead
Maximum power for 48 cavities (with microphonics, with overhead)	303 kW	Use either one source per cavity, to track microphonics locally, or one source for 48 cavities
RMS microphonics offset allowed with a ~300 kW source	9 Hz	For Gaussian distributed microphonics

limit for the number of cavities per source. Some of the factors that influence this choice are listed below.

1. Local energy stability requirements and local/global feedback control

Ideally, with a single source per cavity one could keep the local energy gain very stable given that the main perturbations (microphonics) are mostly slower than the approximately 10 ms cavity fill time. This can also be accomplished with piezo actuators on each cavity. For example, at HZB, microphonic detuning has been reduced from a 3 Hz rms level to a 0.3 Hz rms level with feedback and feedforward (FB/FF), albeit with a different cavity and cryomodule design (see Section 6.4.6.) This result is well within LCLS-II requirements, and the energy gain excursions are only a few tenths of a percent. Tests at DESY achieved similar gradient stability in CW mode with no RF nor PZT feedback but with a 90 Hz BW. The stability achievable using piezo compensation alone for each cavity in a group regulated by one RF source needs to be studied further, under conditions required for LCLS-II. In particular, we need to determine the frequency and amplitude range over which microphonics can be compensated without inducing further Lorentz force driven mode vibrations that lead to a discharge of the cavity stored energy.

Regardless of whether the energy gain of individual cavities, or groups of cavities, are regulated, feedback systems will be required to stabilize the beam energy at key locations. Using dispersion regions in the bunch compressor chicanes and at the end of the linac to measure the bunch energies, the RF systems will be used (either locally or globally) to compensate for any slowly varying energy errors. The electron gun current will also be stabilized on a fast time scale, so that the RF feedbacks do not need to respond as quickly.

2. RF and beam turn on

With one RF source per cavity, one possibility for turning on the beam is to first change the RF frequency to compensate the 100-200 Hz LFD during a slow ramp-up of the cavity gradient with the beam off. The cavity voltage would be maximized by control of the RF drive frequency.

After the cavity is filled, the tuner would be adjusted to move the cavity resonant frequency to the nominal value (1.3 GHz), while also adjusting the drive frequency. Piezo controllers could also be used in a similar manner, that is, the RF power is gradually ramped (at the nominal RF frequency) and the cavity resonant frequencies continually adjusted with the piezo controllers to maximize the cavity voltage. The Cornell SCRF group has demonstrated this for a single, high Q_{ext} cavity where the power was ramped up in about 0.5 seconds. In principle, this could be done with multiple cavities per RF source.

In both cases, RF power is ramped up to about one quarter maximum to achieve the nominal gradient, then to full power as the beam is turned on, ideally increasing both in a single step with matched beam loading. XFEL effectively does this with each RF pulse, although they turn on at full RF power and turn the beam on when the nominal cavity gradients are reached. LCLS-II can do it more slowly, in two steps (beam off and on), to decouple the LFD and beam loading effects on the gradient, and dump the beam before the undulators until the cavity gradients and beam energy reach steady state.

3. Cost

Using one solid state amplifier (SSA) of approximately 6 kW per cavity, the RF system cost would be about two-thirds more per CM than having groups of 48 cavities fed by a single 300 kW klystron powered by a commercial HV power supply (and a factor of about two more if the klystron is power using a refurbished SLAC PEP-II HV power supply). At 6 kW, using klystrons or IOTs instead would not be that much cheaper than SSAs, and would likely be less reliable.

4. Layout

Given the SLAC linac/gallery configuration, having one klystron feed 48 cavities would require only a single air-filled WR650 waveguide every 50 m which would connect between the klystron and the RF distribution system in the tunnel. Single cavity sources would require such a feed every 1.5 m, which still should be able to use nominal-sized waveguides and fit into the 27 inch diameter penetrations between the gallery and tunnel that are located every 20 feet.

5. Availability

SSAs would provide high availability, considering that transistor failures would not reduce the output power from a single unit by much (approximately 1%). Even if the whole unit failed due to a power supply fault, the power could be increased to other cavities to compensate; more cavities than are needed for acceleration are included in the linac design to allow for compensation of this failure mode. A 300 kW klystron failure would shut off the beam until a spare was installed (about eight hours). With a conservative estimate of a 20,000-hour lifetime, 5 klystrons and 4,000 hours per year operation, there would only be an average of one klystron failure per year. Nonetheless, failures of the klystron auxiliaries (e.g., filament power supply) would likely be the dominant source of unavailability, though they would only reduce the availability by less than 1%.

In summary, having groups of 48 cavities driven by one 300 kW klystron provides significant cost savings but adds risk that the cavity fields cannot be stabilized. To manage this risk, simulations will be done of multi-cavity operation with only PZT control of each cavity and actual gradient stability measurements will be made, at least of single cavity operation with no RF feedback. The most realistic tests will be done using the TESLA-style cavities that will be operated at full gradient (16 MV/m) at FNAL and Cornell as part of the high Q_0 program. The cavity power couplers will be modified such that the nominal LCLS-II Q_{ext} of 4×10^7 can be achieved. At minimum, with only slow frequency feedback, we would be able to quantify the gradient stability, and in particular, see if the cavities tend to drive themselves fully off resonance. By the end of 2014, we would then reassess whether to continue with the multiple cavity per source approach, and if not, we would still have sufficient time to change the RF system design to have all cavities powered with individual sources before the production order would need to be placed (this approach will be developed anyway to power the upstream portion of the linac). Finally, if we continue with the multiple cavity per source approach but it turns out to be more difficult than anticipated once the full SLAC Linac is operated, we could reduce the cavity Q_{ext} (by half, to 2×10^7) as LCLS-II will only run at one sixth of the beam power for the first several years (until new undulator lines are installed). Having twice the cavity bandwidth should make stabilizing the gradient much easier.

6.10.2 Technology Options

There are two basic technologies capable of delivering the high-power RF needed to energize the cavities in the LCLS-II linac: (1) vacuum tubes, specifically inductive output tubes and klystrons, and (2) solid state amplifiers in which the output of a number of low power (few hundred watts) transistors are summed. While the multi-kilowatt RF power levels needed for single cavities can be achieved with either technology, significantly higher power levels can be more easily accomplished with vacuum tubes, since they would not require complex combining networks.

6.10.2.1 Vacuum Tubes

Vacuum tubes suitable for modern particle accelerators include triodes, inductive output tubes (IOTs) and klystrons. Klystrons and triodes have been the traditional power source for particle accelerators because they produce high power RF and offer high gain with efficiencies of more than 50%. Triodes are useful at frequencies below approximately 300 MHz, and therefore are not considered for the LCLS-II linac.

IOTs present an attractive alternative to traditional klystrons for accelerators in the lower UHF frequency range. IOTs have recently become available at L-band frequencies with efficiencies around 60% and gains of approximately 20 dB. Still, IOT gain is inherently low compared to that of klystrons (typically 50-60 dB), requiring considerably more RF drive power. Although not established in a long-running accelerator facility, L-band IOTs have been successfully operated, for example, in the ALICE (ERLP) facility at Daresbury [77] and in the cERL at KEK [78]. Also,

IOTs are typically more efficient and can be operated closer to saturation with sufficient LLRF response than klystrons.

Table 6.10.2 lists the operating parameters and output power of several commercially available vacuum tube RF power sources of both types, suitable or adaptable for use in LCLS-II. Current IOTs can provide tens of kilowatts at 1.3 GHz; a principal hindrance in pushing into the 100 kW CW range is the increased RF drive power needed due to their low gain. L-band CW klystrons range in power from several to a few hundred kilowatts.

For LCLS-II, L-3 has proposed to modify the 13 kW klystron (L-4313) they developed for JLAB to deliver up to 7 kW at 1.3 GHz with 40 dB gain and at least 48% efficiency. Their older 8 kW tube would seem a closer match, but is less efficient, even though it uses a permanent magnet rather than solenoid focusing.

6.10.2.2 Solid State Amplifiers (SSAs)

Recent improvements in LDMOS transistor technology have led to increased power capability of solid state amplifiers (SSAs). Individual transistors can reach power levels on the order of a couple of hundred Watts, but by combining many transistors into a single system, several up to tens of kilowatts can be achieved with modest efficiency loss. SOLEIL has built systems that produce 45-50 kW at 352 MHz and 476 MHz. At the higher L-band frequency, Bruker-Biospin has developed for ELBE a 10 kW CW SSA source, successfully operated since 2010. With high power transistors, 16 kW can now be produced in a 10-unit rack. Finally, Cornell recently purchased a 5 kW system from Bruker for the CW SCRF program, and they are satisfied with its performance.

System operating efficiency for such L-band SSAs does not typically exceed 40%. This technology is still emerging, and further advances, including better efficiency, can be expected in the future, likely reaching 45-50%. However, for the same reason — lack of maturity — the reliability of these systems at present is less well established. Since several facilities now have SSAs in place, operational data is continuing to be acquired. The modularity of this option, with its soft failure mode compared to klystrons, is another factor in its favor. As transistor technology advances, “plug compatible” rack inserts are likely to be used to replace failed units (for example, at SOLEIL, a 3% per year transistor failure rate causes no additional downtime, as they are repaired during scheduled maintenance periods.)

6.10.3 Source Selection

For the baseline LCLS-II design, there is one SSA source per cavity for the first three and last two cryomodules (CMs), with the remaining CMs powered by five 300 kW klystrons, each feeding 48 cavities. The last two CMs nominally use SSAs for quantization reasons, not for finer energy control, although this may be useful. More information on how these sources would be configured in LCLS-II are given in the next two sections. This is followed by a section on the 3.9 GHz sources and one on other RF sources that are required. Finally, the last section presents a general plan for vendor qualification and pre-production studies.

Table 6.10.2 Commercially Available Vacuum Tube L-Band CW Power Sources (Klystrons and IOTs).

KLYSTRONS								
Manufacturer	CPI			e2v	L-3		Toshiba	
Model	VKL-7811ST	VKL-7966A	VKL-7967A	K3415LS	L-4941	L-4313	E3750	E37750
Frequency (GHz)	1.3	1.497	1.3	1.3	1.4-1.5	1.4-1.5	1.3	1.3
Beam voltage (kV)	15.5	33.5	61	45	14	14.3	20.5	50
Beam current (A)	2	6.5	8.5	5.5	1.76	1.75	2.5	10
Output power (kW)	10	110	300	120	8.0	13	30	300
Gain (dB)	34	55.5	45.9	45	35	>40	52	40
Efficiency (%)	34	51	58	51	32.5	50.5	60	63

IOTs				
Manufacturer	CPI	e2v	L-3	Thales
Model	VKL-9130A	116LS	L-4445T	TH713
Frequency (GHz)	1.3	1.3	1.3	1.3
Beam voltage (kV)	34	25	34	34
Beam current (A)	1.3	1.1	1.14	0.88
Output power (kW)	30	16	20	20
Gain (dB)	21	20	22.8	20.9
Efficiency (%)	64	60	52	60.4

6.10.3.1 SSAs

While no off-the-shelf SSA sources match LCLS-II needs, Bruker-Biospin (now SigmaPhi Accelerator Technologies) has offered a 6 kW version of existing high-power (5-16 kW) systems. As example, Figure 6.10.1a shows their 10 kW rack unit that consists of eight 1.25 kW water-cooled modules. Each module contains eight 160 W isolated transistor units that are summed to a coaxial output, then coupled into a common WR650 output waveguide. Some of the specifications for Cornell’s 5 kW system are shown in Table 6.10.3. Although a 43% efficiency is listed, the company quotes only 35% overall AC to RF efficiency. For 6.3 kW, a 480 V power supply at the bottom of the rack would supply up to 50 V for the drain voltage. Facilities requirements per rack would be 18 kW AC and 6 gpm cooling water.

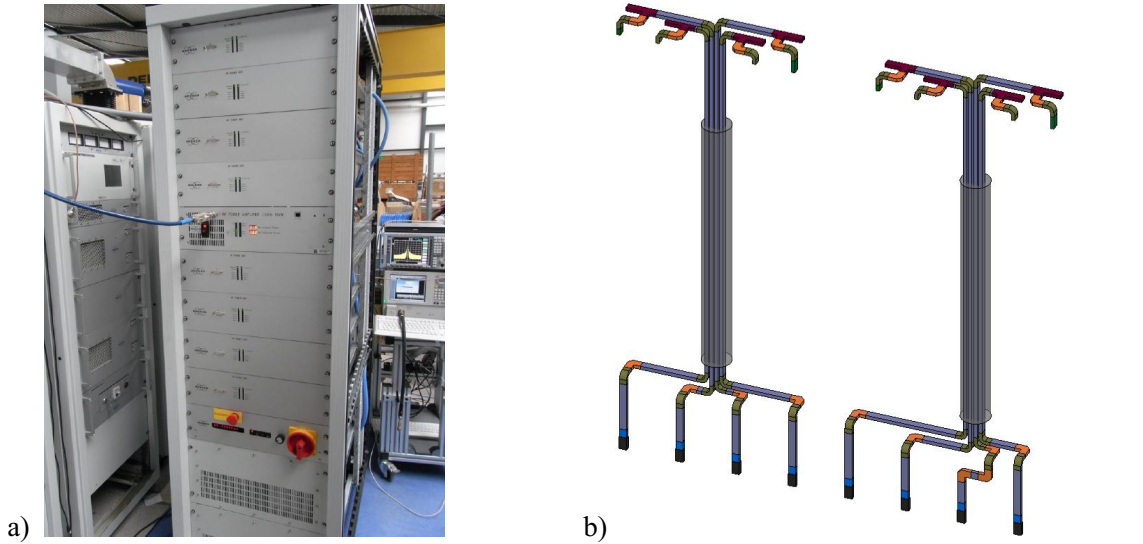


Figure 6.10.1. a) Photograph of the Bruker-Biospin 10 kW 1.3 GHz CW Solid State Amplifier cabinet and b) preliminary layout of waveguide from eight SSA racks feeding a cryomodule through two shafts.

Table 6.10.3 RF specifications of the 5 kW Bruker-Biospin solid-state amplifier used at Cornell.

Frequency range	1,300 MHz \pm 5 MHz
Linear gain	67 dB
Gain flatness in frequency range	\pm 0.2 dB
CW & pulsed output power (1dB Compression)	5,000 W min
Amplifier biasing	class AB operation
RF rise time	< 100 ns
RF fall time	< 70 ns
Input noise figure	8 dB max
Output noise power	-99 dBm @ 1 Hz
IN/OUT impedance	50 Ω
Input VSWR	1.5 max
Output harmonics 2 nd order/3 rd order	-45 dBc min/-60 dBc min
Amplitude stability/temperature	\pm 0.20% / $^{\circ}$ C
Power RF efficiency	43% typ. at 5 kW output
Input power supply	380V/400V 50/60Hz three phase
Max output VSWR	∞ up to 1.5 kW CW

Penetration shafts between the SLAC linac gallery and the tunnel are at 20-foot intervals. The cryomodule length is about twice that, and each houses eight cavities. Therefore, four cavities are

powered through each penetration. Four WR650 waveguides from side-by-side SSA racks can fit through the 27 inch diameter hole, as illustrated in Figure 6.10.1b. If the remaining room is insufficient for cables and related equipment, half-height WR650 or rigid coaxial transmission line may be used. A waveguide isolator for absorbing reflected power will be incorporated at the gallery end of each waveguide feed to reduce heat dissipation in the tunnel. Isolators with pickups incorporated may be used, unless it is determined to be preferable for calibration and phase stability control to bring the forward and reflected RF signals up through cables from bi-directional couplers near the cavity couplers.

6.10.3.2 Three Hundred Kilowatt Klystrons

For the high power source, a strong candidate is the 300 kW CW klystron built by Toshiba (E37750) and installed at the compact ERL demonstrator at KEK [79]. The tube has 63% efficiency and operates at 50 kV (see Figure 6.10.2). The klystron requires no oil tank and operates with a beam voltage of 49.5 kV and beam current of 9.8 A at 63% efficiency. It does, however, require considerable cooling water (more than 100 gpm). A suitable power supply would be the Thomson 540 kVA, 55 kV design used in NSLS II (see Fig. 6.10.3), for which an efficiency of 95% is measured. Though the footprint required for this equipment, particularly the power supply, is large, the resulting RF power is sufficient to feed six cryomodules, or 48 cavities along a span of about 50 m. Space for equipment in the klystron gallery should not be an issue.



Figure 6.10.2. The 300 kW Toshiba E37750 klystron at KEK test stand.



Figure 6.10.3. The 540 kVA, 55 kV PSM switching supply from Thomson (used at NSLS II at BNL) that could be used to power a 300 kW klystron.

Linac operation with multiple cavities driven by a single source has been demonstrated at the FLASH facility and is assumed in the ILC design [38], however without individual cavity resonance control as needed for LCLS-II. Unlike the ILC, which pushes cavities to their gradient limits, LCLS-II does not incorporate expensive power distribution adjusters, but uses equal power division as it is expected that nearly all cavities will operate at 16 MV/m. Figure 6.10.4 shows a preliminary waveguide layout, in which all but two waveguide "T" junctions are equal binary splits, for powering six cryomodules from a 300 kW klystron. An additional feature required in this waveguide system is an approximately 90 degree phase shifter at each cavity (nominally operating at mid-range). Also, the isolators for this shared system must be local, near the cavity couplers. The layout shown uses isolators with built-in pickups and final waveguide Ts with incorporated phase shifters, developed at DESY. Though this layout can be fit in the tunnel, more of the splitting might be done in the gallery and more shafts would be used to minimize tunnel waveguide and heat load.

SLAC has developed and built similar waveguide distribution systems for the cryomodules in the NML Building at FNAL [80], as part of the ILC R&D program. They run pulsed at high power driven by a 10 MW, 1.6 ms, 5 Hz source, demonstrating that peak power at 300 kW can be handled. However, the waveguides will be cooled from the klystron to the second 2:1 splitter, in particular to avoid heating the air in the tunnel.

If the performance of a single cavity degrades significantly, the input waveguide would need to be disconnected in the tunnel, and RF power routed to a load (the cavity would be detuned as well). If the cavity can still be operated at a somewhat lower gradient, the splitter ratio for the final power divider could be changed to lower the power to that cavity and raise power to the adjacent one (similar to the XFEL plan). Splitters with different power ratios can be prepared in advance for such use, and the change out time is expected to be less than four hours. The cavity couplings (Q_{ext}) would also be adjusted accordingly.

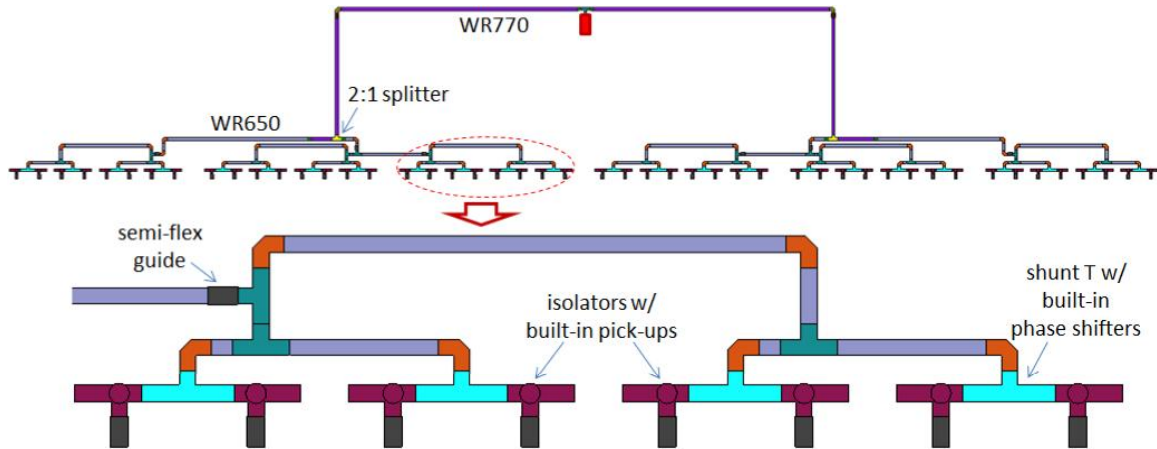


Figure 6.10.4. A possible waveguide system layout for distribution of 300 kW klystron power to 48 cavities, and close-up for one cryomodule.

6.10.4 3.9-GHz RF Sources for the Harmonic Linearizer

Just before BC1 are a set of third harmonic (3.9 GHz) RF cavities used to cancel the curvature in the longitudinal energy profile along each electron bunch (see Section 6.11). Because the bunches need to be nearly 180 degrees off crest, the beam actually loses energy in these cavities. With Q_L and cavity detuning properly adjusted to yield the desired gradient and phase, the steady state field can be maintained from beam loading alone, with essentially no power from the source. To establish the operating field level and sustain it when the beam is off, approximately 400 W RF power would be required, and could be provided by a traveling wave tube (TWT).

However, to increase the cavity bandwidth and hence reduce microphonic effects, we will be likely to use a higher power source, operated even with the beam on, with cavity coupling appropriately set and excess power reflected into an isolator load. At this frequency, a possible source is CPI's VKC-7810F 3 kW CW klystron, which need not be run at full power. The WR187 waveguide output port can be tapered to WR284 (which SLAC has plenty of for its S-band systems) for lower losses in the runs to the cavities.

6.10.5 Other RF Sources

The LCLS-II electron beam originates in a normal-conducting photocathode RF gun and emerges at a beam energy of 750 keV. The gun cavity operates at a frequency of 186 MHz (VHF), the seventh sub-harmonic of 1.3 GHz. While the theoretical gun quality factor and required field level call for about 90 kW input, the source specification with overhead is set at 120 kW. Various RF technologies are available at this frequency.

A gun has been developed at LBNL for the Advanced Photo-injector Experiment (APEX), and has been operated at full gradient using a tetrode tube power source as pictured in Figure 6.10.5 [81]. At LCLS-II, the power will be transported into the tunnel through a pair of four 1/16" coaxial lines and fed to the gun cavity through two magnetic loop couplers.



Figure 6.10.5. High power amplifier and high-voltage power source fabricated by ETM Electronics using two Thales TH571B 60 kW tetrodes to deliver 120 kW 186 MHz CW RF to the gun for the APEX R&D program at LBNL.

Additionally, solid state amplifiers have reached the required level of maturity to deliver high power at this frequency. Bruker/SigmaPhi has proposed a design with a significantly lower cost than the APEX source. They have built a 12 kW CW amplifier at 175 MHz and achieved 60 kW at 88 MHz; a pair of 60 kW CW 186 MHz sources would not be a significant extrapolation.

Also included in the injector beamline, between the electron gun and the L0 cryomodule, is a normal conducting L-band buncher cavity. Due to the copper wall losses, 20 kW of 1.3 GHz RF is required to power this buncher. For a source at this power level, we could use a relatively efficient IOT. But rather than introduce an additional technology to the machine, it is preferable to employ the same SSA technology employed in the linac. A double rack Bruker/SigmaPhi L-band unit, with a waveguide combining T, could provide 20 kW. Figure 6.10.6 shows SSA packages in this power range, which include power supplies and drivers. Isolators would most likely have to be inserted before the combining for average power handling.



Figure 6.10.6 CAD images of proposed double-rack 15 kW and 30 kW CW L-band SSA configurations from Bruker Biospin. 20 kW is needed for the LCLS-II buncher.

6.10.6 Vendor Qualification and Pre-Production Plan

Once the final source selection is made, specifications would be written that could likely be satisfied by vendors with fairly minor modifications to existing designs. In particular, those relating to the AC supply voltage, drain voltage control, controls software (desirable if they are EPICS ready), cooling water pressure, and RF back-termination.

One exception for the SSAs would be to specify Class F amplifiers for higher efficiency provided a viable amplifier module could be developed over the next year. Even if we continue with Class A/B amplifiers, we will aim for at least 45% efficiency, which Bruker/SigmaPhi believes can be achieved within the next two years; again in efficiency of this scale may be achieved by trading off linearity, which is not needed here as much as for other applications like NMR. The 300 kW klystron and modulator specs would not likely require much change from those for commercially available units.

Since both the SSAs and 300 kW klystrons that we are considering are relatively new products, it will be important to have vendors deliver pre-production units early and to test sources from at least two vendors in each case. Test stands at SLAC would be built to do long-term testing of both the SSAs and klystrons into loads, operating 24/7 at least 5,000 hours a year. Based on the results and other factors, the bids for the production units could be placed with reasonable confidence that sources meeting performance specifications would be supplied.

6.11 RF Harmonic Linearizer

6.11.1 Introduction

Space charge effects limit the maximum obtainable charge density from the photocathode, and thus the minimum bunch length. For LCLS-II, a 300 pC bunch will have a length of approximately 1 mm at the exit on the injector. Sinusoidal variation in the RF voltage over this distance will lead to a correlated energy variation, or “chirp,” in the uncompressed bunch and, after bunch compression, to an asymmetric bunch profile. Applying a voltage at a harmonic $\omega_1 = 3\omega_0$ of the fundamental RF frequency ω_0 results in an integrated voltage that is approximately linear over the bunch length, removing the curvature of the beam distribution in longitudinal phase space, and facilitating more efficient bunch compression and controlled bunch charge distribution [82,83]. Linearization of the longitudinal phase space of electron bunches in a superconducting RF linac has proven to enhance beam quality and simplify operation, as evidenced by the performance of the harmonic linearizer cryomodule, ACC39, at the FLASH facility at DESY [84]. Figure 6.11.1 shows results from FLASH, with and without the linearization of the bunch-correlated energy distribution.

6.11.2 The FLASH ACC39 RF Harmonic Linearizer

The ACC39 cryomodule consists of a string of four 9-cell superconducting cavities routinely operating at 2 K and providing of order 19 MV combined voltage. The design, fabrication and delivery of ACC39 was undertaken by Fermilab in partnership with DESY, and an 8-cavity

device is now under fabrication for the European XFEL injector [85]. Both of these applications are for a pulsed RF system with 10 Hz repetition rate and 1.3 ms pulse duration.

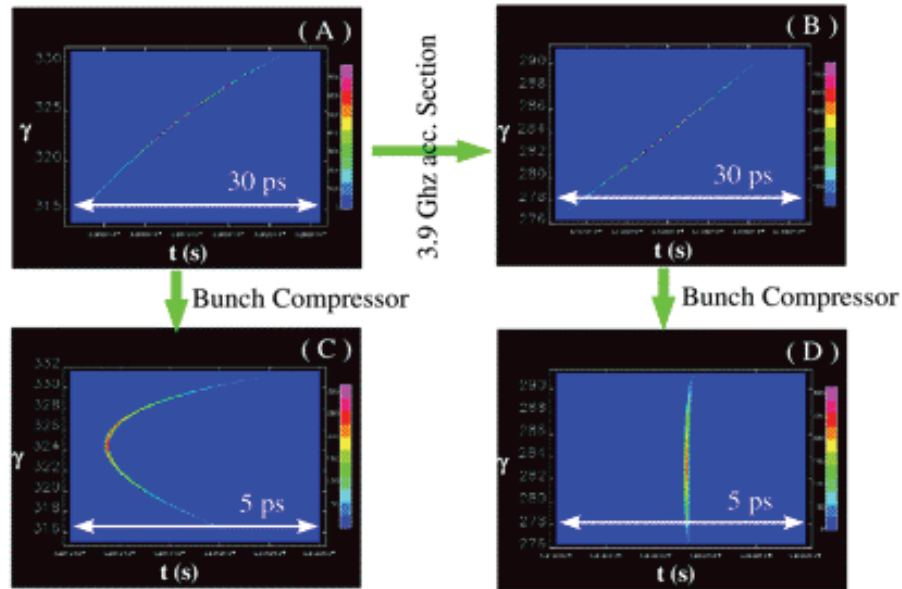


Figure 6.11.1: FLASH longitudinal bunch distribution without (A and C) and with (B and D) the harmonic linearizer. The upper row shows measurements before the bunch compressor, and the lower row after bunch compression. (D) shows the high compression achievable with the harmonic linearizer.

Table 6.11.1: Preliminary 3.9 GHz Cavity Parameters Based on ACC39/FLASH Design.

Parameter	Value
R/Q	750 Ω
$E_{\text{peak}}/E_{\text{acc}}$	2.26
$B_{\text{peak}}/E_{\text{acc}}$	4.86 mT/(MV/m)
$B_{\text{peak}} @ E_{\text{acc}} = 14 \text{ MV/m}$	68 mT
Nominal Frequency and Tuning Range	3900 \pm 1 MHz
$\Delta f/\Delta L$	2.39 MHz/mm
Lorentz force detuning constant, K_{Lor}	6 Hz/(MV/m) ²
Q_{ext}	2.2x10 ⁷
Bandwidth	180 Hz
RF forward power per cavity	415 W
Active length of 9 cells	345.96 mm
Cavity overall length	505.9 mm

The design of LCLS-II specifies 60 MV of linearizer voltage at 3.9 GHz, operating in the continuous wave (CW) regime. A conservative estimate suggests that this voltage could be achieved with 12 cavities of similar design to those used at FLASH, each operating at approximately 15 MV/m. Building on the proven ACC39 design would thus require three such cryomodules. Table 6.11.1 lists major parameters for the LCLS-II 3.9 GHz cavities (with input courtesy W-D Möller, DESY).

6.11.3 Modifications for CW Operation

Most of the mechanical and thermal design factors which must be considered for the LCLS-II 1.3 GHz accelerating cryomodules are also pertinent for the modification of the ACC39 design for CW operation. Preliminary studies suggest modifications to the existing design can readily be made to accommodate CW operation. Further studies and simulations must be carried out to detail the design. Among the factors to be addressed are:

- Heat load and cryogenic piping
- Input coupler power capability and cooling requirements
- Necessity of variable coupling
- HOM heating and beam dynamics
- HOM coupler and feedthrough power handling
- Microphonics and need for fast piezo tuning of the cavity

The heat load is estimated to be of the order of 15 W per cavity at 15 MV/m, and that the total cryomodule heat load should be limited to less than 250 W. Simulations indicate that the existing input coupler should be capable of supporting up to 2 kW in CW operation. Empirical studies using existing spare components are possible to verify the heat load per cavity and power handling of the couplers.

The current HOM coupler design employs a single-post “Formteil” design [86], estimated to have a lower multipacting bound of 25 MV/m. This design is used on two of the four ACC39 cavities and is employed on all eight XFEL harmonic linearizer cavities. The original ACC39 HOM couplers were of a two-post design, with the expected advantage of better cooling, however these experienced repeated incidents of cracking due to overheating in prototype testing, and were not used in production. Two of the cavities now in operation at FLASH exhibit symptoms of HOM overheating, and their gradients are kept low to avoid possible failure. Modeling and prototype testing of both designs should be performed prior to making a final design choice for the LCLS-II. The HOM feedthrough antennae for ACC39 were fabricated with a niobium tip, molybdenum conductor, and sapphire dielectric for improved thermal transfer. At Fermilab, two spare cavities have been retrofitted with new end groups employing the single post “Formteils,” and can be used for initial verification. A recent cavity test resulted in an upper gradient of approximately 22 MV/m, limited by quench. This test included operation in the CW regime. No evidence of heating of the HOM couplers was observed, although it should be noted that, in this

test, the HOM couplers were in direct thermal contact with the helium bath, unlike the case for actual operation in a cryomodule.

Further analysis is needed to verify the robustness of this design for CW operation and/or to investigate cooling schemes, if deemed necessary. Preliminary simulations have been initiated to determine whether high frequency (THz) modes are present in the cavity string which may require absorbing material in the adjacent beam pipe.

In order to minimize design and development time, it is proposed that blade tuners be employed for “slow” adjustment of the resonant frequency. Reliability of such tuners in 3.9 GHz applications has been very good, with no known failures at FLASH or during testing elsewhere. Due to their compact size, these cavities are already relatively stiff and thus resistant to microphonics and Lorentz force detuning. However, it would be prudent to consider the addition of fast piezo tuning or passive microphonics compensation.

Impact of the harmonic cavities on beam dynamics issues must also be considered. Some of the factors include:

- Collective effects (exacerbated by higher frequency). Beam cavity interactions will be evaluated as a part of linac beam dynamics analysis.
- Impact of wakes/impedances on beam quality
- Effect of HOM burden on beam stability
- Beam halo and the impact of a constrained aperture. This will also be evaluated during linac beam dynamics studies.
- RF drive/control. We must take into account the fact that third harmonic cavities decelerate the beam, thus creating the potential for control issues should the power recovered from the beam exceed the forward power provided by the external drive. This circumstance will be avoided by the choice of a low Q_{ext} (1.3×10^6).

6.11.4 Alternate Compression Schemes

Nonlinear control of path length-momentum correlations [87–89] has been utilized in a variety of circumstances and offers a possible alternative to harmonic RF linearizers. Although successfully used in multiple systems providing high CW power in the IR through near UV, and planned for use at shorter wavelengths [90], to date no example system utilizing this methodology has been used in X-ray FEL drivers. Of particular concern is the preservation of high beam brightness during the bending and focusing required to provide the desired control of T_{566} . Control of relevant collective effects is currently being studied [91].

6.12 Linac Beam Dynamics and Tolerances

This section will summarize the SCRF linac single and multi-bunch tolerances and requirements needed to preserve the beam emittance and limit the thermal load in the cryomodules due to wakefields and HOMs. Tolerances for the components in the warm breaks

between the SCRF linacs (laser heater, BC1 and BC2) as well as the tolerances on the post-linac transport will be discussed in Chapters 7 and 10.

The LCLS-II SCRF linac is based on the TESLA 9-cell cavity. Extensive experimental and theoretical studies have been performed over the years on the tolerances and emittance effects in these cavities. In particular, both the short-range and long-range longitudinal and transverse wakefields have been carefully studied for both the 1.3 GHz TESLA 9-cell cavities and the 3.9 GHz cavities that will be used for the RF linearizer upstream of BC1 [92–95]. As a starting point for the CDR, the cryomodule tolerances for the LCLS-II design will be specified to be similar to the European XFEL design, as shown in Table 6.12.1. Future optimization will be performed and is expected to further ease the component requirements.

Table 6.12.1: Assumed rms misalignment tolerances for the LCLS-II cryomodules. These tolerances are close to those of the European XFEL design.

Error Source	RMS error	unit
Cavity misalignments wrt. CM	0.5	mm
Cavity tilts	0.5	mrad
Quadrupole misalignments wrt. CM	0.5	mm
BPM misalignments wrt. CM	0.5	mm
Cryomodule misalignments	0.5	mm
Cryomodule tilt	0.05	mrad
BPM resolution	0.01	mm

6.12.1 Single Bunch Emittance Dilutions

As discussed in Section 7.2, the optics in the SCRF linac are relatively weak, to better balance the single-bunch dilutions of the projected emittance, which is determined by dispersion and transverse wakefields due to alignment errors. It should be noted that neither of these effects has much impact on the slice emittance, which is more critical for the FELs. Upstream of BC1, where

Table 6.12.2. Projected Emittance Dilutions (%) in the LCLS-II from Misalignments Listed in Table 1.

Error Source	L1	L2	L3
Cavity misalignments wrt. CM	6×10^{-2}	0.08	0.15
Cavity tilts	< 1	2.4 / 0.1*	0.4/0.01*
Quadrupoles and BPMs misalignment wrt. CM	< 1	1.5	1.5
Cryomodule misalignments	1.5	2.5 / 1.8*	2.5
Cryomodule tilt	0.35	0.9 / 0.5*	1.1
All misalignments together	<1	5 / 3.8*	< 4.8

* after one-to-one steering

the beam energy is low and the bunch length is long (approximately 1 mm), the effect of asymmetries from the main and HOM couplers should be also taken into account. In general, the weak wakefields of the superconducting 1.3 GHz accelerating structures and the low chromaticity of the focusing lattice leads to harmless beam dynamics in the main linac. The emittance dilutions from different source of misalignments can be easily scaled from ILC and XFEL parameters using analytical formulas [96-99]. The result of simulations of the tolerances and emittance dilution that have been done using the Lucretia and Elegant codes to further refine the estimates are listed in Table 6.12.2.

As shown in Table 6.12.2, the contribution to emittance dilution in the L1 linac is small. In linacs L2 and L3, the chromatic effects due to offsets and tilts of cryomodules, quadrupoles and BPMs, are the dominant source of emittance dilution. Results of simulations of the relative emittance growth, averaged over 40 seeds, are shown in Figure 6.12.1 for the L2 and L3 linacs. All nominal misalignments from the Table 6.12.1 were applied. The initial normalized emittance used in the simulations was 0.35 mm-mrad. Figure 6.12.2 represents the trajectories of the beam in each seed before (blue) and after (green) 1-2-1 correction.

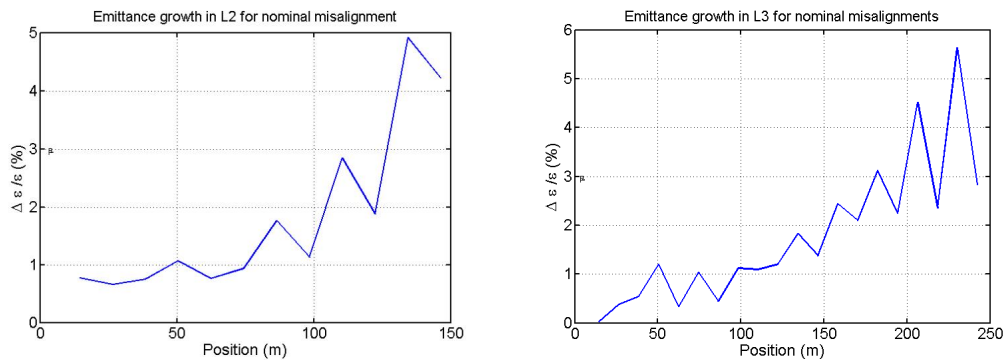


Figure 6.12.1: Relative emittance dilution in linacs L1 (left) and L2 (right) averaged over 40 seeds. All misalignments from Table 6.12.1 are applied.

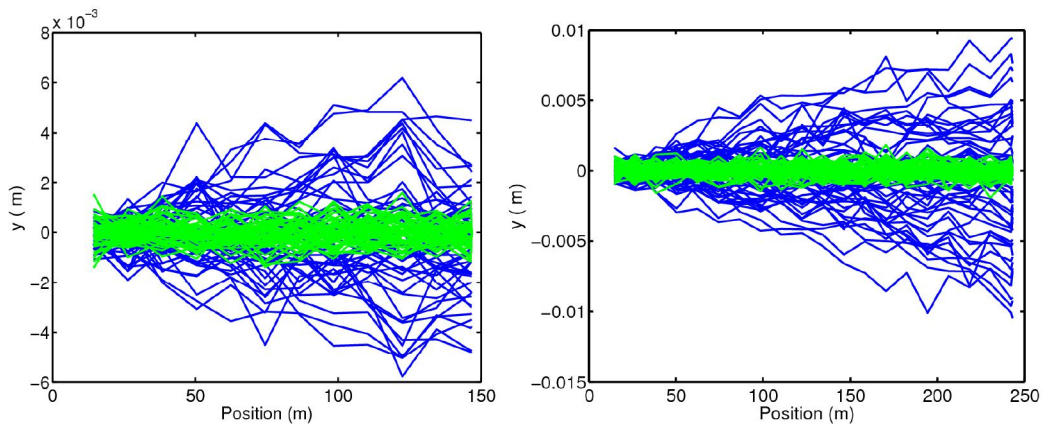


Figure 6.12.2: Beam trajectories before (blue) and after (green) 1-2-1 correction for 40 seeds in the L2 (left) and L3 (right) linacs.

6.12.2 Multi-Bunch Emittance Effects

The effect of the long-range transverse wakefield has been investigated for many different SCRF linacs, including the European XFEL [99]. In a CW linac, the primary limitation is cumulative beam breakup or transients arising during current or orbit changes. In XFEL studies, only trapped modes in the first three passbands (below the cutoff frequency) were considered. Results from these studies, scaled to LCLS-II parameters, show that the expected multibunch emittance effects are small. The cut-off frequency of the TESLA 9-cell cavity beam pipe is about 2.2 GHz, but some higher frequency modes may be also trapped by the periodic structure of the cryomodules or by detuned cells within a cavity. A conservative model, developed for the ILC and Project-X [100-102], has been applied to estimate the maximum transverse effect of the HOMs above cutoff frequency.

The transverse HOM frequencies and the effective impedances $(R/Q)_t$ of the TESLA 9-cell cavity are calculated using the SuperLANS code. Figure 6.12.3 shows the spectrum of the dipole modes. The transverse impedance dependence on the mode frequency can be approximated by an exponential function $(R/Q)_t$ [$k\Omega/m^2$]= $23 \exp(-0.27 f[\text{GHz}])$. The dipole mode density increases approximately linearly with the slope parameter of about 13 modes/(GHz)².

Because propagating modes can be trapped by detuned cavities or the by the bi-periodic structure of a cryomodule, modes up to 9 GHz are considered. Separation between frequencies of dipole HOMs is significant compared to the distance between two adjacent lines in the beam spectrum. Thus, each line of the beam spectrum can interact with only one dipole HOM. The $(R/Q)_t$ of the propagating modes depends on the location of the standing wave, which is evaluated by simulation of cavities with varying beam pipe lengths. In practice, only one dipole mode can be effectively trapped at a time, which means one can safely use 275 $k\Omega/m^2$ (see Figure 6.12.3) as the upper limit for the impedance of the trapped mode. The impedance of other dipole modes is much smaller and their effect on the transverse motion of the beam can be neglected.

To model the LCLS-II, it is assumed that the transverse and longitudinal motions are uncoupled and the monopole HOMs are not simulated when calculating the transverse effects. The LCLS-II beam is represented by a continuous train of electron bunches separated by 1 μs . The bunch charge is 100 pC (this is one-third of the maximum design current), and the cavities' axes are randomly misaligned with a standard deviation of 0.5 mm. The HOM frequency spread is 1 MHz, with an effective impedance of 275 $k\Omega/m^2$ and a quality factor of 10^7 .

In simulations of the transient effects, 10,000 bunches (10 ms of beam) enter the linac with identical energy and position. The HOMs are excited by the first bunch passage. The HOM frequencies are assumed to have a normal distribution. In the simulations, 1,000 seeds were run for the L2 and L3 linacs. The simulations include 2.5% rms errors on bunch charge and 0.5 degree (1.3 GHz) rms errors on the bunch timing.

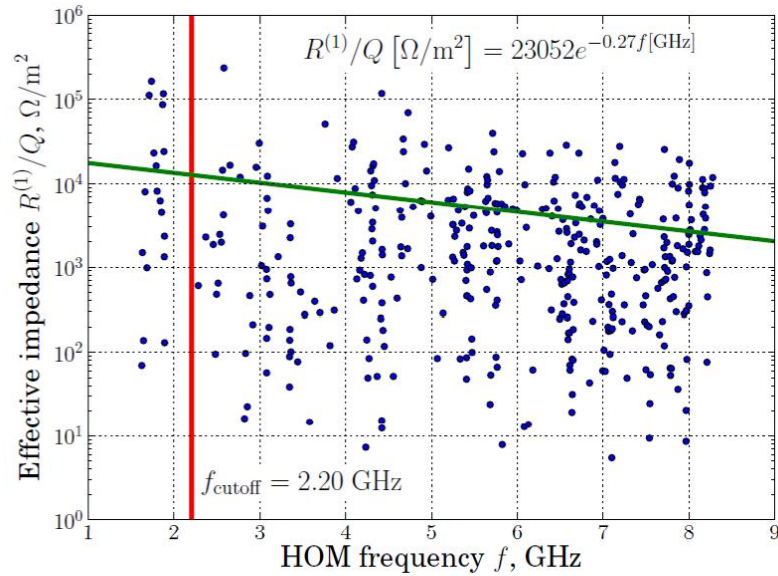


Figure 6.12.3: Spectrum of dipole HOMs in a TESLA 9-cell cavity below ~8 GHz. The green line shows approximation of data with exponential function. The vertical red line shows location of beam pipe cut-off frequency.

The centroids of the 10,000 bunches at the exit of the L2 linac are shown in Figure 6.12.4. For reference, the beam size is about $50 \mu\text{m}$. For a typical value of HOM frequency spread of about 1 MHz, the maximum trajectory deviation never exceeds $250 \mu\text{m}$; the maximum emittance growth, simulated over the phase space distribution of the bunches at the end of the linac, is smaller than 0.01 mm-mrad, with an average value of approximately 10^{-5} mm-mrad. The transient damps away rapidly, and the additional noise due to the fluctuations in the bunch charge and the timing have minimal impact.

In conclusion, the resonant excitation of the dipole HOMs seems not to be an issue for the LCLS-II transverse beam dynamics; and the loaded Q could be relaxed to values of 10^6 or possibly even 10^7 , although the latter needs more study with simulation of higher beam currents. Furthermore, if some HOMs trapped inside a cavity do not couple well to the HOM loads and have Qs higher than 10^7 , the frequency of those modes may be easily detuned by approximately 100-500 Hz to escape the resonance condition with the beam spectral line by detuning the cavity and then retuning it to the correct operating frequency [102]; this tuning and retuning process leaves small deformations that shift the HOM spectrum, and the effect of the deleterious modes will not be larger than in the simulated cases.

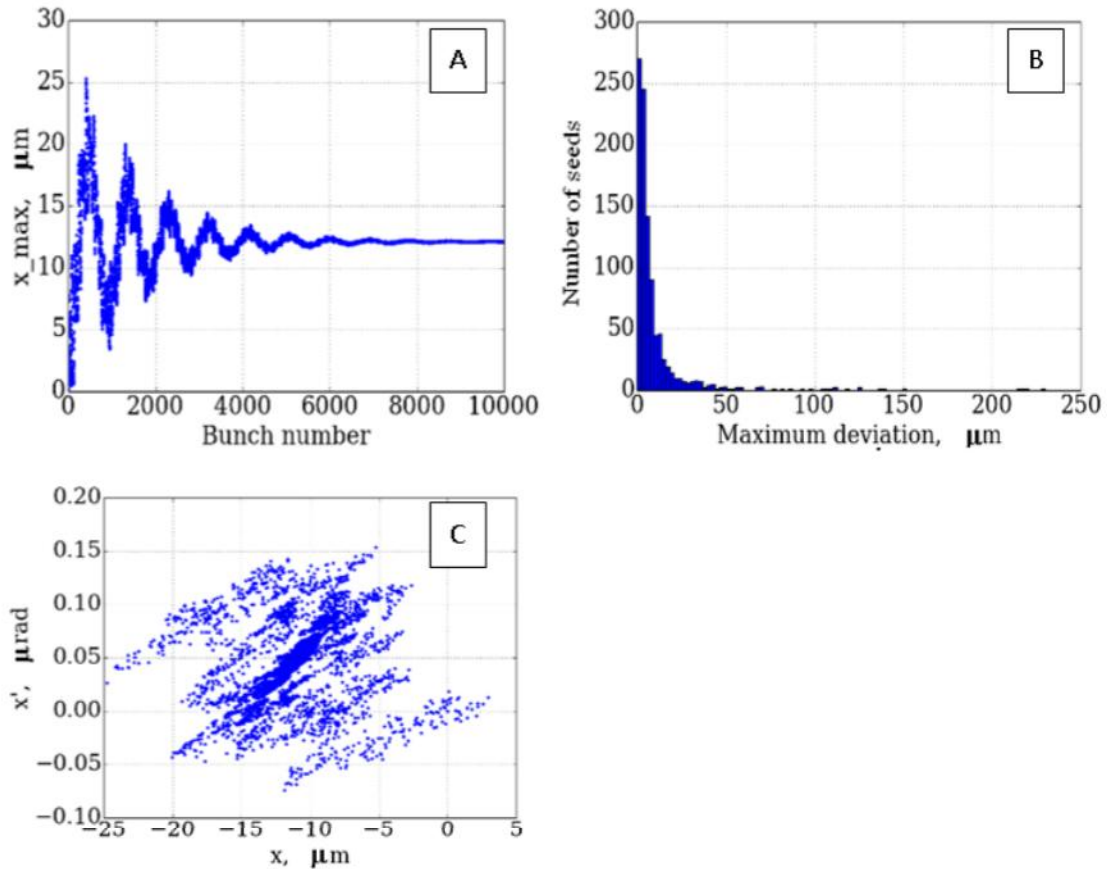


Figure 6.12.4. A) Maximal trajectory deviation for each bunch in one seed (L2 linac). B) Distribution of maximum deviation for 1,000 seeds. C) Phase space distribution of the centroids of all bunches at the end of the L2 linac; the rms beam size is about 50 μm and the divergence is about 0.5 μrad .

6.12.3 HOM Heating Effects

The LCLS-II beam will excite a broad spectrum of monopole HOMs up to THz frequencies. The dipole modes are all lower power than the monopole modes due to the relatively small cavity misalignments. The cut-off frequency of the TESLA 9-cell cavity beam pipe is ~ 3 GHz, but the periodic structure of the cryomodule may trap some higher frequency modes. A conservative model, developed for the ILC and Project-X [100-102], has been applied to estimate the maximum effect of the heating due to both the trapped and the propagating modes.

If a trapped HOM with a high-loaded quality factor, Q_L , is excited close to its resonance frequency, it may absorb significant power. To estimate the effect, the monopole HOM spectrum for the TESLA 9-cell cavity with HOM couplers and absorbers is first calculated using the SuperLANS RF simulation code. The worst trapping conditions for the propagating HOMs, when the (R/Q) values are at their maximum, are found by varying the distance between cavities in our model.

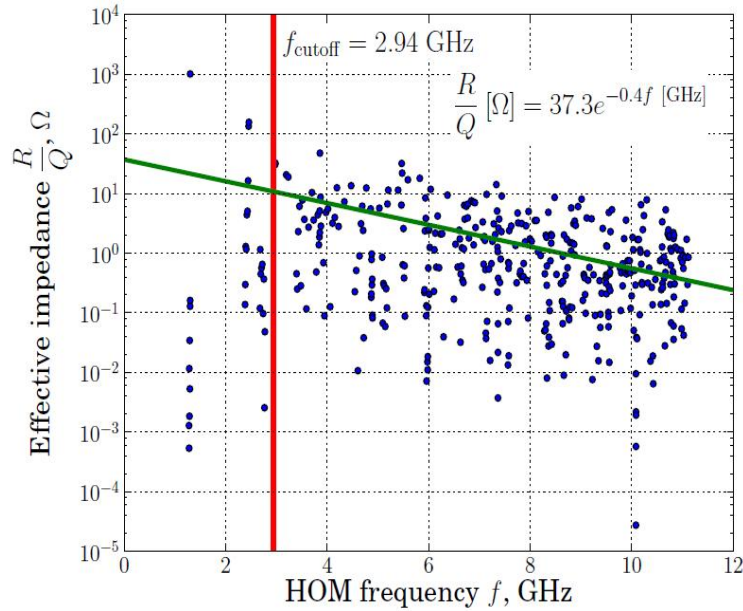


Figure 6.12.5: Spectrum of monopole HOMs of Tesla-type 9-cell cavity. The green line shows approximation of data with exponential function. The vertical red line shows location of beam pipe cut-off frequency.

Figure 6.12.5 shows the effective impedance of all monopole modes below 11 GHz. The red line separates trapped modes (below cutoff frequency) and propagating modes (above cutoff frequency). However, the propagating modes can also be effectively trapped in the cryomodule with multiple cavities due to reflections from neighboring cavities or some detuned cells inside a cavity. To be conservative, it is assumed that all modes below 11 GHz are trapped and have the worst possible (R/Q).

To estimate the heating effect, statistics for 10^4 cavities were simulated with random cavity-to-cavity variations of the HOM frequencies due to fabrication errors, with an rms distribution of $\sigma_f \sim 1 \text{ MHz}$. This sort of variation is similar to that measured in the cavities fabricated thus far. A histogram of the power loss is plotted in Figure 6.12.6, assuming a $Q_L=10^7$. The mean power loss is approximately 0.1 mW per cavity but, due to the random variations, a single HOM in one cavity may come close to resonance, and the power loss may increase up to a maximum of 100 mW. Such a heat loss will be an insignificant addition to the dynamic losses arising from the cavity voltage. Although this model is relatively conservative, it assumes an idealized beam current without time and charge jitter; these effects should be evaluated in the future.

Finally, due to the very short longitudinal bunch size, the LCLS-II beam current spectrum extends into THz range. This means that some sizable fraction of EM energy radiated by bunches is radiated into modes that are above the cut-off frequency and are not trapped. The RF cavities have irises with a radius of 3.5 cm, and the three sequences of cryomodules (for L1, L2, L3) have transitions to 1 cm (radius) pipes at both ends. The two main sources of bunch-induced radiation are these transitions and the irises of the RF cavities themselves (the main source). The optical model of wakefields is used to estimate the power radiated due to the end transitions and the

periodic diffraction model for the steady-state power loss in the cryomodules. For very short bunches, the optical model depends on bunch length as σ_z^{-1} , whereas the periodic diffraction model depends weakly on bunch length, if the bunch is sufficiently short. We assume 1.2 MW of beam power, with charge $q_b = 0.3$ nC and repetition rate of 1 MHz. The rms bunch length $\sigma_z = 1,000, 270, 25$ μm in, respectively, L1, L2 and L3.

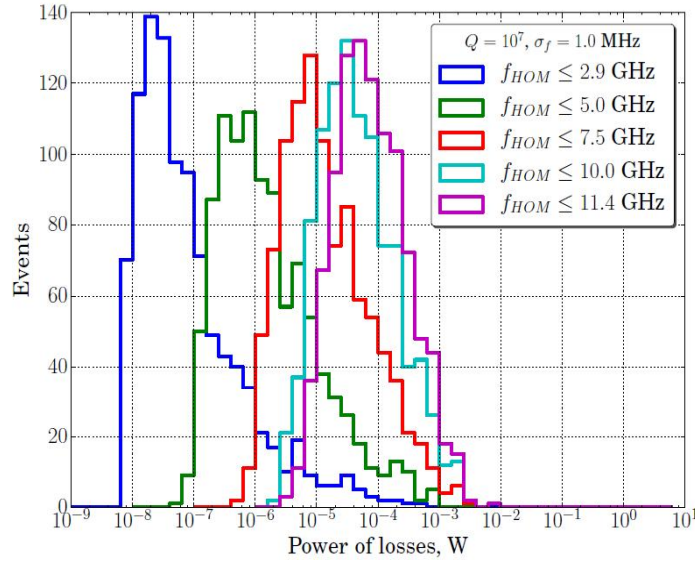


Figure 6.12.6: Distribution of power loss due to resonance excitation of HOMs with the mode frequency spread of 1 MHz and quality factor $Q_L = 10^7$.

The average voltage loss per unit charge of a short Gaussian bunch passing through a step-out transition, going from a beam pipe of radius a to radius b (where b is greater than a) is given by the loss factor [104]

$$\kappa = \frac{Z_0 c}{2\pi^{3/2} \sigma_z} \ln \frac{b}{a}$$

where $Z_0 = 377$ W, c is the speed of light, and σ_z is the rms bunch length. For a step-out transition, half of the beam loss ($\kappa/2$) goes into generating the primary beam field, and half ($\kappa/2$) is radiated away. However, for a step-in transition (in which the beam moves from a larger to a smaller pipe), the beam *gain* ($\kappa/2$) in eliminating primary beam field equals the amount radiated away ($\kappa/2$), and the voltage change of the beam itself is near zero [105]. Thus, the sum of the average radiated power loss due to the transitions at both ends is given by $\kappa q_b^2 f_{\text{rep}}$. For the transition between a pipe of radius $a = 1$ cm to a cryomodule with cavity iris radii of $b = 3.5$ cm, it is estimated that 1, 4, and 46 W are radiated into the ends of the cryomodules of, respectively, L1, L2 and L3. The radiation diffracts into the ends of the cryomodules, transversally spreading as the square root of distance. It is estimated that the fields are radiated, respectively, into the first and last 1, 5 and 50 m of L1, L2 and L3.

The steady-state wake effect of the cryomodules depends weakly on bunch length. For sufficiently short bunches, the loss factor for a length L of any cylindrically symmetric, periodic structure of iris radius a is given by the asymptotic value

$$\kappa_{asym} = \frac{Z_0 c L}{2\pi a^2}.$$

A cryomodule comprises eight cavities, each with an active length of 1.036 m, and with an iris radius $a = 3.5$ cm. Using the asymptotic loss factor (taking $L = 8.3$ m), we find the asymptotic value of steady-state power radiated (per cryomodule) $P_{asym} = 11$ W. A more accurate calculation starts with the point charge wake of a cryomodule, which includes the effects of bellows and pipes between the cavities. The results can be approximated by the simple formula: $W(s) = 344e^{-\sqrt{s/s_0}}$ [V/(pC*cryomodule)], where $s_0 = 1.74$ mm [93]. The loss factor for a Gaussian bunch is given by

$$\kappa = \frac{1}{2\sqrt{\pi}\sigma_z} \int_0^{\infty} W(s) e^{-\frac{s}{4\sigma_z^2}} ds.$$

Using this formula, we find that 7.7, 10.7, and 13.8 W are deposited per cryomodule of, respectively, L1, L2 and L3.

These are steady-state results. When the beam enters the first cryomodule in a string, there will be transients that are different from the results given here. The catch-up distance to steady state can be approximated by $z_{cu} = a^2/2\sigma_z$, which here gives 0.6, 2.3 and 25 m for, respectively, L1, L2 and L3. As long as z_{cu} is small compared to the length of a sequence of cryomodules — which is the case here for all three linacs — the steady-state results can be taken as a good approximation of the cryomodule wake effect.

We conclude that power loss into high frequency HOMs is not significant for the LCLS-II CW linac.

6.13 Commissioning

This section covers linac sub-system acceptance testing, as foreseen prior to installation; tests done during installation; and final full-system commissioning prior to the start of beam operation. Critical subsystems include:

- (1) accelerator SRF cryomodules;
- (2) cryogenic systems (including cryoplant, cryogen distribution and controls);
- (3) high-level RF systems (including power supplies, RF sources and RF distribution systems);
- (4) instrumentation and control (including LLRF controls, beam instrumentation, and cryomodule integrated equipment, such as motors, cryogenics, RF cabling, and internal thermometry);
- (5) magnet power supplies; and

- (6) safety subsystems (including beam-shutoff, radiation monitoring, and cryogenic safety). Supporting utility subsystems include (among other items) water cooling, support adjustment, vacuum inter-connect, cabling, and handling. Safety and utility systems are covered in Chapters 15 and 16, respectively.

All SRF cryomodules are assumed to have been tested at a partner lab that have test-bunkers as well as assembly tooling and related infrastructure. In a practical schedule, if all initial production cryomodules work well, testing at partner labs may be reduced in scope. Thus, the first time a given cryomodule would be fully tested is after it has been installed in the SLAC accelerator enclosure. As a precaution following cryomodule (or cavity) handling and transport, the cavity mode-spectrum is measured with a network analyzer using the cavity field probe and compared with reference data. This is a straightforward measurement and can be done with the cavity either warm (at ambient temperature) or cold (at nominal operating temperature). The cavity mode-spectrum measurement provides an indication of its mechanical integrity and will show micron-level distortions or changes in the cavity shape. Additional checks will include vacuum integrity and shock-sensor recordings.

The goal of the cryomodule test is to show it can achieve the nominal gradient of 16 MV/m, with some margin, and that it has cryogenic losses that are as at least as low as those expected at that gradient. Critical RF control connections are also tested (including cavity RF, cavity resonance, and coupler adjustment and protection); all other internal instrumentation (such as thermometry) and an initial estimate of microphonics (or noise) spectrum is made. High power coupler processing, often a critical-path part of pulsed linac cryomodule commissioning, is not needed for the CW linac.

Assuming the SLAC infrastructure is qualified and prepared to accept cryomodules and that appropriate installation-activity schedule conflicts are properly resolved, lessons learned and know-how at other labs should be used to guide commissioning plans. Experience at JLab and SNS, where the cryogenic system connection to and from each cryomodule can be directly engaged or disengaged using “U-tube” bayonets, shows that full cool-down of a single cryomodule can be done in three to four days. Larger multi-cryomodule systems, such as the five-cryomodule system at DESY (TTF2/FLASH), have been cooled down at a similar rate [106]. Cavity-by-cavity gradient and cryogenic-loss or Q_0 measurements can be done once nominal operating temperature has been reached and subsequent hardware checks have been completed. Experience with the CEBAF upgrade show that measurements (four days) and full 8-cavity operational tests (two days) are expected to take about 20 eight-hour shifts.

Installation, testing and commissioning of the cryogenic plant and distribution system are covered in section 6.7.

The high-power RF system will be tested and qualified in three separate steps: (1) power supply testing using a resistive load; (2) RF source (klystron or solid-state amplifier) testing in a test lab using a microwave load; and (3) waveguide component and sub-assembly testing using a set of testing fixtures. For the latter test, it is important to check active component performance

(phase-shifters that will be used to match waveguide path lengths to the inter-cavity spacing); passive component performance (circulator and loads); and flange connection quality. Depending on the waveguide distribution configuration and the availability of space for maneuvering the cryomodule during installation, tested waveguide sub-assemblies may be pre-mounted on the cryomodule prior to installation.

Cryogenic linac instrumentation and control includes low-level RF (LLRF), beam instrumentation, and cryomodule integrated equipment (motors, cryogenics, RF cabling, and thermometry). The latter is quite inaccessible since it lies entirely within the cryostat; therefore, the motor control system used for cavity tuning (including the low-temperature, high-reliability stepping motor and associated pair of piezo-electric transducer stacks) is one of the most sensitive cryomodule subsystems, and full tests of this system must be an integral part of cryomodule production at partner labs. Throughout the development of the TESLA/ILC cryomodule design, this subsystem has been flagged as not providing the needed reliability performance. Most of the failures, however, can be traced to “operational” or “initial alignment” procedural errors. As a result, we expect improved performance with the present design, which includes lessons learned from these failures.

6.14 References

- [1] H. Padamsee, “RF Superconductivity: Science, Technology, and Applications,” Wiley, Weinheim (Germany), 2009.
- [2] M. Liepe, J. Knobloch, “Superconducting RF for energy-recovery linacs, Nuclear Instruments and Methods in Physics Research,” A 557 (2006) 354–369.
- [3] J. Sekutowicz, et al., "CW and LP Operation Test of XFEL-Like Cryomodule," *Proc. Int. Part. Accel. Conf. 2012*, New Orleans, Louisiana (2012), pp. 2215-2217, <http://accelconf.web.cern.ch/AccelConf/IPAC2012/papers/weppc006.pdf>.
- [4] J. K. Sekutowicz, "Components for CW and LP Operation of the XFEL Linac," *Proc. Int. Part. Accel. Conf. 2013*, Shanghai, China (2013), pp. 1164-1166, <http://accelconf.web.cern.ch/AccelConf/IPAC2013/papers/tupea003.pdf>.
- [5] O. Kugeler, J. Knobloch, and J. M. Vogt, "Pathway to a Post Processing Increase in Q0 of SRF Cavities," *Proc. Int. Part. Accel. Conf. 2013*, Shanghai, China (2013), pp. 3129-3131, <http://accelconf.web.cern.ch/AccelConf/IPAC2013/papers/thobb201.pdf>.
- [6] K. Umemori, et al., "Construction of cERL Cryomodules for Injector and Main Linac," *Proc. Int. Part. Accel. Conf. 2013*, Shanghai, China (2013), pp. 2217-2219, <http://accelconf.web.cern.ch/AccelConf/SRF2011/papers/frioa06.pdf>.
- [7] C. Hovater, et al., "Commissioning and Operation of the CEBAF 100 MV Cryomodules," *Proc. Int. Part. Accel. Conf. 2012*, New Orleans, Louisiana (2012), pp. 2432-2434, <http://accelconf.web.cern.ch/AccelConf/IPAC2012/papers/weppc093.pdf>.
- [8] M. A. Drury and e. al., "CEBAF Upgrade: Cryomodule Performance and Lessons Learned," *Proc. SRF 2013 Conf*, Paris, France (2013), pp. THIOB01, <https://indico.in2p3.fr/getFile.py/access?contribId=48&sessionId=22&resId=1&materialId=slides&confId=8939>.
- [9] A. Burrill, G. K. Davis, C. E. Reece, A. V. Reilly, and M. Stirbet, "SRF Cavity Performance Overview for the 12 GeV Upgrade," *Proc. Int. Part. Accel. Conf. 2012*, New Orleans, Louisiana (2012), pp. 2423-2425, <http://accelconf.web.cern.ch/AccelConf/IPAC2012/papers/weppc089.pdf>.

- [10] For example: T. Powers, "Program for Optimization of SRF Linac Construction and Operation Costs," *Proc. SRF 2013 Conf*, Paris, France (2013), pp. THIOA05, <https://indico.in2p3.fr/getFile.py/access?contribId=48&sessionId=22&resId=1&materialId=slides&confId=8939>.
- [11] A. Yamamoto, M. C. Ross, and N. J. Walker, Status of ILC, *Proc. XXVI Linear Accel. Conf.*, Tel Aviv, Israel (2012), pp. 787-791, <http://accelconf.web.cern.ch/AccelConf/LINAC2012/papers/th3a01.pdf>.
- [12] D. Reschke, "Infrastructure, Methods and Test Results for the Testing of 800 Series Cavities for the European XFEL," *Proc. SRF 2013 Conf*, Paris, France (2013), pp. THIOA01, http://ipnojacow.in2p3.fr/cgi-bin/editor.zipdownload?paper_id=THIOA01&wanted_file=THIOA01_TALK.PDF.
- [13] B. P. Xiao, C. E. Reece, and M. J. Kelley, *Physica C: Superconductivity* **490**, 26 (2013), <http://www.sciencedirect.com/science/article/pii/S0921453413001718>.
- [14] A. Grassellino, et al., *Superconductor Science and Technology* **26**, 102001 (2013), <http://stacks.iop.org/0953-2048/26/i=10/a=102001>.
- [15] P. Dhakal, et al., *Physical Review Special Topics - Accelerators and Beams* **16**, 042001 (2013), <http://link.aps.org/doi/10.1103/PhysRevSTAB.16.042001>.
- [16] A. Grassellino, "New Insights on the Physics of RF Surface Resistance and a Cure for the Medium Field Q-Slope," *Proc. SRF 2013 Conf*, Paris, France (2013), pp. TUIOA03, <https://indico.in2p3.fr/materialDisplay.py?contribId=20&sessionId=14&materialId=slides&confId=8939>.
- [17] J. M. Vogt, "High Q0 Research: The Dynamics of Flux Trapping in SC Niobium," *Proc. SRF 2013 Conf*, Paris, France (2013), pp. TUIOA02, <https://indico.in2p3.fr/getFile.py/access?contribId=19&sessionId=14&resId=1&materialId=slides&confId=8939>.
- [18] O. Kugeler, "Influence of Cooldown on Cavity Quality Factor," *Proc. SRF 2013 Conf*, Paris, France (2013), pp. TUIOA01, <https://indico.in2p3.fr/materialDisplay.py?contribId=19&sessionId=14&materialId=slides&confId=8939>.
- [19] A. Romanenko and A. Grassellino, *Appl. Phys. Lett.* **102**, 252603 (2013).
- [20] B. Aune et al, *Phys. Rev. ST Accel. Beams* **3**, 092001 (2000)
- [21] C. Benvenuti et al., *Physica C* **316** (1999) 153–188
- [22] M. Masuzawa, *Proc. SRF2013*, WEIOD02.
- [23] A.C. Crawford, private communication
- [24] N. Valles et al., "Record quality factor performance of the prototype Cornell ERL main linac cavity in the horizontal test cryomodule," SRF2013 Paris, MOP071.
- [25] M.K. Kelly, et al., in: *Proceedings of the 2003 Particle Accelerator Conference*, Portland, OR, 2003.
- [26] A. Neumann et al., *Phys. Rev. ST Accel. Beams* **13**, 082001 (2010)
- [27] G. Davis et al, "Microphonics Testing of the CEBAF Upgrade 7-Cell Cavity," PAC2001
- [28] J.R. Delayen, et al, "Microphonics and Lorentz Transfer Function Measurements on the SNS Cryomodules," SRF 2003
- [29] M. Liepe, "Experience with Microphonics," ERL 2005
- [30] G. Staats, et al., "Microphonics Measurements at ELBE," ERL 2007
- [31] A. Neumann, W. Anders, J. Knobloch, O. Kugeler, "Microphonics in CW TESLA cavities and their compensation with fast tuners," *Proceedings of SRF2007*, Peking Univ., Beijing, China
- [32] Yu. Pischalnikov, et al, "Tests of a Tuner for a 325 MHz Spoke Resonator," PAC2011
- [33] A. Neumann, et al., "CW Measurements of Cornell LLRF System at HoBiCaT," SRF 2011.

- [34] S. Belomestnykh, "Cornell LLRF Digital System," LLRF05
- [35] D. Proch, "The TESLA cavity: design considerations and RF properties", Proc. of the Sixth Workshop on RF Superconductivity, CEBAF, Newport News, Virginia, USA, Oct. 4-8, 1993.
- [36] B. Aune et al., Phys. Rev. ST Accel. Beams 3 (2000) 092001.
- [37] A. Yamamoto et al., "Advances in superconducting RF technology for the ILC", Proc. of the 2012 Applied Superconductivity Conference, October 7-12, 2012, Portland, OR, USA.
- [38] The International Linear Collider Technical Design Report, SLAC-R-1004, ISBN 978-3-935702-77-5 (2013).
- [39] J. Sekutowicz, "HOM Couplers at DESY," International Workshop on HOM Damping in SC cavities, Cornell 2010.
- [40] C.E. Reece et al., "Optimization of the SRF cavity design for the CEBAF 12 GeV upgrade," Proc. of the 13th International Workshop on RF Superconductivity, October 14-19, 2007, Peking University, Beijing, China (2007).
- [41] A. Romanenko et al., Phys. Rev. Special Topics – Accel. And Beams 16, 012001 (2013).
- [42] P. Dhakal et al., Phys. Rev. Special Topics – Accel. And Beams 16, 042001 (2013).
- [43] A. Grassellino et al., Supercond. Sci. Technol. 26 (2013) 102001.
- [44] N. Valles et al., "Record Quality Factor Performance of the Prototype Cornell ERL Main Linac Cavity
- [45] J. Sekutowicz et al., "Cavities for JLAB's 12 GeV Upgrade," Proc. Of the 2003 Particle Accelerator Conference, (2003)p1395-1397.
- [46] Z. Li, C. Adolphsen, "A New SRF Cavity Shape with Minimized Surface Electric and Magnetic Fields for the ILC," LINAC08 (2008).
- [47] R.L. Geng, Physica C 441 (2006) 145-150.
- [48] P. Kneisel, Private communication (2013).
- [49] G. Ciovati et al., "America's overview of superconducting science and technology of ingot niobium," AIP Conf. Proc. 1352, 25-37 (2011); doi:10.1063/1.3579221.
- [50] W. Singer et al., "Advances in large grain resonators for the European XFEL," AIP Conf. Proc. 1352, 13-24 (2011); doi:10.1063/1.3579220; W. Singer et al., SRF2013.
- [51] W.-D. Moeller for the TESLA Collaboration, "High Power Coupler For The TESLA Test Facility", Proceedings of the 9th Workshop on the RF Superconductivity, 1999, Santa Fe, Vol.2, pp.577-581
- [52] Dohlus et al. "TESLA RF Power Coupler Thermal Calculations," Proc. of LINAC 2004, Lubeck
- [53] H. Hayano (ed.). S1-Global final report - 2012, <http://ilc.kek.jp/S1G/>
- [54] S. Posen, M. Liepe, "Measurement of the Mechanical Properties of Superconducting Cavities During Operation," 2012 International Particle Accelerator Conference, New Orleans, LA, USA (2012).
- [55] S. Posen and M. Liepe, "Mechanical optimization of superconducting cavities in continuous wave operation," Phys. Rev. ST Accel. Beams 15, 022002 (2012).
- [56] Nikolay Solyak, et al., "SRF Cavity Tuning for Low Beam Loading," SRF 2013, Paris, September 23-27, THP080.
- [57] "TESLA Design Report," Hamburg, DESY 2001-11, 2001.
- [58] V.S. Kashikhin *et al.*, "Design and Manufacturing Main Linac Superconducting Quadrupole for ILC at FERMILAB," *IEEE Transactions on Applied Superconductivity*, vol. 18, No. 2, June 2008, pp. 155-158.
- [59] V.S. Kashikhin, *et al.*, "Test results of a superconducting quadrupole model designed for linear accelerator applications," *IEEE Transactions on Applied Superconductivity*, vol. 19, Issue 3, Part 2, June 2009, pp. 1176-1182.

- [60] A. Koski, R. Bandelmann, S. Wolff, "Superconducting magnet package for the TESLA test facility," *IEEE Transactions on Magnetics*, vol. 32, No. 4, July 1996, pp. 2155-2158.
- [61] F. Toral *et al.*, "Design and fabrication study on the TESLA500 superconducting magnets," *IEEE Transactions on Applied Superconductivity*, vol. 12, No. 1, March 2002, pp. 282-286.
- [62] F. Toral, *et al.*, "Magnetization Effects on the Superconducting Combined Magnet Prototype for XFEL," *IEEE Transactions on Applied Superconductivity*, vol. 19, No. 3, June 2009, pp. 1136-1140.
- [63] C.M. Spencer, *et al.*, "Measuring the Magnetic Center Behavior and Field Quality of an ILC Superconducting Combined Quadrupole-Dipole Prototype," *IEEE Transactions on Applied Superconductivity*, vol. 20, Issue 3, May 2010, pp. 1964-1968.
- [64] V.S. Kashikhin, *et al.*, "Superconducting Magnets for SCRF Cryomodules at Front End of Linear Accelerators," Proceedings of IPAC'10, Kyoto, Japan, 2010, pp. 379-381.
- [65] G.V. Velev *et al.*, "A Fast Continuous Magnetic Field Measurement System Based on Digital Signal Processors," *IEEE Trans. of Applied Superconductivity*, Vol. 16, No. 2, June 2006, pp. 1374-1377.
- [66] F. Toral, *et al.*, "Final Design and Prototyping of the Superconducting Magnet Package for the Linear Accelerator of the European XFEL," *IEEE Transactions on Applied Superconductivity*, vol. 24, Issue 3, 2014, Article#: 4000706.
- [67] V.S. Kashikhin, *et al.*, "Superconducting Splittable Quadrupole Magnet for Linear accelerators," *IEEE Transactions on Applied Superconductivity*, vol. 22, Issue 3, Part 2, 2012, Article#: 4002904.
- [68] N. Andreev, *et al.*, "Conduction Cooling Test of a Splittable Quadrupole for ILC Cryomodules," *IEEE Transactions on Applied Superconductivity*, vol. 23, Issue 3, Part 2, 2013, Article#: 3500305.
- [69] R. Carcagno, *et al.*, "Magnetic and Thermal Performance of a Conduction-Cooled Splittable Quadrupole," *IEEE Transactions on Applied Superconductivity*, vol. 24, Issue 3, 2014, Article#: 4001604.
- [70] G. Simon *et al.*, "Status of the re-entrant cavity beam position monitor for the European XFEL project," BIW 2010, TUPSM038.
- [71] D.M. Treyer *et al.*, "Design and beam test results of button bpms for the European XFEL," IBIC 2013, WEPC21.
- [72] Y. Pischalnikov *et al.*, "Lorentz force compensation for long pulses in SRF cavities," IPAC 2012, New Orleans, USA.
- [73] A. Neumann *et al.*, "Analysis and active compensation of microphonics in continuous wave narrow-bandwidth superconducting cavities," *Phys Rev. Spec Topics- Accelerators and Beams*, #13, 82001 (2010)
- [74] C. Hovater *et al.*, "Commissioning and Operation of the CEBAF 100 MeV Cryomodules," IPAC 2012, New Orleans, USA.
- [75] L. Doolittle *et al.*, "Digital Low-Level RF Control Using Non-IQ Sampling," LINAC 2006 Knoxville, TN, USA.
- [76] J. Branlard *et al.*, "The European XFEL LLRF System," IPAC 2012, New Orleans, USA.
- [77] R. Bate *et al.*, "Commissioning of the ERLP SRF Systems at Daresbury Laboratory," proceedings of the 11th European Accelerator Conference (EPAC08), Genoa, Italy, June 23-27, 2008.
- [78] S. Sakanaka *et al.*, "Status of ERL and cERL Projects in Japan," proceedings of the XXV Linear Accelerator Conference, Tsukuba, Japan, September 12-17, 2010.
- [79] S. Fukuda *et al.*, "RF Source of Compact ERL in KEK," proceedings of the First International Particle Accelerator Conference (IPAC'10), Kyoto, Japan, May 23-28, 2010.
- [80] Christopher Nantista *et al.*, "Progress in L-Band Power Distribution System R&D at SLAC," proceedings of the XXIV Linear Accelerator Conference, Victoria, B.C., Canada. Sept. 29-Oct. 3, 2008.

- [81] D. Filippetto et al., “APEX Initial Commissioning Results,” Proceedings of the 34th International Free Electron Laser Conference (FEL2012), Nara, Japan, August 26-31, 2012
- [82] K. Flöttmann, T. Limberg, Ph. Piot, “Generation of Ultrashort Electron Bunches by Cancellation of Nonlinear Distortions in the Longitudinal Phase Space,” TESLA-FEL Report No. TESLA-FEL 2001-06, 2001.
- [83] The TESLA Test Facility FEL Team, “SASE at the TESLA Facility, Phase2,” June 2002 TESLA-FEL2002-01.
- [84] E. Vogel, et al, “Test and Commissioning of the Third Harmonic RF System for FLASH”, Proceedings of IPAC’10, THPD003, Kyoto, Japan (June 2010) <http://www.jacow.org>.
- [85] P. Pierini et al, “Status of the European XFEL 3.9 GHz System”, Proceedings of IPAC’12, WEPPC009, New Orleans, USA (July 2012) <http://www.jacow.org>.
- [86] Khabiboulline, et al, “New HOM Coupler Design for 3.9 GHz Superconducting Cavities at FNAL”, Proceedings of PAC 07, WEPMN098, Albuquerque, USA () <http://www.jacow.org>.
- [87] P. Piot et al., “Longitudinal Phase Space Manipulation in Energy Recovering Linac-Driven Free-Electron Lasers”, Phys. Rev. ST Accel. Beams 6, 030702 (2003).
- [88] R.J. England et al., “Sextupole Correction of the Longitudinal Transport of Relativistic Beam in Dispersionless Translating Sections”, PRST-AB 8 (2005).
- [89] D.R. Douglas and S.V. Benson, “Use of Incomplete Energy Recovery for the Energy Compression of Large Energy Spread Charged Particle Beams”, U.S. Patent Number 7,166,973 (January 23, 2007).
- [90] S. Thorin, “Bunch Compression by Linearising Achromats for the MAX IV Injector”, Proc. FEL2010, WEPB34, Malmo, Sweden (August 2010) <http://www.jacow.org>.
- [91] D. Douglas and C. Tennant, “Management of Synchrotron-Radiation-Driven Beam Quality Degradation During Recirculation Transport of High Brightness Electron Beams”, JLAB-TN-13-036, 19 July 2013.
- [92] A. Novokhatski et al, Single bunch energy spread in the TESLA cryomodule, Preprint TESLA 99-19, 1999
- [93] T. Weiland, I. Zagorodnov, The short-range transverse wake function for TESLA accelerating structure, TESLA 2003-19, 2003.
- [94] I. Zagorodnov et al., Wake Fields Generated by the LOLA-IV Structure and the 3rd Harmonic Section in TTF-II, TESLA Report 2004-1
- [95] F. Marhauser, P. Hülsman, H. Klein, “Trapped Modes in Tesla Cavities,” PAC 1999, New York, USA.
- [96] K. Kubo, PRST-AB 14, 014401 (2011)
- [97] XFEL TDR, chapter 4, http://xfel.desy.de/technical_information/tdr/tdr/
- [98] A. Chao, M. Tigner, *Handbook of Accelerator Physics and Engineering*
- [99] N. Baboi, *Multi-Bunch Beam Dynamics Studies for the European XFEL*, LINAC 2004, Lübeck.
- [100] A. Sukhanov, et al., “Resonance Excitation of Longitudinal High Order Modes in Project X Linac,” IPAC 2012, New Orleans, Louisiana, USA, May 20–25, 2012.
- [101] A. Vostrikov, et al., “High order modes in 650 MHz sections of the Project X linac,” Fermilab TD Note 2011-008.
- [102] A. Sukhanov, et al., “High Order Modes in Project-X Linac, HOMCS12, Daresbury,” UK, June 25–27, 2012, NIMA (in press) <http://www.sciencedirect.com/science/article/pii/S0168900213010796>.
- [103] T. Khabiboulline et al., *Experiments on HOM spectrum manipulation in a 1.3 GHz ILC SC cavity*, PAC 2011.
- [104] G. Stupakov et al, Phys.Rev.ST Accel.Beams 10 (2007) 054401.

- [105] S.A. Heifets and S. Kheifets, Rev.Mod.Phys. 63 (1991) 631—674.)
- [106] S.Barbanotti, et al, “Thermal and Structural Modeling of the TTF Cryomodule Cooldown and Comparison with Experimental Data”, Proceedings of EPAC 2008, Genoa, IT, <http://accelconf.web.cern.ch/AccelConf/e08/papers/wepd038.pdf>.

7

ELECTRON COMPRESSION AND TRANSPORT

TECHNICAL SYNOPSIS

The LCLS-II linac is designed to accelerate electron bunches produced in the high-brightness injector up to 4 GeV and then transport these bunches to one of two FEL undulators located more than 2 km downstream of the end of the LCLS-II linac. The high bunch repetition rate (up to 1 MHz) requires a Continuous Wave (CW) superconducting linac located in the first few sectors of the existing SLAC linac enclosure. An electron bypass line (mostly existing) suspended from the ceiling of the linac is used to transport the 4-GeV beam to the switchyard just beyond sector 30, where a fast kicker or RF deflector is used to distribute bunches to each parallel FEL. This bypass line allows the LCLS-I linac, located in sectors 21-30, to remain fully operational allowing the old 120-Hz copper linac to feed the new HXR undulator as well.

In addition to acceleration, the bunch must be compressed in length to amplify the peak current to about 1 kA, and the energy chirp must be removed for best FEL performance. This is accomplished, as in LCLS-I, by two-stages of magnetic compression using two four-dipole chicanes (BC1 and BC2), located along the linac at 250 MeV (BC1) and 1600 MeV (BC2); a third optional compressor following the linac may be included as well. The RF phases in the linac (1.3 GHz) are typically run off their accelerating crests in order to generate a linear energy correlation along the bunch (a chirp), and each chicane adds a path-length dependence on the relative energy. In this way the typical electron bunch is compressed from about 1 mm to 8 μm rms length, starting after the laser heater, for a net magnetic compression factor of about 85 (12 A after the injector compresses to 1000 A downstream of BC2). A third harmonic RF linearizer section (3.9 GHz) is also included in order to shape the final peak current profile. In addition to compression, the final energy chirp of the bunch needs to be cancelled, which is accomplished by using the longitudinal wakefield of the accelerating cavities, and even more effectively, the resistive-wall wakefield of the long (2.2 km) stainless steel bypass line following the linac.

Adjustable-gap collimators are included along the accelerator in order to remove beam halo and protect the undulator magnets from radiation damage. In addition, pulse-stealing electron diagnostic sections are located along the accelerator at key locations (e.g., after BC1) in order to continuously measure beam energy, energy spread, emittance, and bunch length using kicker magnets and transverse RF deflectors for time-resolved bunch measurements. These are accomplished at a low repetition rate (about 100 Hz) so that intercepting screens and wires can survive. Finally, this chapter also describes the electron transport to each of the two high-power beam dumps and their functionality in terms of beam diagnostics, although they are located well past the FEL undulators.

7.1 Introduction and Overview

The new superconducting linear accelerator is shown schematically in Figure 1. It includes a laser heater chicane (LH), 35 main cryomodules (CM), a 3.9-GHz harmonic linearizer RF section (HL), the first bunch compressor chicane (BC1), a second bunch compressor chicane (BC2), and the four main linac sections labeled L0, L1, L2, and L3. The number of 12-meter-long cryomodules (CM) in each main linac section is as follows: one in L0, two in L1, 12 in L2, and 20 in L3. Each of these CMs includes eight 9-cell cavities resonant at 1.3 GHz, while the 3.9 GHz HL section consists of three specialized CMs, each including four smaller 9-cell cavities. The average accelerating gradient over all powered main cavities is just under 16 MV/m, with about 6 percent of the cavities unpowered, maintained as reserves in each linac section. The 3.9-GHz HL section has a gradient of 14.5 MV/m with a maximum 60-MV on-crest accelerating voltage. Finally, the resistive-wall wakefield of the 2.2-km-long bypass line (LTU) in the linac tunnel removes the remnant energy chirp on the bunch, allowing the L3 linac section to run on crest phase ($\phi_3 = 0$).

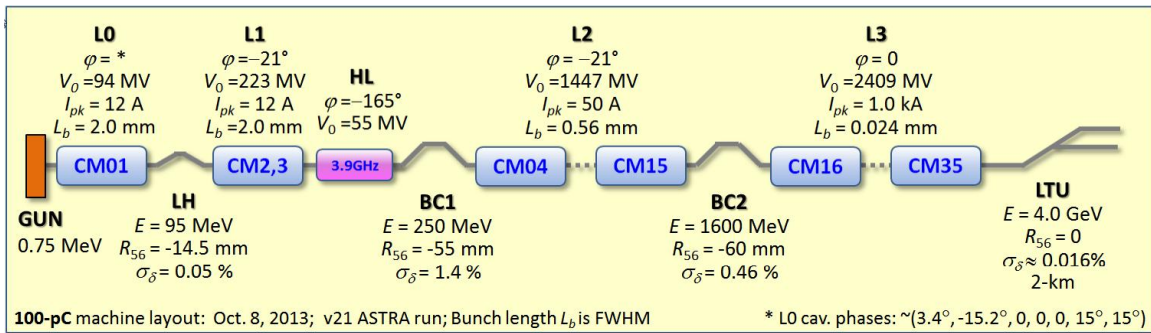


Figure 1. Schematic layout of the LCLS-II injector, linac, bunch compressors, and beam transport, with key parameters listed for CW operation with 100 pC per bunch.

7.2 Linac Lattice

The optical functions along the entire LCLS-II are shown in Figure 2, from the injector output at 95 MeV through the SXR undulator and final beam dump at 4 GeV. The focusing lattice along the main linac sections (L2 and L3) is set using cold quadrupole magnets at the end of each CM. Some warm quadrupole magnets are included around the bunch compressors in order to match the Twiss functions. The best linac focusing structure will be studied in detail, but an initial FODO lattice for the L2 linac section is shown in Figure 3 (30 deg per FODO cell) and for the L3 linac section in Figure 4 (15 deg per FODO cell), each designed using the computer code *MAD* [1] and *Elegant* for particle tracking [2]. With weak transverse wakefields and a short bunch length in the L2 and L3 linac sections the focusing lattice can be quite weak, therefore also minimizing chromatic effects and loosening alignment tolerances and dispersion errors. The effects of coherent synchrotron radiation will also be minimized using careful phase advance selection for partial cancellation between bend systems and by creating small bend-plane beta functions at the exit of the bunch compressors.

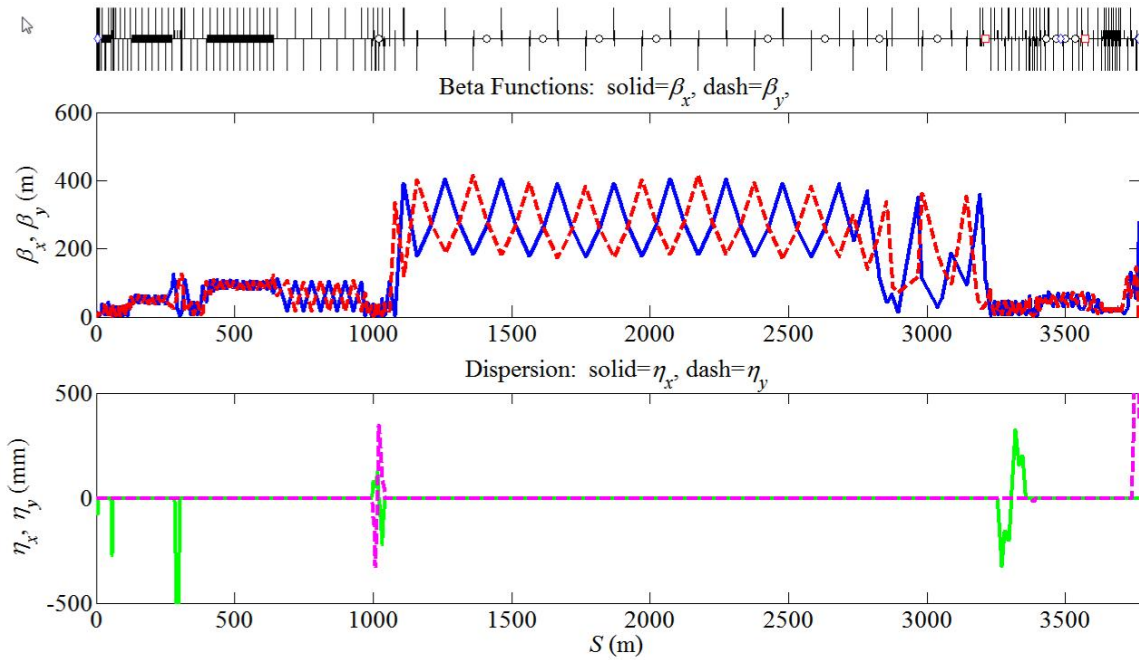


Figure 2. Beta and dispersion functions along the entire LCLS-II, from injector output at 95 MeV through the SXR undulator and final beam dump.

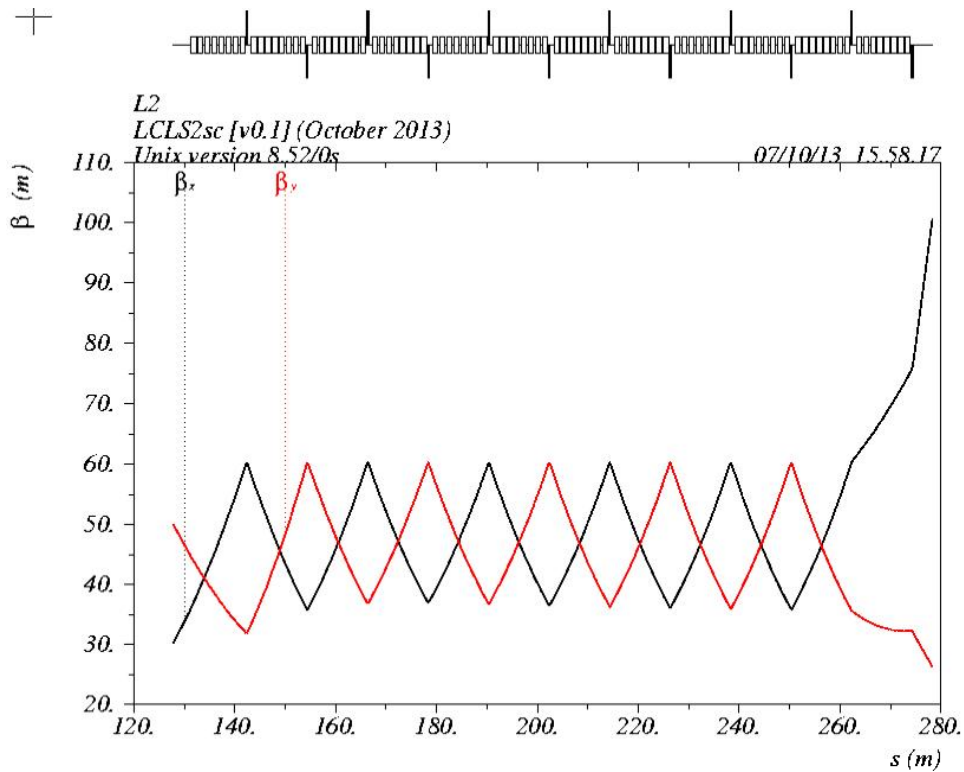


Figure 3. Beta functions along the L2 linac section from 250 MeV to 1.6 GeV (30 deg/cell).

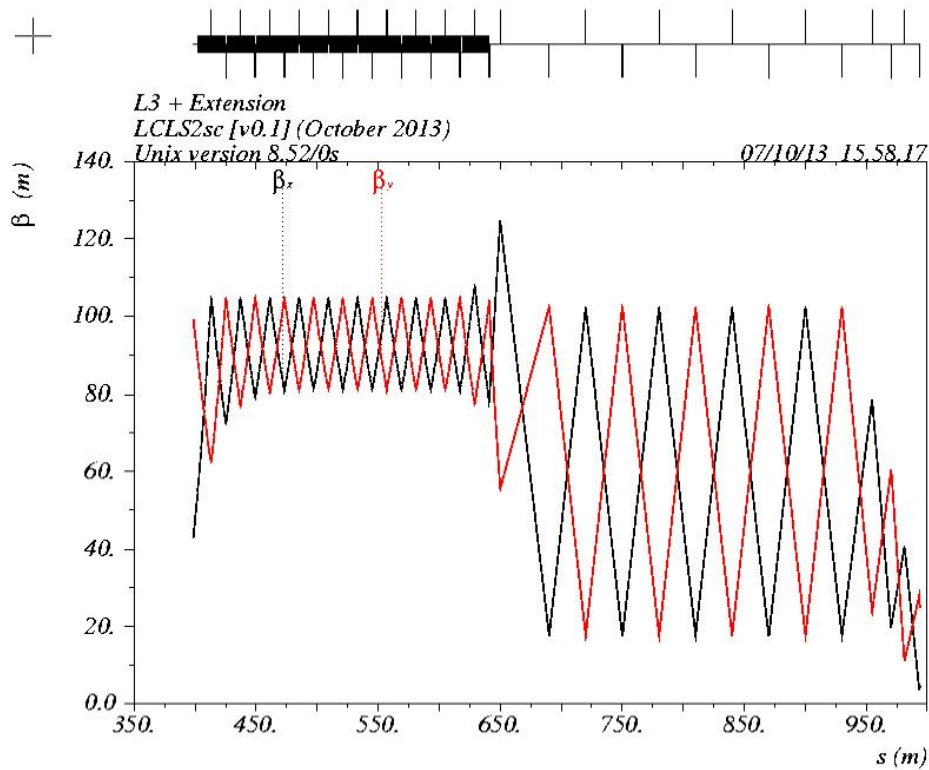


Figure 4. Beta functions along the L3 linac section from 1.6 GeV to 4 GeV (15 deg/cell), and out to the sector-10 extension at $s > 650$ m.

7.3 Alignment

The current linac alignment network is based on the linac light pipe laser alignment system, which needs to be removed in order to install the new superconducting linac. Before it is removed, the linac light pipe and the quadrupole magnets will be transferred to newly installed monuments. The tunnel in sectors 0-6 deforms by about 0.25-0.5mm per year. Periodic remapping of the alignment network will be necessary. Due to the limited space in the tunnel, conventional alignment techniques will be affected by refraction [3]. Under the assumption that the temperature of the wall and air are 1 degC different, the laser tracker is setup in the center of the aisle and a measurement is made to a wall monument 20-m down the tunnel, then the angle measurement is inaccurate by 15 μ rad (300 μ m over 20 m).

The cryomodules pose new challenges for alignment. The internal alignment of the individual components has to be performed before cool-down, without the option of checking the alignment afterwards. The DESY XFEL in Germany has developed a procedure for the fiducialization of cryomodules that should be studied closely. The fiducialization process for the newly designed cryomodules needs to be developed, with its implementation centrally managed by SLAC [4]. Beam-based alignment methods may also be applied.

A new reference network has to be implemented throughout the beam switch yard (BSY) as LCLS-I has only a partial system installed. Existing LCLS components will be used as tie-in points.

The existing alignment network is sufficient to support the installation of the new LTU components. It is expected that only a few monuments will have to be relocated should new components block the line of sight.

7.4 Laser Heater System

The function of the Laser Heater (LH) is to induce a controllable growth in the uncorrelated energy spread as a way to suppress the microbunching instability [5]. Its centerpiece is a short Permanent Magnet (PM) undulator positioned in the middle of a small magnetic chicane. The undulator enables the interaction between the electron beam and a co-propagating conventional laser pulse that results in a modulation of the electron beam energy. This modulation then turns into the desired uncorrelated energy spread as the beam exits the chicane and the electrons slip longitudinally with respect to one another because of their finite transverse emittance. The total uncorrelated beam energy spread is the sum in quadrature of the LH-induced contribution $\sigma_{E,LH}$ and the typically small natural spread acquired by the beam by the exit of the injector (on the order of ~ 1 keV rms).

An upper limit to the heating capacity required of the LH is set by the maximum allowable energy spread at the FEL, $\sigma_{E,FEL}$, and by the total magnetic compression factor, C_T [5]. For $Q = 100$ pC, we have $\sigma_{E,FEL} \simeq 500$ keV and $C_T \simeq 85$, implying that heating from the LH should not exceed about $\sigma_{E,FEL}/C_T \simeq 6$ keV. We believe this is sufficient to suppress the microbunching instability (see section 7.5.3), although further confirmation will be needed. To leave room for other modes of machine operation we set a $\sigma_{E,LH} = 20$ keV rms requirement for maximum heating capacity. This higher power level, if available, will also allow control of the FEL power, providing a straight forward way to suppress the FEL during commissioning and machine experiments.

The choice of $\lambda = 1030$ nm for the laser wavelength is primarily dictated by the availability of high-power, high-repetition rate sources (*e.g.*, Yb:glass fibers). Preliminary beam dynamics studies suggest that this choice should be satisfactory, but a more accurate assessment will be needed to ensure that the small but noticeable additional heating by the trickle effect [6] will not compromise the LH effectiveness. The effect would be reduced by a shorter laser wavelength.

The undulator period, $\lambda_u = 4.71$ cm, is set by the undulator resonance condition, the choice of PM technology, and by the minimum undulator gap requirement ($g_{min} = 3.0$ cm) at the upper end (100 MeV) of the beam energy range at the LH. In our analysis, we have assumed a model for the undulator peak magnetic field given by $B_0 = b \exp(-ag/\lambda_u)$, with $b = 2.08$ T and $a = 3.24$ [7], consistent at the few percent level with the field measurements of the undulator presently installed in the LCLS LH. A moderate number ($N_u = 10$) of undulator periods is selected in order to broaden the bandwidth of the undulator resonance to a few percentage points.

Under optimal operating conditions in which: 1) the electron beam and laser pulse have the same transverse rms sizes, $\sigma_x = \sigma_y = \sigma_r$, 2) the undulator resonance condition is exactly met,

and 3) diffraction effects are negligible, the laser-pulse peak power required to induce the desired energy spread is given by [5]

$$P_L = 4P_0 \left(\frac{\gamma \sigma_{E,LH} \sigma_x}{mc^2 [JJ] K L_u} \right)^2, \quad (1)$$

where $P_0 \simeq 8.7$ GW, γ is the relativistic factor, K the undulator parameter, $L_u = \lambda_u N_u$ the undulator length, and $[JJ] = J_0[\xi] - J_1[\xi]$ with $\xi = K^2/(4 + 2K^2)$. If the laser spot size is set to twice the electron size to accommodate jitter and drift effects, the required laser power will double.

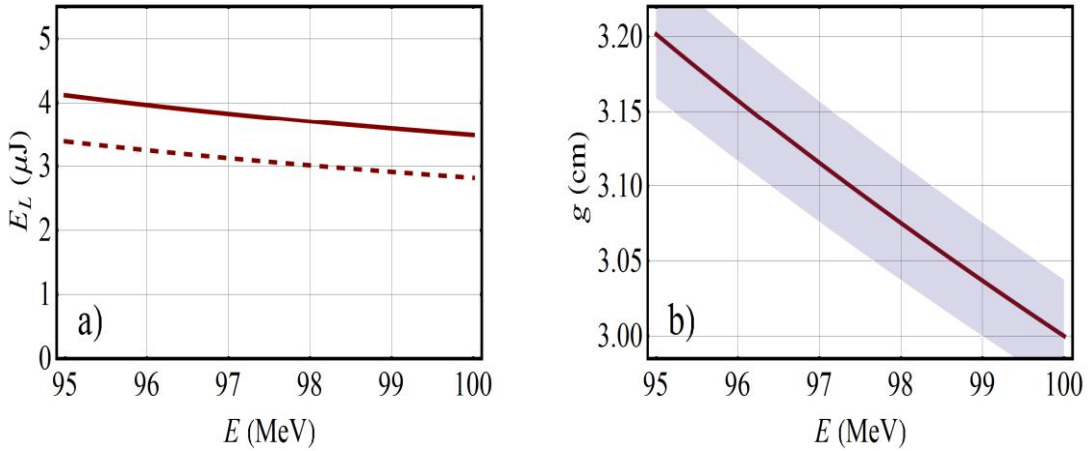


Figure 5. *Left:* Laser pulse energy needed to heat the beam by $\sigma_{E,LH} = 20$ keV rms as a function of the beam energy. The dashed line is from Equation (1), while the more accurate solid line includes an approximate account of the diffraction losses. *Right:* The adjustable undulator gap meeting the undulator resonance condition. The shaded width shows the limits where the induced energy spread is reduced by 15% with respect to the resonance bandwidth.

A plot of the laser pulse energy, inducing $\sigma_{E,LH} = 20$ keV rms heating over a beam energy range about the nominal 98 MeV, as determined by Equation (1) is shown in Figure 5 (*left*, dashed line). The solid line includes an approximate account of the loss of efficiency due to diffraction effects (which is non-negligible, as the Rayleigh range is shorter than the undulator length). At the nominal $E = 98$ MeV, the laser pulse energy is about $4 \mu\text{J}$. Allowing for the laser spot size to be twice the beam size sets the requirement for the laser pulse energy to about $E_L = 8 \mu\text{J}$. The laser pulse energy is calculated for a Gaussian shape of 20 ps FWHM length, a value about three times the 7 ps FWHM length of the baseline electron beam, adequate to insure heating uniformity along the bunch and possibly accommodate longer bunches if needed. Figure 5 (*right*) shows the gap adjustment necessary to maintain the undulator resonance over the beam energy range.

Table 1. Laser heater parameters.

Parameter	Symbol	Value	Unit
Electron beam energy	E	98	MeV
Betatron functions at LH undulator center	$\beta_x = \beta_y$	10	m
Horizontal Twiss function (exit of LH chicane)	α_x	-0.18	-
Normalized transverse emittance used in these LH calculations	$\varepsilon_{nx} = \varepsilon_{ny}$	0.3	μm
Electron beam transverse rms sizes (at LH undulator center)	$\sigma_x = \sigma_y$	125	μm
Chicane dipoles bend angle	$ \theta_B $	0.102	rad
Chicane dipoles lengths	L_B	0.124	m
Drift from 1 st -to-2 nd and 3 rd -to- 4 th dipole	ΔL_1	0.603	m
Dispersion (at undulator)	$ D_u $	7.5	cm
Horizontal offset of undulator from linac axis	Δx	7.5	cm
Momentum compaction (over full chicane)	$ R_{56} $	14.5	mm
Undulator gap (minimum 3.0 cm)	g	3.1	cm
Undulator period	λ_u	4.71	cm
Undulator parameter	K	1.1	-
Undulator peak magnetic field	B_0	0.25	T
Number of undulator periods	N_u	10	-
Laser wavelength	λ	1030	nm
Laser pulse transverse rms size (middle of undulator)	σ_r	125	μm
Rayleigh length	Z_R	19	cm
Laser pulse length (FWHM)	T_L	20	ps
Beam rms-energy spread induced by Laser Heater (max.)	σ_E	20	keV
Laser pulse energy	E_L	8	μJ
Laser pulse peak power	P_L	0.18	MW

Beam heating, occurring at a point of non-zero dispersion, is accompanied by a relative transverse emittance growth. The effect, however, is small. At maximum heating, $\sigma_E = 20$ keV, the expected emittance growth is $\Delta\varepsilon_{nx}/\varepsilon_{nx} = \gamma_x D_u^2 \sigma_\delta^2 / 2 \varepsilon_x \approx 0.8\%$, where ε_x is the geometric rms emittance, $\gamma_x = (1 + \alpha_x^2)/\beta_x$ the Twiss function at the exit of the LH chicane, D_u the dispersion function at the undulator, and $\sigma_\delta = \sigma_{E,LH}/E$ the relative energy spread (a more complete formulation than that of Ref. [5], including the β -mismatch effect).

Finally, we should check the condition for the smearing of the energy modulation into an uncorrelated energy spread. This requires that the reduced laser wavelength $\lambda/2\pi = 0.16 \mu\text{m}$ be much smaller than the emittance-induced longitudinal slippage $|R_{52}|\sigma_{x'}$, where $\sigma_{x'}$ is the beam angular divergence and $R_{52} = -D_u$, the transfer matrix element from undulator to exit of the chicane. This condition is satisfied as $|R_{52}|\sigma_{x'} \approx D_u\sqrt{\varepsilon_x/\beta_x} \approx 0.9 \mu\text{m}$. The laser heater beta and dispersion functions are shown in Figure 6, and the parameters are listed in Table 1.

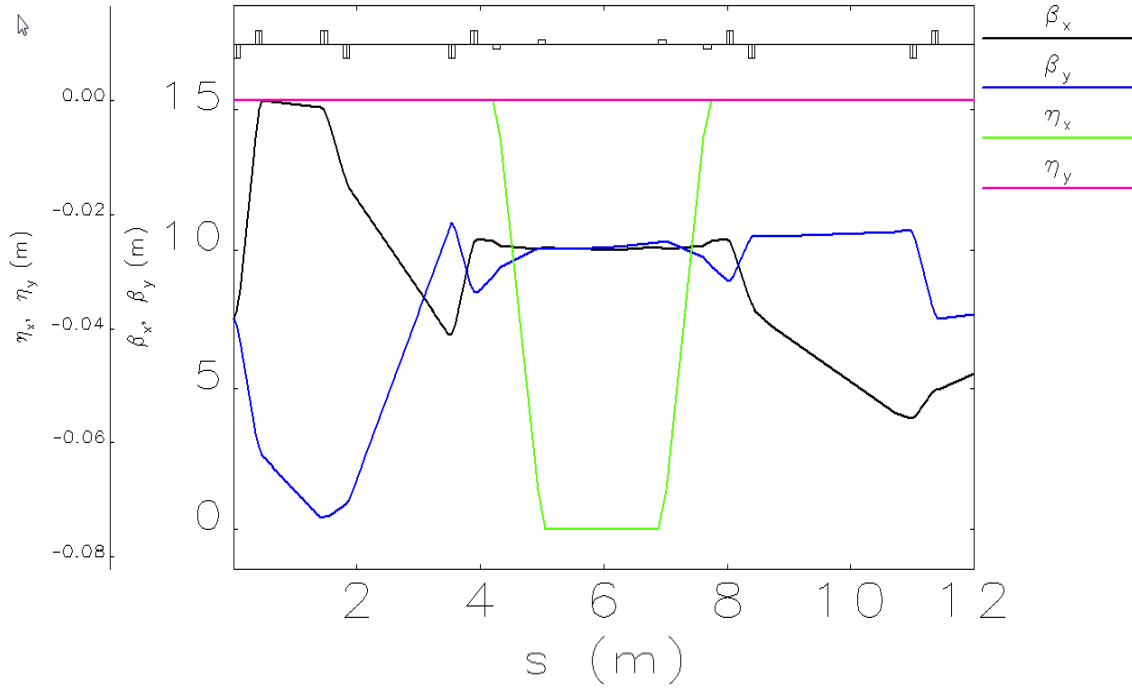


Figure 6. Beta and dispersion functions [2] along the laser heater section, from the exit of CM01 module to within a few meters of the L1-linac RF section. The undulator center is at $s \approx 6$ m. The chicane magnets are similar to the LCLS-I, but somewhat stronger.

7.5 Bunch Compression

In order to drive the FELs, the electrons must be accelerated and the bunch compressed in length to provide about 1 kA of peak current. Bunch compression scenarios have been designed and tested [8] for various FELs and typically require 1-3 bunch compressor chicanes and a linear energy chirp on the bunch induced by off-crest RF phasing. The compression design for the LCLS-II is not very different from LCLS-I, including two compressor chicanes, but also with a third chicane as an attractive option presently under study.

The choice of chicane locations are set by many issues. The first chicane (BC1) should be as close to the injector as possible, but at high enough energy so that space charge forces, magnified by the shorter bunch, do not degrade the beam brightness. As in LCLS-I, a location at 250 MeV is judicious, with the chicane located after the first three 1.3-GHz cryomodules, two of which are run off crest by about 21 degrees (for the nominal 100-pC configuration) to prepare for first stage compression. Note also that a 3rd-harmonic RF section (3.9-GHz) is included just before the BC1

chicane to remove the 2nd-order chirp curvature. Alternate methods for correcting the 2nd-order terms using sextupole magnets in the chicanes are also being investigated.

The second compressor stage (BC2) is located such that the remaining linear energy chirp (after compression) can be completely cancelled by the longitudinal wakefields of the RF accelerating cavities and the resistive-well wake of the long bypass line. This constraint suggests a BC2 location at about 1.6 GeV, following the 15th (of 33) 12-m long cryomodule (CM), where CM 4-15 are also phased off crest by 21 degrees for BC2 compression preparation.

Finally, a 3rd bunch compressor (BC3) is an attractive option as well, although not yet described in the sections to follow. Since the long bypass line has a strong resistive-wall wakefield, it is still possible to remove the linear energy chirp following a 3rd chicane at the end of the linac, but before the bypass line. Adding this final compression allows several clear advantages that are only qualitatively described here:

- The CSR degradation of the bend-plane emittance is greatly reduced since the bunch is longer with a weakened BC2 chicane ($|R_{56,2}| \sim 59 \text{ mm} \rightarrow 55 \text{ mm}$), while the BC3 itself is a very weak chicane ($|R_{56,3}| \sim 12 \text{ mm}$) since it only has to do the final small compression.
- The HOMs in the L3 linac sections will be reduced since the bunch length is about 3-times longer in all of L3 with a BC3 included.
- The CSR-induced vertical (and horizontal) emittance growth (see Ch. 10) of the pre-bypass rolled dog-leg bends is nearly eliminated since the bunch is 3-times longer in this series of rolled bends.

The bunch compressor scheme also incorporates velocity compression in the injector (a factor of about 3 at 100 pC). The magnetic chicane locations are shown in Figure 1, along with the necessary RF phase settings along each linac section.

Alternate bunch compression schemes are also being considered, for example using sextupole magnets for linearization, and/or using the dog-leg bends to refine the compression process, but the simplicity and robust design of 2-3 four-dipole chicanes with off-crest RF phasing, such as used at LCLS-I, FLASH, Fermi, SwissFEL, etc, is difficult to improve upon.

7.5.1 Parameters

Table 2 lists the bunch compression parameters, which are consistent with the parameters shown in Figure 1.

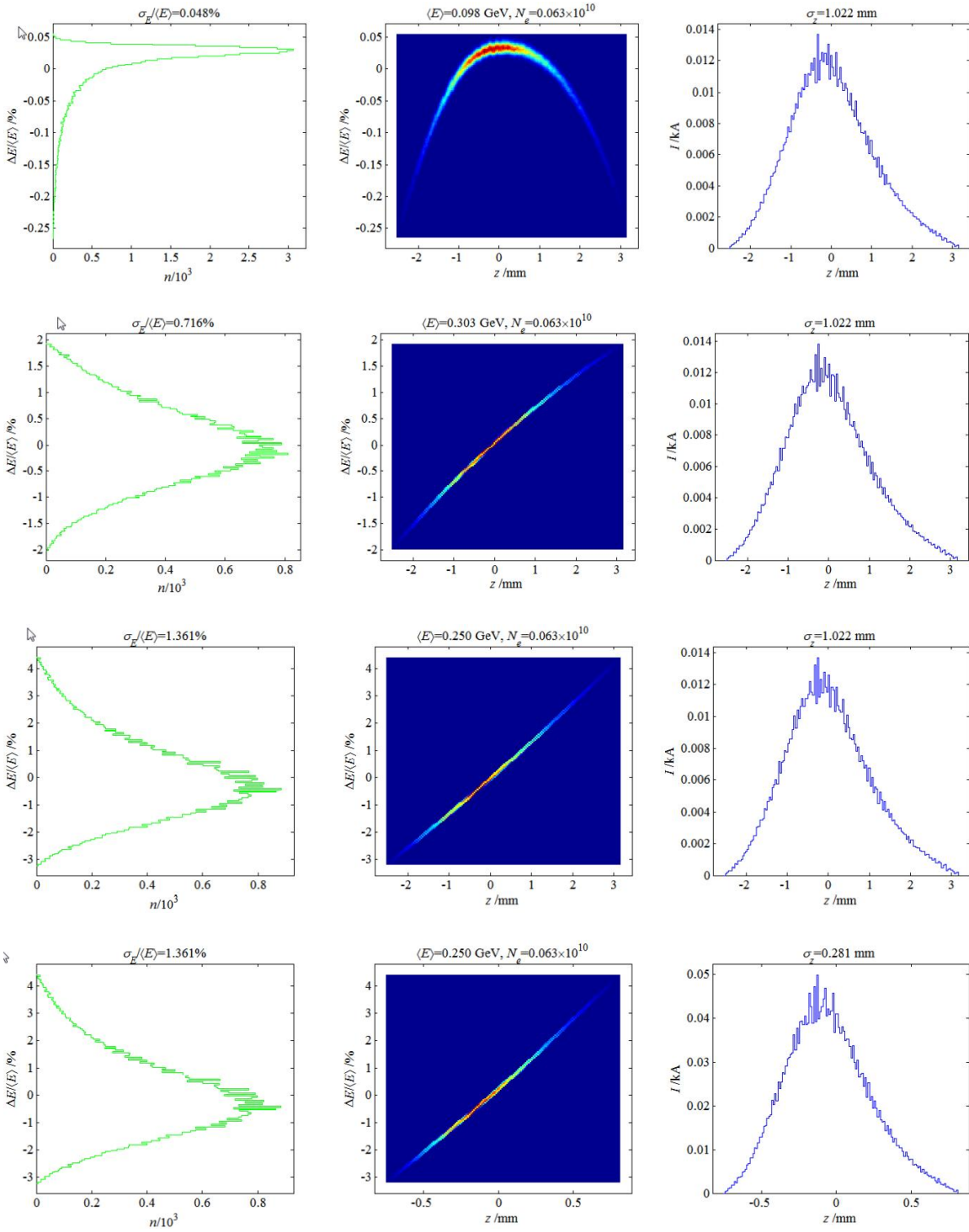
Table 2. List of bunch compression parameters used in the tracking of Figure 7. RF phase settings are defined at zero on crest, and negative values produce a lower energy at the bunch head.

Parameter	Symbol	Value	Unit
Initial electron energy (after CM01)	E_0	95	MeV
Electron energy at BC1	E_1	250	MeV
Electron energy at BC2	E_2	1600	MeV
Final electron energy	E_f	4.0	GeV
Laser heater rms energy spread addition (nominal)	σ_{E-LH}	6	keV
Momentum compaction of BC1	R_{56-1}	-55	mm
Momentum compaction of BC2	R_{56-2}	-60	mm
RF phase of L1 linac section	φ_1	-21	deg
RF phase of HL linac section (3.9 GHz linearizer)	φ_{HL}	-165	deg
RF phase of L2 linac section	φ_2	-21	deg
RF phase of L3 linac section	φ_3	0	deg
RF crest voltage of HL linac section (3.9 GHz linearizer)	V_{HL}	55	MV
Length of stainless steel bypass line	L_{byp}	2200	m
Inside radius of stainless steel bypass line tube	r_{byp}	24	mm

7.5.2 Longitudinal Tracking

The bunch compressor system is designed, optimized and verified using the code *LiTrack* [9], which tracks the bunch length coordinate, z ($= ct$) and the relative energy, $\Delta E/E$, of about 10^5 macro-particles through the linac and chicanes, including the sinusoidal RF curvature, chicane momentum compaction to third order, the longitudinal wakefields of both the 1.3 GHz and the 3.9 GHz RF sections, and the resistive-wall wakefield of the 2.2-km-long, 2-inch-diameter stainless steel bypass line. A simple 2D tracking code is adequate for this stage of the design since the longitudinal particle coordinates are typically not much affected by the transverse extension. In cases where this assumption breaks down we apply the 6D code *Elegant* [2].

The initial distribution is taken from an *Astra* [10] run from cathode to the end of CM01 at 95 MeV. Figure 7 on the next pages shows the longitudinal phase space and projected profiles (energy and time) at eight locations along the accelerator. The final energy is 4 GeV, and the compression result is slightly more than 1 kA peak current at 100 pC of charge per bunch.



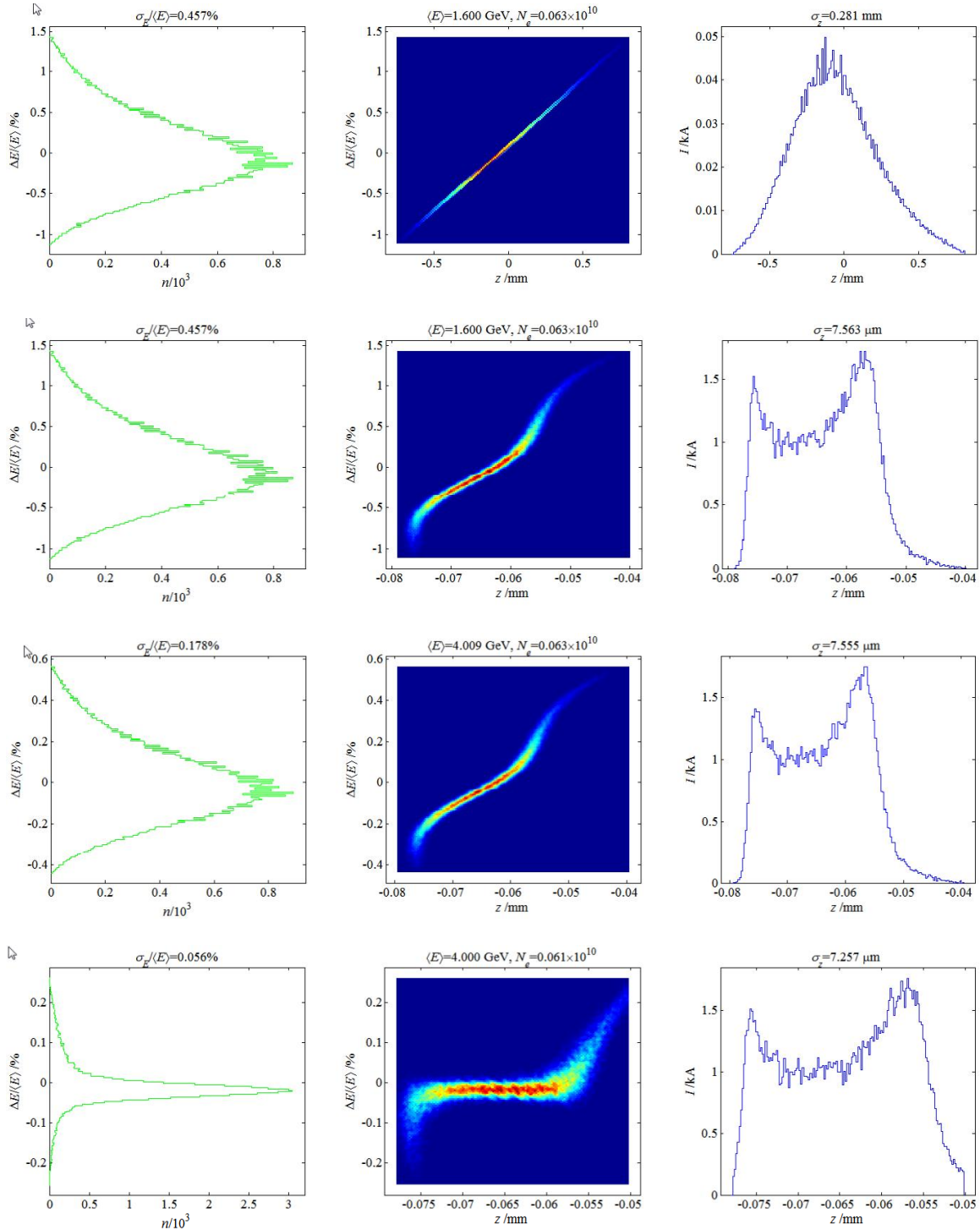


Figure 7. Longitudinal particle tracking through the full accelerator and bypass line, from the end of CM01 to the end of the 2 km bypass line. The left column shows the energy profile, the center column the longitudinal phase space, and the column on the right is the temporal profile. The top row is just after the laser heater at 95 MeV; the second row is just before the 3.9 GHz section at 303 MeV; the third row is before BC1 and just after the 3.9 GHz section at 250 MeV; the fourth row is just after BC1; the fifth row is just before BC2 at 1.6 GeV; the sixth row is just after BC2; the seventh row is after the linac but before the 2.2-km bypass line; and the eighth row is after the 2.2 km bypass line.

The longitudinal resistive-wall wakefield of the 2.2-km long bypass line, convoluted over the simulated bunch distribution, is shown in Figure 8. This beam line is the existing PEP-II high-energy bypass presently suspended from the ceiling of the SLAC linac tunnel with a 24 mm internal radius pipe of stainless steel. The resistive-wall longitudinal wakefield generated by this long cylindrical pipe removes most of the energy chirp from the electron bunch, allowing the L3-linac to run on the RF accelerating crest, which allows using the full RF gradient for acceleration.

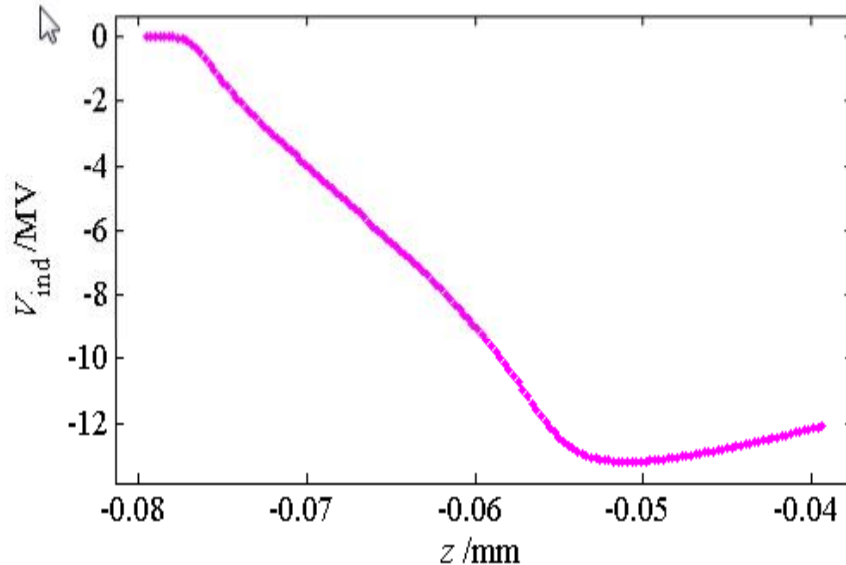


Figure 8. Shown in the tracking above is the resistive-wall wakefield (AC model) generated by the 100 pC, 1-kA bunch. This nearly linear chirp is generated by the 2.2-km-long stainless steel bypass line with 24 mm internal radius cylindrical pipe.

Different bunch charge levels will, of course, generate a different wakefield, but if the bunch is made longer at a higher charge, maintaining the peak current at about 1 kA, then the resistive-wall wake (the slope shown in Figure 8) will be nearly independent of charge. The final chirp can be adjusted using a combination of the RF phase in L2 and the R_{56} value in BC2, however for greater operational flexibility, a variable gap “dechirper” [11] using a special corrugated vacuum chamber will likely be installed in the bypass line to tune the final beam chirp.

7.5.3 Microbunching Instability and Laser Heater Optimization

The impact of the microbunching instability on machine performance can be estimated with an analytical model. The main contribution to beam microbunching comes from the longitudinal space-charge field, which couples to longitudinal perturbations in the beam profile to generate a modulation in the energy distribution. The induced energy modulation is then transformed into a density perturbation by longitudinal motion in the dispersive elements of the beamline (most notably the two bunch compressors). For a high-brightness beam such as that produced by the LCLS-II, the final density perturbation is larger than the initial one (*i.e.*, the system has a high gain). This process is cascaded along the two-stage compression system, generating a strongly perturbed longitudinal phase-space and degrading the FEL performance [5].

The microbunching gain in an amplification stage (*i.e.*, linac + bunch compressor) can be computed with a simple one-dimensional model, using the formulas derived in Ref. [5]. It is a well-known property [5] of any dispersive microbunching process that the final density perturbation is proportional to $\int d\delta_0 V(\delta_0)\exp(i k_f R_{56}\delta_0)$, where k_f is the final microbunching frequency, R_{56} is the chicane longitudinal dispersion, δ_0 is the relative energy deviation with respect to the average beam energy, and $V(\delta_0)$ is the energy distribution function. The microbunching gain is proportional to the Fourier transform of the energy distribution computed at the frequency $k_f R_{56}\delta_0$, which implies that the instability can be damped by increasing the width of the energy distribution with a laser-heater.

To predict and optimize the performance of the laser heater, we estimate the final slice energy spread by adding in quadrature the contributions from the collective space-charge forces, the initial Gaussian spread, and the laser-heater-induced spread (the two latter contributions are multiplied by the total compression factor after BC2). Since the two-stage gain is a high-gain multiplicative process, we can neglect the energy spread induced by longitudinal space-charge before BC2 and integrate the induced energy-spread in the frequency domain using the space-charge impedance following BC2, which includes the 2.2 km bypass line:

$$\sigma_{\gamma,SC}^2 = \frac{1}{2\pi n_z} \int dk |G(k)^2 \Delta\gamma(k)^2| \quad (2)$$

where k is the microbunching frequency, n_z is the beam's linear density, $G(k)$ is the microbunching gain, and $\Delta\gamma(k)$ is the energy modulation per unit bunching factor induced by the space-charge fields. In the calculations we neglect the microbunching gain induced by the two doglegs before and after the bypass line, which are expected to be small contributions. These will be included in a future, more detailed analysis.

Figure 9 shows the final rms energy spread as a function of the laser-heater-induced energy spread for the LCLS-II design parameters. For low values of the heater-induced spread, the final energy spread is dominated by collective effects. Increasing the heater level suppresses the microbunching instability until an optimum setting is reached. Beyond this optimum point, the instability does not substantially contribute to the energy spread; and the final total energy spread approaches $C_T\sigma_{ELH}$, where C_T is the total magnetic compression factor. For the baseline LCLS-II design parameters, the optimal laser-induced rms energy spread is roughly 5 keV, resulting in a final energy spread of roughly 0.5 MeV rms at the undulator entrance, for a peak current of 1 kA. The micro-bunching is being studied at higher charge levels (*e.g.*, 300 pC) to explore its sensitivity.

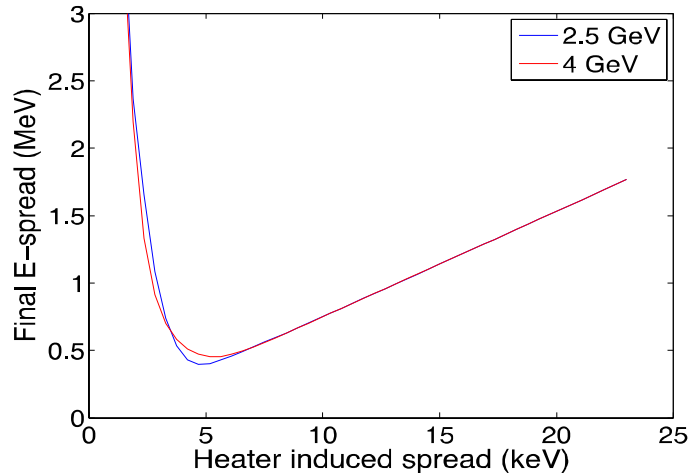


Figure 9. Final rms energy spread as a function of laser-induced energy spread for two different output beam energies (2.5 and 4 GeV), calculated with the linear gain model of the microbunching instability. The 2.5-GeV level is chosen to show a worst case here.

7.6 Electron Diagnostics Sections

The high-average beam power through the linac makes it difficult to use intercepting beam diagnostics, such as screens or wire scanners. Yet there is a strong need for robust beam size measurements and local transverse RF deflectors to time-resolve these measurements. In order to allow routine measurements such as emittance, bunch length, and energy spread, the LCLS-II accelerator will include several pulse-stealing stations with fast kickers to divert a low beam rate (*e.g.*, ~ 100 Hz) to off-axis, short, parallel diagnostic lines, which include beam screens, wire scanners, faraday cups, spectrometers, and RF deflectors where critical. The beam dumps which terminate these low-rate diagnostic lines will only need to absorb up to 120 W (0.3 nC at 100 Hz and 4 GeV). A schematic diagnostics line (following BC1 in this case) is shown in Figure 10 below.

7.6.1 Injector Diagnostic Section

An off-axis diagnostic section will be located after the laser heater at about 100 MeV. A small kicker (~ 1 mrad) with less than 0.5- μ s rise and fall times will fire at 10-100 Hz, stealing electron pulses into this diagnostic line. A magnetic septum will be used to separate the beams after the weak kicker, and the bend-plane dispersion is then closed with a second (DC) bend. An S-band (2856 MHz) or X-band (11.424 MHz) RF deflecting cavity is located past the DC bend and used to measure absolute bunch length and temporal profile. In addition, an OTR and/or YAG screen, along with a redundant wire-scanner after the deflector, is used to measure the horizontal and vertical emittance using a standard quadrupole-scan method. The weak kicker flat-top stability requirement is about 0.1% rms in order to keep the beam stable on the screen to the level of 10% of its rms beam size.

The deflecting cavity is used to also enable sliced measurements (although not with the wire scanners). It may also be useful to add a second rotated deflecting cavity at this one low-energy location to support the other transverse plane and allow slice emittance measurements in both x and y here. A final electron energy spectrometer bend at the end of the line will be used to measure energy and energy spread, including sliced values, before the beam is diverted into a local, low-power dump (less than 3 W at 100 Hz and 300 pC) and Faraday cup. Three or four BPMs are also included in the diagnostic line to allow steering and jitter correction on the wire scanner. This diagnostic system will then continually measure emittance values — both projected and sliced, and in both transverse planes, along with absolute bunch length, absolute beam energy, sliced and projected energy spread, and the bunch's temporal distribution and charge — at several locations along the accelerator, with all measurements at ~ 10 Hz.

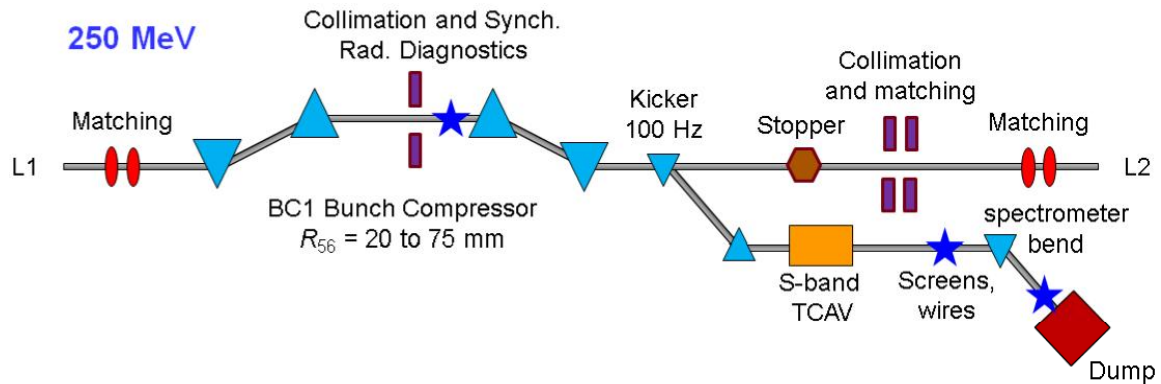


Figure 10. Off-axis, low-rate diagnostic beamline following the BC1 chicane. The 100 Hz kicker steals pulses into an emittance and energy spread measurement section, which includes a transverse RF deflector (S-band in BC1), allowing time-resolved (sliced) measurements, as well as bunch length and temporal distribution.

7.6.2 Post-BC1 Diagnostic Section

A second off-axis diagnostic section will also be located after BC1 at about 250 MeV (see figure above). This system will be identical to the post-laser-heater off-axis diagnostic section, except for use of magnet strengths appropriate to 250 MeV, and may include just one deflecting cavity at this location. The dump power at 100 Hz after BC1 is just 7.5 W at 300 pC of bunch charge.

7.6.3 Post-BC2 Diagnostic Section

A similar diagnostic line *may* be located after BC2 at about 1600 MeV, although will be longer than that at BC1 due to the increased electron energy. This post-BC2 system may not be critical, but is included in the conceptual design until a more thorough study has been made. The dump power at 100 Hz after BC2 is 48 W at 300 pC of bunch charge.

7.6.4 Pre-Undulator Diagnostic Sections

An off-axis diagnostic section will also be located just upstream of each FEL undulator. These systems will also be longer than the BC1 versions, again due to the higher beam energy (4

GeV). The dump power with 100 Hz at 4 GeV is 120 W at 300 pC of bunch charge. Space for RF deflectors will be maintained but perhaps not installed initially.

7.6.5 Dumpline Diagnostic Sections

Diagnostics will also be located along the transport line that leads to the final electron dump, including measurements of energy and energy spread after the FEL. This is described in the section below on the dump and its transport line. The HXR dump line already exists as the LCLS-I dump line and already includes an X-band RF deflector for 1-3 fs time resolution.

7.7 Beam Transport and Switching

The long transport line from the new SRF linac to each undulator is divided into three main sections: (1) the linac extension line (transport from SRF linac to the bypass line); (2) the bypass line (existing PEP-II high-energy transport line suspended from the ceiling of the SLAC linac tunnel), and (3) the LTUH and LTUS (transport from the bypass line to each undulator). This final section has two branch lines: the SXR branch (LTUS) and the HXR branch (LTUH); the beam is switched to each using an RF deflector. These serial transport lines and the switching system must meet the following requirements:

- Transport the high-power, high-brightness electron beam from the end of the new SRF linac to two separate undulators located in the existing Undulator Hall and do it with minimal brightness degradation (less than 10 percent).
- Include a fast (less than 1 μ s) switching system to divert the CW beam to either undulator at up to 1 MHz in each line, but with independently controllable beam rates.
- Include adjustable collimation, beam diagnostics, and tune-up dump systems.
- Generate a small linear, longitudinal wakefield in order to remove the energy chirp from the electron bunch, allowing the L3-linac section to run on RF crest.
- Provide adjustable beta matching and dispersion correction magnets for empirical correction at each undulator entrance.

7.7.1 The Linac Extension

We begin by describing the first section of the long transport line. This section transports the electron beam from the exit of the new SCRF linac in sector 6 to the existing bypass line in sector 11. The first 300 m of this line is a simple, long beam pipe with sparse FODO focusing as shown in Figure 11. The FODO section is followed by two rolled (45 deg) dipole magnets, which deflect almost equally in the horizontal and vertical planes (13.14 mrad per bend horizontally and 13.11 mrad per bend vertically), bringing the beam on line with the existing bypass line suspended from the tunnel ceiling. This rolled “dog-leg” bend system generates a net horizontal translation toward the south of 0.6505 m and a net vertical translation (upward) of 0.6495 m, assuming the new SRF linac beam axis is located at the same transverse location as the old copper linac (as yet to be decided). The x - y coupling of this rolled system has been designed to be insignificant, as

demonstrated in the particle tracking described in Chapter 10. Energy collimation will also be included in the dog-leg bend system (see below). The first 300 m of extension line, prior to the dog-leg, is kept quite simple initially, with no critical functions required (*e.g.*, collimation or diagnostics) so that this can be filled with more cryomodules in the future for an extended energy range of up to about 7.0 GeV.

7.7.2 Bypass Line

The bypass line is an already-existing, long, 2 inch in diameter stainless steel cylindrical pipe running from sector 9 to sector 30. This line was used in the late 2000s as the PEP-II high-energy linac-bypass line at 9 GeV. The line is suspended from the linac tunnel ceiling and includes one quadrupole magnet, BPM, and steering coil every 101.6 m (the length of one linac sector). The LCLS-II linac extension (see above) will connect to the existing bypass line in sector 11 at $s = 1010$ m (downstream of the RF gun). Figure 12 shows the beta and dispersion functions along the bypass line from sector 11 to sector 30. The large quadrupole spacing in the bypass line leads to large beta functions there (200-400 m) with 45 degree phase advance per FODO cell used over the full length. This 45-deg phase advance keeps the quadrupole magnets weak, minimizes vibration effects, allows uniform phase space collimation, and supports a 4-wire emittance measurement section (likely used only at low beam power or perhaps removed from the design). Two horizontal and two vertical adjustable-gap collimators, each pair separated by 90 degrees, will be included along the bypass line (see below) to protect the undulators from an excessive radiation dose due to dark current and beam halo.

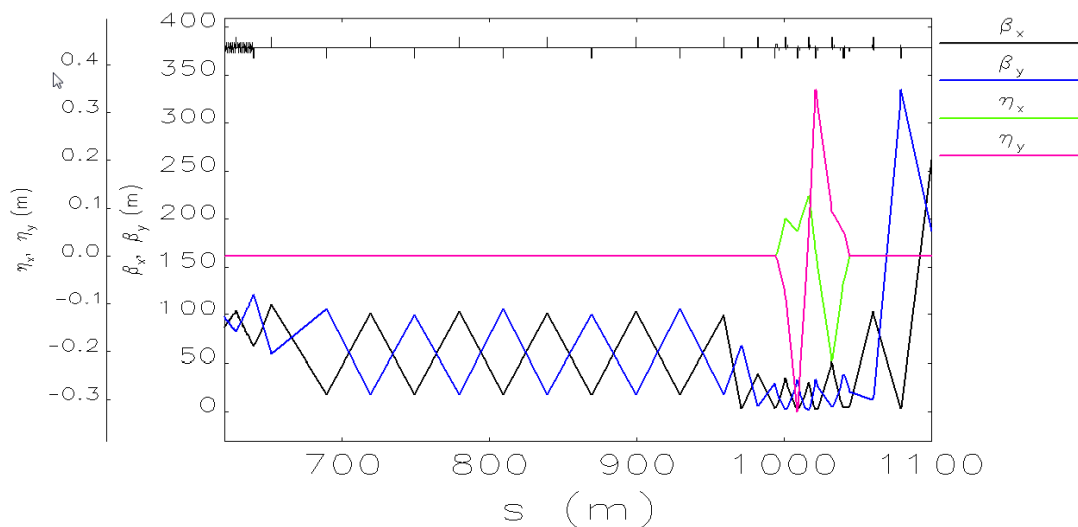


Figure 11. Beta and dispersion functions from the end of the new SRF linac to the start of the bypass line at sector 11. The bends here deflect both horizontally and vertically to bring the beam on line with the existing bypass line suspended from the linac tunnel ceiling.

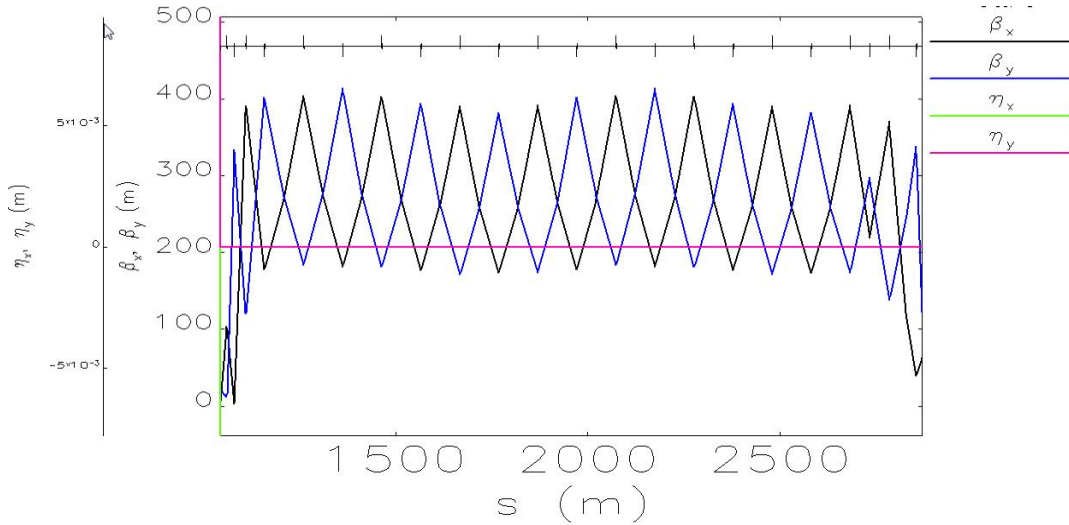


Figure 12. Beta and dispersion functions along the bypass line from sector 11 to sector 30.

7.7.3 Transport from Bypass Line to Undulators

Beyond the bypass line, two nearly parallel branch lines will be in operation, taking beam from the end of the bypass line to one or the other undulator. An RF deflector (spreader) located in sector 30 will deflect the beam to the SXR undulator (90° phase), the HXR undulator (-90° phase), or will not deflect the beam, letting it travel straight ahead to a local dump (zero-crossing phase), depending on the arrival time of the bunch (see spreader section below), which is controlled by the drive-laser timing back at the gun. Only the straight-ahead beam sees a head-to-tail kick variation at the zero-crossing of the RF deflector. The short bunch ($\sim 10 \mu\text{m}$) and the low RF frequency (325 MHz) means this will be an insignificant tilt ($\Delta\epsilon_y/\epsilon_{y0} < 0.1\%$ for $V_{pk} = 4 \text{ MV}$), and then only for the dumped beam. The straight-ahead line is included to provide a high-power dump for commissioning when the undulator hall is occupied or not ready for beam.

After the vertical RF deflector, the beams will enter a three-hole Lamberston septum magnet (or perhaps two separated two-hole magnets) where the small vertical deflection of the transverse RF (up or down) is used to select a much larger left or right horizontal bend in the DC septum magnet. The design, at present, is only conceptual and is shown below in Figure 13 as a three-way spreader system (left, right or straight). The RF deflector kicks up or down (in and out of the paper here) thereby selecting the horizontal bend direction of the three-hole septum magnet. Small vertical “y-correctors” are included to remove the vertical kick and dispersion of the RF deflector. The existing LCLS-I may still be used, of course, to feed the HXR undulator at 3-15 GeV and at a 120-Hz bunch repetition rate by switching off the DC bend at the upper right of Figure 13.

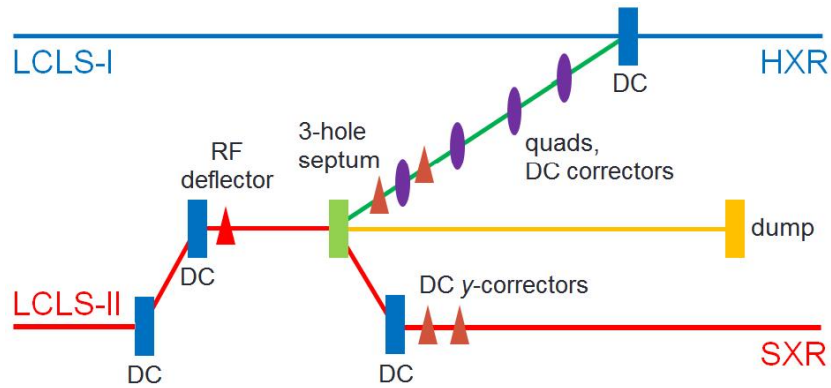


Figure 13. Detail of conceptual three-way spreader system (plan view). The RF deflector kicks up or down (in and out of paper here), thereby selecting the horizontal bend direction of the three-hole-septum magnet. Small vertical “y-correctors” are included to remove the vertical kick and dispersion of the RF deflector. The green section is a combined horizontal/vertical bend. The 300-kW pre-undulator dump is shown as “dump”.

7.7.3.1 LTUS Transport Line

This line transports the LCLS-II beam from the bypass line to the entrance of the SXR undulator, located on the north side of the existing LCLS-I undulator hall (red line in Figure 13). The beamline starts above and to the south of the existing LCLS LTU beamline that will be used for the HXR (blue line in Figure 13); it then crosses (the crossing is not shown in Figure 13) the HXR beamline to the north side and drops to the same elevation. Figure 14 shows beta and dispersion functions along this LTUS transport line from the entrance of the RF deflector to the entrance of the SXR undulator. The large beta functions are needed here to recover the matching after the existing bypass line, with its 400-m beta functions. A very small energy spread and large magnet bores here will mitigate geometric aberrations. Two horizontal dipole magnets (18.6 mrad per bend) after the muon-plug wall (17 m of iron shielding starting at $s \approx 3230$ m) form a horizontal dog-leg bend with a 1.9 m horizontal jog, but ending still parallel to the linac axis. The dog leg has two energy collimators (near dispersion peaks) and is based on a FODO lattice with 90-degree phase advance per cell. This is followed by a four-screen emittance diagnostic section with 45-degrees-per-cell phase advance, including two horizontal and two vertical collimators with 90-degree separation per pair. Two small vertical bends (2.33 mrad per bend) are also included in order to remove the intrinsic SLAC linac downward slope (5 mrad downward angle at station 50, which is defined as being half-way down the linac). Identical vertical bends are used in LCLS-I for the same purpose.

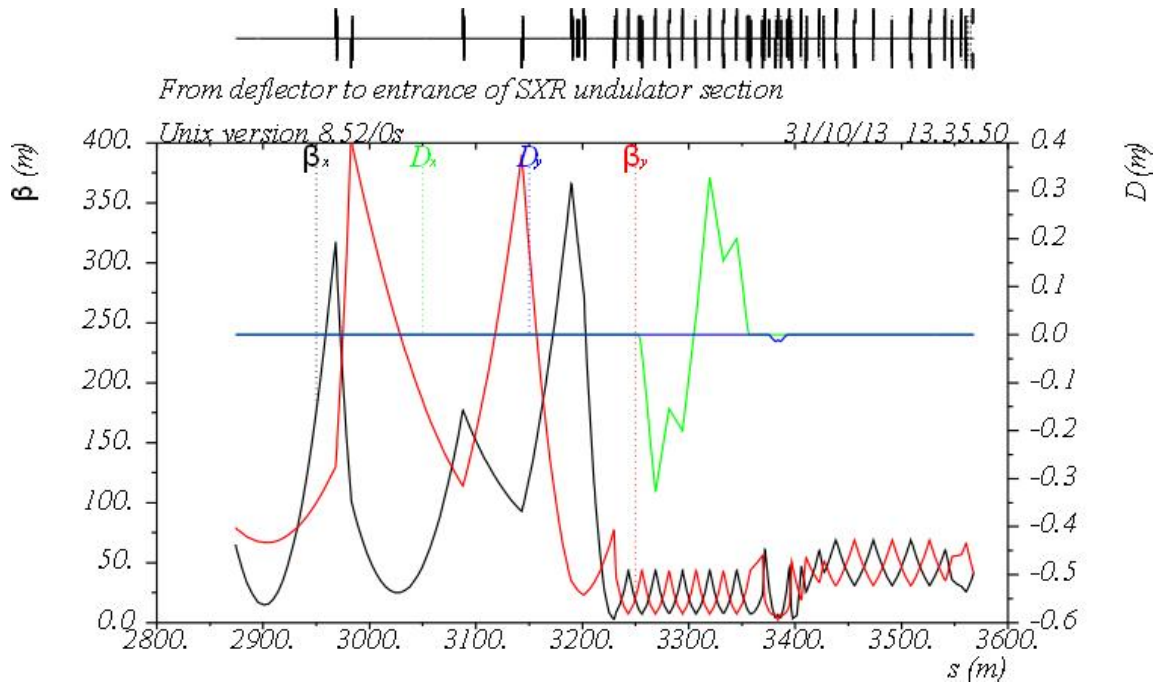


Figure 14. Beta and dispersion functions along the LTUS transport line from the RF deflector entrance to the SXR undulator entrance. Small vertical bends are also included.

7.7.3.2 LTUH Transport Line

This LTUH line transports beam from the bypass line to the entrance of the HXR undulator on the south side of the existing LCLS-I undulator hall (green-to-blue line in Figure 13); this beamline will only be slightly modified from the existing one that is presently in use for the LCLS. Figure 15 shows beta and dispersion functions along the transport line from the entrance of the RF deflector to the HXR undulator entrance. Two 45-degree-rolled dipole magnets (4.6 mrad net x/y angle per bend) form a horizontal and vertical dog-leg with a 0.65 m horizontal and 0.65-m vertical jog, but ending still parallel to the linac axis. Again, x - y coupling is minimal and has no significant effect on the optics, as seen in particle tracking in Chapter 10. A second dog-leg farther downstream places the beam at on center for the HXR undulator. This second existing dogleg has four horizontal dipole magnets (8.7 mrad per bend) with two energy collimators (near dispersion peaks) and adds a 1.25-m horizontal, but parallel jog. This is followed by a four-screen-emittance diagnostic section with 45-degree per cell phase advance, including two horizontal and two vertical collimators with 90-degree separation per pair. Phase advance values are chosen for optimum 4-wire emittance measurements (likely only used at low beam power) and for optical symmetry and dispersion suppression in the dog-leg bends. Two vertical bends (2.33 mrad per bend) are also included in order to remove the intrinsic SLAC linac downward slope. These two vertical bends are about 150 m upstream of the LTUS vertical bends in order to level the two undulators in elevation. Note that the second dog-leg, its collimators, four-screen diagnostics, and horizontal and vertical bends all exist as part of LCLS-I.

7.7.4 Beam Spreader System

A high duty factor, high repetition rate beam spreader is required to switch the beam to three possible destinations: (1) the primary beam dump, (2) the HXR undulator, and/or (3) the SXR undulator. The design is highly flexible, allowing arbitrary beam patterns picked from the nominal 0.929-MHz linac bunch repetition rate (see below) to be directed to any of three destinations on command. A modified version of the NGLS-type three-way, SCRF transverse RF deflecting cavity concept, [12,13] in conjunction with drive laser pulse gating, will be used to distribute the beam accordingly.

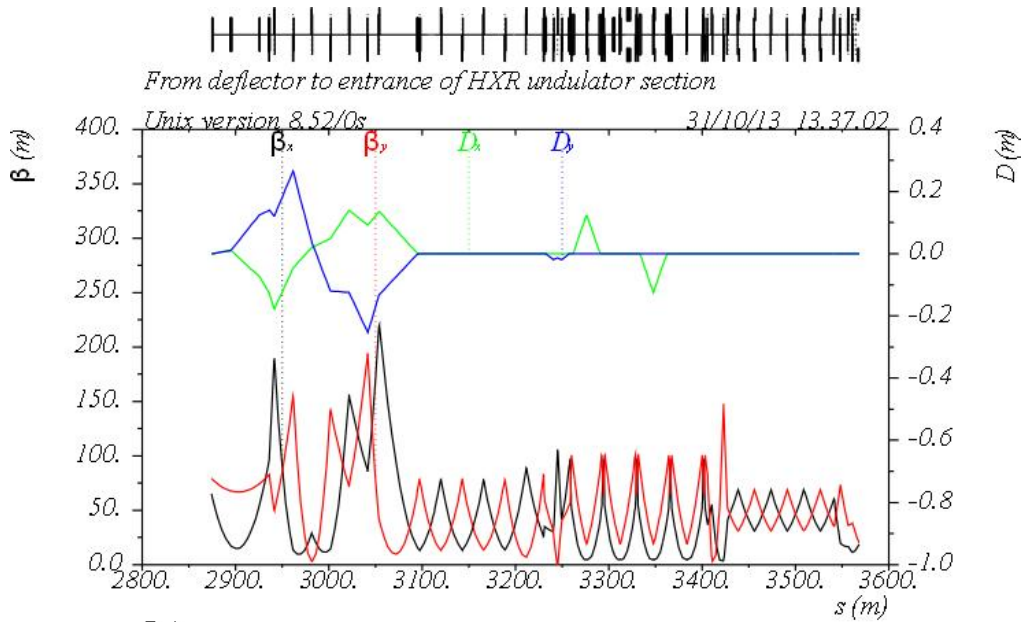


Figure 15. Beta and dispersion functions along the LTUH transport line from the RF deflector entrance to the HXR undulator entrance. Small vertical bends are also included here.

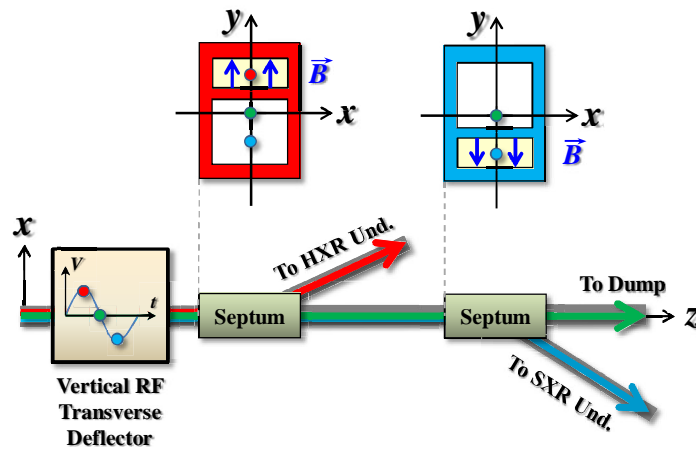


Figure 16. LCLS-II three-way RF beam spreader concept (a two-septum option here). An RF transverse deflector imparts a small vertical kick with direction dependent on beam arrival time and RF phase. Downstream septum magnets provide a strong separation in the horizontal plane, depending on the sign of the vertical kick.

The RF beam spreader concept is similar to a traditional fast kicker system. A fast, weak element will impart a small, 1-mrad-scale vertical deflection to the electron beam in a direction (up or down) dependent on the desired destination. After a drift section, a strong, DC septum magnet (see Section 7.10) then provides a larger horizontal deflection used to fully separate the beam(s) spatially. In the RF beam spreader, the fast pulsed kicker magnet traditionally used is replaced with an RF transverse deflecting cavity to accommodate high-rate (perhaps up to 10 MHz in the long term), high-duty factor operation, as illustrated in Figure 16.

The direction of the initial, vertical deflection depends on the phase between the electron bunch and deflector RF. At the RF zero crossing, there is no net deflection and the bunch passes through the zero-field region of both septum magnets (green dots in Figure 16), continuing to the dump. When the bunch time of arrival is shifted to the positive (negative) crest, it will see a net upward (downward) kick and be directed into the bending field of the HXR (SXR) septum magnet, diverting the bunch to its respective undulator beam line (red/blue dots in Figure 16).

The LCLS-II spreader system will utilize a CW, superconducting RF-dipole deflecting mode cavity operating at 325 MHz (one-quarter of the L-band, 1300-MHz-linac frequency), leveraging ongoing superconducting RF crab cavity research for applications in linear collider luminosity improvements and the NGLS spreader design. Future higher repetition rate switched beams are then also possible without requiring significant hardware changes. At an estimated $\theta_0 = 1$ mrad kick, the peak deflecting voltage required is 4 MV, which can, for instance, be distributed over a 2-m-long cavity. The RF voltage jitter tolerance will be about 0.01% rms ($\approx (\epsilon/\beta)^{1/2}/\theta_0/20$, where ϵ is the emittance, $\beta \approx 10$ m is the beta function, $\theta_0 = 1$ mrad, and the factor of 20 provides a stability of 5% of the rms divergence at the kicker), and the phase jitter tolerances (on crest phase for both deflections) will be very loose: ~ 1 degree. The zero-crossing phase will not have demanding tolerances since this is the dumped beam.

The destination-dependent time delay with respect to the deflector zero crossing will be accomplished by gating the photocathode drive laser oscillator (“seed laser”) before the laser amplifier. The seed laser will operate at a repetition rate of 37.1 MHz (1/35th of the 1300-MHz linac RF). In nominal, full beam rate operation to the LCLS-II electron dump, every 40th seed laser pulse is gated into the drive laser amplifier to produce the phase-locked, maximum linac beam rate of 0.929 MHz, (1/350th of the 325 MHz deflector frequency). With the deflector at zero phase, the beam will pass both septa field-free regions and proceed to the high-power dump in the beam switchyard.

To get the time shift needed to kick a bunch, the laser gate to the amplifier will be fired one seed cycle ($26.9 \text{ ns} = [37.1 \text{ MHz}]^{-1}$) early or late from the nominal 0.929-MHz cycle. As illustrated in Figure 17, a bunch arriving with this phase shift will see the corresponding positive or negative crest of the deflector RF, diverting it to the appropriate septum and subsequent destination.

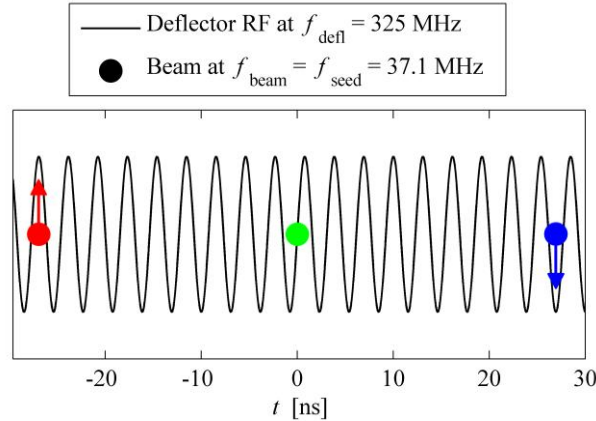


Figure 17. Effect of gating photocathode seed laser one cycle (approximately 27 ns) early or late from the nominal $37.1 \text{ MHz} / 40 = 0.929 \text{ MHz}$. Beam arriving at the spreader deflector will see either a positive or negative deflector crest, respectively, deflecting the tagged bunch to its corresponding septum and subsequent undulator beam line.

This requires the Pockels cell gate between laser seed and amplifier to allow for a logical $\pm 27 \text{ ns}$ shift in an on-demand, phase-locked manner. The laser amplifier gain must not be sensitive to possible variations in consecutive pulse spacing over the range $1.08 \mu\text{s} \pm 54 \text{ ns}$. Where less than full beam rate is desired in the linac, a secondary fast Pockels cell system to suppress the drive laser after amplification with a minimum gate-off width of 108 ns is fired on demand at the nominal 0.929 MHz rate.

Finally, this system requires an irregular (though phase-locked) filling pattern of the beam RF buckets. Linac diagnostics and instrumentation will be designed to accommodate the wide variety of beam patterns and bunch spacings possible from the system described in this section.

The RF-based beam spreader is described for the present design, considering that no significant challenges are expected in terms of available technology. Other options will continue being evaluated going forward, including the use of pulsed magnetic kickers in place of the deflecting cavity to initiate beam separation. Kicker magnets would allow arbitrary pulse picking from the main linac beam without requiring unusual timing patterns, thus greatly simplifying instrumentation. However, it remains to be demonstrated that pulsed kicker magnets can operate with sufficiently high duty factor and low magnetic ripple to satisfy the beam rate requirements, with the ILC kicker already near to firing the rate required (see more below).

7.8 Collimation and Beam Halo Management

Two types of collimators are employed throughout LCLS-II:

- Halo collimators, to protect equipment and reduce radiation due to beam loss, and
- Protection collimators, to keep the beam in its prescribed channels where shielding is adequate to absorb the radiation the beam can produce.

These independent systems have different functions, but both must be able to stop significant amounts of beam and absorb power from beams, wakefields and synchrotron radiation.

7.8.1 Collimation Requirements

Halo collimator requirements are based on the sensitivity of devices to beam loss and the shielding effectiveness in the area the collimators function. The collimators, together with the beam optics, must insure that halo is sufficiently truncated so the beam loss in sensitive areas is limited to the amounts discussed in the next sections. The collimators must also not collimate beam within the acceptance phase space defined below.

7.8.1.1 Undulator Sensitivity to Radiation

Undulators are located in a well-shielded tunnel such that essentially no radiation can escape. However, radiation from lost beam can cause demagnetization and damage the precisely-tuned undulator magnets. To avoid the accumulation of significant damage over a period of many years, the average fractional beam power loss in the undulators must be limited to ~ 0.1 W/m. See Chapter 8 for a detailed discussion of radiation damage to undulators. For the beam power of 120 kW it implies a fractional loss of 10^{-6} per meter. The lattice in the undulator is essentially dispersion free, so only high betatron amplitude electrons are of concern. The quadrupoles form a very weak FODO lattice so chromatic aberrations of off-energy particles should be insignificant (even 5% energy errors only change the beta function by a few percent).

7.8.1.2 BTH Sensitivity to Beam Loss

The shielding of the Beam Transport Hall (BTH) was designed for about **5 W** of beam loss at any one point. To avoid a substantial increase in the BTH wall thickness, the fractional beam loss over this region must be limited to 10^{-4} . Both of these requirements can be met by a system of adjustable-gap collimators located upstream of the BTH that block the beam halo (similar to what is done at LCLS-I).

7.8.1.3 SC Linac Sensitivity to Beam Loss

Beam loss in the area of the superconducting RF cavities of the linac presents an extra thermal load to the cooling system. This has two deleterious effects. More power is required to keep the cavity cool, and over a long period of time the cost of operation is increased. On a shorter time period, a quickly changing thermal load can destabilize the cryogenic system or even cause a quench. The average heat load without beam loss is expected to be about 12 W per cavity (at 2 K). Heating due to beam loss must be kept below about 1 W per cavity at 2K (see Chapter 6). Although no study has yet been performed for LCLS, it is expected a significant portion of the beam loss power will be absorbed at 2K. The angle of incidence of the halo electrons to the inner radius of the cavity cells is very low so the radiation shower will be tangentially aligned with the niobium cell walls; the radiation length of niobium is ~ 1 cm and most of the power is deposited a few, ~ 5 , radiation lengths.

7.8.1.4 Acceptance Phase Space

Collimators, together with the optical design for the beam, must accept sufficient betatron phase space so that in the process of ordinary tuning, beam is not lost on the collimators more often than necessary to protect equipment. The narrow undulator vacuum chamber sets the scale for LCLS-I and will be used for LCLS-II. For LCLS-I, transverse beam excursions of more than 1 mm in the undulator generate a protective beam trip using BPMs. BCS requirements in Chapter 14 include shutting off the beam in 25 to 150 microseconds depending on the hazard. Typical beta peak functions in the undulator are 30 m at 14 GeV. The required betatron acceptance for LCLS-II is scaled from these numbers and amounts to 40σ , where σ is the rms transverse beams size in the undulator, assuming the nominal design parameters. The energy acceptance requirement is set to $\pm 2\%$ relative energy. This is sufficient to allow rapid change of up to $\pm 4\%$ in photon wavelength without adjusting the undulator gap. It also allows a reasonable amount of chirp to be left on the beam without causing beam loss. Greater acceptance would be desirable provided it does not increase beam loss in the sensitive areas beyond the set limits.

7.8.1.5 Protection Collimator Requirements

Protection collimator requirements include the betatron and energy acceptances mentioned above. In addition, protection collimators must be able to either indefinitely withstand the full beam intensity at the location of the collimator or be backed-up with a burn-through monitor (BTM). The latter is usually the case. Additional requirements for protection collimators are given in Ref. [14].

7.8.1.6 Collimator Heat Loads

Incoherent and coherent spontaneous radiation can, in principle, generate significant heat loads, which collimators must absorb. However, the incoherent spontaneous radiation power from bending magnets in the bunch compressors and the dog-leg section is quite low due to the low beam energy and current, and does not present any heating issues. On the other hand, initial estimates indicate that coherent synchrotron radiation beam power can be on the order of up to 45 W. Wakefields, generated by the collimators and by other structures, and can be absorbed by collimators and present a possibly significant heat load. Estimates of collimator-generated wakefield power are of order 70 W per collimator. Collimation and masking of synchrotron radiation is included in the design of the accelerator equipment and not discussed here.

7.8.2 Beam Halo

Although the desired electron beam is extremely bright and small, through a number of different processes the linac will also generate a halo of electrons with widely varying energies, momentum and timing. Some halo electrons originate at the gun from areas of the cathode far from the laser spot, due either to field emission or photoemission of scattered light. Halo electrons are also generated by acceleration of field emission electrons from the SC linac cavities. Beam dynamics effects can also generate halo electrons.

Touschek scattering, whereby electrons within a bunch scatter off each other individually and transfer momentum between transverse and longitudinal degrees of freedom, is one source of beam halo. When such scattering occurs in a dispersive region the energy change can drive electrons at high betatron amplitude which are lost on downstream collimators or other apertures. The rate at which this scattering occurs depends roughly on the inverse on the phase space density of the electron bunch, so the very bright electron beams needed for LCLS-II is of some concern. A calculation was performed for the LCLS-II lattice and beam parameters using code developed and verified at the Cornell storage ring. The total generated Touschek current was found to be only 160 pA and virtually all was lost on collimators. The power associated with 160 pA is less than 1 W so it is unlikely that Touschek scattering will contribute significantly to heating anywhere. It is even unlikely to pose much of a concern for beam loss radiation because a typical shielding design is for substantially more than 1 W.

Intra-beam scattering, while similar to Touschek scattering, concerns the effect of the accumulation of multiple scattering events rather than a large single scattering event generating large amplitudes. It is found not to be important in generating beam halo but can generate energy spread in the core of the beam. A calculation was performed, again using the Cornell ERL code that determined the emittance effect to be negligible. On the other hand the energy spread increased significantly, with estimates ranging from 200 to 300 keV rms. Since the FEL beam energy spread without IBS is estimated to be 500 keV rms, and the IBS energy spread adds in quadrature, the IBS contribution is not detrimental. Further calculations are probing this effect since these initial estimates are only preliminary.

7.8.3 Collimation Scheme

Figure 18 shows optical functions along the accelerator, from the CM01-exit at 95 MeV to the start of the L1-linac section following the BC1 chicane at 250 MeV. Adjustable collimator locations are marked at the top of the plot with an energy collimator (CHXE) in the laser heater chicane, a second energy collimator (C1XE) in the BC1 chicane, and two horizontal and two vertical betatron collimators in the section following BC1 (C1X1, C1X2 and C1Y1, C1Y2). The betatron collimators are paired (*e.g.*, C1X1 and C1X2) with a 90 degree separation (in the appropriate plane) so that beam position and angle are orthogonally collimated in sequence. These are rectangular collimators with independently adjustable jaws. Their names and parameters are listed in Table 3.

Figure 19 shows additional collimators in the BC2 area, with optical functions along the accelerator from the L2 linac exit at 1.6 GeV to the start of the L3-linac section following the BC2 chicane. Additional adjustable collimators are marked at the top of the plot with an energy collimator (C2XE) in the BC2 chicane and with two horizontal and two vertical betatron collimators in the section following BC2 (C2X1, C2X2 and C2Y1, C2Y2); again, these are paired with 90 degree phase advance separations.

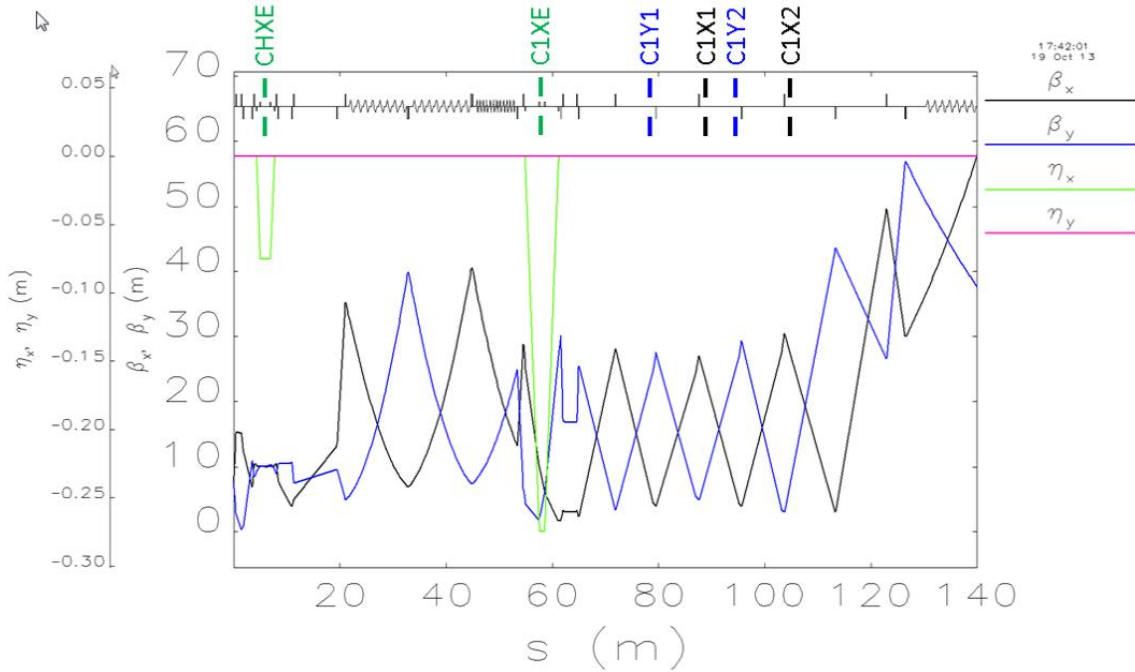


Figure 18. Beta and dispersion functions along the accelerator from the CM01 exit at 95 MeV to the start of the L1-linac section following the BC1 chicane at 250 MeV. Six adjustable collimator locations are marked at top, with names as described in the text.

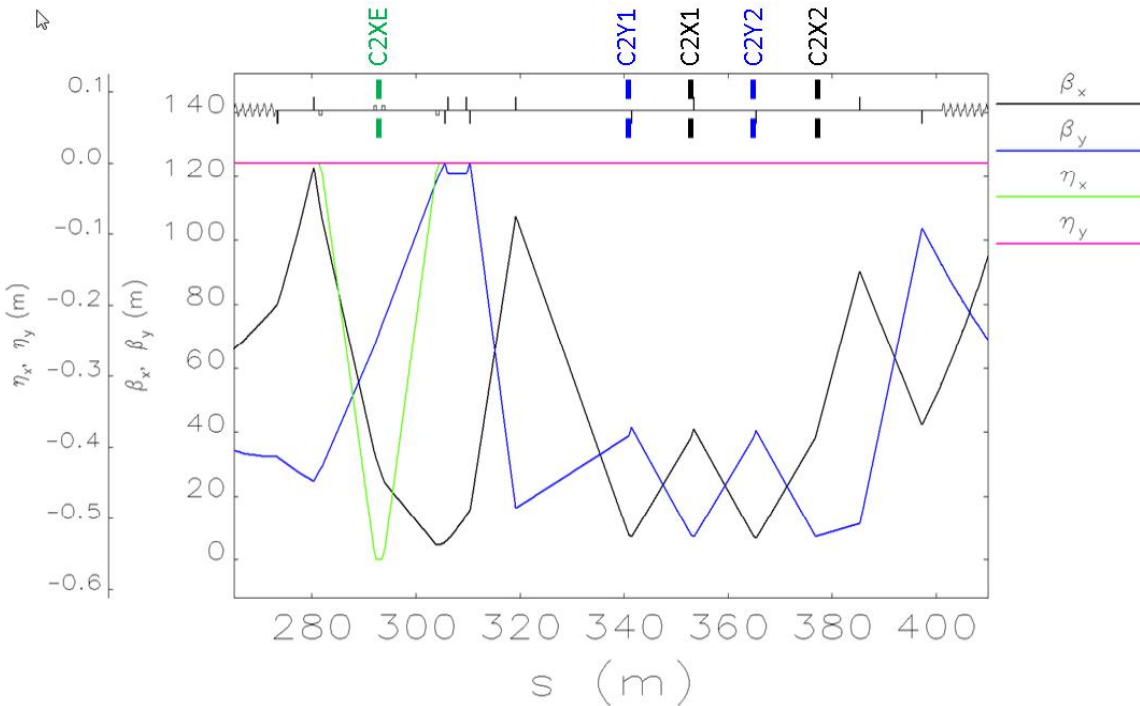


Figure 19. Beta and dispersion functions along the accelerator from the L2 linac exit at 1.6 GeV to the start of the L3 linac section following the BC2 chicane. Five adjustable collimator locations are marked at top, with names as described in the text.

Finally, Figure 20 shows collimators in the post-linac areas, with optical functions along the accelerator from the L3-linac exit, at 4 GeV, to nearly the start of the SXR undulator. Additional adjustable collimators are marked at the top of the plot with an energy collimator (CEBD) in the sector 10 dog leg and with two horizontal and two vertical betatron collimators in the section following bypass line (CX13, CY14 and CX17, CY18), again paired with 90 degree phase advance separations. The SXR branch line has two additional and final energy collimators (CEDL14 and CEDL18) and four more final betatron collimators in x and y (CX31B, CX35B, and CY32B, CY36B). Finally, the HXR branch line similarly has two final energy collimators (CEDL1 and CEDL3) and four final betatron collimators in x and y (CX31, CX35, and CY32, CY36). These last few collimators in each branch line are a final clean-up pass and should not see much beam power, since the primary collimation has been implemented well upstream at several locations and with tighter gap settings (normalized to beam size).

In order to minimize the power load, the betatron collimators are set progressively wider in gap when normalized to rms beam size, with the first collimators (C1X1, C1X2, C1Y1, C1Y2) set at $30\sigma_{x,y}$, the second (C2X1, C2X2, C2Y1, C2Y2) at $40\sigma_{x,y}$, the third (CX13, CY14, CX17, CY18) at $50\sigma_{x,y}$, and the final pass at $60\sigma_{x,y}$. The 2.5 mm vertical undulator aperture, with its 26- μm rms beam size, is then well shadowed at $98\sigma_y$. (The horizontal one is even larger.) Particles scattered out of the collimator jaws have not yet been included and will need to be modeled in some detail, likely using *Elegant* [2].

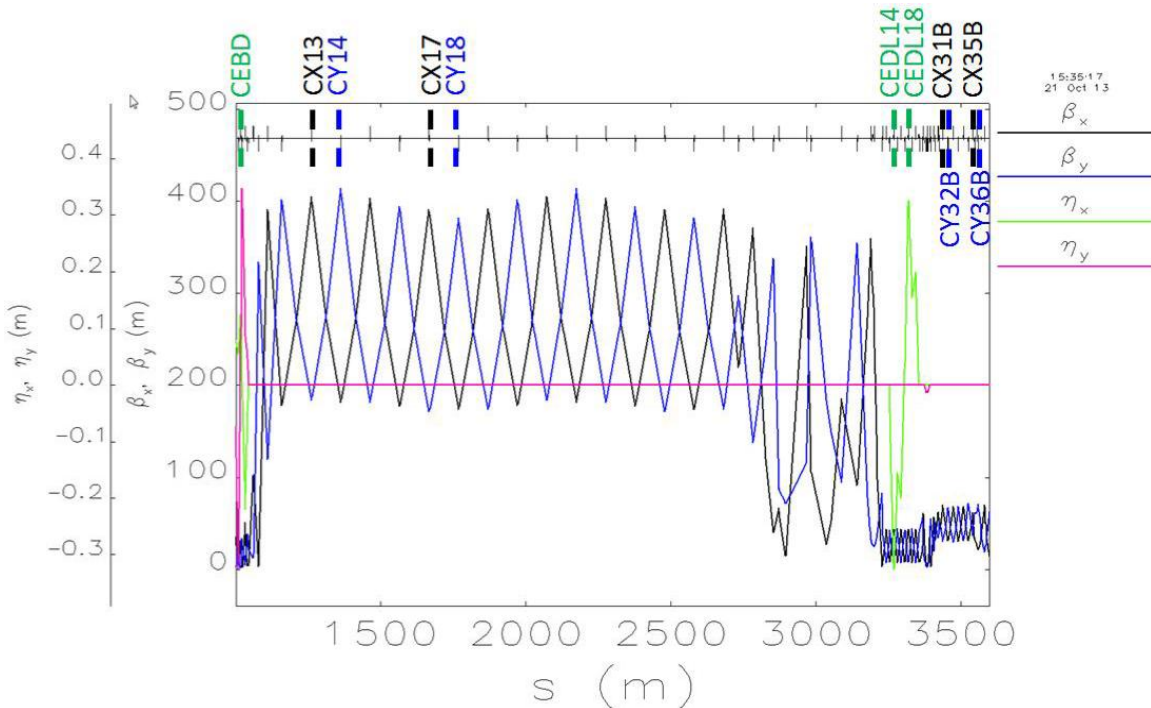


Figure 20. Beta and dispersion functions along the accelerator from the L3 linac exit at 4 GeV to nearly the start of the SXR undulator. Eleven adjustable collimator locations are marked at top, with names as described in the text. Not shown are the LTUH collimators (two energy, two horizontal, and two vertical, similar to the LTUS). (See Table below.)

Table 3. Adjustable collimator parameters (preliminary). Paired collimators are listed on the same row and have a betatron phase advance separation of 90 degrees (except for the energy collimators). The normalized emittance used here to calculate the betatron beam size is 0.45 μm . The last six collimators in the list (last three rows) already exist as LCLS-I components.

Collimator Name	Coll. Plane	E (GeV)	s (m)	σ_z/E (%)	η (mm)	β_x (m)	β_y (m)	$\eta\sigma_z/E$ (mm)	$\epsilon_x\beta_x$ (mm)	$\epsilon_y\beta_y$ (mm)	1/2-gap (mm)	1/2-gap ($\sigma_{x,y}$)
CHXE	$E(x)$	0.095	21	0.05	75	10	10	0.037	0.16	0.16	2.0	-
C1XE	$E(x)$	0.25	73	1.3	275	7	4.0	3.6	0.080	0.060	10	-
C1Y1, C1Y2	y	0.25	94, 110	-	0	4.5	25	0	0.060	0.15	4.5	30
C1X1, C1X2	x	0.25	102, 118	-	0	25	4.5	0	0.15	0.06	4.5	30
C2XE	$E(x)$	1.6	308	0.45	565	28	68	2.5	0.63	0.10	7.0	-
C2Y1, C2Y2	y	1.6	356, 380	-	0	7.5	38	0	0.033	0.074	3.0	40
C2X1, C2X2	x	1.6	370, 392	-	0	38	7.5	0	0.074	0.033	3.0	40
CEBD	$E(y)$	4.0	1022	0.18	287	4.7	25	0.52	0.016	0.038	2.0	-
CX13, CX17	x	4.0	1277, 1684	-	0	390	182	0	0.15	0.10	7.5	50
CY14, CY18	y	4.0	1379, 1785	-	0	182	390	0	0.10	0.15	7.5	50
CEDL14, CEDL18	$E(x)$	4.0	3297, 3348	0.02	156	8.1	40	0.031	0.021	0.048	2.0	-
CX31B, CX35B	x	4.0	3454, 3525	-	0	66	32	0	0.062	0.043	3.7	60
CY32B, CY36B	y	4.0	3472, 3542	-	0	32	66	0	0.043	0.062	3.7	60
CEDL1, CEDL3	$E(x)$	4.0	3293, 3364	0.02	113	4.5	23	23	0.016	0.023	2.0	-
CX31, CX35	x	4.0	3454, 3525	-	0	66	32	0	0.062	0.043	3.7	60
CY32, CY36	y	4.0	3472, 3542	-	0	32	66	0	0.043	0.062	3.7	60

7.9 Main Electron Dump Transport

There is one high-power (about 120 kW) main electron dump at the end of each FEL and one high-power (~300 kW) pre-undulator dump in the existing beam switchyard (see Figure 13), with smaller tune-up dumps in the low-rate diagnostics lines. The beams can be directed to either of the FEL's or the high-power dump with small changes in the injector laser timing. The high-power dump has three primary roles: 1) it allows high-power beam to be established before being sent on across the lightly shielded research yard, and then the undulators, which could be easily damaged by an errant beam; 2) it provides an ability to rapidly vary the train format to the FEL's without large changes to the SCRF linac; and 3) in configurations where the rf deflector is replaced with a magnetic kicker, it provides a BCS or MPS response to a downstream fault much faster than the injector, thereby protecting the undulators and lightly shielded regions of the accelerator.

7.9.1 System Requirements

This section describes a design for the LCLS-II electron transport line leading from the end of each FEL undulator to the main electron dump. The dump is addressed in the chapter on Radiological Considerations, Chapter 17. Here only the dump transport line is addressed, along with its requirements, optics design considerations, beam diagnostics, and beam dynamics issues. The dump transport line requirements are listed below:

The electron dump lines have the following *design requirements*:

- Must transport the electron beam from the end of each FEL line to the designated beam dump with minimal beam loss at any operational electron energy, with an average electron beam power of up to 120 kW.
- Must direct the discarded electron beam in a downward direction, with the beam dump itself located under concrete and iron shielding. In addition, the dump should be located upstream of the experimental hall (EH), and accessible for possible replacement.
- Must include optics or beam spoilers to increase the transverse beam size in both planes on the dump.
- Might need to include a continuously verifiable beam raster system to move the beam around on the dump to dissipate the beam power over a larger area.
- Must include at least two ~ 5 μm resolution BPMs between the end of the undulator and start of the vertical dump bends, in order to support undulator beam-based alignment.
- Must include MPS systems (toroid comparators and beam loss monitors) to switch off or rate-limit the electron beam quickly when significant beam losses occur.

In addition, the electron dump lines have the following *desired features*:

- Should include adequate vacuum chamber aperture to transport a 5 percent off-energy beam.
- Should include an electron energy spectrometer that can resolve relative energy changes as small as 10^{-5} , if possible, and resolve an energy spread of 100 keV rms.
- Should include an insertable beam profile monitor at low rate, able to resolve a 10- μm rms vertical beam size to resolve the FEL-induced energy spread, if possible.
- Should include a “soft” vertical bend magnet ($\theta_s \approx 1$ mrad) before the main dump bends to redirect any coherent optical edge radiation generated by the main dump bends, down and away from the experiments (as was done in the SLC final focus systems).

The transport line(s) leading to the SXR electron dump(s) has not been designed in detail yet, but will be quite similar to the LCLS-I dump line and with much more focus on high average power issues and beam containment. The existing LCLS-I dump line will serve as the HXR dump

transport, and currently includes a horizontal X-band RF deflecting cavity for time-resolved bunch measurements used to quantify FEL performance along the bunch length.

7.10 Kickers, Septa, and Specialized Components

7.10.1 Diagnostic Kickers

The LCLS-II will require several diagnostic kickers (see Chapter 9) that are capable of kicking individual electron bunches at up to a 1 MHz rate — and possibly 10 MHz in the long term. To achieve standby pulses between bunches, a full pulse width of less than 100 ns is necessary (designing for a 10 MHz future). The maximum beam energy is 4 GeV (and perhaps 7-8 GeV longer term) and the maximum kick is about 1 mrad.

To achieve the required length-integrated field of 0.013 T-m, it is preferable to utilize a ferrite loaded magnet. This procedure has the advantage of placing the bulk of the magnetic field energy within the beam pipe, thus reducing the amount of energy required from the pulser. Because the rise and fall time of the magnet are proportional to magnet inductance, it is useful to divide the magnet into several small sections, each driven by a separate pulser. This reduces the inductance each pulser must drive by a factor equal to the number of sections. Initial calculations show that a 4-10 section magnet is possible. Two magnets may be necessary for a 4 GeV beam and possibly four for a 7 GeV beam (with extra space provided for this case). A depiction of each core, as well as a magnet section (with 10 cores), is shown in Figure 21. In the figure to the right, each core is driven by a separate pulser, but for clarity only one is shown here.

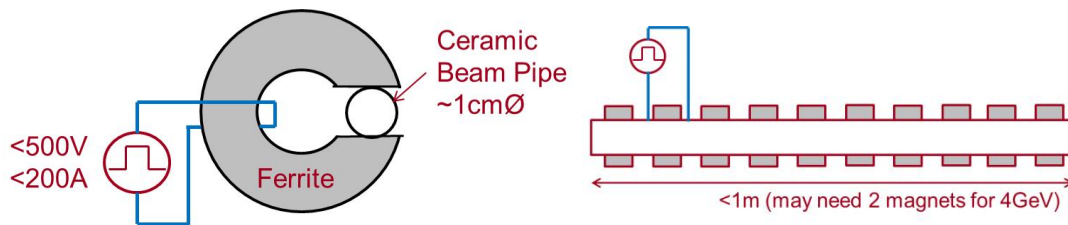


Figure 21. A depiction of a kicker core (left) and the full magnet (right), with 10 sections shown. Each core is driven by a separate pulser, but for clarity only one is shown here.

The fast rise and fall time require tight driver-to-load coupling to avoid excessive ringing. Thus, a co-located magnet and pulser is preferable to avoid long cable runs. The inherently redundant design is useful given that access for pulser maintenance will be limited.

The fundamental pulser topology is an H-bridge. A large bus capacitor is utilized to provide a constant voltage across the magnet sections during the rise and fall time. Through appropriate on/off control of the four switches, it is possible to achieve a rising flat-top, and falling section of the current pulse. The falling section recovers energy back to the storage capacitor. A depiction of the pulser and associated current paths is shown in Figure 22.

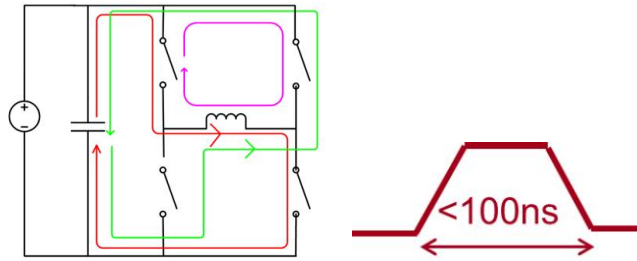


Figure 22. The pulser and associated current paths.

A pulse of less than 200 A-turns is required to realize the magnetic field required. The rise and fall times are proportional to the voltage applied, where 500 V is the maximum reliably switched voltage given the required switching technology. This kicker topology has the added benefit of being capable of several MHz and bipolar operation, should such requirements be beneficial for other LCLS-II applications. The rms amplitude stability required is about 0.01%, which should be achievable with this design, and limits the horizontal shot-to-shot jitter to less than 5% of the beam size.

It is worth noting that the ILC stripline kicker has achieved a 1-MHz rate, but only in burst mode with a duty cycle 1%. These striplines are much faster than needed for LCLS-II (3 ns bunch spacing), driving up the heat load. However, simple scaling from these ILC kicker results to much longer pulses bodes well for the development of a MHz kicker for LCLS-II.

7.10.2 Septum Magnets

The septum is likely a Lambertson magnet such as shown in Figure 23. As an example, this shows a field-free region at nominal beam height (deflector off), and a vertical field-region which is 7 mm below this.

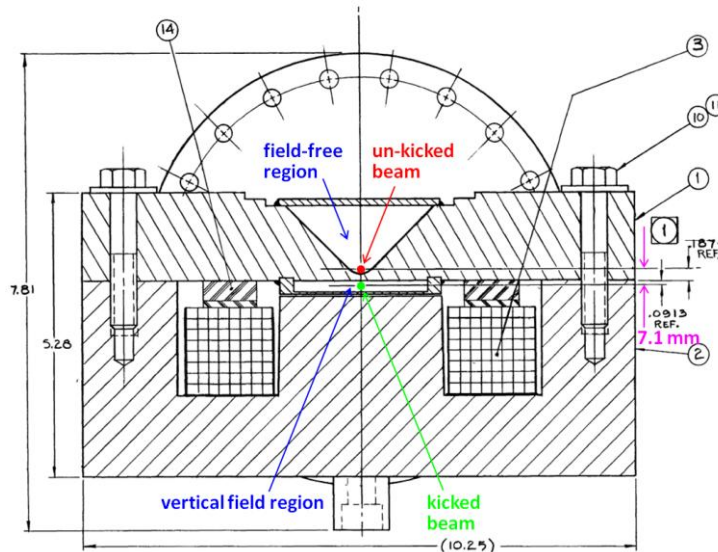


Figure 23. Cross-section of a horizontal deflecting Lambertson septum magnet used in the SLC at SLAC with 7 mm field-transition vertical spacing and a horizontal field integral similar to that needed at LCLS-II [15].

The vertical field in the Lambertson magnet then deflects this electron bunch horizontally into the SXR branch line. Two weak DC vertical dipoles will also be installed in the LTUS line above the septum in order to remove the vertical offset and angle added by the deflector. The small resulting vertical dispersion will also need to be appropriately suppressed. The septum magnet may be a three-hole scheme or perhaps two two-hole septa separated by some optics (see Figure 16). This conceptual design will certainly mature with time.

7.10.3 RF Spreader Cavity

The SC RF-dipole cavity for operation at 325 MHz for particles at $\beta = 1$ is designed for improved electromagnetic and mechanical properties, such as low surface fields and high shunt impedance. An important feature of this cavity is that the fundamental deflecting mode in this cavity corresponds to the lowest order mode, and the wide frequency spacing between the operating and higher-order modes allows for easier dampening of the HOMs. As can be seen in Figure 24, the main contribution to the deflection mode is due to the transverse electric field established between the trapezoidal bars. The straight sections on the inner side of the bar create a uniform transverse electric field at the beam aperture; the aperture region can be further optimized to increase field uniformity, effectively reducing the strength of higher order multipoles of the operating mode. The wide bars connecting to the outer conductor are shaped to reduce surface magnetic fields and decrease multipacting effects. The design and optimization was performed using CST Microwave Studio[®] 2012, using the AKS eigensolver, assuming a loss-free structure, and a tetrahedral mesh. The description and optimization procedure of this type of cavity has been previously reported elsewhere [16,17].

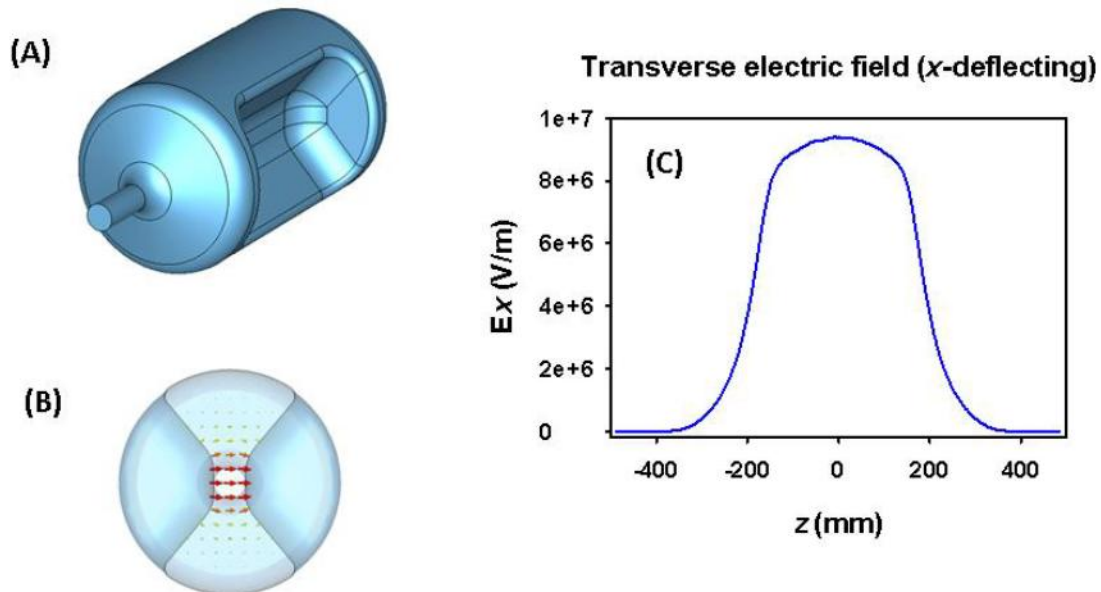


Figure 24. The 325-MHz SC RF-dipole cavity with trapezoidal bars. (A) Perspective view; (B) the vertical cross section and transverse electric field; (C) the deflecting electric field profile along the beam axis.

7.11 References

1. MAD (Methodical Accelerator Design), <http://cern.ch/mad>.
2. M. Borland, “*elegant: A FlexibleSDDS-Compliant Code for Accelerator Simulation*,” Advanced Photon Source LS-287, Sep. 2000.
3. R. Glaus and H. Ingensand, “Tunnel Surveys for New CERN Particle Accelerators”, TS6.2 FIG XXII International Congress, Washington, D.C. USA, April 19-26 2002.
4. Supplemented by private communication with experts at DESY in Hamburg, Germany, 2013.
5. Z. Huang, et al., PRST-AB 7, 074401 (2004).
6. Z. Huang, et al., PRST-AB 13, 020703 (2010).
7. P. Elleuame, et al., NIM-A 455, 503 (2000).
8. The Linac Coherent Light Source Conceptual Design Report, SLAC-R-593, April 2002.
9. K. Bane and P. Emma, “LiTrack: A Fast Longitudinal Phase Space Tracking Code with Graphical User Interface,” Proceedings of the 2005 Particle Accelerator Conference (Knoxville, TN), pp. 4266-4268 (2005).
10. K. Floettmann, “Astra”, DESY, Hamburg, www.desy.de/~mpyflo, 2000.
11. K.L.F. Bane, G. Stupakov, NIM-A 690 106 (2012).
12. M. Placidi, *et al.*, Proc. of IPAC2013, Shanghai, China (2013), p. WEPWA069.
13. M. Placidi, *et al.*, *The NGLS Spreader-Part II*, NGLS Tech. Note 0036, March 18, 2013.
14. *Radiation Safety Systems*, SLAC-I-720-0A05Z-002-R001.
15. SLC Design Handbook, 1984, <http://www.slac.stanford.edu/pubs/slacreports/slac-r-714.html>.
16. S. U. De Silva, J. R. Delayen, “Design Evolution and Properties of the Parallel-bar Rf-dipole Deflecting/Crabbing Cavities”, to be published in PRSTAB.
17. S. U. De Silva, J. R. Delayen “*Analysis of HOM properties of superconducting parallel-bar deflecting/crabbing cavities*” in Proc. SRF2011, Chicago, IL, USA (2011).

8

FEL SYSTEMS

TECHNICAL SYNOPSIS

The LCLS-II project includes two new undulator lines: one for generating hard X-rays (1,000 – 5,000 eV), HXR, and the other one for generating soft X-ray (200 – 1,300 eV), SXR. Each undulator line is comprised of individual undulator segments separated by 1.15-m-long break sections. Each undulator segment will be a variable gap, permanent-magnet planar hybrid device with a nominal minimum gap height of 7.2 mm and a total nominal length of 3.40 m. The HXR undulator line will be made up of 32 individual undulator segments (HXUs), each with 130 26-mm-long periods. The SXR undulator is made up of 21 individual undulator segments (SXUs), each with 87 39-mm-long periods. The poles will be made of vanadium permendur and the magnet blocks of a grade of NdFeB with a high intrinsic coercivity for better resistance to radiation-induced demagnetization. The electron beam will be focused by two separated function Focusing-Drift-Defocusing-Drift (FODO) lattices, using electromagnetic quadrupoles placed between the undulator segments. These focusing or defocusing lenses (quadrupoles) will share the drift spaces (break sections) between the undulator segments with electron beam position monitors, phase shifters, beam loss monitors, and x-ray collimators. The two undulator beam lines are designed to receive electron beams from the new 2 – 4 GeV superconducting linac at high repetition rates. The HXR line will also be able to receive electron bunches from the existing 2.5 – 15 GeV LCLS linac reaching photon energies above 20 keV.

Provision will be made for magnetic tuning of the undulator segments. Tolerances have been developed that will set the magnetic tuning requirements for the individual undulator segments.

The smoothness requirement for the inside surface of the vacuum chamber was analyzed and found to be achievable. Diagnostics for the electron beam will include beam position monitors and beam loss monitors after each undulator segment, and at the ends of the undulator line.

LCLS-II will use a similar undulator alignment strategy as is being used in the current LCLS system, even though there are system differences, such as variable gap, large undulator size, and a smaller available range of electron energies with the superconducting linac, which require special considerations. The electron beam trajectory must be straight to within a few microns at 13.6 GeV over a distance of about 10 m to limit phase errors between electron and photon beams. It is shown here that this specification can be achieved with beam-based techniques.

Self-seeding schemes similar to what is used currently in the LCLS beam line are included to produce nearly transform-limited pulses, minimal jitter in X-ray wavelength and potentially higher spectral brightness by one-to-two orders of magnitude when taken to full saturation.

8.1 Introduction and Overview

The LCLS-II undulator lines will operate as a single-pass Free Electron Laser (FEL) in the self-amplified spontaneous emission (SASE) regime or in self-seeding mode. Exponential gain of the coherent radiation intensity and saturation after about 17 power gain lengths are predicted by theory for the SASE mode. A FEL operating at saturation will have a more stable radiation output. Therefore, a goal in the design of the undulator line is to allow saturation to be reached while minimizing the required undulator line length. Minimizing the undulator line length helped guide many of the parameter choices for the undulator lines and was also used in allocating error tolerances.

8.2 FEL Requirements and Electron Beam Parameters

To generate coherent FEL X-ray beams, the design of the undulator segments as well as the layout of the undulator beamline depends on the parameters of the electron bunches as well as the requirements for the X-ray pulses. A summary of those parameters and requirements is given in this section.

For LCLS-II, the undulator hall will receive electron bunches from both — the existing warm LCLS-I linac (WL) and a new superconducting linac (SCL). The SCL will deliver one beam of high brightness electron bunches at a high repetition rate to the linac-to-undulator beamline (LTU). That beam will be directed to either the HXR or SXR undulator line on a pulse-by-pulse basis. Alternatively, the HXR beamline can receive electrons from the WL while the SCL feeds the SXR beamline. Parameters of the electron beams are listed in the Table 1.

Table 1: Parameters of the Electron Beam from the New SCL and the Existing WL.

Parameter	SCL	WL	units
Electron energy range	2 – 4	2.5 – 15	GeV
Bunch charge range	10 – 100	20 – 350	pC
Bunch repetition rate	≤ 1000	≤ 0.120	kHz
Normalized slice emittance	0.24 – 0.76	0.20 – 0.43	μm
Energy spread	500 ⁺	1400*	keV
Peak current, I_{pk}	≤ 1.0	0.7-5.0	kA

⁺@ $I_{pk} = 1\text{kA}$; *@ $I_{pk} = 3\text{kA}$

The HXR and SXR beamlines will initially be run in both SASE and self-seeded modes. The SXR line will have full self-seeding capabilities. The HXR line will be capable of self-seeding from 4 to 20 keV (self-seeded saturation up to 15 keV) at lower repetition rates. This line will later be upgraded to seeded operation for the intermediate energies from 1 – 4 keV and for high repetition rates. The beamlines should include a sufficient number of undulator segments to saturate in both modes with 20 percent length overhead. The SXR beamline needs to leave

sufficient space (20 m) to later add elliptically polarizing undulators (EPUs). A summary of the minimum photon range requirements are listed in Table 2.

Table 2: Minimum required photon energy ranges for the SXR and HXR with the SCL beam as well as the HXR with the WL beam.

Parameter	SXR SCL	HXR SCL	HXR WL	units
Photon energy range	0.200 – 1.300	1.000 – 5.000	1.000 – 20.000	keV
Seeding support energy range	0.200 – 1.300	1.000 – 4.000	4.000 – 15.000	keV

It is desirable that the X-ray pulse intensity produced with the HXR beamline using the WL beam should be at least 90 percent of the intensity generated by the current LCLS-I undulator for the same electron and photon energies.

8.3 Layout and Operating Range of the Soft and Hard X-Ray FELs

8.3.1 Layout

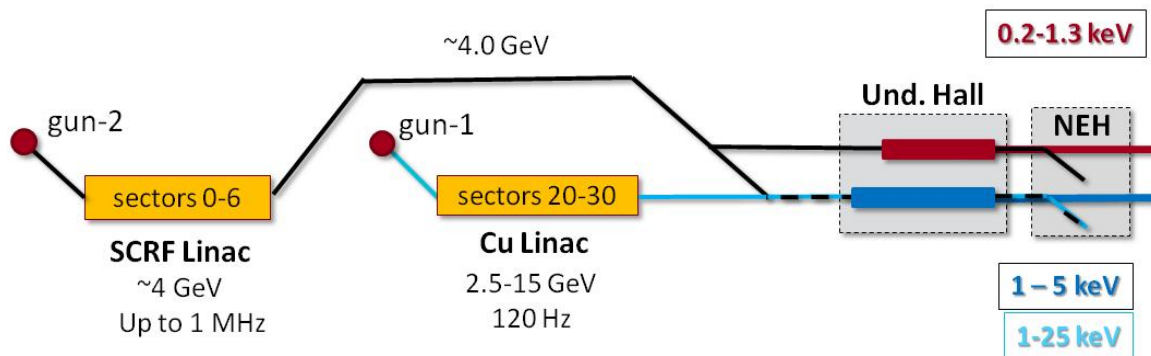


Figure 1: Layout of the to LCLS-II undulators in the existing Undulator Hall. The magnetic/total length of the undulators are 71.25 m / 98.50 m (SXR, top, north tunnel side) and 108.16 m / 149.00 m (HXR, bottom, south tunnel side). Both total length values include an extra 4.55 m for a self-seeding monochromator.

The LCLS-II undulator system will be comprised of two separate undulator lines, one for producing hard X-ray radiation (HXR) the other for soft X-ray radiation (SXR). Both undulator lines will be mounted in parallel and will need to cover different photon energy ranges for the same electron beam energy. A conceptual layout is shown in Figure 1. Each of the two undulator lines will be comprised of individual undulator segments, each 3.4 m in length. These segments will be separated by 1.15-m-long break sections that will house a quadrupole, an RF cavity beam position monitor (RFBPM), a phase shifter, a beam loss monitor, a collimator, and vacuum hardware. A listing of the main dimensions of the undulator lines is given in Table 3.

Table 3: Basic Nominal LCLS-II Undulator Dimensions.

Parameter	Symbol	Unit	HXR	SXR
Individual segment length	L_{seg}	m	3.400	3.400
Number of installed segments	N_{seg}		32	21
Total magnetic segment length	$L_{u,mag}$	m	108.160	71.253
Break section length	L_{Break}	m	1.150	1.150
Self-seeding section length	L_{SS}	m	4.550	4.550
Total undulator line length	L_u	m	149.000	98.950

The two length dimensions given in the caption of Figure 1 and in Table 3 are calculated as follows, based on undulator period length, number of periods per segment, number of segments per undulator, break section length, and length of the self-seeding section:

$$L_{u,mag} = \lambda_u N_{per} N_{seg} \tag{1}$$

$$L_u = N_{seg} L_{seg} + (N_{seg} - 1) L_{Break} + L_{SS}. \tag{2}$$

Table 4: Nominal LCLS-II Undulator Parameters for SASE Operation. The upper photon energy limits are chosen such that the model predict SASE saturation without overhead. In some cases higher or lower limits are achievable but the resulting photon energies would be outside of the base line range. The cases are marked with (*).

Parameter	Symbol	Unit	SXR/SCL	HXR/SCL	HXR/WL
Required K range	K		5.48 – 1.44*	2.44 – 0.47	2.44 – 0.51
Required undulator gap range	g		7.2 – 20.2*	7.2 – 19.4	7.2 – 18.7
Total photon energy range		keV	0.200* – 1.30*	1.00 – 5.00*	1.00* – 25.0*
Photon energy range at 2.5 GeV		keV			1.00* – 1.86
Photon energy range at 3.3 GeV		keV	0.200* – 1.30*	1.00 – 3.58	1.00* – 3.51
Photon energy range at 4.0 GeV		keV	0.243 – 1.30*	1.47 – 5.00*	1.47 – 5.03
Photon energy range at 10.0 GeV		keV			9.17 – 21.9
Photon energy range at 15.0 GeV		keV			20.6 – 25.0*

*Administrative Limit

8.3.2 Nominal X-Ray Parameters and Operating Ranges

As shown in Figure 1, using two different undulator lines (SXR/HXR) and two different electron beam source (SCL/WL), the LCLS-II undulator systems will run three different modes, each with a different energy range:

1. SXR/SCL: Soft-X-ray undulator line using SCL electrons.
2. HXR/SCL: Hard-X-ray undulator line using SCL electrons.
3. HXR/WL: Soft-X-ray undulator line using WL electrons.

The photon ranges available in each of the three modes are listed in Table 4. Graphical representations, including the relative overlap between SXR/SCL and HXR/SCL using the same linac as well as HXR/WL to LCLS-I range, are given in Figure 2 and Figure 3, respectively.

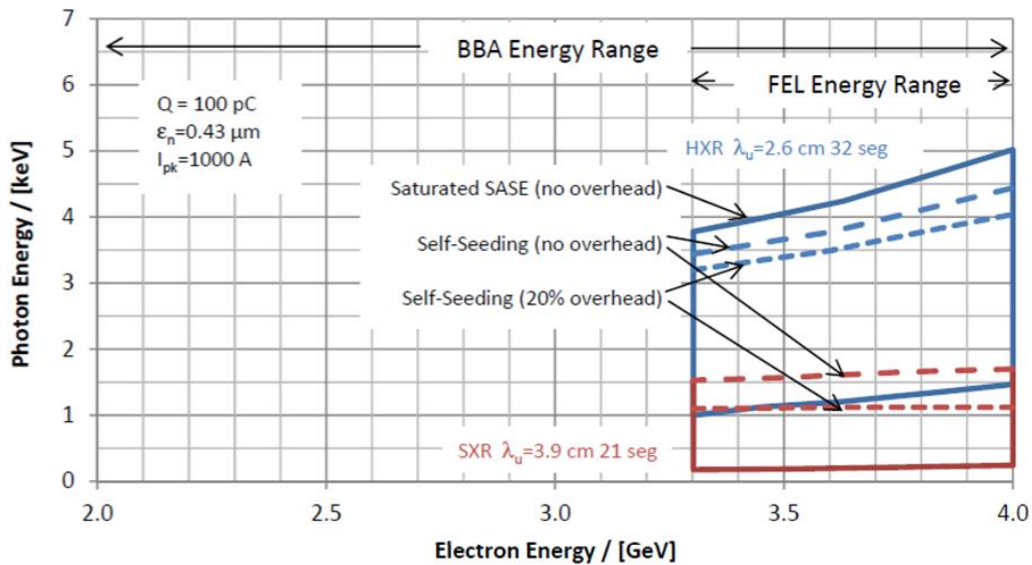


Figure 2: Ranges of available photon energy for the two parallel undulator lines (SXR; red lines, HXR; blue lines) using the same electron beam from the superconducting linac. Note: The lower range is calculated for the smallest undulator gap of 7.2 mm.

The dashed lines in Figure 2 indicate the HXR energy ranges to which seeded operation is to be expected. Please note: even for SASE operation at 4 GeV with otherwise nominal parameters, saturation will only occur reliably for photon energies below 5 keV. Self-seeded saturation should occur up to photon energies of 4.3 keV. The lowest SXR energy of 200 eV will be available over the entire electron energy range of 2-4 GeV. The highest SXR of 1.25 keV will be available for electron energies above about 3 GeV. The lowest HXR energy of 1 keV is available above 3.3 GeV.

As Figure 3 shows, due to its shorter period, the new HXR undulator line will make higher photon energies available. Estimated divergence angles as function of photon energy are plotted in Figure 4 and Figure 5 based on FEL theory [1], Eq. (3), using the photon energy, E_{ph} , the rms

electron beam radius, $\sigma_{x,y}$, and the FEL power gain length, $L_{G,1D}$, with electron beam parameters as indicated in the figures

$$\theta_{FWHM,x,\infty} = \frac{\sqrt{8 \ln(2)}}{\sqrt{\sigma_{x,y}} \sqrt{L_{G,1D}}} \sqrt{\left(\frac{c \hbar}{2 E_{ph}}\right)^3} \quad (3)$$

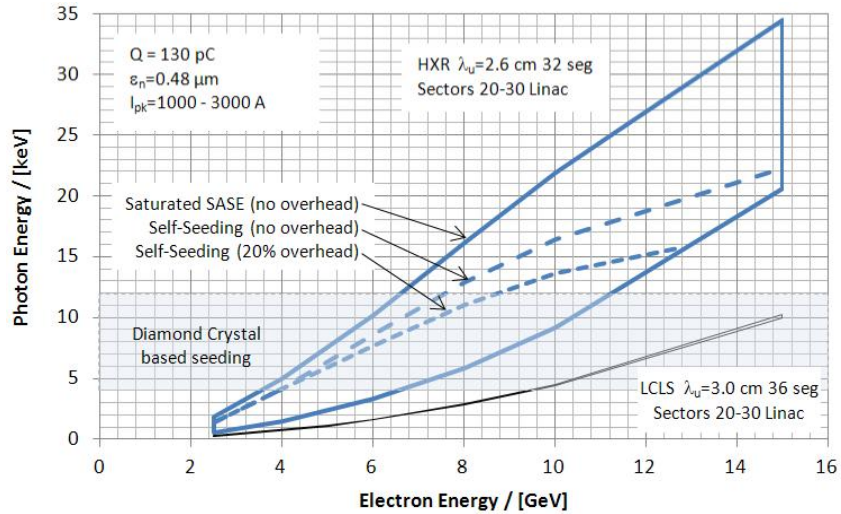


Figure 3: Ranges of available photon energy for the HXR undulator line using the existing warm linac (blue). For comparison, the energy range, available with the existing configuration, has been added (black). Note: the present LCLS-I undulator has a fixed but canted gap of 6.8 mm, while HXU segments will have a minimum gap of 7.2 mm. (Lower line of the blue curve).

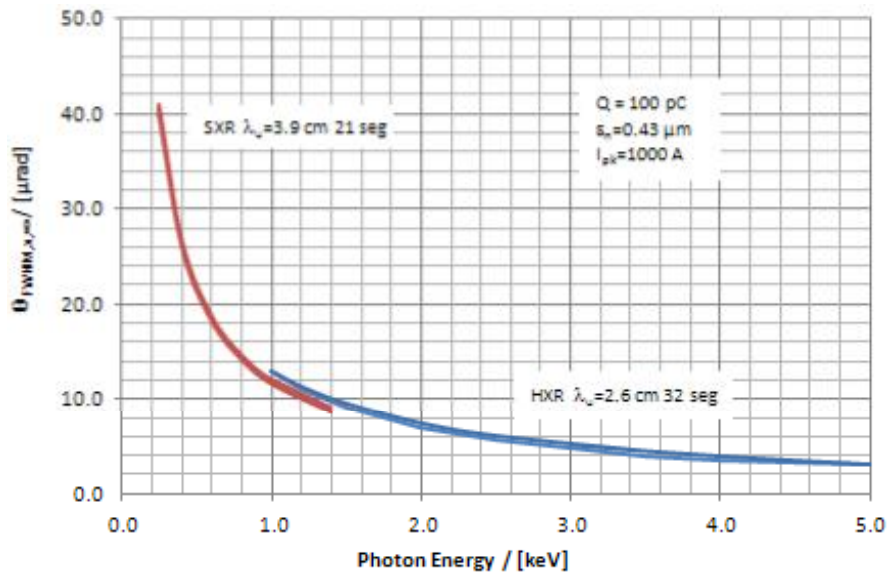


Figure 4: Nominal far-field divergence angles at saturation for the two undulators (red lines for SXR, blue lines for HXR) using the electron beam from the superconducting linac. Note: the indicated ranges are due to the corresponding electron energy ranges at the parameters specified. Working at different electron beam parameters can produce divergences outside the specified ranges.

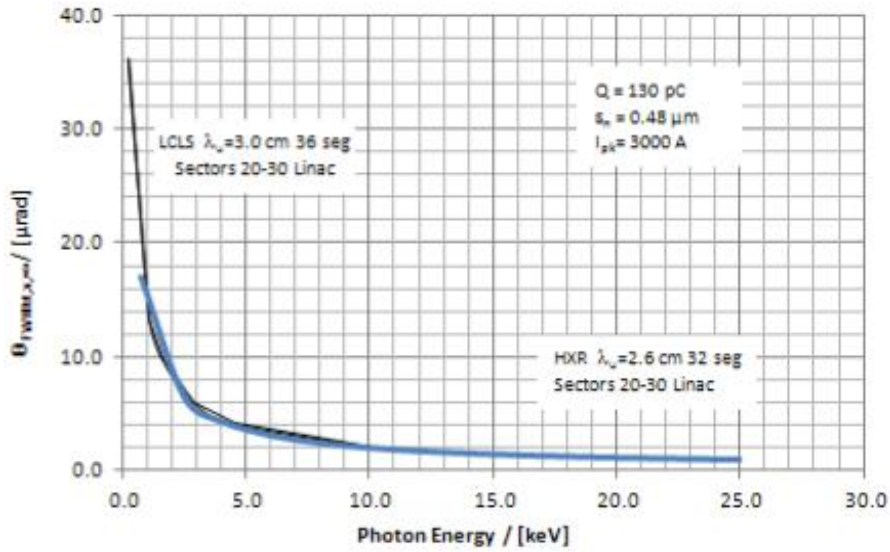


Figure 5: Nominal far-field divergence angles at saturation for the HXR undulator using the electron beam from the warm linac. The values for the present linac are added in black for comparison. Note: the indicated ranges are due to the corresponding electron energy ranges at the parameters specified. Working at different electron beam parameters can produce divergences outside the specified ranges.

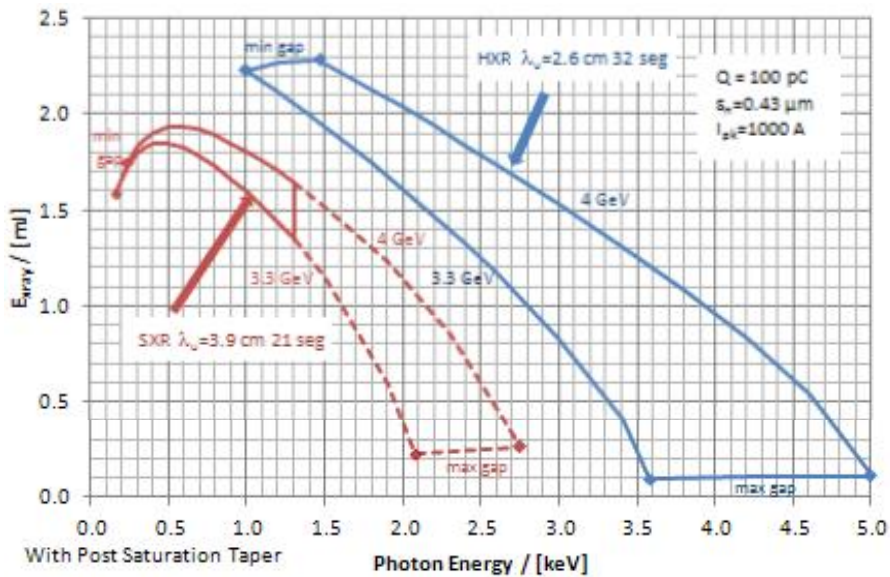


Figure 6: Ranges of per-pulse photon intensity for the two undulators (red lines for SXR, blue lines for HXR) using the electron beam from the superconducting linac. Note, for HXR there is no reliable saturation expected above 4.9 keV for the specified electron beam parameters. The part labeled “max gap” corresponds to the largest gap for which SASE saturation still occurs. The range is 17.5 mm – 19.4 mm for HXR. The dashed SXR lines indicate a region outside the baseline requirements but still reachable with the given parameter set.

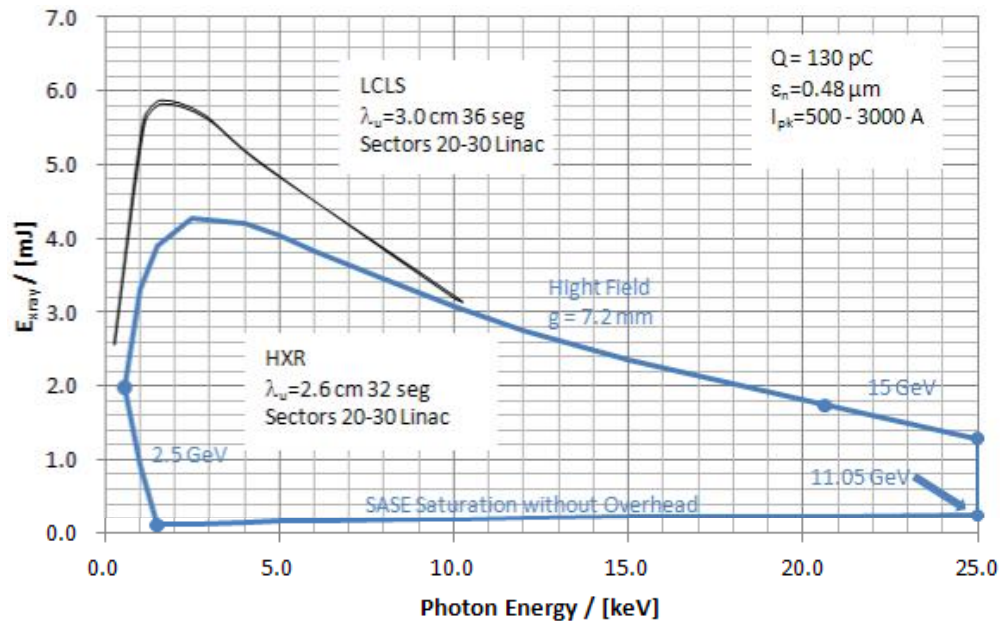


Figure 7: Upper ranges of per-pulse photon intensity for the HXR undulator line using the warm linac (blue line). The blue dots indicate the change of limiting parameters. The top part from (Photon Energy=0.6 GeV, $E_{xray}=1.974$ mJ) to (Photon Energy=20.6 GeV, $E_{xray}=1.7$ mJ) shows operation at the closest possible undulator gap of 7.2 mm. The bottom part shows open gap operation at which saturation still occurs, but without overhead. The performance of the LCLS-I undulator (after the addition of five more segments) has been added for comparison (black lines).

Estimated X-ray pulse intensity ranges in units of mJ/pulse are presented in Figure 6 and Figure 7. The estimates are based on a Ming Xie model [2], modified by peak current, charge, and energy scaling to fit LCLS-I performance measurements. The predictions of that modified model agree well with S2E simulations for LCLS-II (see chapter 10). Note: The allowable maximum average X-ray beam power of 20 W, set for the LCLS-II baseline, could be significantly exceeded if running the FEL at maximum rate with parameters used in Figure 6. Controls will have to be put in place to limit the total average X-ray output power as necessary, such as rate limitation, bunch charge reduction, and X-ray attenuation. Estimated peak and average brightness values are shown in Figure 8 and Figure 9. The average brightness numbers are based on 100,000 pulses per second for LCLS-II SCL, 120 pulses per second for LCLS-II WL and LCLS-I, and for 27,000 pulses per second for the European XFEL.

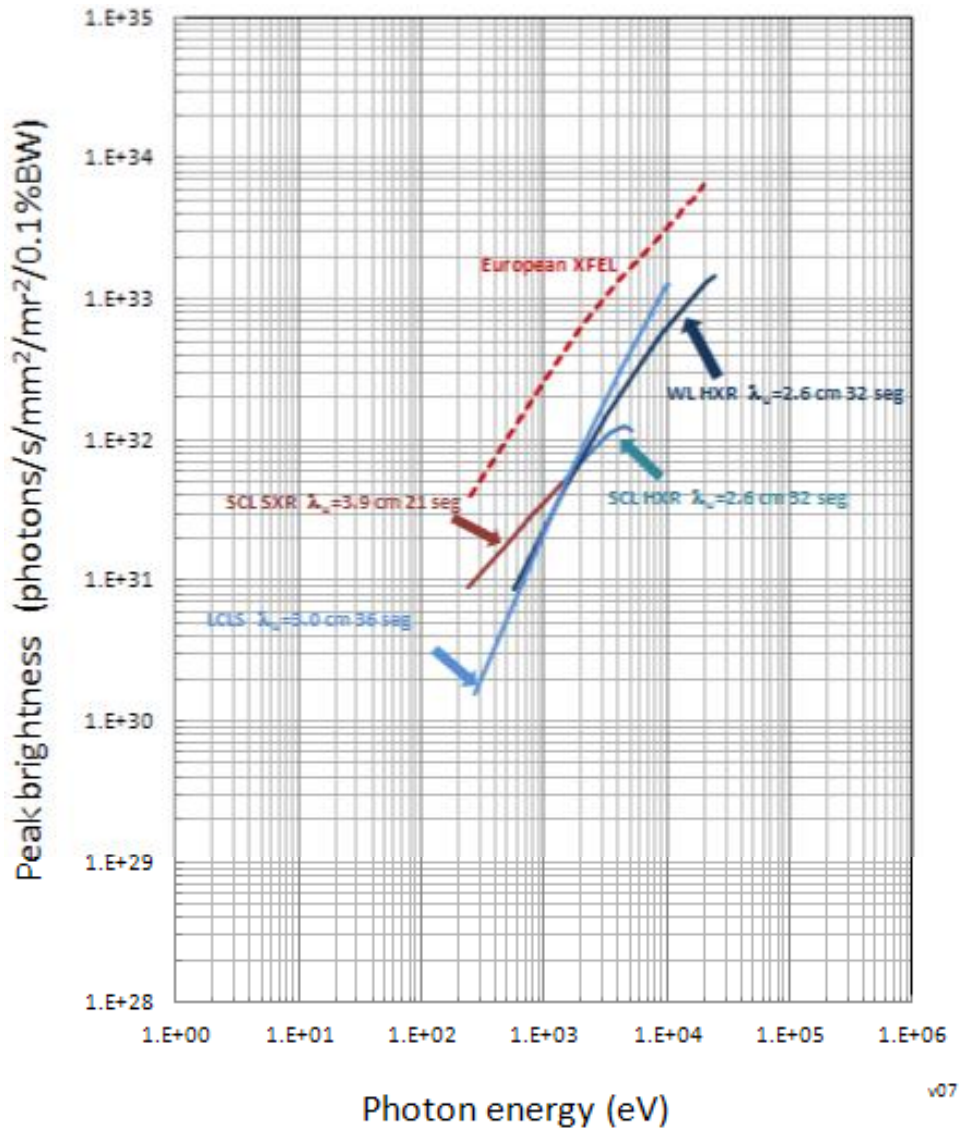


Figure 8: Nominal peak brightness ranges for the two undulators (HXR: dark blue, SXR: dark red) at saturation. In addition, the corresponding ranges for the current LCLS (light blue) as well as the European XFEL (bright red dashed) are shown.

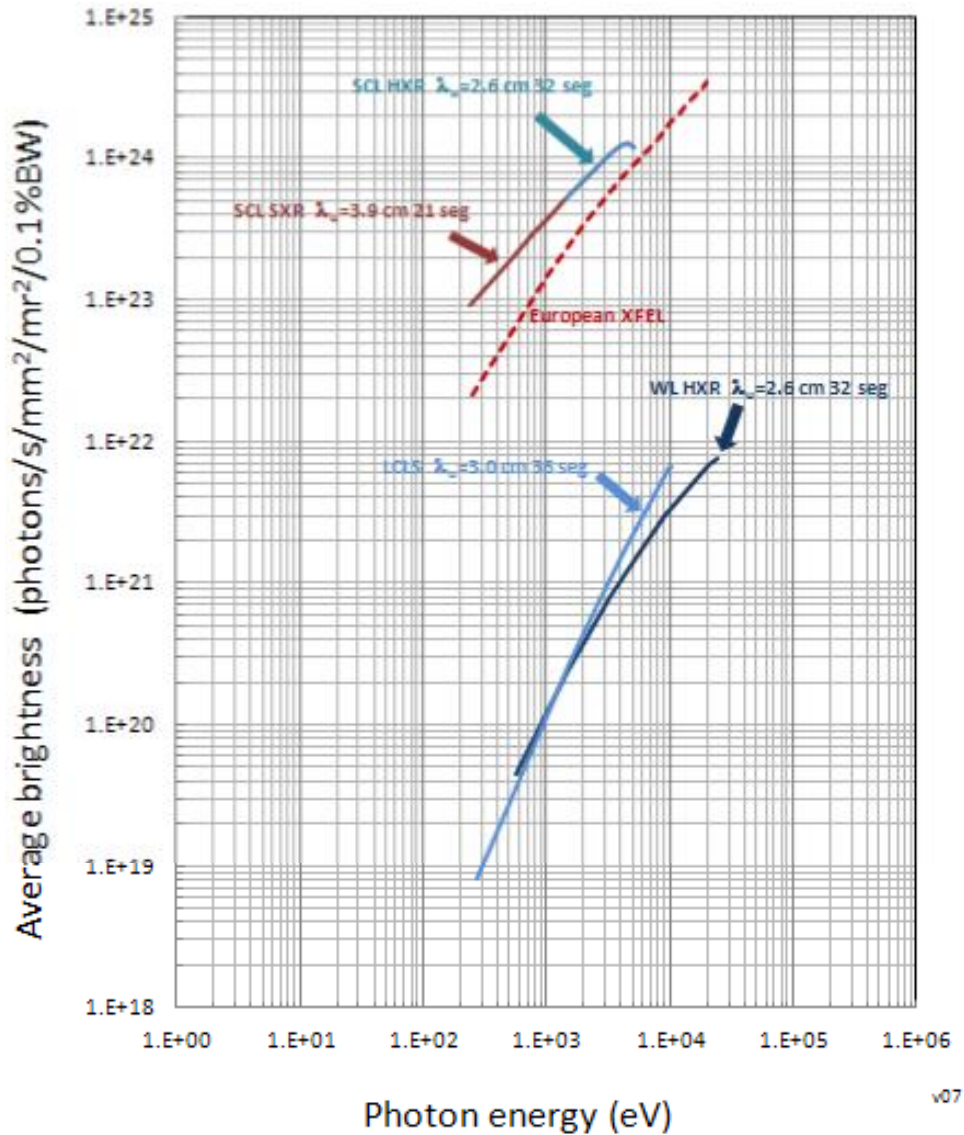


Figure 9: Nominal average brightness ranges for the two undulators (HXR: dark blue, SXR: dark red) at saturation. In addition, the corresponding ranges for the current LCLS (light blue) as well as the European XFEL (bright red) are shown. Note: the HXR and SXR curves exceed the 20 kW limit currently set for LCLS-II.

8.3.3 Electron Beam Arrival Time

The rms of the arrival time jitter of the electron beam at the end of the current accelerator (WL) is expected to be about 50 fs, similar to the measured LCLS-I level. In the LCLS-I, the bunch timing jitter after BC2 with respect to the RF is measured with a BPM after the transverse RF deflector (Figure 10), which effectively converts the arrival time into a transverse “y” position. This BPM y-position jitter is measured with the deflector set at a zero-crossing phase. A calibration is made scanning the deflector phase and recording the BPM y-position, and shows a very linear response: 2.34 mm/deg (970 fs/deg). Consequently, the 0.11 mm rms y-jitter in Figure 10 represents at bunch timing jitter of 46 fs rms, measured with a resolution of 4 fs (0.009 mm).

The rms arrival time of the electron beam from the superconducting linac (SLC) is expected to be smaller.

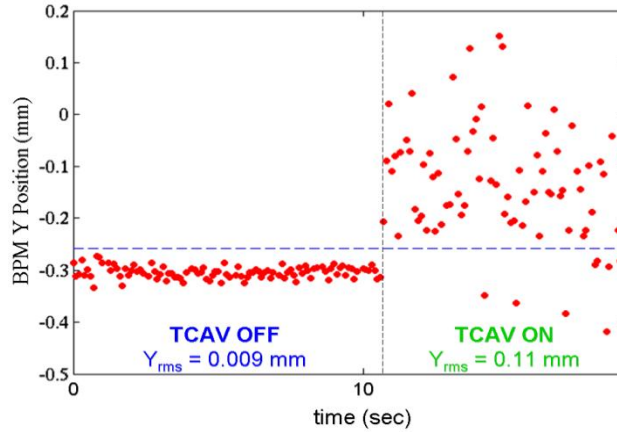


Figure 10: BPM y-position jitter for LCLS-I, measured with Transverse RF cavity 3 (TCAV3) OFF (left side) and ON (right side). The increased y-jitter represents the bunch timing jitter of 46 fs rms with respect to RF.

8.3.4 Pulse Duration

The required peak current for lasing within the designed undulator length is 1 kA for both the HXR and the SXR undulator lines; hence, the maximum allowable electron pulse duration is directly proportional to the core charge. For example, for bunch charges of 100 pC, we expect the electron FWHM pulse length to be about 100 fs or less. At 20 pC, we expect the electron FWHM pulse length to be about 20 fs. Shorter X-ray pulse lengths can be obtained with lower charge (~1 pC) and more aggressive compression; alternatively, they may be obtained with the slotted spoiler method. Thus, the expected photon pulse length range is 100-1 fs. Note: methods for pulse duration control, discussed here, will all affect both the HXR and SXR beamlines and will therefore require coordination between experiments.

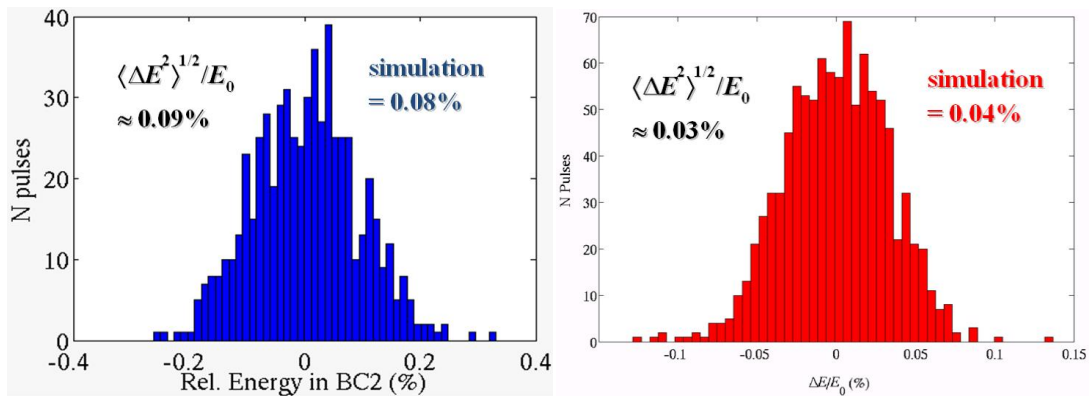


Figure 11: Measured LCLS-I electron energy jitter in BC2 (at 4.3 GeV, blue) and at the linac end (13.6 GeV, red).

8.3.5 Photon Energy

The FEL photon energy ranges are given in Table 4. The expected electron energy jitter from the warm linac at the entrance of the undulator is about 0.03-0.09 percent (see Figure 11), depending on the electron beam energy. The resulting photon energy jitter should be twice as much (*i.e.*, 0.06-0.18 Percent). The photon energy jitter from SCL operation is expected to be smaller.

8.3.6 Bandwidth

The expected FWHM FEL bandwidth for WL operation is about 0.2-0.3 percent for hard X-rays (about 10 keV) and 1-1.5 percent for soft X-rays (1-2 keV). If the bunch is over-compressed in BC2, linac wakefields will add to the rf chirp and produce an energy-chirped electron bunch at the entrance of the undulator. The chirped FEL bandwidth can be as large as 1 percent for hard X-ray and a few percent for soft X-rays. Figure 12 shows the measured LCLS-I hard X-ray spectra under various compression conditions. For SCL operation narrower bandwidths are expected.

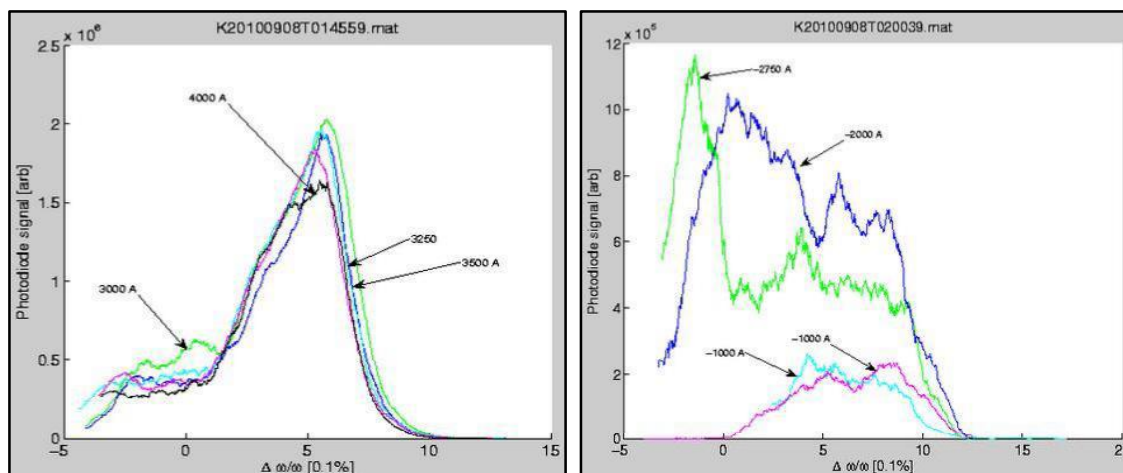


Figure 12: Measured LCLS-I FEL spectrum at 8.3 keV using a scanning monochromator. The negative currents in the right hand side graph indicate overcompression.

8.3.7 Pulse Energy

The estimated per-pulse energies for operation at low repetition rates are given in Figure 6 and Figure 7. Currently an upper limit of 20 W of the average X-ray power does not allow simple repetition rate scaling for average X-ray energy calculations. The 20 W (see discussion in chapter 11) energy cap needs to be applied.

8.3.8 Coherence

The FEL is expected to have high degree of transverse coherence, approaching 80-90 percent at the FEL saturation. The expected temporal coherence length will range from a few hundred attoseconds to a few femtoseconds, depending on the FEL wavelength.

8.4 Undulator Beamline Components

Both undulator beamlines are comprised of equivalent sets of components, as shown in Figure 13. Between the undulator segments, which will be spaced 4.55 m on center, there will be 1.15-m-long (nominal length) break sections. In each these there will be components (i.e., quadrupoles, radio frequency cavity beam position monitors, phase shifters, Collimators, and beam loss monitors, that are necessary for controlling and monitoring the electron beam as well as monitoring radiation levels. Table 5 lists the total number for each component type.

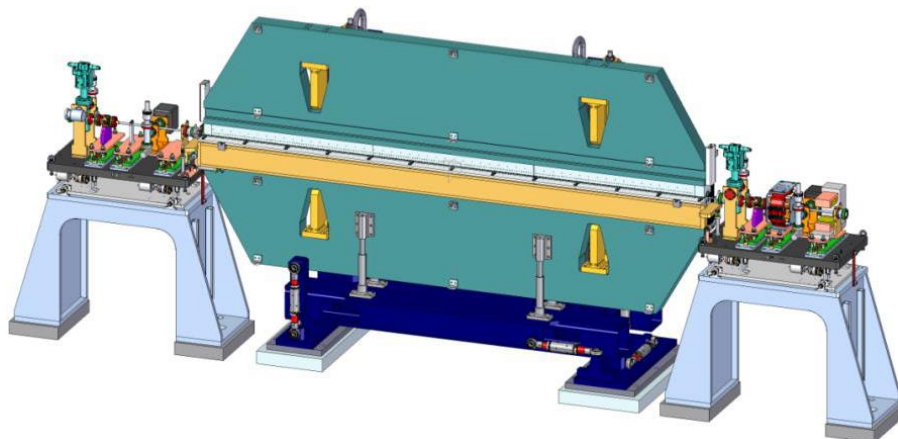


Figure 13: Conceptual layout of a cell in each of the two undulator lines. The board supporting the break section components will be equipped with remote x/y position adjusters in support of beam base alignment.

Table 5. Basic Break Section Parameters.

Parameter	SXR Values	HXR Values	Unit
Number of break sections	22	32	
Break length between segments	1.15	1.15	m
RFBPMs	18	23	
Quadrupoles	22+4	33	
Number of PSs	20	31	
Number of COLLs	21	32	
Number of BLMs	20	32	

These components will be mounted on a common support that can be precisely positioned by remote control. Motion ranges and component stability during motion are listed in Table 6. Some of the break section components are also required upstream and downstream of each undulator line. Only those components between undulator segments and those directly preceding the first undulator segment and following the last undulator segments require motion control.

Table 6. Break Section Components Mover Parameters.

Parameter	SXU Values	HXU Values	Unit
Horizontal motion range	± 1.0	± 1.0	mm
Horizontal motion accuracy (rms)	0.1	0.1	μm
Vertical motion range	± 1.0	± 1.0	mm
Vertical motion accuracy (rms)	0.1	0.1	μm
Acceptable H/V vibration amplitude >1 Hz	<0.25	<0.25	μm
Roll stability over full motion range (rms)	<1	<1	mrad

8.4.1 Segments

The undulator segments shall be planar variable gap, permanent magnet hybrid type undulator magnets. The wiggle plane shall be oriented horizontally, which will produce horizontally polarized radiation. A vertically oriented wiggle plane would be preferable for many experiments, a compact vertically polarizing undulators is being investigated. The basic parameters of the undulator segments are listed in Table 7.

Table 7. Basic Undulator Segment Parameters.

Parameter	HXU Values	SXU Values	Unit
Undulator period length (λ_u)	26	39	mm
Number of effective periods per segment (N_p)	130	87	
Number of poles per segment	260	147	
Undulator type	Planar	Planar	
Undulator magnet type	PM hybrid	PM hybrid	
Gap type	Variable	Variable	
Magnet material	Nd ₂ Fe ₁₄ B	Nd ₂ Fe ₁₄ B	
Wiggle plane	horizontal	horizontal	
Magnetic field symmetry	antisymmetric	antisymmetric	
Minimum operational gap height	7.2	7.2	mm
On-axis vertical effective field at min. oper. gap	1.01	1.51	T
K_{eff} at minimum operational gap	2.44	5.48	
Minimum full open gap height	100	100	mm
Maximum operational gap height	19.4	20.2	mm

8.4.2 Quadrupole & Trajectory Correctors

The quadrupoles in both undulator lines will be air-cooled electro-magnets with laminated core and three separate coil circuits: (1) quadrupole (2) horizontal correction (3) vertical correction. The coils will be dimensioned such that heat dissipation to the tunnel air is minimized. The requirements for the quadrupole are specified in Table 8. There, the item ‘‘Mag. center

stability for $\Delta I_Q = \pm 20\%$ is needed when using the quadrupole excitation current to measure the amount of kick this quadrupole gives to the electron beam. That procedure scans of the quadrupole current amplitude by ± 20 percent and measures the downstream electron beam trajectory to determine the kick amplitude. The item “Mag. center stability under corr variation (rms)” implies that the actual magnetic center change produced by the corrector excitation current should not differ from the expected value by more than the specified amount.

8.4.3 Collimator

Due to the higher electron beam power planned for LCLS-II compared to LCLS-I, the increase in radiation components that could potentially demagnetize the permanent magnets in the undulator segments or damage the vacuum chamber needs to be considered. An x-ray collimator will be installed in front of each undulator segments to remove radiation components from the photon beam that have the potential of being lost were they allowed to travel into that segment’s vacuum chamber. Electron beam collimators will be installed upstream of the undulator hall as part of the LTU.

8.4.4 RF-BPM

The capability to precisely measure the transverse position of each individual electron bunch to sub-micron precision is essential for the application of electron beam base alignment (BBA). The radiofrequency cavity beam position monitors (RFBPMs) used for LCLS-I provide sufficient resolution of better than 250 nm (rms). The use of a similar design on LCLS-II is encouraged. Alignment can take advantage of the fact that the RFBPM body has a circular shape and that the mechanical center of the device coincides with the center of the circular body shape that can be observed when the device is installed. It is important that an RFBPM is installed next to every undulator quadrupole. Two RFBPMs also need to be installed before the first and after the last undulator segment, as well as one RFBPM in each dump line. These are not in the undulator system and therefore not part of this chapter.

Table 8. Quadrupole Requirements.

Parameter	Values	Unit
Integrated gradient range	± 4.0	T
Quadrupole excitation current (I_Q) range	± 6.0	A
Magnetic center stability (rms) > 1 Hz	<2.0	μm
Mag. center stability for $\Delta I_Q = \pm 20\%$	<1.0	μm
Range of integrated horiz. and vert. corr field	± 1.0	mTm
Corrector excitation current range	± 1.0	A
Mag. center stability under corr variation (rms)	<1.0	μm
Maximum energy dissipation	<30	W

8.4.5 Phase Shifter

While travelling along the undulator beamlines, the longitudinal velocity of the electrons, v_z , is less than that of the electromagnetic field of the X-ray beam. Inside the undulator segments, v_z is reduced by the electrons' transverse wiggle motion caused by the alternating magnetic undulator field, such that each electron falls behind the electromagnetic wave by exactly one radiation wavelength in one undulator period. Maintaining this phase slippage is important for obtaining peak FEL performance. This means that when the electron beam travels the distance, $L_{unit} = L_{eff,u} + L_{Break}$, between the centers of two consecutive undulator segments, the total phase slippage, $\Delta\phi_{L_{unit}}$, should be a multiple, ν , of 2π . L_{Break} is the length of the free space distance between undulator segments. This condition will only be true at certain values of the undulator K parameter. For variable gap undulators, this is generally not true. The deviation needs to be corrected by adding a phase shifter device in the break section that delays the electron bunches by a settable amount, such that:

$$\Delta\phi_{L_{unit}} = \Delta\phi_{L_{eff,u}} + \Delta\phi_{L_{break}} + \Delta\phi_{PS} = 2\pi\nu. \tag{4}$$

Here, $L_{eff,u}$, the effective undulator length, is the equivalent distance over which the phase advance is equal to 2π per period. The phase shifter will be based on a short pure permanent magnet undulator design. Requirements for the phase shifter are different for the two beamlines and are listed in Table 9.

Table 9. Phase shifter requirements.

Parameter	SXR Values	HXR Values	Unit
Minimum phase shifter gap, $g_{PS,min}$	10	10	mm
Maximum phase shifter gap, $g_{PS,max}$	100	100	mm
Maximum operational phase shifter gap	40	30	mm
Maximum operational phase integral (PI_{max})	15,840	5,270	T ² mm ³
Minimum phase integral (PI_{min}) estimate at $g_{PS,max}$	80.43	11.94	T ² mm ³
Range of first vertical field integral IIB_y	±20	±20	μTm
Range of second vertical field integral $I2B_y$	±50	±50	μTm ²
Range of first horizontal field integral IIB_x	±20	±20	μTm
Range of second horizontal field integral $I2B_x$	±45	±45	μTm ²
Phase shifter accuracy (rms)	3°	8°	
Minimum phase shifter gap setability (rms)	17	4	μm
Max variation of IIB_y during scan	±2.2	±2.2	μTm
Max variation of $I2B_y$ during scan	±45	±45	μTm ²
Max variation of IIB_x during scan	±2.2	±2.2	μTm
Max variation of $I2B_x$ during scan	±45	±45	μTm ²

8.4.6 Ambient Field Correctors

There will be small ambient magnetic fields present in the undulator hall other than those intentionally created by the beam steering magnets that can modify the electron beam trajectory. The dominant sources are the earth magnetic field and magnetic components such as vacuum pumps, motors, and magnetized steel pieces. The amount of trajectory errors that these fields will generate will depend on the locations of those magnetic components and on the gap height of the undulator segment. In the case of the earth field, those extra field components will be distributed more or less homogeneously along the vacuum chamber and will deflect the electron beam onto a circular trajectory. The BBA procedure (see section 8.8.3, above) will mitigate the effect by reducing the trajectory deviations at the positions of the BPMs, thereby creating a scalloped trajectory through the undulator segments. Those scalloped trajectories still cause a position-dependent increase in path length and thus introduce a phase shake along the segment and a phase error with respect to the next segment. They also affect the convergence of the BBA procedure. In order to further mitigate this effect, dipole steering coils (ambient field correctors) will be integrated in the segment vacuum chamber as described in an LCLS technical note [3]. If powered with two independent power supplies, four insulated single-turn copper wires mounted at the corners of the segment vacuum chamber can provide independently controllable horizontal and vertical corrector fields that are constant along the beam axis. Based on measurements done at the European XFEL undulator laboratory [4], which used large Helmholtz coil arrangements to emulate the external fields, corrector field requirement increases with gap; maximum correction field values of $B_x = 0.6$ G and $B_y = 1.4$ G should be sufficient for all cases. Relevant parameters for the ambient field correctors are listed in Table 10.

Table 10. Ambient Field Corrector Parameters.

Parameter	SXU Values	HXU Values	Unit
Maximum B_x corrector field	± 0.6	± 0.6	G
Maximum B_y corrector field	± 1.4	± 1.4	G
Horizontal corrector wire center separation	14.2	14.2	mm
Vertical corrector wire center separation	5.0	5.0	mm
Maximum current for B_x corrector field	± 1.0	± 1.0	A-turn
Maximum current for B_y corrector field	± 1.4	± 1.4	A-turn
Maximum wire current	± 2.4	± 2.4	A-turn
Maximum dissipated power	1.3	1.3	W
Estimated vacuum chamber temperature rise*	0.2	0.2	K

*without cooling

The dependence of the corrector strength on undulator segment gap height can be determined during operations based on the reading of downstream RFBPMs. This method, however, will only provide information for relative corrector strength change requirements, but will not provide information for the required absolute corrector strength. Those absolute corrector strength values

can only be obtained based on measurements of the magnetic fields along the beam axis when the undulator segments are installed in the tunnel and set to a known gap before the vacuum chamber is installed. The required corrector setting at that gap can be calculated based on the difference of those measured fields to the equivalent fields measured in the magnet measurement facility with the same gap during tuning.

8.4.7 Beam Loss Monitors

Protecting the magnetic material from demagnetization due to radiation generated by the electron beam is very important for a continuous and reliable operation of the facility. Beam Loss Monitors (BLMs) that are integrated in the facility's Machine Protection System (MPS) are instrumental in protecting the undulators. The MPS is to be configured to prevent the electron beam from entering the undulator hall if radiation levels, as detected by the BLMs, exceed a threshold. The devices can be constructed very similarly to those used to protect the LCLS-I undulator, i.e., a quartz Čerenkov radiator, monitored with a photomultiplier. The shape of the radiator needs has been changed in a prototype to reduce the sensitivity gradient exhibited by the existing BLMs [5]. The data acquisition system must be set up for continuous integration of the BLM signals. An upstream wire monitor can be used to calibrate the trip points of the beam loss monitors.

8.5 FODO Lattice Optimization

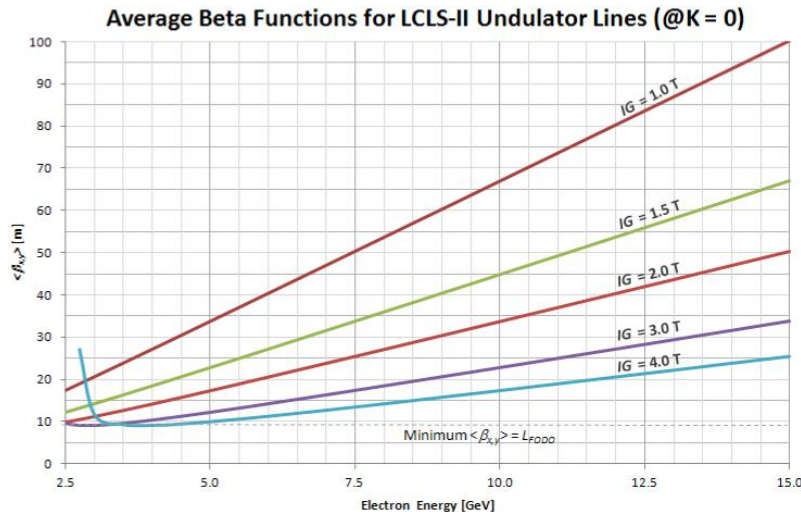


Figure 14: Average beta-functions over the operational energy range for the two undulators

Both LCLS-II undulator lines (HXR and SXR) use a FODO lattice to focus the electron beam and keep the average beta function constant along the undulator. Both FODO lattices have the same cell length of 4.55 m but can have different focal length. The average beta function required for optimum FEL gain is roughly proportional to electron energy for a given gap and undulator period. At a constant (but small) strength of focusing quadrupole magnets, the beta function will be proportional to electron beam energy. Also, the beam-based-alignment algorithm favors a

constant quadrupole gradient. Therefore, at LCLS-II, as was the case at LCLS-I, the FODO lattice will operate a constant gradient. The integrated quadrupole gradients (IG) can be independently chosen for each undulator line but will be kept invariant with energy changes in support of BBA. The integrated quadrupole gradient needs to be below about 2.5 T for SCL operation, while for WL operation higher gradients can be used at a loss of the very low energy range. Figure 14 demonstrates how average beta function depends on beam energy and quadrupole gradient.

8.6 Undulator Magnetic Measurements and Tuning

Most of the magnetic measurement and tuning techniques that were used for LCLS-I can be applied to LCLS-II. Many new challenges must be overcome, however. These include the Earth's magnetic field, fiducializing large undulators, limitations of the Magnetic Measurement Facility (MMF). A summary of the current status and potential challenges follows.

8.6.1 Undulator Tuning

The undulator tuning for LCLS-II will be similar to LCLS-I, but the variable strength of the undulators will require a much more extensive set of measurements. There will also be differences in the shimming techniques used. Finally, the lack of a magnetic shield on the undulators will require measurement and correction of the background magnetic fields.

The principles of undulator tuning have been documented in a technical note [6]. The note shows how most quantities of interest are calculated and which adjustments to the undulator magnetic field must be made to change these quantities. The principles outlined are the same for LCLS-II as they are for LCLS-I.

The implementation of shims for LCLS-II will be different compared to LCLS-I. In LCLS-I, the gap was fixed and the poles were fixed. All correction fields were made by adding magnetic material which altered the undulator field. In LCLS-II there will be (a) individually positionable poles that will allow for field corrections to be made by changing vertical position and angle of each pole and (b) optionally insertable permanent magnet rotor pairs above top poles and below bottom poles to allow for individual pole energization refinement. These two "knobs" have different gap dependencies, which, when appropriately combined, are intended to cancel the net error fields from all sources over the entire range of gap motion. The effect of pole motions and rotor pair strength and orientation will be measured and parameterized. These parameterizations will be used in a computer program or by a tuning expert to determine the necessary adjustments to correct the trajectories, phase, etc. The computer algorithm to determine the shim strengths for LCLS-I undulators is given in [7].

For adjustable gap undulators, the shimming to correct trajectories, phase, field integrals, etc. is first done at a tuning gap near the minimum gap. The tuning gap is chosen to minimize the phase errors caused by undulator jaw deformations due to magnetic forces. By choosing a tuning gap near the minimum gap, the undulator field errors are corrected when the effect of the field errors is the largest. As the gap is increased, the effect of both the field errors and the correction

fields is reduced. If the field errors and corrections do not track each other as the gap is changed, then additional corrections will be made per the above algorithm, to accommodate the range of gap motion. Additional powered dipole coils (see section 8.7.3 below) will make corrections to the trajectories over a large distance for distributed errors, such as compensating external fields whose effect may change as the gap is changed.

8.6.2 Magnetic Measurement Systems

A number of different systems are used to measure undulators in the Magnet Measurement Facility (MMF) [8][9]. A brief list follows. Hall probes carried by a precision bench are used to determine trajectories, phase errors, K value, etc. [10]. The average trajectories are checked using one-period-long coils. This check ensures that errors like the Planar Hall Effect are small. Hall probes are unsuitable for accurate determination of the overall field integrals. A long coil system gives the first and second field integrals [11][12]. The undulators are aligned relative to the bench using a capacitive sensor system and a cam mover system [13]. A temperature measurement system accurately gives the undulator temperature [14][15]. Fiducialization is done using a combination of Hall probe measurements in special high-gradient magnets attached to or mounted near the undulator and either a Coordinate Measuring Machine (CMM) or a laser tracker to locate relevant tooling balls [16][17]. The CMM is also used to do extensive mechanical measurements on the undulator, or various parts thereof. For LCLS-I, the CMM was also used to measure the girder that holds the undulator [18].

The MMF has some capability to repair damaged undulators. A permanent magnet block magnetizer is used to repair radiation damage. Measurement systems must check the blocks before and after magnetization. A Helmholtz coil system is used to measure the magnetic moment of the blocks. A Hall probe mapping system is used to localize radiation damage in magnet blocks.

The MMF also has a system to accurately fiducialize quadrupoles, which is required for the quadrupoles between undulator segments. The fiducialization is done by a vibrating wire system built onto a coordinate measuring machine [19][20][21][22].

The MMF has several calibration systems. A large electromagnet is used to calibrate Hall probes. Both conventional and flowing water NMRs are used. A chiller keeps the probe at room temperature in the magnet. The temperature of the undulators is measured with thermistors. The thermistors are calibrated in a water bath using a reference thermometer [23]. The reference thermometer can be inserted in any thermistor mount to check the measurement in place. The magnets used to fiducialize the undulators need to be calibrated to determine a point with given magnetic field relative to tooling balls [24]. A special fixture allowing magnet flips is used for this purpose.

The MMF employs a number of secondary measurement systems to constantly check for errors. The undulator benches have reference magnets which are measured by the Hall probe and in which an NMR can be inserted to constantly monitor Hall probe accuracy. Survey crews use alignment scopes to check for significant fiducialization errors. Hand-held reference

thermometers verify temperature. Most importantly, reference magnets (undulator or quadrupole) are used to continuously monitor the repeatability of the whole measurement process.

A reference undulator was measured many times during the tuning of the LCLS-I undulators. These data sets give estimates of the random errors in the tuned undulators [25]. The measured trajectories in the reference undulator were stable and straight to within $\pm 2 \mu\text{m}$ (at 13.6 GeV). Changes in the phase errors were less than ± 2 degrees between data sets. The phase advance in the cell varied by less than ± 2 degrees between data sets. The rms variation between data sets of the first integral of B_x was $10 \mu\text{Tm}$, and the rms variation of the second integral of B_x is $17 \mu\text{Tm}^2$. The rms variation of the first integral of B_y was $7 \mu\text{Tm}$, and the rms variation of the second integral of B_y is $12 \mu\text{Tm}^2$. The rms variation of the x-position of the fiducialized beam axis was $35 \mu\text{m}$ in the final production run. This corresponds to an rms uncertainty in the K value of $\Delta K/K = 2.7 \times 10^{-5}$. The rms variation of the y-position of the fiducialized beam axis was $4 \mu\text{m}$ in the final LCLS-I production run.

The MMF presently has all equipment necessary to measure and tune LCLS-I undulators. A laboratory whose temperature is controlled to 0.1°C contains two undulator measurement benches, a high precision, 7 meter bench from Kugler Corp. and a less precise bench by Dover Corp. For LCLS-II, we plan to upgrade the measurement lab and incorporate additional measurement and tuning capacity at LBNL to accommodate the production run schedule.

8.6.3 Earth's Magnetic Field

The LCLS-I undulators were measured in the same orientation as they have in the tunnel [26] [27]. This was done to minimize background field errors. In addition, the LCLS-I undulators had magnetic shields to reduce the effect of the difference of the background field in the tunnel compared to that in the MMF.

LCLS-II undulators will most likely not have magnetic shields because of their variable gap design. This makes background fields a much larger problem. The undulators will continue to be measured in the same orientation as they will have in the tunnel. This will minimize the effect of the external horizontal field, especially as the gap is opened.

Without a magnetic shield on the undulators, further effort to deal with external fields is required. Trim coils will be incorporated into the four corners of undulator beam pipe over its full length [3]. A large Helmholtz coil will be built to apply external fields to a small number of undulators in order to characterize the resulting field in the gap and also the necessary current in the trim windings, in order to correct it. A map of the magnetic field in the tunnel will be made. The difference between the tunnel field and the field in the MMF, along with the characterization from the test undulator in the large Helmholtz coil, will determine how to set the current in the trim windings for each undulator position in the tunnel. A portable system to measure field integrals will be used in the tunnel to check the final field integrals. A portable vibrating wire system for making these measurements in the tunnel is under development [28]. Moving coil measurements as done in the MMF could alternately be performed.

8.6.4 Fiducializing Large Undulators

The LCLS-I undulators were fiducialized in a three-step process [29][30]. First, the Hall probe was positioned to move along the desired beam axis. The distance the Hall probe was required to move from the beam axis to a zero field point in fiducialization magnets at each end of the undulator was recorded. Second, the distance from the zero field point to tooling balls on the fiducialization magnet was determined using a special calibration fixture. Third, the distance from the tooling balls on the fiducialization magnets to tooling balls on the undulator was determined with a CMM.

Sine the LCLS-II undulators are large, the final step of measuring tooling ball positions will not be possible with a CMM. Other measuring instruments, such as laser trackers, are accurate to approximately 50 micrometers and will be used instead of the CMM. A touch probe system which will effectively turn the measurement bench into a CMM is also under development.

8.6.5 Throughput

The throughput of the MMF for LCLS-I undulators was approximately one undulator every two weeks. This included time to come to thermal equilibrium, mechanical measurements on the CMM, mechanical straightening of the gap centerline with checks on the CMM, rough tuning on the Dover bench, fine tuning on the Kugler bench, making a final data set on the Kugler bench, fiducialization on the Kugler bench, fiducialization on the CMM, and final mechanical measurements on the CMM. All this work was done in parallel at the CMM, Dover bench, Kugler bench, and at a separate stand for mechanical work, such as applying shims and gap straightening.

LCLS-II undulators will require all the steps mentioned above. In addition, LCLS-II undulators will have an adjustable gap. This will require a larger tuning effort and a more extensive final data set. Field integral corrections as a function of gap must be determined. We estimate that the throughput of the MMF for adjustable gap undulators will be approximately one undulator every four weeks.

8.7 Undulator Magnet Design

This section will describe the magnetic and mechanical design of the HXU (hard X-ray undulator) and SXU (soft X-ray undulator). The HXU and SXU lines are made up of multiple undulator segments of approximately 3.4 m in length. The following sections will describe features of the design in more detail.

8.7.1 Choice of Magnetic Material

The following are the primary magnet material specifications assumed for the magnetic design:

- The minimum average remanence (B_r) of the finished material at 20 degrees C, after thermal stabilization, shall be equal to or greater than 1.3 T.

- The minimum coercivity (H_c) of the finished material at 20 degrees C, after thermal stabilization, shall be equal to or greater than 970 kA/m (12.2 kOe).
- The intrinsic induction (H_{cj}), after thermal stabilization, shall be equal to or greater than 1670 kA/m (21 kOe). The intrinsic induction versus magnetizing force curve ($[B - \mu_0 H]$ versus H) shall be linear in $[B - \mu_0 H]$ to within 2.5 percent in the second quadrant and to at least 110 percent of the nominal coercive force (H_c) at 40 degrees C after thermal stabilization.
- The dipole moment of each block shall be within ± 1.0 percent of the average obtained for all the blocks of each type at 20 degrees C after thermal stabilization.
- The dipole moment magnetization vector of each block shall be within ± 1 degree of the nominal direction.

The analysis of HXU and SXU magnetic designs shows that magnets with these specifications are likely to result in undulators that are capable of being tuned to meet trajectory and optical phase requirements. The analysis also shows that when installed into the HXU and SXU hybrid structures, the magnets can safely withstand demagnetization when subjected to temperatures of up to 40 degrees C. The intrinsic resistance to demagnetization is also compatible with a radiation environment similar to that of LCLS-I. Magnetic properties may need to be reevaluated for new radiation loads expected in LCLS-II.

8.7.2 Magnetic Design

The magnetic designs for both HXU and SXU are based upon hybrid structures using permanent magnet material and high permeability vanadium permendur poles. The concept is to assemble the magnetic structure into magnetic modules approximately 1 m in length. An undulator segment will consist of a total of six magnetic modules, three on top and three on the bottom. Figure 15 illustrates the magnetic structure design concept.

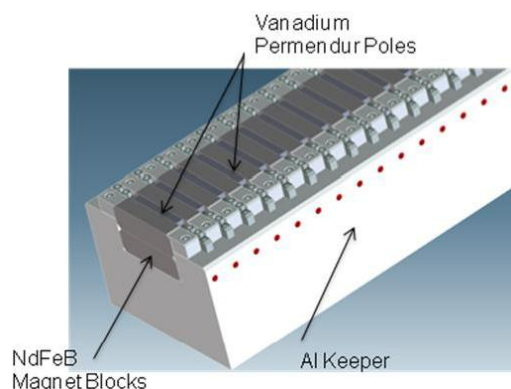


Figure 15. Magnetic Module Design Concept.

An ideal termination of the magnetic structure will allow the electron beam to enter into the periodic field region without a displacement or angle kick. However, for a variable gap hybrid magnetic structure, such as that for the HXU and SXU, this cannot be achieved over the full

range of gaps. There will, in general, be an entrance and exit displacement and kick that will vary with the magnetic gap. The magnetic structures for HXU and SXU incorporate an integral number of periods, which results in entrance and exit displacements that are of the same sign, and therefore add “allowed” entrance and exit kicks that are of opposite sign, and therefore cancel. Entrance and exit kicks that cancel do, nonetheless, result in a trajectory through the undulator that is oblique w.r.t. and unperturbed beam.

Figure 16 shows a finite element analysis (FEA) model of an end-structure design developed for a 32 mm period hybrid undulator. The principle of the design is to use standard-sized poles with reduced-size permanent magnets (PMs) in the last three slots to approximately set the normalized pole scalar potentials at the sequence, starting at the end pole: 0, +0.25, -0.75, +1. For this design, the modified PM heights, normalized to full PM height, are 0.083, 0.36 and 0.76. This design results in a total displacement range of $\pm 15 \mu\text{T}\cdot\text{mm}^2$ over the gap range of 7.2-20 mm. The same design principle will be applied to develop end structures for HXU and SXU.

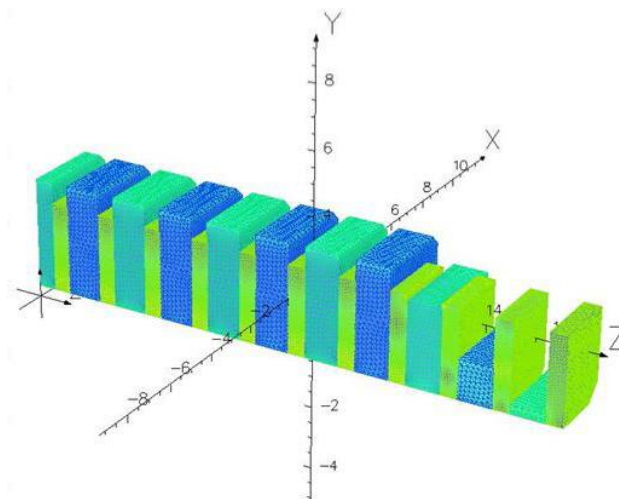


Figure 16. FEA Model of End Structure.

8.7.3 Magnetic Tuning Strategies

An analysis has been made of various expected sources of magnetic errors, including magnetic block strength, angle and dimensional errors, and pole dimension and placement errors. This analysis has helped set appropriate tolerances for the design. It has also been used to look at how the effects of errors change with magnetic gap. A similar study has been made of potential methods for tuning the magnetic field, including vertical pole offsets, introduction of PM rotor pairs (slugs) to modify pole excitation and ferromagnetic shims between poles.

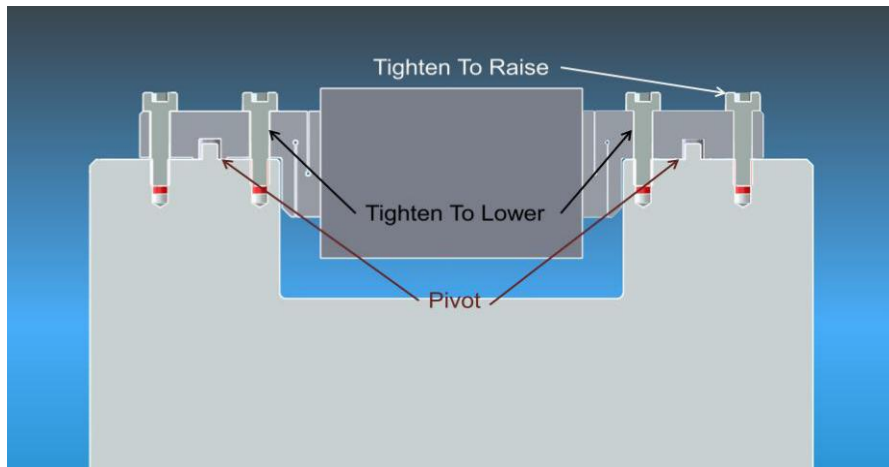


Figure 17. Pole Offset Adjustment.

Figure 17 illustrates a design feature to modify the vertical pole offset. In this design, flexures are cut into the pole mounting tabs. A system of set screws and pivots allow the pole position to be smoothly adjusted. This adjustment mechanism allows for a pure vertical adjustment, which introduces a local variation in the vertical field, and for a pole cant, which will introduce a local variation in the horizontal field.

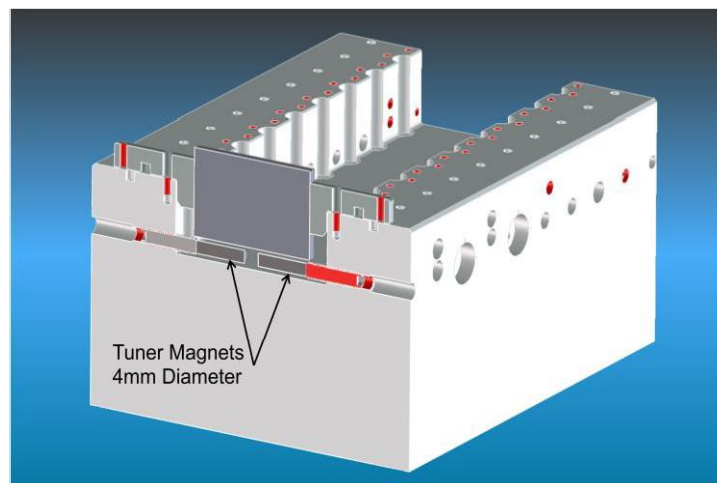


Figure 18. Counter rotating magnet rotors to alter pole excitation.

Figure 18 illustrates a concept for modifying the pole excitation. In this figure the magnetic orientation of the magnet slugs is radial. A system of two rotors (slugs) can be counter-rotated to control the flux into the pole. The rotor pairs as shown allow for up to a ± 1 percent variation in pole excitation. The strength of the excitation perturbation can be adjusted by counter rotating the two rotors. Additionally, if it proves useful/necessary, rotors of the pair can be co-rotated to differentially energize neighboring poles.

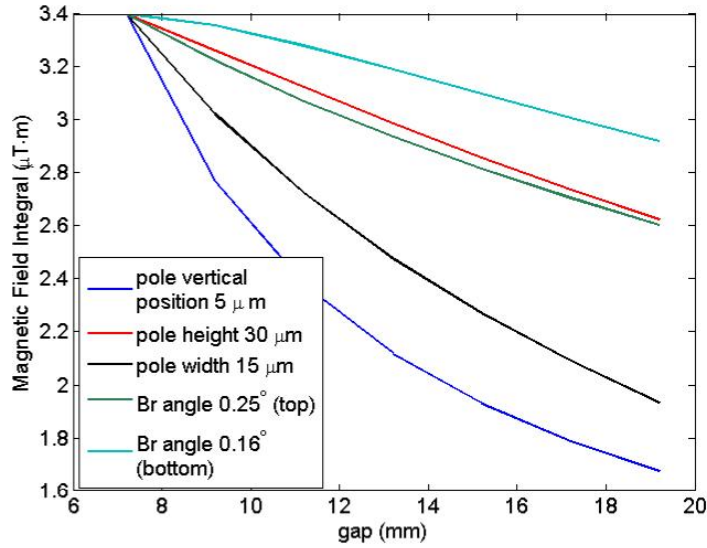


Figure 19. Simulated gap dependent field perturbations of various error sources.

Figure 19 shows simulated field perturbations for various potential sources of dimensional and excitation errors. Figure 20 shows simulated perturbations for vertical pole adjustment and installation of magnet rotors (installed in pairs, adjusted to full strength). By comparing Figure 19 and Figure 20, it is evident that a combination of the two tuning methods can be constructed to deal with any combination of the simulated errors over the full range.

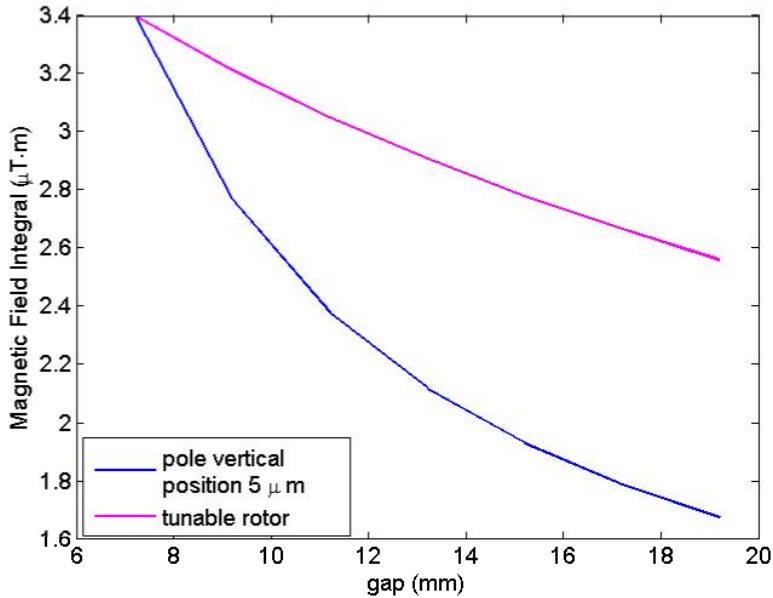


Figure 20. Simulated gap-dependent tuning field perturbations.

8.7.4 Mechanical Design

The undulator mechanical structure consisting of a support frame, strongback supports for the magnetic structure, and a variable gap drive system must be compatible with magnetic requirements and installation constraints. In particular, the latter constraint is a challenge as illustrated in Figure 21, which shows the installation of both HXU and SXU. The assumptions for the illustrated installation are:

- Electron beam separation of 2.5 m.
- The frame is oriented to allow undulator installation and removal without breaking vacuum.

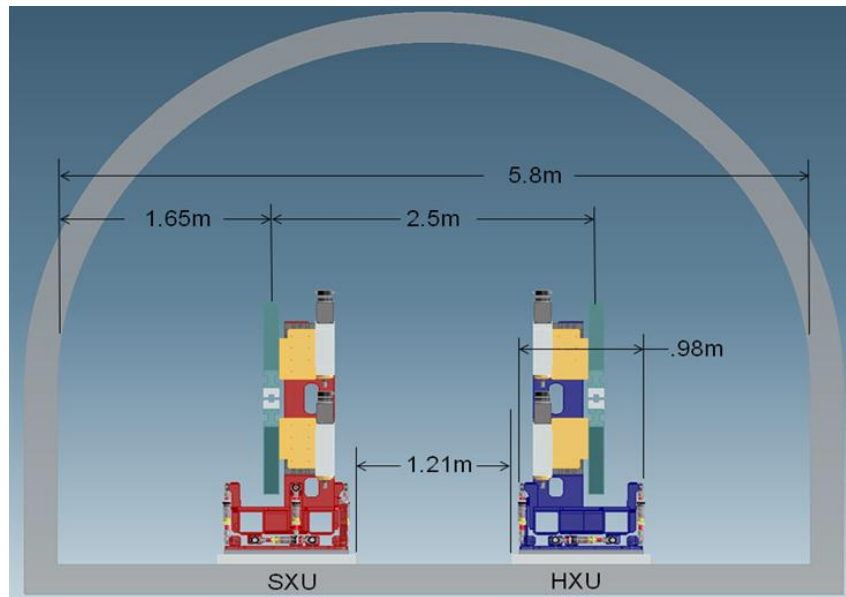


Figure 21. Installation in the LCLS tunnel.

As can be seen in the figure, clearance in the center aisle is very limited for undulator transport. Alternate frame and drive configurations will be examined to improve clearance.

Figure 22 shows the design concept for the mechanical system. The concept is to use the same mechanical system design for both HXU and SXU. The primary features include:

- A welded steel frame with precision machined mounting pads for the drives.
- Four drives to minimize backlash. Each drive consists of servo motor, cross roller bearing slide, and roller screw.
- Flexure plates for mounting the strongbacks to the drives. This feature allows for differential thermal expansion between the frame and strongbacks.
- Strongbacks fabricated from 7075 aluminum to minimize differential thermal expansion between the strongbacks and the magnetic structure. The high profile of

the strongbacks is intended to minimize deflection along the beam axis due to magnetic forces.

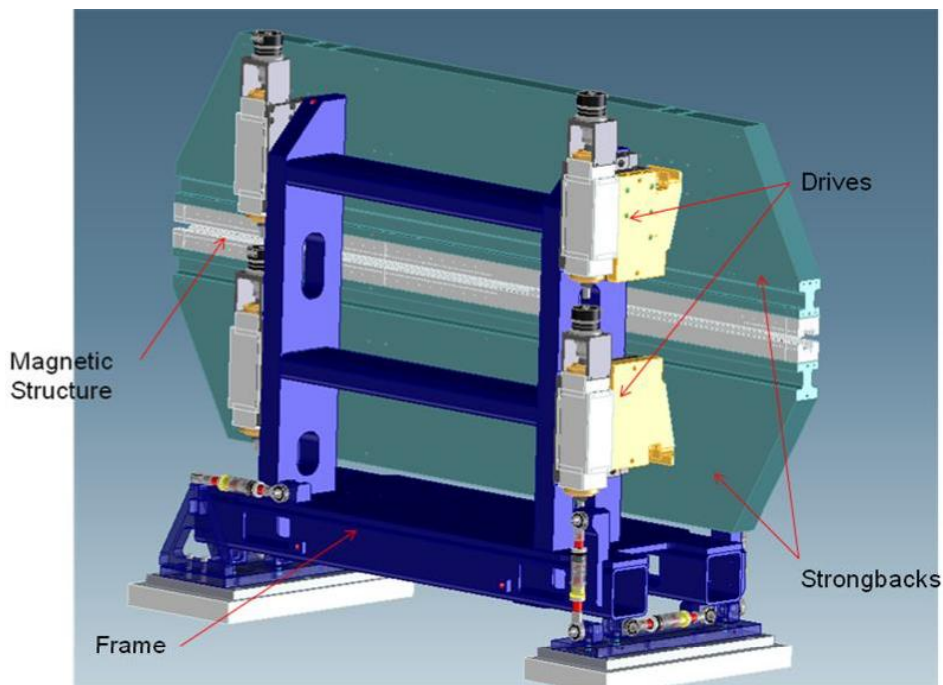


Figure 22. Undulator Design Concept.

8.8 Undulator Alignment

In order for the FEL process to produce optimum gain, three main alignment considerations need to be satisfied:

1. Alignment of the quadrupoles such that the electron trajectory is straight. This will reduce phase errors and improve overlap between the electron and photon beams.
2. Centering of the vacuum chamber to the electron beam to minimize emittance degradation from transverse wakefields.
3. Centering of the undulator to the beam to minimize errors in the undulator parameters (K_{eff}).

All alignment operations will be based on the magnetic or electrical centers (rather than the mechanical shape, with the exception of RF-BPMs) of the components, which will be determined in a separate process and fiducialized to tooling ball (sockets) or appropriate features on the device body.

The tolerances are listed in Table 11. Transverse quadrupole alignment is specified with respect to a virtual straight line. The local straightness requirements refer to a z interval of 10 m (roughly one HXR field gain length), while global straightness requirements refer to the total undulator length. We assume that initial alignment, based on conventional metrological methods,

will provide good local straightness but might suffer from some degree of random walk-off globally. The quadrupoles are the main focus of the alignment procedure, with the other components to be aligned with respect to the quadrupoles. The final alignment tolerances for the quadrupoles are extremely tight and will be met by using electron-beam-based alignment in a similar way as with LCLS (see 8.8.3). A brief summary of the LCLS-II alignment concept is given in the next section.

Table 11. Basic quadrupole alignment requirements with respect to the reference coordinate system.

Parameter	SXU Values	HXU Values	Unit
Initial quadrupole alignment (x,y) (rms)	<100	<100	μm
Maximum random walk amplitude (x,y)	250	250	μm
Final quadrupole position settability (x,y)	0.1	0.1	μm
Quadrupole x/y position stability (rms)	2.0	0.25	μm
Roll tolerance (rms)	<1.0	<1.0	mrad
Pitch tolerance (rms)	<15	<15	mrad
Yaw tolerance (rms)	<15	<15	mrad

8.8.1 Alignment Strategy

The LCLS alignment strategy [31] has been very successful in producing a straight electron beam trajectory sufficient for high FEL gain using first conventional alignment of the undulator system followed by a special beam based alignment (BBA) procedure based on variable electron energies. LCLS-II will use a very similar strategy even though there are system differences, such as variable gap and large undulator size and small available range of electron energies, which require special considerations. The alignment concept for both the SXR and the HXR segments will be similar.

During the BBA procedure, the undulator segments will be at the fixed tuning gap, as measured with linear encoders which have been calibrated during the tuning process in the magnet measurement lab. It is expected that undulator field integrals will significantly vary as the gap is changed. This will change electron beam steering, which will be corrected with the dipole correctors that are incorporated into the quadrupole magnets. The required corrections will first be measured in the magnet measurement lab and later fine-tuned based on RFBPM readings. This is similar to what is currently done at LCLS, where field integrals change and quadrupoles move (due to girder twist) as undulator segments are moved in and out.

During initial installation of the components, the quadrupole magnets, undulator segment strongbacks, and undulator segment vacuum chambers will be pre-aligned using conventional alignment methods. After the first application of the BBA procedure, which precision aligns the quadrupole, the undulator segment strongbacks and the undulator segment vacuum chamber will

be fine aligned with conventional alignment methods. A summary of the conventional alignment of the undulator line is given in Section 8.8.2.

Once lasing has been achieved, BBA should move the quadrupole magnets by less than $\pm 60 \mu\text{m}$, based on the LCLS experience. In LCLS, there are indications that the BBA procedure does not put the electron beam onto a straight line over the entire undulator line but can leave long-range bows in the trajectory with sagitta amplitudes in the order of $20 \mu\text{m}$, which can cause the X-ray beam to change position at the experimental stations after BBA procedures, as well as when changing the number of active undulators. This is currently under investigation at LCLS. It is expected that the additions of extra constraints in the BBA algorithm can reduce the problem.

8.8.2 Conventional Alignment

During initial installation of the components, the quadrupole magnets will be aligned to a straight line within a local error of $100 \mu\text{m}$ (rms) and a maximum random walk amplitude of less than $250 \mu\text{m}$. Both the quadrupoles and the undulator jaws will be equipped with tooling balls that will have been fiducialized to the magnetic axis of the devices. For the undulator this fiducialization will be done at the tuning gap. The undulators, which will be installed independently of the quadrupole magnets, will then be aligned in the tunnel such that their magnetic axes are centered between the magnetic axes of the neighboring quadrupoles. This procedure has been successfully applied several times for the LCLS-I undulator segments since operations began. Using laser trackers, a precision of about $50 \mu\text{m}$ (rms) can be achieved. This alignment technique will be repeated after the first beam-based alignment procedure has set the quadrupoles to the correct positions to allow FEL operation. The vacuum chamber, which needs to be centered on the electron beam, will be supported off the adjacent quadrupole support movers and aligned relative to the quadrupole centers during the initial alignment procedure. We expect that the initial BBA procedure will move the quadrupole positions by less than $250 \mu\text{m}$. The vacuum chamber will move with the quadrupoles. The position of the undulator segment strongbacks will need to be adjusted to stay centered on the vacuum chamber. Encoders that would allow measurements of the relative position between the quadrupole center and the undulator strongback would aid this process and their availability is desirable. There will be sufficient clearance between the quadrupole magnets and the vacuum chamber to allow for this movement.

8.8.3 Beam-Based Alignment

Considering that the accuracy of the conventional alignment for the undulator quadrupoles and BPMs is limited to about $100 \mu\text{m}$, a beam-based alignment (BBA) procedure will be used to achieve the necessary trajectory straightness of a few μm over 10 m. The core feature of the alignment concept is BBA, which measures the trajectory for four different electron energies. For LCLS-II, running with the new superconducting linac, these electron energies will only span the range between 2.0 GeV and 4.0 GeV, which is much smaller than the current LCLS-I range. None of the undulator fields (i.e., quadrupole gradients, corrector strength, undulator gaps) will be varied during the measurements. The measurements can be done in parallel for the SXR and

HXR lines, i.e., for a given setting of the accelerator energy; both trajectories can be measured as the electron beam is switched between the two lines. Alternatively, HXR BBA can be carried out using the current LCLS-I linac (WL) in exactly the same way as is currently done for LCLS-I, which should satisfy the tighter tolerances of the HXR line. As a result of the four sets of trajectory measurements, the BPM offset errors and quadrupole position errors are calculated and independently corrected for each line.

The acquired beam positions at all undulator BPMs are averaged over a few hundred shots at each of the four energy settings. The measured orbit for a particular energy can be described using the known beam optics as a linear function of the beam position and angle at the entrance to the undulators, the offsets of the BPM electrical center to the ideal straight beam axis, and the quadrupole offsets. A linear least square fit of all beam trajectories then determines these parameters, which are implemented by correcting the BPM offsets in the BPM acquisition software and the quadrupole offsets by moving the break section support structure. An additional constraint has to be implemented in the fit to remove the ambiguity of the location of the ideal straight beam axis, because adding any linear function of the z-position along the undulator beam line to the assumed BPM and quadrupole offsets also provides a solution. This constraint can be implemented by forcing the mean quadrupole offset and slope to zero. Several iterations of the procedure might be necessary for it to reach convergence if the BPM scale factors or the optics model are not correct. The final physical quadrupole offsets to the beam axis will, in general, not be zero, but provide necessary kicks to the beam to cancel remaining field integrals from the undulators or Earth field. The correction of the BPM offsets will be done by changing the values of process variables in the control system.

The quadrupole kicks will be corrected by remotely adjusting the quadrupoles' positions. In order to make these adjustments possible, each quadrupole, together with all the other break section components (e.g., BPM, phase shifter, etc.) will be mounted on a common support structure that can be remotely positioned with cam movers, similar to how the LCLS-I girder positions are controlled. This procedure will align the quadrupoles with sufficient precision for the electron beam path to get straightened. This is expected to cause the electron beam to pass the quadrupoles very close to their magnetic axes. A small offset on the order of 20 μm (rms) will remain, just enough so that the small fields related to those offsets compensate any additional remnant field integrals that exist outside of the quadrupoles — i.e., coming from the remnant field integrals of the undulators and phase shifters, from the earth magnetic field, and from any other environmental field components. The tolerances for the fields outside the quadrupoles are 40 μTm for the first and 50 μTm^2 for the second field integrals. The field integrals from the Earth magnetic field will exceed these tolerances and will be corrected with long dipole coils that are integrated into vacuum chamber (see 8.4.6).

This procedure has been successfully implemented at LCLS-I, as shown in Figure 23, where after several iterations of measurement and correction the initial 100 μm orbit deviations were reduced to only a few μm . The differences in the undulator setup have no influence on the algorithm (the new undulators have variable gaps and the break section is supported by its own

motorized support structure). The BBA procedure will be performed at one constant gap setting of the undulators to determine the BPM and quadrupole offsets. Changes to the undulator field integrals from different gaps will not affect the BPM offsets and the straight line location, and the steering correctors embedded in the quadrupoles will be used to obtain a straight trajectory at other gap settings.

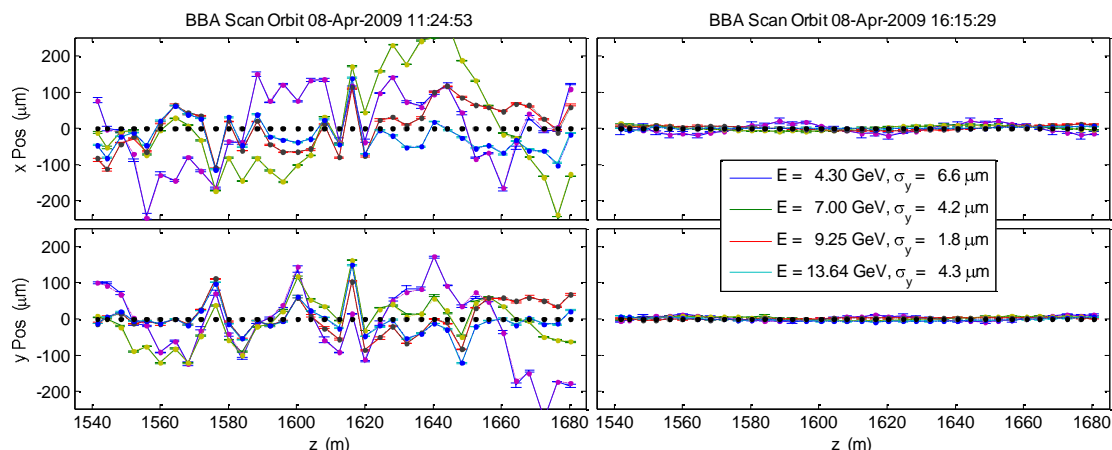


Figure 23: Beam-based alignment procedure for LCLS-I with beam orbits for four different energies before (left) and after several rounds of measurement and correction (right).

8.9 Radiation Damage Issues

8.9.1 Introduction

The undulators used for LCLS-I and LCLS-II are based on rare-earth permanent magnet material (NdFeB), which can be demagnetized by ionizing radiation. Radiation damage studies have been carried out at LCLS-I and at other facilities around the world. The most recent publication shows that high-energy electrons, lost from third- or fourth-generation light source beams, can lead to the generation of star events, which are strongly correlated with the demagnetization of undulator magnets [32].

To protect the LCLS-I undulators from excessive radiation, one Beam Loss Monitor (BLM) (i.e., a Čerenkov-radiator and photomultiplier tube) is installed right in front of each of the 33 undulator segments. The photomultiplier signals are integrated over 1 s and compared to a threshold by the Machine Protection System (MPS), which trips the electron beam in case of a violation. For LCLS-I, the threshold is set such that the radiation from the beam hitting a 40 μm diameter carbon fiber beam finder wire (BFW) is just acceptable. With MARS [33] simulations, it was determined that this threshold should correspond to a maximum neutron fluence in the magnet blocks of 8.4×10^4 neutrons/cm²/nC. The BLM signal for such an event is well above background. A full BFW-Scan (66 wires, about seven interception points per scan and wire, and about 100 hits per interception point) is performed a few times per year, at the most. The MPS does not allow operation with more than one BFW inserted at a time. The BLM signal is very

close to the background when no BFW is inserted. Since BFWs are not included¹ into the LCLS-II design, an alternate calibration device (e.g., upstream wire scanner) will need to be employed.

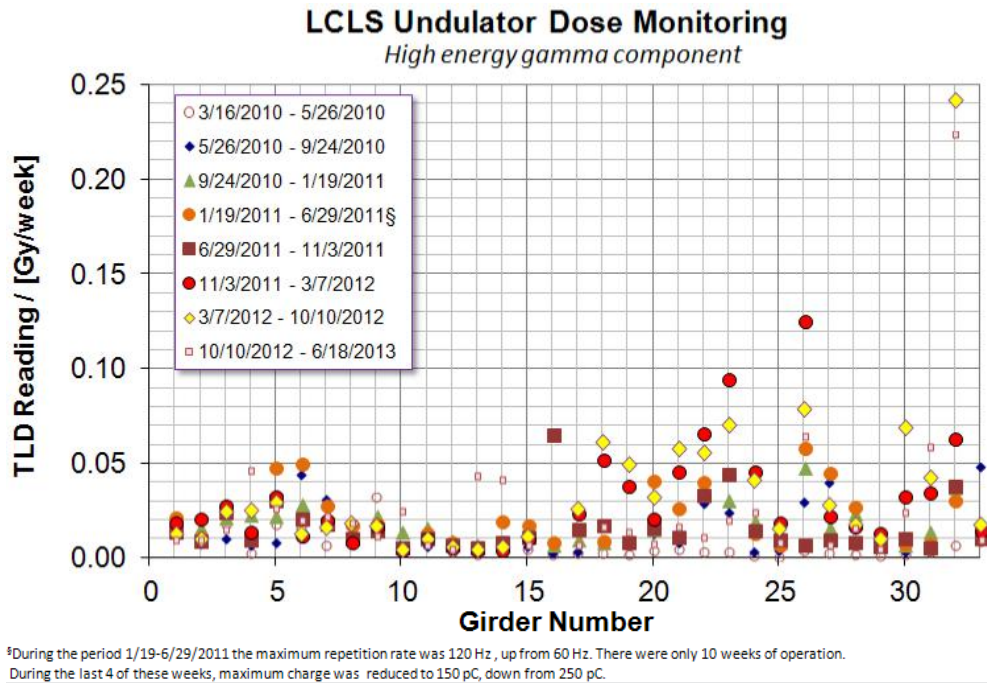


Figure 24: Typical high energy ($> \sim 0.5$ MeV) dose rates (Gy/week) measured at LCLS-I over the span of about three years show the very low levels achieved.

These BLMs constitute just one of several radiation protection layers.

These layers include:

1. A system of beam collimators in the LTU that limit the six-dimensional phase space such that, according to simulations, halo electrons will not be able to reach the undulator vacuum chamber if the steerers, downstream of the last collimator, are set correctly.
2. 33 undulator RFBPMs in the HXR beamline and 22 in the SXR beamline, each monitored by the MPS to keep the beam inside a 1 mm radius envelope relative to the beam pipe center. The girder design together with BBA ensures that a zero reading of the RFBPMs implies that the beam is close to the center of the vacuum chamber to better than 100 μm . The 1 mm radius is sufficient to keep the electron beam that has a diameter of less than 100 μm away from the ± 2.5 mm vertical vacuum chamber extension.

¹The BFWs have been excluded in order to reduce cost. Their original purpose in LCLS-I, i.e., to help with the alignment of the upstream end of the girder, is not needed in LCLS-II due to the lack of a girder. The undulator ends will be aligned relative to the centers of the adjacent quadrupole using a metrology based technique.

3. BLMs that trip the beam if actual radiation levels are detected. Once the trip level has been exceeded, no more than one electron bunch will enter the undulator hall.
4. Two toroids in comparator configuration, mounted before the first and after the last segment that detect larger charge losses along the undulators.
5. A beam collimator mounted in front of each undulator segment to remove the the fraction of the divergent radiation component that otherwise would strike the following segment vacuum chamber wall.

The main protection comes from layer 1. Layer 2 trips the beam occasionally. Layer 3 does not trip the beam in normal operation. Layer 4 never tripped the beam after it was properly calibrated.

8.9.2 Damage Mechanisms

At SLAC, the degree of demagnetization of spare LCLS undulator magnet blocks was measured using high doses of radiation generated by a 13.6 GeV electron beam hitting a copper cylinder. The measured demagnetization levels were correlated to photon doses and neutron fluencies as calculated from a FLUKA [34] model. The experiment (T-493) was carried out in 2007 at End Station A (ESA). Measured magnet damages spanned a range between 0.34 percent and 9.7 percent, and showed a linear correlation with both the estimated photon dose and the neutron fluence in the magnet. The extrapolated neutron fluence required for a demagnetization degree of 0.01 percent is 6.4×10^{10} n/cm². This is more than six orders of magnitude above the BLM threshold. In addition, one thermo-luminescent dosimeter (TLD) is installed right in front of each undulator segment. They are mounted in a quarter-inch-thick lead housing and are read in two-to-four months intervals. The lead shielding sets a threshold of a few hundred keV and attenuates the non-damaging synchrotron radiation component, which can produce a signal 400 times stronger at the last undulator in unshielded TLDs, thus hiding the reading of the damaging component. The readout results are steady (see Figure 24) and show less than 100 mGy/week at 120 Hz beam operation with up to 250 pC bunch charge.

At these levels, no measurable radiation damage is expected during the operational lifetime of the project. Nevertheless an undulator segment is removed from the undulator tunnel roughly every two months and measured in the MMF.

Before the installation of the HXRSS chicane on U16, no significant changes of the K parameter or the field integrals were detected. Since then, an average relative reduction in the K parameter values of re-measured undulator segments around U16 have been observed, with the largest being low by more than three sigma (5×10^{-5}). To establish the significance of these measurements, more observation time will be required. Increased radiation activity has been observed after the HXRSS chicane during initial operation. Due to a slight misalignment of the chicane vacuum chamber, the electron beam halo partially scraped off by the vacuum chamber wall at large chicane amplitudes.

Due to its high repetition rate of operation, there will be up to 1000 times more electrons per second in the LCLS-II beam than there are in the LCLS-I beam. It is therefore important to understand the source of the radiation measured with the TLDs in LCLS-I, as shown in Figure 24, in order to make reasonable estimates for likely LCLS-II damage levels. Three mechanisms for the measured radiation levels are being investigated.

1. Bremsstrahlung from beam electrons on the residual gas background
 - a. The electromagnetic radiation component
 - b. Electrons lost in the vacuum chamber after losing energy in a bremsstrahlung event
 - c. Electrons receiving a large transverse momentum in a bremsstrahlung event
2. Beam halo electrons hitting the vacuum chamber
3. Synchrotron radiation at energies above the Pb filter threshold.

For beam operation that does not use the HXRSS chicane, mechanisms 1 and 2 appear unlikely candidates for explaining the measured dose rate. If mechanism 1 would be an important contributor, the vacuum pressure requirement in the undulator segment chamber would need to be lowered to the 10^{-9} torr range.

8.9.3 Radiation Protection

The undulator magnet material needs to be protected from ionizing radiation of energies above 1 MeV. To achieve this, various protective measures will be implemented, similar to what is used in LCLS. They consist of:

- A complete LTU collimator system to limit the five-dimensional phase space (x, x', y, y', E), such that electrons that pass the collimator system will not be able to get lost in the undulator vacuum pipe if the undulator system components are set correctly. The energy collimators will be incorporated into the dogleg beamline as part of the LTU.
- A machine protection system (MPS) based on the BLMs and RFBPMs to prohibit beam operation at high radiation doses or with trajectory amplitudes outside a ± 1 mm envelope.
- A collimator in front of each undulator segment.

Radiation levels will be continuously monitored by

- Thermo-luminescent dosimeters (TLDs), or equivalent, mounted at the entrance of each segments. If TLDs are used, they will be swapped with fresh TLDs at regular intervals and read out after removal.
- Integrated BLM readings (see Section 8.4.7).

8.10 Temperature and Position Stability

8.10.1 Temperature Monitoring

It is important that the local undulator temperature stays stable to within a ± 0.1 K. A temperature gradient is acceptable as long as the temperature at any given point is stable. The temperature of each undulator segment needs to be monitored redundantly. Each of the two jaws (magnet arrays) needs to be equipped with three independent temperature sensors, each with an accuracy of 0.1 K after calibration. The total long-term drift shall stay within a ± 0.05 K range. In addition, each of the two jaws (magnet arrays) of each phase shifter needs to be equipped with a sensor of the same resolution and long-term drift stability as the undulator segment temperature sensors. Additional temperature sensors are needed to monitor the temperatures of the support pillars for the undulator and the break section, of undulator and phase shifter motors, quadrupole, and ambient air.

8.10.2 Gap Monitoring

The gap height settings of the undulator segments and the phase shifters need to be monitored with absolute linear encoders with a repeatability of better than 1- μm , while for the phase shifter, a single encoder for gap height will be sufficient. The undulator segments require gap height and mid-plane position encoders on both ends of each device.

8.10.3 Wire Position Monitors

X-ray FELs demand that the positions of undulator components be stable to less than 1 μm per day. A precise wire position monitor system (WPM) has been developed and incorporated into the LCLS-I undulator line. This system is capable of measuring x, y, roll, pitch and yaw of each of the 33 undulator quadrupoles with respect to 140-meter-long stretched wires. Instrument resolution is about 10 nm and instrument drift is negligible [35]. Position data of individual quadrupoles can be correlated along the entire 132-meter-long undulator. Even though the measurements showed that the underground tunnel is sufficiently stable to not require a closed loop feedback system based on the wire position monitor readings, the WPM allows monitoring and correcting this important tolerance of the FEL system. The LCLS-I WPM helped identify and characterize the source of quadrupole motion (e.g., coupling to LTU ground motion, girder twist from segment roll in/out activity). Provisions are being made for the future installation of an adapted version of the existing system for the LCLS-II HXR beamline, and a second system will be installed on the LCLS-II SXR beamline.

8.10.4 Undulator Hall Floor Stability

The undulator hall floor stability is a concern. Floor stability is very important since component position monitoring will not be available. Random movement of quadrupoles by 8 μm (rms) will reduce HXR FEL output by about 40 percent, requiring correction based on the WPM system or another application of BBA.

8.11 Undulator Vacuum Chamber

An undulator segment vacuum chamber, meeting the LCLS-II vacuum, mechanical, and physics requirements, will be developed to the conceptual design level.

If a vacuum of 10^{-9} torr is required, the chamber is envisioned to be an aluminum extrusion with an ante-chamber, similar to those in use in the Advanced Photon Source storage ring. The chambers will be fully bakeable, and will be NEG-coated or equipped with NEG strips to achieve the required vacuum. The extrusion profile will be designed to enable abrasive-flow polishing in order to achieve the required surface finish in the beam chamber.

At study, currently underway to characterize the nature of the measured dose rates, gives reason to believe, that gas Bremsstrahlung is not a significant source. This finding, if confirmed, would relax the vacuum requirement.

If the vacuum requirements are relaxed to the level of LCLS-I, the chamber could be nearly identical to the LCLS-I chambers that have been functioning successfully since their original installation. Due to the high rep-rates, they will require the addition of water cooling to handle the heat load from wakefield induced currents. The extrusion profile was designed to enable abrasive-flow polishing in order to achieve the required surface finish in the beam chamber. The technology to manufacture those chambers was already successfully developed for LCLS-I. Costs can be readily extrapolated so long as the surface finish, alignment, and other requirements remain similar.

Table 12. Undulator Segment Chamber Vacuum Parameters.

Parameter	Values	Unit
Maximum vacuum pressure (assuming relaxed requirements apply)	1×10^{-6}	Torr
Segment chamber material	Aluminum	-
Segment chamber inner cross sectional shape	Race-track	-
Segment chamber inner height	5	mm
Segment chamber inner width	11	mm
Beam stay clear radius	2.3	mm
Segment chamber straightness	± 100	μm
Segment rms longitudinal surface roughness slope, α_z	< 15	mrad
Segment rms azimuthal surface roughness slope, α_θ	< 30	mrad
Number of horizontal chamber corrector coils (CUXs)	1	-
Number of vertical chamber corrector coils (CUXs)	1	-

The mechanical vacuum chamber requirements are dominated by wakefield considerations. The interaction between the electron beam and the vacuum chamber generates longitudinal and transverse wakefields (characterized through the vacuum chamber impedance) that can reduce

FEL gain and need to be kept small. There are three main contributors to the vacuum chamber impedance:

- electrical surface conductivity
- surface roughness
- geometric shape

The goal is to keep the contribution from surface roughness and geometric shapes small compared to the unavoidable contribution from the resistive wall conductivity. One component of the latter, AC conductivity [36], can be reduced by the choice of aluminum as surface material. The same requirements apply for the vacuum system of both the SXR and HXR vacuum systems.

The surface roughness slope needs to be monitored by surface scans performed on small chamber samples during the vacuum chamber fabrication process. These scans will yield the surface height $h(z_i, \theta_j)$, which can be used to derive the rms surface roughness slopes (shown for the longitudinal direction):

$$\alpha_z = \sqrt{\frac{1}{m(n-1)} \sum_{j=1}^m \sum_{i=1}^{n-1} \left(\frac{h(z_{i+1}, \theta_j) - h(z_i, \theta_j)}{z_{i+1} - z_i} \right)^2}. \quad (5)$$

8.12 Self-Seeding

The SASE operation will produce X-ray radiation that is transversely, but not longitudinally coherent. The temporal profile exhibits a spiky structure characteristic of the SASE process that starts from shot noise in the electron beam. In the spectral domain, a similar spiky profile has been observed experimentally for both soft and hard X-rays. Seeding (overlapping the electron beam with a monochromatic X-ray beam of sufficiently narrow bandwidth and sufficient power) would force the FEL to produce nearly transform-limited pulses, minimal jitter in X-ray wavelength, and potentially higher spectral brightness by one to two orders of magnitude if taken to full saturation. These enhanced beam qualities will benefit the users by not only improving the measurement efficiency and data analysis, but also enabling experimental studies in many areas of biology, materials, chemistry, and atomic, molecular, and optical sciences, where high spectral brightness or high peak power is essential. An upgrade path to the self-seeding configuration is described in chapter 18.

8.12.1 Self-Seeding for the Soft X-ray Undulator

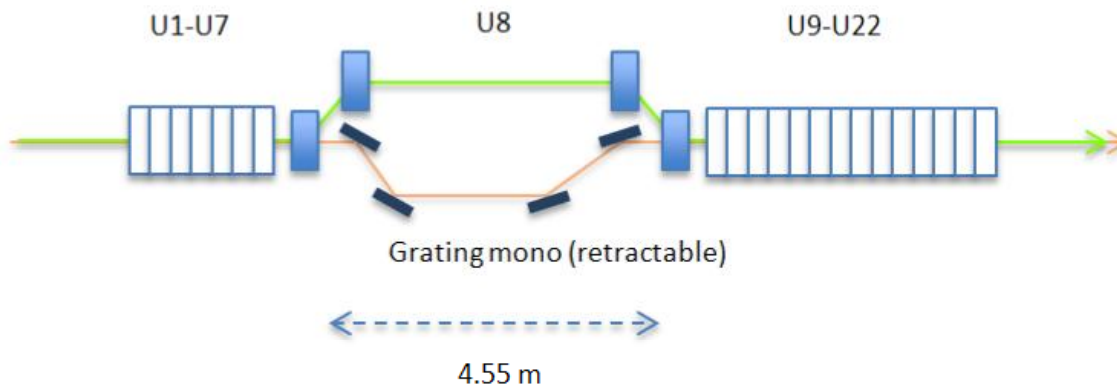


Figure 25. Schematic of a soft X-ray self seeding system, consisting of (from left to right) a toroidal grating, a rotating plane mirror, an exit slit for selecting a narrow bandwidth, a re-focusing spherical mirror, and a plane mirror to redirect the X-ray beam to be recombined with the electron beam, which is deflected around the optics devices by the four bending magnets (B1-B4).

For the soft X-ray undulator line in the energy range of 200 eV to 1.3 keV, the monochromator used to produce a narrow bandwidth seed is necessarily reflection-grating based due to absorption considerations, such as the LCLS-I SXRSS system shown schematically in Figure 25, which will be commissioned in late 2013.

This seeding monochromator system will operate between 0.3 keV (to avoid the carbon edge) and 1.3 keV with a resolving power equal or greater than 5,000 to produce a nearly transform-limited seed pulse with more than 20 kW of seed power, sufficient for initiating the seeding process with optimal spectral properties. The overall size of the grating and mirror system was optimized to be compact enough to fit within a single section of an undulator cell. The grating is a toroidal variable-line spacing (VLS) grating whose tangential curvature and VLS construction disperses and focuses vertically the incident polychromatic X-rays onto the exit slit, where a narrow bandwidth defined by the resolving power is selected. The divergent beam is re-focused vertically by the spherical mirror M2 onto the interaction point, approximately in the middle of the immediate downstream undulator. Horizontal focusing of the incident beam is done by the sagittal radius of curvature of the grating, forming an image of the source in the horizontal direction onto the interaction point. Energy tuning is accomplished by a simple rotation of the plane mirror M1 around a pivot point directly above the center of the grating, compensating for the changing exit angle from the grating with energy. The optical delay is about 1 ps, but variable with energy due to the varying included angle.

The magnetic chicane system contains four dipole magnets, arranged to create an excursion of the electron beam to bypass the optical elements and to match the optical delay for temporally overlapping with the optical seed. In addition, the chicane washes out the SASE micro-bunching produced in the upstream undulator sections.

8.12.2 Self-seeding for the hard X-ray undulator

For the hard X-ray undulator line in the energy range of 4-12 keV, the monochromator used to produce a narrow bandwidth seed will be based on the wakefield seeding scheme using a diamond single crystal, such as the LCLS-I HXRSS system shown in Figure 26, which was demonstrated in early 2012 and later fully commissioned for operation. For energies between 1 and 4 keV and above 12 keV, a grating system and upgrade to the exiting wakefield system will be required and discussed in chapter 18.

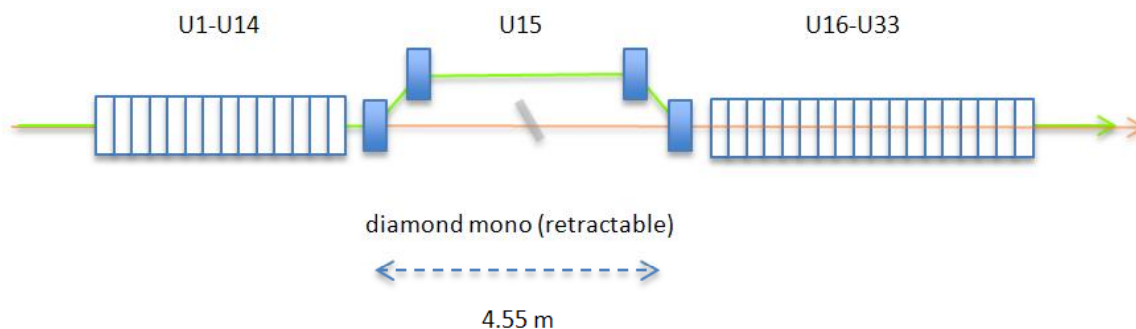


Figure 26. Schematic of the hard X-ray self seeding system, consisting of a thin diamond single-crystal, the four-dipole magnetic chicane is used to deflect the electron beam around the diamond crystal and provide a matching delay to overlap with the seed wakefield.

The seeding monochromator is a thin (about 100 μm) diamond single-crystal operating in the symmetric Bragg geometry, creating a monochromatic reflected beam and a forward-Bragg diffracted beam whose temporal field distribution consists of a main pulse resembling the spectrally noisy input pulse from the upstream undulators and a number of time-delayed trailing satellites (seeds) of decreasing intensity but highly monochromatic. By properly delaying the electron beam to overlap with one of the satellites, seeding is initiated and amplified by the downstream undulators.

The four-dipole magnetic chicane deflects the electron bunch around the diamond crystal, and also washes out the micro-bunching in the bunch after the upstream undulators to prepare the electrons for coherent seeding. It also provides the necessary delay to allow the electron bunch to overlap with one of the optical satellites (seeds) for initiating the seeding process.

For example, for the 4 keV HXRSS, a thin (approximately 100 μm) diamond, configured in Bragg diffraction geometry at the (111) plane will be used. The chicane and the monochromator will be located at the slot for U15. The first 14 undulator segments will generate SASE FEL with peak power around 100 MW. Passing through the monochromator, the seed will have a FWHM relative bandwidth of about 5×10^{-5} , with a peak power of about 250 kW. The seed pulse will recombine with the electron bunch into U16. Exponential saturation will happen at the exit of U27, where the pulse energy is about 60 μJ . When applying taper for the rest of undulator segments, the FEL pulse energy can be about 240 μJ at the undulator U33 exit. The tapered undulator can maintain the FEL FWHM relative bandwidth of 5×10^{-5} . The details are shown in Figure 23 and 24 of Chapter 10.4.4.

8.13 References

1. Z. Huang, K.J. Kim(2007). "Review of x-ray free-electron laser theory". Physical Review Special Topics - Accelerators and Beams 10 (3). doi:10.1103/PhysRevSTAB.10.034801
2. M. Xie, in Proceedings of the 1995 Particle Accelerator Conference (IEEE, Piscataway, NJ, 1995), p. 183.
3. Z. Wolf, Y. Levashov, "Beam Pipe Corrector Study." LCLS-TN-12-1 (2012).
4. U. Englisch, et al. "Ambient field Influence on the 5 m long XFEL Undulator Segments", Talk presented at MMW 17, Terrassa-Barcelona, Catalonia (Spain) 18-23 September 2011. <http://immw17.cells.es/presentations/Wed03-IMMW17-UEnglisch.pdf>
5. J. C. Dooling, W. Berg, B.X. Yang, M.S. Leitner, A.S. Fisher, H.-D. Nuhn, "Modeling the Optical Coupling Efficiency of the Linac Coherent Light Source Beam Loss Monitor Radiator," BIW 2010, JACOW (2010).
6. Z. Wolf, "Introduction to LCLS Undulator Tuning," LCLS-TN-04-7 (2004).
7. Z. Wolf, "Algorithms to Automate LCLS Undulator Tuning," LCLS-TN-06-8 (2006).
8. Z. Wolf, et al., "LCLS Undulator System Tuning and Magnetic Measurements," Proceedings. Part. Accel. Conf. 2009, Vancouver.
9. Z. Wolf, Y. Levashov, H-D. Nuhn, I. Vasserman, "LCLS Undulator Test Plan," LCLS-TN-06-17 (2006).
10. Z. Wolf, "Requirements for the LCLS Undulator Magnetic Measurement Bench," LCLS-TN-04-8 (2004).
11. Z. Wolf, "Undulator Field Integral Measurements," LCLS-TN-05-22 (2005).
12. Z. Wolf, Y. Levashov, "Undulator Long Coil Measurement System Tests," LCLS-TN-07-3 (2007).
13. G. Bowden, "Roller Cam Positioners," LCLS-TN-05-28 (2005).
14. Z. Wolf, S. Kaplounenko, "Temperature Measurements in the Magnetic Measurement Facility," LCLS-TN-05-9 (2005).
15. Z. Wolf, Y. Levashov, "Undulator K Value Temperature Dependence," LCLS-TN-09-4 (2009).
16. Z. Wolf, et al., "LCLS Undulator Fiducialization Plan," LCLS-TN-07-2 (2007).
17. Y. Levashov, Z. Wolf, "Tests of Coordinate Transfer from Magnetic to Mechanical Reference for LCLS Undulator Fiducialization," LCLS-TN-05-10 (2005).
18. Z. Wolf, et al., "Girder Alignment Plan," LCLS-TN-08-3 (2008).
19. Z. Wolf, "A Vibrating Wire System for Quadrupole Fiducialization," LCLS-TN-05-11 (2005).
20. Z. Wolf, "LCLS Undulator Quadrupole Fiducialization Plan," LCLS-TN-07-7 (2007).
21. M. Levashov, Z. Wolf, "Commissioning a Vibrating Wire System for Quadrupole Fiducialization," LCLS-TN-07-8 (2007).
22. S. Anderson, et al., "Magnetic Measurement Results of the LCLS Undulator Quadrupoles," LCLS-TN-09-1 (2010).
23. Z. Wolf, S. Kaplounenko, "Temperature Measurements in the Magnetic Measurement Facility," LCLS-TN-05-9 (2005).
24. Y. Levashov, Z. Wolf, "Tests Of Coordinate Transfer From Magnetic to Mechanical Reference for LCLS Undulator Fiducialization," LCLS-TN-05-10 (2005).
25. Z. Wolf and Y. Levashov, "Reference Undulator Measurement Results," LCLS-TN-09-3 (2009).

26. A. Fisher, H-D. Nuhn, J. Welch, “*Magnetic Measurements of the Background Field in the Undulator Hall with Ductwork and Cable Trays*,” LCLS-TN-08-4 (2008).
27. K. Hacker, Z. Wolf, “*Earth’s Magnetic Field Measurements for the LCLS Undulators*,” LCLS-TN-05-4 (2005).
28. A. Temnykh, Y. Levashov, Z. Wolf, “I,” Nucl. Instr. and Meth. A 622 (2010) 650.
29. Z. Wolf, et al., “I,” LCLS-TN-07-2 (2007).
30. Y. Levashov, Z. Wolf, “*Tests of Coordinate Transfer from Magnetic to Mechanical Reference for LCLS Undulator Fiducialization*,” LCLS-TN-05-10 (2005).
31. H.-D. Nuhn , P.J. Emma, G.L. Gassner, C.M. LeCocq, F. Peters and R.E. Ruland, “*Electron Beam Alignment Strategy in the LCLS Undulators*”, FEL2006 Proceeding, 2006, Berlin, Germany.
32. Y. Asano, T. Bizen, and X. Marechal, J. Synchrotron Rad. 16 (2009), 317-324.
33. N.V. Mokhov, K.K. Gudima, S.G. Mashnik et al, "*Physics Models in the MARS15 Code for Accelerator and Space Applications*", in Proc. of International Conference on Nuclear Data for Science and Technology, Santa Fe, NM, 2004, AIP Conf. Proc. 769, part 2, pp. 1618-1623; Fermilab-Conf-04/269-AD (2004)
34. A. Fasso, A. Ferrari, J. Ranft et al., “*FLUKA: a Multi-Particle Transport Code*”, CERN-2005-10 (2005), INFN/TC_05/11, SLAC-R-773.
35. H.-D. Nuhn, G. Gassner, F. Peters, “*Position Stability Monitoring of the LCLS Undulator Quadrupoles*,” SLAC-PUB-14891.
36. K.L.F. Bane, G.V. Stupakov, “*Resistive Wall Wakefield in the LCLS Undulator*”, Proceedings of the 2005 Particle Accelerator Conference, PAC2005.

9

ELECTRON BEAM DIAGNOSTICS

TECHNICAL SYNOPSIS

The LCLS-II will require electron beam diagnostics for beam setup, tuning, diagnosis, and feedback. While the diagnostics performance is within the state of the art, new engineering designs may be required to meet the specific requirements of LCLS-II. In particular, the beamline devices and front-end electronics will be conventional, but the high average repetition rate of the beam and the need for fast feedback will require high performance data acquisition and control systems. Kickers will select pulses to send to low repetition rate bypass lines so that invasive measurements can provide constant monitoring of beam parameters.

Beam position measurements will use stripline BPMs where they can meet the resolution requirements, and cavity BPMs to provide higher resolution at low bunch charges where needed. Relative bunch length monitors will be based on coherent radiation power, the same technique used at LCLS-I with transverse cavities to provide absolute measurements in specific locations. Beam current monitoring will be performed with conventional toroids.

Based on experience at LCLS-I, the primary transverse profile measurement devices will be wire scanners. Fluorescent and OTR profile monitors may be usable in the injector but are likely to be limited by coherent emission after the compressors. Several possible schemes to mitigate coherent effect and allow for the use of two-dimensional measurements are described in this chapter.

The high average beam power will necessitate the use of beam loss and halo monitors. Several types are described here. Selection of the specific types and locations for loss and halo monitors will be done after a more thorough analysis of the machine is available.

9.1 Diagnostics Requirements

The LCLS-II injector, linac, beam transport, and undulators will require the following diagnostics:

- **Full beam rate monitors:** beam position monitors, beam loss monitors, beam current monitors, and relative bunch length monitors.
- **Single bunch, low readout rate:** longitudinal and transverse profile monitors.
- **Time average:** beam loss, beam halo, and average current, including all dark current.

Some beam diagnostics will be off axis, on parallel beam diagnostic lines operated with approximately 100 Hz deflected beam pulses. Five off-axis diagnostic sections are shown schematically in Figure 1, which allow continual measurement of electron energy, projected and sliced energy spread, projected and sliced emittance, bunch length, bunch charge, and temporal distribution. RF deflecting cavities are used to provide time-resolved (slice) measurements in three of these diagnostics sections. Insertable screens and wire scanners will measure the transverse beam size at a low beam rate without damage. The final two kickers (green) also serve as MPS fast shutoff devices as the MPS shutdown to the gun takes some time to transport.

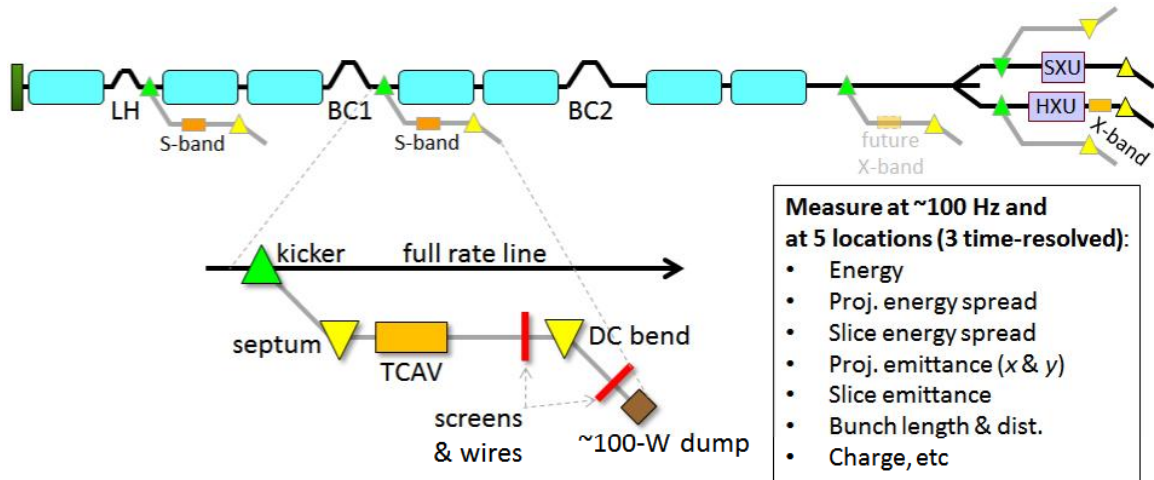


Figure 1. LCLS-II layout with pulse-stealing kickers (green) and beam diagnostics at heater, BC1 after the bypass line, and at each undulator where the beam rate and power are very low, allowing intercepting beam diagnostics to survive. The post-BC1 off-axis diagnostic section is expanded here to show detail. RF deflectors (orange) are used in three of the five diagnostics sections.

LCLS-II diagnostics are required to function over the full range of machine operating modes described in chapter 3, including single shot operation at 10pC. Multiple bunches can be averaged in a train for improved resolution when required. Table 1 lists the electron diagnostics requirements for the LCLS-II accelerator.

Table 1. Diagnostics requirements.

Parameter and Location	Resolution
BPMS: linac and transport, Stripline	50 μm single bunch at 10pC
BPMS: linac and transport, Cavity	10 μm single bunch at 10pC
BPMS: undulator	250 nm single bunch at 10pC
Transverse profile monitors: injector	10 μm resolution
Transverse profile monitors: linac / transport	5 μm resolution
Beam energy monitors	0.003% RMS
Bunch length monitor: injector	20 fs RMS resolution
Bunch length monitor: undulator	2 fs RMS resolution
Bunch length monitor (relative)	1% relative resolution single bunch
Halo monitor	1×10^{-4} of total beam
Beam current monitor	0.1%, 0.5 pC accuracy
Beam arrival time monitor	10 fs RMS, 100 fs jitter

Beam position

Machine simulations are required to determine the required resolution for specific BPMs. Stripline BPMs will be used where resolution requirements are 50 microns at 10pC or less stringent. Cavity BPMs will provide the 10 μm single-bunch resolution required for 10 pC operation in some sections of the linac and transport lines. In the undulator cavity BPMs will provide 250 nm resolution. BPMs will provide position information with less than 1 μs delay for fast feedback and MPS. The BPMs will also provide a fast Big Orbit Abort Trip signal for MPS protection against large orbit excursions.

Transverse Profile Monitors

LCLS-II will primarily rely on wire scanners in the diagnostics lines for beam profile measurement, as screens are likely to be unusable due to COTR effects. Resolution is 5 μm , with scan times on the order of a second for 60 Hz beams. YAG and OTR Screens with 10 μm resolution will be used in the injector for low repetition rate beams for initial setup, and can be used in the diagnostics lines for qualitative measurements. Screens are also used in conjunction with the TCAVs and diagnostic bends to provide time-energy phase space measurements. Synchrotron light monitors are being investigated for use in the chicanes to provide beam size and energy spread measurements.

Beam energy monitors

BPMs in the compressor chicanes and dog-legs will provide shot-to-shot energy measurements with a resolution of less than 0.003 percent. This implies shot-to-shot BPM resolution of 10 μm or better, therefore cavity BPMs are required to achieve this resolution at low beam charge.

Absolute bunch length monitors

Transverse deflecting mode cavities, in conjunction with spectrometer bends, will provide time-energy phase space plots of the beams in the diagnostic lines with few-femtosecond bunch length resolution. To meet this time resolution with reasonable RF power requirements, S-band (2.856 GHz) or third harmonic L-band (3.9 GHz) deflectors will be sufficient before BC1. X-band deflectors (11.424 GHz) will be used in diagnostics after BC1.

Relative bunch length monitors

Coherent radiation monitors after the bends will provide pulse-by-pulse relative bunch length measurements for feedback that can be calibrated against the absolute bunch length measurements.

Halo Monitors

Solid-state ionization detectors located close to the beam in dispersive regions will be used to monitor the beam halo at less than 10^{-4} of the total beam power.

Beam Current Monitors

Beam pickup toroids with less than $1\mu\text{s}$ response will be used to measure the bunch current with 0.1 percent, 0.5 pC accuracy. In addition, a DC current transformer (DCCT) will be used to provide an absolute current calibration to 0.5 percent.

Loss Monitors

Large prompt beam loss will be measured using toroids. Ion chambers will be used to provide shot by shot measurements of small beam losses.

Beam Arrival Time Monitors

RF cavity based beam arrival time monitors will provide better than 10 fs resolution with less than 100 fs drift for single-pulse measurements of the beam arrival time in the linac. A femtosecond beam arrival time system for the experiments is discussed in Chapter 13.

9.2 Beam Position Monitors

Stripline BPMs similar in design and performance to the LCLS_I BPS will be used in areas where a resolution of 50 microns at 10pC is acceptable. Where higher resolution is required cavity BPMs will be used.

Two types of cavity BPMs are foreseen. Cold L-band cavities designed for cryogenic operation will be used in the cryomodules and in large-aperture areas of the chicanes and dump spectrometers (where they will be operated warm). X-band cavities will be used in the rest of the linac, transfer lines, and undulators.

Cavity BPMs will require calibration before use; however, their improved resolution and the reduced electronics linearity requirements relative to striplines make them the preferred choice where high resolution is required.

Table 2. Beam Position Monitors by region.

Region	Cold BPM	Warm BPM
Injector & linac	32	18
Diagnostic sections (4)	-	16
LTU	-	60
Undulator	-	55
Dump	-	12

9.2.1 Cold Cavity BPM

The large aperture of the cryomodules and the chicanes require a low operating frequency for cavity BPMs. A 70 mm aperture requires the BPM operating frequency to be below the TE_{11} mode cutoff frequency of 2.5 GHz. Furthermore integration into the cryomodule requires much tighter control of residual particulates in manufacturing; cleanability is a challenging requirement on design. We expect to use an L-band cavity BPM much like one intended for the ILC cryomodule [1], featuring common-mode-free coupling, a phase reference cavity per BPM, and Q greater than 1,000 to take advantage of the microsecond between bunches. These features make for electronics and processing that is straightforward, simple and compatible with the standard LCLS-II processing electronics (chapter 14). The “re-entrant cavity” BPM from the European XFEL is an existence-proof of a design that has been successfully integrated into a cryomodule, which also meets cleanability requirements [2]. The cold cavity BPMs will also be used at room temperature for measurements in dispersive areas where large apertures and high resolution are required.

9.2.2 Warm Cavity BPM

The undulators require high resolution (250 nm) at low single-bunch charge (10 pC) in a compact package, leading us to choose the X-band cavity BPM developed for the LCLS-I upgrade, whose prototype is presently under test. These cavities feature common-mode-free position couplers and a reference cavity per BPM. Undulator BPMs will be mounted with the quadrupoles on movers for alignment and calibration. The required resolution is within the performance demonstrated for cavity BPMs at LCLS_I and other facilities [3, 4]. Warm cavity BPMs will also be used in other areas requiring resolution not achievable with stripline BPMs.

9.2.3 BPM Electronics

BPM electronics will be based on the standard LCLS-II ADC module (see Chapter 14) with raw signal pre-processed in an analog front-end (AFE) appropriate for each type of BPM. Pre-processing will include appropriate gain, filtering, and down-conversion to an appropriate IF for the standard digitizer module. The ADC module includes programmable logic to decode the BPM signals to provide position and charge at full beam rate. In addition, the BPMs will provide a large-orbit output to the fast MPS system to allow the beam to be tripped off in the event of an unacceptable beam excursion. It may be possible to use the LLRF electronics to read out the similar frequency cold cavity BPMs, but this requires further study.

9.3 Transverse Profile Monitors

The LCLS-II beam is expected to have microbunching similar to that seen at LCLS and at other high-brightness facilities that are likely to prevent the use of diagnostics based on optical measurements (OTR, fluorescent screens etc.), except possibly in the injector. Techniques to mitigate coherent effects are being investigated, including coronagraph-like masking and the use of short wavelength VUV/XUV. Until a suitable solution to coherent effects is found, the baseline will be to use wire scanners for quantitative profile measurements. The screens and wires will be located on the low rate diagnostics lines, or used only on the main beamline at reduced beam rate.

9.3.1 Wire Scanners

Wire scanners are used to measure the transverse profile of the beam in the x, y and u planes. Although profile monitor screens can measure the full transverse distribution in a single shot, wire scanners are now widely used in X-ray FEL machines because they are not susceptible to the disruptive effects of coherent optical transition radiation (COTR). The major consideration for the wire scanner design in this new machine is the higher 1 MHz repetition rate and higher average power of the beam. This is addressed in two ways in the present design. The baseline plan is to place the wire scanners in the special diagnostic beam lines where the beam is only kicked into the line at a much lower rate. In this case, the existing LCLS-I wire scanner designs can be used with diagnostic pulses up to 120 Hz. Also being evaluated is the use of high-speed (about 1 ms^{-1}) wire scanners that will traverse the entire beam before the wire is damaged.

The expected transverse beam sizes throughout the machine are in the range 10-100 μm . Thus at a 100 Hz bypass line beam rate the wire must move at a speed of around 0.1 mm per second to acquire the order of 100 samples. This can be done by the existing wire scanner. A new high-speed wire scanner tested at LCLS also allows the wire to accelerate to the edge of the beam at a much higher speed before starting the scan of the beam, so that an entire scan should only require a few seconds.

If the wire scanner is placed in the beamline straight ahead, it is required to move at a much greater speed so that we can limit the number of 1 MHz bunches hitting the wire without breaking it due to excessive heating. In this case, we require the wire speed to be at least $1 \mu\text{m}/\mu\text{s}$, or 1 ms^{-1} . This allows us to sample of the order of 100 beam pulses during a single scan.

The new high-speed wire scanner [5], tested at LCLS_I, shown in Figure 2 uses an external dc linear servo motor and can accelerate from the park position and move the wire through the beam at 1ms^{-1} . An external position encoder reads the actual position of the wire when triggered by the beam timing system. This allows fast acceleration programs since the actual position not the extrapolated position of the wire is captured by the data acquisition

The fast wire scanner controls will be integrated with the entire LCLS control system so that the photomultiplier tubes can read back the intensity of the electrons intercepted by the moving wire. In addition, the upstream BPMs will be read on the same pulse, so that jitter correction can be applied to compensate for pulse-to-pulse changes in the incoming beam trajectory. This requires the upstream BPMs have a single-shot resolution of $5\ \mu\text{m}$.

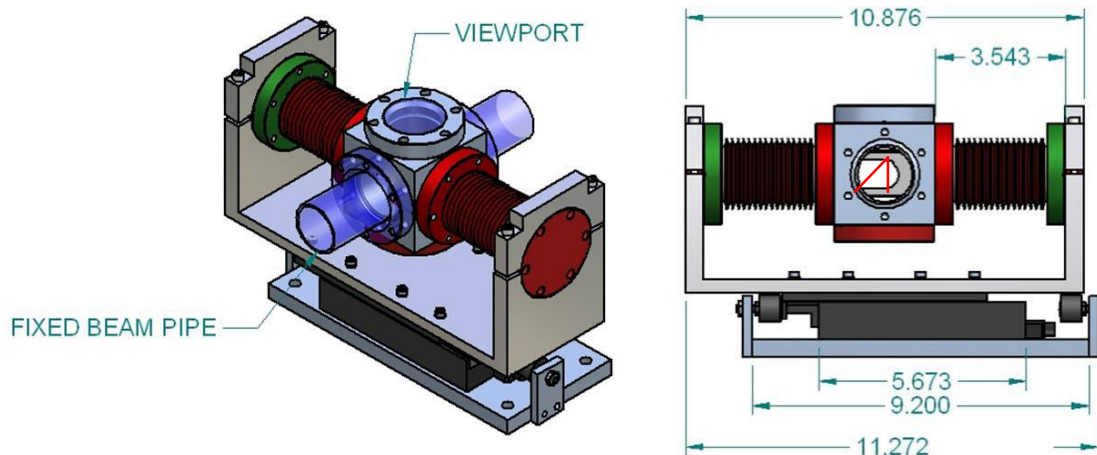


Figure 2. High speed wire scanner used at LCLS-I.

A detection scheme for wire scanners can also be implemented to allow large dynamic range transverse beam profile measurement to measure beam halo and tails. To do this, a fraction of EM shower is converted to visible photons by means of Cherenkov radiation that is detected with PMTs. This signal is then used in a counting mode to provide a very large dynamic range time average measurements [6]. Assuming that the maximum counting rate will be close to the maximum bunch frequency of 1 MHz, and taking in to account that the dark count rate of about 10 Hz is achievable with properly selected PMTs, the dynamic range of about 10^5 can be expected with a single detector. A variety of other techniques that involve integrating the output of the PMT over many pulses can also be applied.

In addition, the angular distribution of the bremsstrahlung (EM shower) can be used to increase dynamic range of the measurements. Several detectors can be placed at different angles relative to the beam direction. The detectors at smaller angles are used for measurements of low intensity parts of the beam. When the beam intensity increases and this detector reaches the upper limit of its dynamic range, a switch is made to a different detector located at larger angle.

9.3.2 Screens

Beam diagnostics screens are essential to obtaining single shot transverse beam profiles, and in conjunction with an RF deflector cavity also longitudinal or time resolved beam profiles and 2D beam distributions. The high average power of the electron beam precludes the implementation of screens intercepting the main beam path at full rate; instead, beam viewing screens will be placed in the low rate diagnostic lines. Optical transition radiation (OTR) screens have the benefit of prompt response, few-micron resolution limit, and low beam loss. However, their use is limited to locations where the longitudinal bunch structure has not been affected by micro-bunching instabilities generating coherent OTR (COTR), which occur for ultra-high brightness electron beams after bunch compression or traversing magnetic bend systems. OTR screens can be considered for the injector prior to bunch compression and at dispersive locations with relatively large beam sizes from energy spread. Cerium doped YAG crystal screens with higher light efficiency will be used in the injector at locations with beam energies below several tens of MeV where the OTR emission is insufficient. Further use of YAG screens at higher energies may be possible because the light emission is less susceptible to coherence effects than with OTR screens, and because mitigation concepts exist to suppress the detection of the COTR emission from the YAG surface by optical or gating techniques [7]. The limitations from saturation of the YAG fluorescence at the high-charge density of a focused beam have been considered in the optics design and screen locations. The same is true for the aging of the crystals that has been anecdotally observed at the main dump screen at LCLS-I, with the light yield locally decreasing over time from prolonged electron beam exposure without any visible damage.

9.3.3 Other Transverse Profile Monitors

Due to the limitations from coherent emission and from high average beam powers, other profile monitor technologies are being investigated. Synchrotron light monitors [8] are an option for non-interceptive single-shot, full or high-repetition-rate energy spread measurement using a small chicane bending the beam perpendicular to the dispersion direction in the bunch compressors or any other dispersive region, including the main dump lines. Use of short (UV, VUV, XUV) wavelengths will reduce sensitivity to microbunching-induced coherent effects, but will increase the system's complexity.

9.4 Halo Monitors

Dark current from the electron gun and from linac cavities at high gradient will produce a halo of electrons around the main beam which could deposit excessive power in the cryogenic systems and activate intercepting beamline components. Detailed simulations will be needed to determine the thresholds and most sensitive locations along the linac. Collimation will be necessary to remove the halo. A beam sweeper or deflector following the gun can remove dark current from gun buckets that are not used for the 1-MHz bunch train (chapter 13). Measurements with beam-halo monitors will allow tuning the collimators and deflector so that the beam can be shut off or rate limited if excessive halo is detected.

Electrons emitted in linac cavities will have substantially lower energies than electrons in the core of each bunch. These halo electrons are easily lost when they fail to pass through apertures and when they are bent through large angles in dipoles. Such losses will be localized after the first bend of the three chicanes (at the laser heater and first and second bunch compressors) and after the dog-leg bends (in the beam-transfer hall, after the linac, and between the undulator and the dump). Additional losses are expected as halo particles closer in energy to the core are trimmed at energy collimators in the middle of the chicanes. In these locations, diamond and sapphire detectors acting as solid-state ionization chambers, can measure the incoming halo population. An array of these small devices after the bend can detect the spectrum of the low-energy halo.

The FLASH FEL at DESY uses a circle of these detectors around the beam pipe to monitor the halo as the beam enters the dump [9]. A similar approach is planned for the European XFEL [10]. The two types, pCVD diamond and single-crystal synthetic sapphire, have different sensitivities and saturation levels and thus extend the dynamic range [10]. The former are 12 mm \times 12 mm \times 0.3 mm, with a bias of 10 to 40 V; the latter are 10 mm \times 10 mm \times 0.5 mm, with a bias of 100 to 400 V. Both types are metalized on both faces. Tests have shown that both tolerate radiation doses of up to 10 MGy.

Halo electrons from the gun differ little in energy and orbit from the core, and as a result are difficult to remove once captured in the linac. However, at 1 MHz, only one gun bucket in 186 should have charge; therefore a deflector or sweeper after the gun that blocks electrons from all other buckets can greatly reduce dark current. The deflected charge can be monitored with additional detectors.

Halo electrons close in energy and orbit to the core emit a comparable synchrotron-radiation spectrum. By imaging the halo while masking the core, it is possible to measure a halo distribution six orders of magnitude below that of the core [11] in the absence of coherent effects. The final dipole of BC2 provides a suitable location where the beam is held at a constant energy, high enough to emit synchrotron light. The masked image shows only the halo from the gun surrounding core bunches, measured at video readout intervals. That should be sufficient since the low-energy halo has already been scraped and the halo from other gun buckets has been deflected. Note, however, that while coherent synchrotron radiation (CSR) from microbunching is substantially reduced in the chicanes, it may still limit the dynamic range of halo measurements. This effect can be reduced by imaging in a narrow bandwidth in the near ultraviolet (UV). Wavelengths around 250 nm still allow the use of ordinary refractive optics and a CCD camera outside the vacuum. This approach should be adequate at the laser heater and perhaps elsewhere. BC1 may require imaging in the vacuum UV using reflective optics. The harder spectrum emitted in the BC2 and LTU dipoles allows the use of the extreme UV or soft X-rays, imaged with multilayer mirrors, or hard X-rays, imaged with either a pinhole camera [12] or a zone plate [13].

9.5 Bunch Length Monitors

Transverse deflecting structures (TDS) in the proposed 100 Hz diagnostic bypass lines provide the most direct bunch length information at rates limited by camera acquisition.

For RF feedback controlling the compression process in the chicanes, a fast bunch length monitor (BLM) is required. In LCLS_1 this was accomplished using pyroelectric detector elements which integrate coherent edge radiation at the exit of the bunch compressors [14]. This provides a relative measurement of bunch length which can be calibrated against TDS measurements. This approach is fully extensible to the LCLS-II linac.

The SLAC-designed pyroelectric detector has demonstrated 100 ns amplified rise times that would be capable of full MHz beam rate operation. Testing is required to verify performance at this rate and to study average power effects.

Alternatively, for bunch durations spanning approximately 3–100 fs, fast mercury cadmium telluride (MCT) detectors may be considered, with the added benefit of improved sensitivity. However, MCT detectors come with the additional cost and complexity of liquid nitrogen cooling.

9.5.1 Relative BLM CW Heat Loading

In 250 pC LCLS_II operating mode, estimates of THz to IR coherent radiation power indicate pulse energies up to several μJ . Thermal effects in the detectors must then be managed to handle Watt-level power from a 1-MHz beam rate. The addition of on-die thermal sensors would provide both thermal signal correction and a path to instrument protection. Where the single-pulse energy exceeds saturation, attenuating neutral density filters in the wavelength range relevant to the local bunch length are used to prevent saturation and sensor damage. With saturation estimated at approximately 100 nJ, as much as 100 mW of continuous power is likely during normal operation. Testing is required to verify if the addition of direct heat sinking or active cooling of the detector elements is necessary in this case.

9.5.2 Advanced BLM Options

Although that pyroelectric relative monitors combined with transverse cavities are the baseline design, other technologies are being investigated to improve performance or reduce costs. An absolute BLM system has also recently been demonstrated at LCLS_I for final bunch compression [15]. The principle is similar to the relative BLM, with the addition of spectroscopy of the coherent beam radiation using a mid-IR prism and linear pyroelectric detector array. With similar limitations as the relative BLM, this solution could also be deployed. It is currently acquisition limited at 10 Hz, but is in principle extensible to 100 Hz, matching the suggested beam rate in the diagnostic bypass lines.

Alternately direct electro-optic (EO) sampling of the beam is also viable for bunch lengths in the range of approximately 50 fs to 3 ps [16]. This implementation is under study at DESY for the European XFEL and requires significant optics and a beam-synchronous Ti:sapph laser pulse at

each diagnostic area. Information about the longitudinal bunch profile is encoded on the laser pulse polarization by nonlinear optical mixing in an EO pickup crystal in the vicinity of the passing electron beam. Analysis of the polarization shift in the IR laser yields detailed information about the bunch profile. Fast, 1D silicon detector arrays operating at the full beam rate are then used for detection. This instrumentation requires nontrivial R&D into the supporting optics, electronics, and FPGA design. More fundamentally, EO pickup crystal damage thresholds under continuous exposure to the passing beam and any potential halo remain to be studied. Should the studies prove direct sampling to be impractical in a CW beam, non-invasive coherent beam radiation could be imaged and probed instead.

9.6 Transverse RF Deflectors

The RF transverse deflecting structures (TCAV) provide a reliable, absolute, single-shot measurement of the bunch length profile. The technique is well established at SLAC where both S-band 2.856 GHz and X-band 11.424 GHz structures are used. The choice of wavelength, λ_{rf} , is chiefly determined by the resolution requirements, given by 17:

$$\sigma_{t,R} = \frac{\sigma_{y0}}{S} = \sqrt{\frac{\epsilon_{N,y}}{\gamma\beta_d} \frac{\lambda_{rf} E_e}{2\pi |eV_0 \sin \Delta\psi|}}$$

where β_d is the beta value at the deflector in the deflection plane, and $\Delta\psi$ is the phase advance to the screen, as shown in Figure 3.

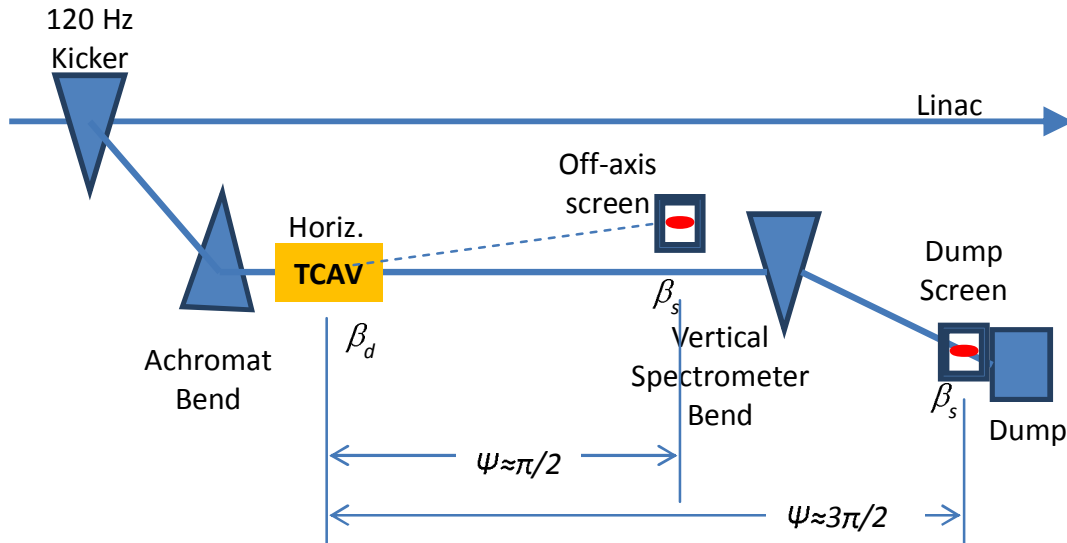


Figure 3. Location of the TCAV in the diagnostic beam lines to measure both slice emittance and slice energy spread.

The resolution requirements and beam energies at the various locations are close enough to those of LCLS-I that the same design choices for RF frequency and power can be made. For example, a 1 femtosecond resolution in the undulator dump beam line can be achieved with an X-band system, whereas the lower energy beam at the injector, BC1 and BC2 diagnostic beam lines

can be served by an existing S-band design. The TCAVs are used in conjunction with emittance and energy spread diagnostics so that the time-resolved slice emittance and slice energy spread can be measured. The deflection plane of the TCAV should be chosen perpendicular to the bend plane where dispersion is generated for the energy measurement.

We envisage installing a TCAV in the injector diagnostic beam line, located downstream from the HXR undulator. Also considered as an upgrade are additional TCAVs after each bunch compressor, the BSY, and after the SXR undulator. The TCAV will be located where the dispersion is nominally zero, and two screens will be located downstream to observe the streaked beam, as shown in Figure 3. The first screen is approximately $\pi/2$ away from the cavity where the dispersion is zero, and can thus be used to measure the vertical slice emittance. The second screen is located after the vertical bend that acts as a spectrometer in the vertical plane. The time-resolved energy spread can be measured if the dump screen is made to be an odd multiple of $\pi/2$ from the TCAV.

To switch between the two screens at the diagnostic line beam rate of 60Hz, either a pulsed magnet can be used or the TCAV phase can be pulsed to steer the beam to an off-axis screen or straight ahead to the dump screen.

The TCAV located downstream of the undulator should be placed in order to best observe the time-resolved energy loss in the beam due to the lasing process in the FEL. The screen should therefore be located downstream of the vertical dump bend, as shown in Figure 4. However, in order to limit the rate and the dose of the beam hitting the screen, it would be placed off-axis and located $\pi/2$ from the cavity. The TCAV will be operated in conjunction with a kicker to ensure that only 120Hz of beam hits the off axis screen. The transverse optics should be configured such that the dump is located another $\pi/2$ from the off-axis screen, so that deflected particles converge back to the dump.

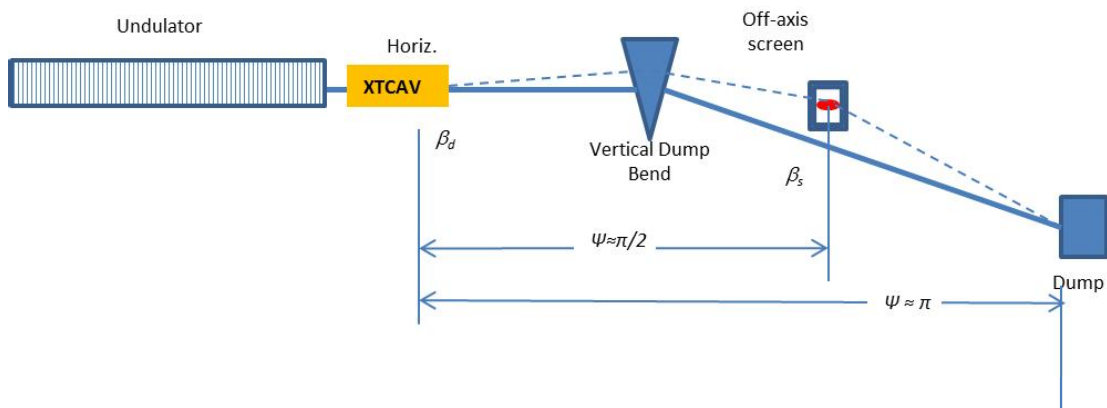


Figure 4. Location of the transverse deflecting cavity for longitudinal phase space diagnostics downstream of the undulator.

Note that while pulsed magnets/kickers can be used to deflect the beam onto the diagnostics screens, it may also be possible to operate the TCAVs slightly off of a zero-crossing to provide

this deflection. Studies are needed to see if this can be done without compromising the measurement accuracy.

9.7 Toroids, Beam Current, and Loss Monitors

Several systems detect and respond to beam losses. They operate on quite different timescales and employ a variety of detectors. The systems are discussed fully elsewhere but are reviewed briefly here to introduce the requirements for detection. The timescales here are estimates and will be further refined by more detailed studies. When the requirements are fully developed, devices will be selected from the following list.

9.7.1 Timescales

Machine Protection System (MPS): approximately 5 μ s

The high beam power makes it critical to detect losses quickly, before a localized loss causes damage. The MPS must shut off or severely limit the beam rate (shifting from the normal 1 MHz to 1 Hz) when a large loss is detected. Losses can be measured on every bunch, allowing a response within a few microseconds, limited by the signal-propagation delay to the gun.

Beam Containment System (BCS): approximately 1 ms

The BCS must respond to the detection of any beam outside its channel (beampipe, linac section, etc.) by halting the beam. Since a localized loss of the entire beam at full rate could melt a hole in copper in about 5 ms, a response time in about 1 ms is needed. Normally MPS will stop the beam far sooner, making a BCS trip unnecessary.

Halo Monitoring: approximately 30 ms

Since the halo electrons should be a small fraction of the total, the response time can be slower. However, the monitors that would detect losses from an unusually large halo have sufficient speed to trip the MPS.

Steady-State Loss Localization: approximately 1 s

A small background of steady-state losses is expected, especially during tuning, when the beam rate is gradually raised. Signals are needed to localize and correct these losses.

9.7.2 Devices

Toroid

Bunch Current Transformers (toroids) will follow electrons from cradle to grave. Toroidal current transformers, measure the charge per bunch passing through a toroidal magnetic core. Comparing pairs of toroids at different locations provides rapid detection of losses of 1 percent or more of the bunch in order to halt the beam at the MPS timescale.

These toroids will be fast enough to measure individual bunches to at least a 10 MHz bunch rate. Therefore the bandwidth will be at least a few times 10 MHz. We expect the resolution to be 0.1 percent or 0.5 pC/bunch, whichever is greater. Toroids will be internally calibrated to about 2

percent accuracy, and cross-calibrated against a precision DCCT to better than 0.5 percent absolute accuracy. Readout will be via an analog front end and digitized by the standard LCLS-II digitizer module. Bunch current transformers will be placed so we can monitor transmission in and out of each machine region.

Table 3. Bunch current monitors.

Region	Bunch Current Monitors	Function
Gun	1	Gun OUT
Laser heater	2	LH IN LH OUT
Diagnostic line 1	1	SDMPB
L1	2	L1 IN L1 OUT
BC1	1	BC1 OUT
Diagnostic line 2	1	DDMP1
L2	2	L2 IN L2 OUT
BC2	1	BC2 OUT
Diagnostic line 3	1	DDMP2
L3	2	L3 IN L3 OUT
BC3	1	BC3 OUT
Bypass line	3	Dogleg IN Dogleg OUT Bypass OUT
BSY	3	Pre RFYKIK Pre BX03 TDKIKB
BTH	2	Pre DKICK3 DDUMP3
UND	5	2 UND IN 2 UND OUT DUMPB
Total	28	

DCCT DC Transformers

In addition to the bunch current monitors, a single DC transformer (DCCT) will provide an absolute current calibration. The DCCT can be absolutely calibrated against either a precision current source or a precision ammeter. This will be placed after the linac, perhaps just before the dog-leg to the bypass line.

Protection Ionization Chamber (PIC)

PICs are compact ionization chambers used to measure localized losses. They are placed at locations where high losses might occur, such as after apertures and collimators. Others look for unusual levels in normally low-loss areas; in the linac, one PIC every 25 to 50 m would be satisfactory.

Long Ionization Chamber (LION)

Losses at points further from a PIC and distributed losses are measured by running a long, air-dielectric coaxial cable (Helix) along the wall next to the beamline. By filling the cable with a suitable gas mixture and biasing it with a high voltage, the cable becomes a long ionization chamber (LION). These operate on the BCS timescale.

Panofsky's Long Ionization Chamber (PLIC)

A coaxial-cable ionization chamber originally running the full 3 km length of the linac became known as "Panofsky's long ionization chamber" (PLIC). A localized loss generates a pulse traveling along the cable in each direction. The arrival time of loss signals at the upstream end gives the distance to each loss point, provided that the repetition interval is less than the time for an electron bunch to travel the length of the cable and for loss signals to return. Loss signals arrive almost simultaneously at the downstream end, since signals in this cable propagate at $0.9c$, and so this pulse measures the total loss. The signal from a PLIC spanning a 100 m linac sector is $0.7\ \mu\text{s}$ long, and would thus be a suitable diagnostic for tuning a 1 MHz beam. A 100 m LION cable could be used for both BCS and as a PLIC for loss tuning.

Solid-state Ionization Detectors

Solid-state detectors after dipoles can detect losses from low-energy halo electrons, as discussed in section 9.4.

Cherenkov Beam-Loss Monitor (BLM)

The permanent magnets of the undulator provide a precisely tailored magnetic field that can be changed by radiation exposure. Losses in the narrow beam channel must be monitored, and the beam must be shut off or rate-limited on the MPS timescale when losses exceed a threshold. Also, the detector must not respond to synchrotron radiation generated in the undulator. A Cherenkov radiator is insensitive to these X-ray photons. In the BLM, electrons and positrons from a loss shower will generate Cherenkov light in two fused-silica blocks above and below the beampipe. Some of this signal will travel along the blocks by total internal reflection to a photomultiplier (PMT) next to the chamber. The beam can be tripped if this signal exceeds a threshold. Since the shower from a grazing-incidence beam loss is seen for tens of meters along the undulator, one

detector per girder is sufficient for MPS. A typical loss will be detected at several adjacent girders.

Fiber-Optic Loss Monitor (Fiber PLIC)

BLMs do not localize losses in the undulator. Instead, we can run a thin optical fiber alongside the beam channel. It will respond to a loss shower by sending a pulse of Cherenkov light in both directions. A PMT detecting this light at the upstream end provides a signal analogous to that of a PLIC. Although the fiber will pick up a signal over many meters, its proximity to the loss point should provide a waveform indicating the position of the loss.

RADFET

Demagnetization of the undulator depends on its accumulated radiation dose over the course of months to years. This is poorly measured by summing the shot-by-shot losses seen by the BLMs. Instead, we propose to use the RADFET, a type of MOSFET transistor. When exposed to radiation, charge is permanently trapped in the oxide, changing the voltage drop for a fixed current. These are commercially available and have been characterized to relate the voltage drop to the radiation dose. One to two RADFETs can be embedded in each undulator section and read every 10 minutes to provide a history of the local dose. These may also be helpful for monitoring the dose to electronics placed in the tunnel.

9.8 Arrival Time Monitors

RF cavity based beam arrival time monitors will be used at the injector site, at each bunch compressor and for each undulator. These will be similar in design to the LCLS Beam Arrival Time system which has demonstrated 7 fs RMS timing jitter and less than 100-fs-long term drift. The RF cavity frequencies will be chosen to be compatible with beam operating modes and the required beam apertures. The cavities will operate away from gun harmonics to reduce sensitivity to dark current. Using 3807.14 MHz is a possible choice. This is one half of the gun frequency below three times the main 1300 MHz RF frequency ($1300 \times 3 - (1300/7)/2$, where 1300/7 is the gun frequency). This frequency is also compatible with the 3808 MHz phase detection electronics that have been developed for the experimental laser locking systems used in LCLS_I and planned for LCLS_II. The frequency locking system needed to generate a 3807.14 MHz reference is described in Section 13.3.

9.9 Beam-Based Feedback

Various transverse and longitudinal beam-based feedback systems have been successfully implemented at LCLS-I to deliver a stable beam orbit, energy and bunch length along the machine for a beam rate of 120 Hz, with loops operating from 1 Hz up to 30 Hz to correct slow drifts and effects from the 60 Hz AC power line. For the MHz beam rate of LCLS-II, two different kinds of beam-based feedbacks will be implemented, as shown in **Figure 5**. Low rate (less than 120 Hz) versions will be used to control the injector bunch charge; to control the beam orbit throughout most of the accelerator, independent or cascaded loops will be used. The slow

orbit feedbacks will mitigate slow drifts of the beam position and will maintain the beam orbit during or after changes of the machine configuration affecting the transverse beam dynamics.

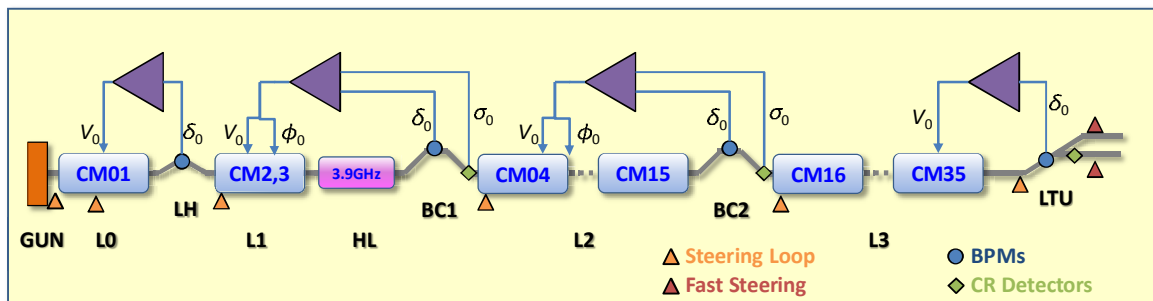


Figure 5. Schematic of LCLS-II transverse and longitudinal beam-based feedback systems.

A high rate feedback system with up to 1 MHz acquisition rate and microsecond latency will be used to stabilize the longitudinal beam parameters throughout the accelerator and the beam orbit in the beam transport lines to the undulators. The longitudinal feedback will be based on single-bunch measurements of beam energy, and bunch length after each subsection of the linac or each bunch compression stage and will control the global accelerating gradient and RF phase of each subsection. The system will take advantage of beam measurements available at full rate to achieve the highest feedback bandwidth. This is particularly important to regulate remaining transients from pulsed bunch train operation which might not get removed by the LLRF feedback or feed-forward schemes and to be able to react immediately to deliberate or safety system induced beam rate changes.

The feedback system will require a highly integrated processing of the beam diagnostics signals, feedback loop computation, and control of the low-level RF or fast kicker/RF-deflector settings, with the feedback latency mainly limited by signal travel time between the different locations of the measurements and actuators.

9.10 References

1. Zenghai Li, SLAC National Accelerator Laboratory, Menlo Park, CA, *personal communication* (2013).
2. C. Simon, O. Napoly, J-P. Prestel, and N. Rouvière, “Status of the re-entrant cavity beam position monitor for the European XFEL project,” *Proceedings of BIW10*, Santa Fe, NM, p. 210 (2010).
3. Y. Inoue et. al “Development of a high resolution cavity-beam position monitor”, *PRST-Accelerators and beams* 11, 062801 (2008).
4. Y. I. Kim et al. “Cavity beamposition monitor system for the Accelerator Test Facility 2”, *PRST – Accelerators and Beams* 15, 042801, (2012).
5. P. Krejcik, M. Campell, N. Fong, J. Frisch, and H. Loos, “Evaluation of New, Fast Wire Scanner Designs for the LCLS”, *Proceedings of BIW2012*, Newport News, VA USA, p. 210 (2012).
6. A. P. Freyberger, “Large dynamic range beam profile measurements,” *Proceedings of DIPAC2005*, Lyon, France, p. 12 (2005).

7. M. Yan, C. Behrens, Ch. Gerth, G. Kube, B. Schmidt, S. Wesch, "Suppression of Coherent Optical Transition Radiation in Transverse Beam Diagnostics by Utilising a Scintillation Screen with a Fast Gated CCD Camera," *Proc. of DIPAC2011*, Hamburg, Germany, p. 440 (2011).
8. Ch. Gerth, F. Ludwig and Ch. Schmidt, "Beam Based Measurements of the RF Amplitude Stability at FLASH using a Synchrotron Radiation Monitor," *Proc. of DIPAC2009*, Basel, Switzerland, p. 342 (2009).
9. A. Ignatenko, N. Baboi, H. Henschel, O. Hensler, W. Lange, W. Lohmann, M. Schmitz, S. Schuwalow and K. Wittenburg, *Application of Diamond and Sapphire Sensors in the Beam Halo Monitor for FLASH*, Report No. TESLA-FEL 2010-05.
10. A. Ignatenko, N. Baboi, H. Henschel, O. Hensler, W. Lange, W. Lohmann, M. Schmitz, K. Wittenburg and S. Schuwalow, "Beam Halo Monitor for FLASH and the European XFEL," Proceedings of the International Particle Accelerator Conference (PAC2012), New Orleans, LA, 2012 May 20–25, p. MOPPR018 (2012).
11. R. Fiorito, A. Shkvarunets, H. Zhang, D. Douglas, F. Wilson, S. Zhang, J. Corbett, A.S. Fisher, W. Mok and K. Tian, "Optical Synchrotron Radiation Beam Imaging with a Digital Mask," Proceedings of the Beam Instrumentation Workshop (BIW2012), Newport News, VA, 2012 April 15–19, p. TUPG031 (2012).
12. F. Sannibale, D. Baum, A. Biocca, N. Kelez, T. Nishimura, T. Scarvie, and E. Williams, "Commissioning of BL 7.2, the New Diagnostic Beamline at the ALS," Proceeding of the 2004 European Particle Accelerator Conference (EPAC04), Lucerne, Switzerland, p. 2783 (2004).
13. H. Sakai, *et al.*, "Improvement of Fresnel zone plate beam-profile monitor and application to ultralow emittance beam profile measurements," *Phys. Rev. ST Accel Beams* **10**, 042801 (2007).
14. H. Loos, T. Borden, P. Emma, J. Frisch, and J. Wu, in *Proc. of 2007 IEEE Part. Accel. Conf.* (Albuquerque, New Mexico, 2007) pp. 4189–4191.
15. T. J. Maxwell, C. Behrens, Y. Ding, A. S. Fisher, J. Frisch, Z. Huang, and H. Loos, *Phys. Rev. Lett.* **111**, 184801 (2013).
16. S. Casalbuoni, H. Schlarb, B. Schmidt, P. Schmüser, B. Steffen, and A. Winter, *Phys. Rev. ST Accel. Beams* **11**, 072802 (2008).
17. P. Emma, "A transverse RF Deflecting Structure for Bunch Length and Phase Space Diagnostics", LCLS technical note LCLS-TN-00-12 SLAC (2000).

10 START-TO-END TRACKING SIMULATIONS

TECHNICAL SYNOPSIS

The expected performance of the LCLS-II accelerator and its two FELs are evaluated by running detailed computer simulations over the three major machine systems: the gun/injector, the linac and compressors, and the free-electron lasers in both SASE and self-seeded operation. These simulations are built up using various computer codes, as has also been done at many facilities in the recent past, including at LCLS-I. The injector simulations are accomplished using the computer codes Astra; the linac/compressor simulations are run using Elegant; and the FEL simulations are carried out using Genesis-1.3. The output particle coordinates of one code are fed as input to the next code in order to string the simulations together consistently for a “start-to-end simulation”.

This chapter summarizes these simulation results for the nominal 100 pC machine configuration, including linear and second order optics, longitudinal wakefields, coherent and incoherent synchrotron radiation in the bends, space-charge forces (mostly in the injector), resistive-wall wakefields in the undulators, the micro-bunching instability, and other well-known effects. Some of the studies also include reasonable component errors and beam-based corrections. In addition, this chapter addresses component sensitivities (e.g., FEL or emittance sensitivity to field errors, RF phase errors, misalignments) and beam-based corrections strategies (e.g., steering, beta-matching, RF phasing, beam-based alignment).

10.1 Introduction and Overview

Particle tracking studies have been performed over the full machine — from injector, through the accelerator, and into the FEL — by stringing together results from several computer codes such as *Astra* [1] (for the injector), *Elegant* [2] (through the linac), and *Genesis-1.3* [3] (through the FELs) [4,5]. Included in the tracking are 3D space charge forces in the injector (to approximately 100 MeV), longitudinal wakefields in the linac, coherent synchrotron radiation (CSR) in the bends and relevant drift sections, incoherent synchrotron radiation (ISR) in the bends, second-order optics (*e.g.*, chromatic and geometric effects), resistive-wall wakefields in the undulators, and 3D time-dependent FEL simulations. All components are initially error free (*e.g.*, in perfect alignment) and no long-range wakes are included (see Chapter 6 for bunch-to-bunch wakefields). A micro-bunching instability study, including CSR and longitudinal space charge forces in the full machine, is included at the chapter end. The following list describes the various effects included in the particle tracking (prior to the micro-bunching study section).

- 0.625×10^9 electrons (using 2.5×10^5 macro-particles) representing a 100 pC electron bunch (as an example) tracked through *Astra*, which includes space charge forces, up to the exit of the CM01 accelerator section at ~ 100 MeV, which is expected to be a high enough energy where space charge forces are unimportant (as is similar in LCLS-I).
- First and second-order optics of dipole, quadrupole, and solenoid magnets (LCLS-II has no sextupole or skew quadrupole magnets yet), and sinusoidal RF fields.
- Short-range longitudinal and transverse wakefields (although with no transverse misalignments yet) of the 1.3 GHz and 3.9 GHz RF accelerating structures.
- Magnetic bunch compression in the two compressor chicanes (to second order, while 3rd order is typically not important).
- CSR applied to all bends using a 1D line-charge model in *Elegant*, including transients and drifts, but ignoring transverse beam dimensions (typically having no impact). 3D studies will be performed after the conceptual design is finished.
- ISR applied to all bends, which impacts the slice energy spread and slice emittance, although by insignificant levels here.
- Longitudinal resistive-wall wakefields of the 2.4-kilometer-long existing bypass line with 2-inch ID and composed of a stainless steel cylindrical pipe (the dominant non-linac wakefield). Linac wakefields are also included, as described above in this list.
- An increased slice energy spread (6 keV rms) at 100 MeV (before magnetic compression) produced by a laser heater system (approximated by a Gaussian profile for this study).
- All components are (at least initially) error-free, including perfect alignment. The local steering effects of the CSR-induced energy loss in all bends are removed, such as would be done in real operation, so that large CSR-induced trajectory errors are not generated.

The simulations are described below separately for the injector, linac, and the two FELs. A short micro-bunching instability study follows. The injector, linac, and bunch compressors are shown schematically in Figure 1 below, including RF phase settings for each linac section, cryomodule numbering, chicane locations, and peak current levels along the machine.

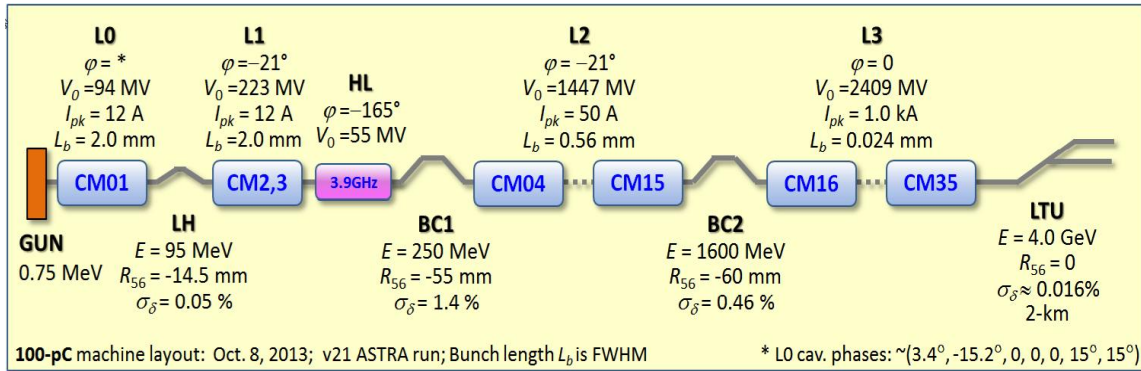


Figure 1. Injector, linac, and bunch compression layout used in the start-to-end simulations presented below (100 pC/bunch). Seven L0 phase are shown since the 8th cavity is off.

10.2 Injector Simulations

The basis of the photoinjector for the LCLS-II is a normal conducting electron RF gun, operating in a continuous wave (CW) mode at 185.7 MHz (1300/7 MHz). A more detailed description of the injector subsystems is given in Ref. [6]. The injector layout is shown in Figure 2. The peak value of E_z at the cathode is limited to 20 MV/m, which is sufficient to guarantee good transverse emittance. The cathode-to-anode gap of the gun is 4 cm, leading to a final beam energy of 750 keV at the gun exit.

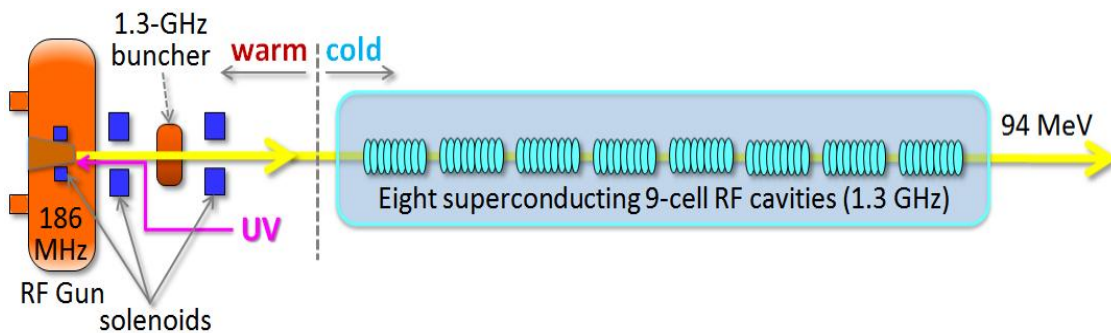


Figure 2. Injector layout from RF gun through first 8-cavity, 12-m long cryomodule (CM01). Parameters are listed in the table below. RF phase settings are defined with zero at max. acceleration while negative values produce a lower energy at the bunch head.

The simulation code used to model the low energy effects, including space charge and $\beta < 1$ effects, is *ASTRA* [1], which has been widely used and extensively benchmarked against experiments as well as other simulation codes. The initial transverse distribution of the bunch is radially symmetric in transverse position and Gaussian in transverse momenta, as expected in the case of photoemission from a cathode illuminated by a transversely uniform laser. For the

longitudinal component, a distribution in the range of a few tens of ps and a rise/fall time of 2 ps is assumed for the emission time, whereas a Gaussian distribution is assumed for the longitudinal component of the momentum. This arrangement provides some velocity-based bunch length compression (a factor of three) over the length of the injector. The beam dynamics simulations from cathode through the first cryomodule are shown below with the parameters listed in Table 1.

Table 1. Table of parameters used in the start-to-end *ASTRA* simulations for the LCLS-II injector.

Parameter	Symbol	Unit	Value
End-of-injector electron energy	E_i	MeV	98
Charge in each bunch	Q_b	nC	0.10
Drive laser FWHM pulse length (flat-top pulse with ramps)	Δt_i	ps	33
Drive laser rise and fall time (10-90%)	Δt_{rf}	ps	2
Drive laser spot size diameter on cathode (radially uniform)	$2r_{cath}$	mm	0.77
Peak current at CM01 exit (after velocity compression)	I_{pk0}	A	12
Bunch length compression factor (velocity compression)	C_v	-	3
Bunch length after CM01 cryomodule (rms)	σ_z	mm	1.0
Gun RF phase (with zero defined as max. acceleration)	ϕ_g	deg	-8.4
Buncher gradient (1.3 GHz)	G_B	MV/m	3.67
Buncher phase (with zero defined as maximum acceleration)	ϕ_B	deg	-84.5
Bucking coil solenoid length-integrated field	$\int B_0 dz$	T-m	0
First solenoid length-integrated axial field ($L_{eff} = 0.184$ m)	$\int B_1 dz$	T-m	0.007784
Second solenoid length-integrated axial field ($L_{eff} = 0.184$ m)	$\int B_2 dz$	T-m	0.005393
Cavity-1 gradient (1.3 GHz)	G_{C1}	MV/m	10.94
Cavity-1 phase (with zero defined as maximum acceleration)	ϕ_{C1}	deg	3.4
Cavity-2 gradient (1.3 GHz)	G_{C2}	MV/m	3.317
Cavity-2 phase (with zero defined as maximum acceleration)	ϕ_{C2}	deg	-15.2
Cavity-3-7 gradient (1.3 GHz)	ϕ_{C3-7}	MV/m	15.47
Cavity-3-6 phases (with zero defined as maximum acceleration)	ϕ_{C3-6}	deg	0
Cavity 7 phase (with zero defined as maximum acceleration)	ϕ_{C7}	deg	15
Cavity 8 is unpowered and held as a spare	-	-	-

Figure 3 shows the transverse normalized emittance, the rms bunch length, and the electron energy across the injector for the parameters listed above. We note that the bunch length is “frozen-in,” in the sense that it does not evolve any further as the energy is increased. The beam emittance is also in the process of being frozen-in in the same sense. We can thus conclude that the low- β and space charge effects associated with low energy are sufficiently small in the downstream linac, although the micro-bunching instability, amplified by space charge forces, is studied separately in Chapter 7.

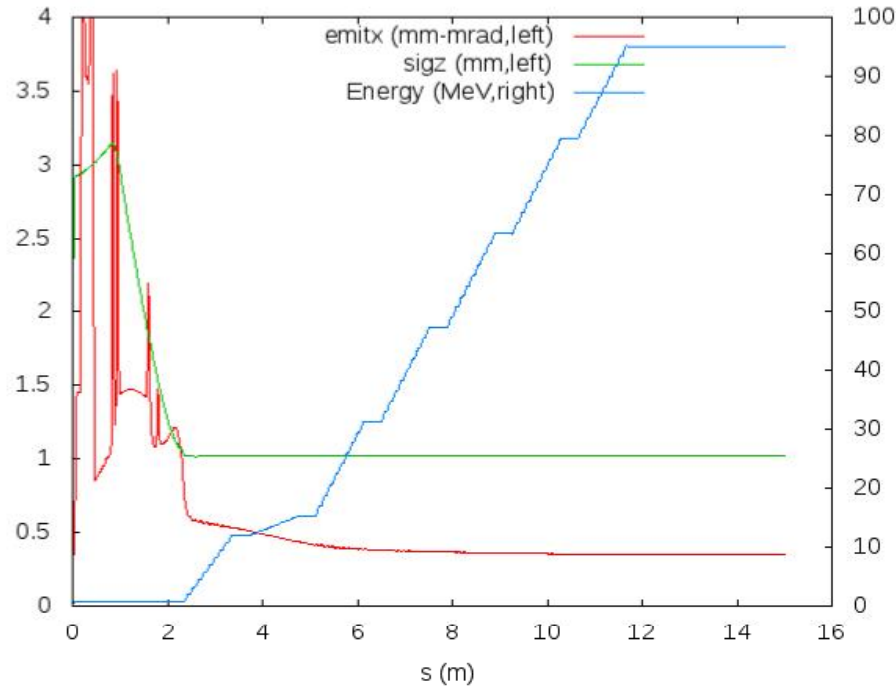


Figure 3. Plot of the transverse normalized emittance (“emitx”), the rms bunch length (“sigz”), and the electron energy across the injector (“Energy”) with a 100 pC bunch charge. The scale at left is for rms bunch length (mm) and normalized emittance (mm-mrad), while the scale at right is for electron energy (MeV).

Finally, Figure 4 shows the temporal profile, sliced transverse emittance values, longitudinal phase space, and the beta mismatch parameter (≥ 1) at 98 MeV, where the beta mismatch parameter is defined as

$$\zeta \equiv \frac{1}{2} \left(\frac{\beta}{\beta_0} - 2\alpha\alpha_0 + \frac{\beta_0}{\beta} \right) \geq 1, \quad (1)$$

where α and β are the beam Twiss parameters, α_0 and β_0 are the design Twiss parameters.

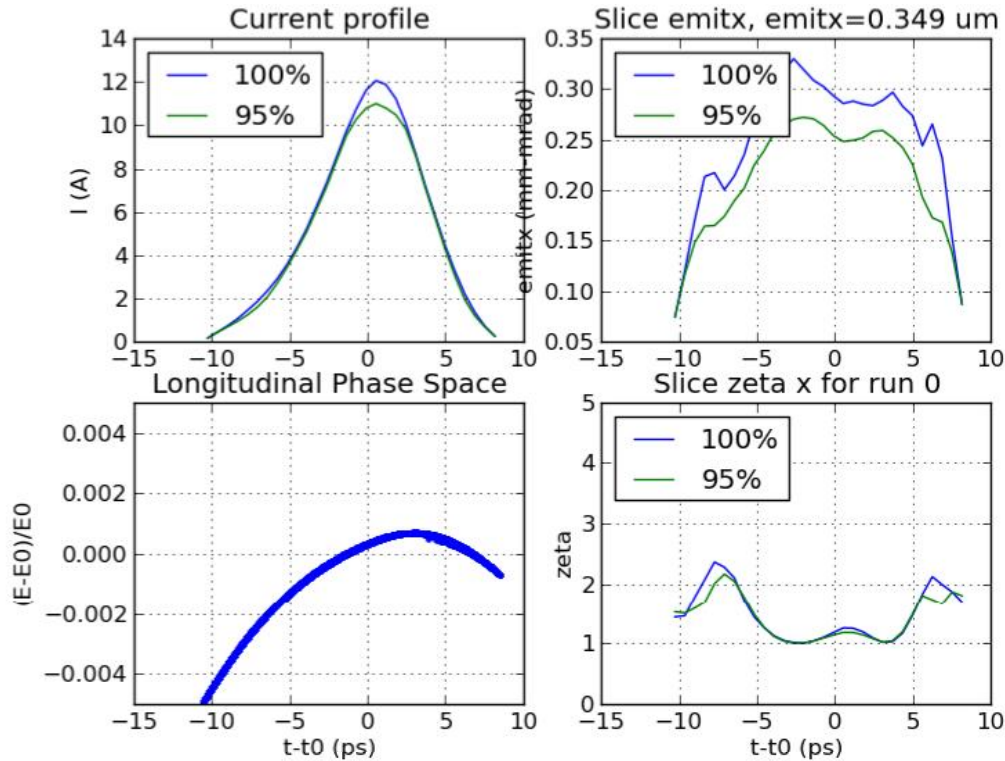


Figure 4. Peak current profile (top-left), normalized slice emittance along the bunch (top-right), longitudinal phase space (bottom-left), and transverse mismatch parameter (bottom-right), all plotted vs. the bunch length coordinate, $t - t_0$, at 98 MeV after CM01 (bunch head at right here), where the mismatch parameter is $\zeta \equiv 0.5(\beta/\beta_0 - 2\alpha\alpha_0 + \beta_0/\beta)$.

10.3 Linac Simulations

The *LCLS-II* linac layout at a 100 pC bunch charge is shown schematically in Figure 1, with the laser heater, the two compressor chicanes (BC1 and BC2), 35 12-m-long, 1.3-GHz RF cryomodules, one 3.9 GHz linearizer RF system, and the final beam switching. The RF phasing, chicane strengths, peak current, energy, and rms energy spread are indicated at each step of the figure. Note that the BC2 spoiler foil [7] is not included and may not survive the beam power.

The macro-particle coordinates from the *ASTRA* run described above are now fed into the linac's next simulation stage, starting from injector output up to the entrance of the SXR undulator. The parameters used for the linac start-to-end simulations (using the computer tracking code *Elegant*) are listed in Table 2. The accelerator optics functions, from the exit of the CM01 injector cryo-module (98 MeV) to the start of the SXR FEL, are shown in Figure 5. In addition, the evolving rms bunch length and rms relative energy spread are shown in Figure 6, where each bunch length reduction occurs at a compressor chicane, and the energy spread is reduced down to 0.01 percent rms through the resistive-wall wakefield of the long bypass line. The electron energy is plotted in Figure 7 along the machine from the CM01 exit at 98 MeV to the SXR undulator entrance at 4 GeV. The flat sections along the plot represent the locations of the laser heater, the BC1, BC2, and the long bypass lines.

Table 2. Table of parameters used in the start-to-end simulations for the LCLS-II linac, from CM01-exit to the SXR undulator entrance.

Parameter	Symbol	Unit	Value
Final electron energy	E_f	GeV	4.0
Charge in each bunch	Q_b	nC	0.10
Laser heater generated sliced rms energy spread	$\sigma_{\delta\text{Htr}}$	keV	5-6
RF phase of Linac-1 (CM02-CM03 cryomodules)	ϕ_{L1}	deg	-21
RF phase of Linac-h (3.9-GHz linearizer)	ϕ_{Lh}	deg	-165
RF phase of Linac-2 (CM04-CM09 cryomodules)	ϕ_{L2}	deg	-21
RF phase of Linac-3 (CM10-CM27 cryomodule)	ϕ_{L3}	deg	0
RF crest voltage of Linac-h (3.9 GHz linearizer)	V_{Lh}	MV	55
Momentum compaction of laser heater chicane	$R_{56\text{-Htr}}$	mm	-14.5
Momentum compaction of BC1 chicane	$R_{56\text{-BC1}}$	mm	-55.0
Momentum compaction of BC2 chicane	$R_{56\text{-BC2}}$	mm	-60.0

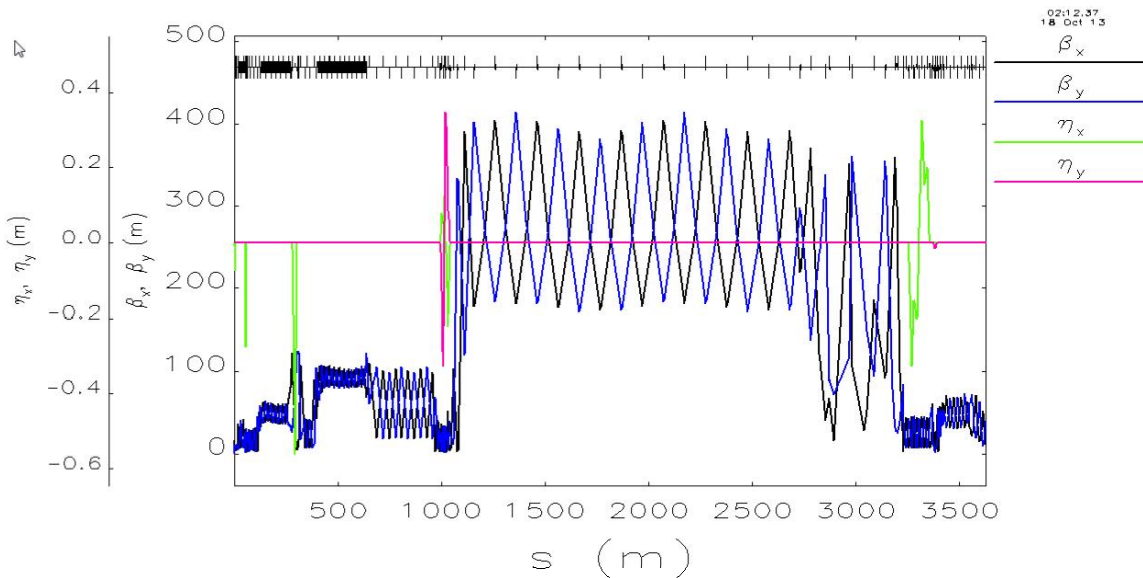


Figure 5. Optics across the entire LCLS-II, from exit of the CM01 injector cryo-module (98 MeV) to the start of the SXR undulator at 4 GeV.

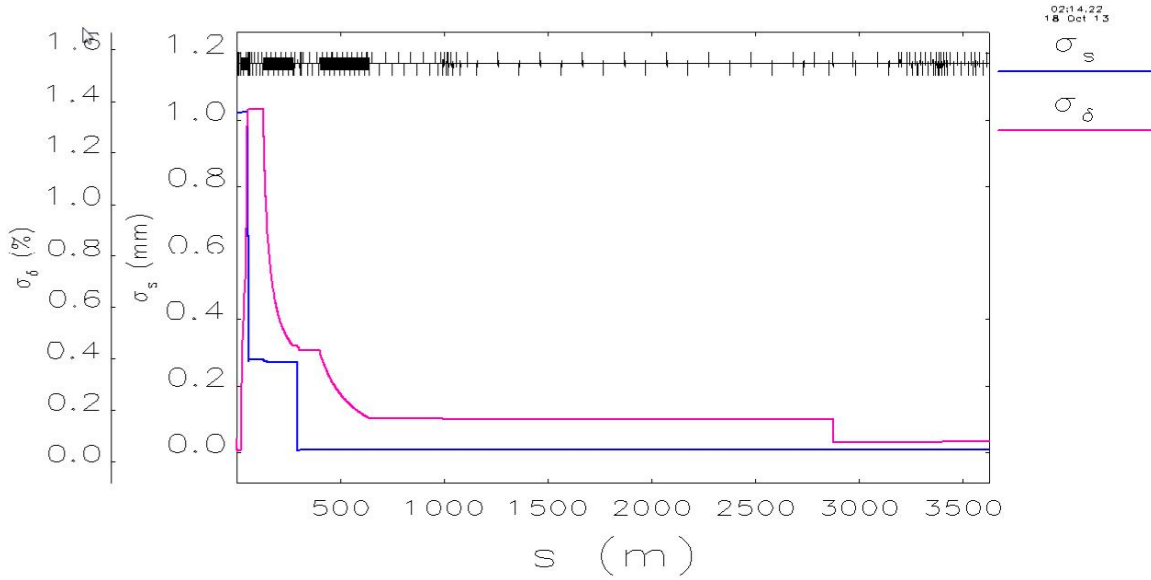


Figure 6. RMS bunch length (blue) and rms relative energy spread (magenta) across the entire LCLS-II, from exit of the CM01 injector cryo-module (98 MeV) to the start of the SXR undulator at 4 GeV. The step down in energy spread at $s \approx 2900$ m represents the accumulated resistive-wall wakefield of the 2400-m-long bypass line, but updated in the plot at just this one point.

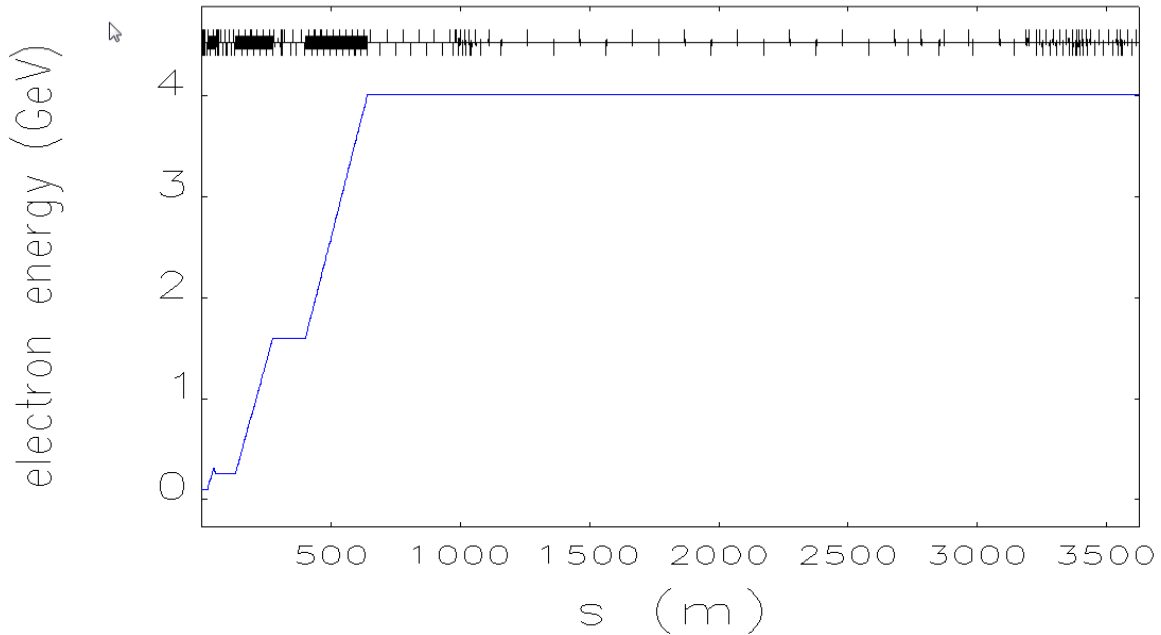


Figure 7. Electron energy (GeV) from the injector output (98 MeV) to the start of the SXR undulator at 4 GeV. The flat sections are the laser heater, BC1, BC2, and the bypass line.

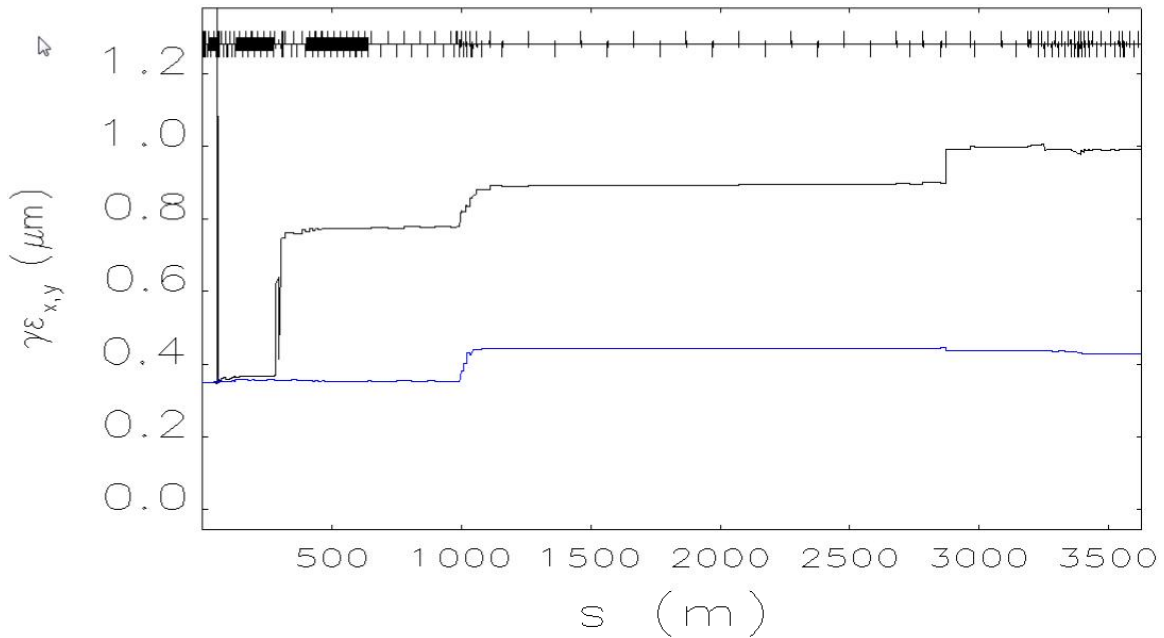


Figure 8. Normalized projected emittance (black is horizontal and blue is vertical) from the injector output (98 MeV) to the start of the SXR undulator. This is the “corrected emittance,” where linear correlations with energy in x , x' , y , and y' are all removed in software. The slice emittance is much less affected. This will improve with future optimization efforts.

Plotted in Figure 8 are the normalized projected x and y emittances along the machine, from the CM01 exit at 98 MeV to the SXR undulator entrance at 4 GeV. The large horizontal emittance increase at $s \approx 300$ m is due to CSR effects in the BC2 chicane. Smaller steps are also seen at $s \approx 1000$ m in both x and y at the rolled dog-leg bends which transport the linac beam up to the bypass line on the tunnel ceiling. Further optimization efforts will concentrate on minimizing these effects by partial cancellation from BC2 to the rolled dog-leg, and by better matching choices. The slice emittance, however, is not much impacted (see below).

The bunch compression process is laid out in the following plots (Figure 9 - Figure 13). Each figure has three plots with the (rotated) energy profile at left, the longitudinal phase space at center, and the temporal profile at right. The first row of three plots (Figure 9) is taken at the CM01 exit (98 MeV), the second row (Figure 10) just after the laser heater (98 MeV), the third row (Figure 11) follows the BC1 compressor (250 MeV), the fourth row (Figure 12) follows BC2 (1.6 GeV), and the fifth row (Figure 13) is at the SXR undulator entrance (4 GeV). The bunch length is compressed from 1.02 mm rms (12 A) at 98 MeV to 8.7 μm rms (1 kA) at 4 GeV over this process. The final energy spread is flattened over the core of the bunch to a 0.012 percent sliced spread (or 500 keV, as better seen in the time-sliced plots below this), defined by the laser heater setting (6 keV rms) and the total compression factor ($1000/10 \approx 100$).

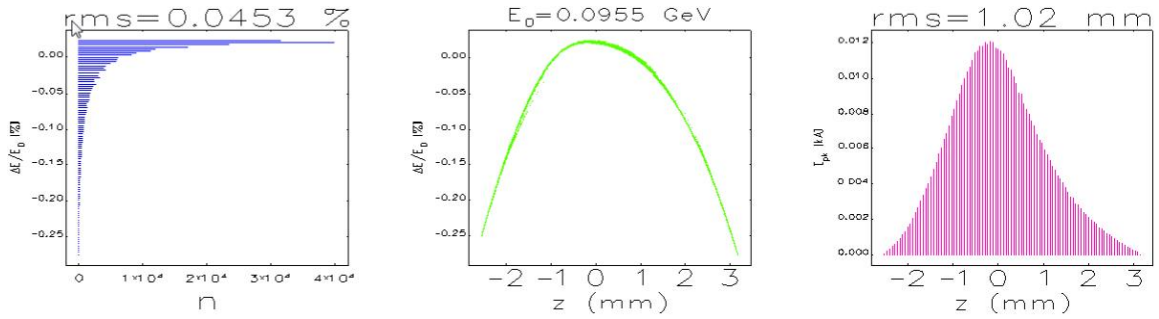


Figure 9. Longitudinal phase space at CM01-exit at 98 MeV, just before the heater, with relative energy spread profile (left), longitudinal phase space (middle), and peak current distribution (right). The bunch head is at left here toward $z < 0$.

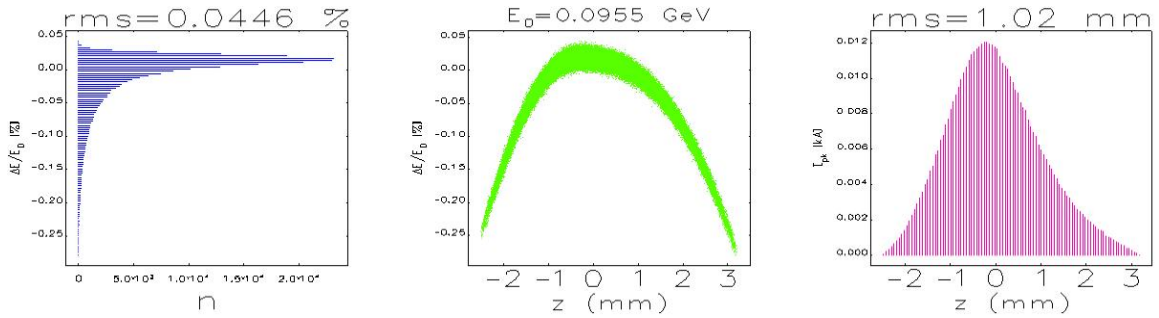


Figure 10. Longitudinal phase space just after the heater at 98 MeV, with relative energy spread profile (left), longitudinal phase space (middle), and peak current distribution (right). The bunch head is at left here toward $z < 0$.

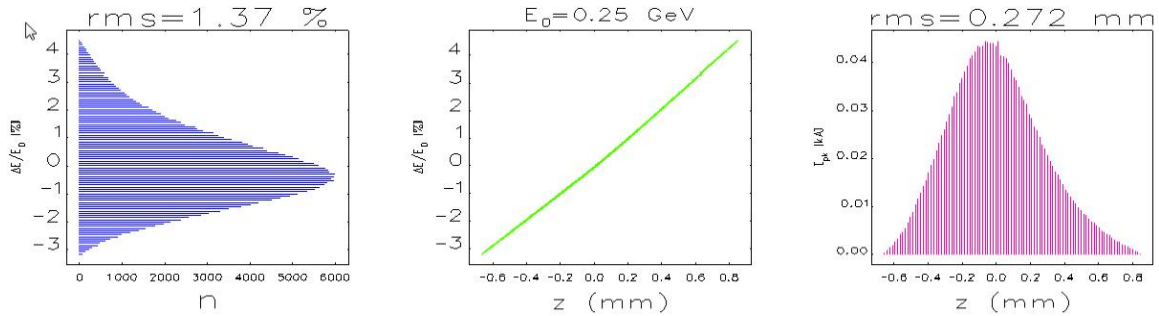


Figure 11. Longitudinal phase space after BC1 at 250 MeV, with relative energy spread profile (left), longitudinal phase space (middle), and peak current distribution (right).

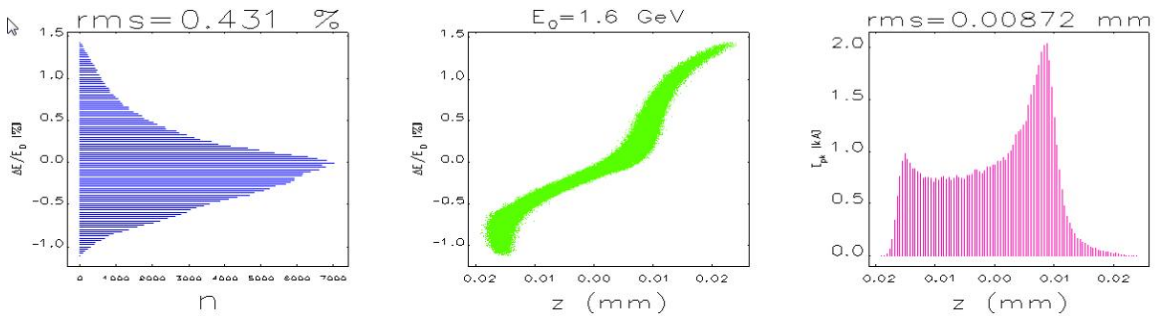


Figure 12. Longitudinal phase space after BC2 at 1.6 GeV, with relative energy spread profile (left), longitudinal phase space (middle), and peak current (right).

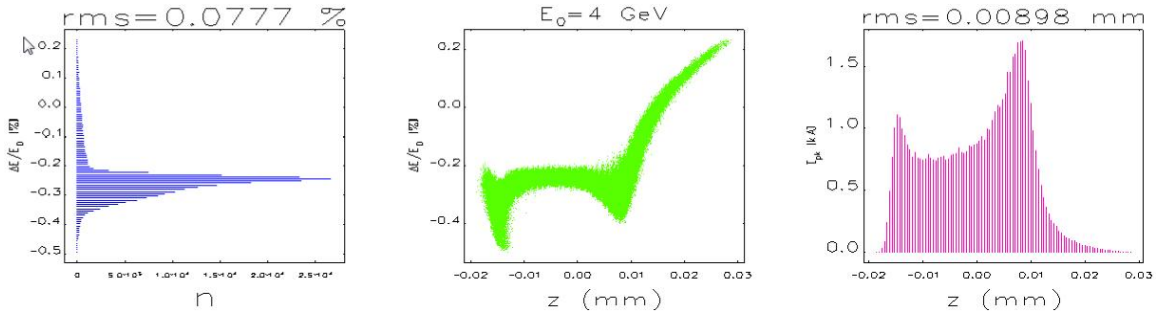


Figure 13. Full phase space at undulator entrance (4.0 GeV) with relative energy spread profile (left), longitudinal phase space (middle), and peak current distribution (right). The bunch head is at left. Efforts are ongoing to remove the tails, but they seem to stem from the injector where space charge forces begin this effect.

Finally, the time-sliced transverse emittance levels and relative energy spread are shown in Figure 14 and Figure 15, respectively, at the SXR undulator entrance at 4 GeV. The time sliced transverse emittance values are almost unaffected in the core of the beam at $\gamma\epsilon_{x,y} \approx 0.3 \mu\text{m}$. Similarly, the time-sliced relative energy spread is 0.012 percent (500 keV) rms in the beam core and defined by the heater setting (6 keV rms) and magnetic compression factor (~ 100).

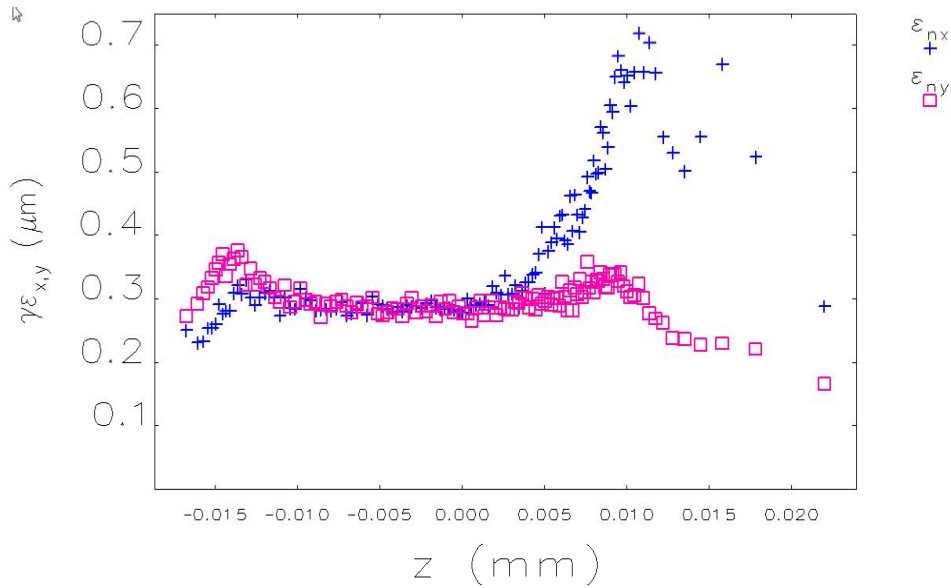


Figure 14. Normalized slice emittance along the bunch length at the start of the SXR undulator at 4 GeV (blue crosses are horizontal and magenta squares are vertical). CSR is included.

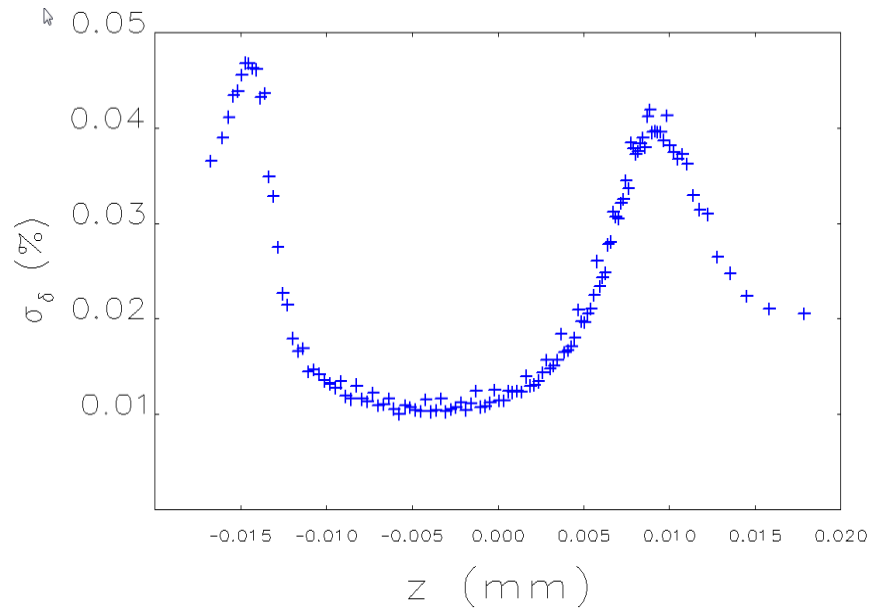


Figure 15. Sliced rms relative energy spread along the bunch length at the SXR undulator (4 GeV). The energy spread level in the high peak current section is about 0.012% rms, which is 500 keV, produced with a laser heater setting of about 6 keV rms. CSR is included.

10.4 FEL Simulations

10.4.1 SXR SASE Simulations

The SXR FEL is simulated, in SASE mode here, at a 1.24-keV photon energy ($K = 2.1$), which is the most demanding level for the SXR FEL, using the output macro-particle coordinates of the *ASTRA* and *Elegant* runs, as described above. The SXU undulator period is 39 mm and the 1.24-keV photon energy is chosen here to highlight the most challenging beam requirements. Undulator parameters are listed in Chapter 3, Table 8. The FEL saturates after about 50 m, as shown in Figure 16. The undulator includes 21 3.4-m undulator segments with 1.15-meter break lengths between segments. The resistive-wall wakefield of the 5-millimeter-high aluminum chamber was included, and the average beta function was chosen at 12 m. Figure 17 shows the 10 GW X-ray pulse (~ 30 fs FWHM) and the SASE spectrum ($\sim 0.3\%$ FWHM).

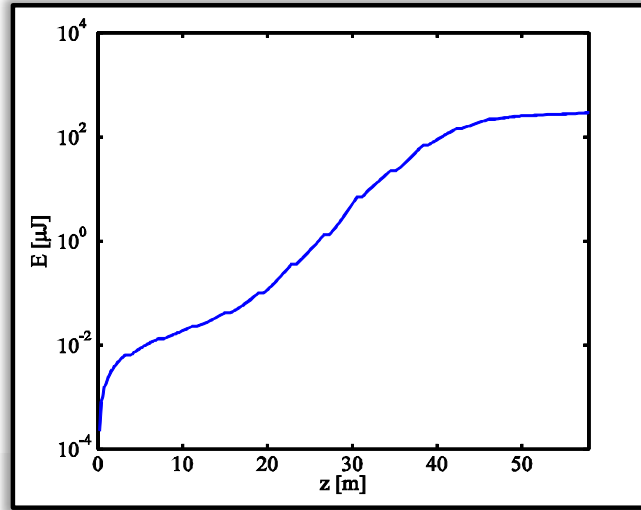


Figure 16. Start-to-end simulations of the SXR FEL in SASE mode at 1.2 keV (a single FEL run here without statistics in this conceptual design study).

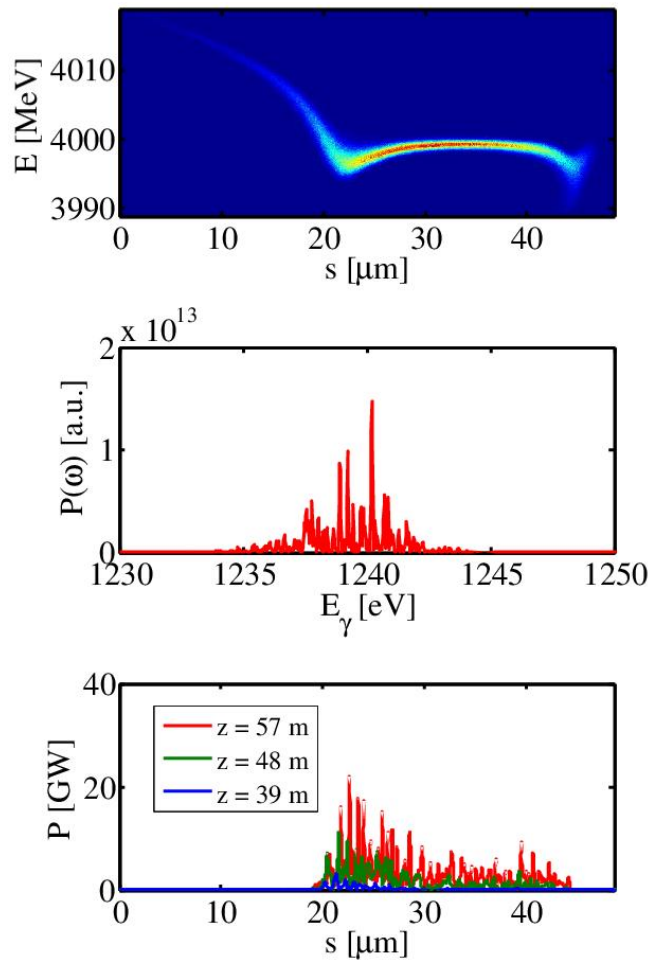


Figure 17. Start-to-end simulations of the SXR FEL in SASE mode at 1.2 keV. The plots show longitudinal phase space (top), SASE spectrum (middle), and the 10-20 GW X-ray pulse (bottom). The bunch head is at the right here. Tapering has not yet been studied.

10.4.2 SXR Self-Seeded Simulations

The SXR self-seeded FEL is simulated using the output of the *ASTRA* and *Elegant* runs, as described above. These coordinates are fed into the FEL computer code *Genesis-1.3* to evaluate the FEL performance with self-seeded operation at 1.24 keV. One segment is removed at the eighth undulator (U8) to install a grating-based monochromator with 0.1 percent net efficiency (including the BW reduction factor). The seed power following 7 undulator segments generates a 15 MW X-ray pulse, which is reduced to 15 kW of seed power at U9 after the monochromator. The FEL saturates at U19 with 300 μJ of pulse energy and a 5×10^{-5} FWHM bandwidth (BW). Figure 18 shows the FEL gain. The monochromator is at $z = 32$ m. Figure 19 shows the self-seeded X-ray pulse following U25 with greater than 0.5 GW and a 30 fs FWHM pulse length.

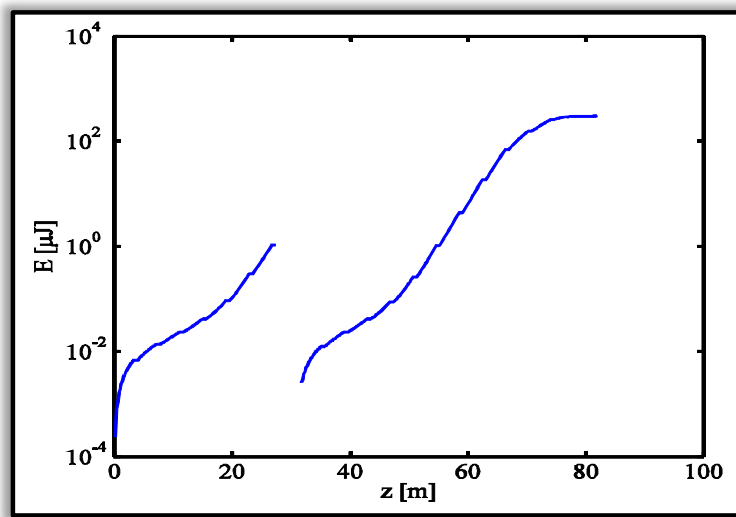


Figure 18. Exponential gain in the SXR FEL at 1.24 keV using the S2E electron beam at 4 GeV. The monochromator is at $z = 32$ m and the pulse energy at the end is 300 μJ .

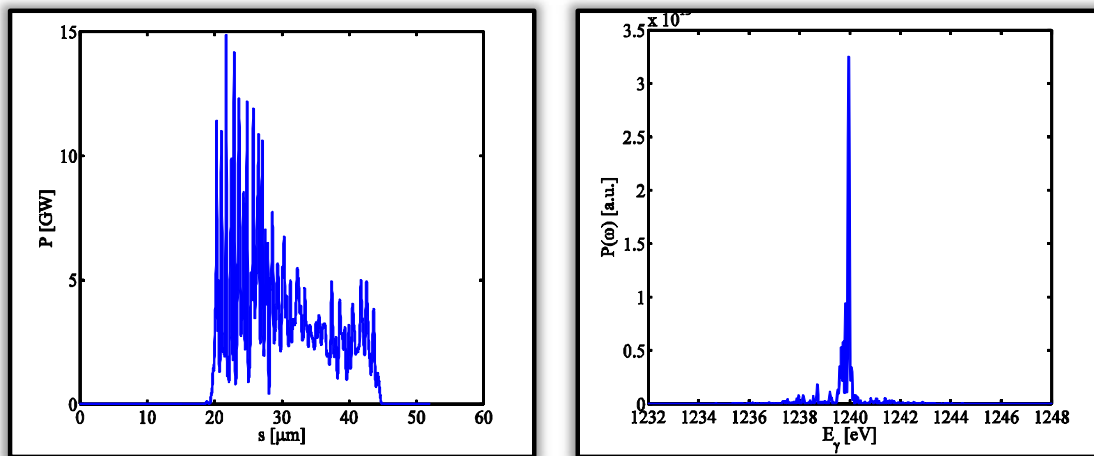


Figure 19. X-ray pulse (left) and SASE spectrum (right) in the SXR FEL at 1.24 keV using the same S2E electron beam. This shows a 10 GW X-ray pulse with ~ 30 fs FWHM duration and a self-seeded spectrum of 5×10^{-5} FWHM BW and 300 μJ of pulse energy.

10.4.3 HXR SASE Simulations

The HXR FEL is simulated at a 5 keV photon energy ($K = 0.58$) using the output macro-particle coordinates of the *ASTRA* and *Elegant* runs, as described above. The HXR undulator period is 26 mm and the 5-keV photon energy is chosen here to highlight the most challenging beam requirements. The FEL saturates after about 140 m, as shown in Figure 21. The undulator includes 32 3.4-m undulator segments with 1.15-m break lengths between segments, an average beta function of 15 m, and a K value of 0.58 at 5 keV. The 16th undulator segment is removed here to allow self-seeding with a monochromator (see next section). The resistive-wall wakefield of the 5-millimeter-high aluminum chamber was included, and the average beta function was chosen at 20 m. Figure 22 shows the 1-2 GW X-ray pulse (~ 40 fs FWHM) and the SASE spectrum (~ 0.1 percent FWHM). The transverse phase space was matched while concentrating on the beam core only. A start-to-end simulation is summarized in Figure 20 showing the electron phase space at the entrance to the HXR undulator.

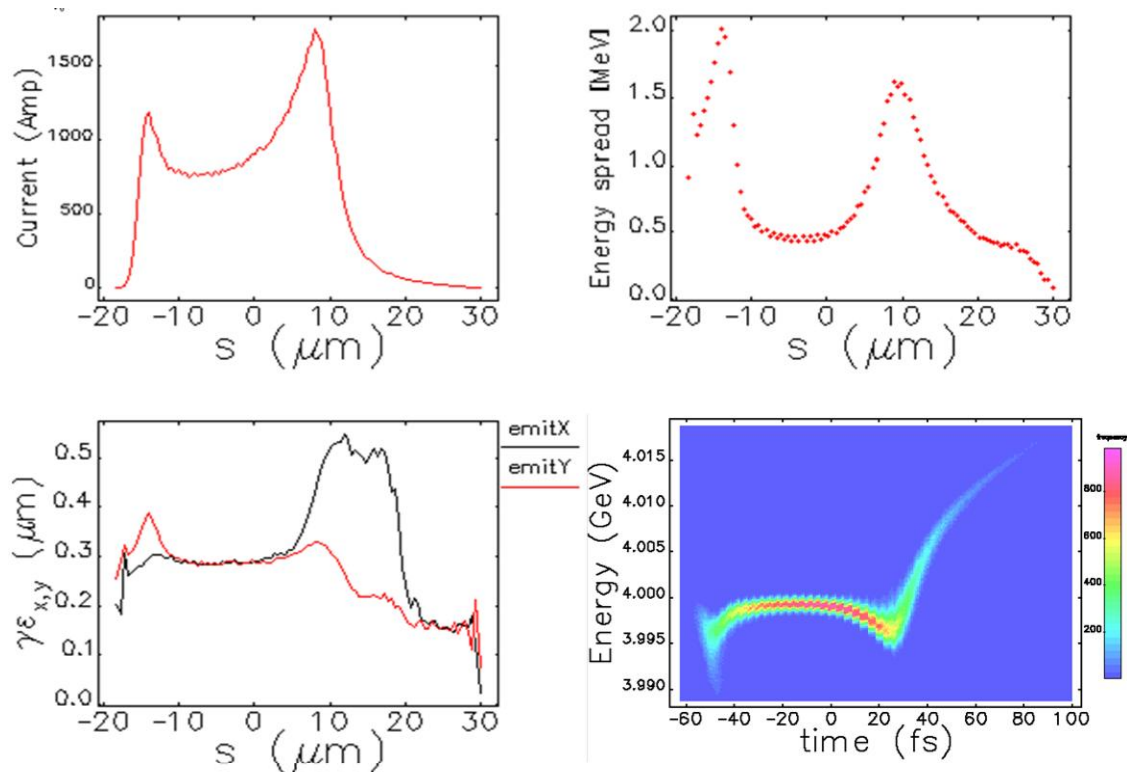


Figure 20. Start-to-end simulations up to the HXR undulator from the *ASTRA* and *Elegant* runs, as described above, and showing the peak current (top-left), the rms energy spread at the undulator entrance (top-right), the sliced transverse emittances (bottom-left), and the longitudinal phase space at 4 GeV (bottom-right). The bunch head is illustrated here at the left.

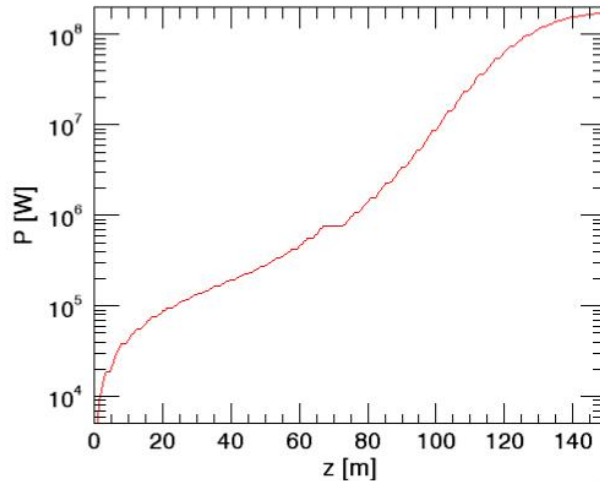


Figure 21. Exponential gain in the HXR FEL at 5 keV using the same electron beam at 4 GeV. The pulse energy at the end of the system is $\sim 18 \mu\text{J}$.

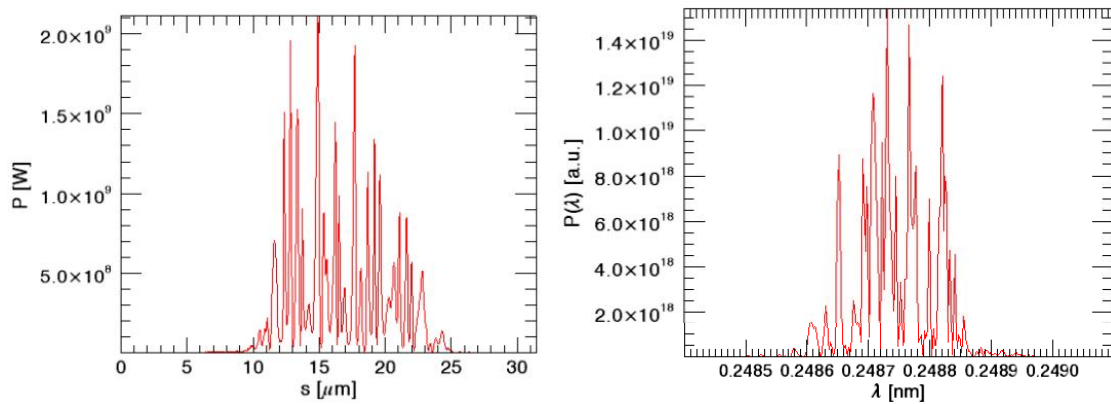


Figure 22. X-ray pulse (left) and SASE spectrum (right) in the HXR FEL at 5 keV using the same S2E electron beam. This shows a 1-2 GW X-ray pulse with ~ 40 fs FWHM duration and a SASE spectrum of $\sim 0.1\%$ FWHM and $\sim 18 \mu\text{J}$ of pulse energy.

10.4.4 HXR Self-Seeded Simulations

The HXR self-seeded FEL is simulated using the output macro-particle coordinates of the *ASTRA* and *Elegant* runs, as described above. These 4 GeV coordinates are fed into the FEL computer code *Genesis-1.3* to evaluate the FEL performance with self-seeded operation at 4.1 keV. One segment is removed at the 15th undulator (U15) to install a 100 μm thick diamond crystal (1,1,1) monochromator with 0.25 percent net efficiency (including the BW reduction factor). The seed power after 14 undulator segments generates a 100 MW X-ray pulse that is reduced to 0.25 MW of seed power at U16 following the monochromator. The FEL saturates at U25 with 13 μJ of pulse energy and a 3×10^{-5} FWHM bandwidth (BW). Figure 23 shows the FEL gain starting from the exit of the monochromator ($z = 0$ here). Figure 24 shows the self-seeded X-ray pulse at U25 with more than 0.5 GW of peak power and a 30 fs FWHM pulse length.

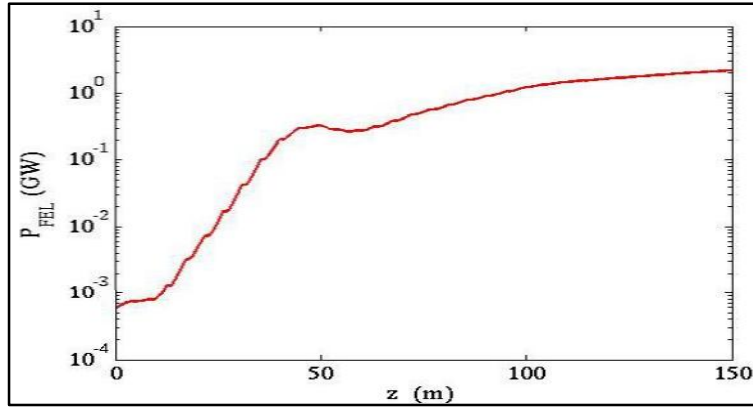


Figure 23. Start-to-end simulation of self-seeded HXR FEL showing exponential gain at 4.1 keV (0.30 nm). The plot starts at the monochromator exit (U15) and shows the seeded power with saturation occurring at U25 (~50 m after the monochromator). Unfortunately little length margin is available in the HXR FEL for field tapering to enhance FEL power.

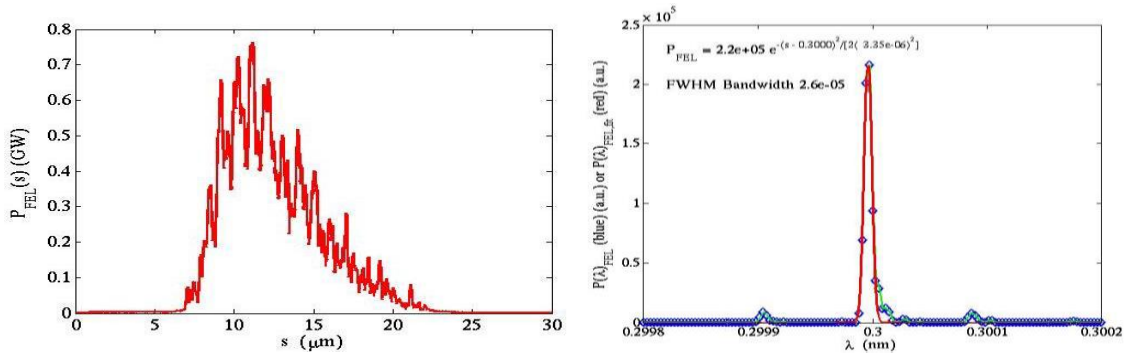


Figure 24. X-ray pulse at 4.1 keV (0.30 nm) with > 0.5 GW of peak power, 30 fs FWHM pulse duration, and 3×10^{-5} FWHM bandwidth.

10.5 Single-Bunch Sensitivities and Tolerances

Single-bunch magnet alignment, strength, vibration, field quality, and chromatic sensitivities are shown in the plots below for all quadrupole and dipole magnets between the end of the injector (98 MeV) and the start of the SASE/SS undulator. These values are “sensitivities” and not tolerances, since they show the effect of one error on one magnet, and do not reflect the overall (tighter) tolerance values, which will need to include all errors on all components simultaneously in a full tolerance budget. These sensitivities do, however, provide some insight into the design, showing which magnets and emittance growth mechanisms are most important as well as pointing out the worst cases. Multi-bunch tolerances are described in the next section. Each data point in the plots of the first three figures below represents a 2% emittance growth. Therefore we would like to have large values here for less emittance growth. For example, the roll angle error of just one of the BC1 (or BC2) bends (see lower plot of Figure 25) must be no larger than 1 mrad in order to keep its associated emittance growth less than 2%. Figure 28 is different. It shows quadrupole magnet vibration sensitivities and chromatic effects for each quad.

This analysis is based on simple analytical formulas that are yet unpublished, but available in private notes [8].

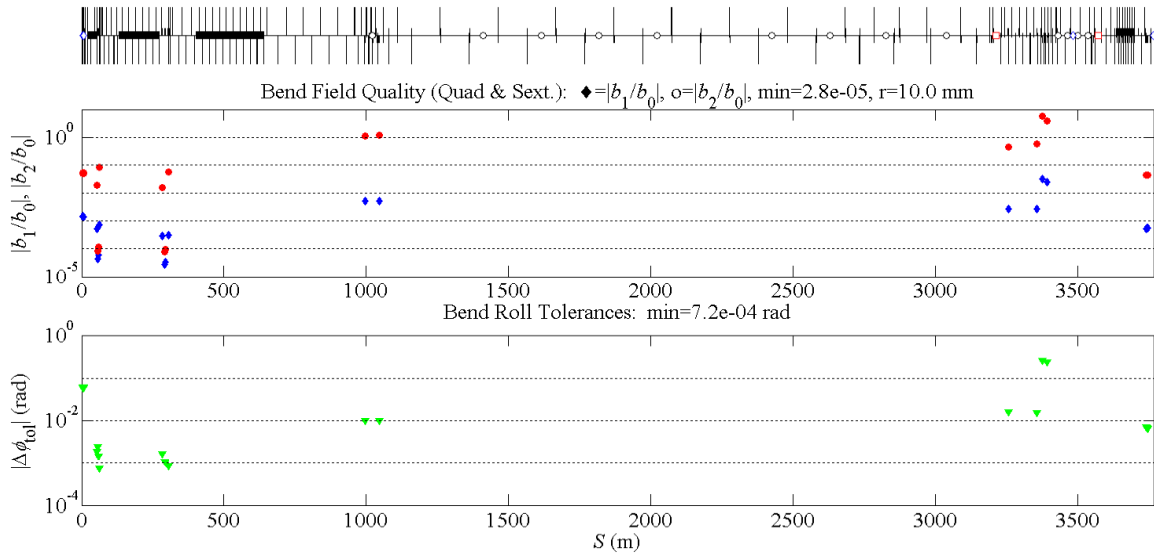


Figure 25. Sensitivities of **dipole magnets**, from injector (98 MeV) to SXR undulator (4 GeV), where each point increases the x and y projected emittances by 2 percent. Dipole magnet field quality sensitivities are shown at top ($|b_1/b_0|$ as relative quadrupole field normalized to dipole field at $r = 10$ mm and $|b_2/b_0|$ as relative sextupole field normalized to dipole at $r = 10$ mm); dipole magnet roll angle sensitivities are shown at bottom. Field quality sensitivities in the BC1 and BC2 magnets are tight (e.g., $|b_2/b_0| < 10^{-4}$ at $r = 10$ mm as the worst case). These are similar to tolerances achieved at LCLS-I. Roll sensitivities are reasonable ($|\Delta\phi| < 1$ mrad as the worst case).

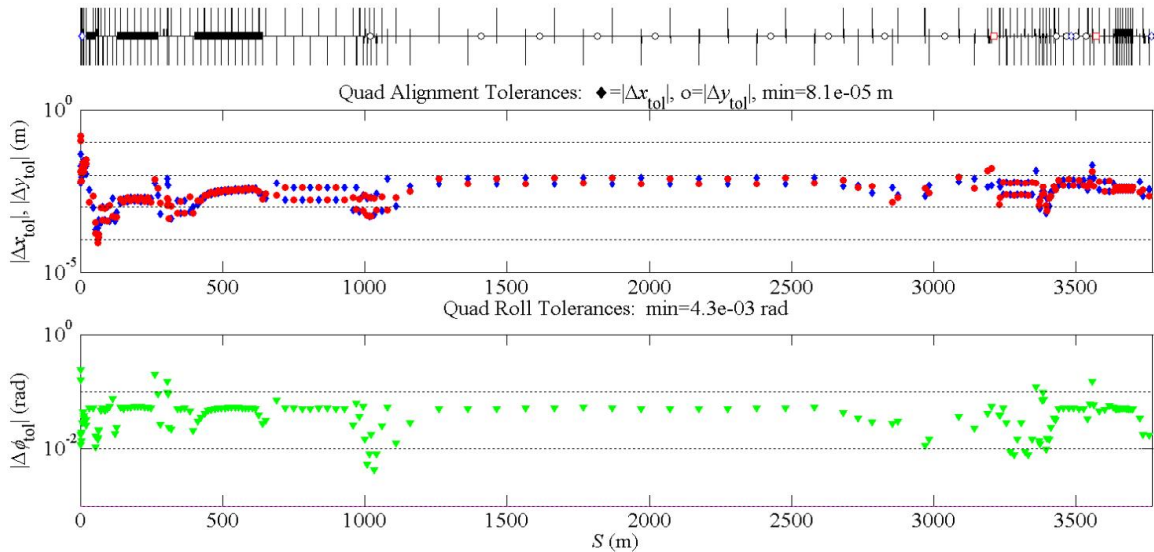


Figure 26. Sensitivities of **quadrupole magnets**, from injector (98 MeV) to SXR undulator (4 GeV), where each point increases the geometric mean of the x and y projected emittances by 2 percent. Quadrupole magnet alignment sensitivities are shown at top ($|\Delta x_{tol}|$ and $|\Delta y_{tol}|$), and quadrupole magnet roll angle sensitivities are at bottom. Alignment sensitivities are not very tight with many at the millimeter level and $|\Delta x_{tol}| < 0.1$ mm as the worst case, and roll sensitivities are also reasonable (e.g., $|\Delta\phi_{tol}| < 10$ mrad as the worst case).

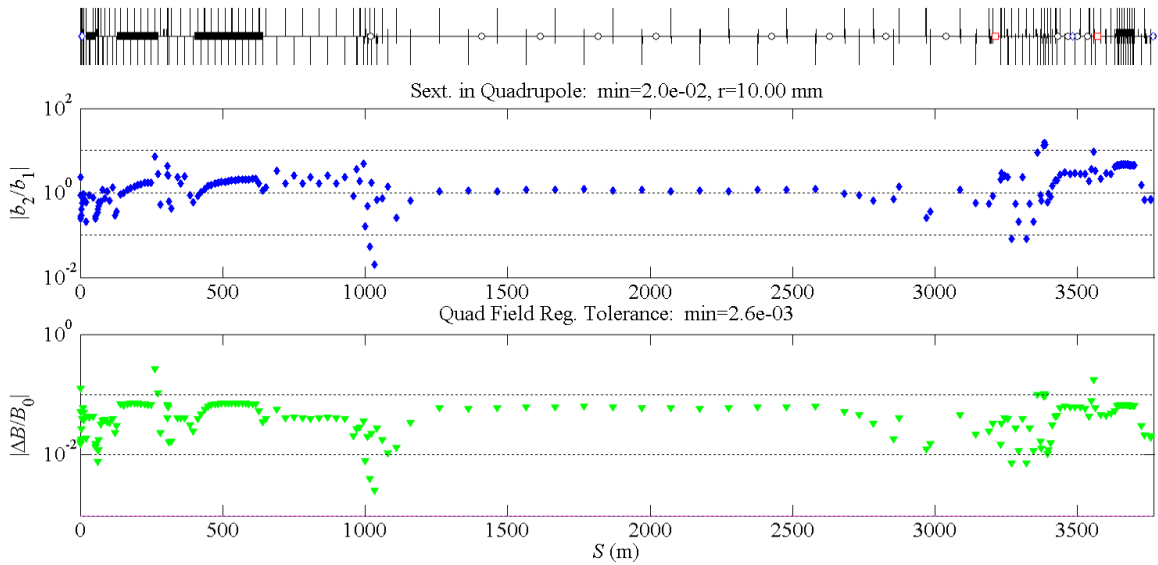


Figure 27. Sensitivities of **quadrupole magnets**, from injector (98 MeV) to SXR undulator (4 GeV), where each point increases the geometric mean of the x and y projected emittances by 2 percent. Quadrupole magnet field quality sensitivities are shown at top ($|b_2/b_1|$) as relative sextupole field normalized to quadrupole field at $r = 10$ mm; quadrupole magnet relative field strength error sensitivities are shown at bottom. Field quality sensitivities are not very tight (e.g., $|b_2/b_1| < 1$ percent as the worst case), and relative field strength error sensitivities are also reasonable (e.g., $|\Delta B/B_0| < 0.3$ percent as the worst case).

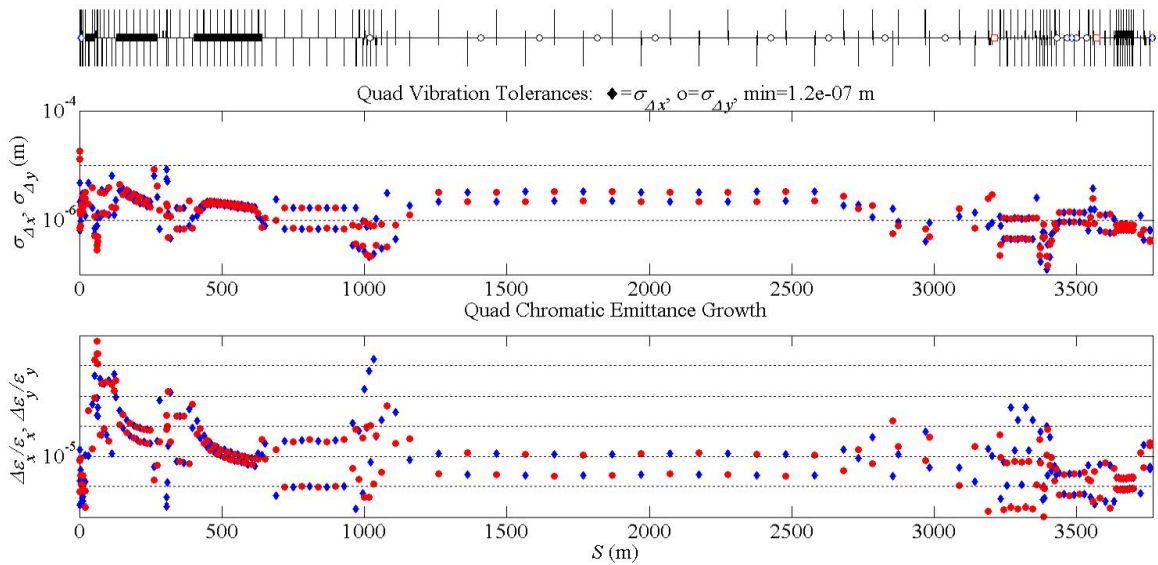


Figure 28. Sensitivities of **quadrupole magnets**, from injector output (98 MeV) to SXR undulator input (4 GeV). Quadrupole magnet transverse vibration sensitivities are shown at top ($\sigma_{\Delta x}, \sigma_{\Delta y}$), where each plotted point will add 5 percent rms transverse jitter (normalized to the nominal rms beam size) in the undulator, and the quadrupole magnet chromatic sensitivities are shown at bottom, where each plotted point is the relative emittance growth due to an individual quadrupole magnet's focal length dependence on particle energy (and relative energy spread at that magnet). Vibration sensitivities are fairly tight (e.g., $\sigma_{\Delta y} < 0.1 \mu\text{m}$ as the worst case), but chromatic sensitivities in the injector are somewhat large (e.g., $|\Delta \epsilon_y / \epsilon_y| \approx 5\%$ as the worst case) and will need more design work. Each vertical line in the lower plot is one decade change.

10.6 Multi-Bunch Sensitivities and Tolerances

The effect of the long-range transverse wakefields has been investigated in many different SCRF linacs, including the European XFEL. In a CW linac, the primary limitation is cumulative beam breakup or transients arising during current or orbit changes. Studies of the multi-bunch effects in the LCLS-II have been performed and are described in Section 6.12. The studies assumed the cryomodule tolerances listed in Chapter 6. In particular, they include 0.5-mm rms cavity misalignments as well as 2.5-percent charge fluctuations and 0.5-degree RF phase errors. These studies are ongoing, but initial results suggest that the HOMs will be a very small perturbation to the beam dynamics even with transverse Q values as high 10^6 . All of the tolerances will be dominated by the single bunch effects described in Section 10.5. Future efforts will study transients and the interaction of the beam response with the feedback systems that are planned for LCLS-II.

10.7 Beam-Based Corrections and Tuning Strategies

10.7.1 Electron Trajectory Correction

The trajectory throughout the LCLS-II will be monitored by beam position monitors (BPMs) near each quadrupole magnet, where weak steering coils will also be located. Steering algorithms will be studied prior to construction and then tested in commissioning. Linac alignment tolerances are not expected to be very tight in comparison to the LCLS-I levels. The undulator orbit correction will be beam-based alignment as routinely used in the LCLS-I, where large energy changes (factor of three) are intentionally set and the BPM responses are used to find a dispersion-free orbit [9].

10.7.2 Electron Beam Matching

The beam size and divergence will be adjustable at several diagnostics stations located after the laser heater, the BC1 compressor, the BC2 compressor, and just before each undulator. Separately powered bipolar quadrupole magnets will be included to allow robust beta matching over various beam conditions, especially from the injector, with the possibility of different charge settings. Off-axis emittance and Twiss diagnostic beamlines will be maintained after each critical area, fed by a fast kicker, to allow low-power beam interception with screens and/or wire scanners in order to measure the matching. This is described in more detail in the Bunch Compression and the Diagnostic chapters.

10.7.3 Electron Dispersion Correction

The sensitivity of the trajectory to deliberate energy variations will be used to measure, using BPMs, the dispersion error at several key locations, including those just past BC1 and BC2, and after each dog-leg bend system. Small “tweaker” quadrupole magnets will be located at high dispersion points in these sections and used to correct residual dispersion using a high-level computer application code. In addition, these quadrupoles can also be used less deterministically

by minimizing the local measured emittance and scanning these “tweaker” quads (see next section) [10].

10.7.4 Emittance Measurements and Minimization

The transverse emittance will be measured at several dedicated diagnostics stations located after the laser heater, BC1, BC2, and just before each undulator. The emittance can be minimized empirically by scanning the strength of several components, including the upstream linac trajectory (wakefield minimization), the dispersion “tweaker” quads in BC1, BC2, and each dog-leg system. The injector emittance will be optimized with solenoid scans, buncher compression settings, and cathode spot size [11].

10.7.5 RF Phasing

The linac RF phasing will be done by varying the phase a few degrees around the crest phase setting and measuring a BPM position reading located at the next downstream dispersion point (e.g., varying the L1 phase and monitoring the BC1 BPM x -position reading as shown for LCLS in **Figure 29**) as performed at LCLS-I [12].

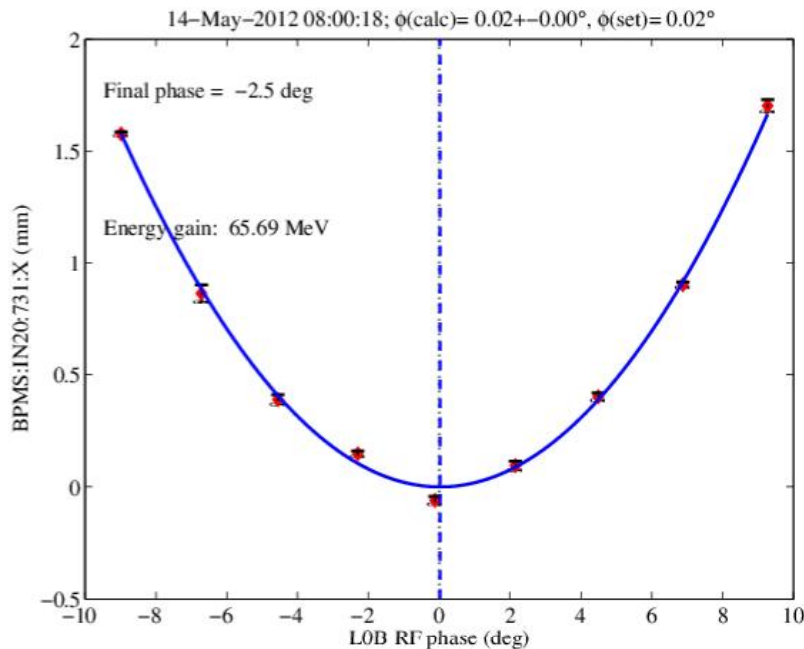


Figure 29. RF phasing scan at LCLS, where the L0 phase is varied ± 9 degrees around crest and the BPM in the DL1 bend system is plotted. Any offset of the phase readback (0.02° here) is then cancelled by choosing an appropriate software offset (phase reference).

10.8 References

1. K. Floettmann, ASTRA: A space charge tracking algorithm. User manual available at <http://www.desy.de/~mpyflo/Astra> documentation.
2. M. Borland, Report No. ANL/APS LS-287, 2000.
3. S. Reiche, Nuclear Instruments and Methods in Physics Research A 429 (1999), pp. 243-248.
4. S. Reiche et. al., Start-To-End Simulation for the LCLS X-ray FEL, Nuclear Instruments and Methods in Physics Research A **483** (2002), 70–74.
5. M. Borland et. al., Start-To-End Jitter Simulations of the Linac Coherent Light Source, In proceedings of PAC-2001, Chicago, IL, USA, June 2001.
6. F. Sannibale et. al., Status of the APEX Project at LBNL, In Proceedings of IPAC-12, New Orleans, LA, USA, May 20-25, 2012.
7. P. Emma et. al., Femtosecond and Subfemtosecond X-Ray Pulses from a Self-Amplified Spontaneous-Emission-Based Free-Electron Laser, Phys. Rev. Lett. **109**, 254802 (2012).
8. P. Emma, unpublished note, private communication, 2012.
9. P. Emma, R. Carr, H.-D. Nuhn, Beam-based Alignment for the LCLS FEL Undulator, Vol. **429**, Issues 1-3, June 1999, Pages 407-413.
10. K. Bane et. al., Measurements of Compression and Emittance Growth after the First LCLS Bunch Compressor Chicane, In proceedings of PAC-2007, Albuquerque, New Mexico, USA.
11. K. Bane et. al., Initial Commissioning Experience with the LCLS Injector, In proceedings of PAC-2007, Albuquerque, New Mexico, USA.
12. R. Akre et al., Commissioning the Linac Coherent Light Source injector, Phys. Rev. ST Accel. Beams **11**, 030703 (2008).

11

PHOTON TRANSPORT AND DIAGNOSTICS

TECHNICAL SYNOPSIS

The LCLS-II is designed to produce high-brightness, short-pulse X-rays from two parallel undulator systems in the existing tunnel. This chapter describes the X-ray transport to deliver these beams to the experimental systems and the diagnostic systems to characterize them. The superconducting linac will initially be able to deliver beam at 1MHz. One undulator is optimized for the production of soft X-rays from 200 to 1250 eV and the second undulator is optimized for intermediate wavelength X-rays, from 1 to 5 keV, at the high repetition-rates with electrons from the superconducting linac, or for intermediate-to-hard X-rays, 1 to 25 keV, at high-pulse energy and low repetition-rates up to 120 Hz, using the Cu linac as the source.

There are two separate X-ray transport and diagnostics systems, one for each of the undulator systems. The soft X-ray system will deliver beam to a single experimental station optimized for high-fluence experiments. The system is laid out to accommodate eventual expansion to four branchlines with separate experimental stations, two monochromatic branchlines and a second high-fluence line. The intermediate and hard X-rays will be delivered to the existing X-ray instruments in Hutch 3 of the Near Experimental Hall and the Far Experimental Hall at either high repetition-rate from the superconducting linac or high-pulse energy from the Cu linac.

This chapter summarizes critical requirements of the beam transport and diagnostics for delivery and characterizing the FEL beams for optimization of operations and normalization of experimental data. Very low figure error mirrors will deliver the X-rays with minimal wave front distortion, which is critical for maintaining intensity in focal spots and uniformity when operating out of focus. The X-ray pulses will be manipulated by attenuation, aperturing and focusing. The pulse energy and spatial distribution will be characterized with energy monitors and imagers. Provisions for future monochromators and spectrometers are described.

11.1 Introduction and Overview

The X-ray Transport and Experimental Systems, XTES, will deliver two FEL beams to experimental stations in existing LCLS facilities. The beam from the Soft X-Ray, SXR, undulator system will be delivered to a reconfigured SXR experimental station in the Near Experimental Hall (NEH). The beam from the Hard X-Ray, HXR, system will be delivered to the four existing HXR stations, one in the NEH and three in the Far Experimental Hall (FEH), as shown in Figure 1 below. This chapter summarizes the requirements for preservation of flux and wave front, band pass and energy cutoffs, as well as the diagnostics to support tuning of the FEL's and experimental data collection. The experimental endstations will be discussed in Chapter 12, the controls and data acquisition systems in chapter 14.

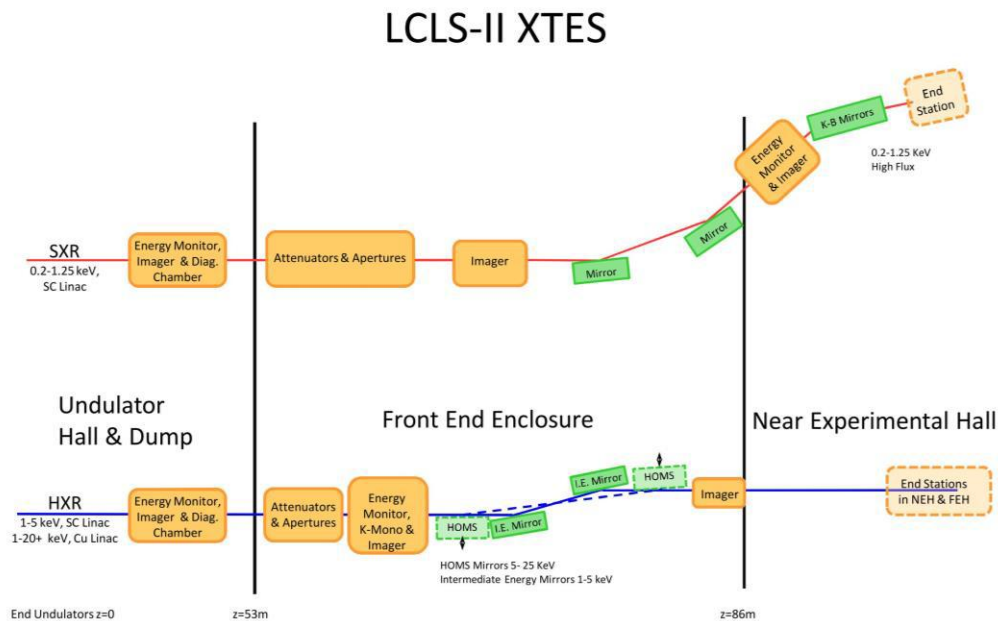


Figure 1. Schematic layout of the XTES. The SXR line is on the north side of the LCLS tunnel and the HXR line on the south. The two lines start just downstream of the beam magnets to the dumps, continue through the front end enclosure and deliver beam to the existing LCLS experimental instruments.

11.2 High Average Power Photon Beamline Requirements

11.2.1 Undulator Performance

The parameters for operation of the FEL for both the high-repetitions rate from the superconducting (SC) linac and at low rate from the Cu linac are described in Chapter 3. The SXR FEL, which is driven only by the SC linac, is summarized in Table 1. The HXR FEL, which operates over the range of 1-25 keV, can be driven by either the SC linac or the Cu linac. The performance when driven by the SC linac is summarized in Table 2, and when driven by the Cu linac in Table 3. The SC linac cannot achieve as high per-pulse-energy as with the Cu linac, but the average power can be considerable. The average delivered FEL beam power will be limited to

20W to prevent damage to filters and deformation of optics. This will be done by a combination of limiting the per-pulse energy and the repetition rates as is best suited for a given experiment.

Table 1. Summary of SXR FEL (SASE/SS[§]) SC linac operational and performance parameters. The values are for 4 GeV electron energy and 100 pC bunch charge. Photon energies down to 200 eV are reached by ramping the electron energy down. A more extensive table of performance parameters is given in Chapter 3.

SXR FEL Parameters (SASE/SS [§])	symbol	$E_{r,min}$	$E_{r,max}$	units
Photon energy (tuning range, fundamental)	E_r	0.25	1.25	keV
X-ray pulse length (FWHM)	$\Delta\tau$	60	60	fs
FEL pulse energy (fundamental, SASE)	$E_r N_p$	1800	1600	μJ
Avg. X-ray beam power <i>delivered</i> in this FEL	P_e	< 20	< 20	W
Photon source size (rms)	σ_s	23	18	μm
Peak brightness (SASE)	$B_{pk,SASE}$	9.3	45	$\times 10^{30}$ *
Peak brightness (SS [§])	$B_{pk,SS}$	140	670	$\times 10^{30}$ *
Average brightness (max delivered, SS [§])	$B_{av,SASE}$	930	4500	$\times 10^{20}$ *
Bandwidth (FWHM, SASE)	BW_{SASE}	0.77	3.5	eV
Bandwidth (FWHM, SS [§])	BW_{SS}	0.03	0.06	eV
Photon far-field divergence (FWHM)	Θ_s	44	8.8	μrad
Beam rate in this FEL	f_{FEL}	ss[†]-1000	ss[†]-1000	kHz

* photons per second, per mm², per mrad², per 0.1% bandwidth

† single shot

§ self-seeded

Table 2. Summary of HXR FEL (SASE/SS[§]) SC linac operational and performance parameters. The values are for 4 GeV electron energy and 100 pC bunch charge. Photon energies down to 1 keV are reached by ramping the electron energy down. A more extensive table of performance parameters is given in Chapter 3.

HXR FEL Parameters (SASE/SS [§])	symbol	$E_{r,min}$	$E_{r,max}$	units
Photon energy (tuning range, fundamental)	E_r	1.5	5.0	keV
X-ray pulse length (FWHM)	$\Delta\tau$	60	60	fs
FEL pulse energy (fundamental, SASE)	$E_r N_p$	2200	200	μJ
Avg. X-ray beam power <i>delivered</i> in this FEL	P_x	< 20	< 20	W
Photon source size (rms)	σ_s	18	17	μm
Peak brightness (SASE)	$B_{pk,SASE}$	53	121	$\times 10^{30}$ *
Peak brightness (SS [§])	$B_{pk,SS}$	790	1800	$\times 10^{30}$ *

Average brightness (max delivered, SS [§])	$B_{av,SASE}$	5300	12000	$\times 10^{20} *$
Bandwidth (FWHM, SASE)	BW_{SASE}	1.1	1.7	eV
Bandwidth (FWHM, SS [§])	BW_{SS}	0.075	0.25	eV
Photon far-field divergence (FWHM)	Θ	8.5	2.7	μrad
Beam rate in this FEL	f_{FEL}	ss[†]-1000	ss[†]-1000	kHz

* photons per second, per mm², per mrad², per 0.1% bandwidth

† single shot

§ self-seeded

Table 3. Summary of HXR FEL (SASE/SS[§]) Cu linac operational parameters. The values are for 2.5 - 15 GeV electron energy and 130 pC bunch charge. A more extensive table of performance parameters is given in Chapter 3.

HXR FEL Parameters (SASE/SS [§])	symbol	$E_{r,min}$	$E_{r,max}$	units
Electron beam energy	E_e	2.5-15	15	GeV
Photon energy (tuning range, fund.)	E_γ	1	25	keV
X-ray pulse length (FWHM)	$\Delta\tau$	43	43	fs
FEL pulse energy (fundamental, SASE)	$E_r N_p$	1500-5100	1540	μJ
Avg. X-ray beam power <i>delivered</i> in this FEL	P_x	0.021-0.052	0.030	W
Photon source size (rms)	σ_s	21-12	9	μm
Peak brightness (SASE)	$B_{pk,SASE}$	4.3-150	840	$\times 10^{30} *$
Peak brightness (SS [§])	$B_{pk,SS}$	66-2200	13000	$\times 10^{30} *$
Average brightness (max delivered, SS [§])	$B_{av,SASE}$	2.3-7.7	44	$\times 10^{20} *$
Bandwidth (FWHM, SASE)	BW_{SASE}	1.0-4.3	22	eV
Bandwidth (FWHM, SS [§])	BW_{SS}	0.05	1.2	eV
Photon far-field divergence (FWHM)	Θ	11-9.4	1.1	μrad
Beam rate in this FEL	f_{FEL}	ss[†]-0.120	ss[†]-0.120	kHz

* photons per second, per mm², per mrad², per 0.1% bandwidth

† single shot

§ self-seeded

11.2.2 Photon Delivery Requirements

The X-ray transport system is required to deliver the FEL beams to experimental stations with a minimal loss in flux and wavefront distortion. The delivered flux is dependent on the grazing angle of the optics, the optical coating, number of optics and the acceptance of the mirrors. The wave front distortion is principally dependent on the figure error of the optics and diffraction from optical and other apertures in the beam path. The requirement for both the HXR and SXR optical systems is to deliver the beam well focused at the sample. A Strehl ratio of

equal to or greater than 0.8 is needed to achieve this requirement. In addition there is a desire to vary the FEL spot size by working out of focus. A Strehl ratio of 0.97 is required to maintain a Gaussian wavefront outside the focal plane.

The requirements for the SXR line are to deliver beams from 200 to 1250 eV and a goal is to have greater than 10^3 suppression of 3rd order harmonic at the oxygen k-edge. There is a single branchline in scope delivering beam to one of several (see chapter 12) experimental stations. There is the potential of expanding the SXR beam line to include up to four branchlines that include both monochromatic and high flux branches. The high-field station will have four mirrors between the source and the endstation. The focusing mirrors will image the beam in a separate chamber for moderately high field studies. These focusing mirrors can be pulled out of the beam path to allow the future installation of a very high field endstation, where the focusing optics are integral with the sample chamber. Monochromatic beam lines would be capable of achieving resolutions $E/\Delta E$ greater than or equal to 30,000 over the 200-1250 eV range. The monochromator will be designed to also vary the energy at which higher orders are suppressed.

The HXR line will deliver the beam to four existing experimental stations. The LCLS High energy Offset Mirror System, HOMS, will continue to be used to deliver X-rays up to 25 keV and at lower repetition rates from the Cu linac to the existing instruments, XPP in the NEH and XCS, CXI and MEC in the FEH. A new pair of mirrors optimized for the 1-5 keV range will be installed to deliver the high repetition-rate beam from the SC linac to these instruments. The front end through to the NEH will be rebuild to handle the high average power beams from the SC linac.

Both the SXR and HXR beamline systems will provide diagnostics to both characterize the beams for FEL tuning and to support the experimental programs at high repetition rates. The basic diagnostics are listed in Table 4 and discussed in more detail in the following sections.

Table 4. Basic required photon beam diagnostics.

Component	Purpose
Pulse energy monitors	Pulse-by-pulse beam and average energy delivered in the FEL beam
Attenuators	Both gas and solid attenuators to limit the intensity on to the sample without changing the FEL operating parameters.
K-Mono capabilities	Measure spectrum from single undulator segments for tuning of the FEL (HXR line only)
Imagers	Image the beam from individual pulse or average over many pulses at specific points along beam path for alignment and characterization

11.2.3 Photon Power and Power Density

The per-pulse photon energy and photon divergences are listed in Table 1, Table 2 and Table 3. The per-pulse energy is limited by the expected performance of the FEL. The total photon

power is limited in this report to 20W to accommodate the practical limits on samples and absorbers at high repetition rates. This power limit is conservative and may be increased after detailed engineering more accurately predicts the damage thresholds at high repetition rates. The nominal peak power densities for the 20W limited beam are shown in Figure 2 for both the SXU and HXU, at the z distance for the first adjustable apertures that could be in the beam path and at the insertable safety stoppers that prevent the beam from entering the experimental areas.

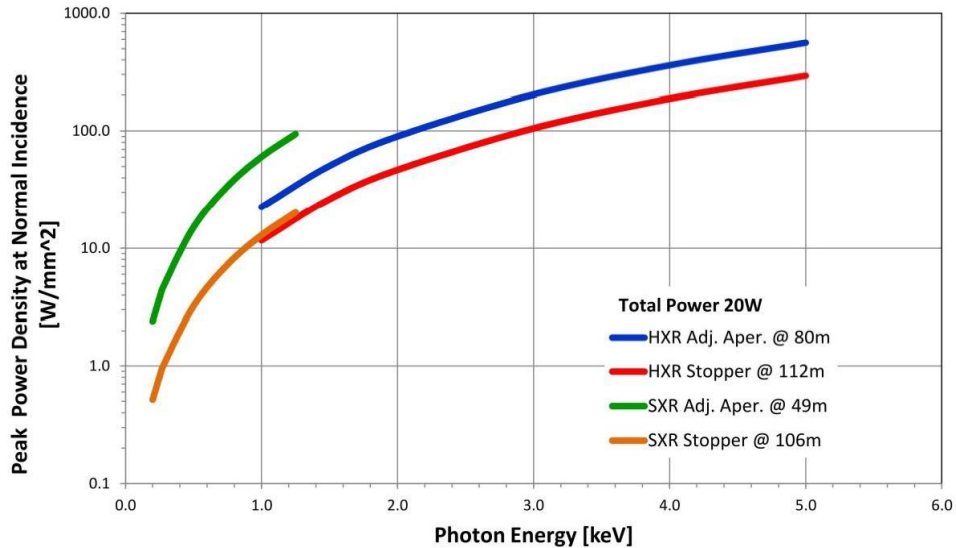


Figure 2. The power density are shown for the unfocused FEL beams from the SXU and the HXU as a function of energy at the z distance of the first adjustable apertures and the safety stoppers in their respective beam lines. The z distances are listed from the source within the undulators.

Both the power density and the dose per pulse are factors in the setting the damage limit in non-reflective absorbers. The principal normal absorber used in LCLS-I is B_4C . The peak dose in this material is shown in Figure 3. The currently accepted damage threshold for B_4C in safety system, such as stoppers, is 0.16 eV/atom. But this assumes low average power. The implications of running with high power and high pulse energy is discussed in section 11.3.1 below.

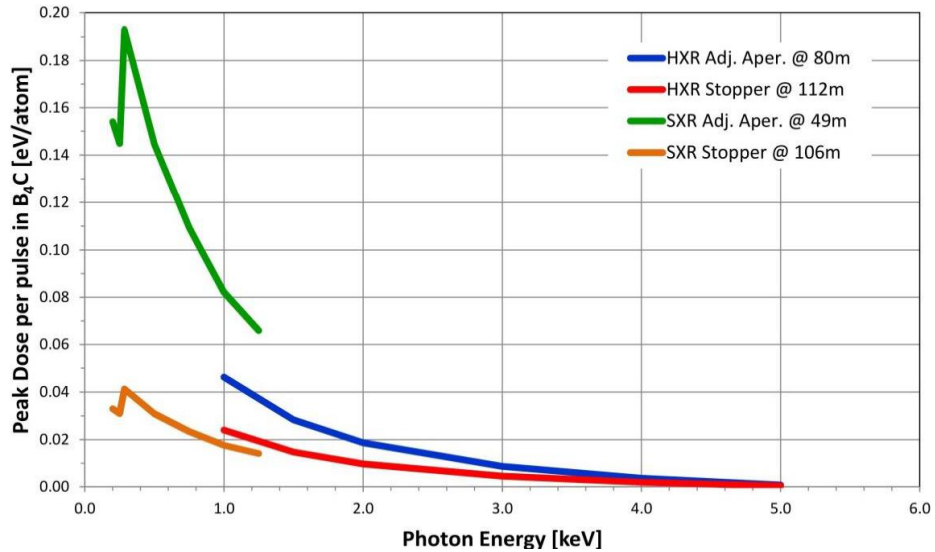


Figure 3. The dose in B₄C is shown for unfocused FEL beams from the SXU and the HXU as a function of energy at the z distance of the first adjustable apertures and the safety stoppers in their respective beamlines.

For mirrors, as discussed in section 11.3.2 below, the energy density per pulse defines the optical damage limit. At the z distance to the first mirror on the SXR line, the peak normal incidence energy density per pulse is $3\text{mJ}/\text{mm}^2$. At the position of the first mirror on the HXR line, the HOMS mirror, it is $10\text{mJ}/\text{mm}^2$.

11.3 X-ray Damage Considerations

11.3.1 Normal Incidence

11.3.1.1 Single shot damage considerations

For low repetition FEL machines, such as the LCLS working at 120 Hz frequency, the damage to optical systems is determined mainly by instantaneous damage mechanisms. The instantaneous damage problem has been studied extensively both theoretically and experimentally at the LCLS and other FEL facilities [1, 2, 3]. The instantaneous damage happens in the time scale ranging from few femtoseconds to tens of picoseconds. The energy of femtosecond photon pulses is first absorbed in the electron system, which then thermalize with the lattice in the time scale of 1–50 ps. When the absorbed dose is larger than the heat of fusion (or a specific heat related to other phase transitions) melting and subsequent damage occur. The typical heat of fusion scale is on the order of 1 eV/atom. Both thermal and non-thermal damage mechanisms have been reported in the literature [2, 4].

Fatigue-related damage should also be considered in addition to instantaneous damage [5, 6]. The theory predicts that fatigue-related damage could occur from thermal cycling of the absorbing material at a fraction of the heat of fusion [7]. For example, in the case of B₄C no multi-shot damage was observed when the B₄C sample was exposed to 650,000 X-ray pulses

depositing 0.17 eV/atom at the surface of the sample (the heat of fusion for B₄C is close to 0.7 eV/atom). Thus, in order to avoid damage, the photo-absorbed photon energy density should be kept below a specific fraction of eV/atom. Therefore, for a low repetition source, the damage can be controlled by one parameter only — a maximum tolerable instantaneous dose.

11.3.1.2 Average power damage considerations

In the case of high repetition machines the situation is more complicated. The element under consideration can reach its melting temperature despite the fact that the instantaneous dose is much lower than the heat of fusion. The average temperature of the element depends on its geometry and its thermal resistance with respect to the environment. Let us consider a simple example of a solid layer which is cooled from one side and exposed to X-ray pulses from the other side, as indicated in Figure 4.

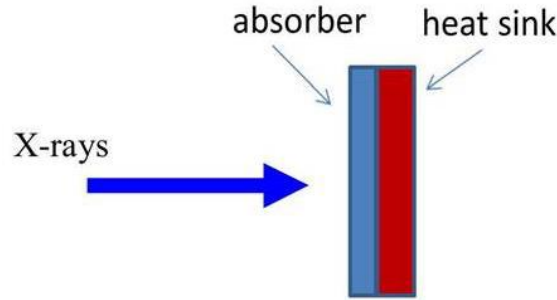


Figure 4. Schematic cross section of a cooled slab exposed to X-ray radiation.

In the steady state condition, the maximum temperature at the surface can be estimated as:

$$T_{\max} \approx T_{\text{ins}} + P_{\text{av}} R_{\text{th}}(d, \sigma, A, k, h) \tag{1}$$

where $T_{\text{inst}} = \frac{F_{\text{inst}}}{C_v l_{\text{abs}}}$ F_{inst} is the instantaneous fluence, l_{abs} is the absorption length, and C_v is the specific heat. Here R_{th} denotes the thermal resistance, P_{av} is the average power, d is the thickness of the element, σ is the rms photon beam size, A is the area of the cooled element, k is the thermal conductivity of the slab material, and h is the convective heat transfer coefficient. In most cases the thermal resistance should be modeled numerically; but for the simple geometry assumed here, an analytical approximation can be used that is often used to calculate spreading resistance in heat sinks [7].

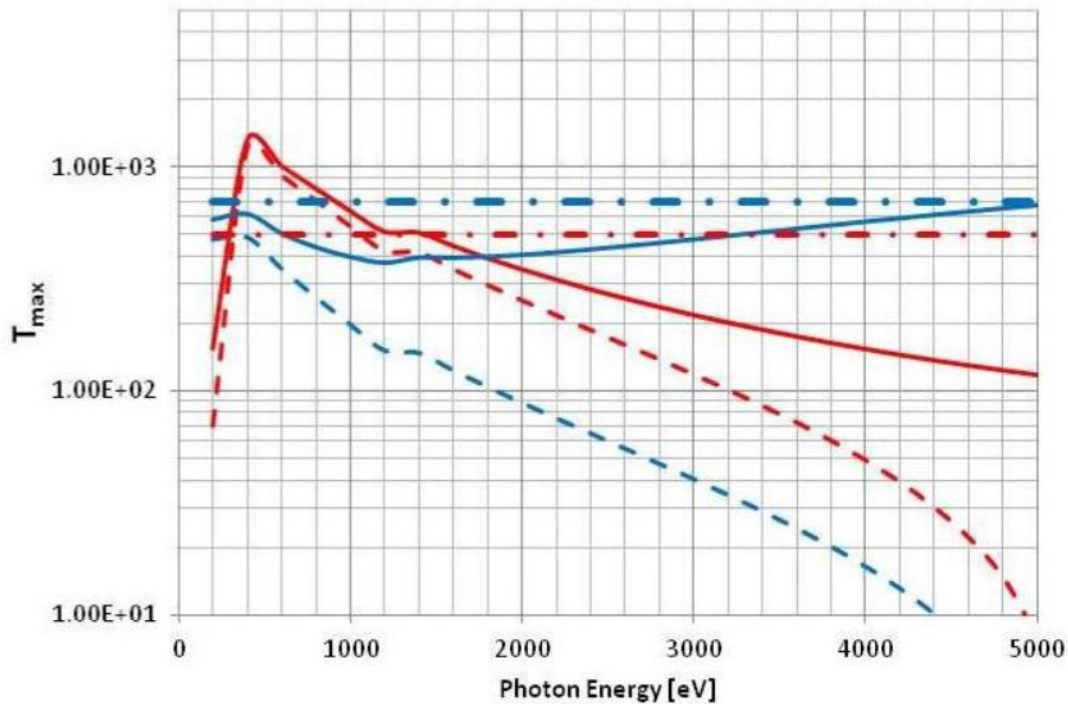


Figure 5. The dependence of instantaneous (dashed lines) and ΔT above ambient (solid line) vs. photon energy calculated for 2-mm-thick B₄C and CVD diamond element back-cooled with the convective heat transfer coefficient of 3000 W/m²K. The dash-dotted lines represent the limits for the maximum temperatures, as determined by maximum allowed thermal stress [6]. The blue color corresponds to B₄C and the red one to CVD diamond.

Let us assume a moderate convective cooling characterized by $h = 3000 \text{ W/m}^2\text{K}$ and investigate the effect of thermal resistance on the maximum temperature given by the Equation 1. Here we assume that the element is located 100 m from the LCLS-II source, the average power is 20 W, and we apply the minimum FEL divergences values. Figure 5 shows the dependence of the maximum temperature T_{max} and the instantaneous temperature of the element as function of photon energy. Curves were calculated for the B₄C and the CVD diamond discs of 10 mm in diameter and thicknesses of 2 mm. The Figure 5 also shows limits for the maximum temperatures determined by maximum allowed thermal stress [6]. The analytical calculations were sampled with finite element analysis (FEA), for example Figure 6 shows the average temperature and the stress distribution in 2-mm-thick CVD diamond disc, calculated by the FEA method for the 5 keV case, and the results agreed within 10 percent.

The results presented show clearly that it should be possible to build devices such as beam stoppers, collimators and slits which could survive the direct hits of the LCLS-II beam when the beam power is limited to 20 W.

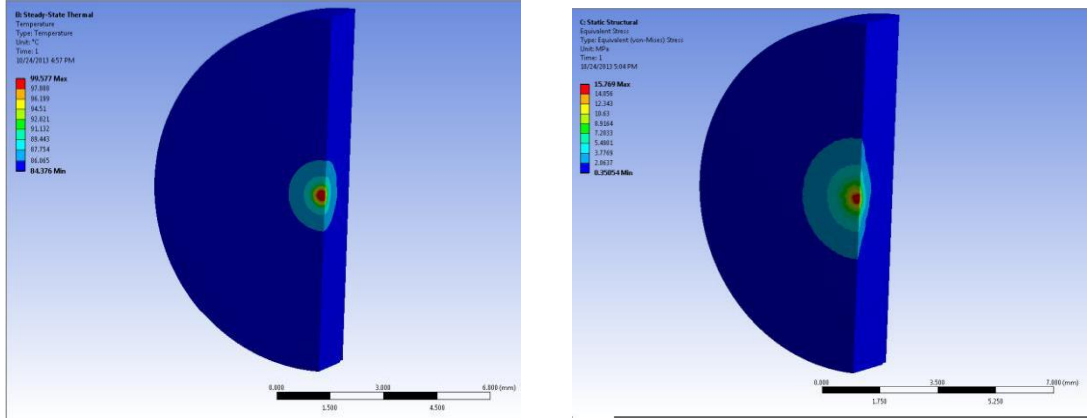


Figure 6. The temperature, 84-99°C, (left) and the stress, 0.4-16 MPa, (right) distribution in 2 mm thick CVD diamond disc, calculated by the FEA method for the 5 keV case.

It should be also straightforward to extend the maximum power limit by a factor of 10 or more by using grazing incidence elements and by increasing heat transfer coefficients.

However, the survivability of all elements, such as solid attenuators or viewers that are exposed to the FEL beam at normal incidence, must be investigated individually in a similar way as is done at the existing synchrotron radiation sources.

11.3.2 Optical Surfaces

The damage problem of grazing incidence optics is similar to the low-frequency operation case when the instantaneous damage is the main concern. The average temperature of grazing incidence optical surfaces is small with respect to normal incidence optics or absorbers, because the beam power is spread over a much larger surface.

The key quantity that helps to assess the damage is the instantaneous absorbed dose per atom at the mirror surface. For the grazing incidence optics this dose can be derived as follows:

For total external reflection below the critical angle, the $1/e$ penetration depth of the evanescent wave is given by [8]

$$d_{1/e} = \frac{\lambda \zeta}{4\pi\beta} \tag{2}$$

with

$$\zeta = \sqrt{0.5(\sin^2\theta - 2\delta + \sqrt{(\sin^2\theta - 2\delta)^2 + 4\beta^2})} \tag{3}$$

and δ and β being the real and imaginary parts of the index of refraction, n , and θ the grazing angle of incidence.

$$n = 1 - \delta - i\beta \tag{4}$$

The absorbed dose per atom at the mirror surface is given by

$$D_{atom} = \frac{(1 - R)P_d \sin\theta}{d_{1/e}\rho_{atom}} \quad (5)$$

where P_d peak is normal incidence power density, ρ_{atom} the number of atoms per unit volume. The evanescent wave has a depth of few nm for the cases of interest, with LCLS-II and some of the energy being transported out of the absorbing volume on a very short time scale by fast photoelectrons; but this decrease in the deposited power is not considered in the analysis below.

The maximum dose at the surface of a mirror is at the critical angle for a given photon energy. The dose monotonically decreases from the maxima as the grazing angle gets smaller, or quickly approaches that for normal incidence as the angle gets larger (see Figure 7).



Figure 7. Dose at surface of a Si mirror for 1mJ/mm² normal incident power as a function of grazing incidence.

The absorbed dose can be used for calculating the maximum instantaneous temperature, which can be compared with the temperature of melting of fatigue-related damage thresholds. As mirrors are costly and time consuming to replace they must be operated below their damage threshold. The damage threshold of various optical coatings are not well constrained. The best studied ones, Si, B₄C and SiC are known to better than a factor of 2 of their nominal values. Other coatings a safety margin of at least 2 should be used.

11.4 Wavefront Preservation and Mirror Acceptance Considerations

11.4.1 Wavefront Preservation

The mirror suite of the photon transport system has to deliver the beam into the experimental chambers with a minimum loss of flux and preservation of the wavefront. This statement carries many implications for the mirror design. To preserve the flux on the sample or, specifically, the peak power delivered, implies high reflectivity, generous acceptance that does not aperture the beam to minimize diffraction effects, and a very excellent mirror figure so as to minimize power into side bands at the focus. LCLS and other FEL facilities also require variable focal spot size. This requirement is the most stringent from the mirror figuring point of view and drives the design of the mirror system. The focal spot size can be varied by adjusting the focal length and moving the sample or by working out of focus. The approach is to vary the spot size by working out of focus. The requirements for wave front preservation are discussed below.

The Strehl Ratio is a measure of reflected beam deviation from the ideal perfect Gaussian profile [9]. It is expressed as:

$$\text{Strehl Ratio} \approx e^{-(2\pi\varphi)^2} \approx 1 - (2\pi\varphi)^2 \quad (6)$$

where φ is the rms wave distortion (phase) and

$$\varphi = \sqrt{\sum_i \varphi_i^2} \quad (7)$$

where $\varphi_i = (2\delta h_i \sin \vartheta_i) / \lambda$ describes the rms phase distortion for the i -th mirror.

The term δh_i is the mirror shape error (rms in this case), ϑ_i is the grazing angle of incidence, and λ the photon wavelength. When optics consist of N mirrors having similar rms figure errors and working at the same grazing incidence angle then the maximum acceptable shape error for a given Strehl Ratio (SR) can be expressed as:

$$\delta h \approx \lambda \sqrt{(1 - SR)/(4\pi \sin \vartheta)/\sqrt{N}} \quad (8)$$

Here we have assumed that the figure errors are uncorrelated. In practice the acceptable figure error could be even larger. This is because as one can sort and orient the mirrors in such a way that the total WF distortions are minimized.

The Strehl Ratio is used as a term to define a properly working optical system. In fact, astronomers and later laser opticians adopted the Marechal Criterion, which stipulates that a good optical system has a Strehl ratio greater than 0.8. This is an adequate criterion for working on-focus. Practically, the criterion ensures that a good optical system has a focal spot with peak intensity greater or equal to 80 percent of the ideal spot.

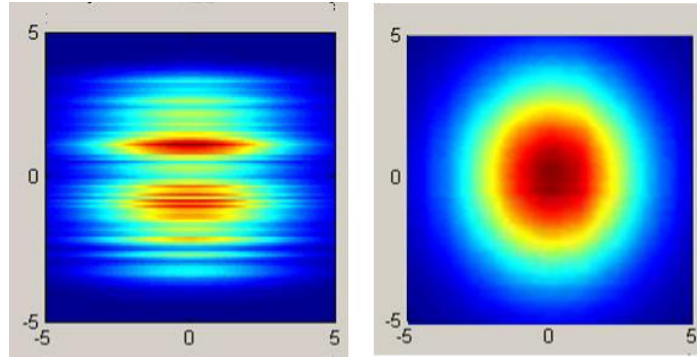


Figure 8. Effect of the shape errors on the beam. The simulations shows an unfocused beam (a.u.) after being reflected by 2 mirrors. The mirrors have 13 mrad incidence angle and the photon energy considered is 1.5 keV. The left image shows an effect of 1.6 nm rms, corresponding to a $SR = 0.8$. The right image shows the effect of two mirrors with 0.3 nm rms shape errors.

This is an inadequate criterion for off-focus beam utilization. An example of the effect of the shape error on an unfocused or defocused beam is shown in and in Figure 8 and Figure 9. In the case illustrated in Figure 8, the effect of two mirror’s shape error is simulated, considering a photon energy of 1.5 keV and an incidence angle of 13 mrad. The standard 0.8 Strehl ratio corresponding to a shape error of 1.6 nm rms is shown on the left. The 0.3 nm rms shape error is shown in the right. Figure 9 illustrates the fact that the quality of the mirror which is sufficient for obtaining a good focus does not preserve intensity uniformity out of the focus. Obviously, to work with a uniform beam out of focus one should go beyond the Marechal Criterion toward much tighter but achievable specifications.

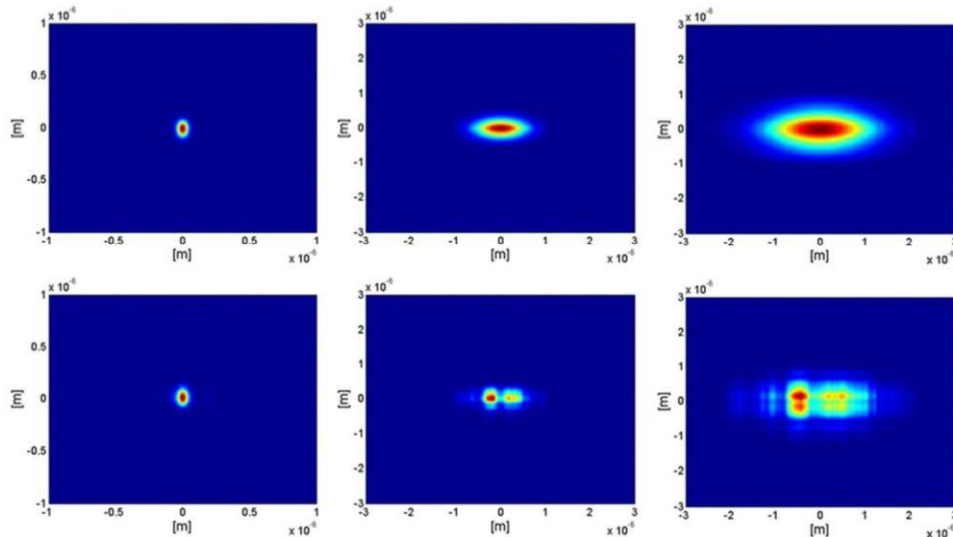


Figure 9. False-color simulated intensity profiles for the 10 keV diffraction-limited example, calculated for a Kirkpatrick-Baez (K-B) pair of mirrors. At the focus (left), 1 mm from the focus (middle), and 2 mm from the focus (right). The upper row simulates a 0.3-nm rms figure height error, while the lower row depicts that of 1-nm rms figure height error. The resultant wavefront error has limited impact on the focus spot size, but even slightly off the focus the beam structure introduced by 1-nm rms figure height error is profound.

The relationship between the out of focus intensity distortion and parameters describing optics quality is much more complicated than for the in the focus case. In particular, there is no simple relationship between the rms height error and the visibility of the fringes which characterize the non-uniformity of the intensity distribution. The visibility depends on details of the spatial frequency distribution of the figure errors and the distance from the focus.

Therefore we have performed wavefront propagation simulations to address this issue. We have used two types of figure error distributions which were based on the metrology results obtained from Zeiss mirrors and JTEC mirrors. We have found from the simulations that JTEC type optics with 0.3 nm rms height error gives excellent out of focus uniformity of the intensity distribution. As a reference we will take the result of the simulation obtained for the case of a beamline which operates at 1.5 keV and consist of three distribution mirrors and K-B focusing optics. The grazing incident angle is the same for all mirrors and is equal to 19 mrad. The SR for this optical system is equal to 97%. The simulated visibility of the out of focus fringes are smaller than 3%. The out of focus intensity distribution for this case is shown in Figure 10.

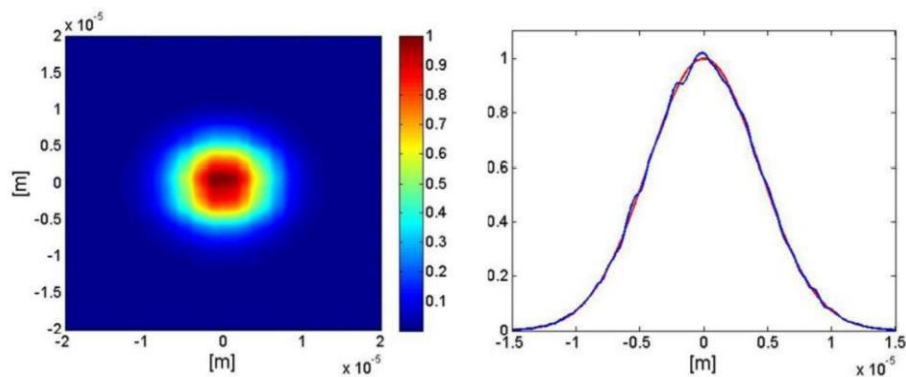


Figure 10. Out of focus intensity profile simulated for a beamline which operates at 1.5 keV and consist of three distribution mirrors and K-B focusing optics. The image shows the result calculated for the position located 10mm downstream from the focus. The right part of the figure is the lineout of the profile along the vertical direction. The red curve represents the intensity simulated for the ideal optics. The grazing incident angle is the same for all mirrors and is equal to 19 mrad. The rms figure error for each mirror is 0.3nm.

11.4.2 Mirror Acceptance

The source brightness should be transmitted to the experimental chamber with a minimal loss. This loss can be due to several factors. The effect of the shape errors and the Strehl ratio were discussed in the previous section. Another important contribution to the reduction of intensity in the focus, as well as out of focus, is the truncation effect.

The first reason is a diffraction effect similar to what happens when a beam passes through an aperture. The larger the truncation, the higher the intensity into the diffracted spot. Moreover, if the combination of wavelength and aperturing is such that the diffracted spot stays within the

central beam diameter, the structures of the diffracted beam alter the structure of the transmitted beam. This is evident in the simulation shown in Figure 11, where a mirror collecting the whole beam is compared to a mirror collecting only one or two FWHM. The effect of the truncation is evident and can be even more serious than the effect of the shape errors.

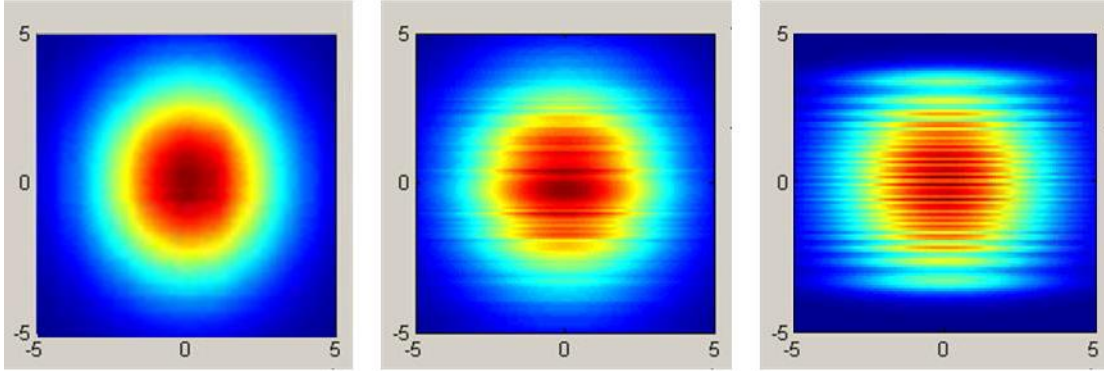


Figure 11. Effect of the truncation on an unfocused beam. The simulations show an unfocused beam (a.u.) after being reflected by two mirrors. The mirrors have 0.3 nm rms shape errors and they collect the whole beam (left), two FWHM (center) and 1 FWHM (right).

However truncation also affects the beam also when it is focused. A limited acceptance can produce a larger spot because of the diffraction limit effect. This effect reduces the fluence in the spot, because of the enlargement. However there is also an overall reduction of power because illumination of the optical aperture is between the two extremes of Gaussian and uniform. A simple formula to calculate the power reduction in this case [10] is:

$$P_L = \exp(-2(D_t/D_b)^2)$$

where D_b is the diameter at 4σ acceptance and D_t is the diameter of the truncation. Even with two FWHM acceptance, there is a reduction of power in the focused spot equal to approximately 6 percent (if the truncation is in both directions). At one FWHM acceptance, such effect increase to 50 percent.

For a given mirror, the grazing incidence angle ϑ and a given mirror length L , the maximum distance from the source D at which two FWHM are collected is given by:

$$D_{hv} = L \sin \vartheta / (2 \text{FWHM}_{hv}) \tag{9}$$

where the subscript hv indicates that the divergence, and therefore the distance from the source at which two FWHM are collected, depends on the photon energy.

The front end enclosure terminates 86m from the end of the undulators. Assuming the downstream soft x-ray mirror is 75m from the end of undulators, then 800 mm long mirrors will collect more than two FWHM down to <250eV at angles down to 11 mrad. In Figure 12, this maximum distance from the source where two FWHM are collected by a 800mm long mirror is plotted as a function of the photon energy for four possible angles of incidence. In the experimental area, where the focusing optics, namely the Kirkpatrick-Baez (K-B) optics, will be located, a larger angle or longer mirrors are required.

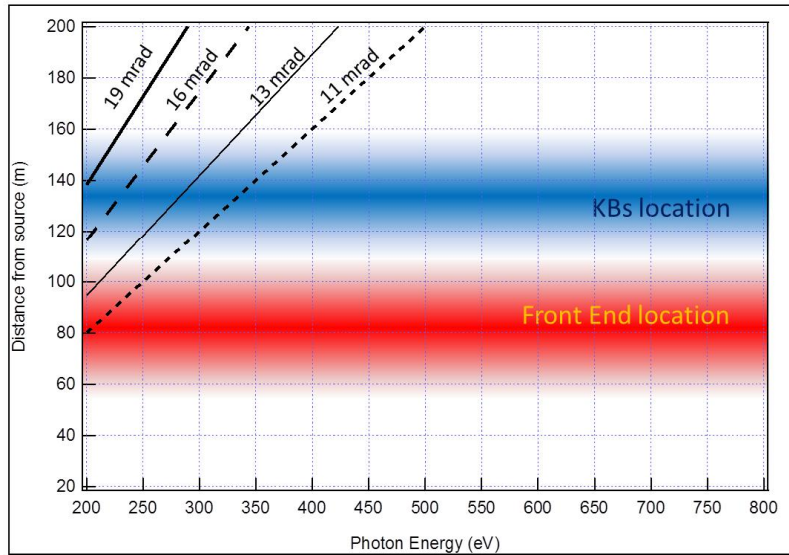


Figure 12. Maximum distance from the source at which two FWHM are collected by 800mm long mirror as a function of the photon energy for four different angle of incidence in the soft X-ray range. The good operating range for a mirror is to the right and below the applicable grazing angle line.

For the HXR line the downstream mirror is assumed to be 80m from the end of the undulator and a similar calculation for 800mm long mirrors is shown in Figure 13. An angle as low as 3 mrad is acceptable for the front-end mirrors, but it should increase to 5 mrad in the Near Experimental Hall to collect two FWHM down to 1 keV. The existing HOMS mirrors are at 1.35 mrad. (LCLS plans to upgrade these, independently of the LCLS-II project, to 800mm long mirrors with very similar figure specifications as are proposed in this CDR.)

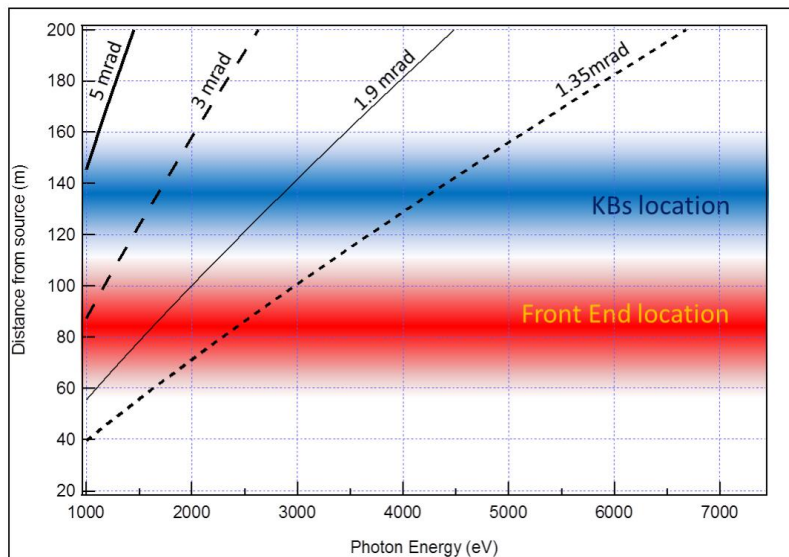


Figure 13. Maximum distance from the source at which two FWHM are collected by 800mm long mirror as a function of the photon energy for four different angle of incidence in the hard X-ray range. The good operating range for a mirror is to the right and below the applicable grazing angle line.

11.4.3 Mirror Figure

The SR of a mirror system depends on the wavelength of the radiation λ and on the angle of incidence ϑ . Lets consider the energy ranges of the fundamental harmonic for the SXR and HXR cases, with a slightly extended range to take into account possible upgraded operative mode (e.g., 0.2-1.6 keV for the SXR and 1-6 keV for the HXR). In the case of three possible angles for the mirrors, the required shape error as a function of the photon energy to have a SR greater than 0.97 after four mirrors are shown in Figure 14 for the soft x-ray and Figure 15 for the hard.

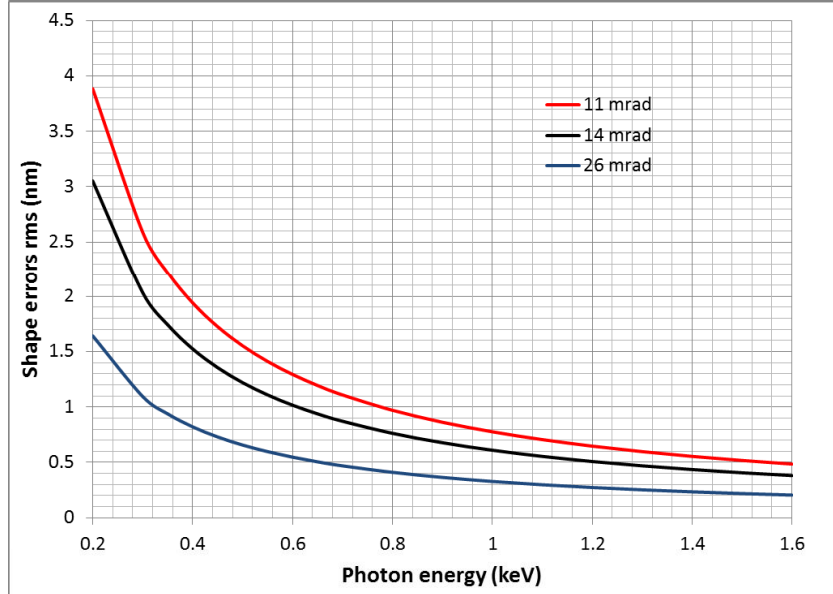


Figure 14. Required shape errors to have an SR greater than 0.97 for the soft X-rays as a function of the photon energy and for three different angle of incidence.

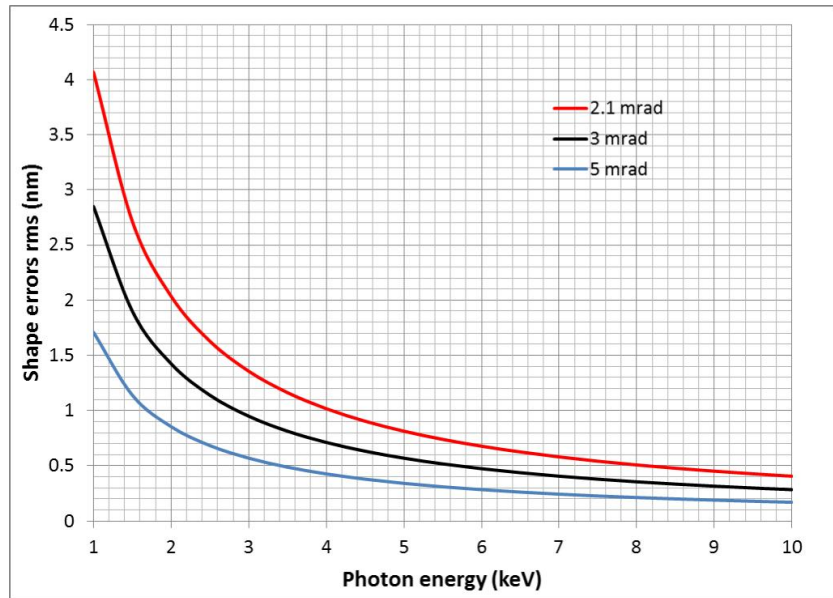


Figure 15. Required shape errors to have an SR greater than 0.97 for the hard X-rays as a function of the photon energy and for three different angle of incidence.

Based on the graphs shown in Figure 14 and Figure 15, the shape errors have to be as low as 0.3 nm rms to be able to work out of focus with a uniform beam after four mirrors. The current mirror technology is such that 0.3 nm rms is feasible only on a limited mirror length, or a portion of the total length. Mirrors of 800 mm length, with 0.3 nm rms in the central 3-400 mm and 1 nm or better overall, are commercially available.

This matches the requirements for LCLS-II mirrors, since the lower shape errors in the central part of the mirror are needed. This is due to the fact that the higher photon energies are the ones demanding the more stringent shape tolerances and are also those having the lower divergence. Considering two FWHM as the footprint of the beam into the mirror, one can plot the graphs of Figure 14 and Figure 15 as a function of the footprint itself. Let's consider the case of a mirror installed in the Front End Enclosure, at 90 m from the source. For each energy, the two FWHM footprints are calculated. For each footprint, a particular shape error is required. This combination of footprint and associated shape error is shown in Figure 16 and Figure 17, for soft and hard X-rays and for the three angles of incidence mentioned above. The figure tolerance is tighter as the angle of incidence increases. Therefore, the SXR case is the most demanding tight mirror profile. It is important to note that if one considers the mirrors into the experimental hutches 50 or more meter downstream, the footprint will increase by 50 percent or more.

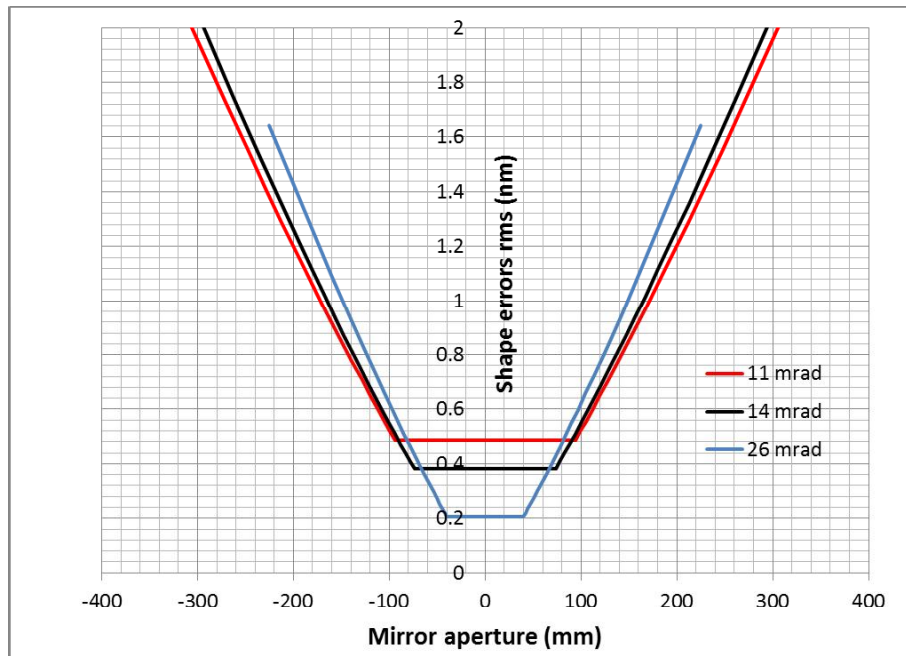


Figure 16. Required shape errors to have a SR agreater than 0.97 for the soft x-rays as a function of the photon energy and for three different angle of incidence.

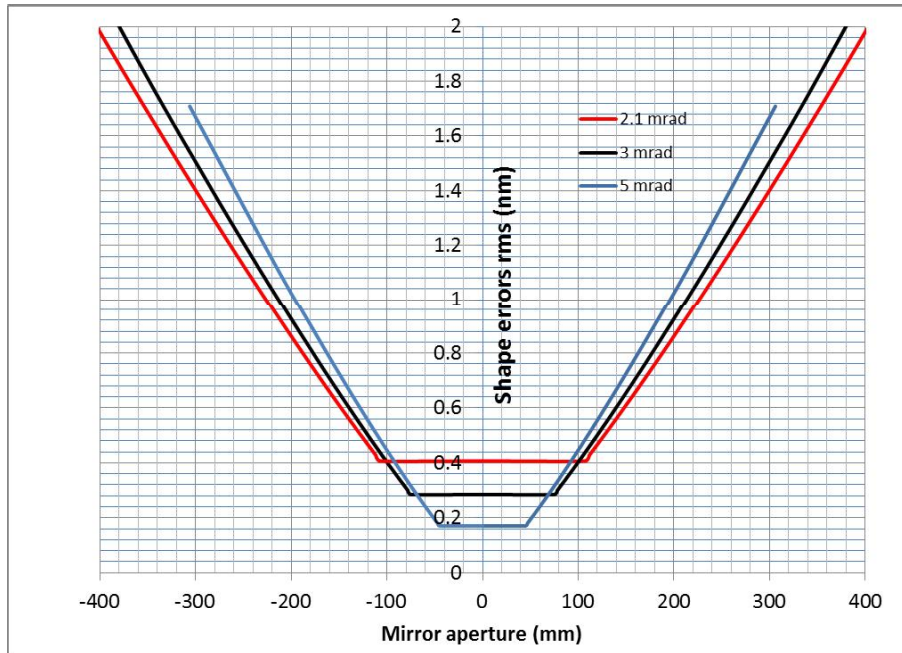


Figure 17. Required shape errors to have a SR agreater than 0.97 for the hard x-rays as a function of the photon energy and for three different angle of incidence.

It is evident that sub 0.5 nm shape error mirrors are required. The maximum length mirror with the central 300-400 mm down to 0.3 nm and 1 nm overall that is commercially available is 1000 mm. The two constrains, to have the best producible residual shape error and the maximum length available mirror, determine the minimum angle for a mirror as a function of the source distance. In fact, in order to collect as much flux as possible, to avoid diffraction effect, and to have a diffraction limited spot or the maximum power on the focused spot into the experimental chamber, one needs to collect a minimum of two FWHM of the beam divergence. The effect of the truncation was explained in section 11.4.2.

11.5 Mirror Reflectivity and Harmonic Rejection

11.5.1 Mirror Reflectivity

Assuming the minimum acceptance is 2 FWHM, the lower limit on the grazing angle is set by the length of the mirror and its distance from the source. The upper limit is set by critical angle above which the transmission at the maximum photon energies is rapidly decreasing. The primary criteria for selecting the coating and angle is high reflectivity over the range the FEL fundamental will operate. A secondary criteria is suppression of higher orders. Ideally suppression of higher orders should be done at every photon energy, but this is only possible with filters or variable angle optics. To meet the first criteria a coating should not contain any material having absorption edges into the required range.

11.5.2 SXR Beamline Optics

On the SXR line, 200-1250eV any carbon-based coatings, the solution adopted for LCLS-I, are excluded. Oxygen is very hard to avoid as most coatings will inherently have an oxide layer. The fluence on the mirror surface and damage threshold of optical surface is a concern at all angles as discussed above in section 11.3.2. All these considerations and constraints limit our choice to a few possible coatings. Transition metal coatings are possible. The disadvantages are several, the reflectivity is low and the cut off energies high relative to coating of lighter elements, and the ablation/damage thresholds could be an issue. Aluminum is the most appealing of the metals, even if some oxidation could prevent its use. Boron could be good from the point of view of reflectivity and damage, but suffers from even stronger oxidation, preventing its use at the oxygen edge and slightly above. A further possibility is the use of silicon borate (SiB_3). This coating has optimal reflectivity property and very good handling of the fluence. Because it is a very new material with many unknowns, studies would have to be performed. The native oxidation on a SiB_3 surface is not well characterized. Bare silicon would be an ideal choice, but it also forms a native oxide layer. It will be necessary to properly passivate the surface to avoid strong oxidation. Bare silicon is a material that can be cleaned *in situ*, which will be critical for operations at the carbon edge.

Examples of these mirrors are shown in Figure 18 for comparison. In this example the overall reflectivity is shown for four mirrors, two of them at 13 mrad in the front end and two of them at 18 mrad in the Experimental Hall.

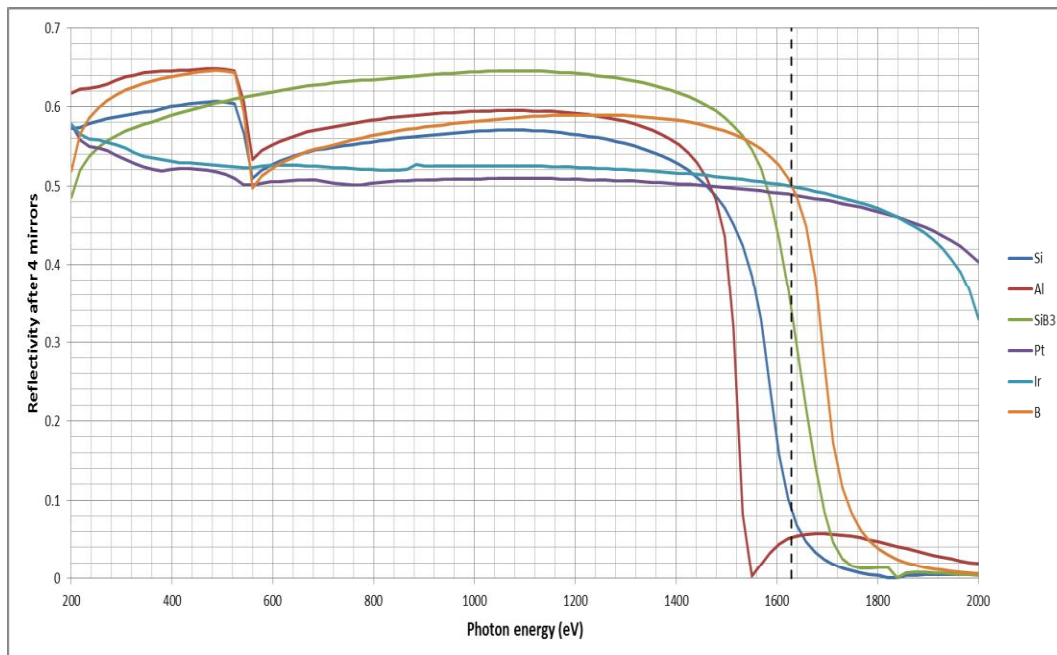


Figure 18. Reflectivity of some possible coating in the soft X-ray region considering four mirrors, two of them at 13 mrad and two at 18 mrad. The dot black line represent the third harmonic position of the oxygen edge, where a suppression of four orders of magnitude is desired. In the case of silicon, boron and aluminum, an oxidation layer is taken into account.

Silicon is well characterized and an excellent optical material that does not require coating after polishing. The safe upper bound for damage in a silicon optical surface is ~ 0.1 eV/atom. To keep the optical surface below this threshold in the front end, less than 80m from the end of the undulator, the grazing angle has to be ≤ 11 mrad. In Figure 19, and the three subsequent figures, Si is compared to SiB_3 , which though it potentially could operate well below its damage threshold, its threshold is not well characterized. At this angle the acceptance for a 800mm mirror is over two FWHM above 250 eV in the front-end enclosure. Though the absorbed dose is close to the damage threshold and going to lower angles would lower the dose, the mirror length would have to increase, and cut off energy would increase.

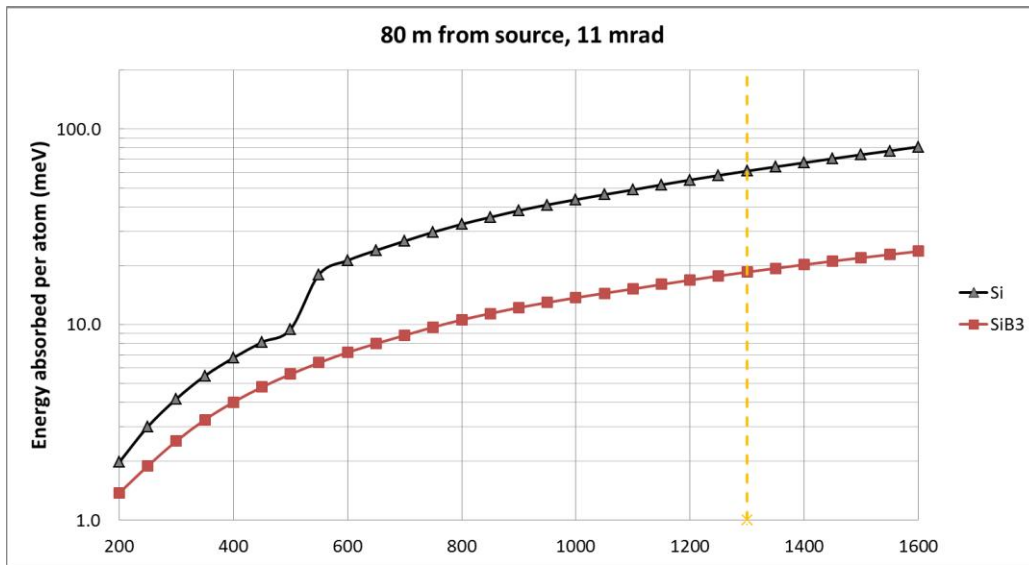


Figure 19. The calculated maximum per pulse dose for Si (with 2nm oxide layer) and SiB_3 at 11 mrad grazing angle and 80m from the SXR source.

To match the acceptance of 11 mrad in the front end with ones in the Near Experimental Hall, at 120m, with the same mirror length, the angle is 14 mrad. The total reflectivity through this optical system with two 11 mrad mirror and two 14 mrad mirrors is shown in Figure 20. The reflectivity is good up to 1750 eV which gives no suppression of 3rd order light at the oxygen k-edge. The optimum angle for suppression of 3rd order at the oxygen k-edge, 1629 eV, with either Si or the SiB_3 is around 20 mrad. The reflectivity at 1250eV is just beginning to drop off while the reflectivity at 1629eV, though not completely suppressed, is 0.02 of that at 543eV for the Si mirrors and 0.028 for the SiB_3 coating.

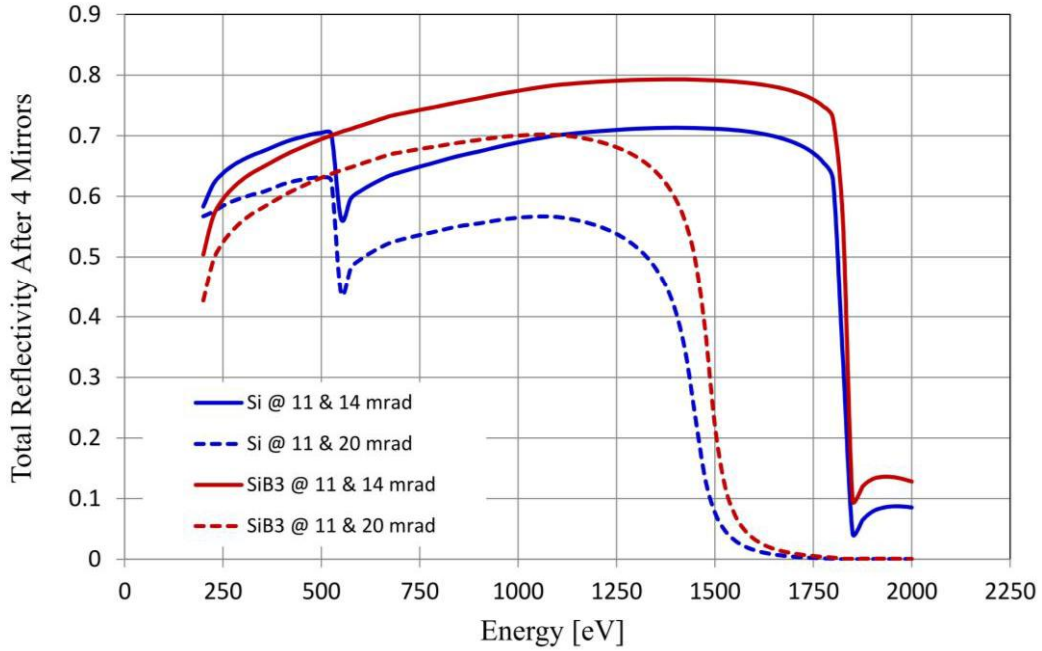


Figure 20. Total reflectivity after four mirrors for all Si and SiB₃ optical surfaces. 2 nm oxidation is assumed on the Si mirrors and none on the SiB₃ ones. The first two mirrors in all cases are at 11 mrad. The second two are at either 14 mrad or 20 mrad.

The dose the 14 mrad mirror is shown in Figure 21. It is lower than for the 11 mrad and angle of incidence could be increased to bring the cut off energy down. In Figure 22 the dose for both the Si and SiB₃ mirrors at 20 mrad is shown. The dose is higher than for the 11 mrad mirror in the front end and exceeds 0.1 eV/atom if it is operated above its cut off energy of 1500 eV.

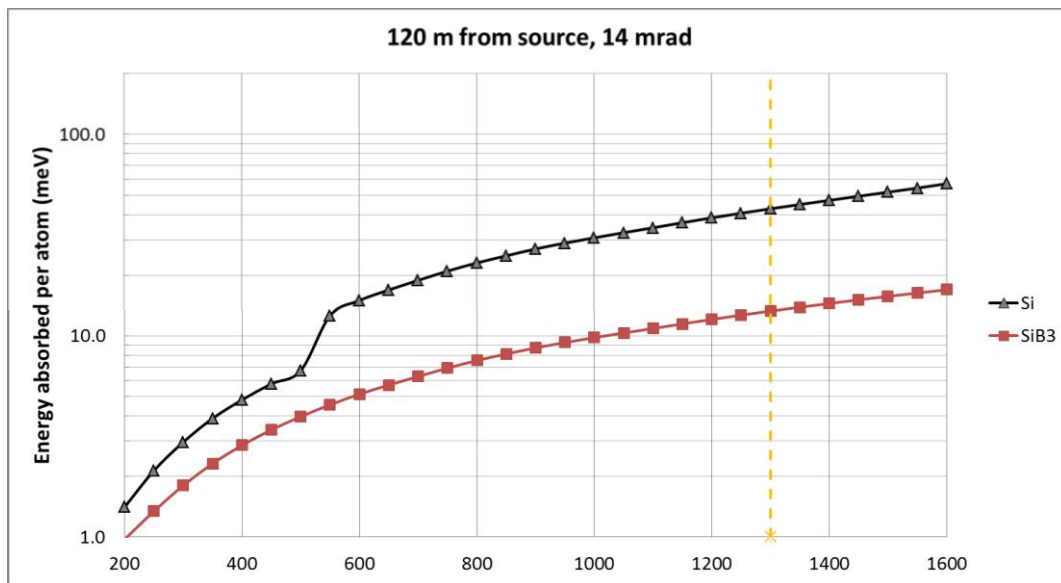


Figure 21. The calculated maximum per pulse dose for Si (with 2nm oxide layer) and SiB₃ at 14 mrad grazing angle and 120m from the SXR source.

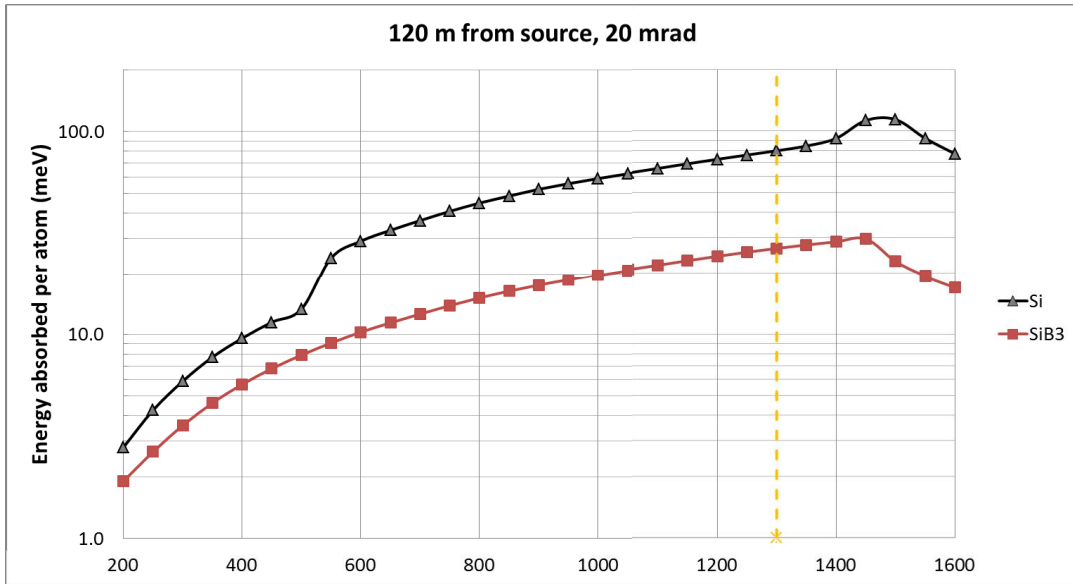


Figure 22. The calculated maximum per pulse dose for Si (with 2nm oxide layer) and SiB₃ at 20 mrad grazing angle and 120m from the SXR source.

The base proposal is to use Si mirrors on first SXR beam line. The mirrors in the front end will be at 11 mrad and the focusing optics in the NEH at angles approaching 20 mrad. Other coatings, including SiB₃, will be considered as they potentially can be used on the optics at angles up to 26 mrad to suppress 3rd harmonic at the oxygen edge.

11.5.3 HXR Beamline Optics

In the hard x-ray line the existing HOMS mirrors will be retained for high energy operations and two new mirrors, optimized for the 1-5 keV and high repetition rate operations will be installed. The LCLS-II mirrors will put the beam on the same optical axis as the HOMS to the XPP and FEH.

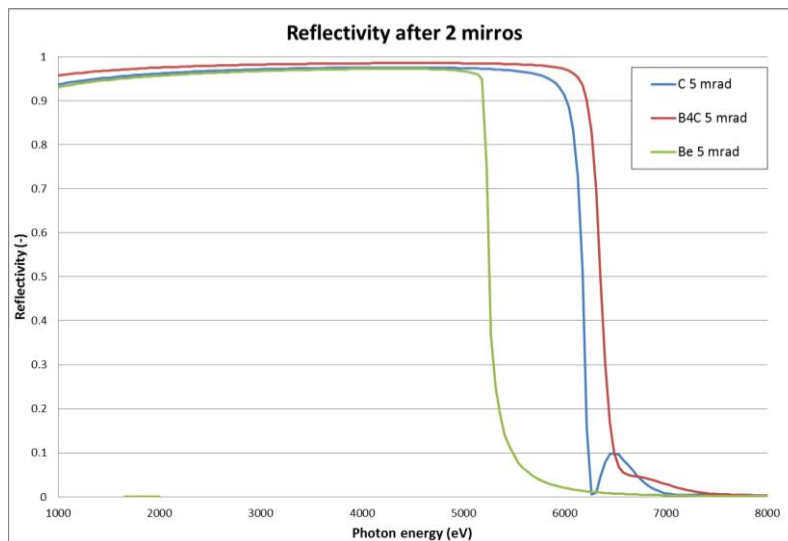


Figure 23. Reflectivity after two: Be, C (diamond like), or B₄C mirrors at 5 mrad.

From Figure 13 it can be seen that a 800 mm long mirror at any angle above 3mrad will have good acceptance down to 1 keV. As coating, three possible alternatives are presented in Figure 23; B₄C, C and Be. From the following graph, it is evident that B₄C is an excellent candidate. Pure Carbon or Beryllium have slightly lower reflectivity but are still good. The Be coating could be a good alternative if we wish to institute *in-situ* cleaning. Working with Be has many issues. At 5 mrad it has a sharp energy cut off just above 5 keV. At 3 mrad the cut off energy is over 8.5 keV. C has the advantage that the coating is well characterized, induces a lower stress into the mirror substrate and is easier and cheaper coat.

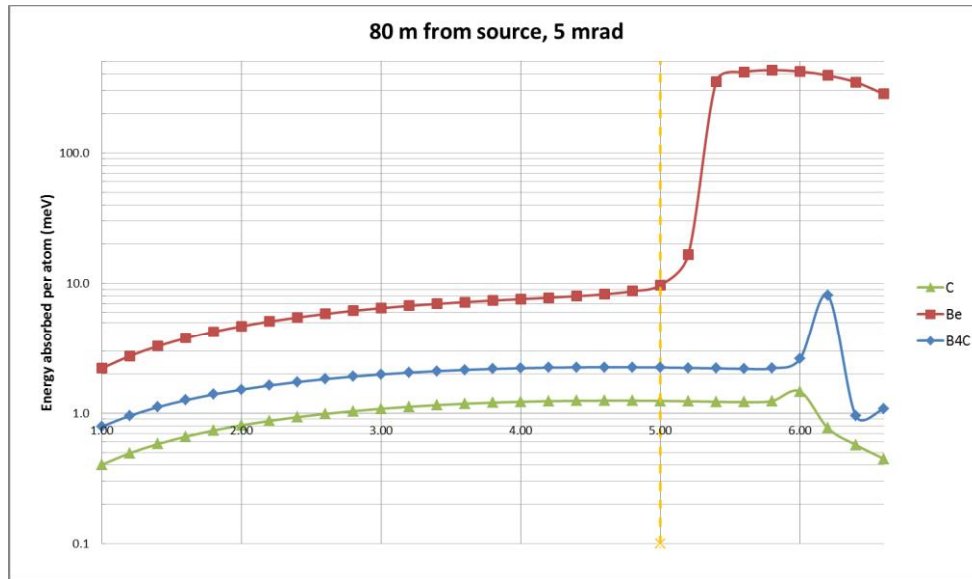


Figure 24. The calculated maximum per pulse dose for Be, C and B₄C at 5 mrad grazing angle and 80m from the HXR source.

The maximum dose is plotted in Figure 24 and B₄C and C are well below their damage thresholds. Be would likely exceed its damage threshold if run at 5 mrad above 5 keV, but as noted above the angle of incidence could be reduced. Considering all these factors, the proposed solution for the HXR line is C-coated mirrors at 5 mrad grazing incidence angle.

11.5.4 Harmonic attenuation

The third harmonic of the emitted radiation can be as high as a few percent of the fundamental in terms of emitted photons or emitted power. Moreover, several experiments can be more sensitive to higher harmonics (or simply to higher photon energy) than to the fundamental, but not all of them. Conversely, some experiments merely require the highest possible flux, without concern for spectral purity (since it is limited to few percent). Just looking at the reflectivity after only four mirrors, the achieved higher order suppression at the oxygen k-edge of 10^3 is not achieved with fixed angle mirrors, as can be seen in

Table 5.

Table 5: Reflectivity and third harmonic suppression at the oxygen k-edge for several possible coatings with two mirrors at 11 mrad and two at 20 mrad. In the case of silicon, aluminum and boron, a 2 nm oxidation layer is taken into assumed.

	Si	Al	SiB ₃	Pt	Ir	B
	Reflectivity after 4 mirrors					
O K-edge	0.553	0.625	0.643	0.455	0.489	0.613
O 3 rd harm	0.011	0.010	0.018	0.437	0.453	0.040
	3 rd harmonic suppression ratio					
3 rd /1 st	0.019	0.015	0.028	0.961	0.927	0.064

Of course, one possible option is to further increase the angle of incidence on the mirrors, with an associated overall reduction of reflectivity and lowering the cut off energy. Another possibility is variable angle harmonic rejection mirrors. The monochromator that is not in scope, but is proposed for future installation, is designed function in higher order sorting mode. In fact, the monochromator is formed (in the proposed design) with a plane mirror and a plane grating. If the mirror and the grating are parallel, the zero order (or reflected order) is directed into the exit slit. Since both the grating and the mirror are flat, there are no constraints in selecting the angle of incidence, except for the ablation issue and, of course, reflectivity. (Actually, by increasing the angle of incidence, the effect of the shape error is more evident, but we can disregard such constraint for now). The damage issue is significant and though there will be clarifications the thresholds as design progresses, it is a given that the per pulse energy in the fundamental will have to be limited to achieve high suppression at the 3rd harmonic over all of the 200 to 1250 eV range.

11.6 Wavefront Preservation in X-ray Transport Systems

11.6.1 Variable Image Size

Most experiments need either a variable spot size or to have the spot focused into two or more different focal position. The most common way used to accomplish this is with two mechanically deformable mirrors. Each of the two mirrors focuses the radiation in one direction only, so that the two mirror are installed at 90 degrees to have a stigmatic focus. This configuration is known as Kirkpatrick – Baez mirror pair [11], or more generally as K-B mirrors.

The ideal shape on which to focus the radiation is the elliptical one. An ellipse focuses all the radiation coming from a source point located in one of its foci into the other foci without aberration. This is the best focus one can have, but ideally it works only for a given point source and image distance and a single angle of incidence. A way to overcome this is by using adaptive optics, namely a mirror substrate bended by two unequal moments at the end of a figured mirror to realize the proper elliptical profile (Figure 25, left). Numerous systems have been developed in

the past. A system was designed and implemented for the LCLS soft X-ray beamlines [12] and have operated successfully (Figure 25 right).

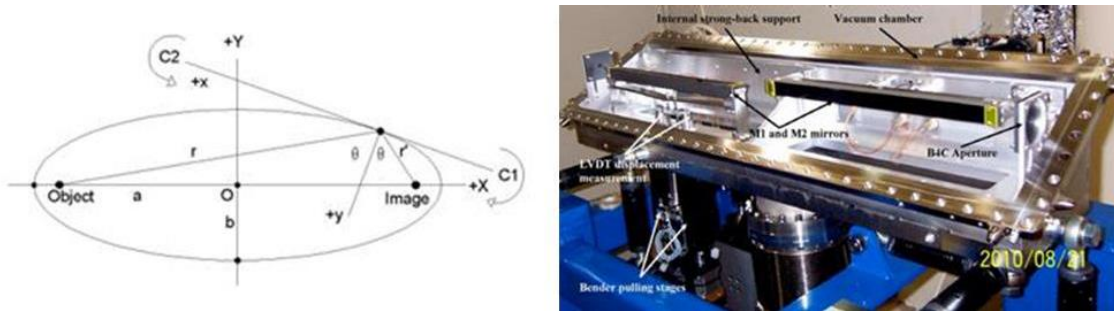


Figure 25. Left: Pictorial description of the bending mechanism necessary to obtain a perfectly focusing mirror starting from a flat surface. Right: The LCLS K-B system used for the AMO beamline.

The system considered for LCLS-II is based on a variable substrate width optimized for a particular position and able to work in a range of focal distance acceptable for the experimental chamber. The mirror lengths will be 800 mm, in comparison to the 450mm for the LCLS-I K-B systems. The LCLS-II K-B mirrors will be in separate vacuum tanks due to the longer mirrors and the requirement that the mirrors be independently translated in the beam to expose different stripes to FEL radiation.

A wavefront sensor would be useful for optimizing the performance of these mirrors [13], but they are not in the baseline scope of the project. Some options are presented in section 11.8.4 below. Space is allocated for installation of such sensors downstream of the experimental end stations.

11.6.2 Thermal and mechanical deformation

LCLS-I was a relatively low- repetition-rate machine, delivering much less than a watt onto the mirrors. LCLS-II can potentially deliver hundreds of watts in the FEL beam. Even if only a small fraction of that is absorbed by the mirror, namely the higher harmonics, most of the spontaneous radiation produced by the undulators (80% at low K and 30% at high K) and a ~10 percent of the fundamental, it is enough to produce significant deformation of a conventionally cooled mirror surface.

Liquid Nitrogen (LN) cooled mirrors have been developed and this approach has the advantage that it brings the mirror to a temperature at which the silicon (the material of which the mirror bulk is made) is near the minimum of thermal expansion and with a high thermal conductivity. This could limit the deformation, but has the drawbacks of higher cost of production, maintenance and operation and more complexity in the mechanical system. The critical drawback though is the LN cool mirrors would have to have the optical figure measured in-vacuum and metrology systems to do this, at the precision required to preserve the wave front, do not exist. The time required to develop such systems is not consistent with the LCLS-II project

schedule. The LCLS-II power loads will have to be limited to what can be handled with more conventional cooling approaches.

The target is to preserve the 0.3 nm rms or to avoid the wavefront distortions as described above. A preliminary analysis shows that limiting the average FEL power to 20W can be handled with conventional water cooling methods. The average power would be limited either through limiting the per-pulse-energy, the repletion rate or a combination of both. At 20W in the FEL beam then no more than ~6 W are absorbed in the first mirror. The first studies will imply the use of side cooling with water at room temperature. This is a classical and well-known system adopted in all the synchrotron sources around the world. The water circulates on pipes cooling some copper block in thermal contact with the mirror, usually with a thin soft material interface in between. For few watts, this is usually enough, and the base plan is the target to preserve a tight shape profile will be met with this approach. The first results (Figure 26) show that the side water-cooling should be enough to preserve required shape errors. However, a detailed study must be made.

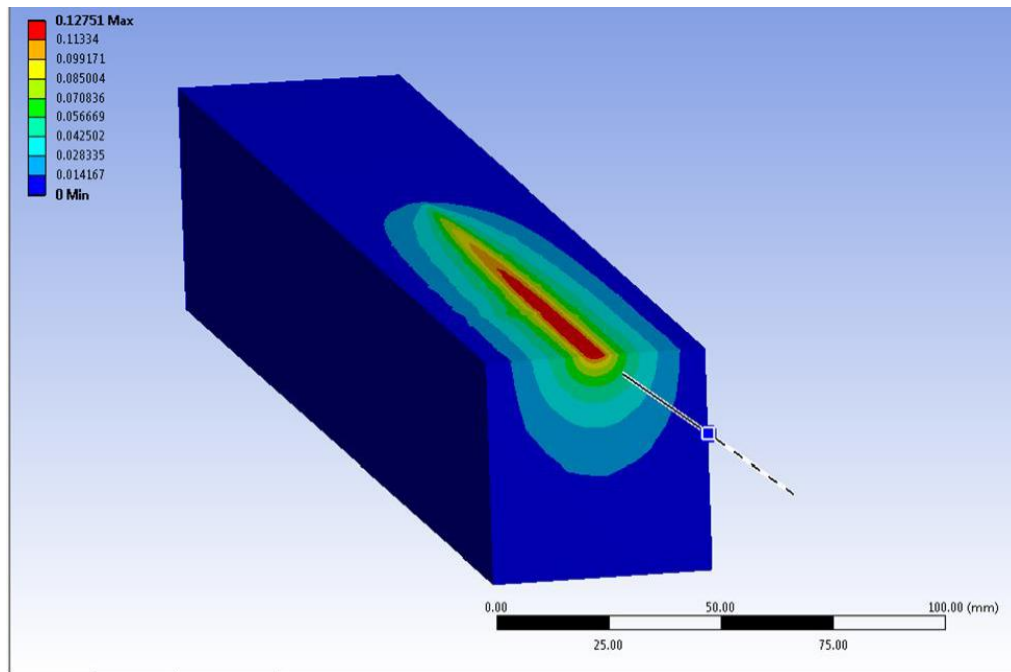


Figure 26. Increase of temperature due to 6 W absorbed by the mirror considering a perfect lateral water cooling scheme. The maximum increase of temperature is of 0.1 degree. Only half of the mirror is shown here.

The mirror support and cooling scheme, must be realized in a way that does not induce mechanical deformation on the mirror. The clamping system, without cooling, was recently studied for the LCLS mirrors. A preliminary solution providing distortion well below 0.3 nm rms was found and will be the starting point for the LCLS-II mirror holder system. The mechanical deformation due to holding the mirror and the thermal deformation after simple side cooling of the mirror described above are shown in Figure 27.

20W in the FEL beam is a relatively safe, but not certain limit for keeping deformation below 0.3 nm rms. If the analysis shows that we will still experience deformations that can reduce the performance of the optics, an in situ correction system, based on mechanical or piezo-electric actuators, may have to be adopted. Conversely after study and development the FEL power limit may be increased.

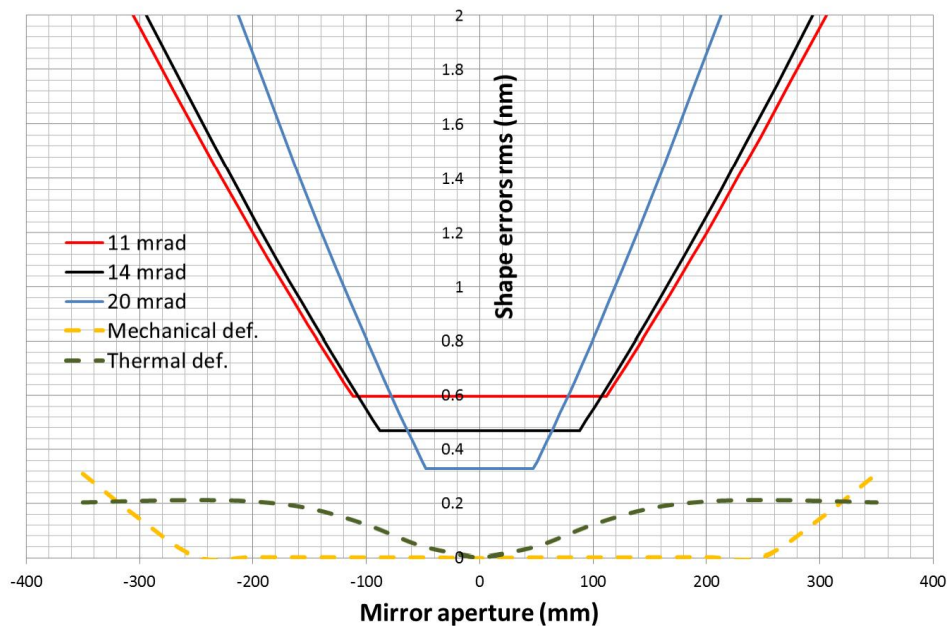


Figure 27. Thermal induced deformation by 20 W incidence FEL beam (~ 6 W max absorbed) for a simple water side cooling system is compared to the required figure errors and mechanical deformation from holding the mirror.

11.7 Monochromators and Pulse Length Considerations in X-ray Transport Systems

11.7.1 Monochromators

The LCLS-II SASE FEL will produce a polychromatic beam having a random distribution of spectral spikes of varying magnitudes, with a typical bandwidth of 0.3 percent. For certain classes of experiments, monochromators will be needed to produce a beam at a fixed energy and with a narrower bandwidth. The monochromators should be capable of sustaining the instantaneous FEL peak power as well as handling the average thermal load. It should be readily tunable, have specified resolving power and reasonable efficiency.

11.7.1.1 Monochromatic Beam Delivery

Soft X-Ray Monochromators

For the soft X-ray undulator line a monochromator has been included in the layout, but is not in the base line plan. The energy range for the proposed monochromator is 200 eV to 1.3 keV the monochromator will be a grating-based system similar to that of the LCLS-I SXR instrument, consisting of a planar pre-mirror, planar variable-line-spacing (VLS) grating, and an exit slit. The VLS grating disperses the incident polychromatic FEL beam and focuses vertically at the exit slit, which then selects a narrow bandwidth limited by the resolving power. The Kirkpatrick-Baez mirror pair is used to refocus the monochromatized beam, with the vertical mirror refocusing vertically the exit slit onto the interaction point and the horizontal mirror imaging the source point horizontally onto the interaction point. The grating will be operated in the “fixed-focus” mode and tuning is facilitated by a concerted rotation of both the pre-mirror and the grating. The rotation of the pre-mirror is pivoted at a point directly above and half the distance from the center of the grating.

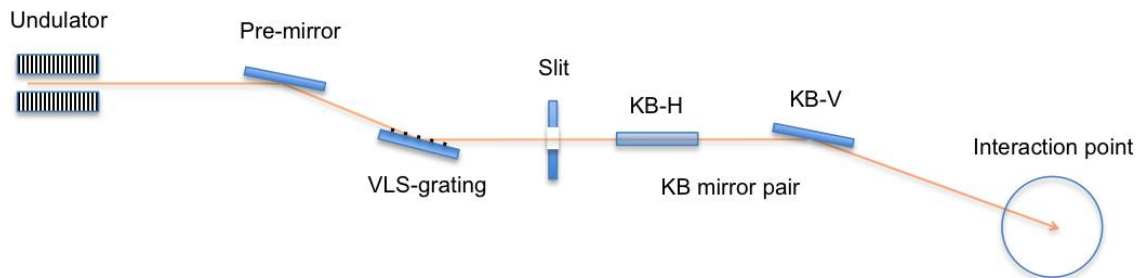


Figure 28. Schematics of the soft X-ray grating monochromator and focusing system. The VLS-grating disperses the incoming polychromatic FEL beam and focuses vertically at the exit slit, where a narrow bandwidth given by the resolving power is selected. The vertical mirror of the KB pair KB-V refocuses the image at slit vertically onto the interaction point, and the horizontal mirror KB-H images the source horizontally onto the interaction point as well. The tuning of the energy is facilitated by rotation of both the pre-mirror and the VLS-grating in the “fixed-focus” mode of operation.

The grating system will operate from 200 eV to 1.3 keV, have a resolving power of 30,000, and a minimum (spectral) efficiency of 5 percent. To achieve the required resolving power, the line density of the grating is quite high, amounting to 1500 lines/mm. The constant-focus condition is $\cos\beta/\cos\alpha = 1.9$. The source and exit slit distances are assumed to be 90 and 5 m, respectively, leading to a demagnification factor of 34 when using Gaussian beam treatment because of the full transverse coherence of the FEL beam. The incident angle varies from 33 to 84 mrad, and the exit angle from 63 to 160 mrad. Because of the large incidence angle, high-Z materials such as platinum are being considered to optimize the efficiency, in conjunction with using a blazed profile. The KB mirror pairs will be designed to produce $1 \times 1 \mu\text{m}^2$ focus at the interaction point. The demagnification factor for K-B-Horizontal differs significantly from that of the K-B-Vertical because it needs to focus the large source point horizontally instead of refocusing the already focused mono beam at the exit slit.

Hard X-Ray Monochromators

For the hard X-ray undulator line in the energy range of 2.5 eV to 25 keV each instrument will provide its own monochromator system. Below 2.5 keV not monochromators are planned.

11.7.1.2 Undulator Tuning (K-Mono)

The LCLS-II undulators for both the soft X-ray and hard X-ray line will be of the variable gap type, in contrast to the fixed-gap type of the LCLS-I. As such, diagnostic tools are needed to make sure that the magnetic parameter K of each undulator matches that of all other undulators within a given tolerance of less than 0.02 percent for the HXU and less than 0.04 percent for the SXU to ensure electrons stay on resonance. The concept of this diagnostic is based on the high precision measurement of the spectrum of the spontaneous emission from an individual undulator. By comparing the spontaneous emission spectra, such as those shown in Figure 29 of two undulators, the relative difference in their K values can be extracted, which could in turn be used for matching. The spectrum is taken by scanning the electron energy while keeping the K fixed.

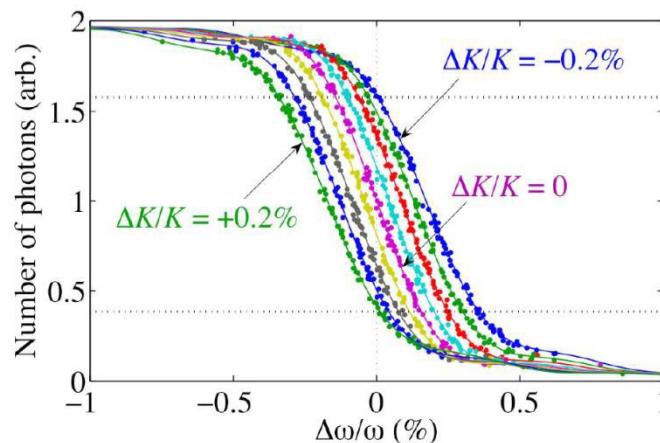


Figure 29. Spectra of spontaneous emission of individual undulators of different magnetic parameter K .

Soft X-Ray Undulator Tuning

For the soft X-ray undulator line there is no monochromator or spectrometer in the base line plan. Tuning of the undulator will rely on the magnetic calibrations of the individual undulators and energy loss measurements of the electron beam as was done for commissioning of LCLS-I.

The proposed future monochromator will also function as a spectrometer in the energy range of 200 eV to 1.3 keV. The spectrum of the spontaneous emission can be measured by using the SXR monochromator operated in the spectrometer mode, whereby the exit slit is replaced by an YAG:Ce screen coupled with an optical camera and two-dimensional spectrographs can be captured. Since no lasing is expected from a single undulator, the spectrograph should be stable,

and time-integration can be taken to enhance the signal-to-noise ratio for better K -value extraction. With this spectrometer no scanning of the electron energy is needed.

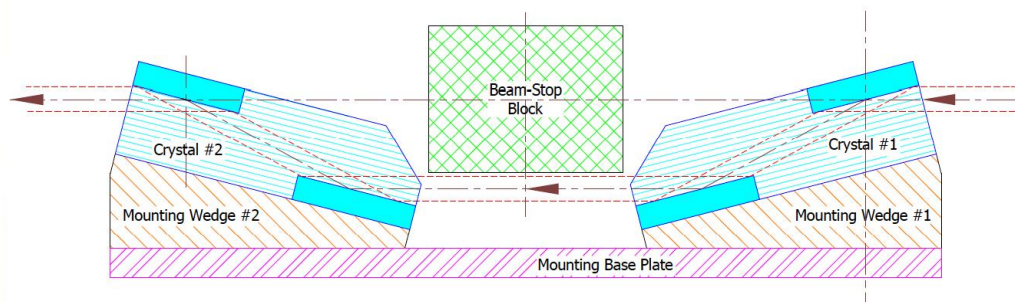


Figure 30. Schematics of the hard X-ray K-mono system, consisting of 4-bounce Si (111) single-crystal monochromator operating at a constant energy of 8172 eV. The spontaneous emission spectrum of an individual undulator is measured by scanning the electron energy.

Hard X-Ray Undulator Tuning

For the hard X-ray undulator line in the energy range from 1 to 25 keV, the same K -mono system shown in Figure 30, developed for the LCLS-I undulators, will be used. The LCLS-I K -mono system uses a 4-bounce Si (111) single crystal monochromator operated for a fixed energy at 8172 eV, with an angular acceptance of 32 μ rad, matching the Darwin width of the Bragg reflection, which is equivalent to 1.2 eV. By varying the electron energy, the spectrum shown in Figure 29 can be traced out, and the relative K value of the undulator can be extracted. The absolute gap could be reset based on the K -mono measurements and gap magnetic field calibration curves measured before installation for each undulator, so the minimum requirement is a fixed energy K -mono.

11.7.2 Pulse Length Considerations

11.7.2.1 Pulse length stretching

When using monochromators, the temporal structure of the pulses will be modified depending on the band pass. Because of the uncertainty principle, or Fourier theory, if the band pass (resolving power) of the monochromator is smaller than roughly the inverse of the length of the input pulse, the length of the exit pulse will be stretched. For a given resolving power and shape of the pulse, such as Gaussian or flat-top, the transform-limited pulse length is plotted in Figure 31. This effect should be carefully considered for time-resolved spectroscopic studies using monochromatic FEL beams.

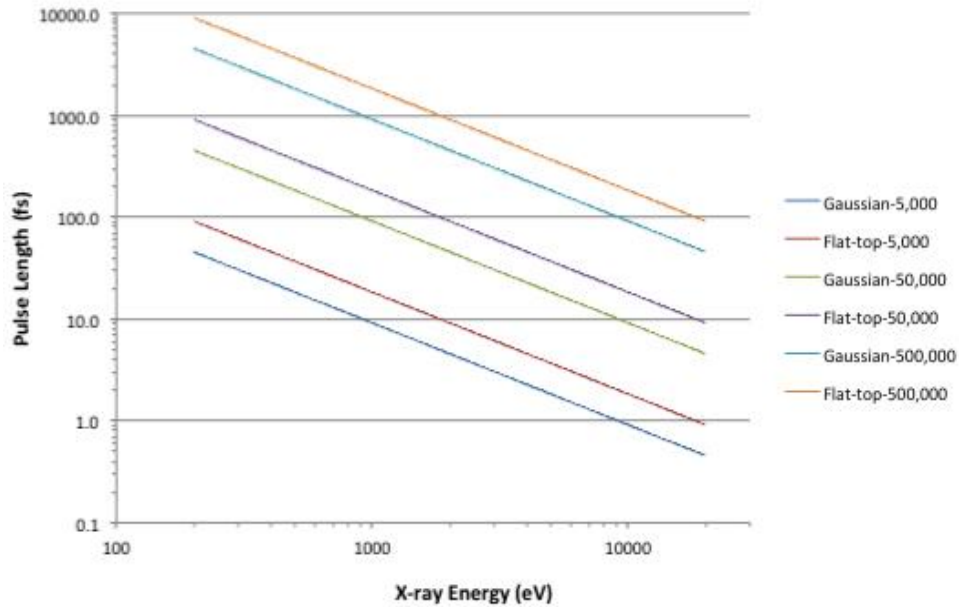


Figure 31. The transform-limited pulse length for a given resolving power of 5,000, 50,000, and 500,000 for Gaussian and flat-top shaped pulses as a function of X-ray energy.

11.7.2.2 Pulse Front Tilt

Pulse front tilt arises if the monochromitization is based on wavefront division, such as gratings. This effect is illustrated in Figure 32, where the grating will introduce a wavefront tilt by requiring one side of the pulse front to advance more than the opposite side by an amount equaling to the wavelength multiplied by the resolving power. The shape of the pulse front is transformed from an originally flat shape to a tilted one, both in the front and in the back, doubling the total length by a factor of two but having the same FWHM beam size as the incident beam. For a monochromator based on amplitude division, such as single-crystals operating in symmetric reflection geometry, no pulse front tilt is present.

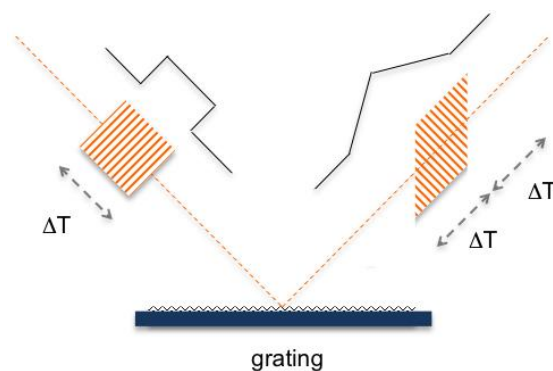


Figure 32. Illustration of pulse front tilt introduced by a wavefront division-based monochromator system (grating). One side of the pulse front must advance more than the other side by an amount equaling to the wavelength multiplied by the resolving power, transforming the original parallel pulse front to a tilted shape, and doubling the total length by a factor of two but with the same FWHM.

11.8 X-ray Diagnostics

The diagnostics described include both those required for science at start up of LCLS-II and are in the base line scope, and those that are to enhance future experimental capabilities, but are not in the base line scope and need to have space allocated. Those that are not in the base line scope are clearly indicated.

11.8.1 Diagnostics for X-ray Tuning

Each photon line has several meters of diagnostics for characterizing and tuning the accelerator/FEL downstream of each undulator, following the separation of the electrons and photons into separate beam lines. Diagnostic devices should include an imaging screen to monitor transverse profile and position, filters to block CSR/bend radiation in the visible spectrum, multi-purpose manipulators for attenuator and edge filter materials, a pulse energy monitor. Most diagnostics are invasive and will likely require reduced beam rate in the undulator to avoid damage.

11.8.2 X-ray Diagnostics Chamber

After each undulator, the spent electron beam is diverted off-axis to a dump line while the X-rays travel straight ahead. Immediately following the separation of the electrons and photons into separate beamlines, X-ray lines have several meters of diagnostics in a long multi-port chamber (essentially a series of ten 4.5" vacuum crosses) set off by vacuum-limiting apertures at either end. There are isolation vacuum valves at either end of the diagnostics section, ion pumps distributed throughout, and a tie-in for local turbo cart vent/pump down. Isolating this volume as much as possible is key to the rapid turn-around of diagnostic devices in the chamber. To minimize internal reflections, the interior of the chamber should not be electro-polished.

11.8.2.1 CSR filters

Broad spectrum bend radiation/CSR from the dump bends immediately upstream will travel along with the X-rays and can swamp imaging diagnostics and light-based detectors (such as PMT-based gas detectors) with visible light. The primary mitigation is the use soft bend magnets just upstream of the main bend magnet to the electron dumps. This minimize the generation CSR. Thin film low-Z material, opaque in the visible spectrum, such as beryllium or carbon (graphite), is suitable for the high-energy FEL, but will significantly attenuate the primary soft X-rays and cause some non-ideal wavefront distortion. The upstream end of each diagnostics section will have two blocking filter actuators for use with the XDC diagnostics or at experimenters request. These filter can be withdrawn for experimental operations that require the best wavefront preservation.

11.8.2.2 Multi-purpose insertion manipulators

There will be several easily reconfigurable manipulators with the capacity to hold a large array of sample materials for use as attenuators and absorption edge filters, as well as materials qualification and testing (for example, scintillator options for soft X-rays). Fixed-angled optical mirrors in adjacent ports will allow observation of either front or back surfaces of exposed samples.

11.8.3 Intensity Monitors

Pulse energy measurement of the FEL beam is an important parameter, which is required for tuning the machine during commissioning and for efficiently changing operating modes. Additionally, during operation basically all user experiments depend on the measurement of the pulse energy, especially for experiments that require normalization of the incoming beam intensity. The requirements for the energy monitors are given in Table 6.

Table 6. Intensity Monitor Requirements.

Parameter	SXR	HXR
Energy	200-1250eV	1-25keV
Repetition rate	1MHz to avg.	1MHz to avg.
Energy per-pulse - relative	0.1%,	0.1%,
Energy per-pulse - absolute	10%	10%

Due to the SASE process, each pulse varies and its pulse energy can differ significantly. Therefore it is necessary to have pulse-resolved energy diagnostics, which are non-beam-intercepting, allowing experiments to operate in parallel. We plan to use gas-based energy monitors, which provide an absolute measure and can also be operated in pulse resolved mode.

On the SXR beamline the gas monitor we are planning to use is based on a PTB/DESY design [14] and one has already been installed permanently and operated at the LCLS-I SXR beamline in the soft X-ray range (280-2000eV). The gas monitor detector (GMD) consists of (1) a rare-gas-filled chamber at low pressures which is ionized by the incoming FEL beam (Figure 33) and (2) the charge detection of ions and electrons by Faraday cups, to provide an average and absolute value which has been cross calibrated to a primary standard at a synchrotron. A slit in the Faraday cups allows a fraction of the ions and electrons to pass through into an open multiplier to allow sufficient sensitivity to be operated into the hard X-ray regime, where the photoionization cross sections are orders of magnitude lower than in the soft X-ray spectral range. Additionally, the open multipliers provide pulse resolved measurements that can be cross calibrated to the absolute average signal.

The energy range easily covers the lower end of the soft X-ray range (250eV, less if necessary) and has been successfully operated up to 2000eV. For operation in the hard X-ray regime up to 25keV, a modified version of the detector needs to be employed that has more sensitive multipliers and employs multiple extraction stages to increase the collection efficiency of the ions and electrons along with a high voltage compatible extraction design. This modified type is already being developed for the European XFEL.

A beam repetition rate of up to 1 MHz is compatible with this design, as the current multipliers are fast enough that the entire charge per pulse can be extracted within the time interval of 1 μ s, so that a distinct separation of the TOF spectra is guaranteed. A calibration mode

which requires a short period of slower extraction times and lower extraction voltages can be performed at a lower beam rate briefly in the beginning of a given experiment.

The detector requires a separate gas inlet system to provide a minimum of two different rare gases in order to span the entire photon energy range and avoid operation at any absorption edges of one particular gas. Integration in the beamline vacuum system requires a differential pumping system to decouple the gas cell from the rest of the beamline vacuum, which also allows one to safely vary the gas pressure to optimize signal levels for a particular spectral range. To ensure the specified accuracy of the absolute and relative measurements, a highly accurate pressure measurement device, i.e. a spinning rotor gauge, needs to be employed in connection with a temperature measurement and stable high voltage supplies.

We plan to position the gas monitors up- and downstream of the attenuator systems in the soft and hard X-ray beam line branches in order to measure the incoming beam intensity and also to monitor the influence of the attenuator system and other beam intercepting elements.

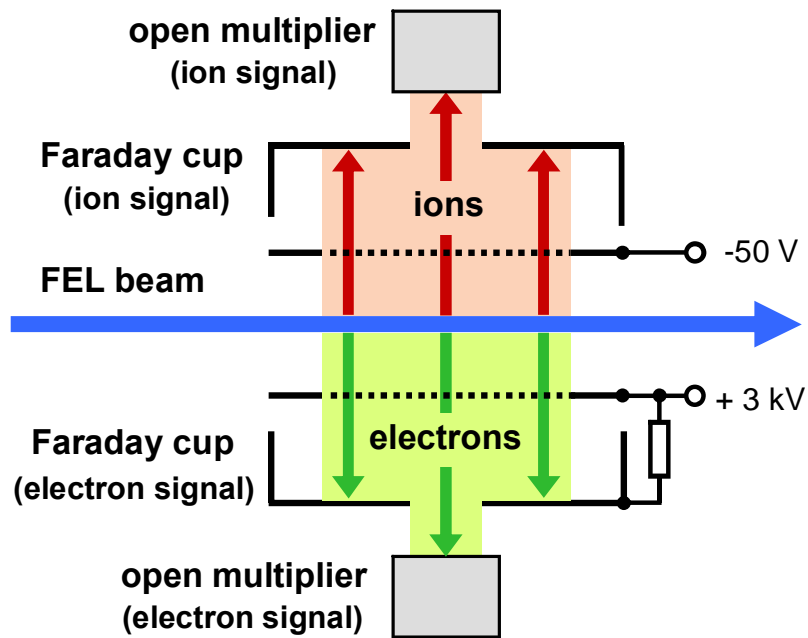


Figure 33. Schematics of the Gas Monitor Detector (GMD) operated at SXR at LCLS-I [14].

On the HXR beam line the existing gas energy monitors will be used. The Gas Detector system [15] has proven reliable over the energy range from below 1 keV to over 8 keV. For higher energies the LUSI Single-Shot Intensity-Position Monitor [16] is a proven system and it is shown schematically in Figure 34. It can operate over the range of 4 up to 25 keV.

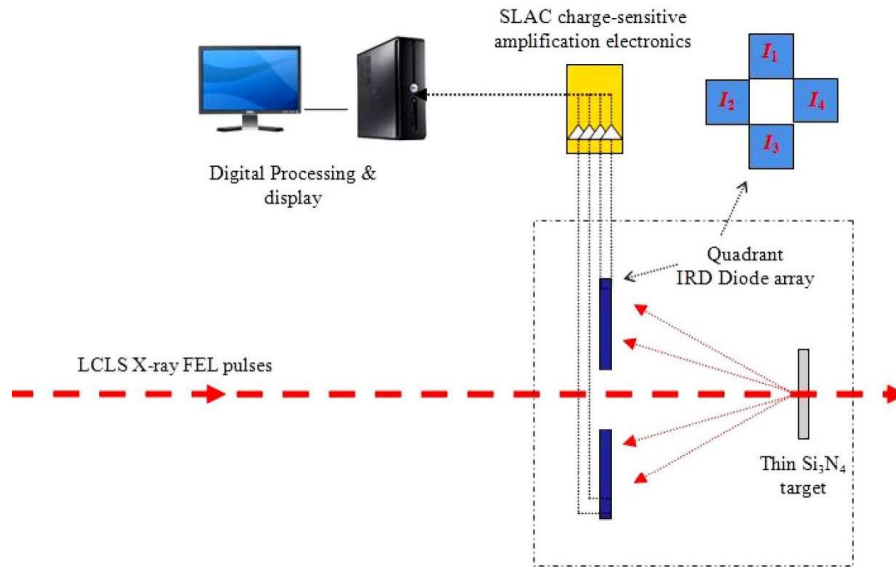


Figure 34. LUSI hard X-ray single-shot Intensity-Position Monitor (IPM), consisting of a thin scattering target, a quadrant diode array arranged in horizontal and vertical pairs positioned upstream of the target to detect back-scattered X-rays, and an electronics assembly [16].

The LCLS Gas Detector system will have its PMT and electronics up graded to operate at very high repetition rates, at or above 1 MHz. Though the Single-Shot Intensity-Position Monitor is capable of operating up to ~100kHz, it will be used only with the Cu linac 120 Hz and needs no upgrades to electronic or for power load on scatter.

11.8.3.1 Attenuators

There are experimental needs when the FEL intensity must be attenuated. The attenuator must be able to not only sustain the (single-shot) peak fluence of the FEL, but also to handle the average thermal loading. The attenuator design must minimize to the extent possible the wavefront distortion and degradation of the transverse coherence of the FEL beam. The attenuator must provide a factor of up to 10^3 attenuation, with a granularity of at least three per decade. The absorbing medium must be void of strong absorption edges in the operating energy range.

Attenuator System for the Soft X-ray Undulator

For the soft X-ray undulator line in the energy range from 200 eV to 1.3 keV at a repetition rate up to 1 MHz, only a gas-based attenuator system will be able to sustain the peak fluence of the FEL beam, such as the that shown in Figure 35. The system consists of a gas volume, a gas handling system, and differential pumping stages on both sides of the gas volume with both fixed and variable apertures. This design is conceptually similar to the one currently installed at LCLS-I. The use of variable apertures stems from the need to use different gas pressure for different X-ray energies while maintaining the same pumping speed. The size of the apertures must be larger than the stay-clear clearance of the FEL beam.

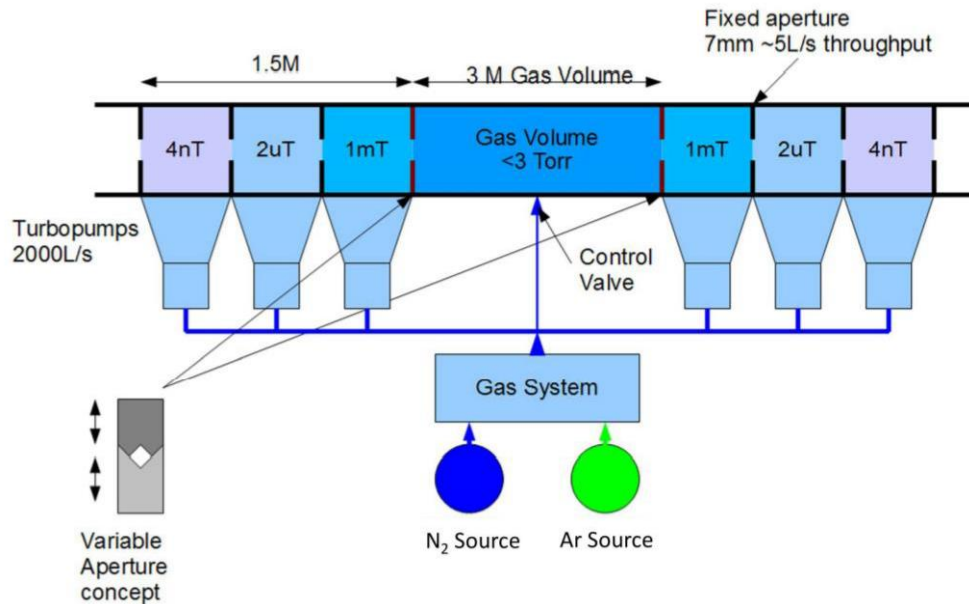


Figure 35. Conceptual design of a variable aperture differential pumps and gas attenuator system.

Attenuator System for the Hard X-ray Undulator

For the hard X-ray undulator line in the energy range from 1 to 5 keV at a repetition rate up to 1 MHz, and from 1 to 25 keV at a repetition rate up to 120 Hz, a combination of gas based and solid based attenuators will be used, with the solid attenuator being downstream of the gas one to sufficiently attenuate FEL beam intensity to below the single-shot damage threshold for the solid material. For X-ray energies below 2 keV, the gas system currently installed on LCLS-I will be reused. In principle, this system is very similar to that shown in Figure 35, but does not use variable apertures and operates with N_2 gas, and is only 4 m long.

For x-ray photon energies above 2 keV, the LCLS-I gas attenuator becomes ineffective without using very high vapor pressure and high-Z gases, which presents challenges to pumping. Moreover, the small angle scattering arising from the density fluctuations may become significant, thus rendering it less desirable, for user experiments aimed at utilizing the excellent coherence properties of the FEL beam. As such, solid attenuators consisting of beryllium foils of varying thicknesses were conceived and used for LCLS-I because of its high single-shot damage threshold. However, it has been found that although the type of beryllium used was of the best optical grade, the residual density non-uniformity has led to speckle patterns that were completely unacceptable to many user experiments. A similar design for the LUSI instruments using single crystal silicon proved to perform much better in minimizing wavefront degradation as well as small angle scatterings. Therefore, the LCLS-II solid attenuator systems will be based on single crystal planar samples, such as silicon and diamond.

11.8.3.2 Beam Imagers

Imaging of the FEL radiation was proven to be extremely valuable in helping diagnose and optimize the LCLS-I lasing process as well as the alignment of various optical elements in the

front-end enclosure. The LCLS-I direct imagers were based on optical imaging of an X-ray scintillation material impinged on by the FEL beam. For LCLS-II, the same design principle will be used. The beam imagers should have sufficient field-of-view (FOV) to capture the entire FEL transverse profile; sufficient resolution for accurate size measurement to within 5 percent of the FWHM, for potentially performing statistical analysis on the FEL transverse coherence. The goal is to be capable of isolating a single-shot at 1 MHz repetition rate. Due to the need for using a solid scintillator, the operation of the beam imager may require attenuation to the incident FEL beam to avoid single-shot damage and cooling of the scintillator at higher repetition rate.

Single crystal Cerium-doped Yttrium Aluminum Garnet (YAG:Ce) is used as the X-ray scintillator, which has been shown to exhibit characteristics suitable for imaging high brightness light sources such as the X-ray FEL. It has a very high melting temperature, high thermal conductivity, and is capable of sustaining unfocused FEL beam at normal incidence with only moderate attenuation. It is a fast scintillator with a maximum luminescence yield at 550 nm, which matches well with the quantum efficiency curve of a typical optical pixelated camera. Its scintillation image is not diffuse as with phosphor materials; as a result, very high spatial resolution can be achieved and is only limited by the numerical aperture of the lens and/or the pixilation of the camera. A similar imaging system used on the LCLS-I X-Ray Pump/Probe (XPP) instrument was demonstrated to have achieved 2 μm resolutions in user experiments. The YAG:Ce screen is positioned with its surface normal parallel to the FEL beam for obtaining high resolution, and its typical thickness of about 20 μm is also optimized for high resolution and sufficient fluorescence yield.

The single-shot damage calculation for the YAG:Ce screen is shown in Figure 36, where the energy dose per atom is calculated at its designed location of approximately 90 m from the source point at 2 mJ/pulse. The divergence of the beam is based on simulations of the LCLS-II soft and hard X-ray undulators. A factor of five attenuation would provide sufficient safety margin to reduce the dose to below 100 meV/atom to minimize potential single-shot damage as well as thermal fatigue from prolonged exposure.

Soft X-Ray Beam Imagers

The need for cooling in this LCLS-II design stems from the fact that the energy of the FEL beam is absorbed entirely by the YAG:Ce screen due to the very short attenuation length (of order 1 μm or shorter) in this energy range. When operating at very high repetition rate, the deposited thermal energy must be removed continuously. Even though the YAG single crystal has relatively good thermal conductivity, edge cooling may not be efficient enough for high repetition rate; instead, a back-plate scheme will be considered, where the back surface of the thin YAG:Ce screen (10 μm thick if feasible) will be coated with a thin gallium-indium eutectic layer, which then makes contact with the cooling plate to promote thermal conduction, as shown in Figure 37.

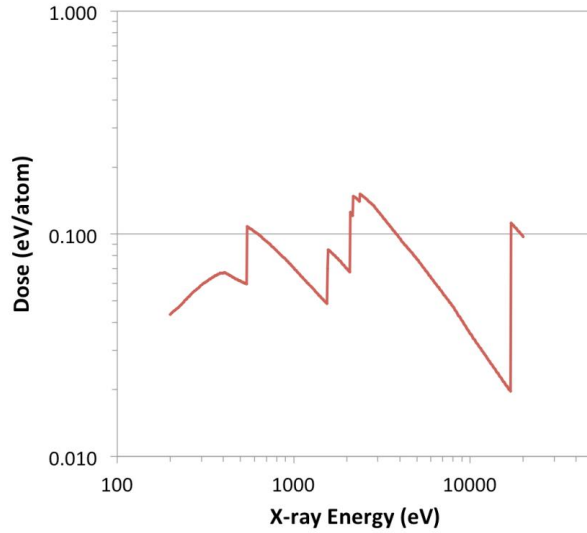


Figure 36. Single-shot dose in the YAG:Ce screen at its designed location of about 90 m from the source point at 2 mJ/pulse. The divergence of the beam is based on simulations of the LCLS-II soft and hard X-ray undulators. A factor of five attenuation would provide sufficient safety margin from single-shot damages.

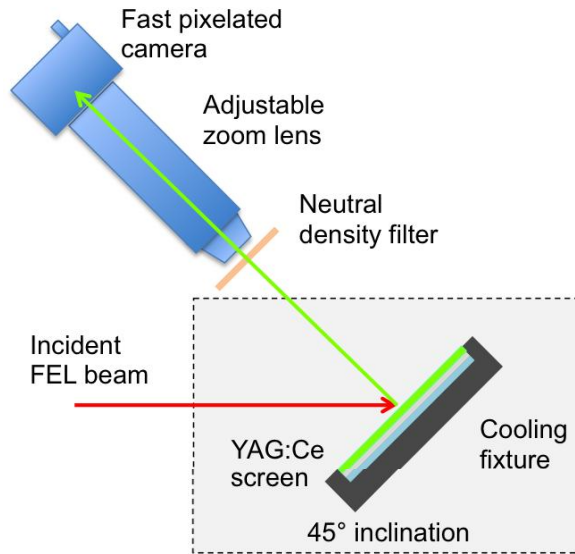


Figure 37. Schematics of the conceptual design of the high repetition rate beam imager consisting of a YAG:Ce screen for X-ray scintillation inclined at 45° with respect to the incident FEL beam, which is cooled to enable high-repetition-rate operation of up to 1 MHz. The axis of the optical imaging system is parallel to the YAG:Ce surface normal.

The optical imaging assembly include a neutral density filter, an adjustable zoom lens, and a fast pixelated camera. The optical axis is aligned parallel to the surface normal of the YAG:Ce screen to ensure the entire image stays in focus. Because of the very short attenuation length in this energy range, the YAG:Ce is entirely a surface emitter and leads to minimal degradation to the spatial resolution, even at the 45 degree inclination with respect to the incident beam direction. The adjustable zoom lens (more than 10x) is used to reduce the FOV when measuring smaller beam profile at higher energies. An optical pixelated camera will be used that has more

than 1 megapixels and 10 bit grey-levels and is capable of gating at $10\mu\text{s}$ for single-shot measurement. At higher repetition rate, the camera will operate only averaging mode, so a manageable number of two-dimensional image frames can be downloaded within a certain time period, or in an on-demand mode that single-shot frames are sparsely triggered for capturing.

Hard X-Ray Beam Imagers

Two types of imagers will be considered for the hard X-ray undulator line in the energy range from 1 to 5 keV at a repetition rate up to 1 MHz, and 1 to 25 keV at a repetition rate of 120 Hz, respectively. For the high repetition rate operation, the design shown in Figure 37 will be used. Since the attenuation length is somewhat larger in this energy range ($8.5\ \mu\text{m}$ at 5 keV), the scintillator is becoming a volume emitter, resulting in loss in spatial resolution due to the 45 degree inclination angle. As such, the inclination direction should be chosen to be in the vertical direction, in which the beam profile is Gaussian-like and not subject to distortion and perturbation by optical surfaces, such as mirrors in the horizontal direction. For the low repetition rate operation at 120 Hz, no cooling is required and a different design should be used, as shown in Figure 38.

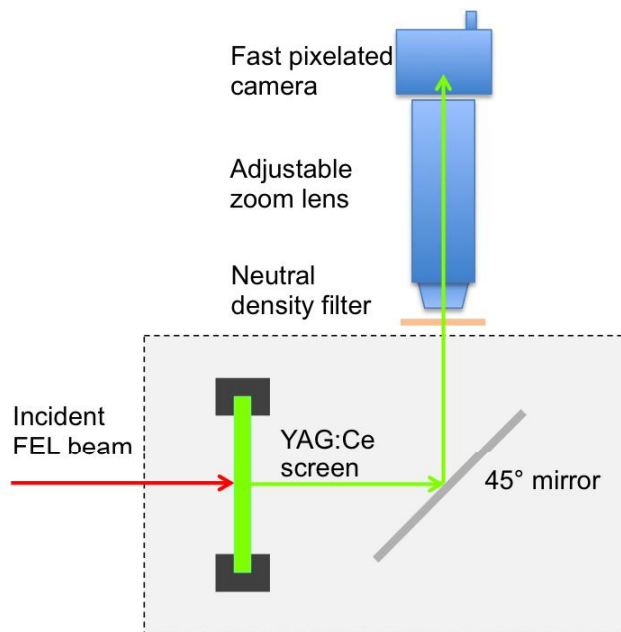


Figure 38. Schematics of the conceptual design of the hard X-ray beam imager consisting of a YAG:Ce screen for X-ray scintillation oriented normal to the incident FEL beam, The axis of the optical imaging system is parallel to the YAG:Ce surface normal via the 45° mirror.

11.8.4 Wave Front Sensors

For optimal performance quantitative analysis of the data obtained in LCLS experiments depends on the knowledge of the intensity distribution of the beam at the sample. The intensity distribution of the LCLS X-ray beam at the sample depends on operating conditions of the FEL, the quality of the optics, and their alignment. It is also subject to long term drifts due to alignment

and changing optical properties and shot-to-shot variations due to the chaotic nature of the process that generates the X-rays in the FEL. Therefore shot-to-shot wavefront (WF) measurements would greatly enhance the quality and scope of the class of LCLS experiments in which the wave front is only minimally perturbed by the sample and which rely on knowledge of the field strength and its distribution across illuminated samples. The wavefront sensors are not required for initial operations of LCLS-II and therefore are not in the base line plans. Space is laid out for install them at several locations along the beam lines.

Hartmann type wavefront sensors are standard instruments that have already been applied in the X-ray regime for the optics characterization and alignment purposes [17,18]. (See Figure 39.) The commercially available X-ray sensor HASO™ X-EUV from Imagine Optics provides the accuracy of $\lambda/50$ in the soft XUV range, 25-7 nm (50-180eV), and $\lambda/5$ in the X-ray range , 1-0.25 nm 91250-5000eV0. The precision of $\lambda/5$ rms error is inadequate for the LCLS purposes, as it corresponds to a 500 percent error in the measurement of maximum intensity provided by the focusing optics.

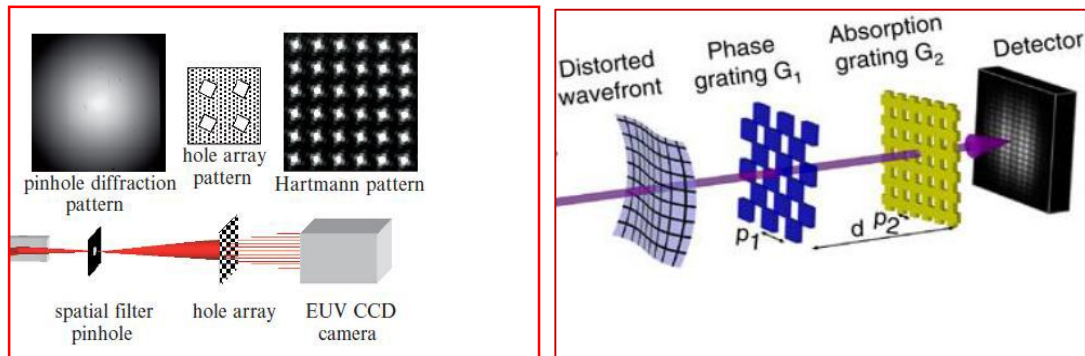


Figure 39. Principles of operation of the Hartmann sensor and the shearing interferometry sensor.

According to an Imagine Optics statement [19], however, there is a possibility to optimize the sensor further for the shorter wavelength range. The LCLS team is working with Imagine Optics and the French group from Laboratoire d'Optique Appliquée (LOA) (which initially developed the WF sensor that was later commercialized by Imagine Optics) on the optimal design for the photon energy range 250 eV- 2500 eV (5nm – 0.5 nm) to achieve the resolution better than $\lambda/15$. The initial experiment performed at the AMO station has shown that the Imagine Optics type sensor is sensitive enough to correct the coma aberration of the K-B optics (see Figure 40). The coma aberration has developed because of carbon deposition on the focusing optics.

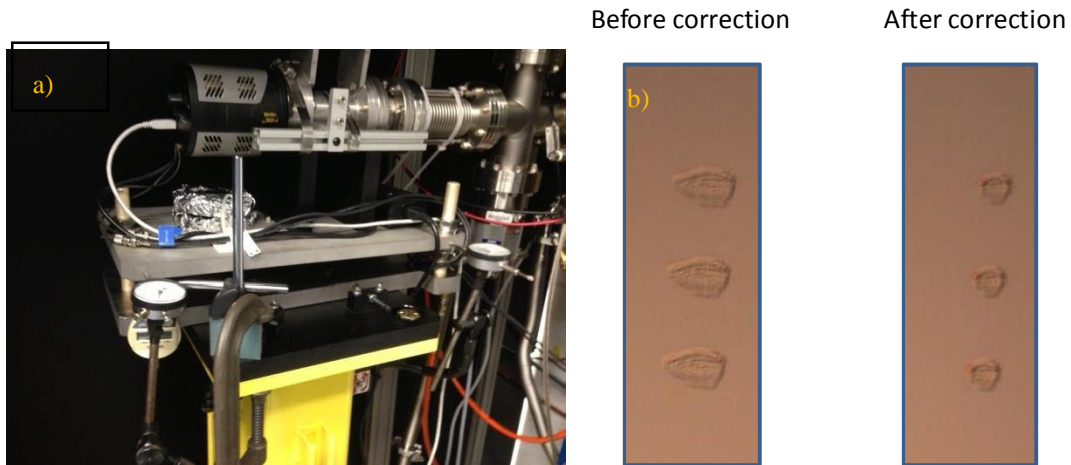


Figure 40. a) Hartmann WF sensor mounted at the AMO station and b) the imprints of focused beam a in a solid sample showing the improved beam shape after the asymmetric bending of K-B mirrors in such a way that it minimized the third order aberration measured by the Hartmann sensor.

A similar effort is needed to improve sensitivity of the Hartmann sensor developed for the hard X-ray regime. The hard X-ray Hartmann sensor developed at SOLEIL has the sensitivity of about 0.02 nm ($\lambda/10$ at 0.2 nm wavelength) [20]. According to Imagine Optics, the sensor could be optimized to achieve accuracy of 1/50 at 0.1nm wavelength [21].

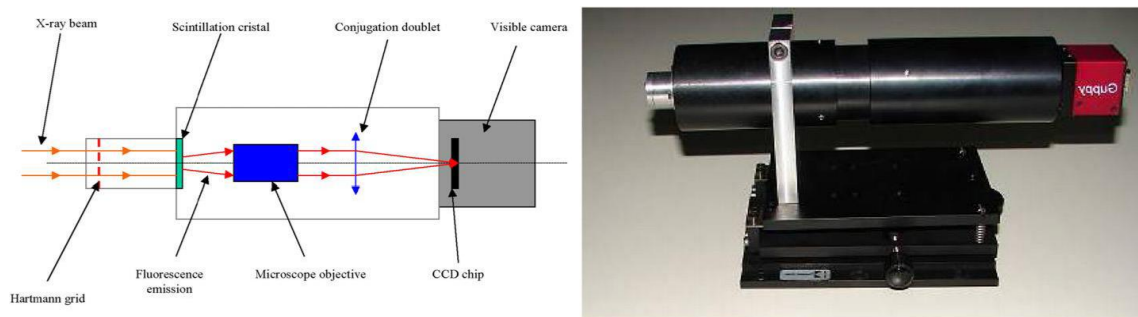


Figure 41. Hard X-ray Hartmann sensor developed at SOLEIL.

The second technique that can be applied is the shearing interferometry WF sensor (Figure 39), a technique successfully tested and applied in the soft [22] as well as in the hard X-ray regime [23]. However, this technique has never been used as a standard diagnostic in an experimental station, and a dedicated effort is needed to solve the practical aspects.

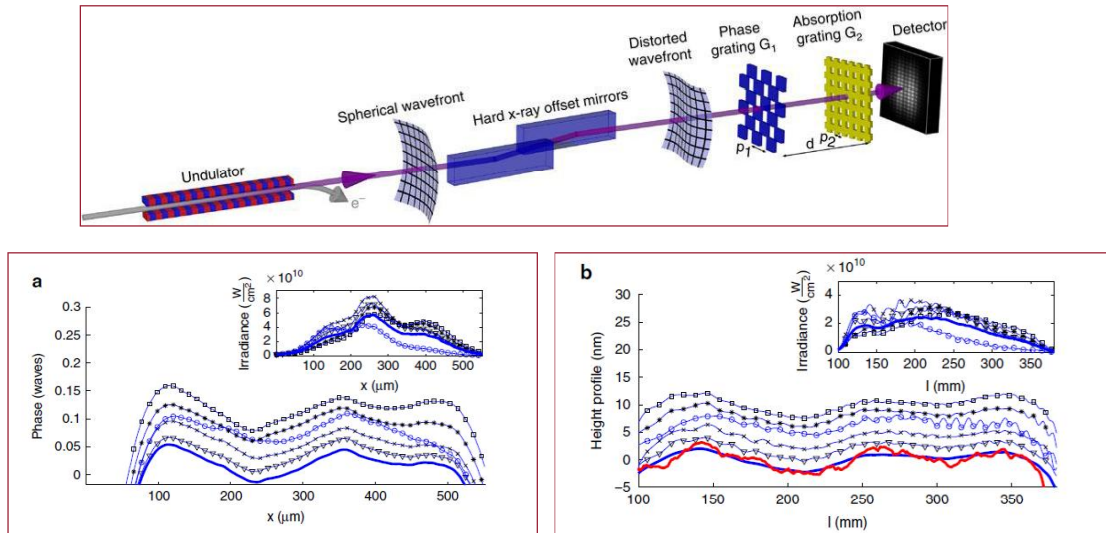


Figure 42. Results of first experiment at 9 keV photon energy performed at the LCLS [6] using a shearing interferometry wavefront sensor. a) A single shot WF measurement result demonstrates accuracy better than $\lambda/40$; and b) reconstructed mirror height profiles where the red curve is the profile measured at the Lawrence Livermore National Laboratory.

In summary, the technology for the WF sensor exists. However, a modest R&D effort is necessary to tailor sensor parameters according to LCLS-II needs.

11.8.5 In-line Spectrometer

The LCLS-II SASE FEL is believed to exhibit pulse-to-pulse temporal and spectral fluctuations in much the same way as the LCLS-I SASE FEL. The temporal fluctuations include jitter in the length of the pulse as well as the temporal profile, which consists of many intensity spikes of varying degrees of width and magnitude. However, the temporal profile has been proven to be extremely difficult to measure, especially for hard x-rays, except for some very coarse measurements of the pulse length. Complimentary measurement can be carried out much more easily in the spectral domain, and spectral diagnostics can be devised to measure the FEL spectrum. For in-line monitoring, the spectrometers should be highly transmissive (greater than 90 percent transmission, if feasible), produce minimal wavefront distortion, and be capable of single-shot measurement at 1 MHz repetition rate, if required. In-line spectrometers are not required for initial operations of LCLS-II and therefore are not in the base line plans.

11.8.5.1 Soft X-Ray Beam Spectrometer

A shot by shot SXR spectrometer is not part of the base line scope. For future only a gas-based diagnostic device, such as shown in Figure 43, should be considered because of the requirement on beam transmissivity. The operating concept will be based on analyzing the kinetic energy distribution of the primary photoelectrons from a gas target excited non-resonantly by the LCLS FEL beam. When the LCLS-II soft X-ray FEL beam impinges on a volume of gas atoms, it ejects photoelectrons with kinetic energies whose distribution is analyzed by a hemispherical analyzer developed for X-ray photoemission spectroscopy. Since the kinetic energy of the

photoelectrons is directly related to the incident photon energy of any given species (e.g. neon *L*-shell electrons). The spectral distribution of the input X-ray beam is thus imprinted onto the electrons' kinetic energies, which are then dispersed and encoded simply as positions on the imaging plane of the analyzer, creating a two-dimensional spectrograph for the FEL.

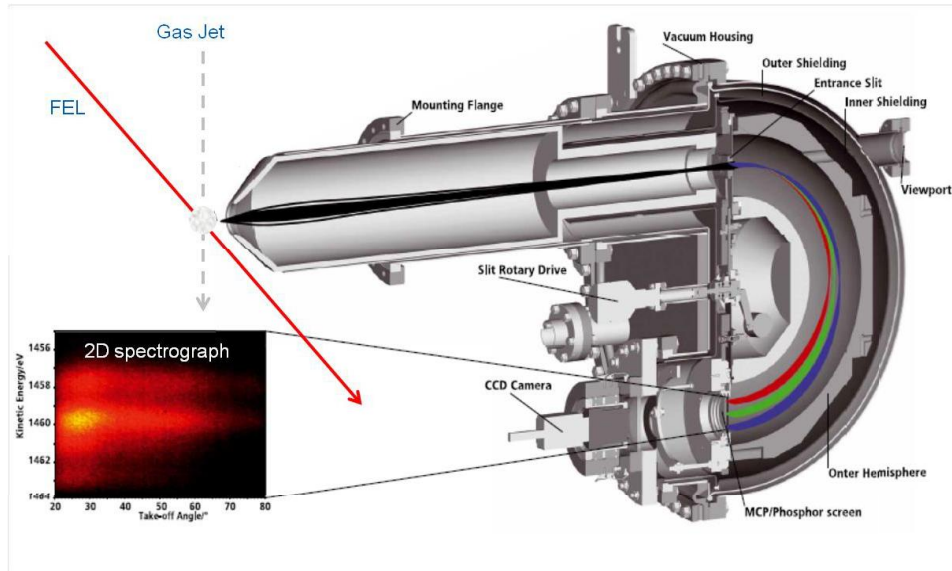


Figure 43. Schematics of the operating principle of the soft X-ray in-line spectrometer. The kinetic energy of photoelectrons excited in a gas volume by the FEL is analyzed by a hemispherical analyzer, mapping the spectral distribution of the incident X-rays and creating a single-shot soft X-ray spectrograph.

The spectral range should be greater than 1 percent, sufficient to capture the full SASE FEL spectrum. The spectral resolution is determined by the lifetime of the electrons in a particular shell (broadening due to space-charge effect and electron optics of the hemispherical analyzer) and the spatial resolution of the electron imaging assembly, including the multi-channel plate (MCP)/electron scintillation screen and pixelated camera. It is expected that 0.1 eV resolution can be achieved for 1 keV X-rays using He gas, i.e., amounting to a resolving power of 10,000. Because of the dilute nature of the sample volume, the transmission of the spectrometer will always be greater than 99 percent. Moreover, any wavefront distortion would be minimal compared to the diagnostics employing solid samples.

To enable high repetition rate operation, an 1D array detector capable of high frame rate (up to 1 MHz) will be used for single-shot measurements. At higher repetition rate, the camera will operate only in the burst mode, so a manageable number of two-dimensional image frames can be downloaded within a certain time period or in an on-demand mode that single-shot frames are sparsely triggered for capturing.

11.8.5.2 Hard X-ray In-line Spectrometer

For the hard X-ray undulator line in the energy range two types of spectrometers will be considered. For X-ray energies from 1 to 5 keV, regardless of the repetition rate, the gas-based

spectrometer depicted in Figure 43 should be used and modified to account for higher kinetic energies of the photoelectrons.

For X-ray energies between 5 and 25 keV and at a repetition rate of 120 Hz, a crystal-based analyzer, shown in Figure 44, will be implemented, where an ultra-thin (10 to 20 μm) curved single crystal disperses a highly collimated polychromatic FEL beam onto a scintillator-based X-ray detector. The spectral range of this design can be as high as 1 percent, sufficient to capture the entire SASE FEL spectrum; spectral resolution as high as 100 meV has been demonstrated using a Si (333) reflection at 8 keV, amounting to a resolving power of 80,000. The transmissivity of the thin membrane is about 60 percent at 5 keV and approaches 99 percent at 20 keV.

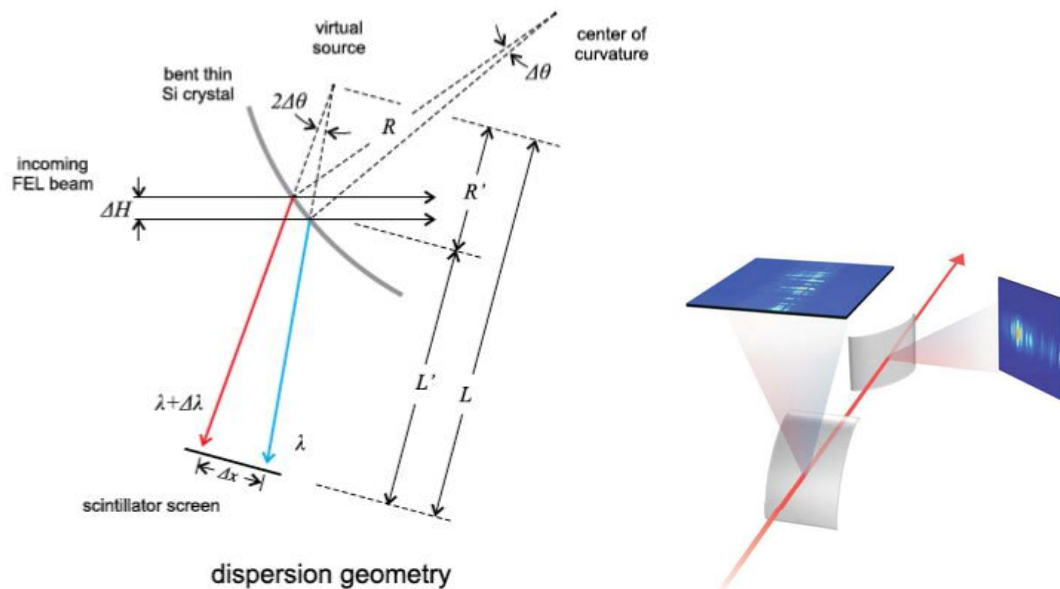


Figure 44. Schematics of the operating principle of the hard X-ray in-line spectrometer for energies from 5 to 25 keV. The cylindrically bent crystal membrane diffract dispersively a small percentage of the incident FEL beam to form a 2D spectrograph (shown on the right), which is recorded on a scintillator-based detector.

11.8.6 Arrival Time Monitors

The LCLS-II SASE FEL is believed to exhibit pulse-to-pulse arrival time jitter in much the same way as the LCLS-I SASE FEL. The arrival time jitter is of critical importance to pump-probe type of experiments, where the precise timing between the pump pulse and the probe pulse must be known or measured to properly analyze the experimental data. This timing information is also best measured at the interaction point (or at least as close as feasible), and various methods have been developed for both soft and hard X-rays using various cross-correlation techniques. As such, the arrival time monitors will be implemented on the instruments and not as part of the base line scope.

11.9 Photon Beamline Layouts

The requirement is to deliver SXR beam to one experimental stations in the NEH and HXR beam to four experimental systems, one in the NEH and three in FEH. The SXR undulator which covers the energy range from 200 to 1250 eV is on the north side of the LCLS tunnel. The HXR undulator, on the south side, can deliver high repetition-rate beam in the intermediate range, from 1 to 5 keV, from the SC linac and low repetition-rate beam, 1 to 25keV, from the Cu linac see Figure 45.

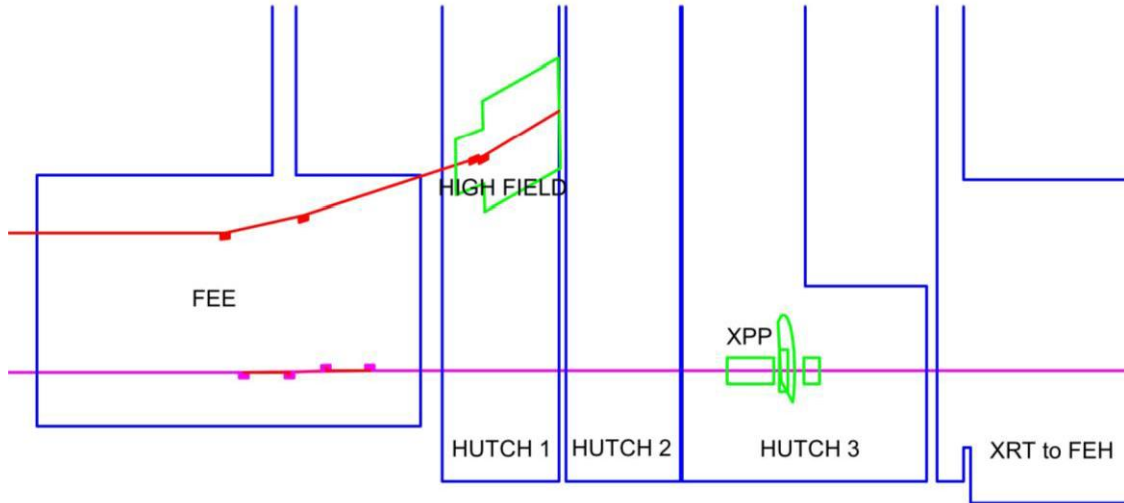


Figure 45. Proposed initial layout of the SXR and HXR beam lines in the FEE and NEH showing the principal optical elements and endstations. The SXR lines, in red, are on the north side of the tunnel, with the experimental stations in Hutche 1 of the NEH. The HXR line, in magenta, is on the south side of the tunnel with experimental stations in Hutch 3 and the FEH. (The Front End Enclosure (FEE) is ~35m along the beam direction and Hutches 1 & 2 are ~10m each. The vertical scale is five times the horizontal.)

11.9.1 SXR Beamline Configuration

The photon diagnostics start just downstream of the bending magnets that direct the electron beam into the dump. The baseline configuration for the SXR is shown in Figure 46.

A suite of movable experimental systems has been built by both LCLS and users groups that can be located at either of the two endstations, according to their individual capabilities and needs. See Chapter 12 for further discussion of the experimental program.

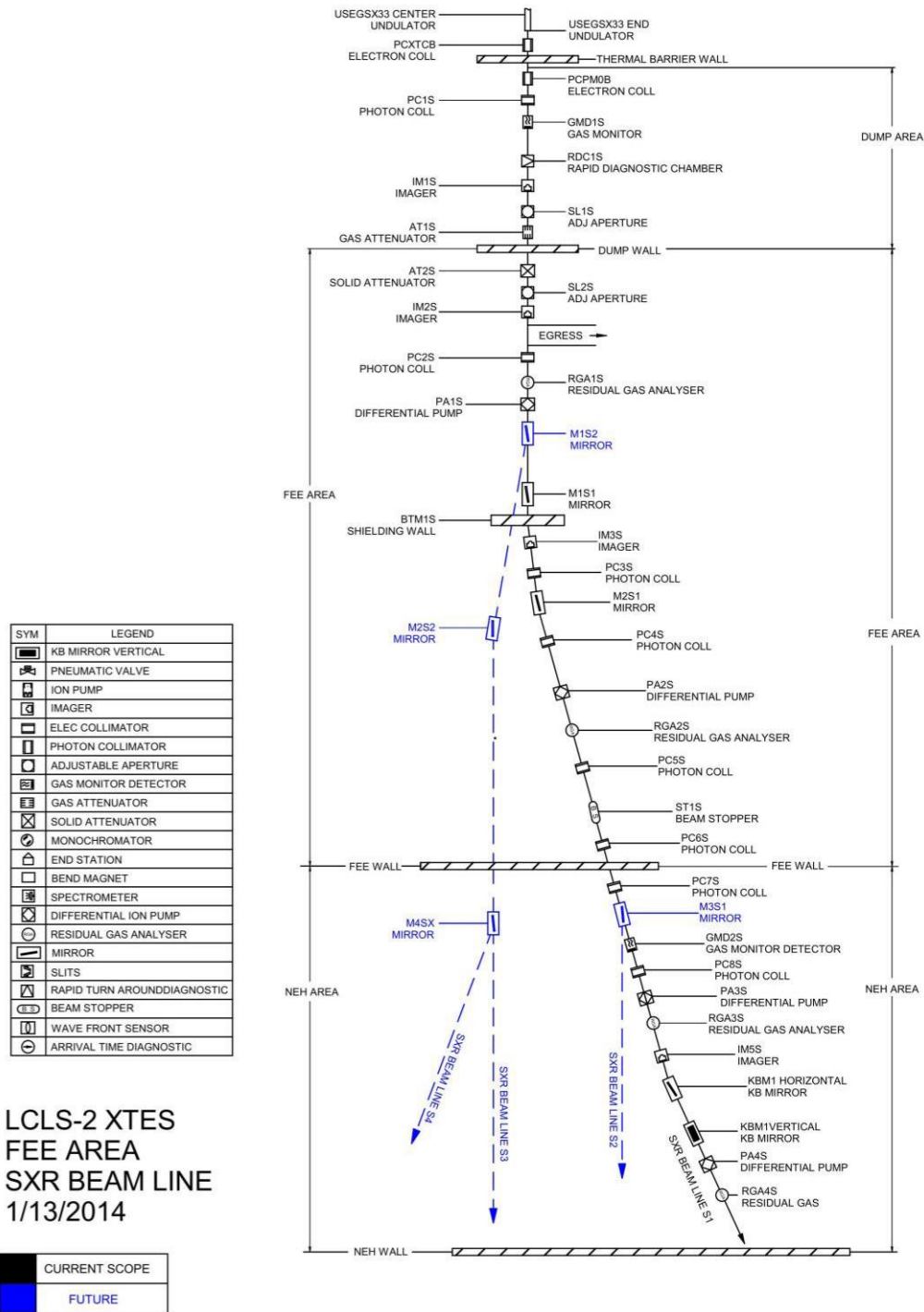


Figure 46. SXR XTES beamline schematic. Baseline scope shown in black. options for additional branchlines shown in blue. The beamline spans the Dump area downstream of the Undulator Hall through to Hutch 1 in the NEH.

11.9.2 HXR Beamline Configuration

The HXR line is designed to deliver both intermediate energy X-rays at high rep-rates, and hard x-rays up to 25keV at low repetition rates. The baseline configuration for the HXR is shown

in schematic in Figure 47. The FEL beam will be delivered to the four existing LCLS HXR experimental stations, XPP in Hutch3 of the NEH and XCS, CXI and MEC in the FEH.

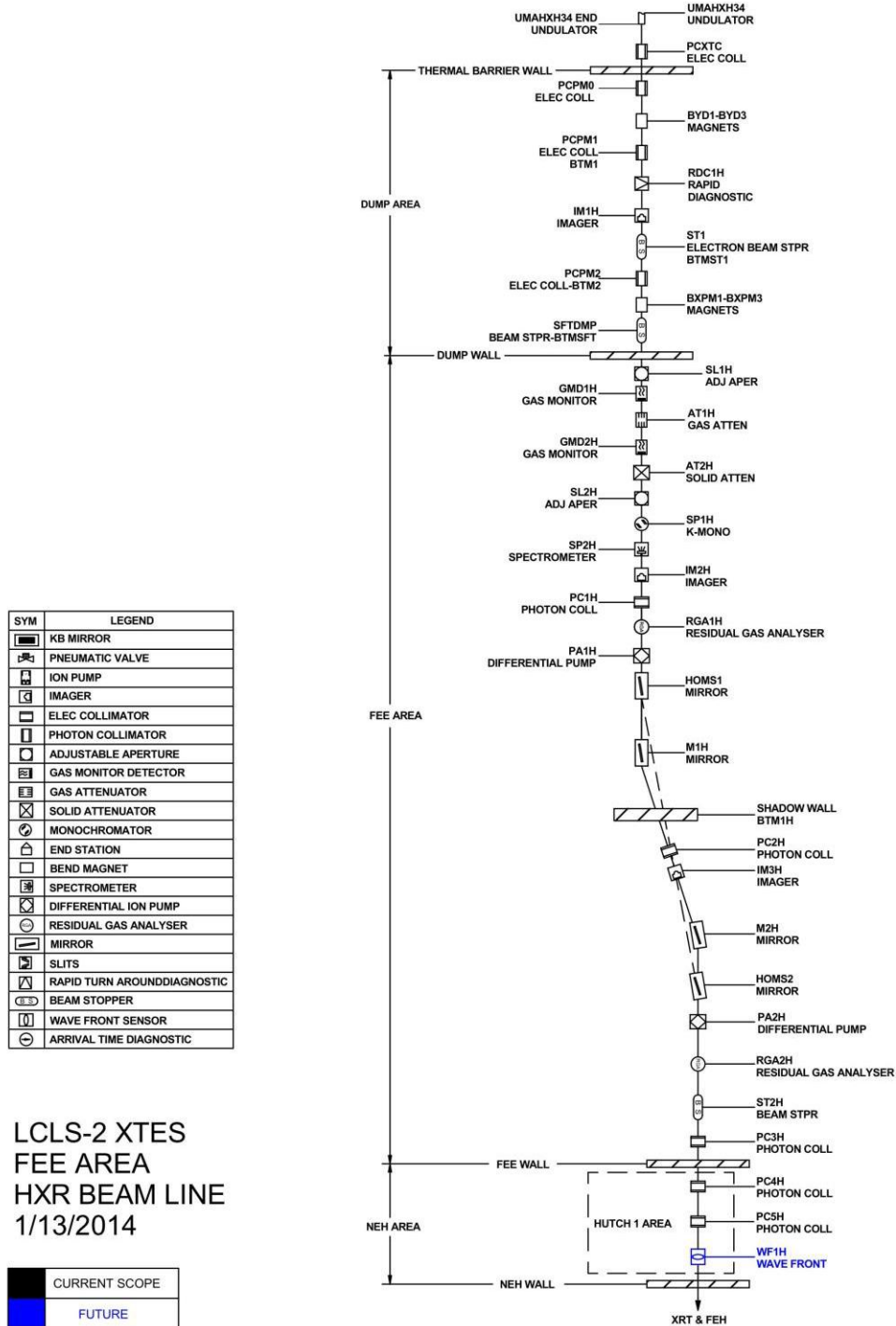


Figure 47. HXR XTES beamline schematic. Baseline scope shown in black. The beam path when using the existing HOMS mirrors is shown with a dashed line. The beamline schematic spans the Dump area downstream of the Undulator Hall through to Hutch 1 in the NEH. The beam is delivered to instruments in Hutch 3 of the NEH and the FEH.

Two pairs of mirrors will be used to handle this wide energy range: (1) the LCLS-I high-energy offset mirrors, HOMS, and (2) a new pair of mirrors that will cut off a little above 5keV and are designed to take the high repetition rate beam from the SC linac. A schematic of this configuration is shown in Figure 48.

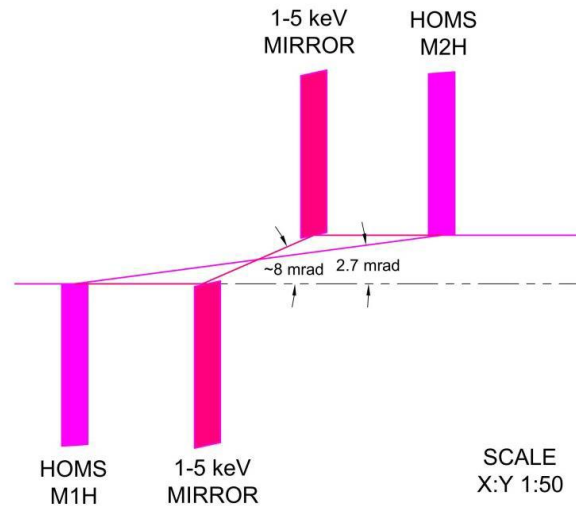


Figure 48. Schematic showing a pair of intermediate energy mirrors: a 1-5 keV mirror, to handle higher power, high-repetition rate operations, and optimized for these lower energies located between the existing HOMS mirrors.

The HXR line configuration starts at the same position as the SXR line at the photon diagnostics start, just downstream of the bending. The baseline configuration for the HXR is shown in

11.9.3 Transport Line/Experimental Area Alignment

The existing alignment network is sufficient to support the installation of the new transport line/experimental area components. (See Chapter 4, Section 7 for a description of the LCLS alignment system.) We expect that only a few monuments will have to be relocated in case new components blocks the line of sight. Fiducialization procedures for components developed for LCLS-I are fully adequate to be used for LCLS-II. X-ray mirrors shall have a port with an optical window to allow direct observation of the mirror surface once installed.

11.10 References

1. S. P. Hau-Riege et. al., Optics Express 18, 23933-23938 (2010).
2. S.P. Hau-Riege et. al., Appl. Phys. Lett. 95,11104 (2009).
3. B. Ziaja, et. al., High Energy Density Phys. 9 (2013) 462-472.
4. J. Gaudin, et. Al, Phys. Rev. B 88 (2013) 060101.
5. S.P. Hau-Riege, LCLS note, LCLS-TN-06-5 (2006).

6. D.D. Ryutov, Rev. Sci. Instr. 74, 3722 (2003).
7. Lee, S., "Calculating Spreading Resistance in Heat Sinks," Electronics Cooling, Vol. 4, No. 1, January, 1998.
8. B. L. Henke, P. Lee, T. J. Tanaka, R. L. Shimabukuro, B. K. Fujikawa, Low-Energy X-ray Interaction Coefficients: Photoabsorption, Scattering, and Reflection, Atomic Data and Nuclear Tables, 27, 1-144 (1982).
9. M. Born and E. Wolf, Principles of Optics, 5th ed. (Peramon, New York, 1975), p 462.
10. Gaussian Beam Optics, CVI Melles Griot tutorial:
<https://www.cvimellesgriot.com/Products/Documents/TechnicalGuide/Gaussian-Beam-Optics.pdf>.
11. JOSA, Vol. 38, Issue 9, pp. 766-773 (1948).
12. WEPC20, Proceeding of FEL 2009, Liverpool, UK.
13. Lorenzo Raimundi, FERMI@elettra: Presentation at the European XFEL Users Meeting January 2013, titled "K-B active optics system optimization through wavefront sensor measurements at Fermi@Elettra FEL").
14. Tiedtke et. Al., New J. Phys. 11 023029 (2009).
15. Stefan P. Hau-Riege, et. al., Near-Ultraviolet Luminescence of N₂ Irradiated by Short X-Ray Pulses, Phys. Rev. Lett. 105, 043003, 2010.
16. Y. Feng et. al., A single-shot intensity-position monitor for hard X-ray FEL sources, X-RAY LASERS AND COHERENT X-RAY SOURCES: DEVELOPMENT AND APPLICATIONS IX Book Series: Proceedings of SPIE Volume: 8140, 2010.
17. Automatic alignment of a Kirkpatrick–Baez active optic by use of a soft-x-ray Hartmann wavefront sensor, P. Mercère et. al., Optics Letters, Vol. 31, 199 (2006).
18. X-ray beam metrology and x-ray optic alignment by Hartmann wavefront sensing, Mercère et al., SPIE, Volume 5921, 63 (2005).
19. HASO™, X-EUV wavefront sensor product brochure, http://www.imagine-optic.com/iop_products_wavefront-analysis_HASO-X-EUV_x-ray-extreme-ultraviolet_shack-hartmann-wavefront-sensor_en.php.
20. M. Idir et al., Nuclear Instruments and Methods in Physics Research A 616 (2010) 162–17.
21. Private communication.
22. In situ fine tuning of bendable soft-x-ray mirrors using a lateral shearing interferometer, D. J. Merthe et al., Nucl. Instrum. Meth. A710, 82 (2013).
23. Exploring the wavefront of hard X-ray free-electron laser radiation, S. Rutishauser et. al., Nature Communications, 3, 947 (2012).

12

EXPERIMENTAL INSTRUMENTS

TECHNICAL SYNOPSIS

For LCLS-II, one new soft X-ray beamline will be installed on the new soft X-ray undulator. The soft X-ray beamline will use the same end stations currently in use at LCLS. For LCLS-II all four of the hard X-ray instruments will remain in use.

Upgrades to the experimental systems infrastructure to exploit the LCLS-II beam parameters like the high repetition rate will be included within the project for the soft X-ray systems. This will include upgrades to the data acquisition and controls systems.

12.1 Introduction and Overview

The experimental end stations for LCLS-II borrow heavily from the existing LCLS-I capabilities. Many of these stations are already in use and more are planned for development. Upgrades to diagnostics and detection systems will begin to provide capabilities to take advantage of the high repetition rate of the LCLS-II beam. The layout of the photon system has previously been described in Chapter 11. This will provide upgrades to the mirror systems that are necessary to handle the higher heat load and broader photon range delivered by LCLS-II.

12.2 Soft X-ray Beamline and End Station

As described in Chapter 11, the soft X-ray undulator source will initially service one photon beamline. The beamline will transport, focus and deliver the X-ray beam to the experimental end station area. Because the transport of soft X-ray photon beams require ultrahigh vacuum conditions, the beamline will end with a vacuum interface to which an experimental end station can be connected. Experimental end stations typically focus on a specific method to address a range of scientific questions. To provide the greatest scientific capability each end station can be used on any of the soft X-ray beamlines.

The end station area will be located in the LCLS Near Experimental Hall (NEH). A new soft X-ray beamline path will be introduced, slightly different from that used by the current AMO and SXR instruments. Therefore much of the current vacuum componentry and controls cabling will be moved or replaced. However, the key support utilities and infrastructure capacities are in place including: electrical power, process cooling water, bridge cranes, compressed air and HVAC. Soft X-ray beam containment for radiation safety can be achieved with proper end station and beamline design without the need to isolate the equipment inside an interlocked hutch. This will be a design target for long-term end station installations. If needed, a personnel exclusion system may be implemented.

Soft X-ray Beamline

The soft X-ray beamline at LCLS-II is described in Chapter 11. The beamline will facilitate scientific studies ranging from atomic and molecular physics to time resolved chemical dynamics in solution. The diversity of experimental environments needed to address these scientific areas requires flexibility of the experimental end stations.

End Station Systems from LCLS

The end station area located downstream of the exit interface flange for the soft X-ray beamline will be designed with the intent to host different end station systems. This has been successfully implemented at LCLS on the SXR instrument. The key to this realization is well-defined interfaces between controls, laser, vacuum and utilities systems. This methodology is under development at LCLS and has been implemented with various degrees of specialization across all of the LCLS hutches. With this in mind it is important to note that fewer changes to instrumentation between experiments provide more efficient operation. This was realized by the

BESAC Subcommittee report on Future X-ray Light Sources, which recommended, “To meet anticipated high demand for this linear device, the linac should feed multiple independently tunable undulators each of which could service multiple end-stations.” [1] Therefore, while modular end-station systems are vitally important to cover all of the anticipated experimental demands on the source, exchanges will be minimized so as to optimize the use of the beamtime.

The end stations described below have either been developed or are in development at the LCLS-I facility and are not within the scope of the LCLS-II project. With upgrades to the detection systems they will be suitable to address the scientific objectives of LCLS-II.

LAMP

The LAMP end station provides soft X-ray coherent scattering capability for gas phase and solid samples. The design is based on the CAMP endstation [2] which was used at LCLS from 2009-2011 in the AMO hutch. The LAMP design provides compatibility with existing components developed for CAMP such as injectors and spectrometers, but the functionality of the instrument has been further improved. The LAMP station is shown in Figure 1.

LAMP End Station System

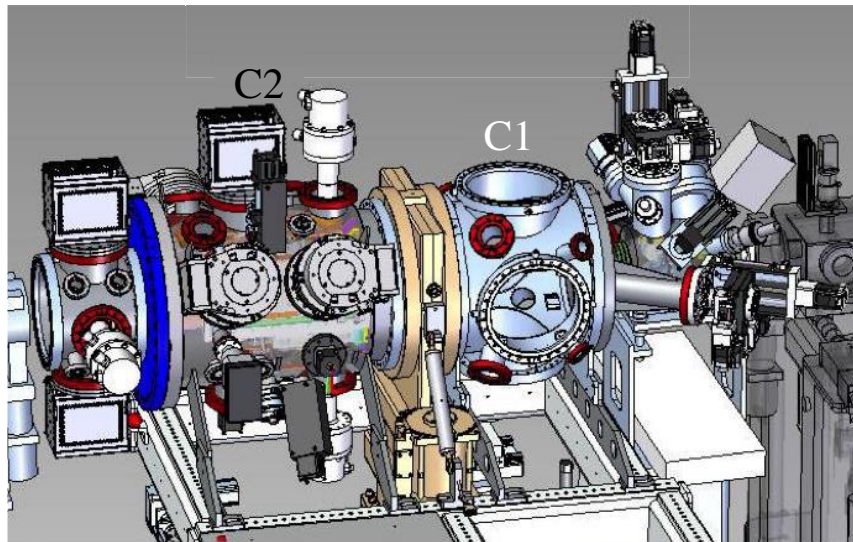


Figure 1: The LAMP chamber began commissioning in Nov. 2013. This figure shows the interaction chamber (C1) as well as the detector chamber (C2).

As shown in Figure 1 the LAMP chamber features a compact differential pumping section that includes laser incoupling capabilities and X-ray beam diagnostics. The end station has two separable vacuum systems: the main interaction chamber (C1) hosts the sample injection systems as well as electron and ion imaging spectrometers and the pnCCD detectors are housed downstream of the large gate valve in the detector chamber (C2). The pnCCD detectors consist of 1024 x1024 75um pixels that are sensitive to the full soft X-ray energy range of 200-1250eV.

The LAMP vacuum chambers are fixed to a six degree of freedom kinematic stand with the capacity to support additional components such as sample injectors and large spectrometers.

Resonant Scattering End Station

This end station is dedicated to resonant diffraction with soft X-rays and is based on the Resonant Soft X-ray Scattering (RSXS) chamber built at LBNL [3]. It will include an in-vacuum diffractometer, a 120Hz low noise CCD, a separate in-vacuum mounting station for long-wavelength optics for pump-probe measurements, and a six-degree-of-freedom cryostat. The general purpose will be to study different types of ordering in condensed matter systems via diffraction, but it will also be used to perform imaging and fluorescence experiments. For instance, observations could be made of charge or spin ordering in strongly correlated systems at low temperatures and with ultra-fast time resolution at the LCLS through studying the diffraction peak while measuring fluorescence in parallel.

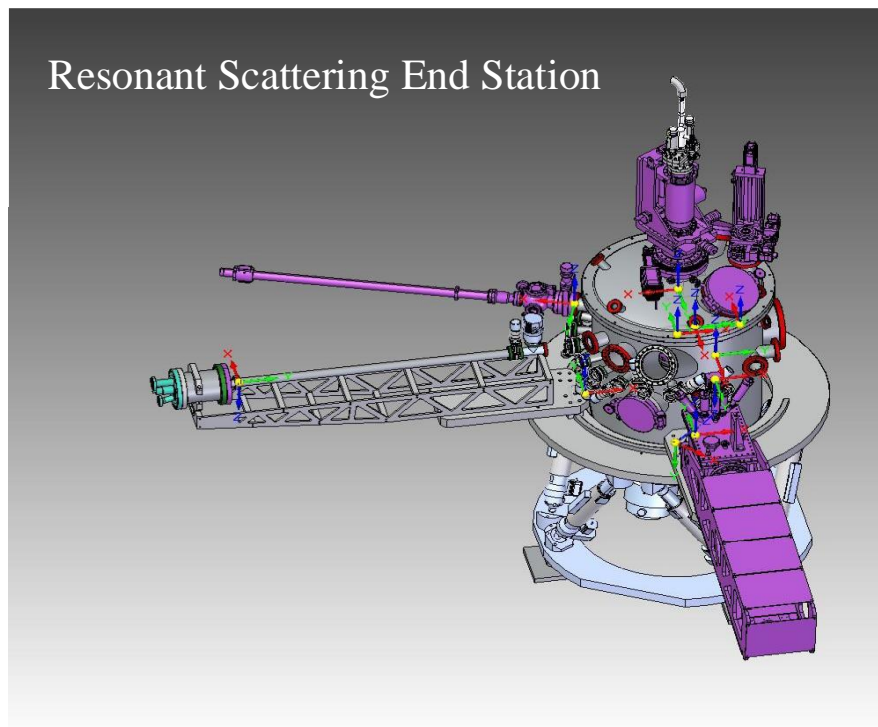


Figure 2: Resonant Scattering End Station. A six-strut motion system supports and manipulates the vacuum vessel. Copious flanges provide flexibility for connecting various diagnostics such as spectrometers and area detectors.

A concept for this system is illustrated in Figure 2. The station is currently under active development as part of the LCLS X-ray improvement project program (with funding from the Operations budget) and thus is not part of the LCLS-II project scope.

High Field Physics End Station

The High Field Physics (HFP) end station was originally designed as a part of the LCLS construction project and was used in the first experiments at the LCLS starting in September 2009. The HFP end station is used primarily for Atomic Molecular and Optical physics studies at LCLS. A skimmed pulsed gas jet is used to introduce sample gas into the chamber where it is ionized/excited by X-rays from the LCLS. One or more optical laser beams can be introduced into the chamber through laser in-coupling mirrors to prepare the sample, for example, by aligning a molecular sample or initiating a dissociation that can be temporally probed by the FEL beam. An array of spectrometers detect the results of the interaction of the X-ray FEL radiation with the sample, including electron, ion and X-ray spectrometers. The entire end station is mounted on a stand with six actuators to precisely control the alignment of the instrument in the six degrees of freedom.

High Field Physics End Station

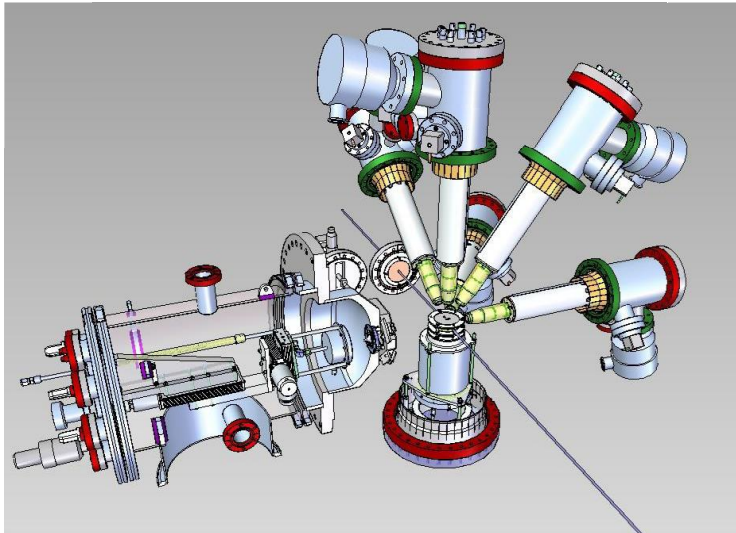


Figure 3: Cut-away CAD drawing of the HFP end-station showing the skimmed gas jet on the left and the five electron spectrometers and the ion spectrometer arranged around the interaction region where the gas jet and FEL beam intersect.

12.3 Hard X-ray Beamline Upgrades

At LCLS-II the hard X-ray undulator will deliver photons to the four existing instruments (XPP, XCS, CXI and MEC). These have been developed on DOE Major Items of Equipment (MIE) projects and commissioned within the operation of LCLS-I. While these instruments were developed for LCLS-I they will continue to support science using both the high repetition rate and extended energy beams from LCLS-II.

Lenses

Beryllium-based Compound Refractive Lenses (CRL) have proven very reliable and application-friendly for focusing of the LCLS X-ray beam. They are the primary focusing method on three of the four hard X-ray instruments (XPP, XCS and MEC). They have been successfully used in all four hard X-ray instruments for focusing FEL radiation in the photon energy range 4-20 keV down to 2 μm focus size. CRLs do not change the X-ray beam trajectory and can therefore be simply added in different combinations into the X-ray beam path to adjust the beam size quickly and flexibly. They take advantage of the photon-energy-dependent refractive index of the lens material. Therefore, the focal length changes for different photon energies and can be adjusted by changing the combinations of lenses. CRLs used under higher heat loads may require cooling to maintain stability.

Focusing Mirrors above 2keV

Currently, CXI is the only hard X-ray instrument using focusing mirrors at LCLS. The CXI Kirkpatrick-Beaz mirrors can produce either a ~ 1 micrometer or a ~ 0.1 micrometer FWHM focus. The mirrors have a clear aperture of ~ 1.1 mm. For operation of LCLS-II, from 1keV-5keV with both high and low repetition rate, the current CXI mirrors would operate at a reduced performance due to the limited acceptance of the mirrors and poor cooling capabilities. The SiC coating on these mirrors provides good reflectivity up to 12keV.

Hard X-ray Monochromators

LCLS hard X-ray monochromators require short and long term angular stability better than 1 μrad . The artificial channel cut monochromator (CCM), currently in use at both the XPP and XCS instruments, is designed for high stability. The LCLS-I CCM systems are entirely based on a design developed and implemented at the Advanced Photon Source [4]. This design has a minimal number of mechanical degrees of freedom and achieves a very high structural stiffness. A water cooling mechanism is incorporated on the first crystal of the LCLS monochromators. However, this mechanism is presently deactivated because it was determined experimentally to be unnecessary. Nevertheless, the system has been operated under high heat load (hundreds of watts) at the Advanced Photon Source with water cooling while maintaining a 1 mrad angular stability. Advanced cooling techniques will be required to improve the angular stability of the system when exposed to high heat load. Fortunately, the CCM system can be modified to cryogenically cool the silicon crystals to a temperature of ~ 100 K. The detailed studies that are required to determine the maximum heat load the system can handle while maintaining a 1 μrad angular stability are not included in the LCLS-II Project. It is noteworthy to point out that the European XFEL will implement this monochromator design with cryogenic cooling [5].

12.4 Detector Systems

The main detector challenge posed by LCLS-II is the high repetition rate. As with the LCLS-I a wide variety of detectors will be essential to take advantage of the myriad experimental

techniques that the science will demand. A list of possible detector architectures and the conditions under which they can record data is given in Table 1.

Table 1. Simplistic list of detector types and the machine pulse rate that can be accommodated by them. Counting detectors allow for one photon per pixel per pulse and are well suited for low signal experiments at high repetition rate. Integrating detectors can accept many photons over one or more X-ray pulses. These higher dynamic range detectors are well suited for experiments with great stability over multiple shots or large signal in a single shot.

Detector Type	Beam Rate	Record Each Pulse	Average Over Pulses	Technology Status
1 D Counting	1 MHz	Yes		In Development at SLAC
1 D Integrating	1Mhz	Yes		Exists at SLAC
Small 2D Counting	100 kHz	Yes		In Development at SLAC
Small 2D Integrating	100 kHz	Yes		Exists at SLAC
Large 2D Counting	1 MHz	No	Yes	In Development at SLAC
Large 2D Integrating	1 MHz	No	Yes	Exists at SLAC
Large 2D Integrating	10 kHz	Yes		Upgrade Existing System

SLAC has an active detector group that is developing detectors for current LCLS experiments with an upgrade path for higher repetition rate operation. These upgrades are planned to take place within the LCLS Operations program and are not within the scope of the LCLS-II project. In addition to local developments, new detector systems envisioned for the European XFEL as well as other detectors developed within DOE Office of Science programs will provide possible solutions as part of a diversified detector plan. This strategy recognizes that rapid global detector development is best coupled to a strong local detector group.

12.5 Controls, Data Acquisition, and Computing

The LCLS-II end station controls will reuse much of the existing capability. For the four hard X-ray hutches the control systems will remain largely unmodified. The controls components for the soft X-ray end stations will be reused in their new location for LCLS-II. This will include vacuum, motion control, vision, high voltage, triggering and pneumatic actuation systems. This relocation is detailed in Chapter 14.

The increased repetition rate at LCLS-II presents many challenges for the Data Acquisition System (DAQ). Addressing the scientific objectives requires efficient use of the high repetition rate. The data acquisition system will be able to record eight one-dimensional detectors (spectrometers, TOFs, etc) at 100kHz. Together all of these detectors should contain no more than 10,000 points per event. The architecture to fulfill these requirements is addressed in Chapter 14.

As higher-repetition-rate area detectors come into operation an augmented DAQ infrastructure will be required. Rack space local to the experimental areas has been allocated for

high throughput and high capacity storage systems at the petabyte level. In addition a new paradigm toward data collection including, triggers, vetoing and compression will be essential. These new approaches are already being developed in conjunction with the LCLS user community. An open approach will be taken to consider viable enterprise solutions for storing the vast data quantities (tens of petabytes) collected.

12.6 Laser Systems

Roughly eighty percent of LCLS experiments involve optical lasers to pump (and on occasion probe) a sample in conjunction with the X-ray FEL. With the exception of the large lasers at the MEC instrument, these optical sources begin with a 120 Hz, 40 fs pulse, with mJ level energy. These lasers can be used to directly pump/probe the sample but in most experiments these 800 nm pulses are wavelength converted to the UV, visible, IR, mid-IR or THz. In many of these cases, the wavelength conversion process involves multiple stages of non-linear frequency conversion. The efficiency of these frequency conversion stages can be as low as 10^{-3} , resulting in μJ pulse energies at the sample. In most cases, these μJ level pulse energies are exactly what is required.

The LCLS-II Project does not include funding for upgrading the experiment lasers. Current LCLS-I laser systems can operate up to 360Hz (and with reduced performance at higher repetition rates). LCLS has a strong and vigorous laser development team. Laser development for the electron gun can be leveraged for high repetition rate experimental laser systems. Though additional R&D is needed there are no physics limitations or engineering problems impeding the development of these laser systems. High repetition rate lasers are critical for many of the experiments at LCLS-II and a straightforward path to their implementation is envisioned.

12.7 Timing Systems

The timing distribution system to the end station areas at LCLS-II is described in detail in Chapter 13. While LCLS-II is expected to have improved timing stability over LCLS-I, arrival-time jitter will remain a problem because each pulse, even when seeded, originates from the SASE process. Therefore, experiments requiring temporal resolution smaller than 10 fs will need to use an X-ray to optical cross correlation method. While these methods currently work at 120Hz R&D will be needed for implementation as described in Chapter 13.

12.8 Scientific Support Infrastructure

Experience at the LCLS and synchrotrons, demonstrates that laboratory space outside of the experimental areas is vital for carrying out a broad scientific program. In some cases this is because the X-ray experimental areas are in high demand leaving little time for setup and testing, while in other cases the X-ray experimental areas simply lack the laboratory environment that is needed to prepare samples that are, for example, light sensitive, toxic or require extensive chemical processing. Table 2 compares current allocation of lab space to what is being planned as part of development outside of the LCLS-II project.

Table 2: Lab space development plan from the current distribution to the timeframe of first light from LCLS-II.

	Current LCLS Lab Space	Planned lab space in 2019
NEH Prep	1248 ft ²	2298 ft ²
FEH Prep	427 ft ²	427 ft ²
Wet Lab	208 ft ²	1408 ft ²
Laser Lab	2672 ft ²	1947 ft ²
Total	4555 ft ²	6080 ft ²

Additional laboratory space cannot be accommodated in the far experimental hall. To remedy this shortage, space in buildings 750 and 757 is under consideration for possible reconditioning to function as laboratory support space. These areas will continue to be developed under the LCLS operating budget and will be a key part of experiment preparation for the LCLS-II upgrades. Overall, there is a plan to develop 6,080 square feet of laboratory space by the time of LCLS-II first light. The additional space will include new wet laboratory and general preparation laboratory areas.

These infrastructure development plans will provide adequate scientific support space for experiments following the LCLS-II upgrade. However, to fully develop the facility, new laboratory space is needed and this is reflected in the long term SLAC laboratory level strategy. Major initiatives are underway to develop new facilities and institutes at SLAC that could be associated with LCLS. These programs will bring faculty expertise and new laboratory buildings to the SLAC site.

References

- 1 http://science.energy.gov/~media/bes/besac/pdf/Reports/Future_Light_Sources_report_BESAC_approved_72513.pdf
- 2 L. Strüder, *et al.*, Nucl. Instrum. Meth. A 614, 483 (2010).
- 3 D. Doering, *et al.*, Rev. Sci. Inst. 82, 17620 (2011).
- 4 Narayanan, *et al.*, J. Synchrotron Rad., **15**, 12-18 (2008).
- 5 European XFEL GmbH 2012 Annual Report, pg. 67.

13 Timing and Synchronization

TECHNICAL SYNOPSIS

The LCLS-II timing system must provide a precision RF phase reference for the accelerator, triggers for pulsed devices and diagnostics, and a high-stability, low-noise beam time reference to the experimental stations.

LCLS-II will operate in conjunction with the existing LCLS-I FEL and experimental stations. LCLS-II is based on a 1300 MHz operating frequency, with its gun operating at the seventh sub-harmonic frequency of 1300 MHz, or 185.7143 MHz with a standard beam rate of 0.9286 MHz. The undulators and experimental stations need to be able to operate with beams from either the LCLS-II or the LCLS-I room temperature linac, which operates at 2856 MHz, with additional RF system frequencies of 8.5 MHz, 476 MHz and 119 MHz.

LCLS-II will use a new combined timing and RF distribution system (Sections 13.2, 13.3). This system will also need to be installed to the undulators and the experimental hutches, where it must be compatible with both LCLS-II and LCLS-I beam timings.

LCLS-II is expected to see some effects from the 60 Hz AC power line. While the beam will typically operate at a nearly constant 1 MHz rate, diagnostics and controls will operate in a 60-Hz-aware mode in a manner similar to that of the existing SLAC system. In addition to providing better diagnostics of 60 Hz power line effects, this project will provide improved compatibility with existing SLAC systems.

The fiducial system will be tied to the existing SLAC system. A “fiducial” pulse will be generated, at 360 Hz, phase locked to the AC power line. This pulse will be re-synchronized to the nearest the highest common subharmonic of all the accelerator frequencies: 71.42KHz. . The existing SLAC EVG/EVR timing system will continue to be used for LCLS-I and will be interfaced to new timing modules to provide triggers to the LCLS-II systems.

Precision (femtosecond) beam timing will be transmitted to the experiments from a beam arrival time monitor located in the Undulator Hall. Separate laser timing systems will be used to provide synchronization with the LCLS-I and LCLS-II beams Figure 1(Section 13.4).

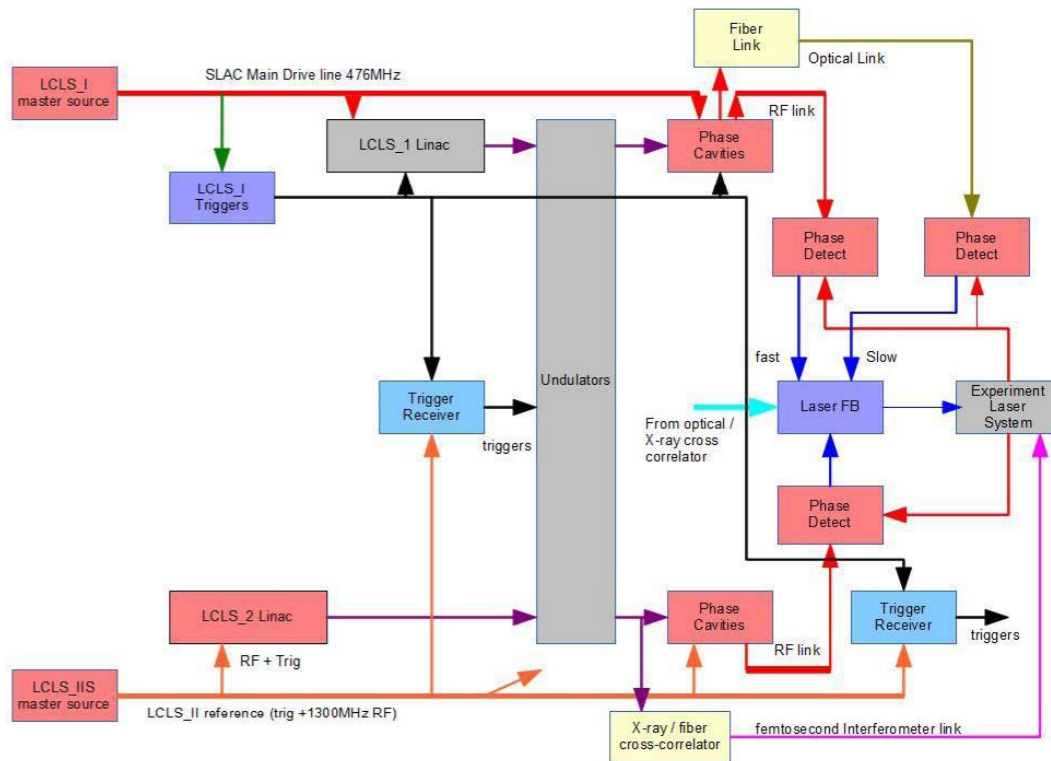


Figure 1. Block diagram of LCLS-II / LCLS-I reference and timing systems.

This chapter provides a number of examples of systems to phase lock different frequency references. For these we show intuitive divider/multiplier systems that could meet the performance requirements. It may be possible to implement these schemes with higher performance and lower cost using Direct Digital Synthesis techniques.

13.1 Master Clock, Frequency Selection, and Conversion

The master clock for LCLS-II will originate in a control rack in the service building at the injector site. A low-noise microwave source will provide the 1300 MHz reference frequency. The source will be frequency locked to a low drift standard, such as an Rb or GPS clock. The required frequency stability of $5e-10$ is set by requiring that the phase shift over the 5 km length of the facility be less than 10 fs, a requirement met by commercial frequency references.

The LCLS-I 476 MHz reference will be phase locked to the LCLS-II reference. This can be done with low noise and drift using a variety of methods. A sample solution is shown in Figure 2. Low phase noise locking can be achieved with frequency multiplication and addition. The LCLS-I master source can either be co-located with the LCLS-II master source, or can be located further downstream in the accelerator and locked to the 1300 MHz main drive line from the LCLS-II.

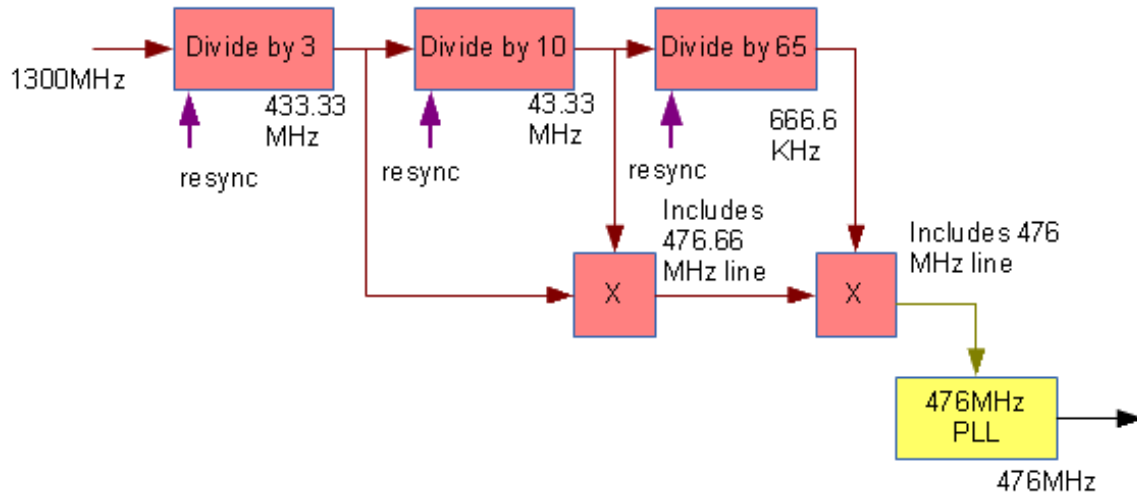


Figure 2. Example system to lock 1300 MHz to 476 MHz.

For reference, various LCLS-I and LCLS-II system-wide clock rates discussed in this chapter are summarized in the following two tables (Table 1). These include their multiplicative relation to their respective, system-wide master oscillator frequencies of 476 MHz (LCLS-I) and 1300 MHz (LCLS-II) that are used to compute the approximate frequencies shown here.

Table 1. Summary of LCLS-I and LCLS-II major component operating frequencies and harmonic relations.

LCLS-I Timing Harmonics	$f_{ref} = 476$ MHz multiplier	f (MHz)
X-band	24	11424
Exp't Timing Modules	8	3808
S-band	6	2856
Master osc.	1	476
Timing Sys.	1/4	119
Exp't Lasers	1/7	68
Fiducial resync frequency (old)	1/56	8.5
Fiducial resync frequency (new)	1/6664	0.07143

LCLS-II Timing Harmonics	$f_{ref} = 1300$ MHz multiplier	f (MHz)
3 ω Linearizers & Deflectors	3	3900
Exp't Timing Modules	41/14	3807.14
Linac RF (L-band)	1	1300
Spreader RF	1/4	325
Gun RF	1/7	185.71
Drive Laser Osc.	1/35	37.14
Exp't Lasers	1/35	37.14
Nom. Beam Rate	1/1400	0.9286
Fiducial resync frequency (new)	1/18200	0.07143

The new fiducial will operate at 360Hz, resynchronized to 71.43 kHz: the highest common subharmonic of all the frequencies shown. This fiducial will be used to insure interoperability between normal conducting LCLS-I components and LCLS-II components for line-locked 120 Hz (and subharmonic) events, as further described in this chapter. Please note that there are a variety of combinations of frequencies that allow operation of LCLS-I and LCLS-II from a common fiducial. One example is described here.

The LCLS-II nominal beam rate shown below is for the baseline; straightforward upgrades will allow beam rates up to the 37 MHz gun laser rate. The actual time between consecutive electron bunches is dependent on desired beam rates and patterns desired at the electron beam dump and undulators, as discussed in Chapter 7 under “Beam Spreader System.”

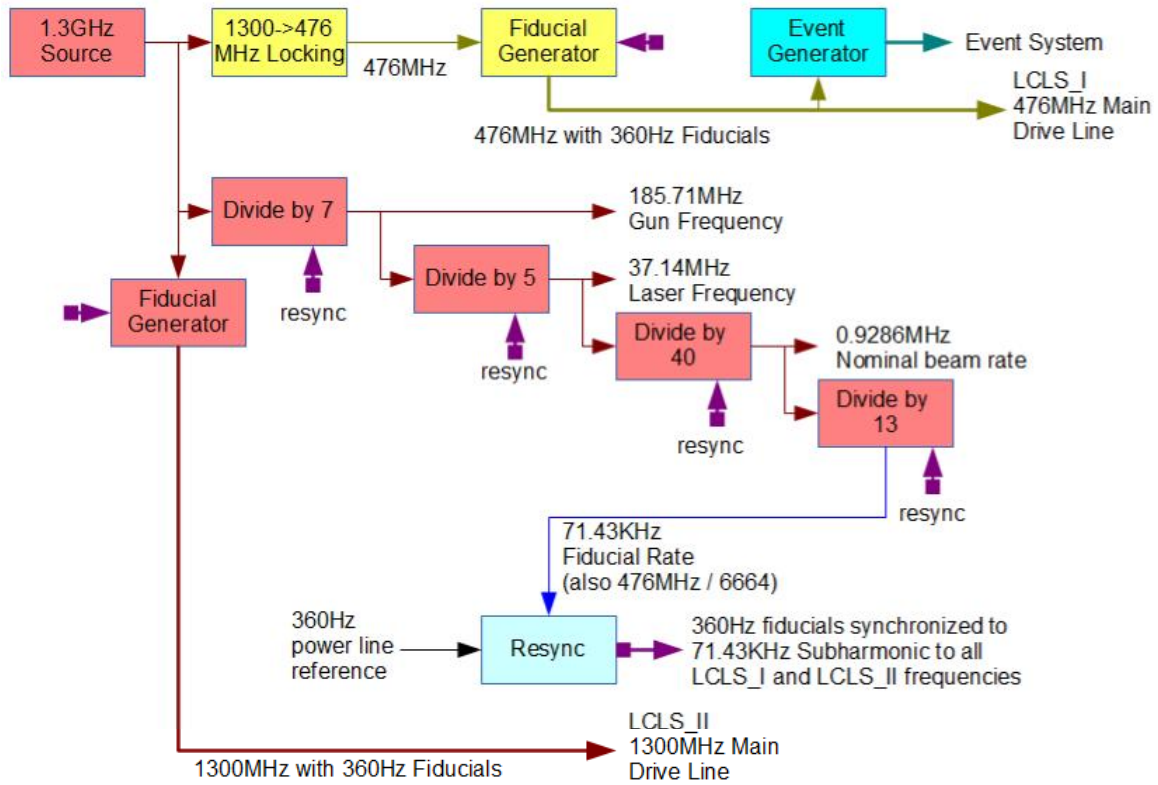


Figure 3. Fiducial generation / frequencies.

13.2 Triggering System

Fiducials are generated at line-locked 360Hz, and all trigger times are set by delays from these fiducials. The time of the 360Hz fiducials is adjusted to match the nearest cycle of the lowest common denominator frequency in the combined LCLS_I and LCLS_II system. A fiducial generator will take the 1300 MHz signal and add timing fiducials at 360Hz. The format of the timing fiducial is yet to be determined, but can probably be described as a tone burst of phase modulation. This tone burst can be designed to not contain significant power near the 1300 MHz carrier. Since the timing fiducials will be out-of-band for the cavity phase determination process, they can be easily ignored by the LLRF phase locking process (but detected and used for synchronization of feed-forward control features).

Triggers will be timed by the 1300 MHz system, with the timing values set through the event system, as described in Section 12.2.4. The system broadcasts events at the beam rate that serves to identify beam pulses and to set the desired delays in countdown timers based on the 1300 MHz distribution. This approach will provide triggers with few picosecond stability and jitter and with

a timing resolution of 1 gun bunch: $1/185.7$ MHz, or 5.4 ns. The EPICS network will distribute pattern information to all timing clients.

Even without a network connection, a utility module connected to the 1300 MHz cable can provide a low-jitter line- and bunch-synchronous tick. With a network and event system connection, any other timing signal related to the bucket filling pattern (e.g., when pulses are diverted to the diagnostics line), can also be generated with few ps-level jitter by cycle counting.

The 1300 MHz reference signal, including fiducial, will provide the low-drift and low-jitter signal to LLRF and other timing clients in the 1 km linac along a phase-compensated tapped reference line in the accelerator tunnel. This reference line is conventional copper-based RF (not optical), which provides a low-cost, low-phase noise solution. The phase compensation network is similar to the cable stabilization system used to transmit low-drift RF timing signals to the LCLS experimental stations, as shown in Figure 4.

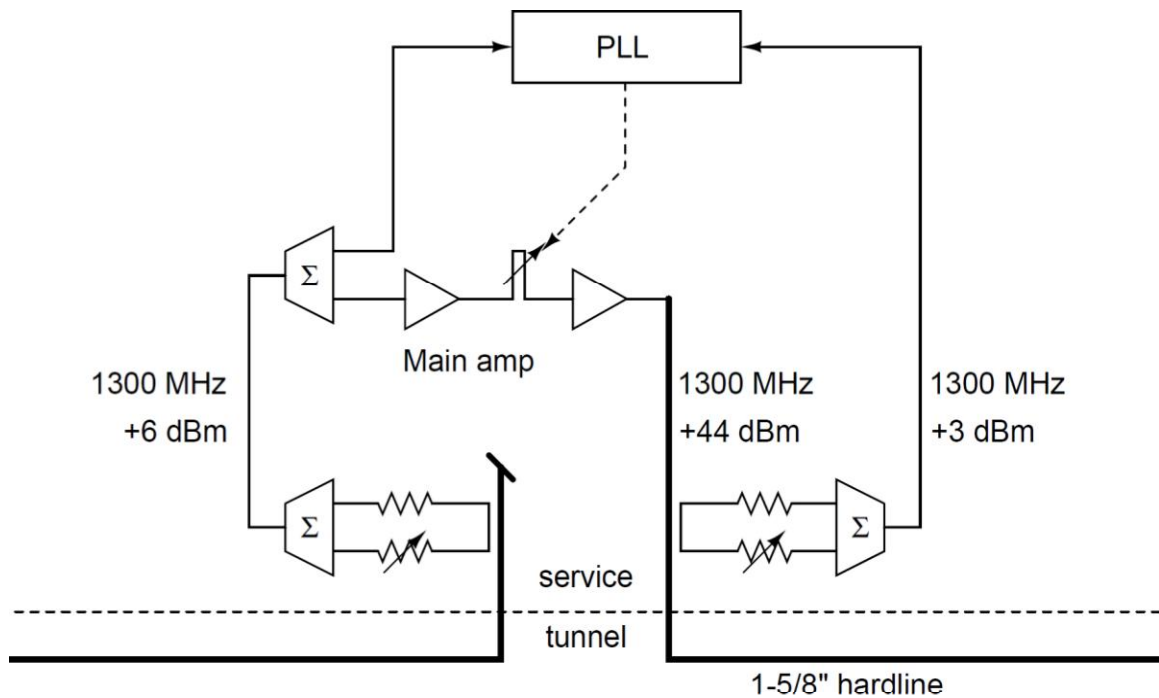


Figure 4. Cable stabilization system (schematic).

Since the RF distribution of 1300 MHz is kept above 0 dBm on copper with a minimum number of active components, the white noise background (additive phase noise) will be less than -160 dB rad^2/Hz , plus a small $1/f$ component. Integrating this over a typical 60 kHz closed-loop noise bandwidth of an individual cavity control gives 3 μrad rms contribution to cavity phase noise, less than that contributed by the local LLRF electronics (ADC).

At periodic intervals, a booster amplifier will regenerate the signal strength to recover losses from cable attenuation. This amplifier must be transparent to the timing fiducial and include the feedback loops needed to support the cable phase compensation scheme.

Based on the performance of the LCLS cable stabilization system, the reference signal drift is estimated at 10 percent of the uncompensated line. Given the temperature stability of the SLAC tunnel (0.1°C), the drift over the approximately 700 m section of active SRF cryomodules is expected to be about 200 fs diurnal. Phase stability over the whole 4 km section (supporting transfer line BPMs) will be in the ballpark of picoseconds, but those clients pose relatively weak demands on the RF phase distribution. The phase drift will be stabilized at the beam arrival time monitor (Section 13.3.1) before being transmitted to the experiment.

If improved phase stability is required, an upgrade path to this system is to first monitor and correct its phase using a high-accuracy optical-interferometer base system at a few points. This would be based on the femtosecond timing system described in Section 13.3.3.

13.3 Timing Distribution to Experiments

Optical/X-ray pump probe experiments require low jitter locking of the experiment pump lasers to the timing of the X-ray beam. The timing requirements are set by the desired resolution of pump/probe timing experiments and limited by the minimum available X-ray and optical laser pulse lengths. This gives desired a timing stability of 10 fs in the near term, and 1 fs in future. Both of these are beyond the current state of the art, so the use of an existing design is proposed for initial turn-on, with R&D to develop improved timing systems. The two systems are described below.

RF based locking system

The LCLS-I RF laser locking system will be modified to operate with either the 476 MHz LCLS-I reference or the 1300 MHz LCLS-II reference. This system provides less than 70 fs timing jitter and less than 800 fs long-term stability, based on the LCLS-I experience (Section 13.3.2).

For many experiments, the RF locking system can be used in conjunction with an X-ray/optical cross-correlator (Section 13.3.4). The cross-correlator will provide shot-by-shot femtosecond timing data to allow offline correction of experiments; it will also provide slow feedback to the RF locking system to correct for drifts.

The cavities in the beam arrival time monitors and the experiment laser locking systems both operate at frequencies near 3808 MHz. For LCLS-I, a 476 MHz phase distribution is used, and the lasers lock to the eighth harmonic, at 3808 MHz.

For LCLS-II, a 1300 MHz distribution will be used with the lasers locking to the third harmonic of the 1300 MHz reference, minus one half of the gun frequency of 185.71 MHz, giving 3807.15 MHz. This will allow reuse of the locking hardware, and only requires that the input reference signal be switched between LCLS-I and LCLS-II. An example of the frequency generation system design is given in Figure 5.

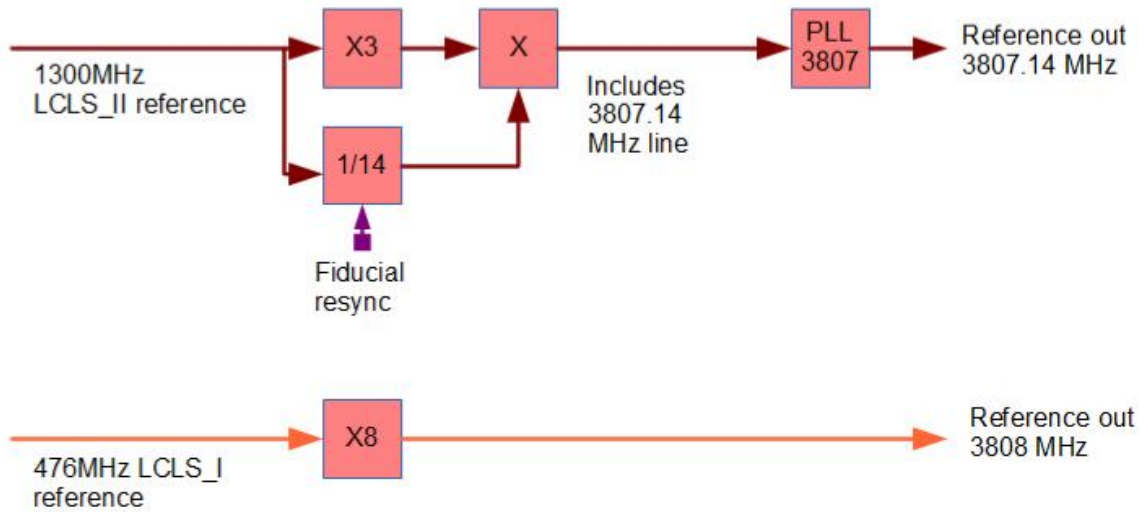


Figure 5. Generation of 3808 MHz reference signals for LCLS-II and LCLS-I.

Interferometric locking system

A laser-locking system based on using optical phase to carry timing information has the potential for sub-femtosecond operation. This would allow femtosecond timing experiments under beam conditions that do not allow for shot-by-shot cross correlation, such as operation at very low X-ray pulse energies. The system would also allow substantially improved non-corrected laser-to-X-ray timing for experiments where offline jitter correction is not practical, and will reduce the timing jitter and required range of the cross-correlators in normal operation. This system requires R&D with a design concept described in Section 13.3.4.

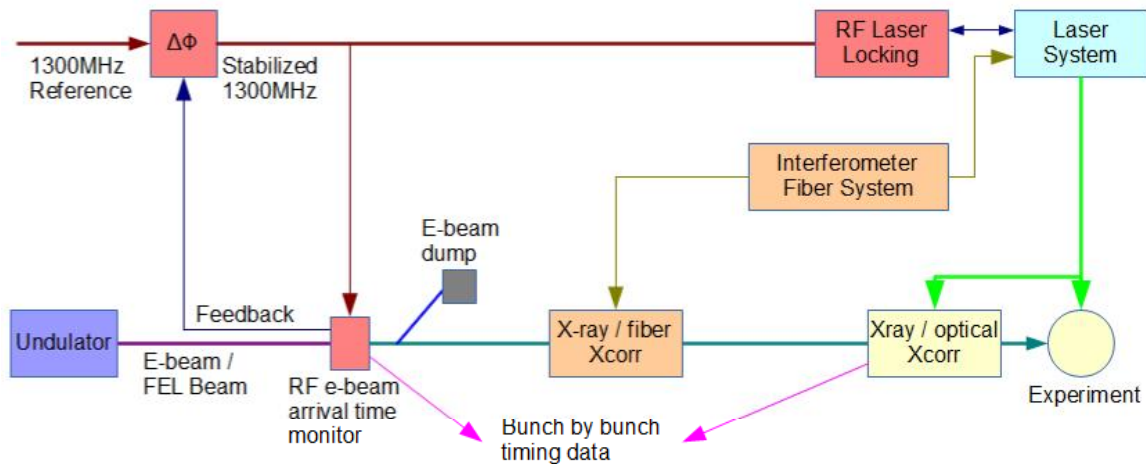


Figure 6. Experiment timing system.

13.3.1 Undulator Beam Arrival Time Monitor

The RF locking system will use an undulator beam arrival time monitor of the same design as that used in the linac and bunch compressors (Chapter 9, Section 9.8) and similar to the LCLS-I system. It will also provide bunch-by-bunch electron beam arrival times with about 10 fs jitter

and less than 100 fs long-term stability. The performance of the LCLS_I system has been measured by comparing two independent phase cavity systems.

The beam arrival time monitor uses a slow feedback to correct the phase of the RF reference from the accelerator to the experimental stations. It also provides pulse-by-pulse data on the arrival time of the electrons relative to the RF. Depending on the timing noise spectrum of the final machine; this data may be used for feedback to the accelerator or provided to the experiment for offline data correction.

The reference for the undulator beam arrival time monitor can be either 3807.14 MHz from LCLS-II or 3808 MHz from LCLS-I (Section 13.3), as shown in Figure 7. With a cavity frequency of 3807.6 MHz, the difference in RF reference frequencies is less than 1 MHz — within the bandwidth of the detection electronics. This frequency is not harmonic with any dark current sources.

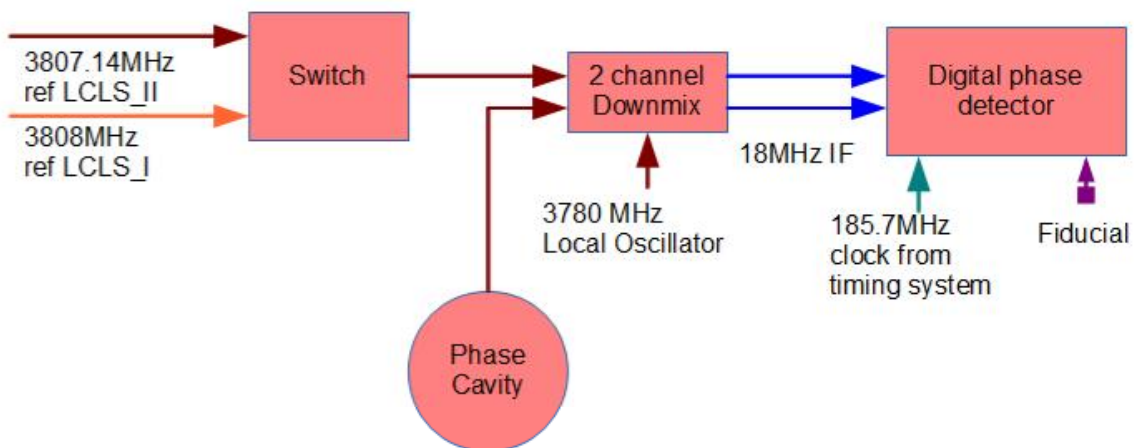


Figure 7. Phase cavity for use with LCLS-II and LCLS-I beams.

An X-ray/optical bunch arrival time monitor for locking the interferometer fiber system is described in Section 13.3.3. It can also be used either in feedback or for experimental data post processing.

13.3.2 RF Laser Locking

Gun and experiment laser systems will be phase-locked to accelerator RF via an analog RF phase detector coupled to a feedback module. Expected performance for a system is less than 70 fs rms jitter (integrated from 10 Hz to 10 kHz relative to carrier) and less than 800 fs long-term drift. The Precision Timing Modules locking system (“Laser Locking System”) already developed at the SLAC will be sufficient for this level of operation. This system is composed of a number of modules that make system setup, maintenance, and replacement incur minimum downtime with a high level of reliability. At this time, systems using these modules are running five source and experiment lasers at SLAC, including the LCLS-I injector lasers and the LCLS-

MEC and FACET experiment lasers. Upgrades to this system are ongoing, and considerably better performance is expected in time for installation in LCLS-II.

If the LCLS-II experiments are operated using a different laser system than the LCLS-I experiments, the LCLS-II laser can be chosen to have the same frequency as the LCLS-II gun laser: 37.14 MHz. This can be locked using the same techniques used to lock the gun laser, by comparing the 105th harmonic of the laser frequency with three times the 1300 MHz reference frequency. Note that the choice of 3900 MHz for frequency locking and 250 kHz for the phase detection frequency match the system currently used for LCLS-I experiment lasers, but may be changed for LCLS-II for optimal performance and compatibility with other LCLS-II RF hardware.

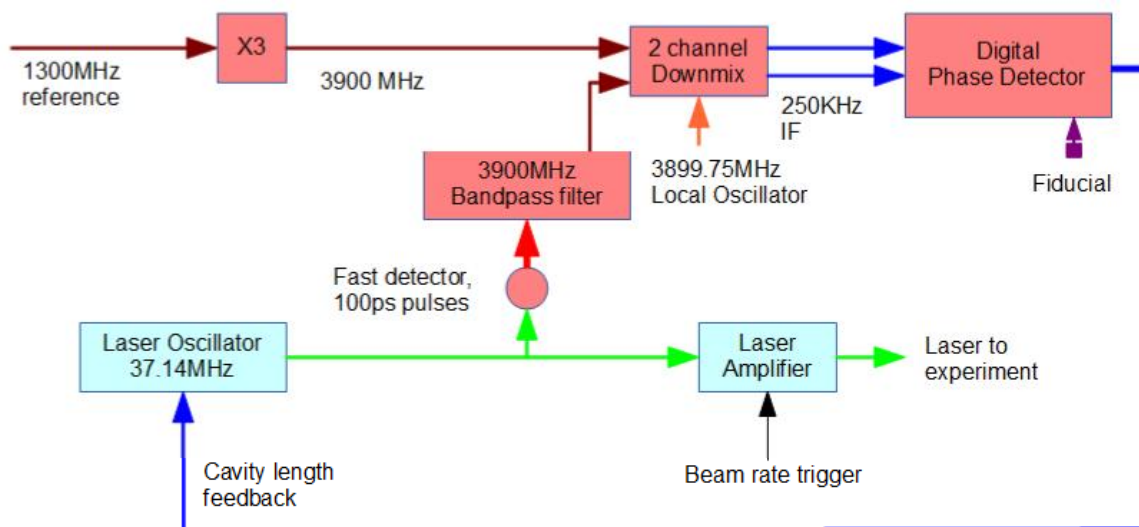


Figure 8. Experiment laser locking system.

If the decision will be made to use the same *Coherent Vitara* Ti:sapphire oscillators for LCLS-II as are used for LCLS-I, these can be retuned to 74.28 MHz and provide locked beams to both systems. In this case, the locking ratios become somewhat complex, but can be implemented in a straightforward manner. By using the $1300 \text{ MHz} * (3 - 3/35)$ gives 3788.57 MHz as a locking frequency (51 times the laser frequency). This is harmonic with all possible beam rates since it is harmonic with the injector laser frequency. Also, 3788.57 MHz can be locked to the LCLS-I reference with $476 \text{ MHz} * (8 - 2/49)$ as the frequency conversion. All of the frequencies are harmonics of the base fiducial rate of 71.43 kHz.

The RF-based laser locking relies on transmitting RF on a feedback-stabilized coaxial cable. An equivalent system is in use on LCLS-I to distribute the accelerator reference RF to the experiment hutches. The system would include coax transmitters located at the end of the LCLS-II undulator section and coax receivers located at each desired endpoint (such as experiment hutches). A coax system would require installation of low-loss, low-drift coaxial cable. A block diagram of this system is shown in Figure 9. As implemented in LCLS-I, this system provides

more than 10 times the reduction in the phase drift of a cable system by averaging the forward and backwards phases in the cable.

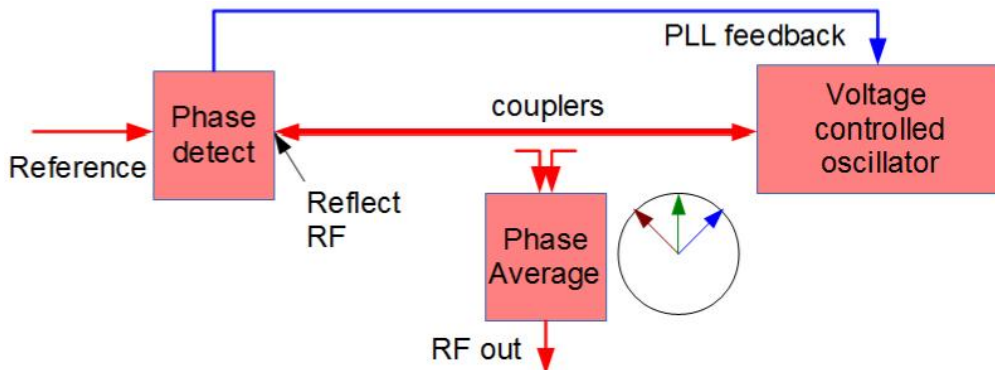


Figure 9. RF cable stabilization system.

In addition, SLAC has demonstrated a fiber-stabilized coaxial system that further stabilizes the reference distribution system by including an optical feedback system using commercially available components, standard fiber optic, and the SLAC Precision Timing Modules. This system would have lower performance than an “all-optical” system, but at reduced cost and complexity. Various companies are developing similar systems that could be used to improve the long-term drift.

13.3.3 Laser Femtosecond Timing

Considering that a soft X-ray beamline will service the AMO and SXR hutches, and a hard X-ray beamline will service the XPP, XCS, CXI, and MEC hutches, two separate femtosecond timing systems will be used, one for each beamline and able to operate simultaneously on two different frequencies. Figure 10 shows a system delivering signals to one hutch.

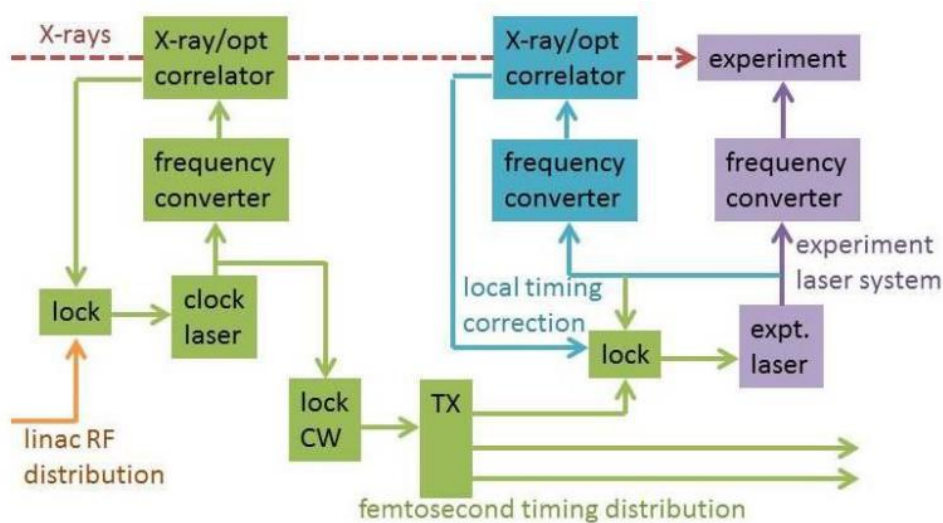


Figure 10. Block diagram of laser femtosecond timing.

The femtosecond timing distribution system starts with a clock laser, which generates RF and optical phase references to be distributed. The clock laser is a CEP-stabilized, mode-locked laser (commercially available), which is initially synced to the linac RF distribution signal or a harmonic thereof. This clock laser also generates pulses used in an X-ray/optical cross-correlator, which could serve as an "optical streak camera" device located in the Front End Enclosure (FEE) before it splits to the respective hutches and is transparent to the beam, save for a small fraction of the energy used to produce photoelectrons from a gas. These photoelectrons are accelerated or retarded by an optical electric field with known phase, and a wave period comparable to the X-ray pulse duration. In the case of, say 10 fs X-ray pulses (and thus photoelectron bunches), the interacting optical field would be in the mid-IR, at around 3-5 μm , produced by nonlinear spreading of the clock laser IR spectrum and difference frequency mixing two components. High pulse energy, mid-IR laser systems have been demonstrated at these wavelengths, which are easier to produce than THz radiation required for longer pulses. After this field perturbs the electron energies, the resultant photoelectron spectrum is recorded, and the relative optical phase/X-ray timing is derived. This scheme has been demonstrated at FLASH and LCLS [1]. Since the important signal is the electron spectral shape, the measurement is relatively immune to large fractional fluctuations in X-ray pulse energy, which are expected from the self-seeded FEL.

Information from the X-ray/optical cross-correlator is fed back to the clock laser to synchronize it to the average arrival time of the X-ray pulses. The clock laser can be well-synchronized, with signals exhibiting jitter frequencies significantly lower than its control bandwidth and sample rate, which is expected from the linac. Depending on electron bunch parameters, there may be a shot-to-shot jitter of the X-ray arrival time with respect to the electron bunch, on the order of a few femtoseconds. This must be accounted for in time stamping using shot-by-shot data from the cross-correlator.

Stability of the clock and its sync to the X-ray pulses is distributed to the experiment lasers via fiber optic. Coarse timing is done by sending a high harmonic of the laser repetition rate, as is done currently on LCLS. Fine timing depends on synchronization of the experiment laser envelope to the phase of an optical signal at 193 THz [2]. The clock laser's envelope and carrier are phase-locked, so the optical phase of a comb line of this laser is synchronous with the clock pulse and the X-rays. One comb line (a CW signal) is selected from the frequency comb of the clock laser and transmitted via fiber interferometer to an experiment laser. This laser also has its carrier stabilized to its envelope (CEP stabilization, an add-on to commercial lasers). The experiment laser beats with the distributed CW light to derive an error signal, and is then synced to the distributed optical phase, so that it is less than 1 fs synced to the clock. All parts of this sync scheme have been demonstrated to the less-than-1 fs level, including locking of two CEP-stabilized lasers to a CW reference [3].

Since the experimental stations are located far from the clock laser and its cross-correlator, additional correction will have to be made to account for drifts in distance and acoustic vibrations. This can be done with another X-ray/optical cross-correlator at each experimental station, driven by the same laser as the experiment, but with a special, fixed wavelength (e.g.

mid-IR for the optical streak camera). The femtosecond timing distribution system enables cross-correlator operation by providing initial close sync, reference, backup, and reduction of jitter range. For instance, without the femtosecond timing system, if the experiment laser jitters by multiple periods of the cross-correlator's optical radiation, results are rendered ambiguous.

13.3.4 X-ray/Optical Cross Correlator

A direct bunch-by-bunch measurement of the relative timing of the amplified optical pump pulse and the X-ray pulse near the experimental chamber provides the best timing reference for experiments. In particular, it can correct for electron beam/X-ray timing variations, and for timing changes in the pump laser amplifier and transport system. This technique is used at LCLS-I to provided precision timing. The system used at SLAC is based in changes in the optical properties (index of refraction and absorption) of a thin film when it is exposed to X-rays.

The films used in the SLAC cross-correlator are not compatible with high repetition rate operation. An R&D program is required to develop a gas-phase system, and a variety of concepts are being investigated. One possible technique is to use the optical fields of the laser to modify the spectrum of the Auger electrons emitted from atoms that are ionized by the X-ray beam. The change in the energy spectrum (for example measured with an ETOF) will indicate overlap of the optical and X-ray beams. Use of a crossing angle between the X-rays and the electron beam, along with multiple detectors, should provide a measure of the relative arrival time.

X-ray/optical cross-correlators are an area of active research at a variety of laboratories around the world. This system is not included in the LCLS-II project, but is considered part of the experimental systems.

13.4 References

1. S. Dusterer et al, "Femtosecond X-ray pulse length characterization at the Linac Coherent Light Source free-electron laser," *New J. Phys.* v.13, 093024 (2011).
2. R. B. Wilcox et al, "Towards attosecond synchronization of remote mode-locked lasers using stabilized transmission of optical comb frequencies," *J. Mod. Opt.* v .58, 16 (2011).
3. R. B. Wilcox et al, "Strategies for achieving sub-10fs timing in large-scale FELs," FEL 2012 conference, Nara, Japan 2012, paper thoai01. http://epaper.kek.jp/FEL2012/talks/thoai01_talk.pdf.

14 Controls and Safety Systems

TECHNICAL SYNOPSIS

The controls system for LCLS-II provides for the control, monitoring, operation, diagnostics, and performance optimization of the entire accelerator facility. Controls provides all the necessary data acquisition and control hardware, software, networking, computing facility, safety systems and the Main Control Center (MCC) operations facility. The system scope and architecture spans from low-level interface and control of beamline components to high level automation and optimization.

Safety systems protect personnel and equipment from potentially dangerous or damaging radiation and beams. These systems couple together the control of many different accelerator systems and subsystems, such as the drive laser, gun RF, injector and accelerator RF, radiation monitors, personnel access gates, mirrors, stoppers, vacuum valves, insert-able diagnostics, and magnets. With the potential for MW-level beam power, the safety systems must be entirely reliable and robust, and in some cases fast acting.

14.1 Control System Overview

The controls system for LCLS-II provides for the control, monitoring, operation, diagnostics, and performance optimization of the entire accelerator facility. Controls provides all the necessary data acquisition and controls hardware, software, networking, computing facility, safety systems and the MCC operations facility. The system scope and architecture spans from low-level interface and control of beam line components to high level automation and optimization. Figure 1 — a screen shot of the LCLS-I top-level operator’s display — presents an overview of the control functions provided for each region. LCLS-II will have an extensive operator’s display package similar to LCLS-I.

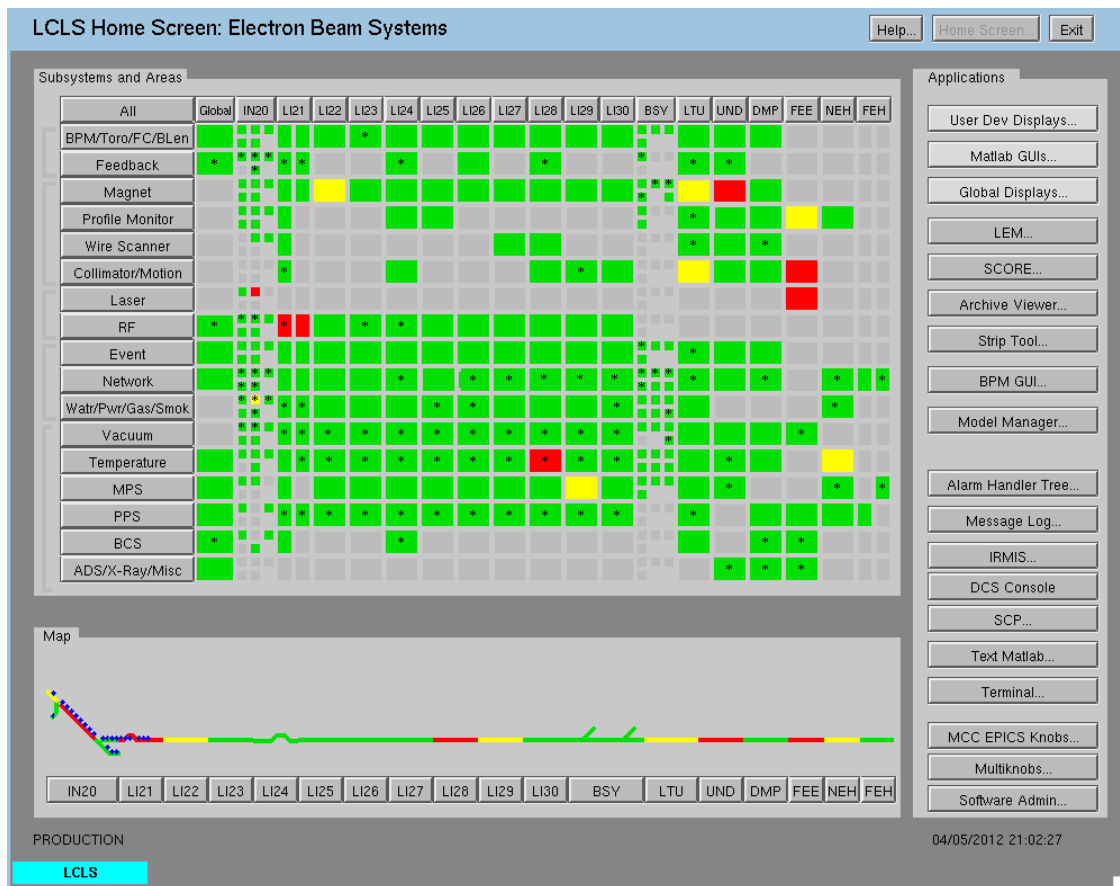


Figure 1. LCLS-I Electron control system main display and overview.

Beamline devices are interfaced directly to the Experimental Physics and Industrial Control System (EPICS) input/output controller (IOC) front-ends, or indirectly to EPICS via programmable logic controllers (PLCs). EPICS channel access (CA) over Ethernet provides the communication protocol for front-end computers and for mid- to upper-level control system elements. Many EPICS “soft IOCs” — processes running in servers — perform important control functions that require little hardware I/O. The distributed controls architecture has a backbone network connection supporting EPICS channel access, plus several dedicated networks for timing, feedback and machine protection. The data rates for recording diagnostics at the 1 MHz

beam rate are high enough that a data acquisition system separate from EPICS will likely be needed.

14.1.1 Controls Requirements

While some requirements for the LCLS-II controls system are almost identical to those of the LCLS-I requirements, e.g. magnet and vacuum control, there are significant new requirements. The system is required to allow control and operation of the facility at up to 1 MHz, with beam synchronized machine data available for diagnostics and automation. The Low Level RF system (LLRF) for this CW machine is completely different from that used for the pulsed linac of LCLS-I.

It is required that EPICS controls be implemented for control of all newly-installed LCLS-II systems. As the capabilities of LCLS-II evolve over its many years of operation, the controls system has to be sufficiently extendable to support more than 100,000 I/O connections and several million EPICS process variables (PVs).

The design of the undulators for LCLS-II is significantly different from that of the LCLS-I undulators and requires new controls development. The Undulator Specific Control System section gives an overview of the new design required for the LCLS-II undulators.

14.1.2 Operations Requirements

Operations control of the LCLS-II linac and the electron beam will be carried out from SLAC's MCC. Necessary data for monitoring and control of the LCLS-II will be available to the operations in MCC, and all user interfaces will be clearly designated so that no confusion arises as to which machine is being controlled. The section on software describes plans for these additional requirements.

14.1.3 Reliability

Overall, the LCLS-II facilities must have an operational availability greater than 90 percent. Controls should contribute only a fraction of the down time, less than 2%. The reliability requirements for LCLS-II are documented in SLAC-I-060-105-000-00. The linac is typically operated about 6,600 hours per year for all purposes. In some cases, improvements of subsystem controls designs will be implemented to improve reliability, based on lessons learned during LCLS-I operations. These changes are described in the following sections of this chapter.

14.2 Global Systems

14.2.1 Controls System Architecture

The controls will be based on the standard three layer client/server architecture. This model has been very successfully implemented for LCLS-I, and the fact that it lends itself to incremental development will allow us to expand it relatively easily for LCLS-II. The system will be based on the proven EPICS toolkit with well-defined interfaces for both the client and server in order to

enable fast integration and development. It will support the use of commonly available hardware and provide an extensive collection of ready-to-use applications software and device drivers.

14.2.1.1 Network Architecture

The LCLS-II controls network will be essentially an upgrade of the ones already in LCLS. It will consist of distribution switches located near the control system devices in each accelerator area. Controls devices will be connected to the distribution switches by CAT6 or fiber cables. The distribution switches will be connected to redundant large core routers in MCC by high speed fiber optic links. A large number of fiber optic cables will be pulled to each accelerator area, and multiple fiber optic cables can be used for increased bandwidth or to isolate traffic, as needed. Redundant fiber links between the distribution switches and the core switches will allow immediate recovery from the failure of a single fiber link.

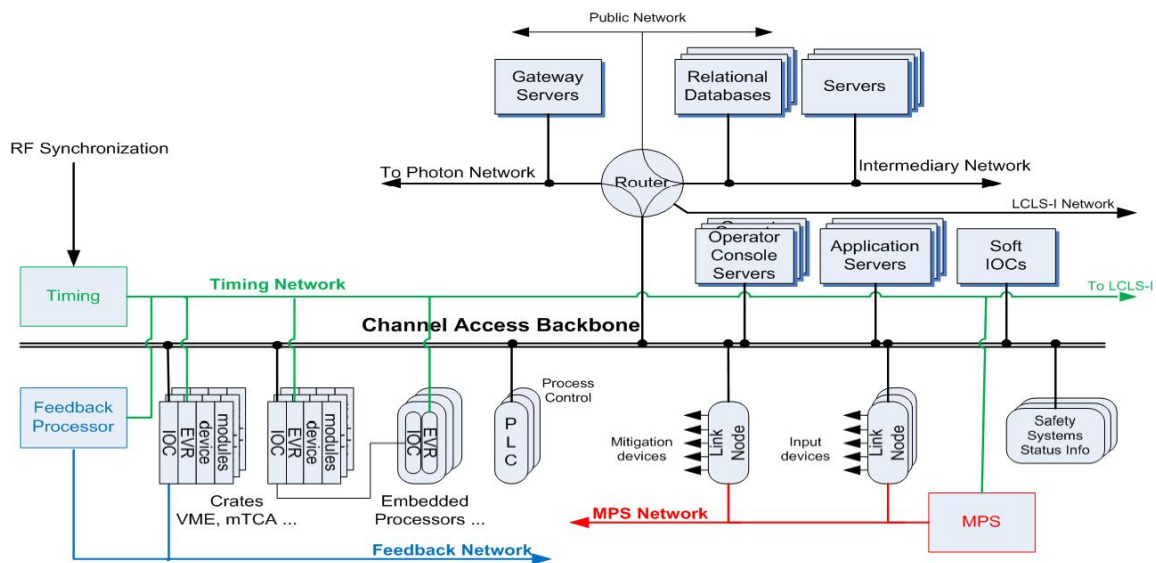


Figure 2. Network-based overview of the controls system.

As indicated in Figure 2, the LCLS-II controls network will consist of many separate networks (VLANs), including computing services, IOCs, instruments, terminals, utilities, video, and Fast Feedback. The Fast Feedback network will use fiber links separate from the other controls networks. The MPS network will use a separate core switch in MCC and separate fiber links to MPS link nodes in the accelerator areas. The timing system network will use separate fiber links and connect directly to timing system devices. The intermediary network (often referred to as the DMZ), which will be shared between LCLS and LCLS-II, will allow limited and controlled access between the controls networks and other SLAC networks through dedicated servers on the DMZ network. The architecture of the switches allows all of these networks to be isolated from each other but to still share the same switches and fiber uplinks. Additional networks can be added when needed. Central redundant core routers will allow controlled connections between any of the LCLS and LCLS-II controls networks, as needed.

The LCLS-II controls network will be isolated from the rest of the SLAC public network. No accelerator control devices will be visible to SLAC campus or Internet networks. This avoids denial of service and reduces vulnerability to other types of hacker attacks from outside of the controls network. Read-only data access will be provided to SLAC public networks by an EPICS Process Variable (PV) Gateway on the MCC DMZ network.

14.2.1.2 Controls Computing Infrastructure

The controls computing infrastructure provides services to controls applications from front-end IOCs, to mid-level software and upper-level operator interfaces (OPIs). It will be hosted in a centralized fashion to support both LCLS and LCLS-II, as shown in the Figure 3 below.

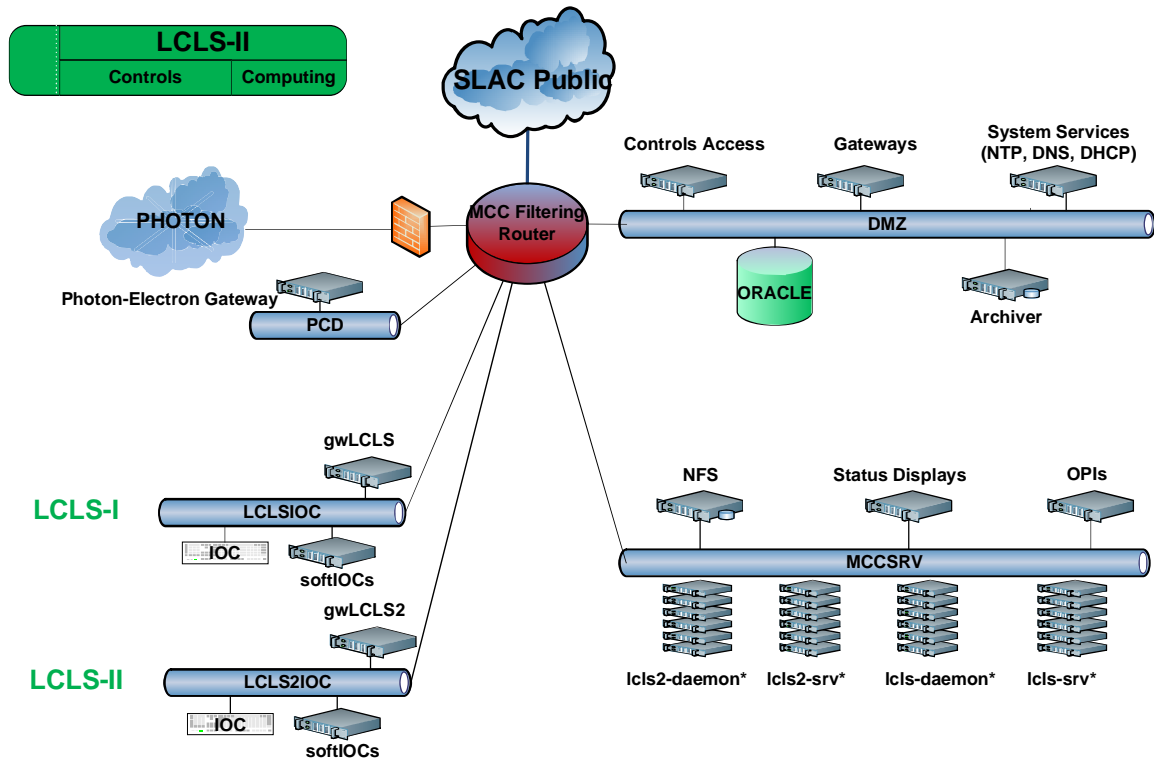


Figure 3. Controls Computing Infrastructure.

IOCs (hard and soft) will be hosted on separated networks, one for LCLS and another for LCLS-II. As shown in Figure 3, a pair of PV gateways will provide channel access traffic controls between LCLS and LCLS-II. As is the case with LCLS, limited and controlled access is provided to the SLAC public via dedicated servers on the DMZ. The channel access communication between photon and electron systems is controlled via PV gateways (photon-electron gateway).

14.2.2 Controls Hardware Architecture

Some LCLS-II requirements for instrumentation and control are largely the same as those for LCLS-I; thus implementations in those cases require copying existing systems. In some cases improvements in design or technology are implemented based on (1) change in requirements (e.g. 1 MHz beam rate, superconducting CW linac), (2) improving reliability, (3) increasing the level of standardization and maintainability of the systems (e.g., aligning the systems with new industry standards), (4) reducing costs either in the development or implementation phases, (5) taking advantage of commercial off-the-shelf hardware, or (6) replacing obsolete or unavailable components.

All subsystems will use EPICS, but different individual subsystems may use various hardware solutions, Micro-TCA, crate-based IOCs, and PLC/soft IOC combinations.

14.2.3 Timing and Event System

The role of the timing event system is to provide pulse-to-pulse coordination (timing patterns) for beam control and data acquisition, and to remain synchronized with both the low level RF phase reference distribution and the 360 Hz AC power line phase. Since LCLS-I and LCLS-II will be operating in the same environment and either accelerator will be able to deliver beam to the HXR undulator, they must share the same synchronization system. The HXR undulator BPMs and photon systems must be able to recognize whether beam is coming from LCLS-I or LCLS-II. The new timing event system will be backwards compatible with LCLS-I so that it can continue to operate with the new HXR undulator. The event system architecture will be similar to the present system except that the event pattern will be scaled up to the new 1 MHz beam rate, as shown in Figure 4.

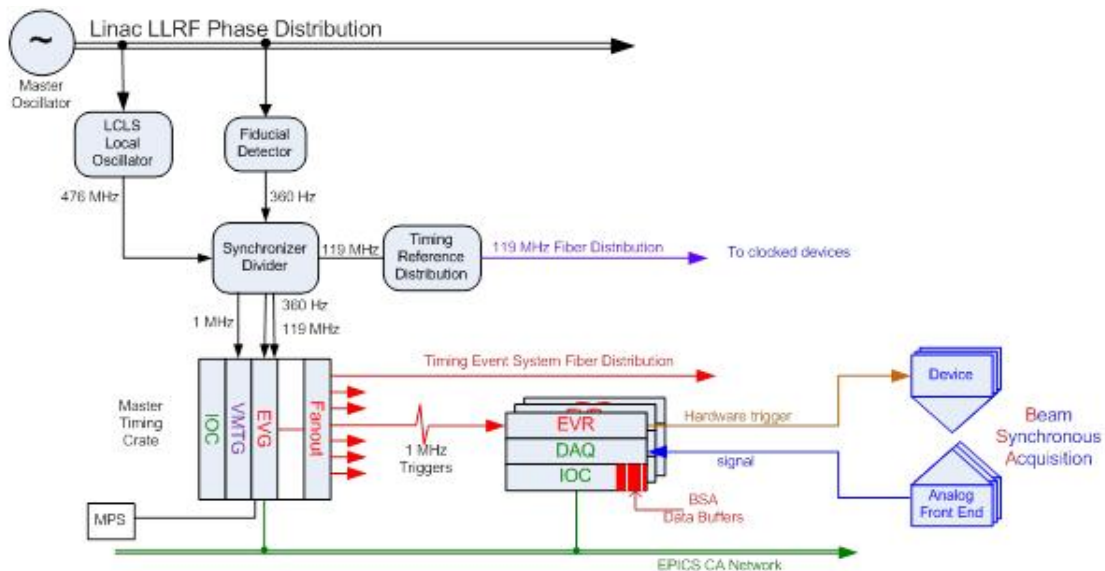


Figure 4. Timing event system block diagram.

The exact beam repetition rate and clock frequencies are discussed in Chapter 13 on the beam synchronization and timing. The new beam rate clock (approximately 1 MHz) will be fed into an existing event generator module (EVG). The present Micro-Research Finland (MRF) EVG can support beam rates up to 125 MHz. This limit is set by the fiber transceiver bit rate of 2.5 GB/s divided by 20 in order to transmit two 8-bit words of data for every beam pulse. This means that an event pattern can be broadcast, as is done now in LCLS-I, such that every beam pulse has a unique event timestamp.

The 1 MHz beam rate clock will be fed into the master timing generator (VMTG) module, which supplies the pattern to the EVG. The EVG also receives a 360 Hz clock, which is synchronized to the power line frequency so that events that coincide with the power line fiducials can be labeled.

In principle, it is possible to operate LCLS-I and LCLS-II from a common EVG, since the pulses to LCLS-I are a subset of those sent to LCLS-II. However, it is operationally more convenient to use two EVGs and have LCLS-I slave off the LCLS-II EVG, so that they remain synchronous but can be operated independently for commissioning and maintenance purposes.

A new requirement for LCLS-II is that the timing triggers remain synchronized to the LLRF to within 1 ps. The timing triggers will therefore be generated directly from the fiducials on the LLRF reference cable, as shown in Figure 5, and the timing event system will only supply the pattern and time stamp information.

The beam codes and timing event system software will be able to leverage off the present LCLS-I design, but new features will be added to account for either of the accelerators being able to deliver beam to the HXR dump. In addition, various start-up and recovery patterns will need to be developed to bootstrap the machine up to the CW operation mode. The timing system will also need to account for the new features of the MPS system, where both slow and fast beam shut-off pathways will be incorporated.

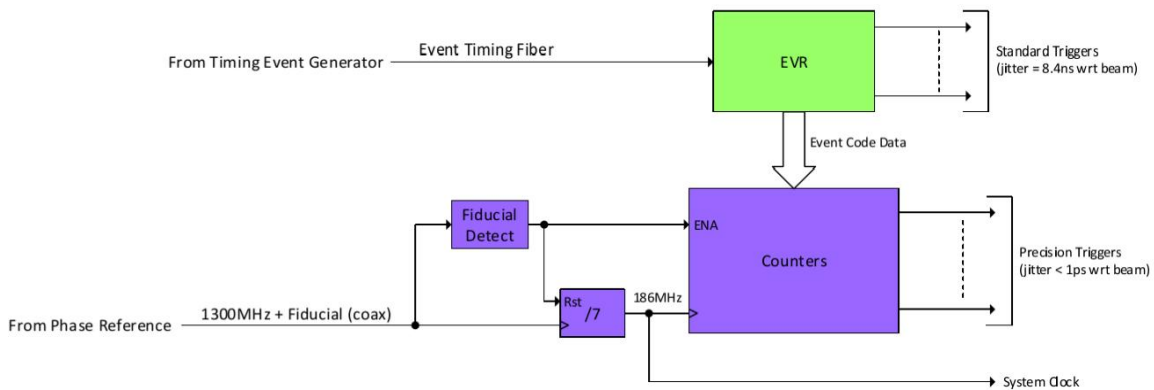


Figure 5. Synchronization of the event pattern with the RF phase reference system.

14.2.4 Beam-based Feedback System

The role of the beam-based Feedback system is to maintain steady beam operation by stabilizing electron beam parameters such as beam position, angle, charge, energy, and bunch length. Feedback loops suppress transients on the beam, can be configured to help minimize known disturbance on the beam, and are used to aid in beam tuning and troubleshooting. In addition, feedback loops calculate and produce beam parameter data that can be shared with the experimental areas. The LCLS-II system requires several beam-based feedback loops operating throughout the accelerator to stabilize electron beam parameters at rates up to 1 MHz.

14.2.4.1 Fast feedback architecture

The LCLS-II Feedback system will have similar high-level architecture to that of the LCLS-I, but will include necessary enhancements to allow feedback loops to operate at rates up to 1 MHz. A fast network (Figure 6) will be dedicated to feedback data transfers. Each feedback loop will include a controller process that is interfaced to the timing system and feedback network, receives sensor data and calculates beam corrections. Also, a set of software applications will support the configuration, maintenance and display of the feedback loops. A graphical user interface and EPICS API will allow the operator to use the feedbacks in beam tuning and troubleshooting procedures.

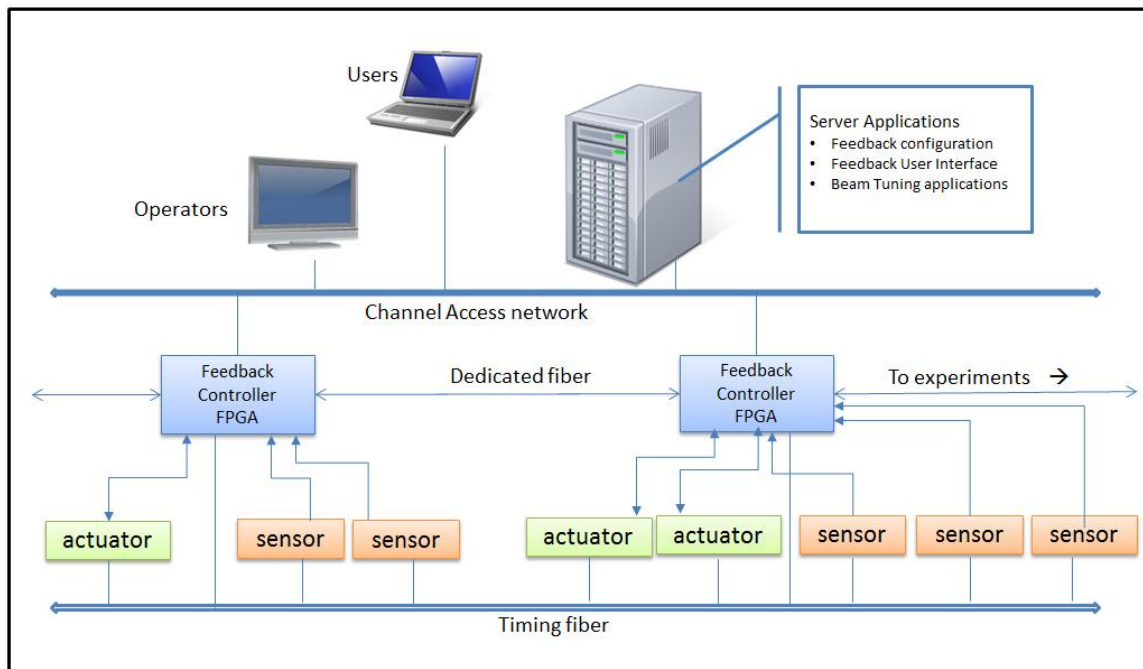


Figure 6. Beam Based Feedback Overview.

Unlike the LCLS-I feedback system, in order to attain the 1 MHz processing rate the LCLS-II Fast Feedback loops will require all sensor, controller, and actuator processing to be accomplished by FPGAs, rather than with microprocessors. Microprocessors will only be used to setup the FPGAs, turn loops on and off, and gather data for displays. Also, devices involved in

feedbacks - such as magnet and LLRF actuators, and diagnostic sensor devices – will include direct fiber connections to a feedback controller in addition to an interface to the timing system.

All the fibers from sensors needed for a single feedback loop converge to a controller board. An FPGA in the controller board waits for a complete set of data and calculates the state of the system (e.g. beam energy or angle) and new actuator settings. The algorithms needed for the FPGA are well understood, but with matrix multiplications and exception handling they will be fairly complex. The controller outputs the actuator settings on fibers, sending one to each actuator. It also buffers sensor, state, and actuator data so they can be read out for diagnostic and display purposes. Finally, the controller outputs its calculated data on another fiber that is shared with other controllers and the experimental area. The links between controllers will be bidirectional so the accelerator feedback loops can also use data from the experimental area.

14.2.4.2 Reliability and Usability

The feedback loops are essential to the operation of the accelerator as is the passing of their data to the experiments. Close attention will be paid to reliability. Redundancies of the fibers between the controllers or of the controllers themselves are being considered. The design will strive to allow a feedback loop to be reconfigured (which will happen relatively frequently) while keeping the communications between controllers running. It will also strive to provide a development platform that makes it fairly easy to change the feedback algorithm, so that a controls engineer is not required for every configuration change.

14.2.4.3 Slow Feedback Loops

The LCLS-I utilizes many slow feedback loops that run at rates less than 10 Hz. These loops are slow enough that MATLAB (or some other language) can be used to read the sensors via the EPICS channel access network, do the calculations, and send requests to the actuators via channel access. These are quick and simple to implement. The design of the LCLS-II Feedback system will not preclude the use of similar slow feedbacks for LCLS-II.

14.3 Beam Diagnostic Systems

The LCLS-II diagnostics fall into two main categories: those that involve analog conditioning followed by a sampling ADC, and those that involve image acquisition. The next two sections cover these two cases.

14.3.1 Sampling ADC based diagnostics

By far, most of the diagnostics need to measure a beam quantity at 1 MHz and make the data available in one of two ways:

1. Time stamped, buffered and transmitted to be stored and/or correlated with other data, or
2. Transmitted as rapidly as reasonably possible for use by MPS, BCS, or beam-based feedback.

All instances will need to do the first, while only a select fraction will need to do the second. The plan is to make all instances capable of doing both, but only connect the requisite communications fibers up to those where the second is required. The diagnostics that fall into this category are BPMs (both cavity and stripline), relative bunch length monitors, halo monitors, beam current monitors, loss monitors, beam arrival time monitors, wire scanners in the main beam and halo secondary emission monitors.

All of these diagnostics can be handled in a similar fashion. Each will have an analog front end that is designed for that diagnostic followed by a sampling ADC that has an FPGA attached. The analog front end typically also incorporates a signal source for calibrating the diagnostic, which can be triggered by a separate event code at convenient intervals. This allows for compensation of drift in the signal processing and continuous monitoring of the health of the system for high reliability. The FPGA will process some number of ADC readings to attain the properly calibrated diagnostic reading, buffer it to onboard memory, and send it out on a fiber if needed. We will strive to minimize the number of types of ADC boards and analog front ends. It looks like we can manage with two types of ADCs and four types of analog front ends.

Table 1 shows what types would be used for each diagnostic. The data can be buffered on the ADC board for seconds if needed and periodically read out by a CPU running EPICS and saved.

Table 1. Analog and Digital Processing for Diagnostic Systems.

Diagnostic	Analog front end	ADC
L band cavity BPM	L band down mixer	125-250 MHz, at least 12 effective bit. May well be the same ADC used for LLRF.
X band cavity BPM	X band down mixer	
Strip-line BPM	Strip-line filter/attenuator	
Relative bunch length monitor	Variable gain amplifier	At least 10 MHz ADC. (Perhaps same as above.)
Halo monitor		
Beam current monitor (toroid)		
Beam loss monitor (several types)		
Beam arrival time monitor		
Wire scanner detector (PM)		
Halo secondary emission monitor		

While it is unlikely we will choose to save all the diagnostic data at 1 MHz, it seems prudent to make sure the system is capable of doing this if it is necessary. Since the data is buffered and there are no hard real time requirements, this is simply a question of bandwidth. A rough calculation of the bandwidth needed for the linac diagnostics is the product of the following numbers:

3. Number of diagnostics of about 100
4. Bunch rate of MHz

5. Bytes per reading of 6 (2 for x, 2 for y, 1 for status, 1 for overhead)

This calculation results in about 600 million bytes per second or about 5 gigabits per second. This performance is well within the reach of modern CPUs and networks, particularly as this is sourced from many CPU's.

14.3.2 Image Acquisition

Profile monitor images are gathered at dump screens, wherever disruptive effects of coherent optical transition radiation (COTR) is not an issue. Some cameras in the LCLS control system are now being upgraded to 120 fps, but there is a large technology jump before we can scale these systems to 1 MHz. If screen materials can be found that can withstand very high repetition rates, the camera readback system will still be a bottleneck. If profile monitors are only deployed in the special diagnostic beamlines where lower beam rates are used, existing LCLS technology can continue to be used.

A standard CMOS camera can perform up to a few hundred frames per second [1], whereas CCD cameras are limited to about 50 fps. Specialized fast cameras [2] that represent state-of-the-art technology have variable regions of interest (ROI) and can presently achieve 7,500 fps for 1,024 x 1,000 pixels, and 775,000 fps if the ROI is reduced to 128 x 24 pixels for a 12-bit image.

Even higher frame rates can be achieved with linear arrays and segmented detectors. Furthermore, if MHz repetition rates are to be considered, then fast shutters using image intensifier technology must be employed, since electronic shutters on CCDs are limited to a few μ s.

14.4 Power Supplies and Power Conversion

14.4.1 Scope

The LCLS-II magnet power supply systems will provide controllable, precise and stable excitation current to dipoles, quadrupoles and solenoids to generate the magnetic field required to steer the electron beam from the injector to the electron beam dump. The electron beam requires very tight magnetic field stability tolerances, which translates directly to current stability for the power supplies. The power supply design will be nearly identical to that of LCLS-I, which has proven stability performance.

14.4.2 Power Supply Designs

The magnet power supply systems will be nearly identical to the LCLS-I design. Power supply types fall into two main categories: intermediate and trim type power supplies. The power supply type for each magnet is selected based on the current and tolerance requirements.

Intermediate type power supplies (Figure 7) are typically provided to magnets that require 750W or more, and/or less than 0.01 percent current stability. Intermediate systems use commercial power supplies controlled by a SLAC-designed Ethernet power supply controller (EPSC). The EPSC uses a PID-based digital control loop along with highly stable current transducers and electronic components to regulate current down to 0.001 percent levels. In

general, these power supply controllers are used for magnets that require higher current and tight tolerances.

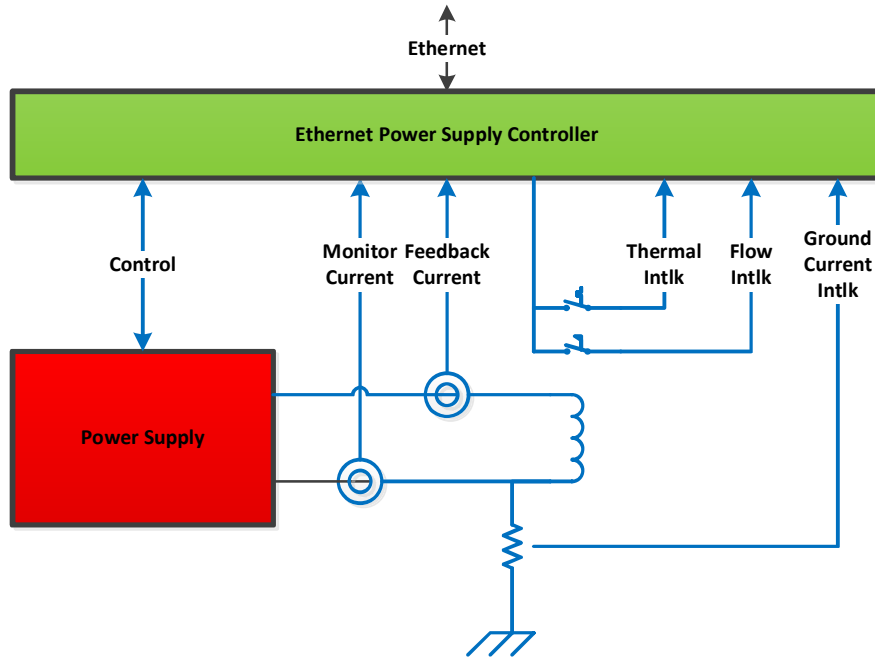


Figure 7. Intermediate power supply diagram.

Trim type power supplies (Figure 8) are provided to magnets that require up to 40V and 30A and more than 0.01 percent current stability. The trim type power supplies are SLAC-designed, crate mounted, modular bipolar power supplies and are available in 1, 2, 6, 12 and 30 ampere ratings at 40 volts. These power supplies have assumed the name MCOR. In general, they will be used for low power magnets that have looser stability requirements, such as trim coils, small quadrupoles and correctors.

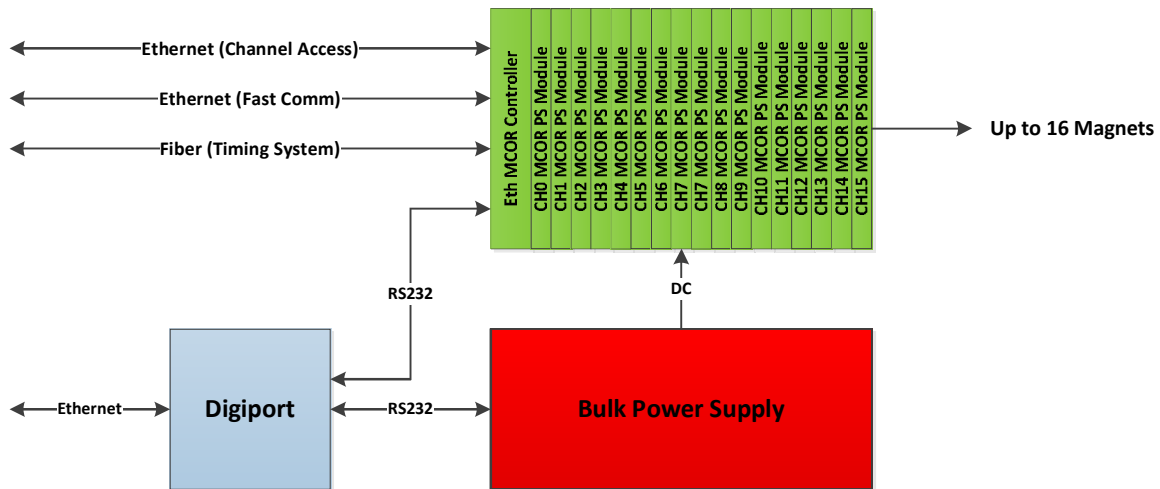


Figure 8. Trim Power Supply Diagram.

14.4.3 Power Supply Controls

The LCLS-II EPICS magnet power supply controls are, in many cases, a copy of the LCLS-I power supply controls. The power supply controls software can be run on three different platforms: VME processors running the RTEMS real time operating system, soft IOC running on Red Hat Linux servers, or COM-X processors running RT-Linux operating system.

The COM-X is an embedded processor onboard the new SLAC MCOR Slot-00 Controller which is currently under development and can be used for low current power supplies. This board also contains an embedded event receiver (EVR), which shall be used to provide pulse identification and timestamp information. This capability may be used in the fast feedback system to both read and actuate the setpoint of a magnet at 120Hz, or for BSA. The SLAC MCOR controller will be capable of controlling up to 16 magnets per crate, in addition to a single bulk power supply.

14.5 Low Level RF Controls

The requirements and proposed high-level system architecture for the LLRF controls of the superconducting linac are presented in Chapter 6, Section 6.9. During the preliminary design stage, we will also review LLRF controls at other laboratories that have similar requirements. For example, the architecture and control electronics for the DESY XFEL, which is Micro-TCA-based with intra-pulse feedback on the 4 MHz pulse train, could potentially work for the 1 MHz CW LCLS-II Linac.

14.6 Undulator Controls

The variable gap undulators will require an expansion and modification of the LCLS-I undulator control. The details of motor control for adjusting the undulators will be different from that used in LCLS-I, but the scope of the work is equivalent.

14.6.1 Undulator Motion Control

The LCLS-II undulator motion controls involves controlling the variable gap undulators (Figure 9), the inter space cams, and the phase shifter (Figure 10).

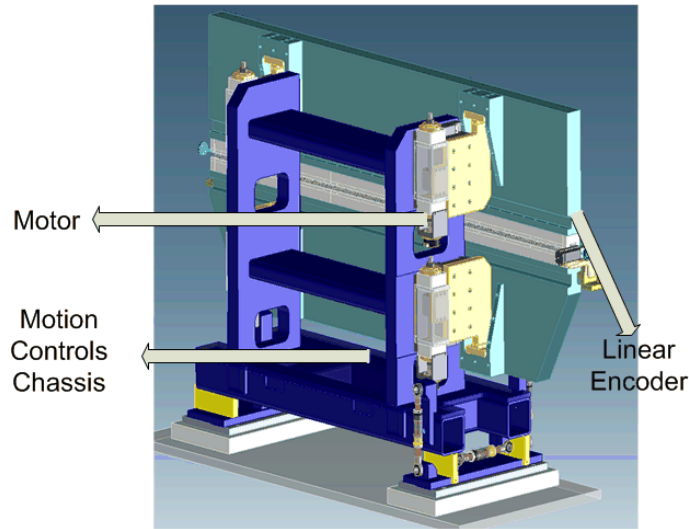


Figure 9. Variable gap undulator.

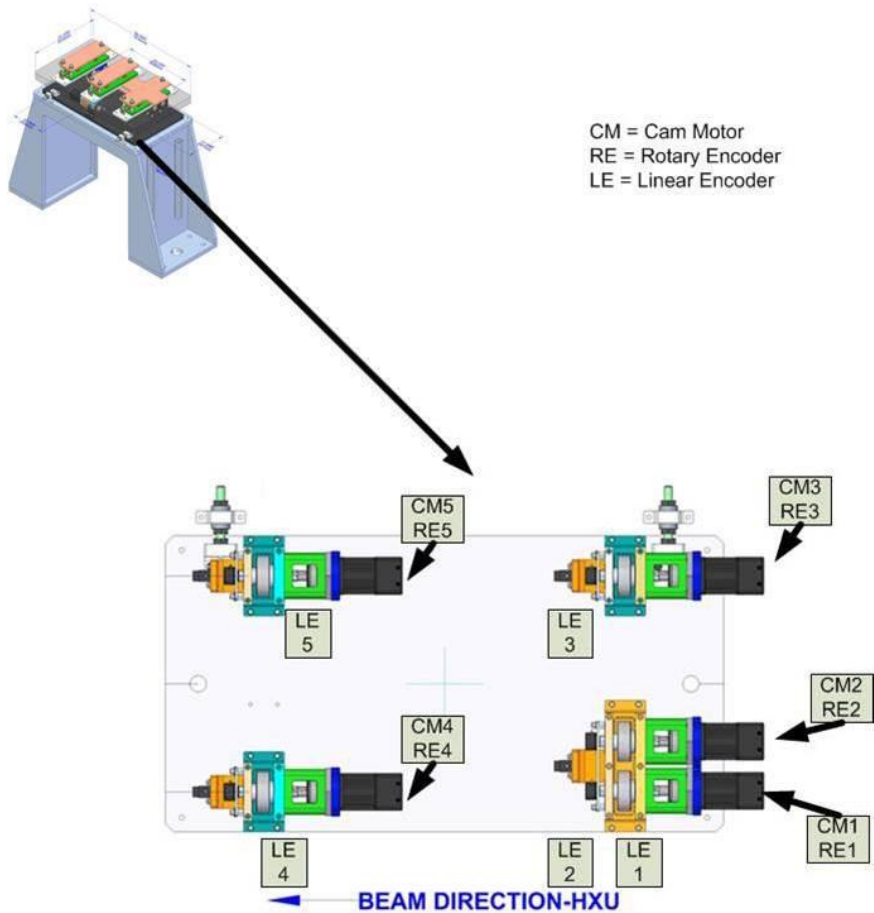


Figure 10. Inter-space motion controls.

Each variable gap undulator will use four motors and a number of position encoders to adjust the gap distance. The system also includes limit switches and emergency stop buttons. The

interspace girders are adjusted using five cam motors and a number of position encoders. The controls for each undulator and interspace will be integrated into a single system that interfaces to an EPICS IOC. A temperature monitoring system will also be integrated into each undulator control chassis, which connects to sensors mounted on the undulator and interspace. An overview of the undulator controls architecture is shown in Figure 11.

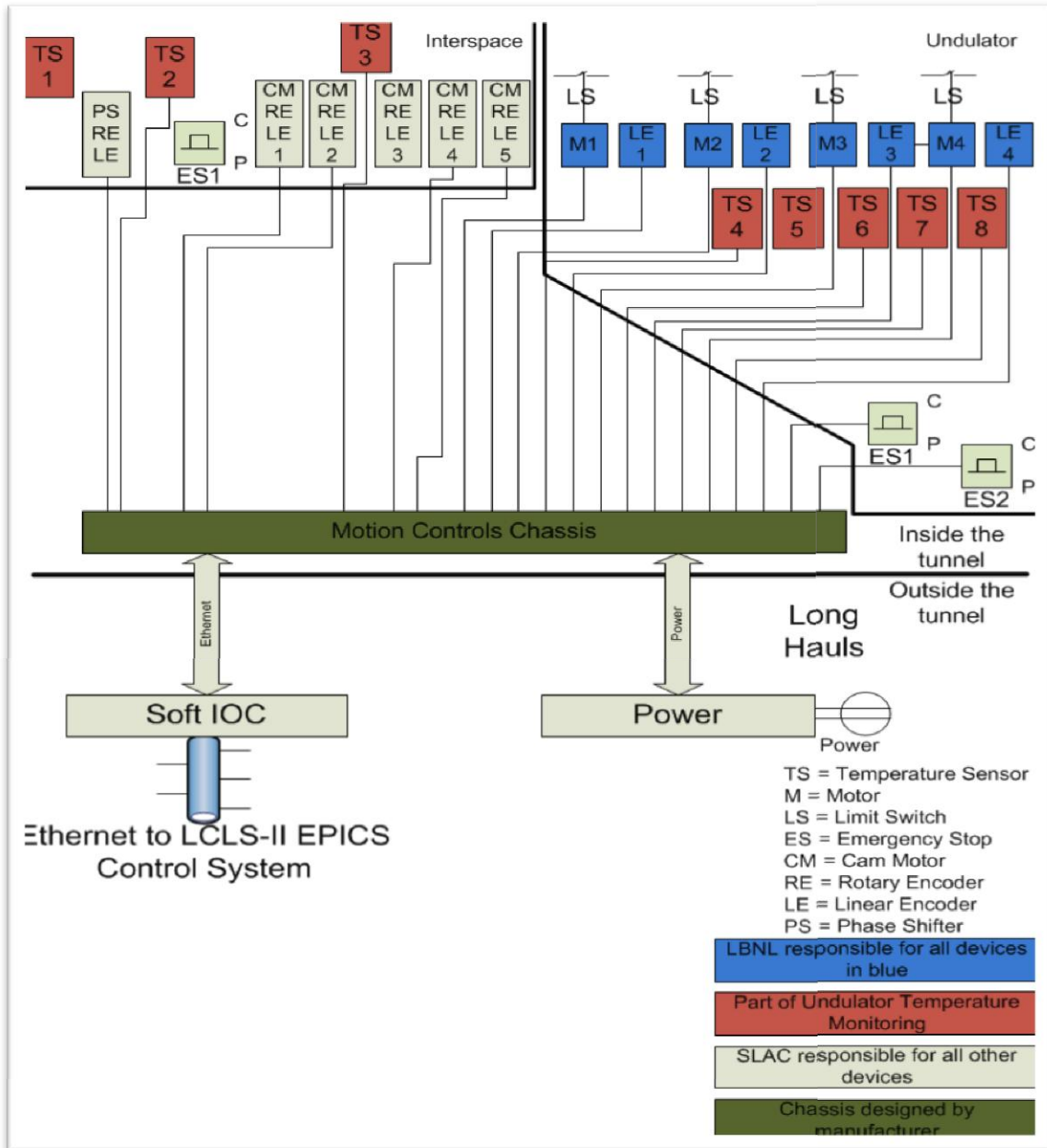


Figure 11. Undulator system diagram.

14.6.2 Undulator Temperature Monitoring

14.6.2.1 Requirements

The temperature of each undulator segment must be monitored redundantly. Each of the two jaws needs to be equipped with three independent temperature sensors, each at a resolution of less than ± 0.05 K. The drift shall be less than ± 0.1 K per month.

14.6.2.2 Design

The LCLS-II undulator temperature monitoring system will provide three temperature sensors for each undulator. It will also provide a minimum of three additional sensors for each undulator/phase shifter/quadrupole/BPM assembly. The additional sensors will be placed in locations likely to have temperature changes, such as quadrupole windings or motors. In addition, this system will provide a minimum of two air and two in-wall sensors.

14.7 Beamline Instrumentation and Controls

14.7.1 Vacuum Control System

The LCLS-II vacuum controls will use the same proven design as LCLS-I. The LCLS vacuum system can be separated into two parts: mechanical vacuum devices and controls vacuum devices. Mechanical devices are those that are physically part of the beamline or waveguide: vacuum valves, vacuum gauges, and vacuum pumps. Controls devices are the remaining hardware needed to build a complete vacuum system: controllers for the vacuum valves, gauges, and pumps; devices used to perform interlocking functions; and the vacuum portion of the EPICS control system.

The vacuum control system will automatically close vacuum valves in order to isolate beamline regions where vacuum pressures exceed allowable limits. The allowable pressure limits will be user modifiable and have capabilities for user bypasses should hardware become faulty. The system will report valve obstructions to the Machine Protection System (MPS) in order to prevent beam from damaging vacuum equipment. The vacuum controls will have interlocks associated with the RF waveguides and shut off klystron modulators when pressure thresholds are exceeded.

14.7.1.1 Vacuum Controls Architecture

A programmable logic controller (PLC) is a small and rugged computer with various input and output cards, widely used in factory automation. The vacuum control system (Figure 12) uses PLCs to monitor and control vacuum devices and to perform interlocking functions. An EPICS soft Input Output Controller (IOC) performs auxiliary control functions and provides an interface to the LCLS global control system.

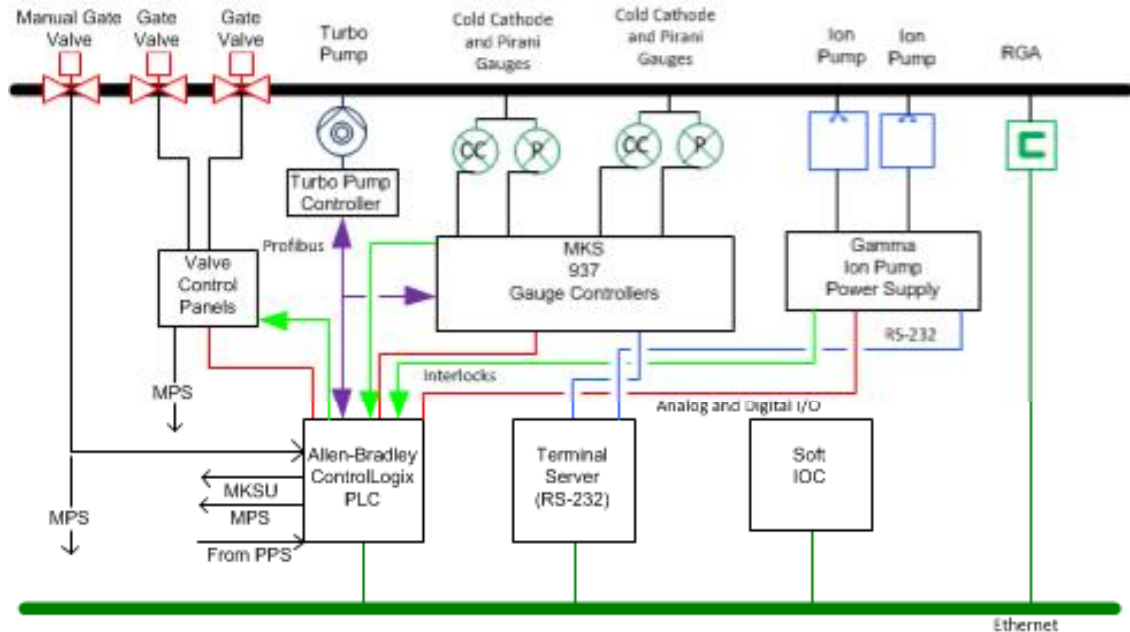


Figure 12. Block diagram of vacuum controls hardware.

The IOC supervises the PLC, which enforces interlock functions. The vacuum PLC serves two purposes: it is the primary control system interface for status and control of vacuum controllers, and it performs vacuum interlock functions. The PLC communicates to the controllers using 24 V digital, 0-10 V analog signals, and Profibus. The PLC communicates to the EPICS control system via EtherNet/IP, an Ethernet industrial protocol. The soft IOC, a Linux process running on a centrally managed server, communicates with vacuum devices in two ways: (1) The IOC sends commands to and receives status from the PLC over the Ethernet using the EPICS Ether-IP driver; and (2) The IOC communicates with some vacuum controllers via RS-232 serial links.

Controls will have similar features to LCLS-I, including operator interfaces, configuration save/compare/restore, data history, alarms and beam-synchronous data for the injector.

14.7.2 Controls System Interface to Cryogenic Plant and Conventional Facilities

The LCLS-II facilities controls will be based on the same system as deployed in LCLS-I. The facilities controls have three parts: facilities distributed control system (DCS) system, facilities HVAC system, and facilities EPICS interface. The hardware and primary control will be handled by the facilities HVAC and facilities DCS control systems, and the EPICS controls will have read access to most of the system and in some case have write access to facilities controls set points. While at this time it is expected that the cryogenic plant will be delivered with a dedicated PLC-based control system (see chapter 15), the controls system interface to the plant and cryogenic distribution will need to be developed including the monitoring of temperature, pressure, flow rates, etc. The EPICS interface to the facilities control system will be based on standard PLC industrial protocols, such as EtherNet/IP, BACnet, and ModBus TCP/IP.

14.7.3 Basic Motion Controls

Basic motion control for collimators and movable beamlines will be implemented with LCLS-I designs as much as possible. Motion controls for wire scanners will be implemented with a new design, which decreases wire jitter and allows for increased scan speeds over the LCLS-I design. With the expected higher beam rate, the time that the wire scanners wire is within the beam must be carefully limited. Motion control designs will limit accelerator tunnel hardware as much as possible to limit controller exposure to damaging radiation.

14.7.4 Temperature Monitoring

Industrial temperature monitor hardware will be utilized as much as possible to monitor accelerator components. Resistance temperature detectors (RTD) will be the preferred sensors due to their increased accuracy over traditional thermocouples. When necessary, temperature signals will be interlocked to the machine protection system to protect hardware from beam-induced temperature damage.

14.8 Controls Software

The software to operate the entire accelerator will mostly be based on the successful three-layer LCLS-I model. The basic low-level device control uses the distributed EPICS control system software, and standard EPICS clients to provide functionality for operator interfaces, IOC management and data archiving. High-level control of the accelerator has been implemented at LCLS-I mostly using Java and MATLAB. A similar implementation is planned for LCLS-II, with the addition of the new functionalities of the emerging EPICS V4 standard.

14.8.1 Operations Software

14.8.1.1 EPICS Software

LCLS-II will continue to use the EPICS software toolkit, libraries and applications to host its distributed control system. It will also take advantage of some of the new service-layer APIs and tools becoming available in the next generation of EPICS, V4. LCLS-II will leverage the LCLS-I EPICS software IOC applications, EPICS modules, and EPICS client application codebases when possible and appropriate. LCLS-I currently has approximately 550 EPICS IOCs networked together to allow communication between the IOCs and other EPICS-based client applications and to provide control and readback for machine devices. EPICS IOCs execute various I/O and local control tasks by setting, reading, and performing math with PVs. “Hard” VME or mTCA-based IOCs perform most of the lowest-level digital and analog I/O to accelerator hardware systems by converting setpoint PVs into analog or digital input that the hardware accepts and, conversely, by converting analog or digital read backs from power supplies, cameras and other beam diagnostic devices into standard-format PVs. Process variables can be set or read back by any IOC or other EPICS client applications using the Channel Access (CA) network protocol.

The “soft” IOCs, hosted on Linux server machines, typically do not perform direct device I/O to accelerator hardware and contain the usual EPICS IOC software. Additional operator workstations and servers provide higher level control and operator interfaces to the systems, as well as perform data logging, archiving, and analysis. LCLS-I is approaching 2 million PVs, 160,000 of which are being archived; more PVs will be archived in the near future via the new EPICS archive appliance developed at SLAC.

14.8.1.2 EPICS Client Application Tools

Many EPICS CA clients as well as SLAC unique EPICS CA multi-facility client tools are used in LCLS-I operations (Table 2). LCLS-II will utilize the same or enhanced applications, when appropriate.

Table 2. LCLS-II will utilize the same or enhanced applications, when appropriate.

Category	Name
Display manager	LCLS-II will augment EDM for rapid development of control system graphical user interfaces (GUIs).
Channel access gateways	Provides access security, name translation, and one connection from many clients to one server.
Electronic logbooks	For operators, physicists and engineers
Machine state and analysis	Bumpless IOC reboot facility – auto-save
	Machine snapshot facility – save/compare/restore configurations.
	Archive appliance (up to millions of PVs) and archive viewers
	Message logging and message log viewer
	Alarm handling and alarm viewer
	Orbit display
	MPS status and history
	Strip tool and other PV diagnostic tools
	PV directory service
	Timing configurations
Model based applications	Model manager
	Linac energy manager
	Steering
Feedback framework	Slow transverse and 120Hz longitudinal feedback loops
	Fast 1 MHz beam-based feedback
MATLAB applications and toolkit	Support for physics group applications

14.8.2 Central Database

An Oracle Relational Database (Figure 3) hosts several databases in support of both operations and engineering teams, including snapshots of operational set points/read backs, machine model design lattice and model-run data, the operations electronic logbook, process variable (PV) data, device parameters, message log data, and machine fault history. Considerable engineering resources are required for management of EPICS-generated PVs and the numerous EPICS client application configurations, which need to incorporate them. PV configuration management automation will be enhanced to support the growing demands.

14.8.3 High Level Applications

As the EPICS software layer provides the infrastructure needed for individual device control and monitoring, high-level software is required for machine operation tasks involving multiple subsystems.

Most of this extensive set of high-level applications is fairly generic and will be used for LCLS-II, as it is not specific to the particular accelerator technology and the much higher beam rate. The main Java-based applications are SCORE (machine parameter save/restore function), LEM (energy dependent machine settings), and an XAL-based online machine model linked to an Oracle database. Plans are underway to replace XAL with a MAD-based online model using the MAD input deck as a single source for accelerator modeling. Furthermore, the new capabilities of EPICS V4 will be used to better integrate higher level accelerator diagnostics and control functions requiring a hierarchical view of the accelerator with the existing EPICS control system.

The 80 different applications written in MATLAB cover most measurement and machine tuning tasks (e.g., beam size, emittance and bunch length measurements, undulator characterizations and settings, as well as accelerator configuration changes). They are highly automated to enable reproducible and fast machine characterization and optimization. They will be adapted for future use of LCLS-II. The MATLAB toolkit contains application-programming interfaces (APIs) for machine control functionality, including setpoint/readback control for PVs, beam synchronous acquisition data, and PV allocation for computed physics data.

14.9 X-ray Transport and Experiment Systems Controls

The Photon Controls and Data Systems (PCDS) provide all the computing capabilities needed to operate the front end enclosure (FEE) and the LCLS instruments and to acquire and analyze the science data generated by these instruments. These three activities correspond to the three core PCDS subsystems: controls, data acquisition (DAQ), and offline analysis.

This section describes the controls and DAQ systems for new photon instruments, diagnostics and detectors that will be located in the Electron Dump, FEE, and experiment hutches. The offline storage and analysis systems are not in the scope of LCLS-II and will not be described in this document.

The core computing services for the LCLS-II photon data systems will be provided by LCLS-I. These include:

- Network file system servers for the user home directories, for the instrument operator accounts, for the user groups, and for the disk-less nodes.
- Disk and tape backups.
- Timing services, naming services, host configuration services, authentication services, web authentication, directory database.
- Experiment database, web server, electronic logbook, system monitoring, and logging services.

A simplified diagram of the photon systems networking is shown in Figure 13. Each instrument has its own controls network and its own DAQ network. Network traffic among the different networks and with the accelerator is managed by the LCLS-I router in the NEH server room. Only one instrument is shown. The bold lines represent Infiniband-HDR connections. The thin lines represent Ethernet (1 Gb or 10 Gb) connections. The blue boxes are IB-HDR switches; the grey boxes are Layer-2 (L2) Ethernet switches.

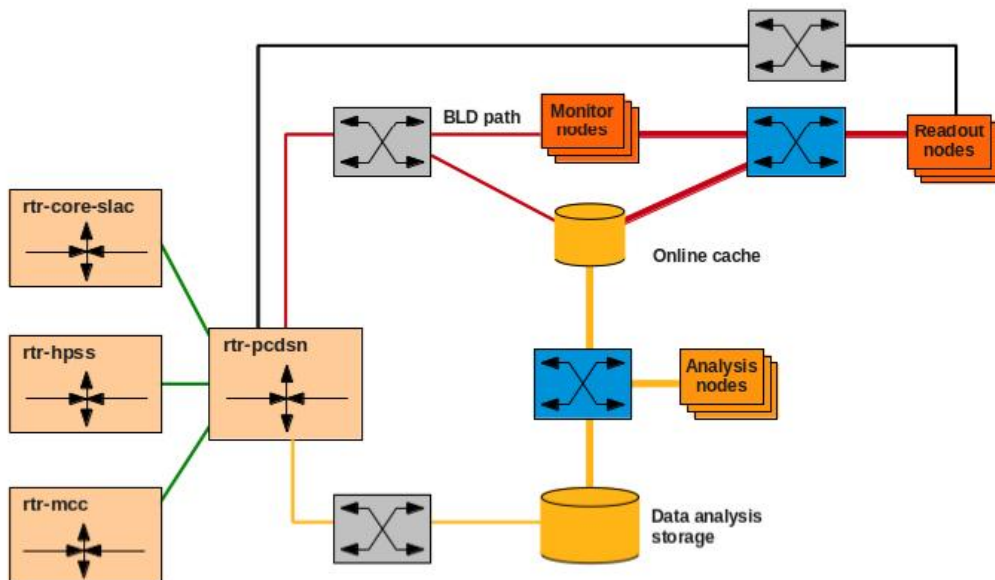


Figure 13. Simplified diagram of the photon systems networking.

14.9.1 Front End Enclosure

14.9.1.1 Guidelines

Instruments: FEE-II will reproduce LCLS-I instruments where they match the requirements. Currently these include the gas energy monitors, gas and solid attenuators, spectrometers, and

pop-in YAG-cameras. There will be technical improvements based on LCLS-I experience, and where kHz-MHz readout is required (gas energy monitors and spectrometers). This incremental approach will significantly reduce engineering and cost risks.

Machine Protection System (MPS): Two types of MPS inputs are foreseen for LCLS-II: Fast signals (μs latency) and slow signals (ms latency). See Section 14.10.3 for details. The mitigation for photon system MPS faults is to turn off the e-beam, since there is no photon shutter that is fast enough. Photon controls will use a network of analog, digital, and position inputs, connected via EtherCat to a central PLC (one for the SXR beamline and one for the HXR beamline) to monitor the slow MPS signals and relaying appropriate inputs to the MPS link-nodes. Fast signals will be input directly to the link-node. The increased beam power of the MHz machine will require water-cooling of all elements that may see beam (slit blades, mirrors, yag-crystals, collimators, stoppers). The MPS-PLC will monitor a network of chilled-water flow meters and thermocouples in addition to slow valves, solenoids, position switches, and absolute encoders. MPS systems on the SXR and HXR beamlines will operate independently (wherever possible) so that a fault on one beamline does not prevent photon delivery to the other.

14.9.1.2 Instruments

The controls for the soft X-ray line and the hard X-ray line instruments are described in Table 3. Generous space will be provided for equipment racks throughout, keeping cable runs short. Thermocouples and pressure/temperature/flow transducers for N₂, H₂O, and compressed air will be provided.

Table 3. FEE2 Instruments.

Instrument	Components	QTY	QTY	Comments
		SXR	HXR	
Slits	Motion	2	2	
Gas detector	HV; LV; pressure; gas handling; digitizer; pumping	2	2	PLC-based 100 KHz readout
Gas/solid attenuator	Pressure; gas handling; digitizer; pumping; motion	1	1	PLC-based
Flat mirrors	Motion	2	2	Possibly with added Piezo and/or feedback
K-B mirrors	Motion	1	-	Possibly with added Piezos
Spectrometer	Motion; 1D-Detector		1	100 KHz readout of a 1-dimensional strip detector
K-Monochromater	Motion		1	Possibly with added Piezos
Imagers	Motion; camera; illuminator	4	3	With zoom and focus lenses; 120Hz
Vacuum	Pumps/gauges/valves	1	1	PLC with EPICS monitoring

14.9.2 Data Acquisition

14.9.2.1 Guidelines

Architecture: The Data Acquisition (DAQ) system will use an updated architecture based on the LCLS-I DAQ system. A diagram of this architecture is shown in Figure 14. Each instrument will have a dedicated DAQ system with a dedicated network. Each of these systems will be built on an IB-HDR (Infiniband/high data rate) network. One or more console nodes will be installed in the control room, a set of readout nodes in the instrument hutch, and a set of data cache and monitoring nodes. The cache/monitoring nodes will be located within 10m of the readout nodes so as not to exceed the maximum practical IB range.

Data rate: The data acquisition system infrastructure will be scaled to accept the kHz-MHz data rate of LCLS-II. In addition to the network backbone upgrade to IB described previously, offline data storage and processing will require significant increases in both capacity and throughput.

Scope: The LCLS-II DAQ will be of sufficient capacity to read, process and monitor data from four 1-dimensional detectors (gas detectors, spectrometers, TOFs, etc.) for a total of 10-thousand elements at 100 KHz, as well as a single mega-pixel X-Ray camera at 1 kHz. The offline storage and analysis systems are not in the scope of this document.

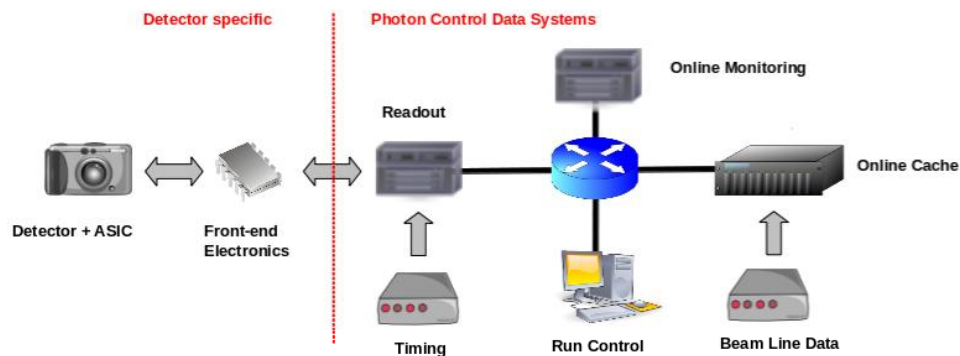


Figure 14. DAQ diagram: architecture of the data acquisition system.

14.9.2.2 Data cache

The data cache nodes store the components received from the different readout nodes in the local file system. These nodes form the online data cache, isolate the DAQ system from users operations and allow the experiments to take data even during outages of the offline system.

The data files will be copied over high speed links from the online cache to the offline storage, where they are made available to the users for offline analysis and for offsite transfer.

14.9.2.3 Monitoring

The online monitoring is implemented by snooping on the multicast traffic between the readout nodes and the data cache nodes. Users will be able to augment the existing monitoring features by dynamically plugging in their code to the core-monitoring framework.

14.9.2.4 Controls System Interface

The DAQ system will be able to interface to the control system in order to store user-selected EPICS process variables together with the science data and to control any device that can be used to perform a scan or a calibration run.

14.9.2.5 Timing System Interface

The existing LCLS-I timing system will be reused (with modifications, see Chapter 13) in LCLS-II.

14.9.2.6 Beam Line Data Interface

Beamline data (BLD) must be transmitted on every LCLS shot and archived together with the rest of the science data. The sources of the beamline data are the FEE gas detectors, the phase cavity, and the accelerator fast feedback system. The BLD contributions of the latter system are the charge, energy and position of the electron beam. These data are used by the scientists to refine the energy and the precision of the beam arrival time on a pulse-by-pulse basis.

Time stamped beam information contained in User Datagram Protocol (UDP) packets is sent via multi-cast to MCC and the experiments interested in it. For LCLS-II there will be two sources of beamline data from FEE to describe the beam parameters, one for each beam-line (SXR/HXR). The same technique as LCLS-I will be used to collect and package these beamline data.

14.9.2.7 RF Cavity Timing

In order to provide timing to the instruments, an updated version of the RF cavity system currently in operation in the LCLS-I Undulator Hall (UH) will be provided for each line of LCLS-II's UH (see Chapter 9).

14.9.3 Relocation of AMO and SXR Instruments

The controls hardware currently in hutch 1 and hutch 2 of the NEH for the AMO and SXR instruments will be relocated to accept beam from the new soft X-ray branch lines. Four control racks will be relocated. Since the physical layout will be different, a new set of rack-to-instrument cables will be provided.

14.10 Safety Systems

Two independent systems — the Personnel Protection Systems (PPS) and the Beam Containment System (BCS) — protect people from accidental exposure to high power beams and radiation. A third system, the Machine Protection System (MPS), is used to protect accelerator equipment. These systems exist for the present LCLS and linac configuration but will be

substantially altered to accommodate the new beamlines and much higher beam power of LCLS-II. In addition to changes in detail, the overall rigor of the systems will be strengthened due to the higher severity of potential accidents. A high-level overview showing these systems is given in Figure 15.

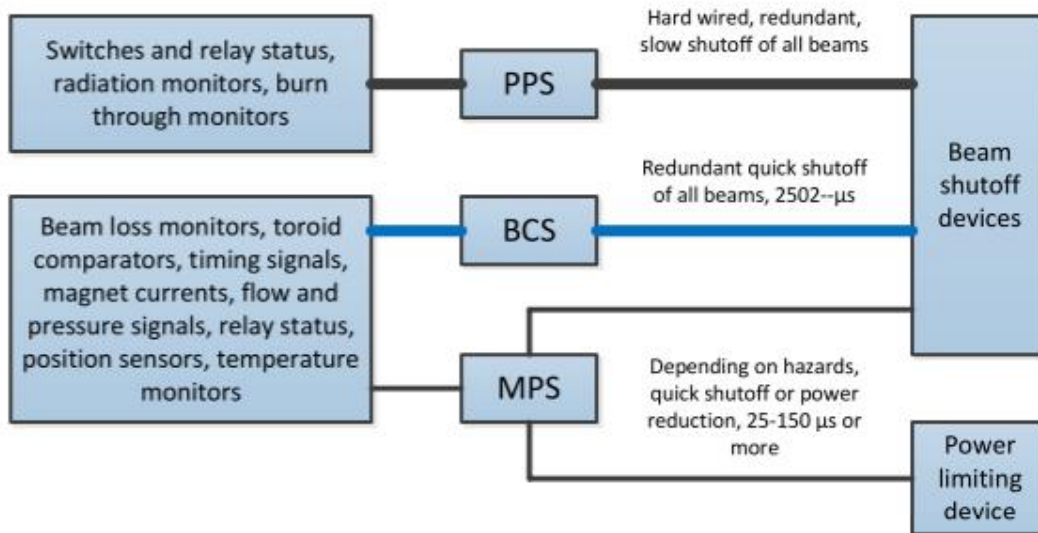


Figure 15. Overview of Controls for Safety Systems.

Safety systems must respond to two main types of hazards. One occurs when beams go astray. Such beams can quickly damage equipment, and they can produce intense radiation fields that are not adequately shielded, thus endangering people outside the radiation area. The other type of hazard occurs when the beam power runs away. In this type of event, the beam may damage a dump and also produce more radiation than the shielding can safely attenuate. The necessary response time and action to be performed depend on the specific safety system and hazard.

Table 4. Response Time Requirements for the Safety Systems for Controls

System	Response Time	Type of Response
PPS	≤ 5 s	Shut off all beams and the high power RF system
BCS	≤ 100 μ s	Shut off all beams
MPS	≈ 150 μ s	Limit beam power

Required response times and actions to be performed for the safety systems related to controls are given in Table 4. The response time is the time between when an event occurs and the time a response is performed by the appropriate devices. In the case of the PPS and BCS system, the response is to turn off all beams. In the MPS case, depending on the location and

severity, the response may be to reduce the beam power by dropping back to a less powerful beam mode (see Chapter 3), or turning off the beam in the most sensitive cases.

The required response time for the PPS system is relatively slow since it deals with access control. The time it takes a person to traverse the shortest distance from outside the accelerator enclosure, through the maze or shaft, to a point where the dose is not meaningfully shielded is estimated to be around 5 seconds.

The BCS system has to deal with the cases where a kicker, suddenly and erroneously puts a high power beam precisely at one point on a protection collimator or erroneously sends a high power beam to a low power dump. In these situations, the collimators and dumps could be damaged by the highly concentrated thermal load, and the beam must be turned off quickly. A conservative estimate of the time to damage a copper collimator with a 1.2 MW LCLS2 beam and minimum beam size range is about 25 μ s. This may be challenging to attain in all cases, particularly since the gun is roughly 3,500 m from the main beam dump. Aluminum collimators or beam dumps would not be nearly as sensitive, and by the same estimate can withstand the worst case beam for at least 100 μ s.

In the MPS case, the response varies depending on the MPS fault and the components at risk. Where the hazard is radiation damage, speed is not an issue, but proper integration or averaging of the radiation levels is needed. Devices which require the fastest response time are those that might be exposed to misdirected beams, such as vacuum chambers, septa, or halo collimators. Just as in the BCS case, these will require a response times ranging from 25 to 150 μ s. Superconducting cavities may intercept mis-steered beams. In addition to the hazard of damage the Nb surface there is a potential for excessive energy deposited into the cryogen system, which could cause an extended disruption. The MPS cannot be made sufficiently fast to avoid quenches, but can prevent more serious damage and allow rapid recovery from a quench.

14.10.1 Personnel Protection System

The radiation safety system (RSS) [3] protects personnel from prompt radiation due to accelerator operation. It is comprised of an access control system (ACS) and a radiation control system (RCS), as modeled in Figure 16. In general, an ACS is “a control system that prevents or controls access by personnel to hazardous areas deemed unsafe due to prompt radiation production. It includes engineered and/or administrative systems” [4]. The ACS for electron beam enclosures is implemented using engineered PPS. The ACS for photon beam enclosures are similarly implemented using an engineered hutch protection system (HPS).

The access control system typically interfaces with circuit breakers and power supply contactors controlling the power to prompt ionizing radiation sources. For some radiation control system functions, using the circuit breakers and power supply contactors already used by the ACS is an efficient choice. In this way, the engineered PPS and HPS for LCLS-II will continue to serve both ACS and RCS functions.

Most of the PPS design concepts for the LCLS-II PPS are already in place for the linac and LCLS-I PPS. The major changes for the LCLS-II PPS designs are reengineering of control circuits and modernizing the electronics for the additional hazards to personnel from high-power beam operations in the linac through Beam Switch Yard (BSY). This would include reintroducing radioactive gas monitors [5] at linac and BSY exhausts as well as adding neutron probes to the Beam Shut Off Ion Chambers (BSOICs) used to detect the radiation levels outside of the enclosures [6].

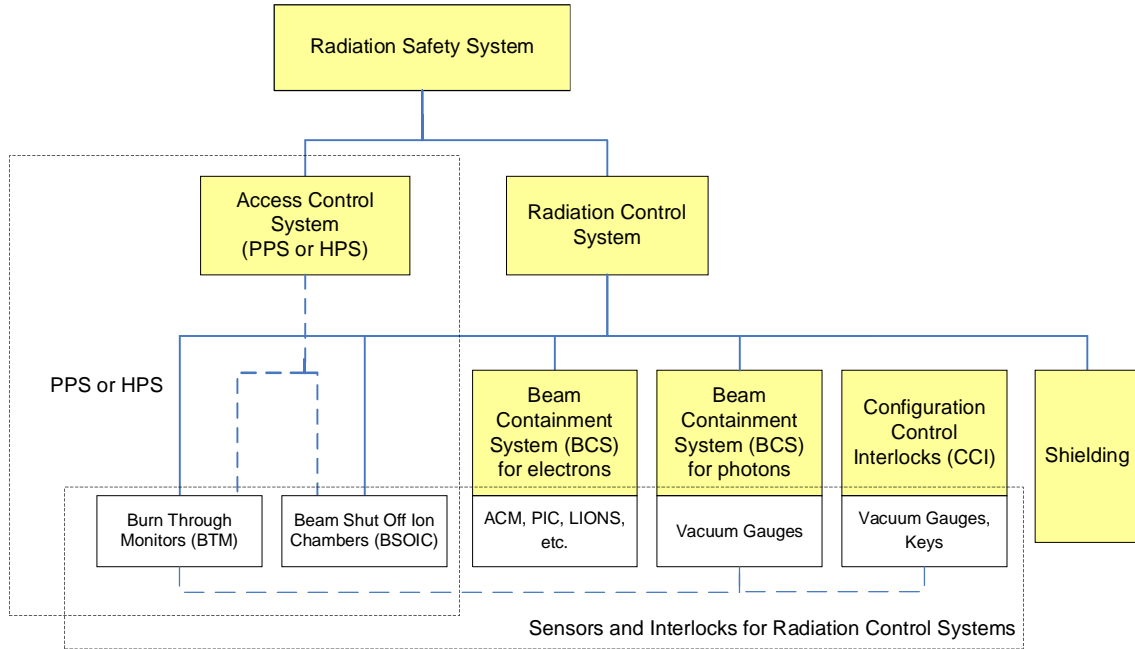


Figure 16. SLAC Radiation Safety Systems Model.

The existing accelerator will require some changes to the allowed operational modes. The current program using the CID gun at the start of the 2 mile accelerator requires, at a minimum for normal operations, that all zones from the injector through BSY be searched, secured, and timed out with a sequence of audible and visual warnings before the gun and RF can be operated in the LINAC.

As shown in Figure 17 LCLS-II beam operations will require the injector through Beam Switch Yard (BSY) and Beam Transport Hall West (BTHW) through Frond End Enclosure (FEE) zones be searched, secured, and timed out with a sequence of audible and visual warnings before the gun and RF can be operated [7]. Chapter 17 includes further details about new shielding and minimum exclusion zones in the research yard (at a minimum, access to the tunnel roof must be prohibited during LCLS-II beam operations).

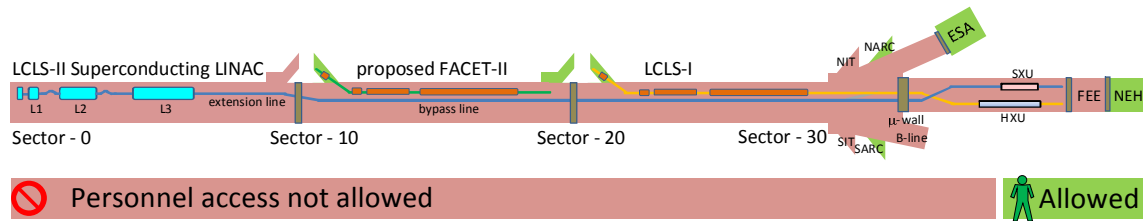


Figure 17. Minimum exclusion zone during LCLS-II normal beam operations.

To minimize the recovery of machine operations after a housing access, there are currently some operational modes that allow limited subsets of hazards to remain on when certain restrictions are met. For example, a Sector 0-gun local mode allows the operation of the existing gun for tuning purposes, but only while injector-area stoppers are inserted to contain the low-energy beam. LCLS-II will similarly have a local mode for low energy beam tuning purposes in the injector, as shown in Figure 18, allowing access to areas downstream of the Sector 10 shield wall [5]. This machine mode allows access to all of the LCLS-I and proposed FACET-II areas while the LCLS-II gun is operational. To prevent the delivery of LCLS-II beam to downstream areas, there will be multiple stoppers to contain the beam within the first third of the LINAC, and all of the LCLS-II RF power supplies downstream of the stoppers will be turned off.

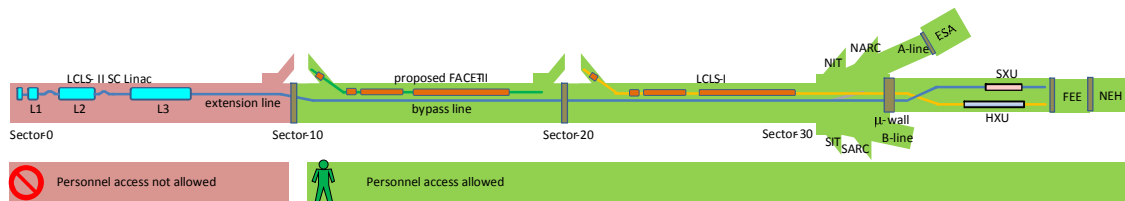


Figure 18. Reduced exclusion zone during LCLS-II low-energy gun-only operational mode.

To implement the changes, some existing PPS zone systems will be modified, and others will be replaced. The ACS hardware for the injector through LI10 shield wall will be a mix of repurposed and new cable plant, interlocks, and relays or safety PLCs for the zones. The remainder of the linac will continue to use the existing relay-based systems for access control. The areas from the BSY muon shield wall through the FEE use programmable safety-relays, allowing for simpler engineering efforts to modify than for an area such as the BSY, which is currently relay-based. For the NEH areas, the Hutch Protection System (HPS) designs use programmable safety-relays with logic that is organized per beamline. This approach would be expanded to accommodate each new beamline in the NEH area.

Key high-level circuits that logically group together the PPS zones and thereby control the hazards in the linac were upgraded in 2010 to redundant safety PLCs that can be reprogrammed with minimal new hardware installations. The high-level circuits will be changed to add new

interlocks and logic for the LCLS-II injector gun, Linac RF power supplies, as well as new RF kickers and deflector cavities.

14.10.2 Beam Containment System

The Beam Containment System (BCS) is a safety system that keeps potentially dangerous accelerator beams within their prescribed channels and within allowed power limits, and hence prevents the generation of excessive level of radiation within occupied areas. The BCS also protects the integrity of safety-related beam line components. It performs this function by monitoring beam power and beam loss, and shutting beams down if a limit is exceeded.

A fault in the BCS will prevent delivery of all beams by three independent methods. The required shut off time is between 25-100 μ s.

The BCS for LCLS has been upgraded as part of a SLAC-sponsored project, and the upgraded designs will be incorporated into LCLS-II. Most notable is the introduction of networked programmable logic controllers (PLCs). As shown in Figure 19 the system has both a fast as well as a “slow” shutoff path. A similar or modified system may be deployed for LCLS-II.

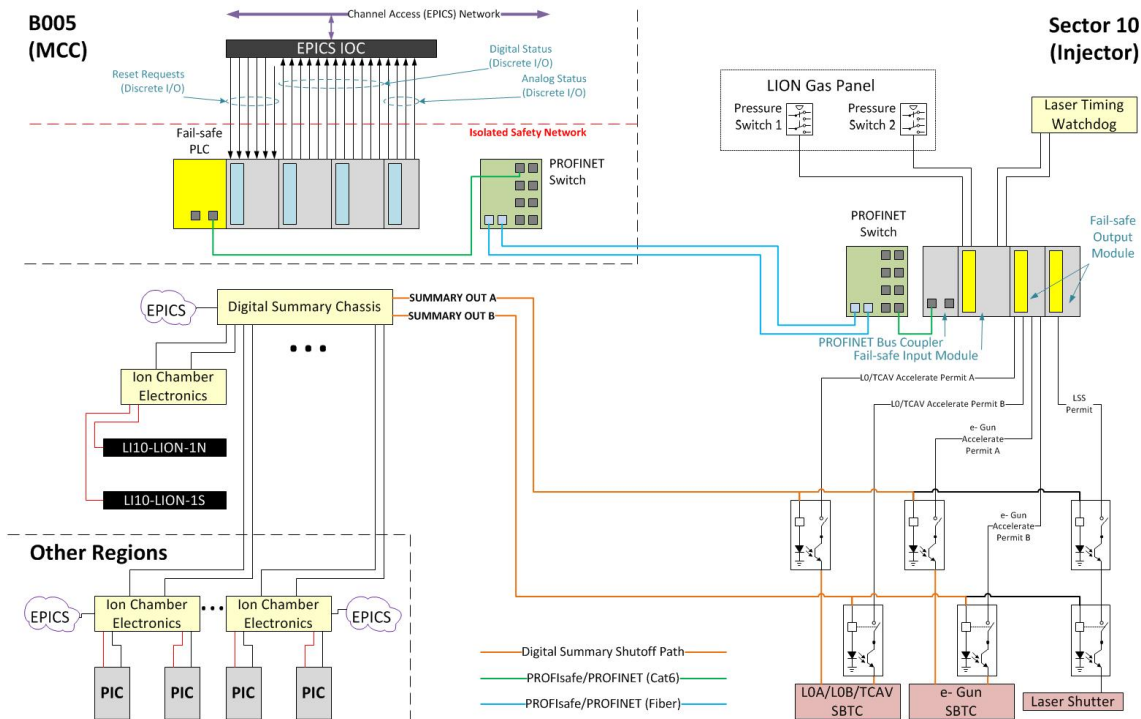


Figure 19. A model of a BCS networked PLC system.

14.10.2.1 BCS Sensors

Currently BCS uses seven types of sensors. New types may be needed for LCLS-II.

1. Protection Ion Chamber (PIC): Typically situated on or near the mechanical device, such as PPS stoppers, that is to be protected.
2. Long Ion Chamber (LION): Typically installed along the inside walls of the accelerator housings where shielding is inadequate.
3. Flow switch & meter installed in cooling water systems for dumps, collimators, and slits.
4. Pressure switch: Installed in PIC and LION gas systems.
5. Microswitch: Used to confirm the correct position of mechanical beam line components.
6. Current Transducer: Used to monitor current in magnet power supply.
7. Toroid: Current transformers that produce an output proportional to beam current.

14.10.2.2 BCS Shut-off Mechanisms

Beam shut off mechanisms comprise a key component in the BCS. There shall be three independent shut off mechanisms for the LCLS-II, which mirrors the requirements for LCLS-I as recommended in the *SLAC Radiation Safety Systems Technical Basis Document*:

1. A dedicated BCS Pockels Cell and mechanical shutter will stop laser light from striking the RF Gun cathode, stopping the production of beam. These shutters will be situated as close to the production point of laser light as practicable.
2. To shut off the beam in 25 μ s, starting from the fault occurrence to no beam delivered will require inhibiting the gun. This will need careful analysis of the time it takes the VHF normal-conducting-radio-frequency (NCRF) gun referenced in Section 5.4 Electron Gun and Buncher to stop beam production.
3. To prevent beam or dark current acceleration, the RF in the accelerator must be set to a staggered standby state.

In some cases a BCS fault in either LCLS I or LCLS II could require both LCLS I and LCLS II to be shut off.

14.10.3 Machine Protection System

The role of the machine protection system (MPS) is to turn off the electron beam or limit the average power by lowering the repetition rate of the beam when a fault is detected. This measure is not a life safety system [see descriptions of Beam Containment System (BCS) and Personnel Protection System (PPS)], but is designed to prevent excessive losses of the electron beam, which would otherwise cause damage to sensitive machine components. Architecturally, LCLS-II MPS (Figure 20) will largely be a copy of the LCLS-I MPS with an additional fast shut-off layer. The MHz pulse rate of LCLS-II requires the MPS to shut off the beam in sub-milliseconds in order to protect accelerator components during major faults (Table 4). Faults requiring sub-millisecond shutoff will be classified as Level 1; the rest will be classified as Level 2 faults.

The MPS takes input from many different devices, such as vacuum valves, beam charge monitors, beam loss monitors, protection ion chambers, and beam position monitors (see Chapter

9 for more detail). These inputs are fed into the MPS via dedicated custom electronics boards (Link Node). Based on the severity of the input signals, the MPS may either rate limit or completely shut off the beam. The mitigation devices include the gun laser Pockels cell, the gun laser mechanical shutter and a downstream RF deflecting cavity located in the Beam Switch Yard. The deflecting cavity will distribute the beam to the soft X-ray and hard X-ray undulators or let the bunch pass to the straight ahead high power beam dump.

The choice of mitigation device to be used depends on the location of the fault, the type of mitigation desired (rate limiting vs. beam shut-off) and the fault level. Level 1 faults will be summarized internally in each MPS link node's internal FPGA, and a permit signal will be transmitted via a dedicated, fast connection to fast MPS supervisor FPGAs that collect the various MPS link node permit signals. The fast MPS supervisors relay the permit signal to the mitigation control link nodes. Two fast MPS supervisors will be implemented such that signal propagation times are minimized. A fast MPS supervisor will be located near the injector mitigation devices and one near the BSY's RF deflector. Level 1 fault logic will result in a global zero rate beam inhibit. Level 2 faults will be interpreted by the MPS processor to determine the appropriate response. The MPS processor is capable of processing Level 2 faults in complex protection algorithms, and will determine the allowable beam rate for each destination. All MPS faults and rate transitions will be logged to a MPS history system for postmortem analysis.

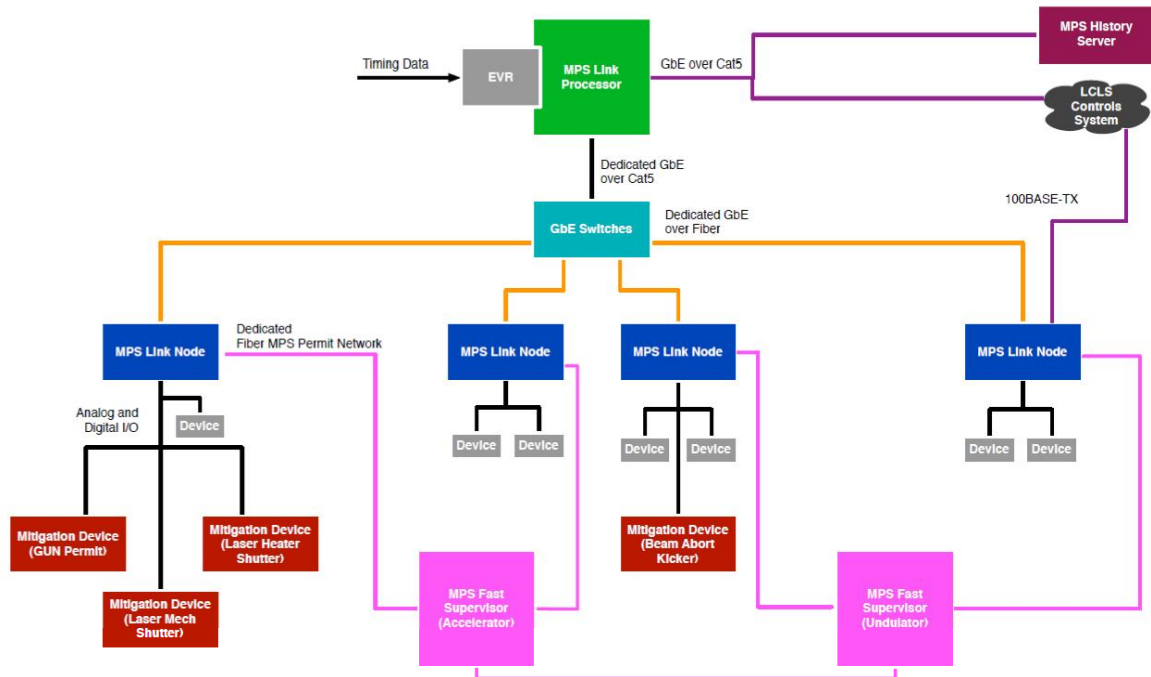


Figure 20. MPS System Architecture.

14.11 References

1. "OVERVIEW OF IMAGING SENSORS AND SYSTEMS USED IN BEAM INSTRUMENTATION", Enrico Bravin, Proceedings IBIC 2013, International Beam Instrumentation Conference, Oxford, 16-19 September 2013.
2. Photron Fastcam SA5, http://www.photron.com/datasheet/FASTCAM_SA5.pdf.
3. SLAC Radiation Safety Systems Technical Basis Document, ESH Division, SLAC-I-720-0A05Z-002-R004.
4. ANSI/HPS N43.1-2011 Radiation Safety for the Design and Operation of Particle Accelerators.
5. The Stanford Two-mile Accelerator, Chapter 2, Protection Systems, Section 3 Radiation Monitoring; Radioactive gas Monitor (GW).
6. RP-RPG-131119-MEM-03, "BCS Requirements for LCLS-II Project Electron Beamlines".
7. RP-RPG-131119-MEM-02, "PPS Access Requirements for LCLS-II Project."

15 INFRASTRUCTURE & FACILITIES

TECHNICAL SYNOPSIS

The LCLS-II infrastructure support system is based on the requirements of the technical systems to be installed in each area, as defined by the physical boundaries. Engineered design solutions will provide the infrastructure by taking advantage of the existing facilities at SLAC. LCLS-II will use the first third of the existing 3-kilometer-long linear accelerator (linac). A new injector will be installed in the Collider Injector Development area. The drive laser will be housed in the existing enclosure. The existing linac infrastructure will be re-used and supplemented with new systems to support the superconducting linac.

The beam transport segment, downstream of the injector, will be a combination of existing and new equipment. The linac between sector 0 and sector 10 will be replaced by a superconducting accelerator system. The resulting beam will be carried through the existing PEP II High Energy Ring (HER) transport line, with some modifications to the transport line through the Beam Switchyard. The new electron beam will continue through the existing Beam Transport Hall.

The Undulator X-ray Tunnel, which is comprised of the Undulator Hall, Electron Beam Dump, and Front End Enclosure, will house the undulator magnets, electron beam dumps, and front-end X-ray diagnostics and optics, finally delivering the new X-FEL light to the experimental stations at the Near Experimental Hall.

In the injector area, electrical power will be provided to meet the requirements for the new injector and accelerator section. Similarly, mechanical systems, including cooling water, ventilation and water collection systems will be modified as required to support the new installations.

The Beam Switchyard will be modified to accommodate the new beam line. The Beam Transport Hall and Electron Beam Dump will require local shielding and access control. Depending on the specific location, the modifications will consist of additional shielding made of concrete, iron, or a combination of concrete and iron based on radiation analyses. The Front End Enclosure will require structural modifications due to the additional beamlines. All areas from the Beam Transport Hall through the Front End Enclosure will require utility relocation and additional utility distributions for the new beamline. Two experimental hutches in the Near Experimental Hall will be modified to accommodate the XTES experimental stations. Utilities will be reconfigured to support the new experiments.

SLAC, as a federal facility, is required to comply with Executive Order (EO) 13423 “Strengthening Federal Environmental, Energy, and Transportation Management,” dated

January 24, 2007. The order sets goals in the areas of energy efficiency, acquisition, renewable energy, toxics reductions, recycling, renewable energy, sustainable buildings, electronics stewardships, fleets, and water conservation. The proposed LCLS-II project will comply with EO 13423.

15.1 Introduction and Overview

The infrastructure systems to be provided include mechanical wet and dry side utilities, electrical power, compressed air, and specialty gases. The existing injector area, referred to as Collider Injector Development, or CID, will be reconfigured, and a new injector system will be installed for the superconducting RF cavities. The linac tunnel between sectors 0 through sector 10 will be outfitted with piping, cabling, and ventilation to support new installations and to meet the current building codes and federal requirements. The necessary existing infrastructure will be re-used where possible. Infrastructure that is replaced will comply with applicable codes. The Beam Transport Hall (BTH) crosses the Research Yard (RSY) and connects to the Undulator X-ray Tunnel (UXT). The UH extends under the ridge between the RSY and the Electron Beam Dump (EBD) and Front End Enclosure (FEE) complete the (UXT). The Near Experimental Hall connects to the FEE and is where new experimental stations will be installed (See Figure 1). The scope for infrastructure and facilities includes the SLAC effort for commissioning the reconfigured and new infrastructure systems.

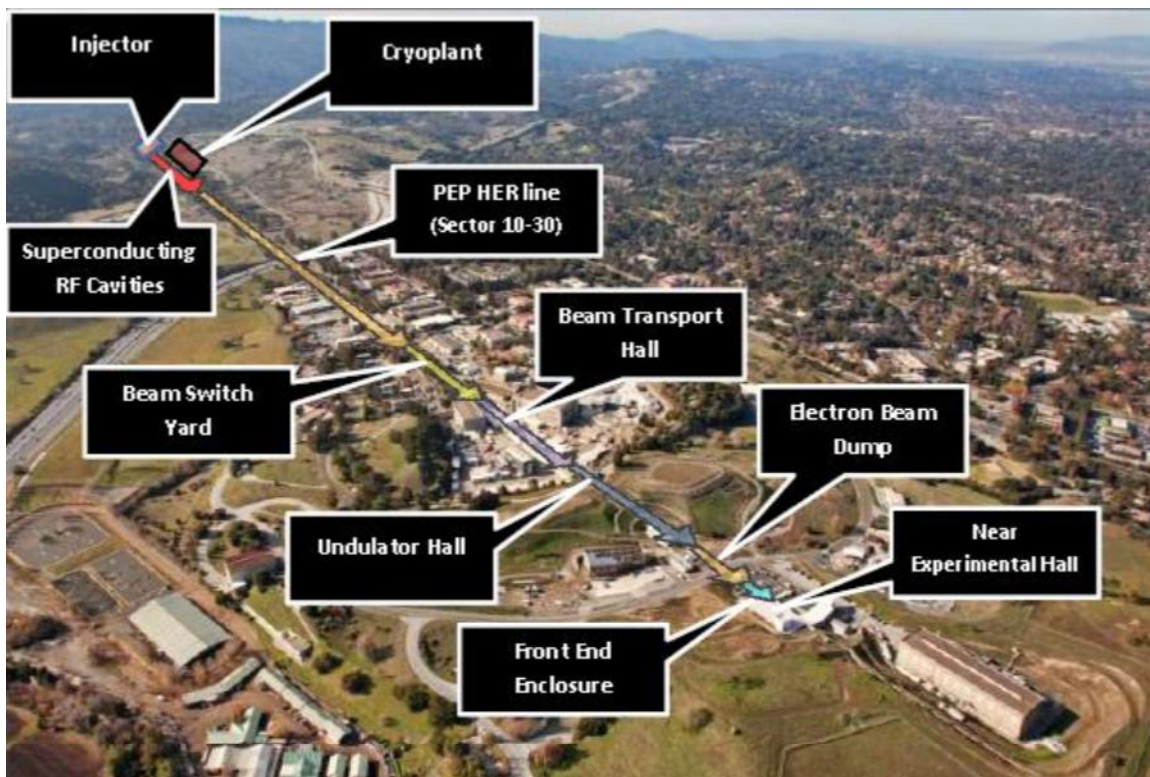


Figure 1. LCLS-II Location Plan.

15.2 Infrastructure Requirements

This section describes the infrastructure requirements for the LCLS-II project for each affected area, starting from the injector and proceeding to the experimental stations.

15.2.1 Injector

The project includes the reconfiguration of the existing infrastructure supporting the injector located west of the Klystron Gallery in preparation for the installation of a new injector in the CID.

The scope includes the reconfiguration of the existing utilities inside and surrounding the injector facility, and preparation for connecting the new components.

15.2.1.1 Mechanical

The injector facility requires conditioned spaces and process cooling. The existing HVAC system will be modified as necessary to provide cooling for HVAC and process cooling water. The HVAC system will provide stable temperatures and humidity control for the spaces. Cooling systems are required for injector, laser, accelerator, waveguide, and bunch compressor systems.

15.2.1.2 Electrical

The available electrical power is adequate for the injector. Electrical systems will be cleaned, repaired and prepared for re-use. The new components will be connected to serviceable breakers, panel boards and motor control centers.

15.2.1.3 Fire Protection

The existing fire protection and detection systems will be preserved. Fire extinguishers will be provided in accordance with NFPA 10 throughout the injector facility. The injector facility will meet current life-safety standards, including one-hour-rated barriers and fire-rated exit doors. The access/exit doors will include an interlock that is integrated into the existing Personnel Protection System (PPS). Exit signs will be edge-lit with concealed lamp and integral lettering on a clear lens. Where low-level exit signs are required, they will be backlit and set flush with the adjacent wall.

15.2.2 Cryogenic Plant Infrastructure

The infrastructure requirements for the cryogenic plant are described in this section. A complete description of the cryogenics is presented in Chapter 6 on Superconducting Linac Technologies.

15.2.2.1 Civil

The new cryogenic plant to be installed near the west end of the linac is expected to be approximately 10,000 square feet in size, with roughly an additional 20,000 square feet of equipment pads, tanks, storage, and parking and outdoor equipment to be installed at various locations (see Figure 2). Civil infrastructure requirements include the reconfiguration of the north access road, leveling and grading for the cryoplant building pad, installation of the cryoplant structure, site improvements, storm water retention features and site restoration.

Approximately 30,000 cubic yards of soil will be excavated to provide a level area on which to build the cryogenic plant and appurtenant features. To the extent possible, the excavated material will be placed nearby to shield the site visually and acoustically.

New domestic water and sanitary sewer line laterals will be installed from main lines near the Klystron Gallery.

Storm water collection drains and piping will be installed in the cryogenics plant area. Section 438 of the Energy Independence and Security Act (EISA) of 2007 requires the project to maintain or restore, to the maximum extent technically feasible, the predevelopment hydrology of the property with regard to the rate, volume, and duration of flow. This dictates that a storm water retention basin be installed down-gradient of the cryogenics plant installation to collect the flow. Overflow from the retention basin will drain to the existing storm drain system in the vicinity.

Approximately 800 feet of the existing north access road will be relocated to the north of the new cryogenics plant area. This road will be designed to match the existing road.



Figure 2. Cryogenic Plant Site.

15.2.2.2 Mechanical

The cryogenic plant will require approximately 3,600 GPM of cooling tower water, which will be facilitated by using the existing linac cooling tower 1201. Cooling tower water lines will be provided at the cryogenic plant site.

Cryogenic piping (24-inch pipes) from the plant to the accelerator will make use of the existing 27-inch diameter linac penetrations which will be modified to accept the cryogenic piping.

15.2.2.3 Electrical

Cryogenic plant power provided by others from existing services, consists of double-ended, 12 KV-rated main substation/switchgear, powered by dedicated 12 KV feeders from the existing spare breakers located in the master substation at B016. Distribution of power for the warm compressors will come from the new 4160 V-rated, double-ended unit substations powered by the main substation mentioned above. Power for the various small compressors, pumps motors, HVAC, and others will be provided from new motor control center, powered from the new 480V-rated, double-ended unit substation mentioned above.

New electrical power for the new cryogenic equipment house power, cold box room power, and the local cryogenics control room will be provided from a new switchboard powered from the 480 V-rated unit substations used for powering the motor control centers mentioned above.

15.2.3 Linac Facility Sectors 0 through Sector 10

15.2.3.1 Mechanical

Existing mechanical systems in Sectors 0 through 10, including the Klystron Cooling System (KCS), Accelerator Cooling System (ACS), and Waveguide Cooling System (WCS) will be reconfigured to provide cooling the linac klystrons, waveguide, injector and bunch compressors, and electronics. The Sector 10 HER extraction line cooling system will be upgraded.

Ductwork and air distribution: Exhaust fans for all linac superconducting (SC) sectors will utilize existing ventilation system as possible.

Controls for process systems (LCW, PCW, CTW) will be available via the existing linac distributed control system. HVAC controls will be handled by the site-wide BACnet protocol DDC, integrated with EPICS for system monitoring.

Linac water cooling systems: Cooling is required for the klystrons, modulators, and for the injector and bunch compressors. Modulator and rack cooling will be provided in the Klystron Gallery. The waveguides will be temperature stabilized. Each sector has existing independent LCW cooling systems. The waveguide and klystron cooling systems will utilize the existing linac cooling tower water system. Cooling water will be provided for the injector and bunch compressors. The PEP-II HER transport line magnet cooling piping distribution system will be reused.

15.2.3.2 Fire Protection

The fire protection system includes a VESDA smoke detection and sprinklers for fire safety; a wet pipe system (NFPA 13) will be installed.

15.2.3.3 Electrical

All existing electrical systems will be reused to the extent practicable. Existing components and cables include: panels, bus ducts, lighting systems, controllers, transformers, disconnects, motor control centers, power distribution systems, unit substations and various other systems located in the gallery and the tunnel.

The lighting level shall be designed in accordance with recommendations from the Illuminating Engineering Society (IES) and will be suitable for the gallery area application. No new lighting is anticipated.

The fire alarm and detection systems will integrate with the existing campus network. The fire alarm and detection systems will comply with NFPA 72 and all associated codes and regulations.

The existing telecommunication system will be used to support voice, data and low-voltage networks.

15.2.4 Beam Switch Yard

The BSY modifications include the use of an existing beam dump for the new beam. The dump will be serviced by an existing closed-loop cooling system. This effort will require modifications of the selected beamline to accept the new beam. Cooling systems will be provided for the transport line bend and quadrupole magnets.

15.2.5 Beam Transport Hall

The existing BTH is constructed of formed concrete. The project will install a second array of beamline components on the northern aisle of the BTH. Considerations for this second beamline were provided during the design and construction of the LCLS. These considerations primarily provide the space required to install a second beamline and to provide long-term utilities, ventilation, lighting, and power for two similar beamlines. The scope of work in the BTH will consist of installation of utility distribution networks for the second beamline. The majority of the installations will consist of power, cooling water systems, and radiation safety systems. The existing ventilation consists of exhaust fans, with no air conditioning capability available for the BTH.

Service buildings are also included in the BTH section. There are currently three existing service buildings of varying size on top of the BTH. These service buildings were originally sized to hold the controls and power racks for two beamlines.

Due to the increased power of the electron beams, additional, local radiation shielding, or administrative control is required around the BTH housing. During beam operations, access to the BTH and service buildings will be under Controlled Access protocol.

Controlled access to the interior of the BTH includes two entrance mazes on opposite ends of the Research Yard. The west end of the BTH access points are currently plugged with removable panels. These panels may be removed for access to the facility.

The floor level is to remain constant throughout the entire length of the LCLS-II, at 247.25 feet. The radiological requirements are stipulated in Chapter 17 Radiological Considerations.

Local shielding to meet the radiological requirements of the higher energy beam may be required in specific areas. Fencing and access control will be installed around the BTH as part of the radiation protection requirement.

15.2.5.1 Mechanical

BTH has an existing ventilation system that is activated when the beam is off. The ventilation system provides more than two air changes per hour (ACH). A roof-mounted exhaust fan with ductwork provides the necessary ventilation. The fan is monitored and controlled by SLAC's Energy Management System.

Relocation of existing chilled water piping will be required to accommodate distribution to the new undulators.

Supplemental LCW supply and return piping with pressure gauges and isolation valves will be mounted on the north wall of the BTH.

Supplemental clean, dry compressed air at 100 psig will be provided along the length of the BTH. Compressed air piping is mounted along the south wall, with shut-off valves and pressure gauges. The compressed air piping will be extended to the north wall for the second beamline components. The compressed air piping system is connected to the SLAC site-wide compressed air piping. The estimated demand for two beamlines is 20 SCFM.

Modifications to the current fire water main line supports will be required to accommodate transportation paths of the new undulators.

15.2.5.2 Service Buildings 911, 912, 913

Current AHUs are installed on the roof of the BTH, next to the service buildings. Air distribution ductwork (supply and return) is provided inside the building. The operation of the AHUs is controlled and monitored by SLAC's Energy Management System (EMS). Existing duct mounted smoke detectors were installed per California Mechanical Code (CMC).

The BTH service buildings have a wet fire sprinkler system. Zone control valve with supervisory and flow switches are provided where the piping system enters the building.

15.2.5.3 Electrical

The 480V or 120V/208V distribution panel boards will be installed to provide power to various systems located in the BTH and the service building 911, 912, 913 I&C racks, power supply racks, and PPS racks. Low profile fluorescent lighting is provided in the entire length of the BTH.

New electrical power for the new BTH equipment and control racks will be provided as required by the existing and new panels located inside service buildings 911, 912, and 913 routing cabling through the existing penetrations to the I&C, PPS, and power supply racks.

Lighting will be in accordance with IES recommendations and suitable for the building application.

The fire alarm and detection systems will integrate with the existing campus network. The fire alarm and detection systems will be designed to comply with NFPA 72 and all associated codes and regulations.

The existing telecommunication system will be used to support voice, data and low voltage networks.

15.2.6 Undulator Hall

The UH is approximately 170 meter-long and houses the electron beam and the undulator. The tunnel is in line with the BTH. The downstream part connects to the EBD in the vicinity of the existing service building 921.

The LCLS-II undulator requires stringent temperature control, which is provided by a dedicated HVAC facility near service building 921.

The utilities required in the tunnel for the LCLS-II are to support the technical systems for photon and electron beams. New utility resources are required, including new plumbing, wiring, and power.

Due to the configuration of the variable gap undulator magnets, the height of the utilities in the UH will have to be modified. The existing utilities are generally 8 feet above the finished floor. The variable gap undulators will require nine-foot clearance from the finished floor to the lowest utility. This will require that all existing utilities be rearranged within the tunnel envelope.

The UH is physically defined by two thermal barriers, which are located at the end of the BTH to the west and before the start of the EBD to the east. It is geometrically defined as a horseshoe tunnel with internal cross-sectional dimensions of 14'6"x14'10" (HxW). Service access into the UH will be modified to allow for taller variable gap magnets. This access point is from the BTH.

15.2.6.1 Mechanical

The existing UH HVAC system will be used to maintain space temperature and gradient inside the tunnel stable. The existing air handling units (AHUs) serving the UH are located at the ground surface adjacent to the current UH Service Building 921.

The current AHUs have pre-heat coils, temperature control valves, supply and return fans, heating and cooling coils and economizers. Chilled water (CHW) and hot water (HW) piping are connected to the AHUs. The operation of the existing AHUs is monitored and controlled by SLAC's EMS. Duct mounted smoke detectors are installed, per California Mechanical Code (CMC). The current HVAC system will be upgraded to accommodate the anticipated heat load increase in the UH.

Relocation of existing chilled water piping will be required to accommodate transportation paths of the new undulators.

Supplemental low conductivity water (LCW) piping will be necessary to accommodate XTCAV systems in the UH. Supplemental LCW piping system will be connected to existing 1801 LCW piping. The 1801 LCW supply temperature is 87 degrees, with a total demand of approximately 90 GPM for two XTCAV systems.

Supplemental insulated supply and return PCW piping with pressure gauges, isolation valves, and circuit setters will be mounted on the wall of the current UH. PCWS and PCWR connections for technical equipment will be spaced along the wall of the tunnel. The PCW system currently located inside the UH service building 921 at ground level will be upgraded to accommodate a second XTCAV system in the UH tunnel. PCW supply temperature is 65 degrees, with stability of 0.1 degrees and a total estimated demand of approximately 30 GPM. The operation of the current PCW system and equipment is controlled and monitored by SLAC's EMS.

Supplemental clean, dry compressed air at 100 psig will be provided along the length of the UH tunnel. Compressed air piping will be mounted along the UH wall with shut-off valves and pressure gauges. The compressed air piping system will be connected to SLAC site-wide compressed air piping. The estimated demand for two beamlines is approximately 30 SCFM.

15.2.6.2 Fire Protection

The UH currently has a wet fire sprinkler system. Zone control valves with supervisory and flow switches are provided where the piping system enters the tunnel. Modifications to the current fire water main line's supports will be required to accommodate transportation paths of the new undulators.

Current sump pumps along the existing tunnel collect any accumulated water, and drainage piping that route the water to an existing outdoor storage tank, located outside of the BTH. The storage tank drains into the sanitary waste piping once the water has been tested. A high level indicator monitors the level and is connected to the SLAC Distributed Control System (DCS) network. No modifications will be required.

15.2.6.3 Service Building 921

The current air handling unit (AHU) with cooling coils, economizer and chilled water piping and air filters provides conditioned air to the service building. The AHU removes the heat generated by the electronic racks.

In the service building, the current fire protection piping system is designed to meet NFPA 13 and Life Safety Code 101.

15.2.6.4 Electrical

Electrical power for the UH new equipment I&C, PPS and power racks will be provided from the existing and new panels located inside the service building 921 and 913 routing conduits

through the existing penetrations in the floor on both the north and south side of the service buildings.

15.2.7 Electron Beam Dump

No modifications to the existing HVAC system serving the EBD will be necessary to accommodate the technical requirements for the new beamlines.

The existing outdoor exhaust fan serving the tunnel area between FEE & EBD removes any excess heat when the beam is off. Operation of the exhaust fans and AHU is interlocked, and all equipment is controlled and monitored by SLAC's Energy Management System.

Modifications to the existing beam dump pits will be required to provide room for the beam pipes leading to the beam dump devices. The modifications resulting from the increase power of the beams will include the addition of iron shielding in strategic locations.

Utilities will be provided for both beamlines, which will require a reconfiguration of the existing utilities as well as additional utilities for the second beam line.

15.2.7.1 Mechanical

An isolated LCW cooling system is required due to the increased beam power and possible activation.

Supplemental LCW piping will be necessary to accommodate cooling requirements for the components of the new beamlines.

Supplemental clean, dry, compressed air at 100 psig will be installed along the length of the EBD tunnel. Compressed air piping drops will be mounted along the north wall, with shut-off valves and pressure gauges. The compressed air piping system will be connected to SLAC site-wide compressed air piping. The estimated demand for the two beamlines is approximately 40 CFM.

Current sump pumps in the dump pits are routed to the UH drainage system.

The current fire protection piping system for the EBD is designed to meet NFPA 13 and Life Safety Code 101. The EBD is classified as an Ordinary Hazard (Group I) facility.

15.2.7.2 Electrical

Electrical power for the EBD new equipment will be provided, as required, by the existing panels located inside the service building 921 routing conduits and by wires through the existing penetrations in building 921. Any electrical utilities located in the new beamline area will be relocated or removed as required to accommodate installation of the new equipment.

15.2.8 Front End Enclosure

Modifications to the existing structure will be required to provide for the additional beamlines. The modifications will include structural modifications, a new entrance, and coring through the common wall leading into the experimental stations.

Utilities will be provided for both beamlines through a reconfiguration of existing utilities. Additional utilities will be provided for the second beamline.

15.2.8.1 Mechanical

The FEE tunnel is currently sharing a HVAC system with the EBD to provide ventilation and conditioned air. The air handling unit (AHU) serving both FEE and EBD is located in the Near Experimental Hall's basement mechanical room.

A supplemental supply and return PCW piping with pressure gauges and isolation valves will be mounted on the wall of the FEE tunnel. PCWS and PCWR connections for experimental equipment will be spaced along the wall of the tunnel. The PCW serving the FEE is currently being fed from an existing PCW piping system installed in the Central Utility Plant (CUP), and the current PCW system includes recirculating pumps, plate heat exchanger, control valves, temperature and pressure sensors, valves and piping. The current PCW system will be modified to accommodate the anticipated increase in loads in the FEE. Chilled water (CHW) piping from the Central Utility Plan is connected to the heat exchanger to remove the heat from the PCW system.

The operations of the current HVAC and PCW systems serving the FEE are both controlled and monitored by SLAC's Energy Management System.

15.2.8.2 Fire Protection

Minor modifications to the existing fire protection piping system serving the FEE will be required to accommodate installation of new science equipment supporting the new beamlines.

15.2.8.3 Electrical

New electrical power for FEE area equipment will be provided, as required, from both existing and new panels located inside the NEH and FEE area alcove. All electrical utilities located on the north side of the FEE will be relocated or removed, as required, to accommodate installation of the new beamline equipment and any control racks.

Electrical distribution panel boards (480V or 120V/208V) will be installed to provide power to various systems, I&C racks, and personnel protection system (PPS) racks located in the FEE and maze alcove.

15.2.9 Near Experimental Hall

Modifications to the Near Experimental Hall will consist of reconfiguring the first two experimental hutches. Hutch 1 and Hutch 2 are located at the sub-basement level within the NEH. The hutches will be converted for installation of two experimental end stations. Modifications will include the relocation of existing wall-mounted power, mechanical, ventilation, and cooling systems. Coring of the structural shear wall between the hutches will be required to allow for the installation of beamline components or experiment chambers. Radiation protection for the existing experimental hutches includes lead-line soft (sheetrock) walls with multiple utility penetrations and access doors. All radiation protection will be restored during the remodeling.

15.2.9.1 Mechanical

In order to accommodate the reconfigured experimental Hutch 1 and Hutch 2 and related support areas, the following upgrades and changes will need to be made:

- Modifications to the current HVAC system's chilled water piping, hot water reheat coils piping, conditioned air, and exhaust ductwork
- Equipment upgrade and piping modifications to the current PCW system
- Supplemental control points installation to the current energy management system
- Modifications to the current compressed air piping distribution system
- Minor modifications to the existing fire sprinkler system serving the sub-basement level

15.2.9.2 Electrical

All the hutches have existing electrical utilities (lighting, outlets etc.) and panel boards located inside and outside the hutches that support all the electrical requirements for the experimental areas, including controls and monitoring system, such as the ODM. Power to these panel boards inside and outside the hutches is provided by the main distribution panel located in the NEH electrical room. This panel is powered by the unit substation, located in the Central Utility Plant in B950A.

15.3 LCLS-II Standards

All infrastructure systems will comply with the following LCLS-II system standards for new renovations or for modifications of existing infrastructure.

15.3.1 Architectural Standards

Planning and development of new facilities at SLAC is guided by the SLAC Long Range Development Plan. The campus planning framework is summarized in the following [1]:

“SLAC’s scientific and support facilities were constructed on a strongly conceived framework established in the General Development Plan (1961) and the Master Plan (1966). For nearly four decades SLAC grew within this original framework; however, over the years, many small support, storage buildings, and increased parking demands have crowded the core research areas and obscured the original circulation plan. This next stage of facilities development at SLAC cannot be accommodated by “filling in” parking and scarce open space. The Long Range Development Plan (LRDP) utilizes strategies that will make room for growth: redevelopment of low-density areas into high-density, expansion and intensification of existing facilities, and importantly, careful consideration of expanding into undeveloped areas.

The LRDP will gradually implement the replacement of small, outdated structures with more efficient and well-planned development, with the clear organizing principles of the original Master Plan will be restored and reinforced. The logic of well-planned development will make room for research program expansion and the human support systems (offices, parking, food service, short term lodging, and computer facilities) necessary to serve those programs. SLAC users and visitors will find their way safely and efficiently through an ordered campus system. All of this is compatible with the casual, naturalistic feeling of the SLAC landscape and will reserve areas for the creative work of enterprising scientists.

The LRDP was created by a group of dedicated experts, both the SLAC LRDP Working Committee and the

professional land use, environmental and campus planners from the Stanford University Architect and Planning Office. The LRDP thus combines the entrepreneurial spirit, scientific knowledge, and working experience of SLAC employees with sound planning expertise to produce the LRDP. This effort will ensure that planned future development at SLAC will reflect the highest and best use of financial, land, and human resources to meet the Center’s research goals.”

Building on these principles, the project will select appropriate sites, layouts, exterior finishes and site lighting with consideration for the Long Term Development Plan, the local environment, existing facilities and structures, the safety of personnel, staff, visitors, and guests.

Sound level mitigation measures are required for the new facility, including the cryogenic plants. The specified sound level limit at the SLAC site boundary is 60 dB during normal business hours. During the evening hours, when traffic on the adjacent freeway is limited, the sound coming from SLAC is prominent; this will require special facility design considerations.

15.3.2 Structural Standards

Structural work includes assessment of the existing condition of the structures proposed for structural modifications. The necessary modifications of the facilities will comply with current state codes, SLAC and DOE guidelines.

Structural Design Criteria

The selected structures will be evaluated against and conform to CBC 2013 requirements, as well as SLAC Building & Site-Wide Design guidelines (DS-018-000-01-R0) and Seismic Design Specification for Buildings, Structures, Equipment, and System (SLAC-I-720-0A24E-001-R003).

Table 15-1. General Structural Design Parameters.

Parameter	Value	Comment
Structure dead load	ASCE 7	Minimum loads
Structure live load	varies	As calculated
Floor live load	150 psf or equipment weight	Use greater value
Collateral dead load	5 to 10 psf or as calculated	Use greater value
Laser room, service building, HVAC deck live load	350 psf or equipment weight	Use greater value
Platform, stairs and corridors Live Load	100 psf	
Wind Load	ASCE 7, 85 mph, Exposure C	Basic “3 second gust”

Seismic Design

The structures which are identified for modification will be analyzed for seismic loads and deflection limits generated by strong ground motion during a seismic event.

Table 15-2. General Seismic Design Parameters.

Parameter	Value			Comment
Occupancy category	II			Importance factor I=1.0, Ip=1.0
Soil class	varies			Based on Geotechnical Report, Assume Class D
Seismic coefficients - CID				
Latitude:: 37.41230 deg.	Ss= 2.438g	S1=1.238g	SMS=2.438g	SDC=E (ASCE 7.05, article 11.6)
Longitude: -122.2397 deg.	SMI=1.856g	SDS=1.625g	SDI=1.238g	Fa= 1.0 Fv=1.5
Seismic coefficients - BTH				
Latitude:: 37.416928 deg.	Ss= 2.414g	S1=0.997g	SMS=2.414g	SDC=E (ASCE 7.05, article 11.6)
Longitude: -122.200955 deg.	SMI=1.495g	SDS=1.609g	SDI=0.997g	Fa= 1.0 Fv=1.5

15.3.3 Mechanical Systems Standards

Occupied spaces and specific technical equipment installations will require process cooling water for various technical components. Technical components are housed in various areas, and as such, will require independent clean or general air conditioning zones to handle each specific space temperature set points. A mechanical equipment plant will provide the infrastructure space for cooling and hot water needs.

Chilled Water System

The cooling plant will consist of suitably-sized packaged, air-cooled chillers with associated circulating chilled water pumps to support the air handling system.

Heating Hot Water System

The heating hot water system will consist of an electric boiler with associated circulating pumps and distribution piping for heating hot water.

Air Handling System

Air handlers and distribution systems will be sized to provide the required volume, temperature and pressures for the intended areas. Specific rooms may require additional, smaller package air handlers. The air handlers will be a packaged fan-wall type, furnished with 30 percent pre-filter, 95 percent high efficiency filter, chilled water coils, hot water reheat coils, humidifier, HEPA filters, where applicable, and associated variable frequency drive (VFD).

Ductwork and Air Distribution

The air flow delivery system consists of lined, rectangular or round, galvanized supply ducts. It returns ductwork extending from the air handler, located at the nearby mechanical equipment plant, and terminates inside the service areas. Supply air will terminate at engineered heights derived from installation stay-clear envelopes and equipped with Lami-Vent or equivalent supply air diffusers placed at equal distances throughout the service area.

EMS and Controls

The site WebCTRL Direct Digital Controls (DDC) System will be provided to monitor and control the mechanical systems and equipment, and it will be integrated with EPICS through BACnet protocol.

Cooling Water Systems

Cooling water systems will include cooling tower water (CTW), low conductivity water systems (LCW) and process cooling water (PCW) systems. Cooling is required for the injector components, klystrons and modulators, bunch compressors, and electronics racks. The waveguides will be temperature stabilized at 86 degrees Fahrenheit. Each sector will have independent LCW cooling systems.

Fire Protection System

The fire protection piping system will be a wet type fire sprinkler system per NFPA 13, for Ordinary Hazard (Group 1). The sprinkler system is connected to the nearby existing riser sprinkler main. Sprinkler system is designed per NFPA 13 at 0.10 GPM/FT², with 155 degrees Fahrenheit heads. Each head is spaced to cover a maximum of 130 square feet. Each single zone includes zone control valve with supervisory and flow switches where the system enters into the building. A fire department connection will be provided at the sprinkler system riser.

15.3.4 Electrical Systems Standards

The site electrical master substation systems provides 12.47 KV underground power distribution system to the all the site buildings, including the Gallery B002 substations. From there it will be distributed to various electrical equipment, such as MCCs and distribution panels that will provide power for all mechanical infrastructure and science support equipment in the gallery and the tunnel. Advanced metering will be provided for all installations and meters will be connected to SLAC's metering system.

Unit Substation

The power source will be from outdoor 12.47 KV 1,000 KVA unit substation, which shall have a draw out main circuit breaker "MCB" primary section, outdoor FRP3 based oil-filled transformer of 12KV to 480/277V, and a secondary distribution section with a main circuit breaker (MCB) and feeder breakers of the Magnum DS type. All unit substations will be installed on a concrete pad.

Motor Control Center (MCC)

The 1200A, 480V/277V rated MCC will be furnished with a 100-percent-rated solid state main circuit breaker with LSIG trip unit, branch circuit breakers, starters, power monitoring, and metering instruments.

Power for the Sector 0 injector laser rooms, gallery and injector area I&C racks, power supply racks, and PPS racks will be provided from new electrical distribution panel boards fed from the above-mentioned MCC through step-down transformers.

Distribution Panel Boards

480V or 120V/208V distribution panel boards will be installed to provide power to systems and support equipment. Distribution panel boards will be dead-front, dead-rear, solid-state-type main circuit breaker. Branch circuit breakers are group mounted, front accessible, bolt-on thermal magnetic molded case type, with adjustable magnetic trip settings. Full-length busses are required for both voltage and 200 percent neutral bussing on 208V distribution panels.

Dry Type Transformer

The transformer will be NEMA TP-1 compliant, Energy Star labeled to step down voltage from 480V to 120V/208V, three-phase/four-wire, and K13 rated with 200 percent neutral and individual neutral wire for each of the phase wire.

Arc Flash Rating

For the 480V system, solid-state type breakers will be used for coordination selectivity to reduce fault-clearing time; for the 208V system, limit step-down transformers will be provided to 112.5 KVA.

Lighting System

An existing lighting system is provided for the existing enclosures, vaults, and tunnels consisting of industrial fluorescent and recessed fluorescent light fixtures. New installed lighting levels shall be designed in accordance with IES recommendations and suitable for the specific application. Fixtures shall be fluorescent type, with energy saving T8 lamps, 3,500 Kelvin color temperature with high efficiency electronic ballasts with 95 percent power factor, and total harmonic distortion (THD) of less than 10 percent. Lighting control will be designed to meet or exceed the requirement of Title 24 and other project requirements. Exterior lighting at the entrances, landings, and equipment pad shall be LED, with photocell controls and bypass switch.

Grounding and Bonding System

Service grounding will be designed as required by the California Electric Code and the National Electric Code requirement. All ground buss will be tied back to the area grounding. All systems and equipment will be bonded as per NEC and NFPA requirements.

Fire Alarm and Detection System

The fire alarm and detection systems will integrate with the existing campus network. The fire alarm and detection systems will be designed to comply with NFPA 72 and all associated codes and regulations. New fire alarm system installations will consist of, but not be limited to a fire alarm control unit, alarm initiating devices, occupant notification appliances, and associated ancillary equipment for interfacing the new fire alarm system with the existing SLAC alarm receiving equipment. The fire alarm system will also communicate with other life safety systems and building system equipment, as applicable.

The fire detection system will be VESDA Air Sampling and Early Warning Smoke Detection. The VESDA system will consist of, but not be limited to, the sampling pipe network, highly sensitive LASER-based smoke detectors, aspirators, filters, detector assembly network, and digital communication ports. The fire detection system will also communicate with other life-safety systems and building system equipment, as applicable.

Telecommunication System

The existing telecommunication system is provided to support the physical transmission facility for voice, data and low voltage networks. The system consists of, but is not limited to the following:

- Telecommunication backbone pathways, which include a dedicated point-to-point (BDF to IDF) pathway system.
- Telephone and data structure cabling systems that comply with the requirement of EIA/TIA 569 Commercial Building Standard for telecommunications pathways and spaces. The cabling system will be upgraded to comply with pertinent codes, rules, regulations, and laws of the authorities having jurisdiction.

15.3.5 Site Utilities Standards

Site civil utilities improvements includes storm drainage, site sanitary sewer service, potable water service, and fire protection water service systems, and will conform with all current applicable codes and CBC 2013 requirements. Design guidelines set in SLAC Building & Site-Wide Design guidelines (DS-018-000-01-R0) will be considered.

Excavation and Grading - Site Earthwork

Earthwork will be designed in accordance with the recommendations provided in the project geotechnical report.

Consideration will be given to the use of recycled roadway base and asphalt pavement as part of the site earthwork fill requirements for the site.

Site grading design will be done to minimize the need for imported fill material.

Existing asphalt, concrete, and soil to be excavated will be characterized by SLAC for possible contamination to determine disposal and/or reuse prior to start of work.

Parking Lot, Roadways and Sidewalks

New parking lots will be provided at areas of new personnel concentration, such as the cryogenic plant. They will be provided with charging stations for government electric vehicles and with minimum lighting of 1 foot candle. Parking lots will have curbs and gutters, and the drainage system will be connected to groundwater recharge systems.

Primary roadways, as applicable, will be designed for H20-44 truck loading, fire truck loading, and FL-40 forklift loading (98,500 pounds for each front wheel and 9,500 pounds for rear wheels). Roadways will have curb and gutters and catch basins where needed. Catch basins will be connected to existing drainage system. Rerouted roads will be constructed to match existing.

Domestic Water

The domestic and fire water service connections will be designed based on all applicable codes and on the sizing requirements for the building. Metering for the domestic service, backflow prevention, and valve control for services will be included. Approval for fire services will be under the direction of the SLAC fire marshal. All water connections — domestic, fire and irrigation — is supplied from one master source on the SLAC campus.

Pipe will have a minimum cover of three feet. A cover of less than three feet may be considered, but only if some other protection is provided and the proposed installation is approved by SLAC.

Sanitary Sewer System

Toilet and utility rooms will be provided with hot and cold domestic water and vent and sanitary-waste plumbing. The sanitary waste will connect and discharge to the existing sanitary sewer system. Additional loads to the existing sanitary sewer system will be evaluated for capacity, and modifications engineered and installed.

Sewer service for the new installations will be designed to provide capacity for the calculated sewer flows. The minimum slope for the pipe will be determined based on a minimum design velocity of 2.0 feet per second at peak flow and a minimum of four inches in diameter.

15.3.6 Environmental Standards

Storm Water Management

Section 438 of the Energy Independence and Security Act (EISA) of 2007 requires the final design, construction and maintenance of all projects with a footprint that exceeds 5,000 square feet in order to maintain or restore to the maximum extent that is technically feasible the predevelopment hydrology of the property with regard to the rate, volume, and duration of flow. Rainfall up to the 95th percentile rain event shall not enter the storm drain system, but be accommodated by one or more alternative methods, such as permeable pavements, landscaping or sediment basins. (The 95th percentile rainfall event is the event for which the measured depth of precipitation over a 24-hour period is greater than or equal to 95 percent of all 24 hour storms

over a 30 year period.). The project will be engineered and installed in accordance with these requirements.

15.4 Sustainability Standards

SLAC, as a federal facility, is required to comply with Executive Order (EO) 13423, “Strengthening Federal Environmental, Energy, and Transportation Management,” dated January 24, 2007. The order sets goals in the areas of energy efficiency, acquisition, renewable energy, toxics reductions, recycling, renewable energy, sustainable buildings, electronics stewardships, fleets, and water conservation. In EO 13423, Section 2(f), federal agencies are required to ensure that new construction and major renovation of agency buildings comply with the Guiding Principles for Federal Leadership in High Performance and Sustainable Buildings set forth in the Federal Leadership in High Performance and Sustainable Buildings Memorandum of Understanding (2006).

The approach to be taken by the project toward this initiative includes:

- Meet High Performance and Sustainable Buildings practices for new construction and renovations in the conventional facilities scope for LCLS-II.
- Meet Leadership in Energy and Environmental Design (LEED) gold certification practices for new construction, as applicable.

For additional information, see <http://www.fedcenter.gov/programs/greenbuildings/>.

BES has concurred that the LCLS-II project scope does not need to implement High Performance and Sustainable Building provisions because no federal buildings will be constructed. This fulfills the HSPB requirement for CD-1.

15.5 References

1. SLAC Building and Site-Wide Design Guidelines, Binder 2, DS-018-000-01-R0, SLAC National Accelerator Laboratory, Menlo Park, California, 28 July, 2010.

16 ENVIRONMENT, SAFETY, HEALTH, AND QUALITY

TECHNICAL SYNOPSIS

SLAC is committed to the success of the mission objectives of the LCLS-II Project and to the safety of its users, staff and the public. It is our vision to construct LCLS-II with zero incidents or injuries. The SLAC Worker Safety and Health Program will be the primary vehicle for the LCLS-II Project to meet that vision, and is therefore essential to the safety of the workers as well as the successful completion of the project. LCLS-II management will design and build the project with the assistance of a fully involved quality assurance program. The LCLS-II Quality Assurance (QA) program will implement quality assurance criteria in a way that achieves adequate protection of the workers, the public, and the environment, taking into account the work to be performed and the associated hazards. The primary objective of the Quality Assurance Program is to fully satisfy LCLS-II Project requirements and expectations.

16.1 Introduction and Overview

It is SLAC's policy to integrate safety and environmental protection into its management and work practices at all levels and to achieve its scientific mission while protecting the worker, the public and the environment. To achieve this policy, SLAC has developed and implemented a Worker Safety and Health Plan (WSHP) [1]. SLAC's WSHP was developed to be compliant with 10 CFR 851 [2] and with DOE's Integrated Safety Management System (ISM). SLAC has taken the additional step of combining ISM and the DOE's Environmental Management System [3] into one integrated system: the Integrated Safety and Environmental Management System (ISEMS) [4].

To align with SLAC's policy and ensure that all aspects of the design, manufacturing, installation, testing, operational, and decommissioning phases of the project are reviewed and consistent with that policy, LCLS II has adopted SLAC's WSHP. This action meets the Critical Decision 1 requirement for the Project to have an integrated safety management system. The LCLS II project director is responsible for implementing the SLAC policy for the project through the adoption of the SLAC WSHP. Supporting the project director in this effort are the project's representatives for Environment, Safety, And Health (ES&H) and for Quality Assurance (QA). These representatives advise the project director and the project staff on E&SH and QA aspects of the project, helping to ensure LCLS-II meets both its DOE and SLAC ES&H and QA requirements and goals. The *LCLS-II Project Management Plan* will describe high level responsibilities and authorities and position descriptions that define the responsibilities of the ES&H and QA Representatives.

The existing and mature programs at SLAC will be followed to ensure that all aspects of the design, decommissioning, installation, testing, and operational phases of the project are reviewed to meet regulatory requirements and SLAC's policies and procedures. SLAC's Project Review Procedure [5] provides a systematic, streamlined, and effective review of projects to ensure the ES&H aspects are adequately identified and mitigated before authorization and release of project activities. The thresholds and applicability determination for reviews; the experimental project review and conventional project review processes are described in the Procedure.

The hazards and selected mitigations will be identified through the hazards analysis process, as described in Section 16.2 of this document. SLAC has several decades of experience operating electron accelerators, free-electron lasers (FELs), and their accompanying user facilities. Engineered safety systems, policies, and procedures have been developed to control the hazards and risks associated with them. Upon completion of the installation activities, the hazards and mitigations will be included in the LCLS-II Safety Assessment Document (SAD).

The LCLS-II project will not generate new hazards that have not already been identified and addressed at SLAC or across the DOE complex. The potential hazards that have been initially identified can be mitigated through established SLAC ES&H policies and procedures. Additionally, LCLS II will use the experience, hazard analysis, documentation, and Lessons

Learned of other DOE laboratories in order to evaluate our mitigation efforts against potential and identified hazards. The LCLS II Project is shown schematically in Figure 1.

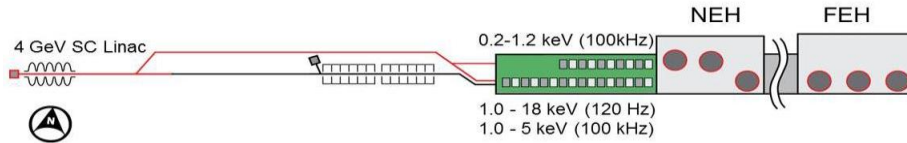


Figure 1. The LCLS II Project is shown schematically above.

16.2 Preliminary Hazards Analysis (PHA)

A principal component of an effective ES&H program is to ensure that all hazards have been properly identified and controlled through design and mitigations (policies and procedures). To ensure that these issues are understood at the conceptual phase, a preliminary hazards analysis (PHA) has been conducted to identify the hazards that will be encountered during the various phases of the project. In addition, some sections of the PHA were also used to meet the safety requirements defined in DOE Order 420.2C, “Safety of Accelerator Facilities” [6].

Generally, all hazards and risks anticipated to be encountered at LCLS II, as identified in the PHA, are well known to SLAC, LCLS II, and across the DOE complex. This institutional knowledge has been used to generate well-defined design criteria and controls to eliminate and/or control these risks. Table 1 summarizes the hazards that have been considered at this stage of the projects development.

Table 1. PHA Identifier and Hazard List.

PHA Identifier	Hazard List
<u>LCLS II – PHA-1</u>	<p>Demolition and decommissioning</p> <ul style="list-style-type: none"> Welding Asbestos Nuisance dust Work at elevations (steel, roofing, MEP) Utility interfaces, (electrical, steam, chilled water, compressed air) Noise Powered tools Slips, trips, and falls Crushing Vehicles and traffic Limited egress Animals and insects

	<p>Weather-related conditions</p> <p>Transition to operations</p>
<u>LCLS II – PHA-2</u>	<p>Natural phenomena hazards</p> <p>Seismic</p> <p>Flood</p> <p>Wind</p> <p>Precipitation (snow, ice and rain)</p> <p>Lightning</p>
<u>LCLS -II – PHA-3</u>	<p>Environmental hazards</p> <p>Construction impacts</p> <p>Storm-water discharge (construction and operations)</p> <p>Operations impacts</p> <p>Soil activation</p> <p>Air activation</p> <p>Cooling-water activation (HVAC and machine)</p> <p>Oils/chemical leaks</p>
<u>LCLS-II – PHA-4</u>	<p>Waste hazards</p> <p>Construction phase</p> <p>Facility maintenance</p> <p>Experimental operations</p> <p>Industrial</p> <p>Hazardous</p> <p>Radiological</p>
<u>LCLS-II – PHA-5</u>	<p>Fire hazards</p> <p>Facility occupancy classification</p> <p>Construction materials</p> <p>Storage of flammable /combustible liquids</p> <p>Flammable gasses</p> <p>Egress/access</p> <p>Electrical</p>
<u>LCLS-II – PHA-6</u>	<p>Electrical hazards</p> <p>Facility</p> <p>Experimental</p> <p>Laboratory-built equipment</p> <p>Low voltage/high current</p> <p>High voltage/high power</p> <p>Maintenance</p> <p>Cable tray overloading/mixed utilities</p>
<u>LCLS-II – PHA-7</u>	<p>Noise/vibration hazards</p> <p>Construction tools</p> <p>Industrial vehicles</p>

	Compressors SCRF cavities HVAC and air handling fans
<u>LCLS-II- PHA-8</u>	Cryogenic hazards Oxygen deficiency Thermal Cryogenic distribution system Pressure LN2/LHe vent/spill/leak
<u>LCLS-II- PHA-9</u>	Confined space hazards Hazardous gases Oxygen deficiency Hot work Limited egress Electrical
<u>LCLS-II- PHA-10</u>	Ozone hazards Toxic
<u>LCLS-II- PHA-11</u>	Chemical/hazardous material Toxic Extremely toxic Compressed gas Carcinogens, mutagens, teratogens Combustibles Explosives Flammable gases Lead (shielding)
<u>LCLS-II- PHA-12</u>	Accelerator/Beamline hazards Vacuum/Pressure Cooling water Compressed gas Electrical Heavy equipment handling Magnetic Cryogenic Shielding Mechanical (moving shutters, valves and actuators)
<u>LCLS-II- PHA-13</u>	Ionizing radiation hazards Prompt radiation (scatter, neutrons, bremsstrahlung) Radioactive contamination Activation (equipment) Radioactive material (experimental)
<u>LCLS-II- PHA-14</u>	Non-ionizing radiation hazards

	RF & microwave Magnetic fields Laser
<u>LCLCS-II – PHA-15</u>	Material handling hazards Overhead cranes/hoists Fork trucks Manual material handling Delivery area distribution Manual movement of materials Vehicle and traffic
<u>LCLCS-II – PHA-16</u>	Experimental operations Electrical equipment Transportation of hazardous materials Biological materials Chemicals (corrosive, reactive, toxic, flammable) Nanomaterials (particulates) Elevations Dark-room hazards Clean-room hazards Ionizing radiation Ozone production Slips, trips, falls Machine tools/hand tools Stray static magnetic fields Research gasses (corrosive, reactive, toxic, flammable)

16.3 Construction Hazards (LCLCS-II PHA – 1)

SLAC has a mature construction safety program, with recent experience in constructing the LCLCS Project, the Research Support Building (65,500 square feet) the Sector 10 injector facility, and several other projects. Lessons Learned from these projects as well as those from other construction projects within the DOE complex will help establish the controls necessary to minimize the risk associated with installation and construction activities at the LCLCS-II project. SLAC's Work Planning and Control (WPC) process supports the program by helping workers to understand the scope of work, identify qualified workers, identify hazards and mitigations, and communicate hazards and mitigations to all the workers, either employees or subcontractors. The typical installation and construction hazards anticipated during LCLCS-II include the following:

- Demolition and decommissioning
- Welding
- Asbestos
- Nuisance dust

- Work at elevations (steel, roofing, MEP)
- Utility interfaces, (electrical, steam, chilled water, compressed air)
- Noise
- Powered tools
- Slips, trips, and falls
- Crushing
- Vehicle contact; backing, traffic
- Access and egress
- Animals and insects
- Weather-related conditions
- Transition to operations

16.4 Natural Phenomena Hazards (LCLS-II PHA-2)

Natural phenomena hazards (NPHs), including winds, floods, earthquakes, precipitation, and lightning are considered in the design and operation of LCLS-II. The LCLS-II design will follow DOE-STD-1020-2012 [7] and the California Building Code (CBC) 2013 at the time of its construction and installation.

LCLS-II is categorized as Seismic Design Category 1 (SDC-1) per DOE-STD-1020-2012, which is Risk Category II per ASCE 7-10 [8], except where some systems may require a higher risk categorization (e.g., high-powered beam dumps; Risk Category IV). Note that Table 3-1 of DOE-STD-1020-2012 is used in conjunction with ASCE 7-10 to determine the response modification coefficient to be utilized for design.

LCLS II will contain only some quantities of activated materials during demolition and deconstruction. Some hazardous chemical materials may be used during its installation and operation. If a NPH were to cause significant damage, the impact would be mission related and would not pose a hazard to the public or the environment.

DOE O 420.1C [6] requires structures and facilities to be evaluated for the effects of seismic hazards every decade. This evaluation assists the contractor in determining what, if any, actions are required to update the affected structures or facility. The SLAC Seismic Study [9] confirmed that accelerator facilities at SLAC were built to the appropriate national consensus codes and standards at the time of their construction and have a seismic performance rating consistent with Life Safety (ASCE 31-03)[10] or better.

16.5 Environmental Hazards (LCLS-II PHA 3)

Installation of LCLS-II requires the removal of some hardware (magnets and vacuum chambers) and the installation of new components (cryomodules, electrical distribution and

cooling systems) suited to the proposed facility. Removal of these materials and the subsequent installation activities will produce quantities of nonhazardous, hazardous, and radioactive waste that will be managed through SLAC's defined processes. Past operating experience indicates that normal operation of the accelerator does not typically produce significant quantities of waste but, some hardware may have induced radioactivity associated with its proximity to the beam. Other components may contain hazardous materials as part of their design (e.g., mineral oil in electrical components, or radioactive contamination from the LCW system).

All material removed from the accelerator and gallery will be surveyed for residual radioactivity or contamination, labeled, and appropriately disposed of as defined in the SLAC Radiological Control Manual [11] and The SLAC Radioactive Waste Manual [12]. Items that show residual radioactivity or contamination will be stored onsite until ultimately disposed of offsite.

Component manufacturing and system installation may also produce hazardous wastes, such as spent solvents from degreasing baths or spent cutting fluids. These wastes are managed and controlled routinely during operations at SLAC in full compliance with its policies on the management of hazardous materials and waste minimization. The LCLS-II partner laboratories will produce wastes from their manufacturing and assembly work. They will follow their approved Environmental Management Systems requirements for minimizing the generation of wastes, collecting and disposing of those wastes safely.

16.6 Waste Hazards (LCLS-II PHA-4)

Waste-related hazards from LCLS-II include the potential for releasing waste materials (oils, solvents, chemicals, and radioactive material) to the environment and personnel contact or injury. Typical initiators would be transportation accidents, incompatible materials, insufficient packaging/labeling, failure of the packaging, and natural phenomena.

During the installation and operation phases of LCLS-II it is anticipated that minimal quantities of hazardous materials will be used, such as paints, epoxies, solvents, oils and lead in the form of shielding. There are no current or anticipated activities at LCLS-II that would expose workers to levels of contaminants (dust, mists or fumes) above permissible levels.

The ES&H Industrial Hygiene Group provides program management and guidance to SLAC and subcontractor employees who are subject to waste related hazards. Their staff identifies workplace hazards at the earliest stages of the project and implements controls to eliminate or mitigate these hazards to an acceptable level. Industrial hygiene hazards will be evaluated, identified, and mitigated as part of the hazard assessment process.

Site and facility-specific procedures are in place for the safe handling, storing, transporting, inspecting and disposing of hazardous materials. These are contained in the *SLAC ES&H Manual*, Chapter 17, "Hazardous Waste" [13] which describes minimum standards to maintain for compliance with Title 40, Code of Federal Regulations.

The field construction manager (FCM) or project manager has responsibilities for subcontractors' use of chemicals and other materials that can become hazardous waste. They ensure subcontractor personnel are aware of, and remain in compliance with *SLAC ES&H Manual* Chapter 40, "Chemical Lifecycle Management" [14], Chapter 52 [15], and Chapter 53 [16]. They also keep affected SLAC personnel informed of hazardous material usage and the associated hazards and risks.

16.7 Fire Hazards (LCLS-II PHA – 5)

The probability of a fire at LCLS-II is very low, similar to that for present operations, as accelerator and beamline components are primarily fabricated out of nonflammable materials and combustible materials in general are kept to a minimum. Operational experience at SLAC and at accelerators throughout the DOE complex has demonstrated that most fires in accelerator facilities are electrically initiated, typically by component failure. All other potential sources of fire are also considered in the design of the LCLS-II facility and installation. They include the combustibility of building construction materials, the accumulation of combustible materials by occupants during installation and operation, the use of pyrophoric or reactive materials, improper storage or use of flammable materials and gasses, lightning storms, and static discharge.

16.8 Electrical Hazards (LCLS-II PHA – 6)

LCLS-II will have subsystems that either produce or use high voltage or high current, either of which can present an electrical hazard to personnel. Since LCLS-II will operate similarly to other accelerators at SLAC, control and work procedures for electrical subsystems and entry into the accelerator housing are well understood. Mitigations for these hazards consist of deenergizing equipment, placement of barriers, PPE, and the use of Lockout and Tagout (LOTO) procedures [17] as specified in *SLAC's ES&H Manual*, Chapter 51, Control of Hazardous Energy.

The design, upgrade, installation and operation of electrical equipment will be in compliance with the National Electrical Code, Title 29 Code of Federal Regulations, Parts 1910 and 1926 (as applicable) and SLAC's policy on electrical safety, *SLAC ES&H Manual*, Chapter 8 [18]. Entry into the accelerator housing requires the mitigation of electrical hazards through either the lockout of power supplies or selective use of mechanical barriers, interlocked to further reduce the risk of exposure to electrical shock. Various levels of electrical safety training and LOTO training are provided by SLAC for all personnel who may work on or near potential electrical hazards.

16.9 Noise and Vibration Hazards (LCLS-II PHA – 7)

Hazards from noise and vibration can result in permanent hearing loss, also known as Permanent Threshold Shift. Vibrations at various frequencies can affect personnel, the surrounding area and community, and equipment and machinery operations.

LCLS-II will incorporate a wide variety of equipment that will produce a wide range of noise and vibration. Support equipment for cooling water circulation, compressed air, air handling and exhaust fans as well as equipment that compress and refrigerate gases into cryogenic liquids contribute to the ambient and point source noise levels. The majority of LCLS-II areas will be below the OSHA noise threshold. Certain areas however, could exceed that requirement and will require periodic monitoring, postings, and personal protective equipment. [19]

16.10 Cryogenic Hazards (LCLS-II PHA – 8)

Large volumes of liquid helium will be used to cool the super conducting linac (SCRF). In addition, liquid nitrogen will be used for precooling the cryogenic facility, cooling experimental samples and to cool beamline and detectors. The use of these cryogenics will include the potential for oxygen-deficient atmospheres in the event of catastrophic failure of the cryogenic systems; thermal hazards (cold burns) from cryogenic components; and pressure hazards. Initiators could include the failure or rupture of cryogenic systems from overpressure, failure of insulating vacuum jackets, mechanical damage or failure, magnet quenching, deficient maintenance, or the use of improper procedures.

The extreme low temperatures of cryogenic liquids and gases have a significant adverse effect on the human body, as well as on inanimate objects. These effects range from destroying human tissue to altering the physical characteristics and properties of materials, such as size, strength and flexibility of metals and other materials.

Liquid helium will be used to cool the superconducting accelerator components. Liquid nitrogen will be used for precooling the cryogenic facility and will be used for cooling experimental samples such as protein crystals, and also to cool beamline equipment, such as detectors, for enhanced sensitivity

16.11 Confined Space Hazards (LCLS-II PHA – 9)

Hazards from confined spaces could result in death or injury due to asphyxiation, compressive asphyxiation, smoke inhalation, or impact with mechanical systems. Initiators would include failure of the cryogenic systems releasing liquid, the release of gas, fire, or failure of mechanical systems.

The LCLS II facility will have several types of confined spaces. They include those associated with the facility's support and maintenance, and typically include sump pits and HVAC plenums that can only be accessed by facilities maintenance personnel or escorted vendor personnel. An additional confined space will be the beam dump or dump pits. Other confined spaces can be created by the experimental programs and may include vessels or chambers.

16.12 Ozone Hazards (LCLS-II PHA-10)

Beamlines can generate radiation from the beam coming into contact with beamline components during operations. Resulting electromagnetic cascades deposit some of the beam energy onto the surrounding air, leading to ozone production. During the design and review phases of the project this hazard will be further evaluated and mitigated.

16.13 Chemicals and Hazardous Materials (LCLS-II PHA – 11)

The LCLS-II Project anticipates a minimal use of chemical and hazardous materials, based on the construction of LCLS and its subsequent operations. Exposure to these materials could result in injury or in exposures that exceed regulatory limits. Initiators could be conventional and technical installations, experimental operations, transfer of material, failure of packaging, improper marking/labeling, failure of fume hood or glove box, reactive or explosive events, improper selection (or lack) of personal protective equipment, or natural phenomena.

As explained in Section 16.6, SLAC has site- and facility-specific policies and procedures for the safe handling, storing, transporting, use, and disposal of these materials. These materials are managed throughout their life-cycle from purchase to removal/disposal.

16.14 Accelerator/Beamline Hazards (LCLS-II PHA – 12)

Hazards from the accelerator and beamlines include activated cooling water, chemicals, compressed gas, electrical, material handling and magnetic/cryogenic/radiation, access and egress, falls, and walking and working surfaces.

The accelerator and beamlines will have medium- and high-voltage electrical equipment and associated power supplies. High-power equipment includes RF, vacuum pumps, vacuum gauges, detectors, and beam-position monitors (higher voltage-biased system).

Access and egress from the linac tunnel is limited by its location. Fixed ladders provide the access and egress from the tunnel at all locations (sectors) with some sectors having stair access. Ladder hazards include falls, hand or feet slipping, hard contact with the ladder, and muscle strain.

16.15 Ionizing Radiation Hazards (LCLS-II PHA – 13)

Potential hazards from ionizing radiation include prompt radiation (X-rays, neutrons, bremsstrahlung) produced during machine operation; induced activity in machine components; and radioactive material (use and storage). Typical initiators of radiation exposure would include operating machines, maintenance work, and the use of radioactive materials. Accidental exposure could result from failure of an interlock or other protective system, inadequate design or control of shielding, or an inadequate procedure.

To address these issues, the LCLS II design will incorporate the requirements specified in 10 CFR 835 and the accelerator-specific safety requirements as set by DOE Order 420.2C, "Safety of Accelerator Facilities." The facility will be designed and operated in a manner to maintain radiation exposure to staff, users, and the general public within DOE and SLAC dose limits and control levels [20] [21] [22].

16.16 Non-Ionizing Radiation (LCLS-II PHA – 14)

Non-ionizing radiation will be comprised of radio frequency and microwave radiation and magnetic fields and lasers at LCLS-II. SLAC's policies and procedures, Lessons Learned, and safety measures based on present operations will provide the controls to address these hazards.

The LCLS-II RF systems will produce radio frequency radiation which, when not controlled, could have an adverse health effect on personnel working on or near the system.

LCLS-II will utilize equipment and devices that generate magnetic fields. The concern with these devices is the strength and extent of the fringe fields and how they may affect people and equipment in their vicinity. Fringe fields in excess of 5 gauss are of particular concern because they could affect medical electronic devices (pacemakers), while fields over 600 gauss could impact ferromagnetic implants (artificial joints) and other material (tools).

The LCLS-II operations and experimental programs utilizing Class 1, 2, 3R, 3B, and 4 lasers can present hazards to personnel. Direct exposure of laser radiation can adversely affect human skin or eyes if it exceeds certain levels. In addition, Class 4 lasers intensity can exceed the combustibility thresholds of some materials. Laser-target interactions may produce laser-generated air contaminants and hazardous plasma radiation at very high intensities.

16.17 Material Handling (LCLS-II PHA – 15)

A wide variety of equipment and material must be removed and installed during the decommissioning, deconstruction, installation, and operational phases of the LCLS-II Project. Hazards associated with these moves and material handling has included vehicle impact with building or personnel, back strain or injury, being caught in a pinch point, the striking of body parts against equipment, cuts and bruises, as well as slips, trips, and falls. Additional material handling hazards from forklift and tow cart operations include injury to the operator or personnel in the area and contact with equipment or structures. Crane and hoist will be used during fabrication, testing, removal, and installation of equipment. The hazards associated with this type of work include irregular shaped loads, awkward load attachments, limited space, obscured sight lines, and poor communication.

16.18 Experimental Operations (LCLS-II – PHA-16)

Based on existing experimental facilities operational hazards and how they affect personnel and equipment are well understood at SLAC. Initiators would include the release or unexpected

reaction of hazardous material, protective systems failures, laser hazards, the use of radioactive and biological materials, operator error, Operations lack of training, poorly designed or installed equipment, equipment failure and unexpected chemical reactions. Many of the anticipated hazards are discussed in the specific hazard analysis sections in this document (e.g., ozone, non-ionizing radiation). Various research gases will be used in experiments (e.g. inert, flammable). Inert gases include nitrogen, helium, and argon. Flammable gasses can include hydrogen, propane, and butane. Various toxic gases may be used in small quantities at the experiment. Small-scale use of oxygen and halogens is also anticipated. Liquid nitrogen and helium will be used to cool experimental samples such as protein crystals.

16.19 NEPA and NHPA

The LCLS-II Project is required by the National Environmental Protection Act (NEPA) to perform an evaluation of its potential environmental impacts during construction and operation of the project. DOE Order 451.1B Change 3 [23] provides the directive for complying with NEPA for DOE facilities. The project will perform an Environmental Assessment (EA), which will include a detailed analysis of potential environmental impacts and the safety and health hazards identified during the design, construction, and operating phases of LCLS-II.

The project is also required to comply with the National Historic Preservation Act (NHPA), 36 Code of Federal Regulations, Part 800. The details contained in the project's scope will describe in narrative form the project's potential effects on historic buildings. The potential effects include the modifications of buildings and change-out of technical systems. To comply, the project will perform a Section 106 process that evaluates the buildings and structures for historic significance against National Register criteria [24].

16.20 Quality Assurance

LCLS-II project management will design and build a world-class user facility for scientific research with the assistance of a fully involved quality assurance program.

The LCLS-II Project Director is responsible for achieving performance goals. The LCLS-II Quality Assurance Manager (QA) is responsible for ensuring that a quality system is established, implemented, and maintained in accordance with requirements. The QA manager will provide oversight and support to the project participants to ensure a consistent quality program.

A quality assurance plan has been prepared by the QA manager and approved by the LCLS-II project director. This plan specifies the program requirements that apply to all LCLS-II work. The primary objective of the QA program is to implement quality assurance criteria in a way that achieves adequate protection of the workers, the public, and the environment, taking into account the work to be performed and the associated hazards. The objectives include:

1. "Designing in" quality and reliability.

2. Assuring that all personnel involved in the project uphold the LCLS-II quality assurance plan [25].
3. Promoting early detection of problems to minimize failure costs and impact on schedule. Records of the nature of nonconformities, and any subsequent actions taken shall be maintained.
4. Developing appropriate documentation to support construction and operational requirements.
5. Assuring that personnel have the necessary training, as needed, before performing critical activities, especially those that have environmental, safety, security, or health consequences.
6. Defining the general requirements for design and readiness reviews, including environmental, safety, security, and health issues related to LCLS-II and collaborator and contractor hardware, software, and processes.

16.21 References

1. SLAC-I-720-0A21B-001-R006, "SLAC Worker Safety and Health Program."
2. PART 851—Worker Safety and Health Program.
3. SLAC-I-750-0A03H-002-R4, "Environmental Management System Description."
4. ISEMS contract clause from the DOE Acquisition Regulations [DEAR], specifically DEAR 970.5204.-2, "Integration of Environment Safety and Health into Planning and Execution."
5. SLAC-I-720-0A24C-001-R006, "Chapter 1: General Policy and Responsibilities ESH: Project Review Procedure."
6. DOE Order 420.2C, "Safety of Accelerator Facilities."
7. DOE-STD-1020-2012, "DOE STANDARD Natural Phenomena Hazards Analysis and Design Criteria for DOE Facilities."
8. ASCE/SEI 7-10, "Minimum Design Loads for Buildings and Other Structures".
9. 10 YEAR SEISMIC STUDY FOR SLAC, July 2011.
10. ASCE/SEI 31-03, "Seismic Evaluation of Existing Buildings."
11. SLAC-I-720-0A05Z-001-R007, "Radiological Control Manual."
12. SLAC-I-7602A08Z-001-R002, "Radioactive Waste Manual."
13. SLAC-I-720-0A29Z-001-R023, SLAC ES&H Manual, Chapter 17 "Hazardous Waste."
14. SLAC-I-730-0A09L-004-R000, "SLAC ES&H Manual, Chapter 40, Chemical Lifecycle Management".
15. SLAC-I-730-0A09L-003-R000, "SLAC ES&H Manual, Chapter 52, Hazardous Materials and Waste Transportation."
16. SLAC-I-730-0A09L-005-R000, "SLAC ES&H Manual, Chapter 53, Chemical Safety."
17. SLAC-I-720-0A29Z-001-R000 SLAC ES&H Manual, Chapter 51 "Control of Hazardous Energy."
18. SLAC-I-720-0A29Z-001-R007, SLAC ES&H Manual, Chapter 8 "Electrical Safety."

19. SLAC-I-720-0A29Z-001-R023, SLAC ES&H Manual, Chapter 18 "Hearing Conservation."
20. SLAC-I-760-0A05S-003-R000, "Radiological Safety, Facility Design and Operation Requirements."
21. SLAC-I-760-0A05T-001-R000, "Radiological Safety, Related Programs and Documents."
22. SLAC-I-760-0A05S-002-R004, "Radiological Safety, Radiological Work and Area Entry Requirements."
23. DOE O 451.1B Admin Change 3, National Environmental Policy Act Compliance Program.
24. 36 CFR part 63, "National Register criteria."
25. Quality Assurance Plan, LCLSII-1.1-PM-0007.

17 RADIOLOGICAL CONSIDERATIONS

TECHNICAL SYNOPSIS

This chapter covers the radiation protection measures and radiological impact of the LCLS-II project. Experience with LCLS-I and previous high power beam operations provided an excellent basis for the development of the preliminary requirements and concepts needed for shielding, the Beam Containment System (BCS), the Personnel Protection System (PPS), and to mitigate the radiological impact. Every effort is made to use existing infrastructure, especially existing accelerator housing and dumps. Changes to the existing protection systems are required to account for the new beamlines and faster response times needed for beam mis-steering events. Shielding modifications are required in some places to accommodate the much high beam power compared with LCLS-I.

17.1 Overview and Design Requirements

LCLS-II is designed to ensure that radiation doses above background received by workers, the public, and the environment are As Low As Reasonably Achievable (ALARA), as well as to prevent any person from receiving more radiation exposure than is permitted by SLAC radiation safety requirement.

Several technical, operational, and administrative systems were taken into account to implement the radiation safety program for LCLS-II as described in the SLAC Radiological Control Manual [1] and the Radiation Safety Systems Technical Basis Document [2]. These systems are part of the SLAC Radiation Safety System (RSS); a combination of active and passive safety systems used to protect personnel from prompt radiation. The primary components of the SLAC RSS include:

- Shielding, which attenuates radiation.
- A Personnel Protection System (PPS), and the Hutch Protection System (HPS) for X-ray beam lines, an access control system that prevents personnel from entering areas in which dangerous levels of radiation could be present.
- A beam containment system (BCS) that keeps excessive levels of radiation from penetrating the shielding enclosure. The BCS is comprised of a combination of electronic protection devices including current toroids, meter relays, protection ionization chambers (PIC), Long ionization chambers (LION), and mechanical devices (such as collimators and beam dumps) that:
 1. monitor and limit the beam power in a beam line to the allowed value,
 2. limit the losses along a beam line,
 3. protect safety-related beam line components from damage, and
 4. shut off the beam if excessive radiation levels are detected, or can be generated in occupied areas.

Other safety systems, such as burn-through monitors (BTMs) and beam shutoff ion chambers (BSOICs) active area monitors, are also integrated into the SLAC RSS. BTMs are pressure vessels located near shower maximum that are designed to rupture when the device being protected absorbs greater than its allowed beam power, thus detecting the onset of damage to mechanical protection devices such as collimators, beam stoppers, and beam dumps. BSOICs are interlocked radiation detectors that are used to detect prompt radiation and terminate accelerator operation if excessive radiation is detected in potentially occupied areas. BSOICs trip limits are typically set at 10 mrem/h or 100 mrem/h, depending on the location of the detector and the occupancy of the area. Figure 1 shows an overview of the RSS components used in LCLS-II.

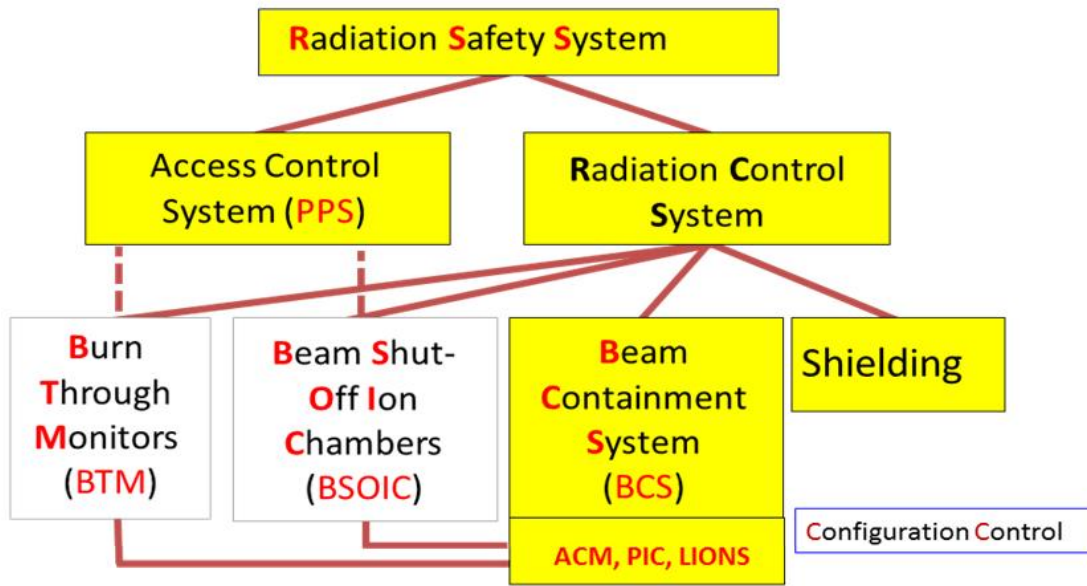


Figure 1. Overview of the LCLS-II radiation safety system (BCS components tied to PPS are in white boxes).

SLAC has operated high power beams in the past, LCLS-II presents several additional challenges, namely: the use of superconducting RF cryogenic modules for acceleration of electron beams, the transport of high power beams through Beam Transport Hall, the undulators at forward angles with respect to the LCLS Experimental Hall, long periods of beam operations (large use factor).

Potential radiological impacts to the public and the environment include: 1) direct prompt radiation dose to the public, 2) doses to the public due to the production and release of airborne radioisotopes, 3) activation or release of radioisotopes to groundwater, 4) activated LCW systems and storm water pollution. The impacts from LCLS-II operations mainly come from high beam loss points such as main dumps. Requirements from regulations (e.g., from DOE and EPA) and SLAC radiological environmental protection program, including ALARA principle, are satisfied with appropriate safety system design as well as operational controls for LCLS-II. This is described in more details in section 17.6.

17.2 Criteria for Shielding and Radiation Safety Systems

The SLAC Radiological Control Manual specifies an administrative control level of 500-mrem total effective dose (TED) per year and a dose-management “ALARA Level” of a maximum of 360 mrem TED per year above natural background levels for radiological workers. The actual dose that the majority of personnel at SLAC typically receive is well under these levels. This will continue to be the case for LCLS-II operations, with very little to no doses expected from prompt radiation generated during beam operations.

The following radiation dose criteria have been used in the design of the LCLS-II radiation safety systems:

1. The effective dose to personnel working inside and around the experimental halls should not exceed 100 mrem in a year (2000 work hours) for normal beam operation. The users of the LCLS-II who will be working in the experimental halls are not classified as radiological workers.
2. During normal operations the LCLS / LCLS-II electron beam enclosures are be shielded to an average dose rate of less than 0.5 mrem/h in accessible areas of the accelerator and research yard and to 0.05 mrem/h for general public areas.
3. The maximum effective dose rate in accessible areas at 30 cm from the shielding or barrier should not exceed 400 mrem/h for mis-steering conditions, defined as conditions that are comprised of infrequent or short-duration situations in which the maximum allowable beam power, limited by Beam Containment System (BCS) devices is lost locally or in a limited area.
4. The effective dose-rate in the event of the Maximum Credible Incident (MCI) should not exceed 25 rem/h, and the integrated effective dose not exceeding 3 rem [2]. The MCI considers the unlikely scenario of failure of safety systems and is defined as the highest beam power that the accelerator can deliver to a point, assuming that all the BCS devices that limit beam power have failed.
5. In addition to shielding (bulk and local), the LCLS-II radiation protection systems have a Beam Containment System (BCS) and Personnel Protection System (PPS) in the tunnel, and the Hutch Protection System (HPS) in the X-ray beam lines.

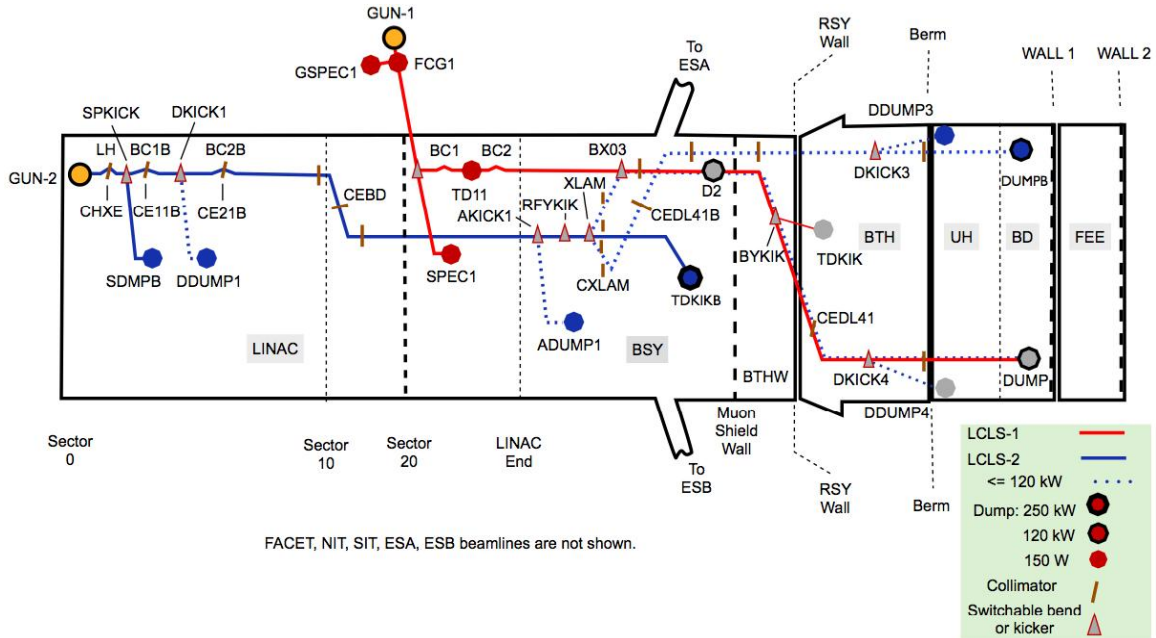


Figure 2. Overview of LCLS-I and LCLS-II electron beam sources and dumps.

17.3 LCLS-I and LCLS-II Beam Distribution System.

The electron beam distribution system for the LCLS-I/LCLS-II complex involves multiple destinations for each source, different modes of operation, and a number of high and low power beam dumps. The scheme and the parameters for the dumps are chosen to provide the flexibility of more or less arbitrary bunch distributions to be sent to either the SXR or HXR undulators independently. Moreover, lower power diagnostic lines “steal” a few pulses that are characterized and used for feedback to maintain high beam quality. These diagnostic lines can also be used for a fast abort function.

A schematic showing both electron guns and all dumps is given in

Figure 2. Starting at the LCLS-II gun, labeled GUN-2 in the figure, following the solid blue line representing the high powered CW beam there is a dump labeled SDMPB. It is at the end of a diagnostic line used to measure the laser heater energy spread. Next are low power diagnostic lines and dumps to measure emittance and compression after each of the two bunch compressors. A special fast acting “abort” dump ADUMP1 near the three-way RF kicker (RFYKIK) roughly 3000 m from the GUN-2 serves to both absorb a low power diagnostic beam and also to absorb a high power beam for roughly 100 μ s while, in the event of a fault, the BCS or MPS system is in the process of shutting off the gun.

At the three-way RF kicker, RFYKIK, there are three possible beam paths. The beam that is not kicked out to the undulator lines is directed to the highest power dump TDKIKB. Beam kicked toward the SXR line passes by another diagnostic line and dump just before the undulator and is finally terminated in a high power dump DUMPB. Beam kicked toward the HXR line

joins the existing LCLS-I beam path. This beam then passes by the existing BYKIK/TDKIK kicker/dump combination, but as that dump was only designed for a maximum of 5 kW LCLS-I beams, it will be of limited use for the high power LCLS-II beams. Finally, the CW HXR beam passes by the last diagnostic line and dump just before the undulator hall and is terminated in the high power dump labeled DUMP. Both DUMP and DUMPB share the same shielding enclosure and are installed in existing pits, side by side. However, the shielding on top and down beam of the dump are modified to be commensurate with the higher average beam powers.

Beams that start with the LCLS-I gun will see the same dumps that are in operation prior to LCLS-II, but they will be terminated on a much higher power dump (DUMP), which will replace the current LCLS-I dump. The LCLS-I beam power limit for DUMP was 5 kW.

17.3.1 Dump Performance Parameters

Basic power parameters for the dumps are listed in Table 1. CW operation generally determines the power limits except for existing elements such as TDKIK and D2, for which the beam power is BCS limited. “Nominal Beam Power” refers to the beam power chosen to be consistent with operation at 100 pC/bunch and 1 MHz repetition rate. “Maximum Beam Power” numbers assume either 300 pC/bunch at 1 MHz or a power that is limited by a BCS device, whichever is lower. Generally each dump must be rated at a power no lower than the Maximum Power. In the case of TDKIKB the beam power is limited by the BCS to 240 kW even though the Linac has the capability of 1.2 MW beams (TDKIKB can take beams of up to 300 kW)..

“Average (1 yr) Beam Power” is a conservative design value for the overall time-average power the dump will absorb. Unbiased estimates of the time-average dump powers were made for the main dumps. The results are 53, 24, and 18 kW for TDKIKB, DUMPB, and DUMP respectively – comfortably below the design values in Table 1. The estimates were made by taking, for each accelerator mode of operation, the power going to each dump and the percentage of time the accelerator is in that mode, and calculating weighted average of the power. The following assumptions were also made:

- FEL X-ray beam power is limited to 20 W per beamline by mirrors.
- FEL X-ray beam will be delivered to experimental stations either as 1 W for tuning up the experiment or 20 W for data taking.
- The experimental program requires seeded beam for the majority of the experiments, and seeded beam pulse energies will be around 100 uJ/per pulse.
- A negligible number of experiments will require harmonic operation: ~1 uJ/per pulse at maximum beam power.
- 1 kW of beam power is always maintained on a high power dump for MPS/BCS reasons and diagnostic purposes.

- The Linac is tuned up at 80 kW x 2 + 1 kW and maintained at this current. Current in excess of that going to the SXR or HXR lines is sent to TDKIKB (80 kW is derived from $4 \text{ GeV} \times 100 \text{ pC} \times 20 \text{ W} / 100 \text{ uJ}$, seeded operation).
- The LCLS-I beam is 5 kW. This is a conservative simplification.
- Operational time when beam is scheduled to be delivered to users is estimated to be 5000 hours per year.

Table 1. Design parameters for LCLS-II electron beam dumps.

Symbol	Max Beam Energy [GeV]	Nominal Beam Power [kW]	Max Beam Power [kW]	Average (1 yr = 5000 h) Beam Power [kW]
SDMPB	0.1	0.001	0.003	0.001
DDUMP1	0.25	0.003	0.01	0.003
TDKIKB	4	240	240	120
ADUMP1	4	0.048	0.144	0.048
DUMPB	4	40	120	60
D2	4,15	0.245	0.9	0.012
TDKIK	4,15	0.245	0.9	0.024
DDUMP4	4,15	0.014	0.045	0.014
DUMP	4,15	40	120	60

‘Max Power’ values are used to design the shielding of dumps for prompt and residual radiation, while ‘Average Power’ values are used to determine shielding needed to protect the environment from long-term operations.

Note that for most photon wavelengths it is possible to deliver SASE pulse energies of 1 mJ or more and reach the 20 W FEL X-ray power limit on the mirrors with as little as 8 kW of electron beam power. However, for the ‘Average Power’ estimates it was assumed that effectively all of the delivered beam is seeded and has a pulse energy of only 0.1 mJ. With this assumption it takes 80 kW of electron beam to reach the mirror limit. Maximum beam power, 120 kW, is required only when the FEL efficiency is extremely low, such as when generating harmonics. Another assumption used to determine average power estimates is that the TDKIKB dump takes remainder of 80 kW beam in the Linac that is not sent to DUMP or DUMPB. This arrangement insures independent operation of two beamlines. When one beamline changes repetition rate or even turns off their beam entirely, the other will not notice. Lastly, at minimum a beam of 1 kW to TDKIKB is always maintained to keep feedbacks active and verify that beam path is viable in case of an MPS fault.

Table 1 is the starting point for the design of shielding for prompt and residual dose rates (typically designed for the Max Beam Power) as well for environmental protection (usually based

on Average Power). These and all other loss sources along with their potential radiological impacts have been systematically identified and cross-linked in [3].

17.3.2 Upgrade Scenarios

The beam distribution system for LCLS-II is designed with the expectation of adding beamlines in future upgrades. The SC Linac is capable of 1.2 MW beam power and could support 10 or more beamlines. For the baseline only 240 kW is required and this will be the operation safety envelope. For dumps, there are two basic options for upgrading to more beamlines. One option is to upgrade the TDKIKB dump to 1.2 MW. This option is attractive because of the simplicity of all unused beam going to one location that can be well shielded. A few megawatt class dumps already exist at SLAC and could be employed. The near-term disadvantage is the additional cost to the project. The other option is to add ~300 kW class dumps as new beam lines are incorporated. This option gives more flexibility to locate the new beamlines. A combination of the two options is also possible.

17.4 Preliminary Shielding Design

This section presents the conceptual shielding design for LCLS-II. For outstanding radiological areas of LCLS-II, like the high power dumps and the BTH building (which was not designed for beams of hundreds of kW) specifications are based on actual preliminary computation analysis. For other components, such as lower power dumps in the LINAC (where high power dumps were already operated), or for elements similar to those in use at LCLS-I (like the tune-up dumps), no dedicated analysis has been carried out yet, but applicable guidelines are described and relevant studies are referenced.

17.4.1 LCLS-II Injector, LINAC and Beam Switch Yard

Existing shielding of the SLAC 2-mile Linac and the Beam Switch Yard (BSY) is sufficient for prompt radiation that is generated from beam losses in the accelerator, by-pass transport line and in the Beam Switch Yard.

There are two beam dumps (SDMPB and DDUMP1 in

Figure 2) for beam tune-up along LCLS-II injector and LINAC before the main beam dump, TDKIKB. These dumps are planned to work at 120 Hz only and will receive beams from an upstream kicker, so the beam pulse rate can be controlled by the kicker. Since there a few watts of beam parked on these dumps, shielding for residual activity will be according to the expected use factors, average beam powers, and access requirements [4, 5] and will range between 4" and 8" of iron or code row steel.

The dark current is another source of radiation in the LINAC. It is estimated [6] ~10 μA of dark current will be generated at the LCLS-II gun, out of each only 1 μA will be accelerated at the gun cryomodule. The 9 μA dark current lost at that stage is at low energy (~1 MeV), and thus carries a low power level (~9 W). The sweeper will then knock the dark current that is

propagated downbeam the LINAC by another factor of 10. The remaining 0.1 μA dark current will be accelerated and lost on several collimators at various energies. These collimators will be locally shielded (not only for dark current, but for primary beam as well). Dark current from field emission in the SRF cavities is mainly localized, and simulations at Cornell show a relatively small current (pA level) travels appreciably.

Other sources of beam loss have also be looked at (e.g. beam gas, Touschek) and found to be in the pA level.

17.4.2 Shielding of LINAC Penetrations

Shielding of the radiation streaming from the LINAC to the klystron gallery through the penetrations is provided by borax filling those. Such shielding will be verified and topped to the full height of the penetration where needed. To avoid radiation leakage, collimator locations must be adjusted in the optics design (MAD deck) so that they are not directly below Linac penetrations. With beta functions of typically 10 meters or more, the required few meter shifts usually can be accomplished without significantly affecting the collimator function. In the cases where that circumstance (alignment of a loss point with a penetration) could not be avoided, local shielding on top of the component would need to be added accordingly.

17.4.3 Shielding of TDKIKB

With beam powers of hundreds of kilowatt, the electron beam dumps and their associated shielding are a major aspect of the LCLS-II facility. Indeed, LCLS-II includes several beam dumps and stoppers of different power and energy ratings, as indicated in Table 1. This section covers the dump taking the highest peak beam power, 240 kW, i.e., TDKIKB.

SLAC has several dumps in stock that can take beams of 240 kW: D10 (250 kW), SL10 (500 kW) and D-400 (2.2 MW). Considering its relatively compact size, the existing D10 dump in its current position at BSY C-line has been preliminary retained as TDKIKB.

Since several key factors will be fully determined later (e.g. residual dose rates), the following shielding requirements should be regarded as preliminary. Among those are the shielding necessary to ensure groundwater below the tunnel is not impacted and the shielding/coverage needed to attenuate prompt dose to the surface.

FLUKA Monte Carlo code [7] [8] tritium production simulations performed in [9] for a 1.2 MW/10% duty factor beam have been scaled down to the 120 kW average power assumed for TDKIKB (Table 1). As a result, it was concluded that 4 ft of iron are necessary between the 2 ft concrete floor and the dump (if more space is available it should also be filled with iron). With such shielding, the saturation activity for ^3H and ^{22}Na in the groundwater table (estimated at a depth of just 10 ft below the concrete floor in BSY) would be minimal and undetectable (of the order of 12 pCi/L for ^3H , and half that value for ^{22}Na). In this scenario, activation of moisture right below the floor and migration of it to the water table is not considered because sandstone in

this zone is very dry as rain water has no direct (or remotely short) path from the surface to the water table due to the large width of the BSY, which blocks that line of sight.

Shielding requirements on top of D-400 were also analyzed in [9]. In that case, with a one-foot plate of iron (below) and an equally thick plate of concrete (above) dose rates at the surface, 30 ft above BSY tunnel, were found to be in the order of 0.05 mrem/h for beam powers of 1.2 MW. Thus, the upper shielding will also be sufficient for the lower D10 beam powers. However, in order to minimize residual dose rates in the upper floor of BSY above D10 at short and medium cool-down times, the sequence of the plates should be inversed, i.e. concrete right over the dump and iron on top of it, as shown in Figure 3.

In summary, *TDKIK shielding design includes a thick layer of iron below the TDKIK (4 ft or even up to 6 ft, depending on space constraints), 1 ft of concrete + 1 ft of iron on top and iron filling most of the available space in the C line to the sides of the dump.* Additional shielding may be installed to the side closest to the lateral ground. Moreover, like for other high-loss areas, the TDKIKB dump area should be painted adequately to minimize the production of loose-contamination from concrete/shotcrete dust.

These aspects, as well as residual activity and its mitigation will be addressed in the future in a similar fashion as in section 17.4.6.

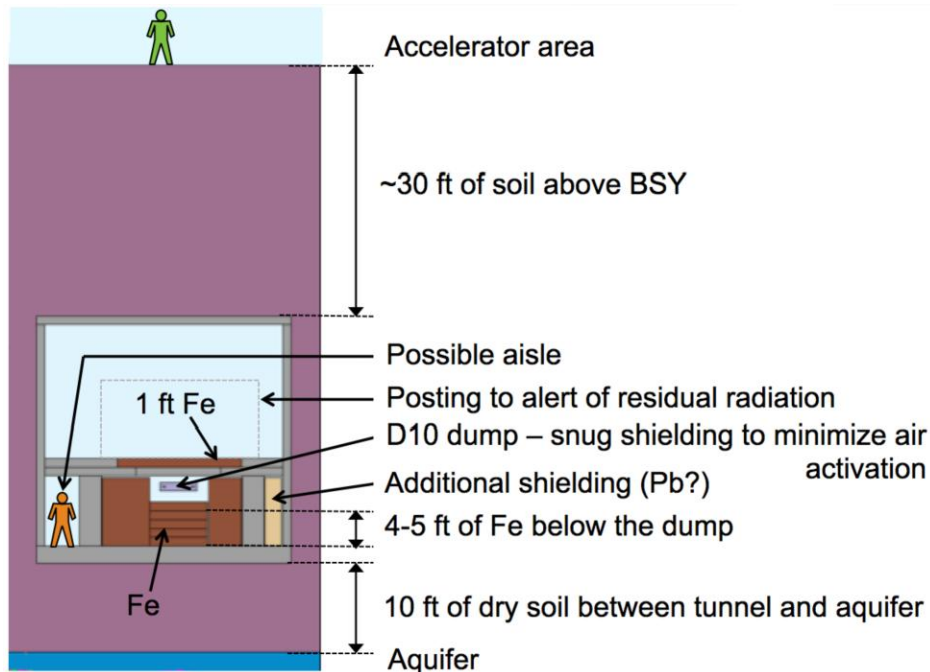


Figure 3. Cross section of the BSY at the TDKIKB (D10) location. The aquifer is 10 ft below the tunnel and the tunnel is 30 ft below ground. Available space around the dump should be filled with shielding. A possible aisle is located to the side of the dump as residual radiation in the second floor will be significant.

17.4.4 Head House, BTH, Undulator and Roof Buildings

The Head House (HH) and the BTH are the structures built for LCLS-I to link the BSY complex and the Undulator tunnel. Those buildings cross the Research Yard (RY), which is accessible to personnel but does not belong to the general public accessible area. Thus (see section 17.2), the walls of these buildings were designed so that normal dose rates in the RY would not exceed 0.5 mrem/h. This principle also applies to the roof below the service buildings on top of BTH. The rest of the BTH roof and the HH roof were dimensioned so that dose rates on top of those buildings would not exceed 3 mrem/h, and sky-shine at the site boundary would be below the SLAC design goal.

With exception of beam losses at beam dumps, shielding design for the 5 kW LCLS-I allowed for point losses of up to 1‰ (i.e. ≤ 5 W) anywhere along the beamline. This loss threshold is guarded by long ion chambers (LIONs). Consequently, concrete walls of the HH and BTH were made 6 ft thick, while the roof was made 4 ft anywhere except below (or near) the service buildings, where it is also 6 ft thick. Such design ensures normal dose rates below 0.5 mrem/h in the accessible areas (Research Yard and service buildings), 5 mrem/h on the roof, and the accident dose rate for 150 kW MCI under the SLAC 25 rem/h limit.

The superconducting LCLS-II is projected to carry up to two 120 kW beams through the LTU. If such beam power was carried with a loss fraction tolerance like that of LCLS-I, then side

walls would need to be augmented substantially, by about to 4.5 ft. To avoid such a major retrofit, it was decided that loss rates above 0.1‰ would trigger LION shut-off.

In that scheme, *2 ft of concrete* should be added on the outside of the BTH walls. This requirement could be further reduced to just *1.5 ft* if comparators in each line were set to prevent losses above 12 W to occur on either beam-line. Alternatively, a fence with PPS access gates could be installed at 18 ft from the BTH. Hybrid solutions could also be implemented, e.g. 1-foot additional concrete and a PPS fence 5 ft from the added concrete. As for the head-house walls, those would also need to be made thicker, but not as much as for BTH, due to the broader size of that building.

The previous solutions are not feasible for the roof of the BTH below the service buildings 911-913. Thus, *PPS will preclude access to those buildings* when LCLS-II beam goes through LTU. Moreover, calculations in [10] show that sky-shine dose rates to public due to neutron leakage through the roof are acceptable and do not dictate any supplemental concrete in the roof. However, higher loss rates are compensated by also imposing a *restriction on the sum of losses for HH/BTH LIONs* (36 W for the first three and 40 W for the last four pairs of LIONs) on top of the individual 24 W limits established for each pair of LIONs.

Borated polyethylene slabs (2-4 inch) will be installed in the outer doors of the BTH East and West mazes, so that increased neutron fluxes are contained within the LTU enclosure.

The requirements above assume that the loss fraction can be made an order of magnitude smaller than that assumed for LCLS-I. This may not be achievable for some components. For those, and *for all other devices where non-negligible losses are regularly expected, local shielding needs to be installed snugly around the full perimeter* of the source to attenuate prompt radiation (including sky-shine) and residual radiation, and to minimize air activation.

In the previous paragraphs 2 additional ft of concrete or 18 ft clearance were specified to keep dose rates from a 24 W beam loss at 0.5 mrem/h. The effectiveness of those measures was therefore equal to $24 \text{ W}/(0.5 \text{ mrem/h}) = 48 \text{ W/mrem/h}$. SLAC prompt dose limit for an accident case in which BCS fails and the full accelerator power is lost is 25 rem/h. Thus, the augmented BTH enclosure or fence solution would comply with the accident case for a beam of up to $25000 \text{ mrem/h} \times (48 \text{ W/mrem/h}) = 1.2 \text{ MW}$.

17.4.5 Tune-up Dump Shielding

Each undulator will be preceded by a diagnostic tune-up dump similar to TDKIK in LCLS-I, which should take a beam-power no larger than that at the corresponding tune-up dump of LCLS-I (TDUND). Thus, a similar shielding design [11] to that of TDUND can be used, including tungsten (to break EM showers), lead (to shield the undulators), borated polyethylene (to moderate and absorb neutrons) and outer panels of marble (to shield gammas).

17.4.6 Shielding of Main Dumps, DUMP/DUMPB

Normal beam power operation on each of the main dumps, DUMP and DUMPB will typically range between 40-120 kW (delivered by superconducting Linac), or, for DUMP, also ≤ 5 kW (delivered by the copper Linac). In particular, as shown in Table I, total beam power in the dump hall will peak at 240 kW, while power over calendar years is not expected to exceed to 120 kW. These power levels exceed substantially the present capabilities of the LCLS-I dump and the enclosure (dump pits), both of which were designed for an average beam power of 5 kW. This section examines a shielding solution for the main dumps that preserves the integrity of the main dump hall concrete structure. Figure 4, rendered with Flair [12] over a FLUKA simulation geometry input, shows the LCLS-II shielding design for DUMP and DUMPB, in which the dump lines have been raised and bent inwards, and top iron and concrete shielding has been added to compensate for the increased beam power and for the elevated location of the dumps.

The raised shielding on the two main dumps captures the photon beam-pipes. From a radiation protection perspective, this is a desirable feature, as this configuration will also help shield NEH from bremsstrahlung showers generated at upstream components. Moreover, the front face of the dump shielding can also serve as a dump for safety dump line that is shown also in Figure 4.

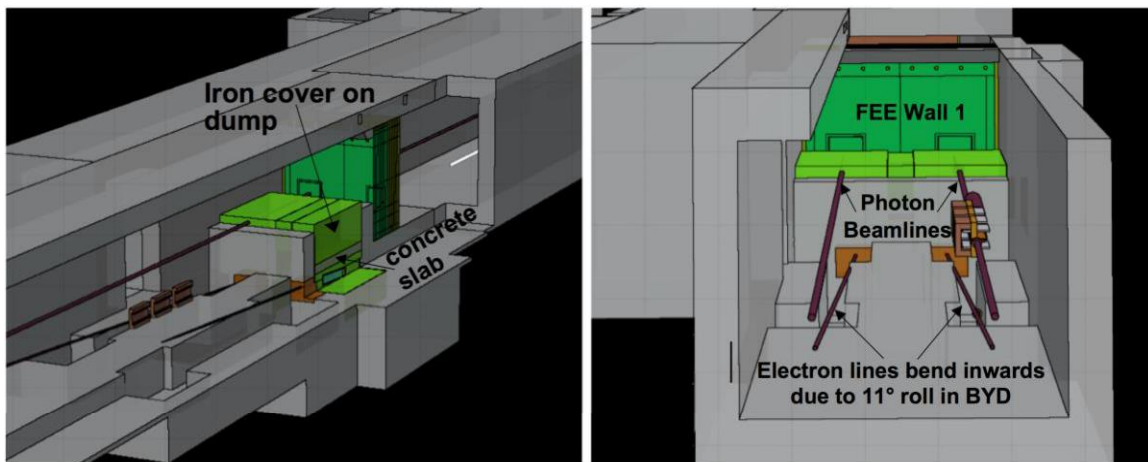


Figure 4. 3D rendering of the model used for LCLS-II main dump hall simulations, where the BYD bends are rolled by 11° and the strength of the kick has been reduced to 3.9° . A 1 ft thick concrete slab (gray) and 5 ft iron (green) are stacked on top of the dumps providing also photon collimation, safety dump capabilities, and supplementing Wall 1 shielding.

17.4.6.1 New Design for DUMP and DUMPB Stoppers

A preliminary design for the main dump stoppers has been produced to cope with the higher power requirements [13]. The new stoppers are cylinders made of 146 cm (16.5 radiation lengths) of aluminum alloy 1100 (of high thermal conductivity), backed with 16.5 cm of tungsten (47 radiation lengths). A radius of 6 inches is sufficient to maintain maximum peripheral energy

flux leakage below 2 W/cm^2 while keeping moderate temperature gradients between the axis and the cooling water coil.

17.4.6.2 Shielding of Groundwater Below DUMP & DUMPB Against Radioisotope Contamination

Radiation escaping the dump pits may either reach occupied areas or activate equipment and the environment. In the latter case, the main concern is the generation of radioisotopes in soil, which could eventually reach the groundwater, located about 30 ft below the dump pits. LCLS-I shielding was designed to conservatively mitigate this risk. In order to compensate for the higher average power on LCLS-II (with respect to LCLS-I), the shielding inside the DUMP and DUMPB pits has been redesigned while leaving the outside enclosure unaltered. The easiest way to achieve was to raise the location of the dumps (by reducing the vertical bend of the main bends to 3.9°) and to bring the dumps closer together towards the center of the tunnel (by adding an 11° roll to the bends). The space vacated below (51 cm) and to the sides (31 cm) of the dumps is filled with iron to further attenuate the high-energy neutron fields, which are mainly responsible for generation of radio-isotopes in soil.

Simulated radioisotope production rates [14], folded with a conservative, build-up/decay hydrogeological model for an hypothetical groundwater column trajectory, dropping from the surface towards the water table (located about 30 ft below the pits) at constant speed, show activation values that in the *worst* case (for speeds of 2 ft/year instead of the presumed 3.3 ft/year), and for this high estimate of the average power, would reach 3400 pCi/L for ^3H and 120 pCi/L for ^{22}Na . These values would be well below the EPA drinking water limits (20000 pCi/L and 400 pCi/L, respectively), but they are just slightly above the detection limits of 1000 pCi/L, and 86 pCi/L (see 17.4.6.2). However, considering other factors such as lateral diffusion towards less-irradiated areas, it is expected that *actual radioisotope concentrations in dripping moisture before it dilutes into the volume of the ground water table would be minimal, and certainly undetectable. To further insure that assumption, a geomembrane should be installed covering the top berm and periodically inspected to reduce the direct rain-water flow near the dump area.*

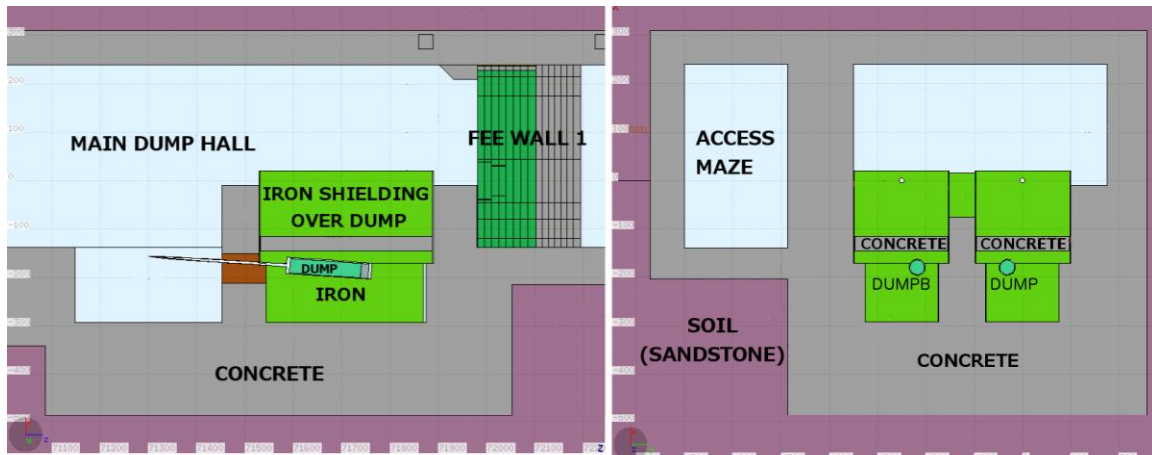


Figure 5. Elevation and transverse sections of the main dump pits showing the position of DUMP and DUMPB as well as the concrete cover plates (gray) on top and the iron (A36 steel) shielding (green) on top and in the dump pit. The grid is at 1 m intervals.

In the longitudinal direction, for LCLS-I, the soil was shielded by $25.92+1.23$ cm of copper+tungsten ($18+3.5$ radiation lengths) in DUMP, followed by 146 cm of A36 steel (~ 83 radiation lengths) shielding in the pit (and 150 cm of air) and 6 ft of pit concrete. As for LCLS-II, after filling the entire length of the pit with iron (actually steel A36), as shown in Figure 5-(left), the longitudinal direction will be shielded by the $146.8+16.5$ cm of aluminum+tungsten ($16.5+47$ radiation lengths) in the DUMP/DUMPB stoppers, followed by about 110 cm of steel A36 (62.6 radiation lengths) before the 6 ft-thick concrete pit. The latter shielding is equal to that in the vertical direction, which in the preceding paragraphs was considered sufficient to shield radio-isotope production in soil from high-energy neutrons generated in electronuclear showers in the dump. For high-energy beams, the dominant dose at small angles is due to showers induced by photo-muons, but those will be drastically less abundant in LCLS-II because at 4 GeV their production is very low, as evidenced by comparing Figure 6-(left) with Figure 7.

As the configuration of the dump and its shielding are frozen, detailed radio-isotope generation simulations including three-dimensional diffusion of water towards the groundwater table could be performed to confirm that the radio-isotope concentrations in groundwater are undetectable.

17.4.6.3 Shielding of the DUMP and DUMPB for Prompt Radiation Fields to Occupied Areas

During operation, low intensity high-energy neutron fields will reach the upper ground surface where the general public can access, while dose to the experimental areas will be dominated by high-energy muons and the associated showers.

With the configuration shown in Figure 5, consisting of an immediate cover of 15-20 cm iron (A36 steel), followed by a 30 cm thick concrete plate and a 135 cm tall A36 steel block, and with the indicated front shielding, the prompt radiation field at 4 GeV with 240 on the main dumps is shown in Figure 6. *At those power and energy levels, radiation fields to the NEH (or even FEE)*

are very small and, as advanced earlier, irradiation of the downstream soil is moderate. As for vertical neutron streaming both peak and yearly average dose rates in the upper ground exceed the instantaneous dose rate limit (~0.3 mrem/h and ~0.08 mrem/h, instead of 0.05 mrem/h) with the initially designed shielding. Thus, 4 inches of iron were added to the starting design, leading to a total shielding on top of the dump of 15-20 cm A36 steel + 30 cm concrete + 135 cm of A36 steel.

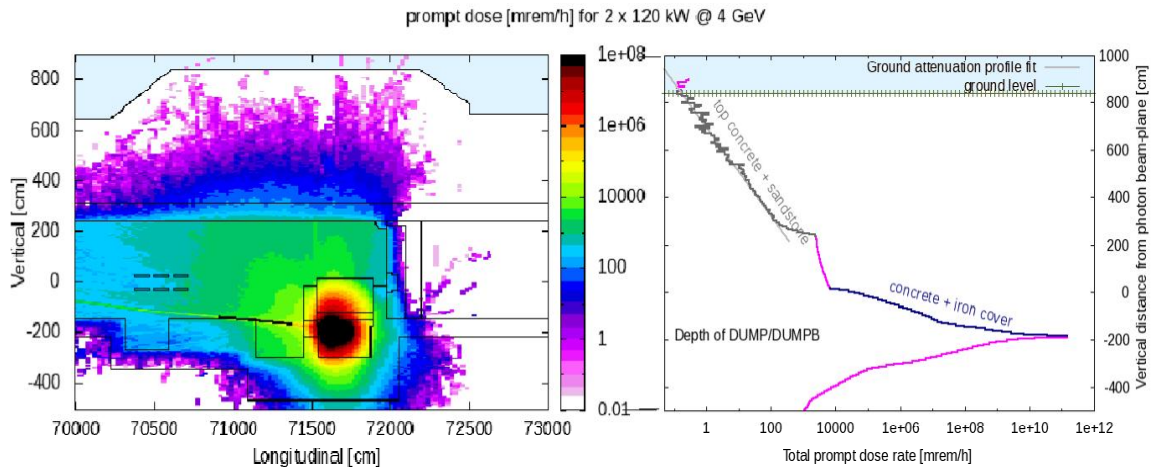


Figure 6. 2D prompt dose rate plot [mrem/h] and 1D projection to the vertical direction above the dump pits for 120 kW @ 4GeV simultaneously for each of DUMP and DUMPB.

The initial design of the dumps included 16.5 cm of iron in the back. For such design, if the superconducting Linac was upgraded to provide 240 kW 10 GeV beams, then peak dose rates in NEH could reach ~0.8 mrem/h (Figure 7), which is above the reference value of 0.05 mrem/h. The current design proposal for the dump substitutes that thickness by tungsten, which also helps reduce the irradiation of the downstream soil.

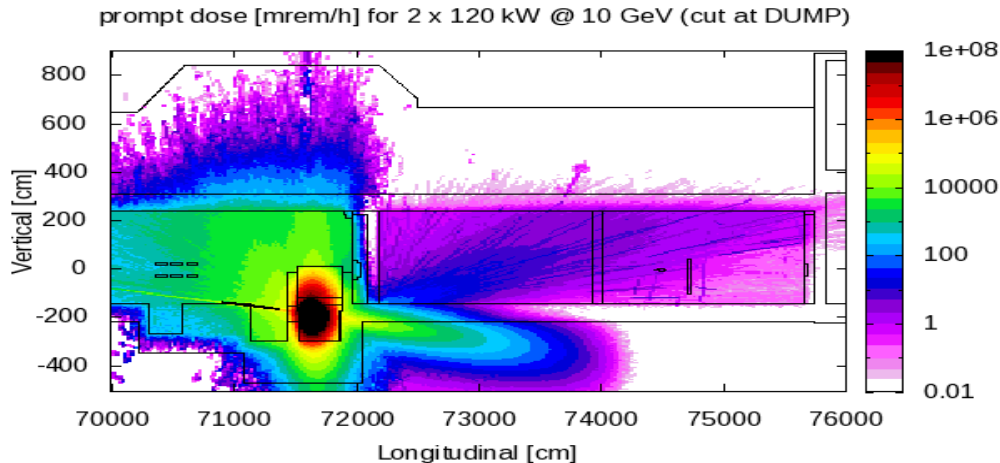


Figure 7. 2D prompt dose rate plot [mrem/h] for 10 GeV upgrade option (2 x 120 kW on DUMP/DUMPB), prior to dump redesign that includes 47 radiation lengths or tungsten.

17.4.6.4 Residual Dose Rates in the Main Dump Hall

When beams are off, an access to the LCLS/LCLS-II complex will be through a maze that communicates the beam dump hall with the Front End Enclosure (FEE) and Near Experimental Hall (NEH). It is therefore important to ensure that shielding around the dumps minimizes the residual dose rates in this area.

For that sake, a plate of 30 concrete (see Figure 5) has been included as part of the shielding that covers the main dumps. The purpose of this component is to reduce low energy neutron fluence to the tunnel walls, which is responsible for ^{24}Na activation decays. In previous LCLS-II studies, residual dose rates at typical access times (within one to few hours of beam off) were an order of magnitude smaller after application of this intermediate shielding component.

On top of the concrete plate, a thick (135 cm) A36 steel cover will shield prompt high-energy neutrons (that activate other decay mechanism in the concrete and beam-lines) and it will also attenuate decay-gammas from the activated dump and concrete slab. These two components (concrete+iron covers) were already introduced in the previous section as part of the shielding for the prompt dose to the upper ground.

Figure 8 shows the simulated residual dose rates [mrem/h] after the first day of irradiation at 2 x 120 kW and one hour cool-down. It is remarked how *residual dose rates at accessible areas near the dump remain below 5 mrem/h*, except for on top of the simulated 1 cm gap for tolerance between the dump pit and the iron plates and in the diagnostic pits in front of the dump pits (~10 mrem/h). Activities from short-lived isotopes will have saturated at 1 day irradiation while those of longer-lived will continue to build up as days and months of irradiation pass.

Figure 9 shows the equivalent plots after the first full year at 2 x 120 kW. For that case it is observed how dose rates are just slightly higher, and this seems mostly due to radio-isotopes from components inside the pit (dump+shielding) rather than from the beam dump hall.

In summary, *the proposed shielding in place seems adequate to allow access through the FEE maze after one hour cool-down. Radiation Area barriers to the dump area may be put in place as activities build up, based on radiation surveys and readings from area monitors. Additionally, shutters could be installed to suppress gamma-leakage from the irradiated dump during beam-off. Moreover, like for other high-loss areas, the second half of the main dump hall should be painted adequately to minimize the production of loose-contamination from concrete/shotcrete dust.*

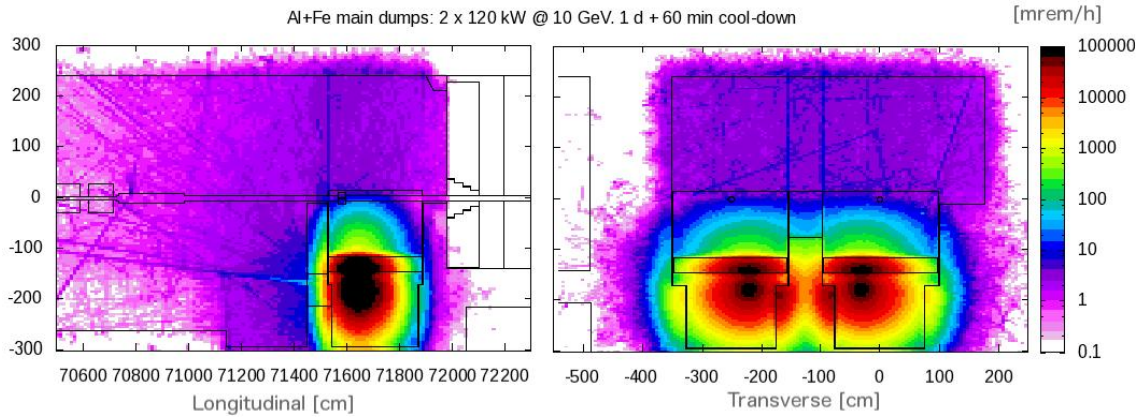


Figure 8. Elevation and cross section residual dose rate maps [mrem/h] for 1 day of operation at 2 x 120 kW, and 1 hour cool-down.

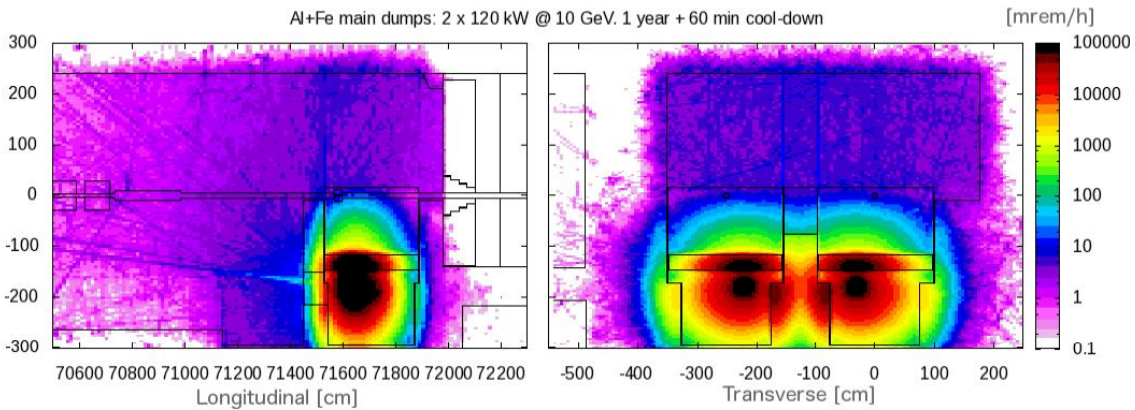


Figure 9. Elevation and cross section residual dose rate maps [mrem/h] for 1 year of operation at 2 x 120 kW, and 1 hour cool-down.

17.4.7 Shielding and Beam Collimation for NEH Access

To allow access to the NEH during beam operations (soft X-ray beams to end-stations and/or hard X-ray beam passing through to downstream hutches), radiation to the NEH must be reduced to meet the shielding criteria. In normal operations, electrons will be sent to the main electron dumps without entering the front electron enclosure (FEE). According to the simulations shown before (Figure 6), prompt radiation from the main beam dumps hosted at the existing LCLS-I pit locations does *not* contribute to dose rates in NEH. However, before being sent to the dump,

electrons generate bremsstrahlung radiation through collisions with residual gas molecules; in beam loss processes occurring mainly in the last bending dipoles before the main dump [15]; and from beam interception by diagnostics. The gas bremsstrahlung power at pressures as high as 10^{-6} Torr represents merely $1.7E-9$ of the total beam power (0.2 mW at 120 kW beam), and thus does not contribute to the dose in NEH. There should be no beam intercepting devices at high repetition rate. The major source of bremsstrahlung is from the small fraction of the beam lost on the main bending dipole before the main beam dumps, DUMP, DUMPB.

To limit dose rates to the NEH, the losses in the main vertical bends (named BYD in accelerator deck files) should be limited to 120 W, i.e. 0.1% of the full 120 kW beams. However, combined losses in BYDs should not exceed 24 W (0.01 %) to avoid the additional shielding around BYD that would be required for the excessive prompt (towards the groundwater and to the upper campus) and the residual dose (in the dump hall). In accident scenarios, e.g., power loss of the dump line bending magnets, electrons may be sent downstream. Permanent clearing magnets (already existing in LCLS-I system) will be required in HXR to prevent electrons from entering FEE, since the hard X-ray beamline has only about 3 cm offset. This requirement does not apply to SXR beamline due to its larger offset (~40 cm [16]).

There are two radiation pathways to NEH: direct penetration through the walls between the dump hall and NEH (Wall 1 and Wall 2), and leakage along beam pipes. The direct penetration can be reduced by adding local steel shadow shielding (80 cm thick and 100 cm \times 100 cm lateral) in FEE [17]. The requirement for the local shielding is dominated by the bremsstrahlung generated in normal operations. The leakage along beam pipes can be reduced by the beam collimation system [17], including not only photon collimators (3-5 along each branch beamline) with high-Z material (e.g. 8 cm thick tungsten heavy alloy) inside FEE, but also electron collimators (2 for each dump line, 60 cm thick steel) between dump line and FEE. Meanwhile, photon collimators with high-Z material in NEH as well as local shielding around collimators and beam transport pipes will be installed to reduce the dose from radiation leakage. It should also be noted that during LCLS-II operations, access to FEE will not be permitted by PPS system.

Finally, according to simulations (see section 17.4.6.3), regular high-power on the main beam dumps hosted at the existing LCLS-I pit locations does *not* contribute to dose rates in NEH (just to FEE).

17.4.8 Experimental Systems and Hutches

The new experimental systems will include two soft X-ray beamlines in existing SXR and AMO hutches, and upgrade the existing hard X-ray beamlines in current hutches. The high rep-rate FEL energy will be 200 – 1250 eV for soft X-ray beamlines, 1 – 5 keV for the hard X-ray beamline in NEH Hutch 3, and 1 – 20 keV (with low rep-rate and limited power high rep-rate) for hard X-ray beamlines in the Far Experimental Hall (FEH).

The beam collimation system described in 17.2.6 helps limiting the high energy bremsstrahlung radiation from entering into NEH. The soft X-ray mirrors cutoff high energy

spontaneous radiation, so that soft beam enclosures (e.g. beam pipes, chambers, etc.) are still expected to supply enough protection. But there may still be noticeable amount of high energy spontaneous radiation for hard X-ray beamlines, since their mirrors have higher cut-off energies and the hard X-ray FEL power entering hutches will increase much as well, the hard X-ray hutches shielding requirements will be re-evaluated. The new operational modes with simultaneous soft and hard X-ray beamlines shall also be studied with proper hutch protection systems (HPS), beam containment systems (BCS) and configuration control [18].

17.5 PPS and BCS Requirements

17.5.1 PPS Design Requirements for LCLS-II

The PPS for LCLS-II will prohibit access to the accelerator shielded enclosure from the LCLS-II injector through FEE during beam or RF operation with the exception of a few areas. Positron Vault, LCLS-I Injector Vault, ESA, NEH and downstream areas can be accessed with the existing SLAC PPS system. Access to Sector 10 vault will be prohibited with PPS during the LCLS-II beam operation. To allow tuning of the LCLS-II gun during access to areas down stream of Sector 10 wall, the LCLS-II Gun Local Mode is envisioned. In this mode, the gun and the Injector Cryomodule are on, 100 Hz Kicker can be on or off. All LCLS-II RF must be off except the RF connected to Injector Cryomodule, and three insertion PPS stoppers must be in. The first PPS stopper must be able to take maximum operation power of 30 kW.

PPS will also turn off LCLS-II beam, or in Gun local mode for access to the fenced area surrounding the BTH. The detailed requirements for PPS are listed in reference [19]; the specifications are described in Chapter 14 of this CDR.

17.5.2 BCS Design Requirements for LCLS-II

The LCLS-II Beam Containment System (BCS) monitors and limits the beam power and beam energy from Linac, to the dumps ensuring that they are within the allowed limits, it also limits beam losses in these areas. Additionally, BCS protects safety-related beam line components from damage due to excessive beam power deposition in them. BCS will shut off the beam if excessive radiation levels are detected, or can be generated in occupied areas, or limits set in BCS sensors are exceeded.

It is imperative the LCLS-II Beam Containment System (BCS) to be redundant and fail-safe since high power beams could quickly burn-through collimators, beam pipes, dumps, and then strike the shielding enclosure generating high radiation doses outside of the enclosure. Fast BCS beam shut-off time is essential to protect the radiation safety components. To protect safety-related beam line components from melting by high power beam up to 300 kW, the BCS response time should be less than 1 millisecond [20]. Burn-through monitors (BTMs) are designed to shut-off the beam for burn-through scenarios that assume BCS failure. Additionally, Beam Shut Off Ion Chambers (BSOICs) with both photon and neutron probes are required to detect radiation

levels outside the enclosures including the neutron component of radiation that may stream through penetrations and shafts.

For LCLS-II, key BCS design requirements beyond recent LCLS-I designs include:

1. Faster shut-off time
2. Compatibility with high repetition rate
3. Toroid comparators with sufficient resolution to detect loss of approximately 24 Watts.
4. The LIONS will need to include a sealed radiation source reference to use for self-calibration

For each area 1) LINAC, 2) BSY, 3) BTHW, BTH HH and BTH, 4) Undulator, 5) Dumpline, 6) FEE, detailed ray-trace studies need to be performed to ensure that all mis-steered beams are contained by BCS collimators backed-up by burn-through monitors. These BCS collimators and BTMs are protected by fast shut-off BCS devices. Average current monitors will limit the beam power to be delivered to each area. Beam energy will be monitored and limited by Dual Trip Comparator or equivalent BCS devices. Beam loss monitor with BCS collimator system will detect any mis-match between magnet setting and the delivered beam energies.

BCS beam loss monitors such as protection ion chambers and LIONS, are critical BCS devices to protect the personnel outside shielding enclosure, especially for BTH. LIONS require radiation sources for a function check and calibration of losses. Furthermore, the existing HH and BTH LION segments will need to be reconfigured, resulting in two segments on the north side of the tunnel and two segments on the south side, with each segment set up to trip off the LCLS-I and LCLS-II beams when 24 Watts of loss is detected. New BCS average current comparators will be required to monitor the beam losses along the beam lines, including LINAC from Sector 10 – 30, TDKIKB dumpline, LTU lines for each LCLS-I and LCLS-II line, LCLS-I and LCLS-II dumpline. BCS requirements for LCLS-II are described in detail in [21].

BCS requirements for the SXR dump line (north side) will be similar to those of the HXR (south side) [22], except for the permanent magnet safety dump line. Such line will *not* be required *only if* the design for the soft X-ray beam line remains with an offset between photon beamline and electron zero degree line larger than 40 cm.

Two additional radiation safety systems will be added to detect and monitor radiation levels in the BSY. A residual radiation dose monitoring system will be linked to PPS in BSY, and BSY ventilation system will be equipped with radiation monitoring detectors to ensure radiation levels are below preset limits prior to access to this area.

17.6 Radiological Environmental Issues

In this section potential radiological impacts to the public and environment from radiation and releases of radioactive materials due to LCLS-II operations are evaluated. The requirements and issues are identified, and measures to mitigate and monitor the radiological hazards are described.

The main impacts include direct radiation (skyshine of neutron and photon radiation) dose to the public, radioactive air effluent and its resulting dose to public, protection of groundwater and soil activation around the high beam loss points, LCW system and wastewater management, and stormwater protection. The impacts to the public and environment shall be below the DOE/EPA [23][24][25][26], state and local regulatory limits, as well as SLAC administrative limits, and are to be maintained ALARA.

The DOE Order 458.1 imposes an annual dose limit to the Maximum Exposed Individual (MEI) of a general public member of 100 mrem/y from all exposure pathways, including skyshine, radioactive air effluent, contaminated groundwater, release of potentially contaminated materials. Doses must also be kept ALARA.

The impacts and issues for LCLS-II are similar to those considered for past high power beam operations at SLAC. The areas of concern are associated with the high beam loss points such as the high power kW main dumps as listed in Table 1 and those collimators with high average power losses.

17.6.1 Skyshine Dose at Site Boundary and Monitoring Systems

Potential sources for direct radiation to the public are skyshine radiation and leakage x-rays from the klystrons in the LINAC Klystron Gallery. Skyshine radiation is caused by neutrons and photons that transmit through the accelerator housing roof, scatter off air molecules, and return to the ground. High-energy neutrons (> 20 MeV) dominate the skyshine radiation from LCLS accelerators and shielding is the main measure to reduce the skyshine impact. The SLAC shielding design guideline for skyshine radiation is 10 mrem/y to the MEI from all facilities and 5 mrem/y from any single facility at SLAC [27].

Since Linac, BSY, undulators and main dumps are heavily covered with thick earth shielding (~ 30 ft), the annual doses from the dumps and collimators in these areas are negligible. For example, conservative calculations for LCLS-I show that the maximum dose to the MEI was 0.4 mrem/y, dictated by 170-W TDUND and 5-kW main dump [28]. The other skyshine source is from normal beam losses at collimators located in BTH, where the roof is just 4-ft concrete. Mitigation options are adding local shielding and/or relocating these collimators to other places such as BTH-W or BSY.

The skyshine neutron/photon radiation are monitored through the site-wide radiological environmental monitoring program, including passive and sensitive dosimeters placed around SLAC site boundary. Due to the high average beam powers of LCLS-II, the active RP Perimeter Monitoring Stations (PMSs) are also utilized to monitor neutron and photon radiation at the SLAC site boundary.

17.6.2 Radioactive Air Effluent and Monitoring Systems

Radioisotopes (mainly the short half-life ^{11}C , ^{13}N , ^{15}O and ^{41}Ar are of concern) will be generated in the ambient air from electron beam losses and then released to environment due to ventilation during accelerator operation and access. These radioactive air releases can produce

potential dose to the MEI. The annual regulatory dose limit for the MEI is 10 mrem/y, and a continuous air effluent monitoring system is required for the release point that is expected to exceed 0.1 mrem/y [29] [30].

Optimum bremsstrahlung yield targets, reasonable air paths surrounding the targets, and beam loss scenarios are used to calculate radionuclide yields. Conservative accelerator operational scenarios and reasonable air exchange rates for accelerator housing are then used to estimate the annual release of airborne radioactivity. The EPA approved code CAP88-PC is then used to calculate the annual dose to the MEI and the collective dose to the population up to 80 km from SLAC. For CY2012 LCLS operations, an annual dose to the MEI (which was located at East-End of SLAC site boundary) was calculated to be $\sim 2 \times 10^{-4}$ mrem/y [31], well below the 10 mrem/y limit and 0.1 mrem/y threshold.

For the high-power LCLS-II operation, the production of airborne radioisotopes and ozone are minimized by adding local shielding, and thus reducing the air paths, surrounding the high beam loss points such as dumps and collimators. The local shielding needed to reduce airborne radioactivity can be integrated with the local shielding needed to minimize the impact to groundwater. To reduce releases to environment, independent ventilation zones and limited air exchanges at high beam loss points during accelerator operation are implemented as needed.

Continuous air monitoring systems (AMSs) for release points [32] at BSY, BTH and the main LCLS-II dump enclosures are used periodically to measure the production of airborne radioactivity and to ensure that the 0.1 mrem/y threshold from each release point is met so that no continuous air effluent monitoring is required. Radioisotopes such as ^3H and ^7Be are also produced in the air, but with activities 2 orders of magnitudes lower than the above short-lived radioisotopes. Their dose impacts to the public MEI are minimal, but they may present contamination impact to the workers entering accelerator enclosures and impact to groundwater, which are addressed by operational radiation protection controls as needed.

17.6.3 Groundwater Protection and Soil Activation and Monitoring Systems

High-energy neutrons produced from electron beam losses are the most penetrating and are the main cause for radioisotope production in environment media (soil and groundwater) outside accelerator shielding walls surrounding the beam loss points. The main radioisotopes produced in soil are ^3H (12.3-year half-life) and ^{22}Na (2.6-year half-life). For groundwater protection, ^3H is the main radionuclide of concern due to its high leachability (nearly 100%) from soil to groundwater. Groundwater may not be impacted [33][34], which in practical terms means that the groundwater cannot have detectable radioactivity due to LCLS-II operation. This is compared to the EPA-required detection limit of 1000 pCi/L for ^3H in drinking water. The ALARA principle should also be followed for soil and groundwater protection [27].

Past high beam power ESA operations have resulted in detectable ^3H in groundwater wells located very close to the beam dump D400. This issue was anticipated during the design of the project [35] and the situation is regularly monitored [36].

The safety design for LCLS-II high loss points includes extensive shielding to minimize the impact to soil and groundwater surrounding the beam loss points. For example, compared to existing LCLS-I dump, extra shielding (by at least a factor of 10 or more attenuation) has been incorporated in the design of the two LCLS-II main dumps to compensate for the increase in total beam power such that the potential activation for the water reaching the groundwater table below the dumps is insignificant (i.e., non-detectable).

Additional groundwater monitoring wells will be installed for areas near the high loss points such as BSY, and LCLS-II main dumps.

17.6.4 Wastewater Management and Stormwater Protection

Wastewater includes regular LCW replacement and discharge, as well as water originating from within the accelerator housing. Wastewater is collected at sumps at various locations and pumped to holding tanks outside accelerator housing. Storage, radiological monitoring and analysis, and discharge of wastewater into sanitary sewer are managed per various requirements [37] to satisfy the regulatory discharge limits (e.g., 5 Ci/y of ^3H and monthly concentration limits in wastewater permit from the South Bayside System Authority) [38] and SLAC radiological environmental program requirements.

Protection of stormwater from potential spill of the LCW systems and possible leakage to the soil and storm drains is also regulated and is considered both in the design and for operation.

17.7 Operational Radiation Protection Issues

The operational radiation protection issues that will be encountered at beam power levels of LCLS-II include higher levels of residual activity at beam dumps, collimators and other beam loss locations; increased level of air activation and radioactive contamination; and fixed and removable contamination.

Activated air and ozone are present mainly during high power beam operation and shortly after beam is turned off. Few longer-lived radioisotopes such as ^{41}Ar (half-life of 110 minutes) and ^7Be (half-life of 53 days) can also be produced. Installation of Continuous Air Monitors, delay in access to enclosure, controlled venting of the enclosure prior to access, installation of radiation monitoring system that measures dose rate before access to high loss points is allowed, as well as addition of local shielding and/or barriers around beam dumps and collimators will be used as part of management of hazards from these sources.

The typical sources for contamination in the accelerator enclosure include dust, flaking or peeling paint, beam-line components, spilled water from closed loop cooling systems for dumps and collimators, flaking or peeling paint chips and liquids created when activated material or equipment is machined or refurbished or otherwise damaged. Removal of excess components and legacy beam lines in the accelerator, especially in the BSY, and taking strong measures to control the dust (e.g. using paint to seal the enclosure) and debris reduces the magnitude of the contamination problem.

Programs that are part of the SLAC operational radiation protection will support LCLS-II operations. These include a program to ensure that activated material is not removed from accelerator housing without proper surveying and labeling, and processes and procedures that designate locations for storing radioactive materials on site, transport of radioactive materials to machine shops for disassembly and repair, as well as radioactive waste disposal.

17.7.1 Radiation Damage Fields to Beam-Line Components

Potential radiation-induced damage to sensitive components like electronics and permanent magnets will continue to be studied through measurements and simulations. The on-going program of investigating radiation environment in LCLS-I undulator (synchrotron radiation, Bremsstrahlung losses) will continue and potential damage to LCLS-II undulators can be simulated and mitigated.

17.7.2 Repair and Maintenance Considerations

Accelerator operation with several hundred kW beams requires all beam-line components to be chosen such that activation and generation of mixed (hazardous and radioactive) waste is minimized. Similarly, components should be designed and installed in such a way that they can be extracted quickly from the beam-line for repairs, or they can be maintained *in situ* with minimum exposure to residual radiation. Similar to LCLS-I, intervention to components that may result in high doses to personnel will be assessed to ensure that the ease of potential repairs and maintenance have been considered. During operations, cool-down time and optimum work control plans will be utilized to keep doses during maintenance and repair ALARA.

17.7.3 LCW System Design and Activation of Water in Dumps

The LCLS-II high-power dumps and collimators require LCW for cooling, and thus the LCW connected to these systems may contain large amount of radionuclides, especially, ^3H , ^7Be and corrosion products. Potential leakage and spills from these systems can generate potential exposure and contamination issues to workers and environment. Independent LCW systems, similar to those for ESA-BDE, SLC NFF/SFF Dumps, SL10/30, or BSY Collimators systems, are needed for the LCLS-II high-power dumps. Radiological protection of workers for repair and maintenance of activated LCW systems and its resin filters and piping systems will be considered in the design and operation of the LCLS-II.

17.8 References

1. SLAC ES&H Division, Radiological Control Manual, SLAC-I-720-0A05Z-001-R005, SLAC National Accelerator Laboratory, Menlo Park, CA, 2010
2. SLAC ES&H Division, Radiological Safety Systems, SLAC-I-720-0A05Z-002-R003, SLAC National Accelerator Laboratory, Menlo Park, CA, 2010
3. M. Santana, "Response to LCLS-II (2013) CD1 Directors Review Recommendation to RP", RP Memorandum, RP-RPG-140109-MEM-01, January 2014.

4. S. Xiao, M. Santana and S. Mao, "Shielding Studies for Prompt and Residual Radiation from LCLS-II Injector Dumps", RP Note RP-12-04, 2012.
5. S. Xiao, M. Santana and S. Mao, "Linac Sector 10-20 Radiation Shielding Analysis for LCLS-II Operations", RP Note RP-12-05-R1, 2013.
6. Christopher Mayes, Cornell University, personal communication.
7. G. Battistoni, S. Muraro, P.R. Sala, F. Cerutti, A. Ferrari, S. Roesler and A. Fassò and J. Ranft, "The FLUKA code: Description and benchmarking", Proceedings of the Hadronic Shower Simulation Workshop 2006, Fermilab 6-8 September 2006, M. Albrow, R. Raja eds., AIP Conference Proceeding 896, 31-49, (2007).
8. A. Ferrari, P.R. Sala, A. Fassò, and J. Ranft, "*FLUKA: a multi-particle transport code*", CERN-2005-10 (2005), INFN/TC_05/11, SLAC-R-773.
9. L. Nicolas, "Preliminary calculations around a MW class dump", RP Memorandum, RP-RPG-131025-MEM-01, November 2013.
10. M. Santana and S. Mao, "Sky-shine neutron dose to public from new LCLS-II operation", RP Memorandum, RP-RPG-131105-MEME-01, November 2013.
11. M. Santana, J. Vollaie and S. Roesler, "Radiation protection studies for the undulator tune-up dump of LCLS", RP Note, RP-07-28-r2, November 2008.
12. V. Vlachoudis, FLAIR: A Powerful But User Friendly Graphical Interface, *Proc. Int. Conf. on Mathematics, Computational Methods & Reactor Physics (M&C 2009)*, Saratoga Springs, USA, 2009.
13. D. Walz, "Investigation of 100 kW SLC FF Extraction Dump for Use in LCLS-II", SLAC Memorandum, October 30 2013.
14. M. Santana, "First radioisotope production evaluations for DUMP/DUMPB of LCLS-II MHz project", Radiation Physics Note, RP-13-22.
15. S. Xiao, "Radiation Protection Studies for Electron Losses in LCLS-II BYD Magnets", RP Note RP-13-06-R1, 2013.
16. "LCLS-II CDR Chapter 11: Photon Transport and Diagnostics", LCLSII-1.1-DR-0001, 2013.
17. S. Xiao, M. Santana and L. Nicolas, "Radiation Shielding Studies for LCLS-II XTOD", RP Note RP-13-14, 2013.
18. S. Xiao, "Radiation Shielding Studies for LCLS-II XES Baseline Design", RP Note RP-13-05, 2013.
19. S. Mao, K. Turner, "PPS Access Requirements for LCLS-II Project", RP Memorandum RP-RPG-131119-MEM-02, 2013.
20. J. Welch, e-mail comuncation 11/10/2013 BCS response time.
21. Stan Mao, Kristina Turner, "BCS Requirements for LCLS-II Project", RP-RPG-131119-MEM-03, November 19, 2013
22. T. Sanami and X. S. Mao, "Safety analysis for safety dump line of the LCLS facility", RP-07-03, January 31, 2007
23. DOE-2011: Radiation Protection of the Public and the Environment, DOE Order 458.1, Feb. 2011.
24. EPA-1987: U.S. EPA, "National Pollutant Discharge Elimination Systems (NPDES)", 40CFR122, 1987.
25. EPA-1989: U.S. EPA, "National Standards for the Emission of Radionuclides Other Than Radon from Department of Energy Facilities (NESHAPs), 40CFR61, Subpart H, 1989.
26. EPA-1992: U.S. EPA, "National Primary Drinking Water Regulation (NPDWR), Environmental Protection Agency", 40CFR141, 1992.

27. RE-200: SLAC Radiological Environmental Protection Program Manual, Radiation Protection Department, RE-200, March 2012.
28. RPD-2008: Linac Coherent Light Source (LCLS) Radiological Environmental Impact Analysis Report, Radiation Protection Department, November 2008.
29. RE-022: SLAC National Emission Standards for Hazardous Air Pollutants (NESHAPs) Program Technical Manual”, Radiation Protection Department, RE-022.
30. EPA-1989: U.S. EPA, “National Standards for the Emission of Radionuclides Other Than Radon from Department of Energy Facilities (NESHAPs), 40CFR61, Subpart H, 1989.
31. SLAC-2013: SLAC NESHAPs 2012 Annual Report, Radiation Protection Department, May 2013.
32. RE-021: Technical Basis Document for SLAC Air Monitoring System, Radiation Protection Department RE-021.
33. EPA-1992: U.S. EPA, “National Primary Drinking Water Regulation (NPDWR), Environmental Protection Agency”, 40CFR141, 1992.
34. RWQCB-2009: California Regional Water Quality Control Board (RWQCB), San Francisco Bay Region Order No. R2-2009-0072, 2009.
35. K. Kase, Tritium in Ground Water at the Stanford Linear Accelerator Center, RP-02-17, SLAC National Accelerator Laboratory, Menlo Park, CA, 2002.
36. RWQCB-2009: California Regional Water Quality Control Board (RWQCB), San Francisco Bay Region Order No. R2-2009-0072, 2009.
37. RE-019: Approving Sanitary Sewer Release of Water Containing Radioactivity: Rationale and Process, Radiation Protection Department, RE-019, SLAC-I-760-2A16Z-000.
38. SBSA-2011: South Bayside System Authority (SBSA), Mandatory Wastewater Discharge Permit WB 111216, 2011.

18 FUTURE UPGRADE OPTIONS

TECHNICAL SYNOPSIS

The LCLS-II is designed to meet several baseline requirements with two separate FELs driven by a new superconducting CW linac. Although the baseline design is clear, it is useful to envision future expansion concepts and enhanced performance so that present design decisions will not exclude these avenues. This chapter briefly describes some of these future expansion ideas, including an energy upgrade, an increased bunch repetition rate, expanded FEL facilities, external laser seeding with HGHG, HHG and EEHG FEL designs, and several other concepts.

18.1 Introduction and Overview

This section describes several upgrade or expansion schemes that are being envisioned and considered at the present time. These may provide extended wavelength range, higher X-ray power, a higher pulse rate, narrowed bandwidth, and additional user capacity. Baseline design decisions will be made in order to preserve these possibilities, where practical.

18.2 Electron Energy Upgrade

The electron energy of the new SCRF linac was chosen to be 4 GeV, including some small operational margin. Enhanced FEL performance and a wider spectral tuning range are possible with an increase in electron energy. Described here are two ways of increasing the energy. The first option (pulsed mode) might need very little initial investment but runs at a lower duty cycle, while the second option (upgrade) will require installation of more cryomodules and a second cryogenics plant.

18.2.1 Higher Gradients in Pulsed Mode

The baseline linac design includes 35 installed cryomodules, each with eight 9-cell L-band RF cavities for electron acceleration up to at least 4 GeV, using an average gradient over the powered cavities of just under 16 MV/m. Given the off-crest RF phasing needed for bunch compression and the fact that 6 percent of RF cavities are typically held in reserve as spares, even in the best of circumstances the final energy cannot be increased much above 4.4 GeV when the baseline RF is run in a CW mode. It may be possible, however, to run the RF in a pulsed mode rather than CW operation, with a lower beam current and a reduced duty cycle, allowing the average RF gradients in the linac to be run perhaps as high as 24 MV/m. This concept needs further study but may allow a final electron energy of up to 6.4 GeV with pulses of 200 μ A at 25~40% duty cycle. The duty cycle would be determined by both cryogenic heating (scaling as the gradient squared) and by possible RF ramping issues. To limit thermal transients, the cycle times would be limited to <1 second and an example cycle might be 25 msec of an rf ramp, followed by 100 msec of 1 MHz bunches and then followed by 125 msec with the rf and beam off with a macro-pulse repetition rate of 4 Hz. The transport lines extending from the exit of the linac to each final electron dump will be designed and built to support up to a 10 GeV beam in order to keep these upgrade possibilities open. A 6.4-GeV energy would allow 6-7 keV FEL photons from the HXR undulator. More study is needed before such a low duty cycle operation could be proposed.

18.2.2 Additional Installed Cryomodules

The 35 cryomodules included in the baseline design extend from the beginning of the existing SLAC linac tunnel to about the mid-sector-6 location (101.6 m/sector). This stretch constitutes about 650 m of accelerator length, accommodating the injector, bunch compressors, and several beam collimation sections. The available (unused) tunnel length leading up to the start of the

bypass line at mid-sector-10 is then about 300 m. This empty tunnel might be filled in the future with (up to) an additional 22 cryomodules (13-m period). There are two ways in which this upgrade might be adopted. First, with the baseline single cryoplant, the gradient would need to be decreased as $1/\sqrt{L_{acc}}$ allowing a final electron energy in sector-10 of about 5.5 GeV with a 12.5 MV/m average gradient. Second, with an additional cryoplant comparable in power and scale to the initial LCLS-II system, the gradient could be maintained at 16 MV/m reaching a final energy in excess of 7.0 GeV. This upgrade would allow the full CW, high-rate operation of the SXR and HXR FELs with a significantly extended wavelength range into the hard X-rays, approaching 8-10 keV in the HXR FEL.

18.3 Future FEL Lines

The LCLS-II baseline project includes two FEL's feeding six experimental stations. Operationally, such a configuration is useful because it allows each FEL to supply X-rays to one or two stations while the other stations modify their experiments for another user. Of course, the SCRF linac is capable of supplying beam to many additional FELs which the SLAC site could support. The original LCLS project, constructed in 2009, anticipated two paths for subsequent expansion:

- installation of a second undulator in the existing tunnel, and
- construction of a new beamline and tunnel on either the north or south sides of the existing Beam Transport Hall (BTH) and tunnel which could support long undulators.

The first path is developed in this Conceptual Design Report. The second path was developed to the point of readiness to receive DOE approval for construction (CD-3). In addition, other facilities exist on the SLAC site, such as End-Station A (ESA) and End-Station B (ESB), which might be modified to support short, soft X-ray FELs. These options are illustrated in Figure 1.



Figure 1. Options for future expansion of the LCLS FEL complex. The existing LCLS and the new LCLS-II (referred to here as LCLS-2020 and described in this CDR) are indicated in gray and green. Future expansion possibilities are indicated in orange and include a new tunnel proposed for an earlier version of the LCLS-II to the South of the existing tunnel, as well as a new tunnel to the North as described in Section 18.3.1. In addition, the SLAC facility has existing tunnels to two of the original SLAC End-Stations, End-Station A to the north of the existing LCLS, and End-Station B to the south as described in Section 18.3.2.

18.3.1 New Beam Transport, Undulator Hall, and Experiment Hall to the South

Until September 2013, the LCLS-II Project proposed to build a new tunnel and experiment hall on the south side of the existing facility. This design was documented in a Preliminary Design Report prepared to support approval of CD-2 for the project. Elements of this project ranging from the tunnels and experimental facilities to the normal conducting linac in Sectors 11-20 could be resurrected as a follow-on upgrade of the LCLS and LCLS-II facility. The long tunnel of the original LCLS-II project is ideally suited for long undulators that would be heavily tapered and generate intense hard X-ray pulses in a ‘TeraWatt’ configuration [1].

This earlier LCLS-II Project was designed to provide the following facility enhancements:

- A hard X-ray undulator source (2,000-13,000 eV).
- A soft X-ray undulator source (250-2,000 eV).
- A dedicated, independent electron source for these new undulators, making use of Sectors 10-20 of the SLAC linac.
- Construction of an annex to the Klystron Gallery to house a laser for the photocathode gun.
- Modifications to sectors 10-20 of the SLAC linac, primarily to install two bunch compressor chicanes.
- Adaptation of an existing beam transport line to carry electrons past the LCLS linac through the existing Beam Switchyard.
- Expansion of the existing LCLS Beam Transport Hall in the SLAC Research Yard to house new transport lines to the new undulator sources.
- A new shielded enclosure that is roughly 300 meters in length for the two new undulator sources, beam dumps, and X-ray front ends.
- A new experiment hall capable of accommodating at least four experiment stations.
- A high-field physics experiment station served by the soft X-ray undulator.

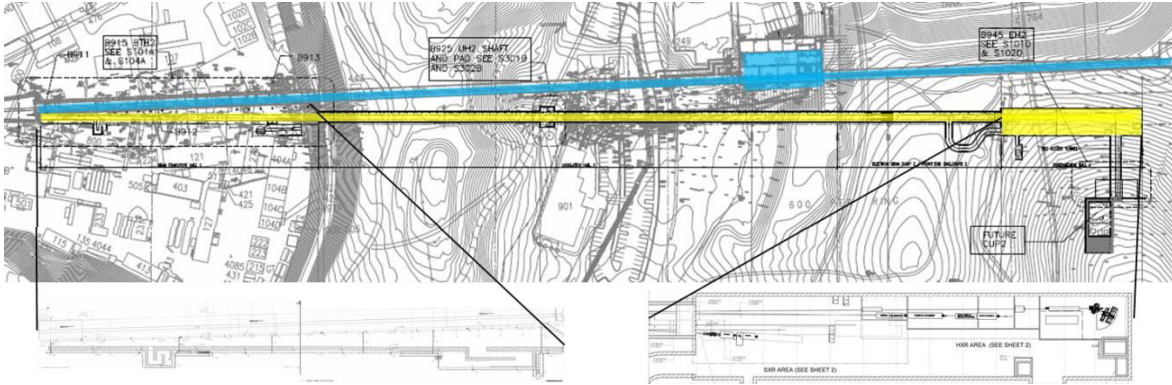


Figure 2. Layout of LCLS-I and earlier version of LCLS-II. Items tinted blue are existing LCLS facilities. Items tinted yellow are possible new LCLS-II facilities. Blowups of the Beam Transport Hall extension and the new Experiment Hall are shown below the site layout.

Table 1. Sample operating parameters for the SXR and HRX beamlines illustrate the range of photon energies, beam energies, bunch charges, peak currents, and possible parameter sets for the HXR and SXR. Self-seeding configurations are also included (SXRSS & HXRSS).

Parameter	"Earlier" LCLS-II Operational Configurations									
	SXR	SXR	SXR	SXR	SXR	HXR	HXR	HXR	HXR	HXR
Undulator line	SXR	SXR	SXR	SXR	SXR	HXR	HXR	HXR	HXR	HXR
Operational mode	SASE	SASE	SASE	SASE	SXRSS	SASE	SASE	SASE	SASE	HXRSS
Photon energy [keV]	2.0	1.0	0.50	0.25	1.0	13	13	5.0	3.7	8.3
Final electron energy [GeV]	13.5	13.5	10.0	10.0	10.0	13.5	13.5	10.0	10.0	13.5
Laser pulse length (FWHM) [ps]	3.0	3.0	3.0	3.0	3.0	3.0	3.0	3.0	3.0	3.0
Laser iris diameter [mm]	0.6	1.0	1.0	1.2	0.8	0.6	1.0	1.0	1.2	0.6
Bunch charge [pC]	20	150	150	250	150	20	150	150	250	40
Slice emittance ϵ_n [μm]	0.19	0.41	0.41	0.51	0.41	0.19	0.41	0.41	0.51	0.23
Bunch length (rms) [μm]	0.58	4.3	4.3	11	6.5	0.58	4.3	4.3	14	0.87
Undulator K []	5.4	7.8	9.0	9.9	4.8	2.5	2.5	2.6	3.5	3.3
Undulator period [mm]	63	63	63	63	63	32	32	32	32	32
Undulator gap [mm]	14.6	10.0	8.3	7.2	16.2	10.2	12.2	10.1	7.6	8.1
Magnetic undulator Length [m]	50.1	50.1	50.1	50.1	63.4 [§]	67.8	67.8	67.8	67.8	109 [§]
$\langle\beta_{x,y}\rangle$ [m]	20	20	15	15	15	20	20	15	15	20
Peak power [GW]	70	68	70	37	>190	62	34	56	18	580
Pulse duration (FWHM) [fs]	6.7	50	50	125	75	6.7	50	50	167	10
Waste size (FWHM) [μm]	23	32	32	43	38	19	23	26	34	16
Beam divergence. (FWHM)	12-	17-	30-61	49-98	17	2.7-	2.2-	5.0-	5.6-	4.0
Photons per fs [$\times 10^{10}$]	22	43	88	94	119	3.0	1.7	7.0	3.0	43
Pulse intensity [mJ]	0.47	3.4	3.5	4.7	14	0.41	1.7	2.8	2.9	5.8
Photon bandwidth [$\times 10^{-4}$]	16	17	22	22	1.0	10	9.3	13	12	0.5
Peak brightness [$\times 10^{33}$]*	0.29	0.14	0.051	0.016	12	1.5	1.1	0.37	0.11	630

* $\text{Ph}/(\text{s}\times\text{mm}^2\times\text{mrad}^2\times 0.1\% \text{BW})$. Peak brightness occurs at saturation in non-seeded mode.

[§] The SXRSS case uses four extra undulator segments that are in the baseline. The HXRSS case assumes 12 additional undulator segments.

[†] In non-seeded mode, smallest divergence occurs at saturation; post-saturation divergence has been measured up to two times larger.

The undulator sources were designed to produce spatially coherent plane-polarized X-rays by self-amplified spontaneous emission (SASE). They were designed to be compatible with future upgrades, to include full temporal coherence (*i.e.*, seeding) and polarization control. The

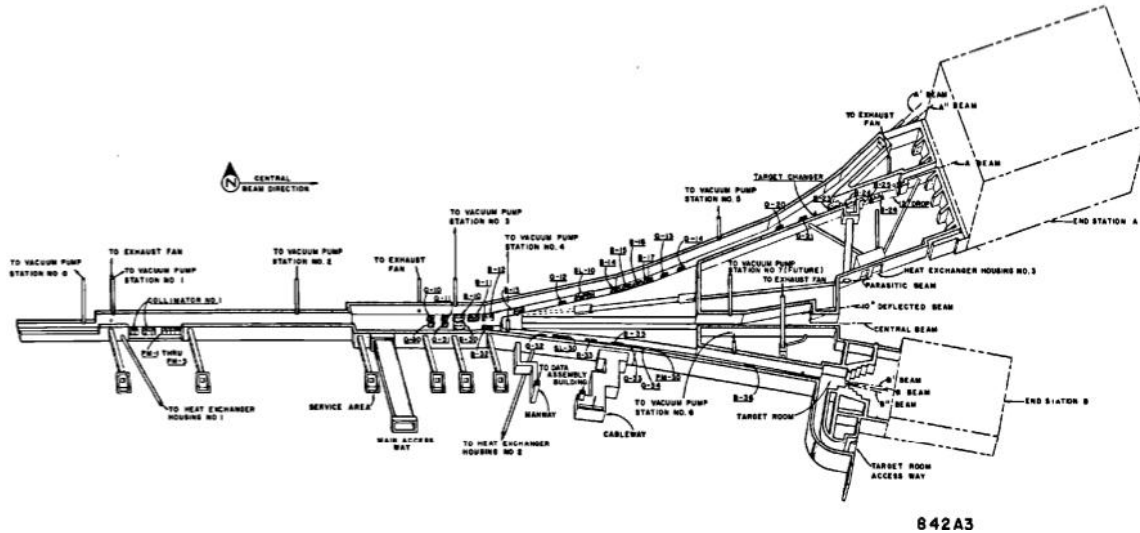


Figure 4. Cutaway view of the Beam Switchyard. ESA is at upper right and ESB at lower right.

18.4 Seeding and Other Techniques for Improving Coherence

18.4.1 Self-Seeding

The baseline LCLS-II design will implement self-seeding in the SXR and HXR for X-ray wavelengths between 0.2 and 1.3 keV and from 4 to about 12 keV, as described in Chapter 8. These self-seeding insertions will be similar to those that are being developed for the LCLS. An R&D program will develop self-seeding techniques for the intermediate range between 1.3 keV and 4 keV. Space is available in the SXR and HXR undulators to accommodate this planned upgrade, which was also described in Chapter 8.

18.4.2 External Seeding

External seeding, in principle, can offer many advantages over self-seeding, including better synchronization with an external laser signal for pump-probe experiments, detailed control of the temporal and spectral properties of the output pulses, and shorter total undulator lengths to reach the same saturated power levels. Over the past year, the seeded FERMI FEL at Trieste [5] has produced transversely- and longitudinally-coherent output pulses at the 10 microjoule energy level down to 5 nm wavelength, utilizing the fresh bunch technique in a two-stage, HGHG configuration (High-Gain Harmonic Generation). FERMI's near-term goal is to reach the carbon K-edge at 280 eV with its 1.5 GeV electron beam. Reaching even shorter output wavelengths (*e.g.*, 2 nm or shorter) with good longitudinal coherence is very challenging but may be feasible with the brighter and more energetic LCLS-II electron beams. The goal of this section is to show a preliminary design of a two-stage HGHG that satisfies the following criteria:

- Nearly transform-limited soft X-ray pulses over an initial range of 250 eV to 600 eV photon energy (5 nm to 2 nm radiation wavelength).

- Length of the entire FEL line of less than 80 m, allowing placement in the existing End-Station A (ESA) tunnel.
- Highly stable output pulse timing, spectral bandwidth, and central FEL wavelength.

Upgrade options would allow possible HHG seeding (High Harmonic Generation) or reconfiguration to an EEHG design (Echo-Enabled Harmonic Generation) in order to reach output photon energies of 1.2 keV or greater. An ongoing R&D program will make detailed studies of these different approaches to external seeding to understand the detailed implications.

18.4.3 Two-Stage HGHG

As with the standard LCLS-II design, the electron beam is produced by the high repetition rate, high-brightness, RF photocathode gun and accelerated by the superconducting CW linear accelerator. Relative to the SASE configuration, an HGHG FEL requires smaller energy spread; moreover, the fresh bunch technique needs a relatively long bunch, generally a factor of at least 2.5 greater than the seed laser pulse length. We therefore choose a lower peak current (500 A) than the baseline LCLS-II peak current (1 kA) and a smaller incoherent energy spread (250 keV versus 500 keV). For a 100 pC bunch charge, the usable portion of the bunch length is about 50 μm FWHM. Higher charge options (up to 300 pC) for higher peak current and/or longer bunch duration are possible but are not considered here. The electron beam parameters assumed for this HGHG study are summarized in Table 2.

Table 2. Final electron beam parameters for a possible HGHG FEL.

Parameter	Value	Unit
Final electron energy	4	GeV
Peak current	500	A
Slice energy spread (rms)	250	keV
Normalized emittance (x & y)	0.45	μm
Bunch length (FWHM)	50	μm
Bunch repetition rate	100	kHz

The two-stage, HGHG LCLS-II design (see Figure 5) is based on the FEL-2 configuration presently operating successfully at FERMI in Trieste [5]. Each stage includes a “modulator” undulator, a dispersive chicane, and a “radiator” undulator. Between the two stages is a delay chicane; for LCLS-II this would require an equivalent R_{56} of approximately 100 microns or less. Beginning with a 70 fs (FWHM), 300 MW peak power external laser pulse at 210 nm, the first stage is run at a harmonic upshift ratio of 15 to reach 14 nm output with a peak power of 700 MW. After passing through the delay section, second modulator, and dispersive section, the electrons enter a second radiator section consisting of eight LCLS-II baseline SXR undulator

segments that produce 2 GW of peak power at a final resonant wavelength of 2 nm (see Figure 6 and left plot of Figure 7). Details of the undulator parameters and required section lengths are given in Table 3. Our initial time-dependent simulations show that for an idealized electron beam (*e.g.*, temporally flat current and energy) and external laser (perfect Gaussian temporal profile with no phase noise), the spectral output is within a factor of two of the transform limit for a Gaussian pulse (see right plot of Figure 7). The undulator beamline, including chicanes and break sections, required to attain saturation of 2 nm output wavelength is about 60 m. Additional final radiator sections can be used to extract more FEL pulse energy or to accommodate seeded FEL operations at shorter wavelengths.

Table 3. Undulator parameters.

Parameter	Value	Unit
Mod1 polarization	linear	-
Mod1 period	15	cm
Mod1 K	< 20.6	-
Mod1 resonant wavelength	< 261	nm
Mod1 length	4.5	m
Rad1 and Mod2 polarization	circular/linear	-
Rad1 and Mod2 period	7.5	cm
Rad1 and Mod2 K (rms)	< 8	-
Rad1 and Mod2 resonant wavelength	< 40	nm
Rad1 and Mod2 segment length	3.4	m
Rad2 polarization	linear	-
Rad2 period	3.9	cm
Rad2 K	2.07-5.5	-
Rad2 resonant wavelength	1-5	nm
Rad2 segment length	3.4	m

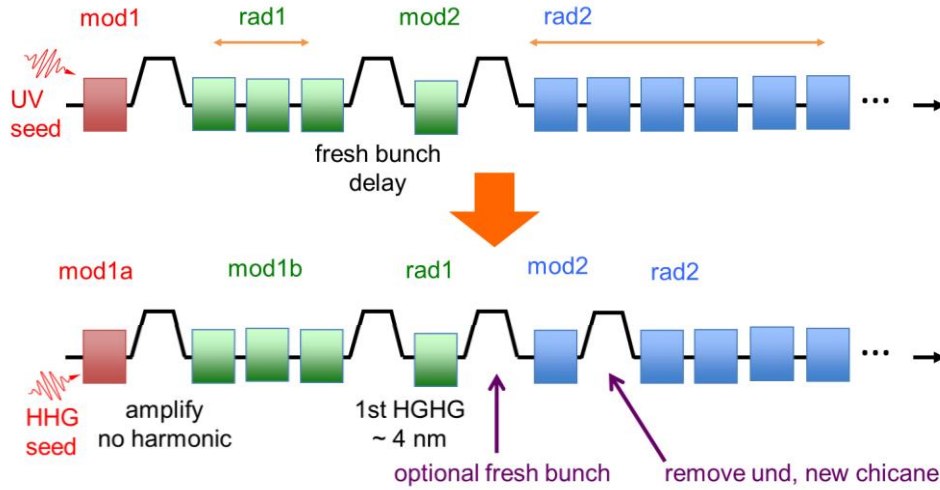


Figure 5. Schematic layout of a two-stage HGHG seeded by a UV laser at 210 nm (upper plot) and a second rebuild-option configured with an HHG laser at 30 nm (lower plot) where the HHG laser bunching is increased with the 1st chicane and then a 4th chicane is added by removing an undulator section.

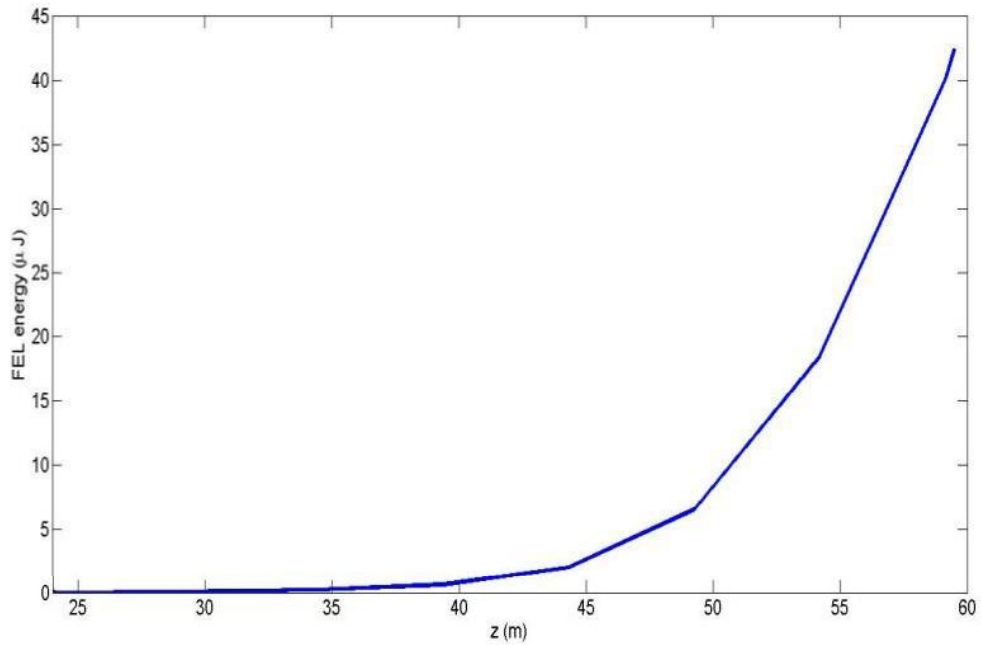


Figure 6. Seeded FEL pulse energy (up to 40 μJ) at 2 nm radiation wavelength along the final radiator (“rad2”). Here z=0 marks the beginning of the first stage’s modulator (“mod1”).

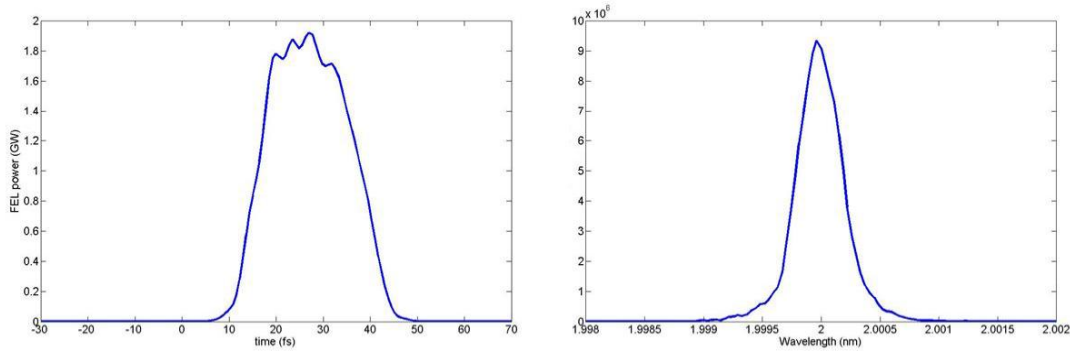


Figure 7. *Left:* Simulated 2 nm FEL power profile at $z=60$ m showing a 25 fs FWHM X-ray pulse duration. *Right:* Corresponding spectral content of the X-ray pulse shows 2×10^{-4} relative bandwidth (FWHM).

18.4.4 HHG Modification

It will be extremely challenging to reach 1 nm from the HGHG beamline because of the extreme large harmonic jump (>200) from a UV laser. On the other hand, HHG sources offer more modest harmonic jumps and the possibility of extending to shorter wavelengths. The HHG beamline can use almost the same configuration as the two-stage HGHG beamline described above (see Figure 5). One undulator section in the final radiator can be replaced by a chicane, or, alternatively, the beamline could already have an extra chicane in it. However, the various undulator sections and chicanes will be repurposed. While the beamline still uses two stages of HGHG with a fresh-bunch delay section in between, the harmonics targeted will be much more modest to reach 1 nm wavelength, which would be very challenging when starting with a UV laser as a seed. The HHG laser seeding will begin with a harmonic component of roughly 30 nm wavelength. A peak power of approximately 5 MW and a pulse duration of about 20 fs FWHM for the HHG seed are assumed.

The main difference between the HHG beamline and the UV-seeded HGHG configuration is that the 30 nm radiation is amplified using an optical klystron (OK) configuration instead of using a single undulator section for modulation. The first undulator section generates a weak modulation, which is then followed by the first chicane, which generates moderate bunching leading to significant radiation and modulation in the following three undulator sections. This OK configuration makes the HHG seeding less sensitive to initial power requirement. The first stage harmonic upshift is 8, and the second stage harmonic upshift is 4. At about 75 m of the beamline distance, the output pulse energy at 0.94 nm radiation wavelength is more than 20 μJ (see Figure 8). The output pulse at 0.94 nm has a duration of about 15 fs FWHM, with the relative bandwidth of about 3×10^{-4} , about three times the transform limit (see Figure 9).

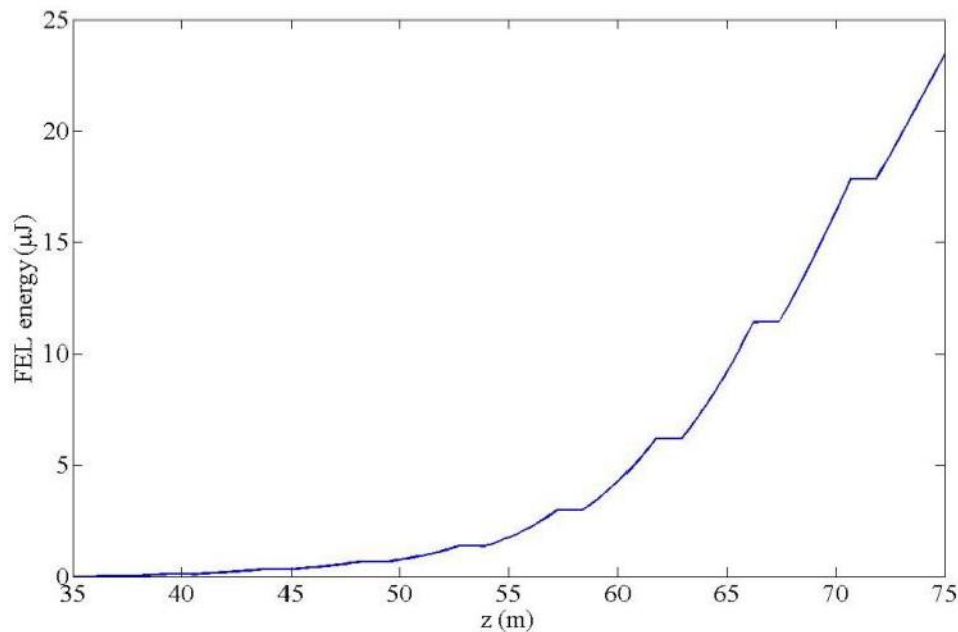


Figure 8. Seeded FEL pulse energy at 0.94 nm radiation wavelength along the final radiator ("rad2"). Here $z=0$ marks the beginning of the first modulator ("mod1").

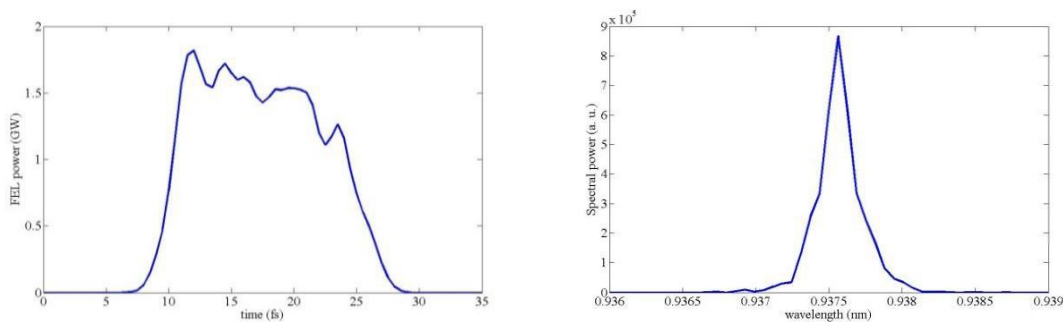


Figure 9. *Left.* Simulated 0.94 nm FEL power profile at $z=75$ m showing a 15 fs FWHM X-ray pulse duration. *Right.* Corresponding spectral content of the X-ray pulse shows 3×10^{-4} relative bandwidth (FWHM).

18.4.5 EEHG Modification

EEHG [6] is capable of generating significant power output at high harmonics of the seed laser with relatively small energy modulation of the beam in a single stage with two modulators and two chicanes. It is particularly suited for cases where the beam slice energy spread is relatively large, limiting the harmonic number achievable in other seeding schemes. To implement the EEHG scheme using the two-stage HGHG beamline discussed previously, the chicane and radiator in the first stage of HGHG should be replaced with a stronger chicane (a few mm R_{56}). The modulator in the second stage of HGHG may be used as the second modulator for EEHG, provided it uses a variable-gap undulator that allows the resonant wavelength to be changed from a few tens of nm to about 200 nm.

Compared to the HGHG and HHG schemes, the EEHG scheme could provide a smaller FEL bandwidth because it does not use the fresh bunch technique. As a result, a longer seed laser pulse can be used. Moreover, analysis shows that EEHG is less sensitive to beam imperfections, such as nonlinear energy chirp that may increase the FEL bandwidth for schemes such as HGHG. However, it should be pointed out that EEHG is still in the early experimental development stage. Experiments at SLAC and SINAP have demonstrated the concept and generated ~ 10 harmonics of a seed laser but at wavelengths of 100~200 nm. Much more experimental work is needed to demonstrate the capability EEHG in reaching nm output wavelengths.

18.4.6 Two-Bunch Seeding Option

As another alternative to the fresh-bunch seeding technique described above, the LCLS-II might also be able to support two-bunch seeding [7] where the seed is generated by one bunch and the seeded radiation is generated by an unperturbed second bunch that closely follows the first. This approach has some benefits over the fresh-bunch technique in that it can operate with shorter, higher-current bunches and has the potential to generate narrower bandwidth radiation with higher-peak-power and higher-pulse energy. However, to be effective, the two bunches must be closely spaced. Although the baseline LCLS-II design does not support bunches with ns-level spacing (the closest spacing of about 27 ns is dictated by the injector and RF spreader), a modest upgrade of the injector and spreader, such as a DC gun and magnetic kicker, would allow 0.7 ns spacing in the future.

18.4.7 Improvement of Temporal Coherence by *iSASE*

It is also feasible to control the spectral properties of a SASE FEL by various techniques using the undulator system itself. For example, the reduction of the SASE bandwidth using the “improved SASE”, or *iSASE*, scheme has been studied both theoretically and experimentally. A proof-of-principle experiment has been performed recently at LCLS [8,9]. The *iSASE* techniques should be readily applicable to the superconducting LINAC based LCLS-II.

The *iSASE* technique employs a scheme to effectively increase the cooperation length. The concept is to introduce, in the FEL undulator divided in modules separated by a break, additional slippage (*i.e.*, localized shifts of the electron bunch) by repeated delays of the electron beam with respect to the radiation field. The shifts are introduced with small magnetic chicanes at the end of each module. A delay of the order of the cooperation length introduces a correlation between the electromagnetic field phases and amplitudes of the spikes, in effect increasing the slippage length and the longitudinal coherence. The most important parameters in the mixing process are the electron delay, δ , the cooperation length L_c , the number of delays introduced, and the gain in each module.

With a geometrically increasing series of 5 or 6 delays, the bandwidth reduction is about a factor of ten and for some X-ray wavelengths the resulting pulse is nearly transform limited. Combining *iSASE* with a tapered undulator, the X-ray peak power and brightness can be significantly increased by one or two order of magnitudes.

The main advantages of *iSASE* are as follows:

1. It can operate at any repetition rate, since it does not require external lasers or monochromators which are subject to thermal effects at high repetition rate;
2. It is completely tunable over the entire LCLS-II energy range, even in the 1 to 5 keV range where the efficiency of self-seeding monochromators is not optimal;

However, to implement in the LCLS-II, it requires 5 or 6 small chicanes, with a maximum length of about 60 cm. These might be inserted in the LCLS-II undulator breaks but a careful assessment is needed to determine whether the break lengths allow this addition.

18.4.8 Improvement of Temporal Coherence by *pSASE*

Another scheme called *pSASE* (purified SASE) has also been proposed to potentially improve the temporal coherence of a standard SASE FEL [10]. The *pSASE* configuration consists of 3 undulator sections (U1, U2 and U3), with U1 and U3 being resonant at the target FEL wavelength, λ_0 , and U2 resonant at a sub-harmonic wavelength, $n\lambda_0$. In U2 the average longitudinal velocity of the electrons is reduced, which effectively increases the FEL slippage length that allows the radiation fields to communicate phase information over larger portions of the electron beam to improve the FEL temporal coherence. Simulation using realistic beam and undulator parameters shows that this method can be readily used to enhance the temporal coherence and spectral brightness of a SASE FEL by a factor of 5 with U2 tuned at $7\lambda_0$. When combined with tapering, *pSASE* may enhance the spectral brightness by two orders of magnitude compared with standard SASE, as reported in a recent study from the European XFEL [11].

It is worth pointing out that the implementation of *pSASE* at the LCLS-II over a large wavelength range is straightforward and no additional hardware changes are needed. Only the gap of a few (2 to 3) undulator sections where FEL is in the middle of the exponential growth regime needs to be reduced to increase the resonant wavelength to $n\lambda_0$. This system will be straightforward to apply on the SXR for photon energies between 0.75 and 1.25 keV where the variable gap undulators have a large tuning range. It may also be useful for producing narrow-bandwidth radiation at 3 to 5 keV where the monochromators required in the self-seeding schemes have limited efficiency. However, the bandwidth narrowing may be limited to a factor of 3-4 since the tuning range for the HXR undulator is only a factor of 5. The full range of applicability for this option is being studied.

18.5 Upgrade to Self-Seeding Schemes

Both soft and hard X-ray schemes require upgrades for achieving better performances in terms of handling higher repetition rate, operating in a wider energy range and producing seeds with narrower bandwidths for potentially increasing spectral brightness.

18.5.1 Self-seeding for the Soft X-ray Undulator

The baseline design based on the LCLS-I SXRSS system shown in Chapter 8 is limited to a resolving power of 5,000, and is not optimized in the overall system throughput due to the mode of operation not being “fixed-focus” when tuning the X-ray energy, thus producing an enlarged image of the source at the interaction point and reducing the overlap with the electron beam. These characteristics were results of compromises made to minimize design complexities and meet other non-technical requirements. The LCLS-I SXRSS system has been installed and will be commissioned in late 2013. Potential upgrades to the system include higher resolving power in the range of 10,000 to 20,000, and “fixed-focus” mode of operation to maximize X-ray-electron overlap. For higher resolving power, a higher line density for the VLS grating will be needed, and a longer distance to the exit slit. To operate in the “fixed-focus” mode, rotation is required for the grating in addition to the M1 mirror. As such, the sagittal focusing function of the grating must be taken up by either the M2 or the M3 mirror. The more efficient overlap between the X-rays and electrons is especially important for the high repetition rate operation because of increased concern over the thermal loading on the optics.

18.5.2 Self-seeding for the Hard X-ray Undulator

For the hard X-ray undulator, the baseline seeding scheme only covers the energy range of 4 to 12 keV using the diamond wake-field monochromator shown in chapter 8. To extend beyond 12 keV, Si in either (333) or (440) reflection should be considered. These two reflections have a Darwin width comparable to that of diamond (400) at 8 keV, and the lateral shift of the forward Bragg diffracted beam is comparable to that of diamond (400) at 8 keV.

For seeding below 4 keV, the diamond (400) crystal should be replaced by a diamond (111) crystal in the symmetric Bragg geometry to minimize absorption. This would extend the X-ray energy down to slightly above 3 keV. To mitigate the concern in sample damage due to the peak power or the average thermal loading on the small seeding crystal, a two-stage diamond wake-field approach [12] will be used. In such a scheme, the first stage is designed to take less incident power and will pre-seed the beam before the quasi-seeded beam proceeds to the second stage for enhanced seeding performance.

Between 1 and 3 keV, a grating-base system would be more feasible due to the increasing absorption by either diamond or silicon crystals, although the efficiency of the grating tends to drop off dramatically towards higher X-ray energies, especially when higher resolving power is required to produce transform-limited pulses of equal duration at lower energies. The complete system for the hard X-ray undulator from 1 to 20 keV is shown in Figure 10.

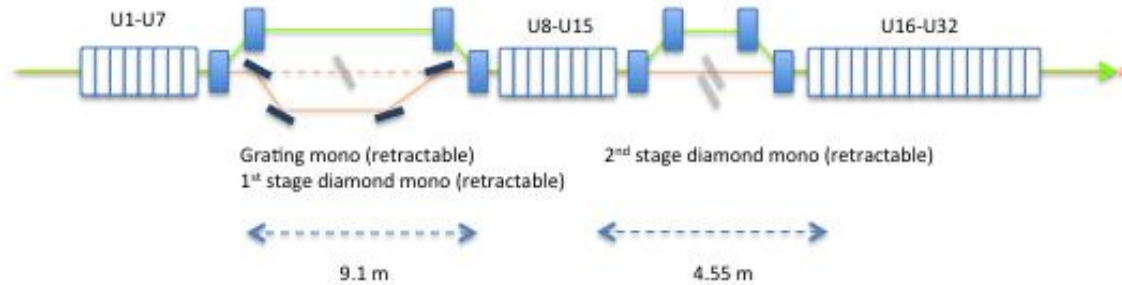


Figure 10: Schematics of the complete self-seeding system for the hard X-ray undulator, consisting of a two-stage diamond wake-field monochromator seeding sections, and a grating monochromator seeding section. For seeding above 3 keV, the grating system is retracted while both the 1st and 2nd diamond systems are retracted for below 3 keV. Between 3 and 5 keV, both the 1st and 2nd diamond monochromators are in and use (111) crystals, and above 5 keV, only the 2nd diamond monochromator using a (400) crystal is inserted and everything else retracted.

18.6 Polarization Control for the SXR FEL

The LCLS-II is designed to generate linearly polarized, intense, high-brightness X-ray pulses from planar variable-gap undulators. While the planar undulator design is well understood and expected to be tunable within tight FEL tolerances, it lacks polarization control, which is of great importance for soft X-ray experiments. The design provides space to add polarization control — APPLE or DELTA type polarizing undulator segments. The polarization control undulator segments will work as so-called “afterburners,” producing right or left circular, elliptically polarized FEL radiation from the micro-bunched electron beam generated by a few of the regular LCLS-II SXU undulator segments. Switching between right and left polarized radiation will be achieved via row position adjustment in the added polarizing undulator segments. The linearly polarized radiation produced by the regular SXU undulator segments during the micro-bunching process will be a small background component, keeping the total degree of polarization slightly below 100 percent. With 12 m of polarizing undulators for the 39 mm SXU period, polarization degrees above 90 percent are expected at millijoule-pulse-energy levels for the 250–1250 eV photon energy range. The pulse-to-pulse fluctuations of the polarization degree should be below the 1 percent level. Increasing the number of polarizing undulator segments can be used to further enhance both the intensity and the degree of the polarized radiation.

18.7 Beyond 1 MHz

The maximum beam rate in the linac is limited by the average beam power on the electron dump. A working limit of 120 kW has been set on each electron dump at the end of each FEL. For example, 300 pC of charge per bunch, 4 GeV, and a 100 kHz bunch rate per FEL results in an average beam power of 120 kW per dump. We can also imagine, for example, a reduced bunch charge at 30 pC, allowing a 1 MHz bunch rate in each FEL simultaneously. This might be carried to an extreme with 10 pC per bunch and a 3 MHz rate per FEL, or possibly even lower charge levels, but the 10-pC bunch charge has been selected as the present lower limit for operations.

However, a bunch rate up to 10 MHz, or perhaps higher, is not excluded as long as the beam power is within practical limits (less than 120 kW). The diagnostic kickers have a fast enough rise and fall (less than 100 ns), and the machine protection system (MPS) response time is fast enough to shut down the beam before damaging components. Note also that for a constant peak current over the electron bunch, the bunch length will need to be reduced linearly with a lower charge. The much shorter bunch may not be well matched to a two-stage HGHG scheme, for example, where a fresh-bunch manipulation may not function well.

18.8 References

- [1] G. Geloni, V. Kocharyan and E. Saldin, "Scheme for generation of fully coherent, TW power level hard x-ray pulses from baseline undulators at the European XFEL", DESY 10-108 (2010).
- [2] R. B. Neal, ed., *The Stanford Two-Mile Accelerator*, (1968) W. A. Benjamin Inc.; Library of Congress Catalog Card Number 68-24364; also available online at the SLAC website.
- [3] H. Geng, Y. Ding, P. Emma, Z. Huang, Y. Nosochkov and M. Woodley, "Optics Design for a Soft X-Ray FEL at the SLAC A-Line," Proceedings of PAC09, Vancouver, BC, Canada, WE5RFP043, available at <http://www.JACOW.org>.
- [4] H. Geng, Y. Ding, P. Emma, J. Galayda, Z. Huang, and Y. Nosochkov, "Design of a Soft X-ray FEL in the SLAC A-Line," Proceedings of FEL2009, Liverpool, UK, WSEPC63, available at <http://www.JACOW.org>.
- [5] Allaria, E. et al., "Highly coherent and stable pulses from the FERMI seeded free-electron laser in the extreme ultraviolet," *Nature Photon.* 7, 913 (2013).
- [6] Xiang, D., Stupakov, G., "Echo-enabled harmonic generation free electron laser," *Phys. Rev. ST Accel. Beams* 12, 030702 (2009) (2009).
- [7] Y. Ding, Z. Huang, and R. D. Ruth, "Two-bunch self-seeding for narrow-bandwidth hard x-ray free-electron lasers," *Phys. Rev. ST Accel. Beams* 13, 060703 (2010).
- [8] J. Wu, A. Marinelli, C. Pellegrini, "Generation of longitudinally coherent ultra-high power X-ray FEL pulses by phase and amplitude mixing," *Proc. of FEL2012*, Nara, Japan, TUPD07 (2012).
- [9] J. Wu, et al, "X-ray spectra and peak power control with iSASE," *Proc. of IPAC2013*, Shanghai, China, WEODB101 (2013).
- [10] D. Xiang, Y. Ding, Z. Huang and H. Deng, "Purified self-amplified spontaneous emission free-electron lasers with slippage-boosted filtering," *Phys. Rev. ST Accel. Beams* 16, 010703 (2013).
- [11] S. Serkez, V. Kocharyan, E. Saldin, I. Zagorodnov and G. Geloni, "Purified SASE undulator configuration to enhance the performance of the soft x-ray beamline at the European XFEL," DESY 13-135; see also arXiv:1308.0172.
- [12] G. Geloni, V. Kocharyan, and E. Saldin, "A Cascade self-seeding scheme with wake monochromator for narrow-bandwidth X-ray FELs", DESY 10-080 (2010), <http://arxiv.org/abs/1006.2045>.

A

LCLS-II ACRONYMS

Acronym	Meaning
1D	one Dimensional
2D	two Dimensional
3D	three Dimensional
6D	six Dimensional
AC	Alternating Current
ACC39	3.9-GHz ACCelerating cryomodule
ACH	Air Exchanges per Hour
ACS	Accelerator Cooling System
ADC	Analog to Digital Converter
AFE	Analog Front End electronics.
AHU	Air Handling Unit
ALARA	As Low As Reasonably Achievable
ALICE	Accelerators and Lasers In Combined Experiments
ALS	Advanced Light Source (at LBNL)
AMO	Atomic, Molecular & Optical science instrument at LCLS
AMS	Air Monitoring Systems
ANL	Argonne National Laboratory
ANSI	American National Standards Institute
AOM	Acousto-Optic Modulator
APEX	Advanced Photoinjector Experiment
APS	Advanced Photon Source (at ANL)
ARPES	Angle Resolved Photoemission Spectroscopy
ASCE	American Society of Civil Engineers
ASME	American Society of Mechanical Engineers

ASTA	Advanced Superconducting Test Accelerator
ASTRA	A Space charge TRacking Algorithm code
BACnet	Building Automation and Control Network
BBA	Beam Based Alignment
BC1	Bunch Compressor #1
BC2	Bunch Compressor #2
BC3	Bunch Compressor #3
BCP	Buffered Chemical Polish
BCS	Beam Containment System
BCS	Bardeen Cooper Schrieffer (theory of superconductivity)
BDF	Building distribution frame in telecommunications
BESAC	Basic Energy Sciences Advisory Committee
BFW	Beam Finder Wire
BLD	Beam Line Data
BLM	Bunch Length Monitor (unfortunately this acronym is overloaded)
BLM	Beam Loss Monitor. (unfortunately this acronym is overloaded)
BOA	Born Oppenheimer Approximation
BPM	Beam Position Monitor
BPV	Boiler and Pressure Vessel
BSOIC	Beam Shut-off Ion Chamber
BSY	Beam Switch Yard
BTH	Beam Transport Hall, section of the existing facility
BTHW	Beam Transport Hall West
BTM	Burn-Through Monitor
BW	Band Width
C100	cryomodule for the 12 GeV upgrade of the CEBAF facility
CA	Channel Access
CAD	Computer Aided Design
C-band	Radio frequency equipment operating at roughly 6 GHz.
CBC	California Building Code
CCD	Charged Coupled Device
CCM	Channel Cut Monochromator

CD-0	Critical Decision 0: approval of mission need
CD-1	Critical Decision 1: Approval of alternative selection and cost range
CD-2	Critical Decision 2: approval of performance baseline
CD-3	Critical Decision 3: approval of start of construction
CD-3a	Critical Decision 3a for long-lead procurements
CD-4	Critical Decision 4: approval of project completion
CDR	Conceptual Design Report
CEBAF	Continuous Electron Beam Accelerator Facility
CEP	Carrier Envelop Phase-locked laser.
cERL	compact Energy Recovery Linac
CERN	European Organization for Nuclear Research
CFM	Cubic Feet per Minute
CFR	Code of Federal Regulations
CGA	Compressed Gas Association
CHL	Central Helium Liquifier (<i>e.g.</i> , at TJNAF)
CHW	Chilled Water
CID	Collider Injector Development (location of electron source in area of accelerator)
CM	Cryo Module
CMC	California Mechanical Code
CMM	Coordinate Measurement Machine
CMn	Cryo Module number n , where $n = 01, 02, 03, \dots, 35$
CMOS	Complementary Metal Oxide Semiconductor
CODR	Coherent Diffraction Radiation
COHE	Control of Hazardous Energy
COTR	Coherent Optical Transition Radiation
CPA	Chirped Pulse Amplification
CPI	Communications & Power Industries
CPU	Central Processing Unit
CRL	Compound Refractive Lens
CSR	Coherent Synchrotron Radiation (beam dynamics issue in bunch compressors)
CTW	Cooling Tower Water
CUP	Central Utility Plant

CVD	Chemical Vapor Deposition
CW	Continuous-Wave
CXI	Coherent X-ray Imaging; or, the Coherent X-ray Imaging instrument at LCLS
DAC	Digital to Analog Converter
DAQ	Data Acquisition system
DC	Direct Current (also refers to a system with constant output wrt time)
DCCT	Similar to toroid but measures continuous beams.
DCS	Distributed Control System
DDC	Direct Digital Controller
DESY	Deutsches Elektronen-Synchrotron (SLAC's sister lab in Hamburg, Germany)
DI	De-Ionized
DL	Dog-Leg (jogging bend system for electron transport)
DMZ	De-Militarized Zone (Intermediate Network)
DOE	United States Department of Energy
DYN	Dynamic
EBD	Electron Beam Dump section of the UXT
EIA/TIA	Electronic Industries Alliance/Telecommunications Industry Association
EISA	Energy Independence and Security Act
EJMA	Expansion Joint Manufacturers Association
ELBE	Electron Linear accelerator with high Brilliance and Low Emittance
EM	Electro-Magnetic
EMS	Energy Management System
EO	Electro-Optical device (measures bunch length).
EOM	Electro-Optic Modulator
EP	Electro-Polish
EPA	Environmental Protection Agency
EPICS	Experimental Physics and Industrial Control System
EPSC	Ethernet Power Supply Controller
ERL	Energy Recovery Linac
ERLP	Energy Recovery Linac Prototype
ES&H	Environment, Safety, and Health
ESA	End Station A

ESD	Engineering Specifications Document (for LCLS & LCLS-II projects)
EtherNet/IP	Ethernet/Internet Protocol (industrial protocol)
eV	Electron Volt
EVG	Event Generator
EVR	Event Receiver
FACET	Facility for Advanced Accelerator Experimental Tests
FB	Feed-Back
FCM	Field Construction Manager
FDR	Final Design Report
FEA	Finite Element Analysis
FEE	Front End Enclosure section of the UXT
FEH	Far Experimental Hall
FEL	Free-Electron Laser
FF	Feed-Forward
FIR	finite impulse response
FLASH	Free-electron -LASer in Hamburg (at DESY)
FNAL	Fermi National Accelerator Laboratory, or Fermilab
FODO	Focusing-drift-Defocusing-drift (electron optics lattice focusing type)
FOV	Field-Of-View
FPGA	Field-Programmable Gate Array
FRIB	Facility for Rare Isotope Beams
FRP3	High performance Flame Retardant Plastic from Laminations Inc.
fs	Femtoseconds
FT2	Square feet
FWHM	Full Width at Half Maximum
FY	Fiscal Year
GB	Giga Byte
GeV	Giga-electron Volts
GMD	Gas Monitor Detector
GPCR	G Protein-Coupler Receptor
GPM	Gallons Per Minute
GPS	Global Positioning System (navigation)

H-ARPES	High Energy Angle Resolved Photoemission Spectroscopy
HEPA	High Efficiency Particle Absorption
HER	PEP-II High Energy Ring
HFP	High Field Physics
HH	Head House
HL	Harmonic Linearizer (3.9 GHz RF section)
HoBiCaT	Horizontal Bi-Cavity Test-facility (at HZB)
HOM	Higher Order Mode (RF field modes)
HOMS	Hard X-Ray Offset Mirror System
HP	Horse Power
HPR	High-Pressure Rinse
HPS	Hutch Protection System
HPSB	High Performance and Sustainable Buildings
HV	High Voltage
HVAC	Heating, Ventilation, Air Conditioning
HW	Hot Water
HXR	Hard X-Ray
HXRSS	Hard X-Ray Self-Seeding
HXU	Hard X-ray Undulator
HZB	Helmholtz-Zentrum Berlin
I&C	Instrumentation and Control
I/O	Input/Output
IBS	Intra Beam Scattering
ICT	Integrating Current Transformer
ID	Inside Diameter
IDF	Intermediate distribution frame in telecommunications
IES	Illuminating Engineering Society
IF	Intermediate Frequency
ILC	International Linear Collider (e^+e^- collider facility proposal)
INFN	Istituto Nazionale di Fisica Nucleare
IOC	Input Output Controller (EPICS computer)
IOT	Inductive Output Tube

IQ	In-Phase, Quadrature
IR	Infra-Red
ISEMS	Worker Safety and Health Plan
ISM	Integrated Safety Management
ISR	Incoherent Synchrotron Radiation
IXS	Inelastic X-ray Scattering
JLAB	Jefferson Laboratory (same as TJNAF)
kA	Kilo-Ampere
K-B	Kirkpatrick-Baez optics
KCS	Klystron Cooling System
KEK	Kō Enerugī Kasokuki Kenkyū Kikō, Japan High-Engy Acc. Resrch Org.
keV	Kilo-electron Volts
KPP	Key performance parameters
KV	Kilo Volts
KVA	Kilo Volt-Amperes
kW	Kilowatt
L0	Injector linac section in LCLS-II layout (1 cryo module)
L1	First multi-cryo module linac section in LCLS-II layout – before BC1
L2	Second multi-cryo module linac section in LCLS-II layout – before BC2
L3	Third multi-cryo module linac section in LCLS-II layout – after BC2
LAMP	Soft X-ray Scattering Experimental End Station
LASA	Laboratorio Acceleratori e Superconduttività Applicata
L-band	Radio frequency equipment operating at roughly 1.5GHz.
LBNL	Lawrence Berkeley National Laboratory
LCLS	The Linac Coherent Light Source Facility
LCLS-I	LINAC Coherent Light Source (uses SLAC linac)
LCLS-II	Linac Coherent Light Source II Project
LCW	Low Conductivity Water
LED	Light Emitting Diode
LEED	Leadership in Energy and Environmental Design
LFD	Lorentz Force Detuning
LH	Laser Heater

LHC	Large Hadron Collider
LHe	Liquid Helium
LINAC	LINEar ACcelerator
LION	Long Ionization Chambers
LLRF	low-level Radio Frequency
LN	Liquid Nitrogen
LN2	Liquid Nitrogen
LOA	Laboratoire d'Optique Appliquée
LOTO	Lock Out Tag Out
LRDP	Long Range Development Plan
LSIG	Type of circuit breaker (long-time+short-time+instantaneous+ground fault)
LTU	Linac-To-Undulator (electron transport line)
LTUH	Linac-To-Undulator: for Hard x-ray side (electron transport line)
LTUS	Linac-To-Undulator: for Soft x-ray side (electron transport line)
LURE	Laboratoire pour l'utilisation du rayonnement électromagnétique.
LUSI	LCLS Ultrafast Science Instrumentation
M&O	Managing and Operating
MAD	Methodical Accelerator Design (charged particle optics software)
MAD	Multi-wavelength Anomalous Dispersion
MCB	Main Circuit Breaker
MCC	Motor Control Center
MCI	Maximum Credible Incident
MCOR	Magnet Controller
MCP	Multi-Channel Plate
MCT	Mercury Cadmium Telluride detectors for mid-infrared light.
MEC	Matter in Extreme Conditions; or the "MEC" instrument at LCLS
MEI	Maximum Exposed Individual
MEP	Mechanical Electrical Plumbing
MeV	Million electron Volts
MHz	Megahertz
MMF	Magnet Measurement Facility
MNS	Mission Need Statement

ModBus	Modicon Communications Protocol
MPC	Multi-Particle Coincidence
MPH	Miles Per Hour
MPS	Machine Protection System
MTCA	Micro Telecommunication Control Architecture
MVA	Mega-Volt-Ampere
MW	Megawatt
NCRF	Normal Conducting Radio-Frequency
NEC	National Electric Code
NEG	Non-Evaporative Getter
NEH	Near Experimental Hall (at LCLS)
NEMA	National Electrical Manufacturers Association
NEPA	National Environmental Protection Act
NFPA	National Fire Protection Association
NGLS	Next Generation Light Source (FEL proposal at LBNL)
NHPA	National Historic Preservation Act
NML	New Muon Laboratory
NMR	Nuclear Magnetic Resonance
NPH	Natural Phenomena Hazards
NSF	National Science Foundation
NSLS-II	National Synchrotron Light Source–II project
ODH	oxygen deficiency hazard
ODM	Oxygen Deficiency Monitor
OPC	Other Project Costs
OSHA	Occupational Safety and Health Administration
P3	Physics of Photocathodes for Photoinjectors
PCDS	Photon Control and Data Systems
PCW	Process Cooling Water
PCWR	Process Cooling Water Return
PCWS	Process Cooling Water Supply
PDR	Preliminary Design Report
PEP-II	Positron-Electron collider, Asymmetric B-Factory facility at SLAC

PES	Potential Energy Surface
PHA	Preliminary Hazards Analysis
PIC	Protection Ionization Chambers
PID	Proportional, Integral, and Differential (feedback loop components)
PITZ	Photo Injector Test Center at DESY-Zeuthen
PLC	Programmable Logic Controller
PM	Permanent Magnet (usually referring to undulator magnets)
PMS	Perimeter Monitoring Stations
PMT	Photo Multiplier Tube
PMU	Permanent Magnet Undulator
pnCCD	Soft X-ray Area Detector (Charged Coupled Device)
PPB	Parts Per Billion
PPE	Personal Protective Equipment
PPS	Personnel Protection System
PRD	Physics Requirement Document (for LCLS & LCLS-II projects)
PSI	Pounds per Square Inch
PSIG	Pounds per Square Inch, Gauge
PTB	Physikalisch-Technische Bundesanstalt
PZT	Piezo Tuner
Q	Quality factor
QA	Quality Assurance
QAP	Quality Assurance Plan
QE	Quantum Efficiency
Q_{ext}	External quality factor
Q_L	Loaded quality factor
Q_o	Unloaded quality factor
R&D	Research and Development
RADFET	RADFET: Radiation Detector FET.
Rb	Rubidium stabilized frequency source, typically stable to < 1e-9.
RCM	Radiological Control Manual
RCS	Radiation Control System
RDR	Reference Design Report (of the ILC)

RF	Radio Frequency
RF-BPM	Radio-Frequency Beam Position Monitor(s)
RIXS	Resonant Inelastic X-ray Scattering
RMS	Root Mean Square
ROI	Region Of Interest
RRR	Residual Resistance Ratio
RSS	SLAC Radiation Safety System
RSXS	Resonant Soft X-ray Scattering End Station
RSY	Research Yard area of SLAC
RTD	Resistance Temperature Detector
RTEMS	Real-Time Executive for Multiprocessor Systems
RWM	Radioactive Waste Manual
RY	Research Yard
S2E	Start-to-End simulation
SAD	LCLS-II Safety Assessment Document
SAD	Single-wavelength Anomalous Dispersion
S-ARPES	Spin resolved Angle Resolved Photoemission Spectroscopy
SASE	Self-Amplified Spontaneous Emission (an FEL lasing process)
SAXS	Small Angle X-ray Scattering
S-band	Microwave band of EM spectrum; usually 2.856 GHz as the SLAC RF frequency
SC	SuperConducting
SCF	Standard Cubic Feet
SCFM	Standard Cubic Foot per Minute
SCL	Super Conducting Linac
SCRf	SuperConducting Radio Frequency (RF accelerating systems)
SESAM	SEmiconductor Saturable Absorber Mirror
SLAC	SLAC National Accelerator Laboratory
SNS	Spallation Neutron Source
SOLEIL	Source Optimisée de Lumière d'Énergie Intermédiaire du LURE
SR	Strehl Ratio
SRF	Superconducting Radio Frequency (RF accelerating systems)
SS	Self-Seeding (an FEL seeding method)

SSA	Solid-State Amplifier
SSMC	Single Source Multiple Cavities
SSR1	Single-Spoke Resonator 1
SSSC	Single-Source, Single Cavity
SuperLANS	Software for Evaluation of Electromagnetic Fields and Resonances
SXR	Soft X-Ray
SXRSS	Soft X-Ray Self-Seeding
SXU	Soft X-ray Undulator
TCAV	Transverse deflecting RF CAVity
TCP/IP	Transmission Controls Protocol/Internet Protocol
TDR	Technical Design Report
TDS	Transverse Deflecting Structure (same as TCAV).
TEC	Total Estimated Cost
TED	Total Effective Dose
TESLA	TeV Energy Superconducting Linear Accelerator
THD	Total Harmonic Distortion
THz	Terahertz radiation – frequencies above a few hundred GHz, but below optical.
TIG	Tungsten Inert Gas
TJNAF	Thomas Jefferson National Accelerator Facility
TJNAF	Thomas Jefferson National Accelerator Facility
TLD	Thermo Luminescent Dosimeter(s)
TOF	Time Of Flight
TPC	Total Project Cost
Tr-ARPES	Time Domain Angle Resolved Photoemission Spectroscopy
TTF	Tesla Test Facility
UDP	User Datagram Protocol
UH	Undulator Hall section of the UXT
UHF	Ultra-High Frequency
UHV	Ultra-High Vacuum
UV	Ultra Violet
UXT	Undulator X-ray Tunnel (includes undulator hall, e^- dump, & front end enclosure)
VESDA	Very Early Smoke Detection Apparatus

VFD	Variable Frequency Drive
VHF	Very High Frequency
VLAN	Virtual Local Area Network
VLS	Variable-Line-Spacing
VME	Versa Module Europa (data bus)
VMTG	VME Master Trigger Generator
VSWR	Voltage Standing Wave Ratio
WAXS	Wide Angle X-ray Scattering
WCS	Waveguide Cooling System
WebCTRL	Building automation software system from Automated Logic Corporation
WF	Wave Front
WL	Warm Linac – existing SLAC copper linac
WPM	Wire Position Monitor
WR284	Waveguide, Rectangular, 2.84-inches inside dimension
WR650	Waveguide, Rectangular, 6.5-inches inside dimension
WSHP	Worker Safety and Health Plan
XAS	X-ray Absorption Spectroscopy
X-band	Microwave band of EM spectrum; usually 11.424 GHz as 4th harmonic frequency
XCS	X-ray Correlation Spectroscopy; or the XCS instrument at LCLS
XDC	X-ray Diagnostic Chamber
XES	X-ray Emission Spectroscopy
X-EUV	E-ray-Extreme Ultra-Violet
XFEL	X-Ray Free-Electron Laser (typically the Euro. XFEL in Hamburg, Germany)
X-FEL	X-ray Free Electron Laser
XPP	X-ray Pump/Probe; or the XPP instrument at LCLS
XPS	X-ray Photoelectron Spectroscopy
XTCAV	X-Band Transverse Deflecting Cavity
XTES	X-ray Transport and Experimental Station
YAG	Yttrium Aluminum Garnet
YAG:Ce	Cerium-doped Yttrium Aluminum Garnet